Alma Mater Studiorum – Università di Bologna

DOTTORATO DI RICERCA IN
Scienze della Terra, della Vita e dell'Ambiente

Ciclo XXXIV
Settore Concorsuale: 04/A2 - GEOLOGIA STRUTTURALE, GEOLOGIA STRATIGRAFICA, SEDIMENTOLOGIA E PALEONTOLOGIA
Settore Scientifico Disciplinare: GEO/02 - GEOLOGIA STRATIGRAFICA E SEDIMENTOLOGICA

Subsidence history, thermal maturity, and structural inversion of the Greater Caucasus-Kura-Adjara-Trialeti basin system of central-eastern Georgia

Presentata da: Dott. Thomas Gusmeo

Coordinatore Dottorato:
Prof.ssa Maria Giovanna Belcastro

Supervisore:
Prof. William Cavazza

Co-supervisori:
Prof. Massimiliano Zattin
(Università di Padova)
Prof.ssa Sveva Corrado
(Università di Roma Tre)
Dott. Andrea Schito
(University of Aberdeen)

Esame finale anno 2022

LIST OF CONTENTS

ACKNOWLEDGMENTS

This work would not have been possible without the help and support of many people. First of all, a huge thank you must be said to my advisor Prof. William Cavazza for his guidance and support during the course of my Ph.D. journey, for the patience and the fundamental insights during research, data interpretation, scientific discussions, manuscripts design, and writing of this dissertation. I am deeply grateful to Prof. Massimiliano Zattin and Dr. Andrea Schito for the help in data acquisition and interpretation, for the precious insights and the guidance during manuscripts design and writing. Much gratitude is owed to Prof. Sveva Corrado for guidance during fieldwork and samples collection, data acquisition and interpretation, precious insights and help in manuscripts design and writing. I thank Prof. Victor Alania, Dr. Onise Enukidze and Tamar Beridze for their guidance during fieldwork and samples collection in Georgia. The Georgian Oil and Gas Company is warmly thanked for kindly granting me access to industrial seismic, borehole and thermal maturity data. I am very grateful to Dr. Silvia Cattò (Padua University) for all the time spent on my training in the lab and support during data acquisition and interpretation. Dr. Irene Albino is acknowledged for the help during samples processing and lab work. Funding from MUR (Italian Ministry of Research; PRIN 2017-2021) and the University of Bologna is gratefully acknowledged. Prof. Paolo Ballato and Prof. Marco G. Malusà are warmly thanked for their constructive reviews and comments on an earlier version of this thesis. I would like to express my gratitude to my colleagues Alberto, Barbara, Bruno, Francesco, Giulia, Lisa, Sharon, and particularly to my roommate Costantino, for the fruitful discussions and the support during the hard periods. My family deserves a special thank for their everlasting and unconditional support. Last but not least, a special mention goes to Chiara for her love, support and trust.

ABSTRACT

This study aims at a better definition of the tectonic evolution of a portion of the Caucasian region which experienced a complex pattern of deformation events throughout Mesozoic and Cenozoic times. Particularly, this dissertation focuses on the Adjara-Trialeti fold-and-thrust belt, the western Kura Basin and the southern slope of the central Greater Caucasus in Georgia. An integrated approach, combining low-temperature thermochronology and thermal maturity analyses on sedimentary rocks, was applied to unravel the thermo-tectonic history of those three inverted sedimentary basins from burial to exhumation. Additionally, this study provides examples of structural inversion of sedimentary basins in response to far-field transmission of compressional stresses away from collision zones, thus contributing to elucidate the dynamics of stress partitioning during continental collisions.

The first domain studied is the Adjara-Trialeti fold-and-thrust belt in south-western Georgia, resulting from the structural inversion of a Middle Eocene continental back-arc rift basin opened arguably as a consequence of the Northern Neotethys slab rollback. The results of thermal maturity analyses on its sedimentary fill, thermal modelling of borehole data and apatite fission-track and (U-Th)/He analyses quantitatively define the subsidence and exhumation history of the Adjara-Trialeti basin, constraining the Middle Miocene timing of inception of its structural inversion, arguably in response to northward transmission of far-field compressional stresses from the coeval Arabia-Eurasia collision along the Bitlis suture.

The second domain studied is the western Kura Basin, a flexural foreland basin which registered periods of contrasting subsidence in response to the advancement of the adjacent orogenic belts (i.e. the Lesser Caucasus to the south and the Greater Caucasus to the north). Continued convergence between such oppositely verging orogens lead to shortening and deformation within the basin, which began in the Middle Miocene and is still ongoing. Thermal maturity analyses and thermal modelling of borehole data constrain successive and competing episodes of flexural subsidence during Oligocene-Miocene times in the western Kura Basin, followed by partial inversion through thick- and thin-skinned tectonics in response to the advance of the adjacent orogenic belts.

The third domain studied is the southern slope of the central Greater Caucasus, in north-eastern Georgia. This orogen results from the structural inversion of a Jurassic continental back-arc basin but the timing of its growth is still debated. This long and complex orogenic belt was studied along an across-strike transect in its southern central domain through thermal maturity assessments and low-temperature thermochronological analyses (zircon (U-Th)/He and apatite fission-track and (U-Th)/He analyses). The results indicate that this sector of the Greater Caucasus experienced two phases of structural inversion, in response first to the Sevan-Akera (Late Cretaceous-Paleocene) and then to the Bitlis (Middle Miocene) continental collisions.

Overall, the dataset obtained from the study area points to a complex and episodic history of incremental deformation, characterised by successive phases of extensional and compressional tectonics which developed in response to sequential terrane accretion at the southwestern margin of Eurasia since Late Cretaceous times, that eventually determined the current configuration of the Arabia-Eurasia collision zone. The latest deformation phases occurred following the northward transmission of far-field compressional stresses from the Bitlis continental collision since Middle Miocene times.

RIASSUNTO

Questo studio mira ad una migliore definizione dell'evoluzione tettonica di una porzione della regione caucasica, interessata da una complessa successione di eventi deformativi durante il Mesozoico e il Cenozoico. In particolare, questa dissertazione si focalizza sulla catena orogenica di Adjara-Trialeti, sul Bacino di Kura occidentale e sul versante meridionale del Grande Caucaso centrale in Georgia. Un approccio integrato, che combina termocronologia di bassa temperatura con analisi sulla maturità termica delle rocce sedimentarie, è stato utilizzato per definire l'evoluzione termo-tettonica di questi tre bacini sedimentari invertiti, a partire dal seppellimento fino all'esumazione. Questo studio fornisce esempi significativi dell'inversione strutturale di bacini sedimentari in risposta alla propagazione a lungo raggio di sforzi compressivi a partire da zone di collisione, quindi contribuendo ad elucidare la dinamica di ripartizione dello stress durante le collisioni continentali.

Il primo dominio analizzato è la catena orogenica di Adjara-Trialeti nella Georgia sud-occidentale, il risultato dell'inversione strutturale di un bacino di rift di back-arc continentale apertosi nell'Eocene Medio probabilmente in risposta al rollback dello slab subduttivo della Neotetide settentrionale. I risultati delle analisi sulla maturità termica del suo riempimento sedimentario, della modellazione termica di dati di pozzo e dell'analisi delle tracce di fissione e dell'(U-Th)/He su apatite definiscono quantitativamente la storia di subsidenza ed esumazione del bacino di Adjara-Trialeti, vincolando la tempistica di inizio dell'inversione strutturale al Miocene Medio, probabilmente in seguito alla propagazione a lungo raggio verso nord di sforzi compressivi a partire dalla contemporanea collisione tra Arabia ed Eurasia lungo la zona di sutura di Bitlis.

Il secondo dominio studiato è il settore occidentale del Bacino di Kura, un bacino flessurale di avampaese che ha registrato una serie di contrastanti episodi di subsidenza in risposta all'avanzamento delle catene orogeniche circostanti: il Piccolo Caucaso a sud e il Grande Caucaso a nord. La progressiva convergenza tra questi due orogeni a vergenza opposta ha portato al raccorciamento del bacino e alla sua deformazione, iniziati nel Miocene Medio e ancora in atto. L'analisi della maturità termica dei sedimenti e la modellazione termica dei dati di pozzo hanno vincolato episodi successivi e contrastanti di subsidenza flessurale durante l'Oligocene e il Miocene, seguiti da inversione parziale dovuta a tettonica sia profonda che pellicolare in risposta all'avanzamento delle adiacenti catene orogeniche.

Il terzo dominio analizzato è il versante meridionale del Grande Caucaso centrale - nella Georgia nord-orientale. Questo orogene risulta dall'inversione strutturale di un bacino di back-arc apertosi nel Giurassico, la cui tempistica di chiusura e strutturazione è oggetto di dibattito. Questa lunga e complessa catena orogenica è stata studiata lungo un transetto trasversale alla catena, nel suo settore centro-meridionale, utilizzando l'analisi della maturità termica delle successioni sedimentarie e la termocronologia di bassa temperatura (analisi delle tracce di fissione su apatite e (U-Th)/He su apatite e zircone). I risultati indicano due fasi di inversione strutturale, raffreddamento e raccorciamento, le cui tempistiche (fine Cretaceo-Paleogene e Miocene Medio) coincidono rispettivamente con quelle delle chiusure del ramo settentrionale (Sevan-Akera) e meridionale (Bitlis) della Neotetide.

Nel complesso, i risultati ottenuti nei tre domini studiati indicano che la regione caucasica ha registrato una storia complessa ed episodica di deformazione incrementale, caratterizzata da fasi successive di tettonica sia estensionale che compressiva che si sono sviluppate in risposta all'accrezione progressiva di blocchi tettonici e microcontinenti al margine sudoccidentale di Eurasia a partire dal Cretaceo Superiore, fino a determinare la configurazione attuale della zona di collisione Arabia-Eurasia. Gli ultimi incrementi deformativi sono avvenuti a partire dal Miocene Medio in seguito alla propagazione a lungo raggio di sforzi compressivi associati alla collisione continentale lungo la sutura di Bitlis.

Chapter 1

INTRODUCTION AND GOALS

1.1 Introduction

Studies on the dynamics and mechanisms of stress generation, transmission and partitioning have direct implications for the building and evolution of orogenic systems, since these are determined by the accommodation of strain within Earth's crust. Classic Plate Tectonics predicts that deformation can occur only along plates boundaries, which are considered rigid and non-deformable at their interiors. Conversely, a growing body of evidence indicates that plates interiors can indeed be deformed, for example as a consequence of far-field transfer of compressional stresses away from collision fronts (Zoback, 1992; Ziegler et al., 1995, 1998, 2002; Cloetingh et al., 2005). Such collision-related stresses can travel for distances in excess of 1700 km from the plate margin (Ziegler et al., 2002), bypassing portions of rigid continental or oceanic crust and eventually focusing along rheological discontinuities and in already stressed sectors of the lithosphere. Intraplate deformation can occur in the form of buckling and folding at lithospheric scale, upthrusting of basement blocks, structural inversion of extensional sedimentary basins, and reactivation of older structures (Cloetingh et al., 1982; Jolivet et al., 1989; Ziegler, 1993; Ziegler et al., 1995; Faccenda et al., 2009) both on the upper and lower plates of the converging system (Fig. 1.1).

Numerous factors influence the dynamics of stress transmission and partitioning, including the nature of the plate interface, the amount of coupling between the plates and the presence of pre-existing crustal structures (Cloetingh et al., 1982, 1989; Jolivet et al., 1989; Ziegler, 1993; Ziegler et al., 1995, 1998; Faccenda et al., 2008, 2009; Sokoutis and Willingshofer, 2011; Vogt et al., 2017). Stronger mechanical coupling between the colliding plates leads to more efficient stress transmission and partitioning. Reactivation of existing faults and discontinuities is invariably preferred over the creation of new ones, but the nature of such pre-existing structures and their orientation with respect to the direction of the main axis of stress propagation have compelling implications on the mechanics of reactivation. In general, the weakest portions of the foreland (or hinterland) are rift areas, characterised by a thermally destabilised, stretched and faulted crust (Ziegler et al., 1998; Ziegler and Cloetingh, 2004). Similarly, strike-slip faults can be easily reactivated, whereas thrust faults and ancient suture zones require greater amounts of stress to be compressionally reactivated (Ziegler et al., 1995). Analogue experiments and real case studies have shown that fault reactivation is favoured if the strike of the discontinuity/structure to reactivate is broadly perpendicular to the stress propagation direction (Nalpas et al., 1995; Ziegler et al., 1995; Brun and Nalpas, 1996).

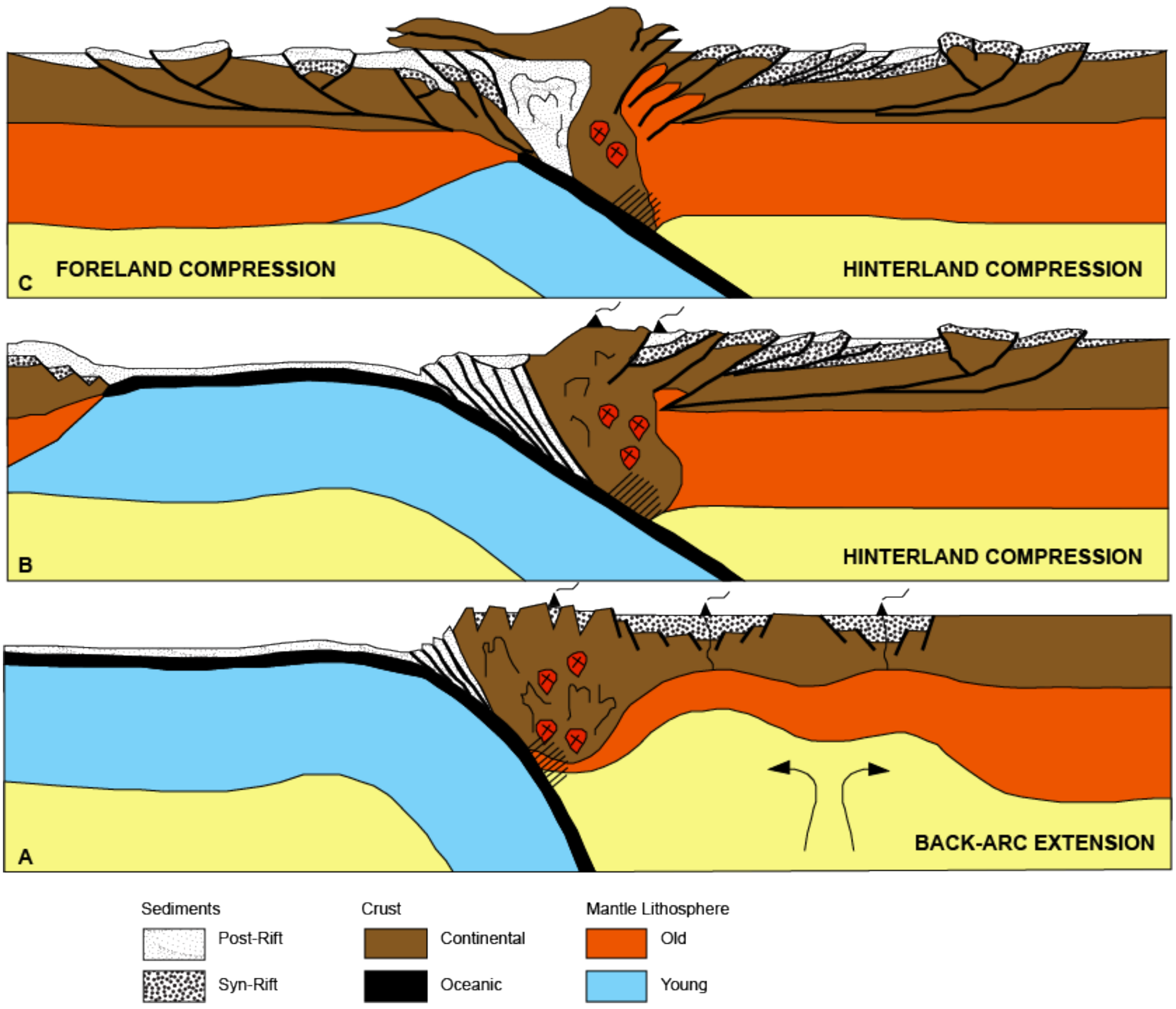

Figure 1.1: Conceptual model illustrating intraplate (A) back-arc extension, (B) back-arc (hinterland) compression and (C) collisional foreland and hinterland compression (not to scale) (Ziegler et al., 1998).

Back-arc rift basins (Fig. 1.2) open following a decrease in plates convergence rates, steepening and rollback of the subducting lower plate slab, and ensuing upper plate extension (Uyeda and Kanamori, 1979; Uyeda and McCabe, 1983; Doglioni et al., 2007; Miall, 2013). Prolonged back-arc rifting along active continental margins can produce deep marine basins floored by highly extended continental lithosphere, and eventually lead to crustal separation and opening of oceanic basins (e.g. South China Sea, Tyrrhenian Sea, Sea of Japan). However, back-arc basins are usually transitory and can undergo structural inversion following a renewed increase in convergence rates, with subsequent shallowing of the subducting slab (Uyeda and McCabe, 1983; Cloetingh et al., 1989; Jolivet et al., 1989; Letouzey et al., 1990; Ziegler, 1990; Nikishin et al., 2001; Hall et al., 2011; Munteanu et al., 2011). Structural inversion of such basins can also occur because of far-field compressional stress transmission from continental collisions (Zoback, 1992; Ziegler et al., 1995, 1998, 2002; Cloetingh et al., 2005; Cowgill et al., 2016). Continental back-arc rift basins represent rheological discontinuities where far-field collision-related stresses can focus: in this context basin inversion is favoured by the existence of structural weaknesses (i.e. the normal faults which accommodated extension), the lower density and strength of the sedimentary fill with respect to the surrounding crust, and in the case of young rift basins the not yet dissipated rift thermal signature (Ziegler et al., 2002; Buiter and Pfiffner, 2003; Ziegler and Cloetingh, 2004; Cloetingh et al., 2005; Buiter et al., 2009; Granado and Ruh, 2019).

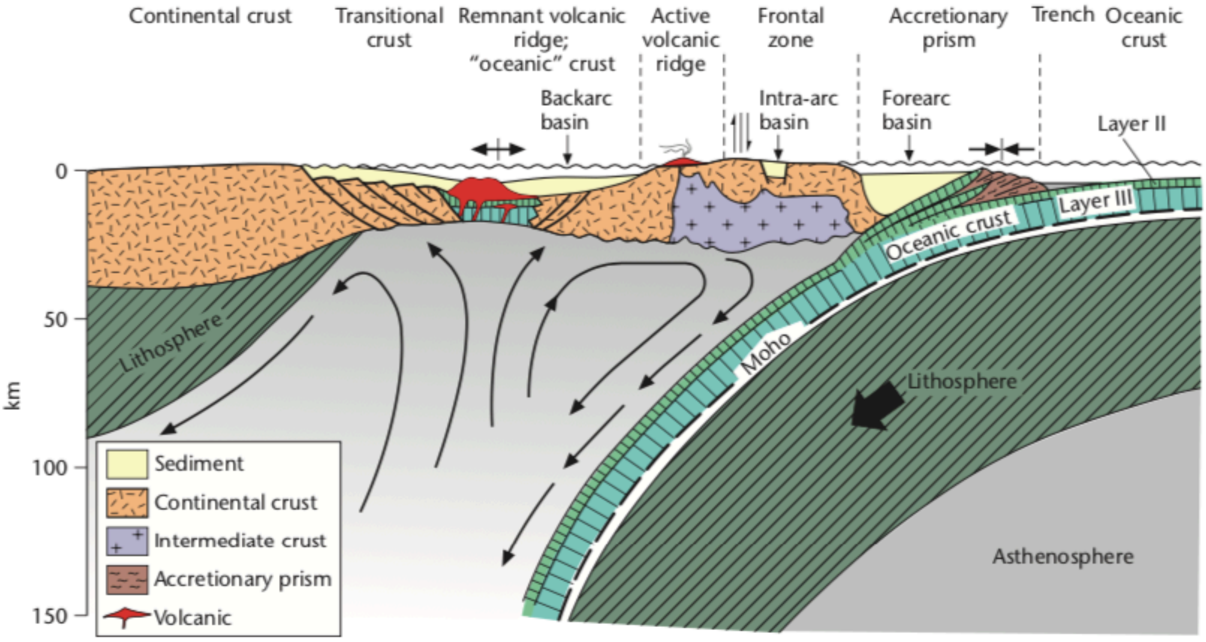

Figure 1.2: A convergent ocean-arc boundary showing the location of the trench, accretionary wedge, forearc basin, intra-arc and backarc basins (Allen and Allen, 2013; modified after Dickinson and Seely, 1979).

Numerical and analogue models suggest that structural inversion of back-arc basins is facilitated if (i) it occurs within about 25 My from the end of rifting and (ii) the lower crust is rheologically weak (Ziegler and Cloetingh, 2004; Buiter et al., 2009). Inversion of extensional basins is mainly controlled by the reactivation of pre-existing discontinuities, whereas the creation of new faults that cut through older structures is subordinate (Van Wijhe, 1987; Hooper et al., 1995; Brun and Nalpas, 1996; Buiter and Pfiffner, 2003).

The topic of this dissertation is the study of the tectonic evolution of a sector of the Caucasian region which experienced episodic and incremental deformation in an intraplate setting. The burial and exhumation history of two structurally inverted back-arc basins (the Adjara-Trialeti fold-and-thrust belt and the Greater Caucasus) and of a partially inverted flexural foreland basin (the Kura Basin) are constrained through thermal maturity analyses, thermal modelling of wells data and low-temperature thermochronological analyses.

This thesis includes three chapters which correspond to published or in preparation manuscripts, a further chapter exposing newly acquired and published thermochronological results for the Greater Caucasus, and a final chapter containing a comprehensive discussion integrating all the results exposed in the other chapters. Chapter 2 is a manuscript published in *Tectonophysics* in February 2021 which contains low-temperature thermochronological constraints on the structural evolution of the Adjara-Trialeti back-arc basin. Chapter 3 is a manuscript published in *Marine and Petroleum Geology* in May 2021 which contains the results of the thermal maturity analyses performed on surface samples and borehole cuttings from the sedimentary fill of the central-eastern Adjara-Trialeti, western Kura and southern central Greater Caucasus inverted basins. Chapter 4 is a manuscript in preparation, discussing the subsidence/exhumation history of the easternmost Adjara-Trialeti fold-and-thrust belt and the southernmost western Kura Basin, constrained through thermal modelling of data obtained from hydrocarbon exploration wells integrated with new low-temperature thermochronological constraints and interpretation of an industrial seismic line. Chapter 5 presents a compilation of all available thermochronological data for the Greater Caucasus and exposes newly acquired low-temperature thermochronological results along the southern slope of the central Greater Caucasus, discussing them together with published results. To date, most of the data available for this orogen are concentrated in the western Greater Caucasus, whereas detailed studies in the central and eastern portions are rare and focused on circumscribed areas (Kral and Gurbanov, 1996; Sobornov, 1996, 2021; Somin et al., 2006; Vincent et al., 2007, 2011, 2016, 2020; Avdeev, 2011; Avdeev and Niemi, 2011; Bochud, 2011; Somin, 2011; Cowgill et al., 2016; Trexler, 2018; Tye et al., 2020; Vasey et al., 2020). Given the rather limited datasets available, the knowledge of the structural architecture and tectonic history of such a huge and complex orogen is far from satisfactory. The new datasets presented here contributes to the definition of the tectonic evolution of the central Greater Caucasus, but it must be stated that such evolution cannot be extended to the whole orogenic belt, which needs further studies. In the final discussion (Chapter 6), all the results exposed in the previous chapters are integrated and combined with published structural, geochronological, geomorphological and stratigraphic data providing a comprehensive review of the current knowledge regarding the tectonic evolution of the study area.

1.2 Goals of the study

This study aims at a better definition of the tectonic and thermal evolution (subsidence history, thermal maturity, and timing of exhumation) of selected tectonic domains of the Caucasian region in Georgia. The investigated area comprehends portions of two structurally inverted continental back-arc rift basins (the Adjara-Trialeti fold-and-thrust belt and the southern slope of the central Greater Caucasus) and the western sector of the intervening Kura Basin, a flexural foreland basin which has later undergone compressional shortening and deformation. The added value of this study is the integration of several analytical techniques related to low-temperature thermochronology, thermal maturity assessments on sedimentary rocks based both on organic matter and clay minerals, and thermal modelling of borehole data.

Such integrated approach allowed to quantitatively constrain the time-temperature evolution of the three domains analysed, throughout their whole tectonic history from burial to exhumation. The results point to episodic deformation in the study area, which evolved in response to successive phases of extensional and compressional tectonics at the southwestern margin of the Eurasian Plate during Mesozoic and Cenozoic times. Apart from the regional interest, this study provides further evidence of intraplate deformation and structural inversion of former back-arc rift basins as a consequence of far-field stress transfer away from continental collisions, thus on the dynamics of stress partitioning in the hinterland of collision zones.

1.3 Geological background

This section provides a synthetic regional overview of the study area within the context of the overall goals of my Ph.D. project. The specific geological background of the study area is presented in more detail in the introductory sections of Chapters 2, 3, and 4.

The Caucasian region (Fig. 1.3) forms part of the long and complex Alpine-Himalayan orogenic system, which developed following the progressive convergence between the Eurasian and the African-Arabian-Indian plates with consumption of the Tethyan oceans during late Mesozoic-Cenozoic times and the ensuing collisions (Dewey et al., 1973, 1989; Stampfli et al., 2001; Reilinger et al., 2006; Stampfli and Hochard, 2009; Sharkov et al., 2015). In this context, the Arabia-Eurasia collision zone (Fig. 1.4) was shaped by the progressive

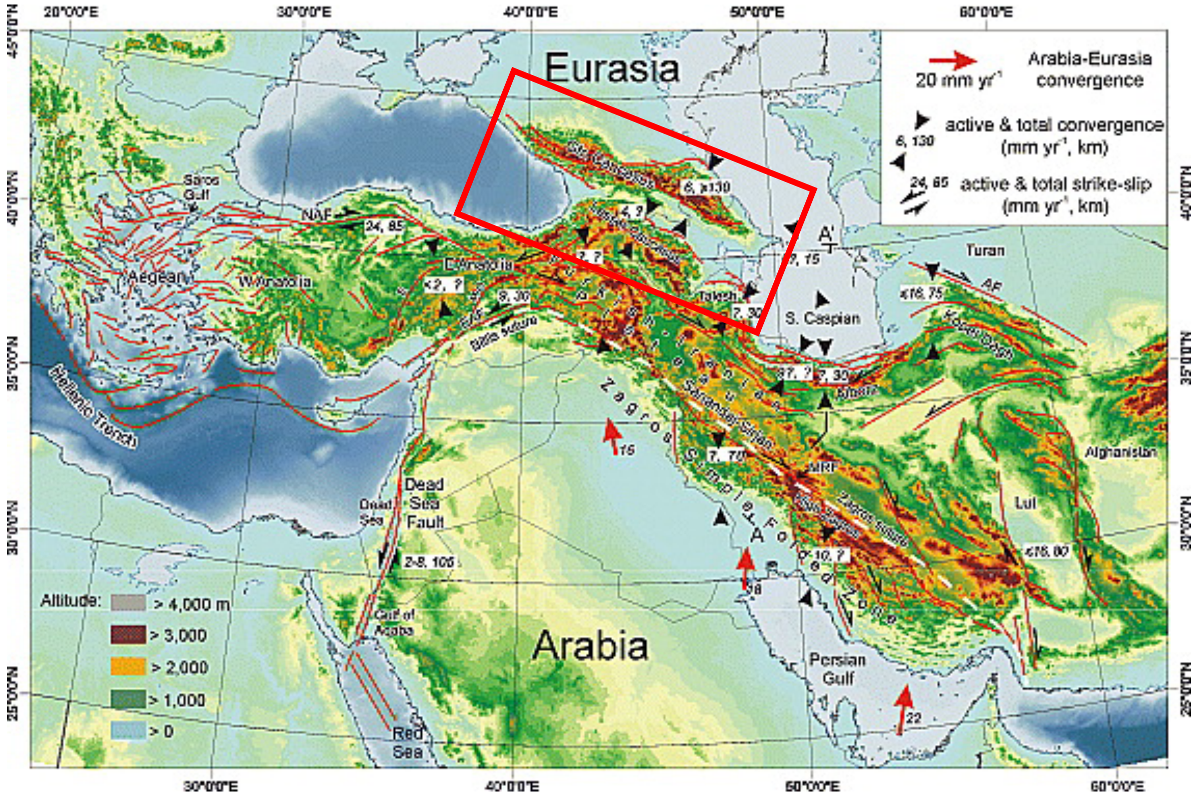

Figure 1.3: Topography, structure, current deformation rates and finite strain of the Arabia-Eurasia collision zone (Allen et al., 2004). Red rectangle identifies the Caucasian region.

closure of the two northern and southern branches of the Neotethys ocean, and from the ensuing continental collisions. The Northern Neotethys ocean closed during Late Cretaceous-Paleogene times forming the Izmir-Ankara-Erzinçan-Sevan-Akera suture zone, which extends from western Anatolia to the Lesser Caucasus (Okay and Tüysüz, 1999; Stampfli et al., 2001; Cavazza et al., 2004; Barrier and Vrielynck, 2008; Rolland et al., 2009, 2016; Barrier et al., 2018). Timing of closure of the Southern Neotethys ocean and subsequent collision between Arabia and Eurasia to create the Bitlis orogenic prism has long been debated, with estimates ranging from the Late Cretaceous to the Pliocene (Dewey et al., 1986; Philip et al., 1989; Alavi, 1994; Jolivet and Faccenna, 2000; Robertson et al., 2007; Allen and Armstrong, 2008), but recent thermochronologic data point to a Middle Miocene collision (Okay et al., 2010; Cavazza et al., 2018).

The Caucasian region (Fig. 1.5) is constituted by two main orogenic belts, the Greater Caucasus to the north and the Lesser Caucasus to the south, comprised between the Black Sea to the west and the Caspian Sea to the east and separated one from the other by a flexural foreland basin. Such foreland basin is in turn subdivided by the Dzirula metamorphic basement salient into the Rioni Basin, plunging towards the Black Sea, and the Kura Basin, plunging towards the Caspian Sea (Adamia et al., 2010, 2011b; Alania et al., 2017; Tibaldi et al., 2017;

Tari et al., 2018). To the south of the Dzirula Massif is located the E-W-trending Adjara-Trialeti fold-and-thrust belt (FTB) (Banks et al., 1997; Adamia et al., 2011b). This study focuses on a portion of the Georgian territory comprising the Adjara-Trialeti FTB, the western Kura Basin and the southern slope of the central Greater Caucasus (Figs. 1.4 and 1.5).

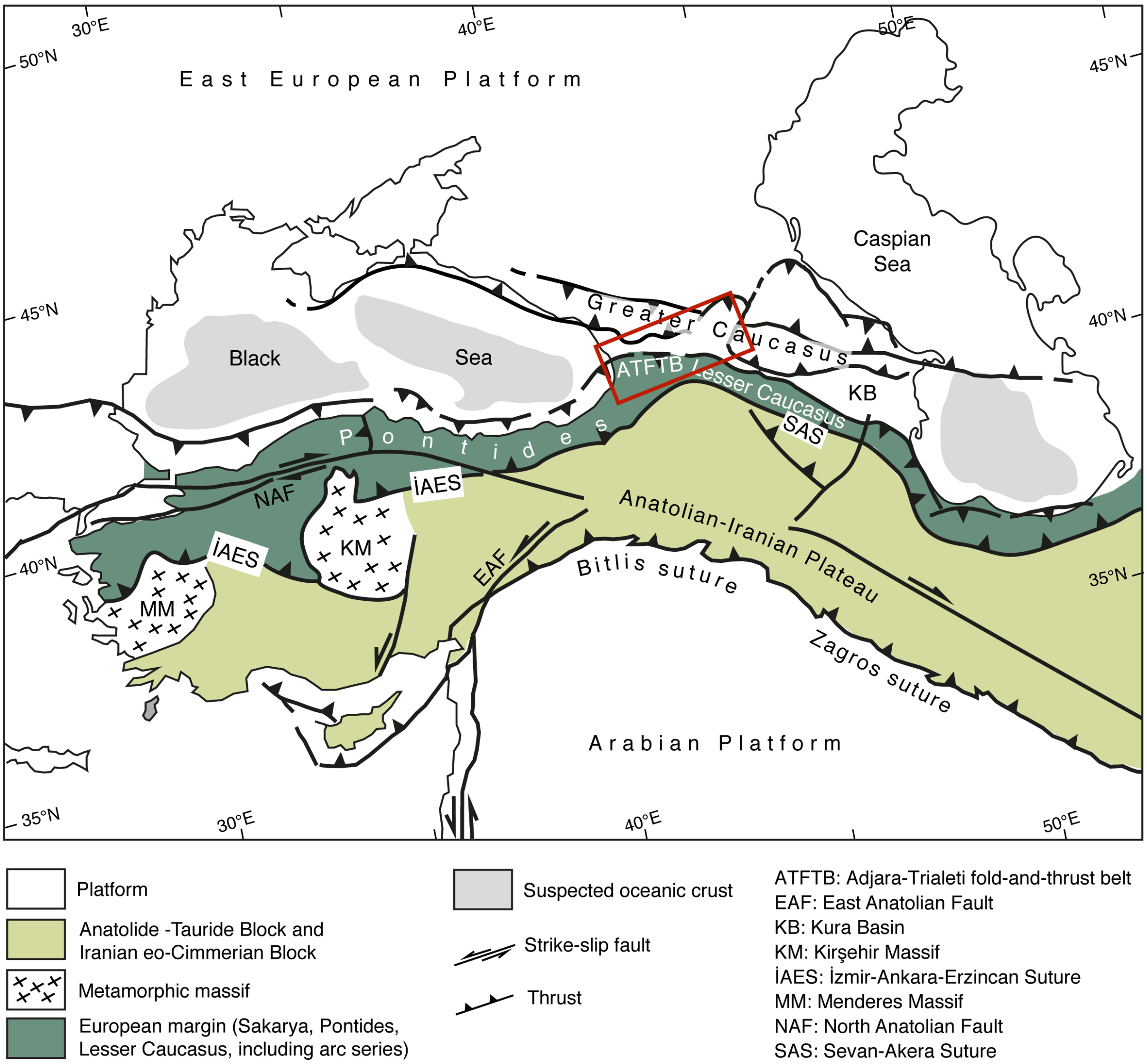

Figure 1.4: Tectonic sketch map of Asia Minor and the Caucasus region (Cavazza et al., 2019). Red rectangle outlines the study area.

The main characteristics of the Adjara-Trialeti FTB are presented in Chapter 2. This orogen resulted from the structural inversion of an Eocene back-arc rift basin developed behind the Lesser Caucasus, arguably as a consequence of the Northern Neotethys slab rollback (Adamia et al., 1977, 1981, 2010, 2011b; Banks et al., 1997; Yılmaz et al., 2000, 2014; Okrostsvaridze et al., 2018). Significant subsidence in the Adjara-Trialeti area began in the Paleocene with the deposition of a thick section of deep-marine turbidites (Borjomi Flysch, Paleocene-Ypresian) behind the Erzinçan-Sevan-Akera orogen (Gamkrelidze, 1949; Adamia et al., 1981, 2011b;

Yılmaz et al., 2000, 2014). A Middle Eocene pulse of rifting is testified by the deposition of volcaniclastic turbidites interbedded with submarine volcanic rocks, reaching a thickness of more than 5,000 m in the western sector of the Adjara-Trialeti inverted basin and decreasing to about 2,000 m in the eastern portion (Adamia et al., 1974, 1981, 2011b; Gamkrelidze et al., 2019). Such deposition was accompanied by the intrusion of a number of hypabyssal plutonic bodies, mostly concentrated in the central-western sector of the orogen (Okrostsvaridze et al., 2018, 2021). Closure and inversion of the Adjara-Trialeti basin was generically attributed to the Oligocene or Miocene (Adamia et al., 2011b, 2017): this dissertation provides compelling constraints on its Middle Miocene structural inversion (Chapters 2 and 4).

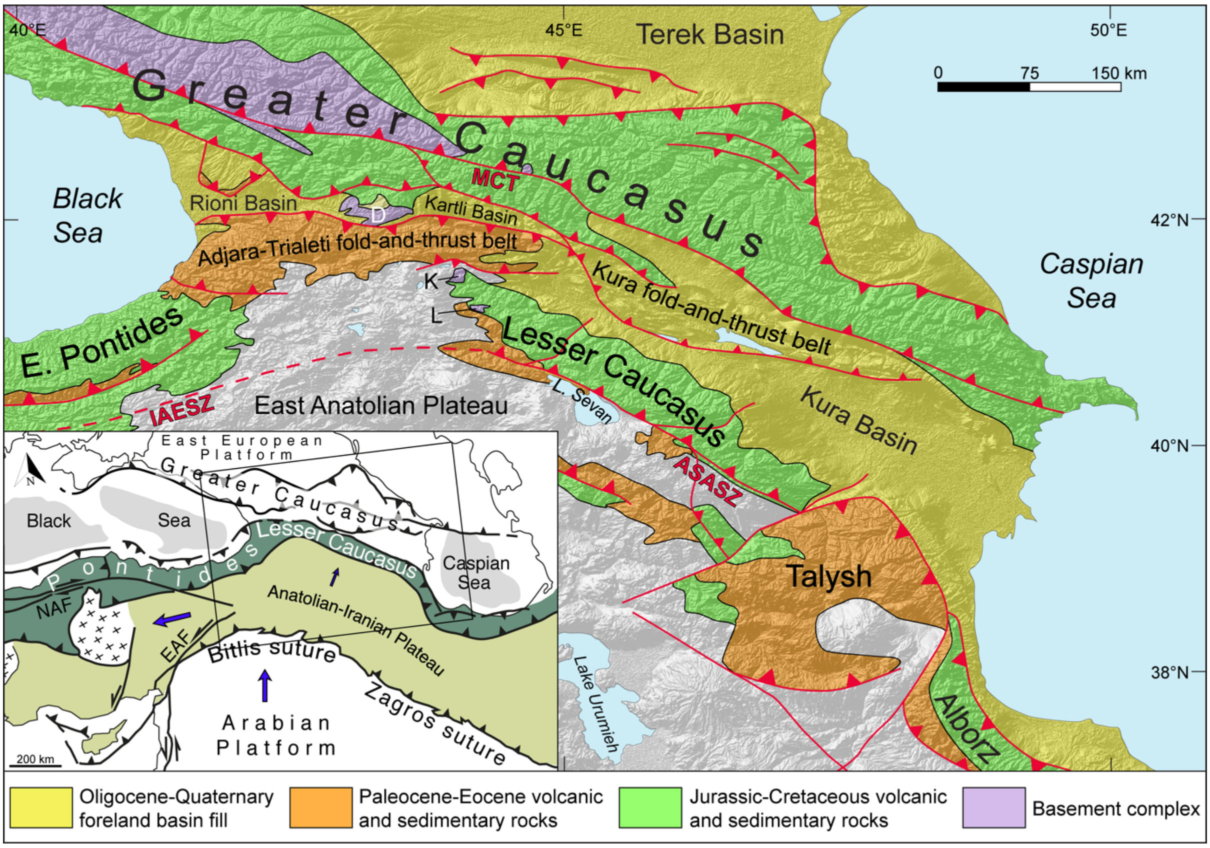

Figure 1.5: Main tectonic units of the Eastern Anatolian-Caucasian region (Gusmeo et al., 2021).

The Kura Basin developed as a flexural foreland basin since Oligocene times, in response to the growth of the retrowedge of the Lesser Caucasus (Banks et al., 1997; Adamia et al., 2010; Nemčok et al., 2013). Such basin was filled with a thick succession of Oligocene-Lower Miocene sedimentary rocks (Maikop Group) deposited within the anoxic-dysoxic environment of the Paratethys (Boote et al., 2018; Pupp et al., 2018; Sachsenhofer et al., 2018, 2021). Marine sedimentation continued until the Tortonian, when the western portion of the basin started emerging and the marine connection between the Rioni and Kura basins was interrupted

(Adamia et al., 2010; Shatilova et al., 2020, 2021). Since then continental conditions prevailed. Nemčok et al. (2013) recognized competing and asymmetrical episodes of flexural subsidence during the evolution of the western Kura Basin, attributed to the progressive convergence between the Greater and Lesser Caucasus. Continued convergence led first to thick-skinned and later to thin-skinned deformation within the basin.

The >1200-km-long Greater Caucasus orogen results from the structural inversion of a back-arc basin opened in the Early Jurassic, with Middle Jurassic lavas and volcaniclastics marking the main phase of rifting (Lordkipanidze et al., 1989; Zonenshain et al., 1990; Nikishin et al., 2001; Saintot et al., 2006; McCann et al., 2010; Mosar et al., 2010; Adamia et al., 2011b; Vincent et al., 2016; Vasey et al., 2021). The Greater Caucasus back-arc basin was probably underlain by thinned continental crust and never reached the oceanic spreading stage (Ershov et al., 2003). Sedimentation within the Greater Caucasus Basin lasted from the Early Jurassic to the Late Eocene. Post-rift thermal subsidence started at the Middle/Late Jurassic boundary, and since then both calcareous and siliciclastic turbidites were deposited in a mostly deep marine environment (Saintot et al., 2006; Adamia et al., 2011b, 2011a).

The term Transcaucasus traditionally defines the region comprised between the Greater Caucasus and the Lesser Caucasus. The Transcaucasus in the geological past connected two basins of great potential in terms of petroleum exploration: the underexplored but promising Eastern Black Sea and the Caspian Sea, hosting a world-class petroleum province (Boote et al., 2018; Tari et al., 2018; Pape et al., 2021; Tari et al., 2021). The Transcaucasus hosts proven hydrocarbon reservoirs within the Rioni and Kura basins, associated especially to the maturation of the Maikop Group source rock. The connection between the Black and Caspian seas was interrupted in early Late Miocene times because of the convergence between the south-verging pro-wedge of the Greater Caucasus and the north-verging retro-wedge of the Lesser Caucasus orogenic prisms (Nemčok et al., 2013; Shatilova et al., 2020, 2021). This convergence is interpreted as a far-field effect of the Middle Miocene continental collision between the Eurasian and Arabian plates along the Bitlis-Zagros suture zone (Okay et al., 2010; Cavazza et al., 2018), which caused diffuse deformation and induced reactivation of older structures (including structural inversion of pre-existing sedimentary basins) and widespread strike-slip deformation in a broad portion of the hinterland, comprising the Eastern Pontides, part of the Lesser Caucasus, the Talysh and the Alborz Mountains (Axen et al., 2001; Guest et al., 2006; Gavillot et al., 2010; Madanipour et al., 2013, 2017; Albino et al., 2014; Cavazza et al., 2017, 2019; Barber et al., 2018).

Chapter 2

Manuscript 1:

Structural inversion of back-arc basins – The Neogene Adjara-Trialeti fold-and-thrust belt (SW Georgia) as a far-field effect of the Arabia-Eurasia collision

Manuscript 1

Structural inversion of back-arc basins – The Neogene Adjara-Trialeti fold-and-thrust belt (SW Georgia) as a far-field effect of the Arabia-Eurasia collision

Thomas Gusmeo, William Cavazza, Victor Alania, Onise Enukidze, Massimiliano Zattin, and Sveva Corrado

Submitted to Tectonophysics on 1st October 2020, accepted on 3rd December 2020, first published online on 10th February 2021.

Tectonophysics 803, DOI: 10.1016/j.tecto.2020.228702

Tectonophysics 803 (2021) 228702

Contents lists available at ScienceDirect

Tectonophysics

journal homepage: www.elsevier.com/locate/tecto

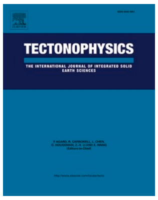

Structural inversion of back-arc basins–The Neogene Adjara-Trialeti fold-and-thrust belt (SW Georgia) as a far-field effect of the Arabia-Eurasia collision

Thomas Gusmeo [a,*], William Cavazza [a], Victor M. Alania [b], Onise V. Enukidze [b], Massimiliano Zattin [c], Sveva Corrado [d]

[a] *Department of Biological, Geological and Environmental Sciences, Univ. of Bologna, Italy*
[b] *Institute of Geophysics, I. Javakhishvili State University, Tbilisi, Georgia*
[c] *Department of Geosciences, Univ. of Padova, Italy*
[d] *Department of Sciences, Roma Tre University, Rome, Italy*

A R T I C L E I N F O

Keywords:
Fission-track analysis
(U-Th)/He analysis
Lesser Caucasus
Rift inversion
Far-field tectonics
Arabia-Eurasia collision

A B S T R A C T

The 350 km-long Adjara-Trialeti fold-and-thrust belt of southwestern Georgia is the result of the structural inversion of a continental back-arc basin developed in the Paleogene on the upper (Eurasian) plate of the northward subducting northern branch of the Neotethys. Low-temperature thermochronological data [fission-track and (U-Th)/He analyses on apatite] from sedimentary and plutonic rocks provide robust constraints on the tectonic evolution of the Adjara-Trialeti orogenic belt. Fission-track central ages range from the Middle Eocene to the Middle Miocene (46–15 Ma); helium ages are clustered in the Late Miocene-Pliocene (10–3 Ma). Time-temperature paths obtained integrating thermochronologic, stratigraphic, and radiometric data show that the volcanosedimentary basin fill of the Adjara-Trialeti back-arc basin underwent progressive burial heating prior to final cooling/exhumation in the late Middle Miocene-Pliocene. These new data show that the Adjara-Trialeti back-arc basin was inverted and developed as a fold-and-thrust belt starting at 14–10 Ma, in tune with widespread Middle-to-Late Miocene shortening and exhumation across wide areas of the Middle East, from the eastern Pontides of NE Turkey to the Lesser Caucasus in northern Armenia and NW Azerbaijan, and the Talysh and Alborz ranges in northern Iran. Such a supraregional tectonism is interpreted as a far-field effect of the Arabia-Eurasia collision along the Bitlis suture ca. 400 km to the south of the study area.

1. Introduction

Back-arc rifts develop in response to a decrease in plates convergence rates, inducing steepening and rollback of the subducting lower plate lithospheric slab and concurrent upper plate extension (e.g. Doglioni et al., 2007; Miall, 2013; Uyeda and McCabe, 1983). Back-arc rifting along active continental margins can lead to crustal separation and the opening of deep marine basins floored by either oceanic or highly extended continental lithosphere (e.g. South China Sea, Sea of Japan, Tyrrhenian Sea). However, as plates convergence rates are variable in time and space, back-arc basins are usually transitory. Following an increase in convergence rates and the ensuing shallowing of the subducting lower plate, back-arc extensional basins are liable to structural inversion by compressional stresses (Cloetingh et al., 1989; Hall et al., 2011; Jolivet et al., 1989; Letouzey et al., 1990; Munteanu et al., 2011; Nikishin et al., 2001; Uyeda and McCabe, 1983; Ziegler, 1990).

Back-arc basins can be also deformed and inverted during continent-continent collisions, when horizontal compressional stress can travel far from suture zones inducing the formation/reactivation of an array of compressional/transpressional structures, such as lithospheric folding, basement upthrusting and overall basin inversion both in the foreland and the hinterland (Cloetingh et al., 2005; Cowgill et al., 2016; Ziegler et al., 2002, 1998, 1995; Zoback, 1992). Collision-related stresses can bypass the orogenic wedge and focus along rheological discontinuities at distances in excess of 10^3 km from the collisional front (Ziegler et al., 2002). Basin inversion is favoured by the existence of preexisting structural weaknesses as well as the lower density and rheological strength of the sedimentary fill compared to the surrounding crust. In

---

* Corresponding author at: Piazza di Porta San Donato 1, 40126 Bologna, Italy.
E-mail address: thomas.gusmeo2@unibo.it (T. Gusmeo).

https://doi.org/10.1016/j.tecto.2020.228702
Received 1 October 2020; Received in revised form 30 November 2020; Accepted 3 December 2020

addition, young sedimentary basins can localize shortening more efficiently because the extensional thermal signature not yet dissipated makes them weaker.

In this paper, we present the first low-temperature thermochronological dataset on the Adjara-Trialeti back-arc rift basin of southwestern Georgia, which developed along the Eurasian continental margin during the latest stage of northward subduction of the Neotethys (Adamia et al., 2010; Yılmaz et al., 2014, 2000). Our data indicate that the Paleogene sedimentary fill of the Adjara-Trialeti basin has been structurally inverted and developed as a fold-and-thrust belt starting from the late Middle Miocene. Coeval compressional deformation took place over a wide area comprising –from west to east– the eastern Pontides of northeastern Turkey, portions of the Lesser Caucasus in northern Armenia and northwestern Azerbaijan, and the Talysh and Alborz ranges of northern Iran (Albino et al., 2014; Ballato et al., 2013; Cavazza et al., 2019, 2015; Guest et al., 2006; Madanipour et al., 2017). We interpret this overall state of compression and selective reactivation of older structures as a far-field effect of the coeval Arabia-Eurasia continental collision along the Bitlis-Zagros suture, located more than 400 km to the south of the Adjara-Trialeti fold-and-thrust belt.

2. Geological and geophysical background

The Adjara-Trialeti fold-and-thrust belt (ATFTB) of southwestern Georgia is an E-W-trending orogen spanning some 350 km from the Black Sea coast to east of Tbilisi (Fig. 1). The maximum surficial width of the belt is about 50 km close to the Black Sea and decreases progressively to the east. In eastern Georgia, the ATFTB plunges to the east and it is covered by highly deformed Oligocene-to-Miocene sedimentary rocks of the Kura basin fill. To the west it continues offshore in the eastern Black Sea, where it is known as Gurian fold belt (e.g. Tari and Simmons, 2018).

Geodetic data indicate that the ATFTB is tectonically active and accommodates 3–6 mm/yr of the present convergence rate between the eastern Anatolian Plateau and Eurasia (Reilinger et al., 2006; Sokhadze et al., 2018) (Fig. 2). The major earthquakes within the fold-and-thrust belt are characterized by transpressive focal mechanisms (Sokhadze et al., 2018; Tsereteli et al., 2016). Seismicity is higher in the Rioni-Kartli-Kura foreland basin to the north (Adamia et al., 2017a; Tibaldi et al., 2017) where fault-plane solution data indicate ongoing north-south-oriented compression and convergence rates can reach 12 mm/yr (Forte et al., 2014, 2013; Karakhanyan et al., 2013; Reilinger et al., 2006). Crustal thickness along the ATFTB ranges between 35 and 45 km, whereas the lithospheric thickness is 130–140 km (Adamia et al., 2017b; Motavalli-Anbaran et al., 2016).

The ATFTB is bordered to the north by frontal thrusts and associated fault-propagation folds (Adamia et al., 2017b, 1992; Alania et al., 2018; Banks et al., 1997; Nemčok et al., 2013) (Fig. 2). Shortening along the northern frontal structures is estimated at ca. 15 km (Bazhenov and Burtman, 2002); northward propagation of such frontal structures has induced deformation of the southern margins of the Rioni and Kartli foreland basins (Alania et al., 2017; Banks et al., 1997; Nemčok et al., 2013). The Dzirula massif, a polymetamorphic salient in central Georgia (Figs. 1, 2), was already at the surface during the development of the ATFTB (Vincent et al., 2011) and acted as a relatively rigid indenter during the northward propagation of the belt, as shown by the curvature of the frontal thrusts close to the massif (Fig. 2). Surface relationships between the ATFTB and the Khrami Massif to the south are hidden by a thick cover of latest Miocene-to-Quaternary subaerial lava flows and pyroclastic deposits (Adamia et al., 2017b, 2011, 2008, 1981; Okrostsvaridze et al., 2018b). The boundary and structural relationship between the Adjara-Trialeti and the Eastern Pontides (NE Anatolia) orogenic belts are unclear due to a thick vegetation cover.

Fig. 3 shows the overall stratigraphy of the eastern sector of the ATFTB. To the west precise correlation is hampered by limited exposure. The age of the pre-rift sedimentary succession ranges from the late Early Cretaceous to the Early Eocene. The Aptian-Cenomanian volcanics and volcaniclastics of the ATFTB have been interpreted as connected to either (i) the Eastern Pontides-Lesser Caucasus subduction-related magmatic arc, located immediately to the south (Adamia et al., 1992, 1981; Yılmaz et al., 2014) or (ii) to the opening of the Eastern Black Sea (Nikishin et al., 2015a, 2015b). While there is ample evidence that the western Black Sea opened in late Early Cretaceous times (e.g. Finetti et al., 1988; Görür, 1988; Munteanu et al., 2011; Nikishin et al., 2011, 2001), arguably as an extensional back-arc basin related to the northward subduction of the Neotethys (e.g. Letouzey et al., 1977; Nikishin

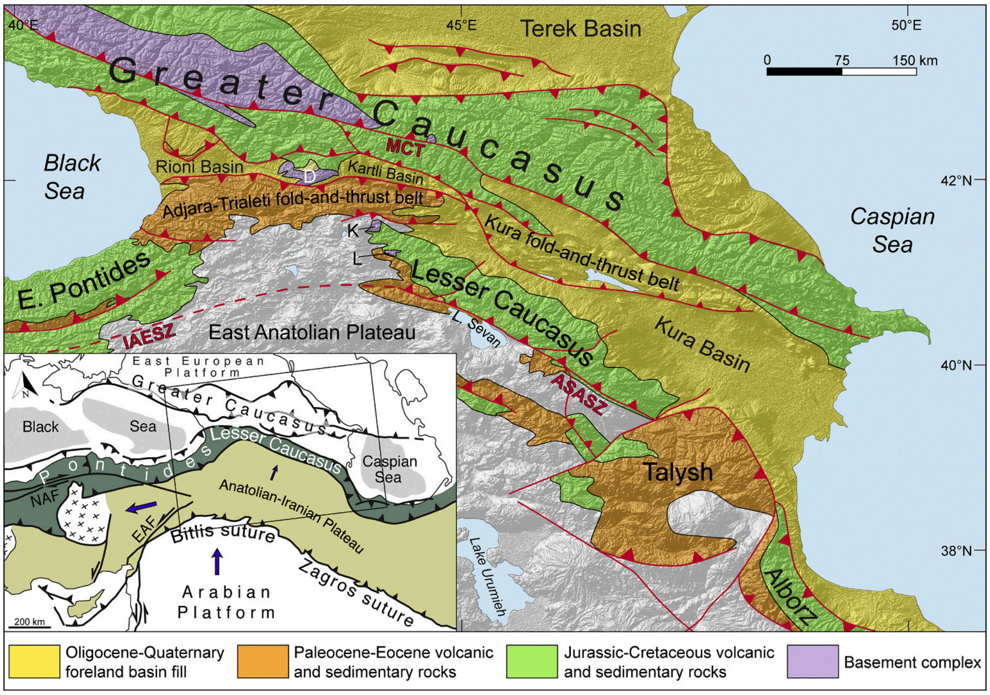

Fig. 1. Main tectonic units and structures of the Eastern Anatolia-Caucasian region superimposed on an ASTER GDEM shaded relief map (source: USGS). ASASZ = Amasia-Sevan-Akera suture zone; D = Dzirula Massif; IAESZ = Izmir-Ankara-Erzinçan suture zone; K = Khrami Massif; L = Loki Massif; MCT = Main Caucasian Thrust. Red lines with triangles indicate thrusts; red lines are normal, strike-slip or unknown kinematics faults. Inset: Tectonic sketch map of the Arabia-Eurasia collision zone modified after Cavazza et al. (2019) and Sosson et al. (2010). EAF = Eastern Anatolian Fault; NAF = Northern Anatolian Fault. (For interpretation of the references to colour in this figure legend, the reader is referred to the web version of this article.)

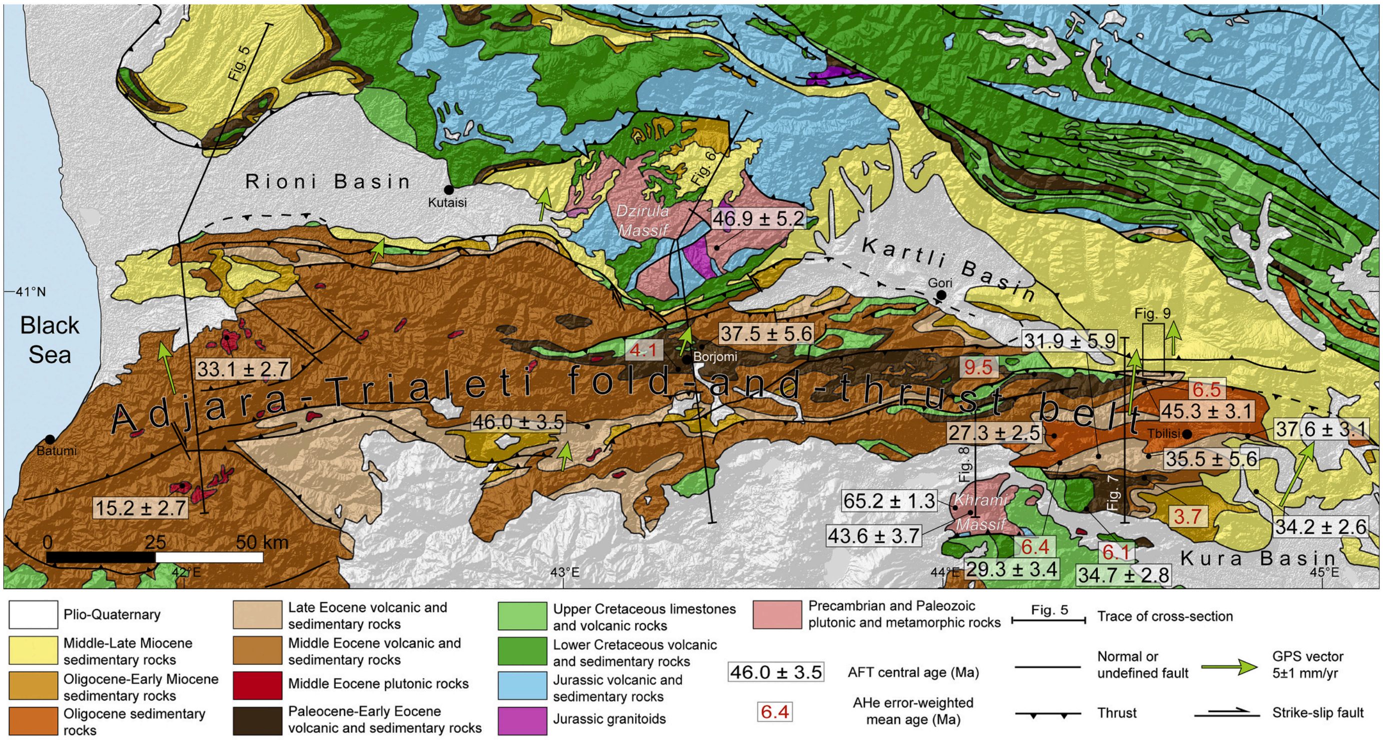

Fig. 2. Geological sketch map of the Adjara-Trialeti fold-and-thrust belt and the surrounding regions (modified from Adamia, 2004; USSR Geological Survey, 1957a, 1957b, 1956a, 1956b, 1956c). For analytical details of apatite fission-track central ages and (U-Th)/He mean ages and exact samples locations, see Tables 1 and 2. Traces of geological cross-sections of Figs. 5, 6, 7 and 8 and location of Fig. 9 are also shown.

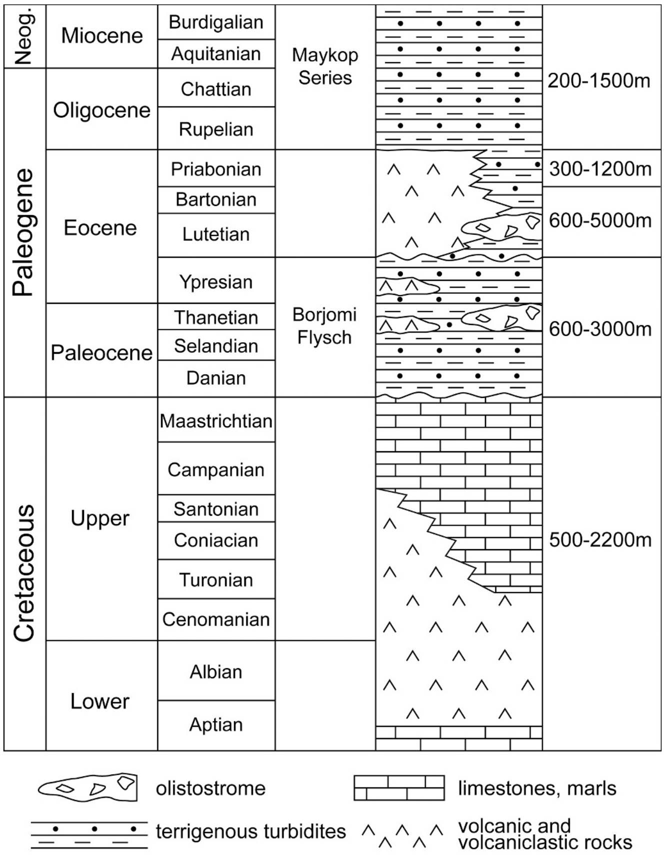

Fig. 3. Schematic chronostratigraphy of the Adjara-Trialeti region. Sources: Adamia et al., 2017b, 2011; Gamkrelidze et al., 2018; Yılmaz et al., 2014, 2000.

et al., 2011; Okay et al., 1994), the timing of opening of the eastern Black Sea has been variously interpreted as coeval with the western Black Sea (e.g. Nikishin et al., 2015a, 2015b, 2003; Okay et al., 1994; Zonenshain and Le Pichon, 1986), as late Campanian-Danian (Vincent et al., 2016), Paleocene-Early Eocene (Robinson et al., 1996, 1995a, 1995b; Shillington et al., 2008; Spadini et al., 1996) or as Eocene (Kazmin et al., 2000). As a whole, the formation of the Black Sea basins has been explained in terms of geodynamic models derived from the study of modern back-arc basins, where extension is driven by slab roll-back. For example, Stephenson and Schellart (2010) interpreted the Black Sea as an asymmetric back-arc basin bordering a subduction slab undergoing asymmetric anticlockwise slab roll-back, a model compatible with an earlier onset of extensional structures in the western compared to the eastern sub-basin.

Adjara-Trialeti subsidence increased rapidly in the Paleocene, with the development of an east-west-trending elongate basin and the deposition of a thick succession of terrigenous turbidites (Paleocene-Ypresian Borjomi Flysch; Fig. 3) (Adamia et al., 2011; Banks et al., 1997; Yılmaz et al., 2014, 2000). During this period, the Adjara-Trialeti region was located in the northern foreland of the Erzinçan-Sevan-Akera orogen and was experiencing flexural subsidence. The flexural interpretation of the Borjomi subsidence is supported by the progressive eastward thickening of the Borjomi Flysch (Gamkrelidze, 1949; Yılmaz et al., 2000), as the oblique collision between the Anatolide-Tauride terrane and the southern Eurasian margin (Barrier et al., 2018) induced a gradient of increasing subsidence from west to east (Fig. 4). Back-arc rifting occurred in the Middle Eocene (Fig. 4), as shown by a thick succession of volcaniclastic turbidites interbedded with submarine volcanic rocks (Adamia et al., 2011, 1981, 1977; Okrostsvaridze et al., 2018a). The Middle Eocene section thickens dramatically toward the Black Sea coast, where it reaches ca. 5000 m (Adamia et al., 2011; Gamkrelidze et al., 2019; Okrostsvaridze et al., 2018a) and volcanic/hypabyssal rocks are most abundant (Okrostsvaridze et al., 2018b). In the Late Eocene, mostly epiclastic turbidites were being deposited in the

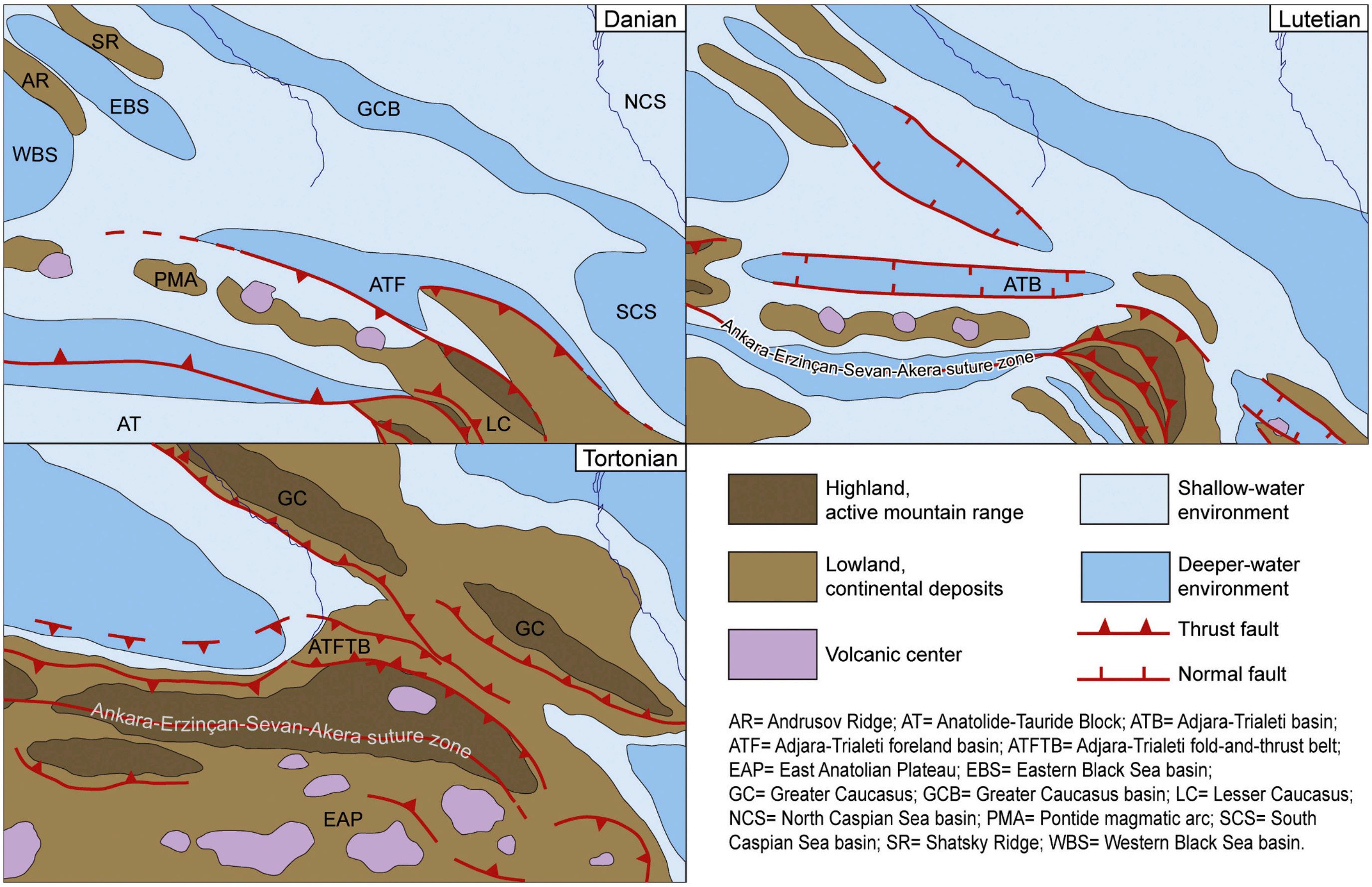

Fig. 4. Paleogeographic sketch maps of the Black Sea-Caucasian region (modified from Barrier et al., 2018). During the Danian (Early Paleocene), the Adjara-Trialeti region was affected by flexural subsidence related to the progressive development of the Ankara-Erzinçan suture to the south. In the Lutetian (Middle Eocene), the rollback of the Neotethyan slab induced upper-plate extension and the development of the Eastern Pontides intra-arc/back-arc extensional basin, partly superposed on the Adjara-Trialeti basin which was then experiencing peak subsidence. In the Tortonian (Late Miocene), following complete Arabia-Eurasia collision, the Adjara-Trialeti-Eastern Pontides rift system was inverted.

eastern sector of the ATFTB, whereas volcaniclastic turbidites interbedded with lava sheets and pyroclastic rocks were predominant in the central and western sectors (Adamia et al., 2017b, 2011; Gamkrelidze et al., 2018). Seismic data show that the ATFTB continues offshore in the Eastern Black Sea and suggest coeval extension in the Black Sea - Pontide domain and in the Adjara-Trialeti basin (Banks et al., 1997; Robinson et al., 1995b, 1996, 1997; Shillington et al., 2008; Tari et al., 2018).

During Oligocene-Early Miocene (Maykopian) times the Adjara-Trialeti basin saw the deposition of terrigenous turbidites, locally interbedded with shales, marls and fine-grained sandstones indicating an anoxic/disoxic environment (Pupp et al., 2018; Sachsenhofer et al., 2018) (Fig. 4). The youngest deposits are Sarmatian (ca. 12–10 Ma) shallow-water siliciclastics and oolitic limestones (Adamia et al., 2017b, 2011; Gamkrelidze et al., 2019). Inversion of the Adjara-Trialeti back-arc basin has been generically indicated as Oligocene-Miocene (Adamia et al., 2010, 1981, 1977; Banks et al., 1997; Sosson et al., 2016). The chronological definition of such a structural inversion and its interpretation in a wider geodynamic scenario is the objective of this study.

3. Analytical methods

3.1. Apatite fission-track analysis and modelling

Fission-track dating is a useful tool to unravel the cooling histories experienced by rocks in the upper crustal levels and to give a measure of their exhumation (for a review, see Donelick et al., 2005). Fission tracks are linear radiation damages within the crystal lattice, caused by the nuclear fission of radioactive isotope ^{238}U, which can be etched and counted under an optical microscope. Concurrently, neutron irradiation is used to induce the decay of ^{235}U, generating radiation damages on the surface of an external detector. Grain-by-grain determination of both spontaneous and induced fission-track densities yields a single-grain age representing the cooling of the grain below a closure temperature of ~100 °C. Fission tracks in apatites have the same initial length of about 16 μm (Donelick et al., 1999; Ketcham et al., 1999) but anneal at rates proportional to temperature, starting at about 60 °C. Over geological time periods, partial annealing of fission tracks occurs at temperatures between about 60 and 120 °C (the Partial Annealing Zone or PAZ; Gleadow and Duddy, 1981). Because tracks shorten in relation to the degree and duration of heating, the measurement of fission-track lengths gives information about the thermal evolution in the PAZ temperature range. A quantitative evaluation of the thermal history can be carried out through modelling procedures, which find a range of cooling paths compatible with the fission-track length frequency distribution (Ketcham, 2005). In this work, inverse modelling of track length data was performed using the HeFTy program (Ketcham, 2005), which generates the possible T-t paths by a Monte Carlo algorithm. Predicted AFT data were calculated according to the Ketcham et al. (2007) annealing model for fission tracks revealed by etching. Dpar values (i.e. the etch pit length) were used to define the annealing kinetics.

3.2. Apatite (U-Th)/He analysis

(U-Th)/He (AHe) dating is based upon the decay of radioactive isotopes ^{238}U, ^{235}U, and ^{232}Th to give as products ^{206}Pb, ^{207}Pb, and ^{208}Pb, respectively. ^{4}He nuclei (α particles) are emitted at each step of this decay series and hence are the daughter nuclides for this dating system (Lisker et al., 2009; Reiners, 2005). In (U-Th)/He thermochronology, the closure temperature (Tc) is depending on a number of factors, such as crystal size, eU and radiation damage (Flowers et al., 2009; Gautheron et al., 2009). Moreover, production-diffusion model predicts that the effective He closure temperature of apatite will vary with cooling rate and effective U- and Th-concentration, and may differ from the commonly assumed temperature of 70 °C by up to ±15 °C (e.g. Farley, 2002, 2000; Farley et al., 1996; Flowers et al., 2009; Shuster et al., 2006; Shuster and Farley, 2009; Wolf et al., 1998, 1996). It follows that AHe ages should be younger than AFT ages because of the lower closure temperature (for a review, see Peyton and Carrapa, 2013). The He Partial Retention Zone (PRZ) is the temperature interval where some He can be slowly lost through diffusion. The PRZ in apatite is usually assumed to be between ~40 and 70 °C, but experimental data have demonstrated that this range can widen depending on the diffusion kinetics of the grains (Flowers et al., 2015, 2009; Gautheron et al., 2009; Shuster and Farley, 2009). Another important issue in AHe thermochronometry is that α particles emitted during decay can travel for 20 μm inside the crystal lattice of apatites: thus some He can be lost if emission occurs within that distance from the crystal edge, and ages should be corrected accordingly (Farley, 2002; Farley et al., 1996).

3.3. Sampling strategy and sample preparation

Twenty-one samples were collected from sedimentary rocks of the ATFTB, four samples were collected from intrusions in the central and western ATFTB, two samples were collected from the Dzirula Massif, and four samples from the Khrami Massif, for a total of thirty-one samples. Sedimentary rocks from the ATFTB are sandstones ranging in age from the Aptian-Albian to the Early Miocene. The intrusives are diorites and syenites of Eocene age. One sample from the Dzirula Massif is a Bajocian andesite, the other is a Late Paleozoic (Variscan) granitoid. Three samples from the Khrami Massif are Variscan granitoids, whereas one is a Paleozoic dioritic gneiss.

Apatite grains were concentrated by crushing and sieving the samples, followed by hydrodynamic, magnetic, and heavy-liquid separations. Apatites were embedded in epoxy resin, polished in order to expose internal surfaces within the grains, and the spontaneous fission-tracks were revealed by etching with 5 N HNO_3 at 20 °C for 20 s. Mounts were then coupled with a low-uranium fission-track-free muscovite mica sheet (external detector method) and sent for irradiation with thermal neutrons at the Radiation Center of Oregon State University (see Donelick et al., 2005, for details). Nominal fluence of 9×10^{15} n cm^{-2} was monitored using a CN5 uranium-doped silicate glass dosimeter. Induced fission tracks were revealed by etching of the mica sheets in 40% HF for 45 min at 20 °C. Spontaneous and induced fission tracks were counted under an optical microscope at x1250 magnification, using an automated stage and a digitizing tablet.

Fifteen samples yielded apatites suitable for AFT dating (Table 1). Central ages were calculated using the zeta calibration approach (Hurford and Green, 1983), using Durango (31.3 ± 0.3 Ma) and Fish Canyon Tuff (27.8 ± 0.2 Ma) age standards within grains exposing c-axis-parallel crystallographic planes. Track-length distributions were calculated by measuring horizontal confined tracks together with the angle between the track and the c-axis of the apatite crystal. Confined tracks constitute a small portion of all the AFT populations, therefore additional concentrates were mounted, polished, and etched for analysis. Ultimately, five samples provided statistically significant numbers of confined tracks for a robust inverse modelling.

Six samples, which yielded the best apatite grains (euhedral, inclusion-free crystals with widths >60 μm), were selected for AHe analyses (Table 2). Three to five apatite grains for each sample were hand-picked, photographed, and measured before being wrapped into 0.8 mm Nb tubes. They were then degassed with a Nd-YAG laser and after cryogenic purification ^{4}He was measured by quadrupole mass spectrometry. The concentrations of U, Th and Sm were measured using an inductively coupled plasma mass spectrometer (ICP-MS). Standard procedures are described in Reiners et al. (2004). The alpha ejection correction has been applied to the obtained AHe ages, to take into account the partial He loss due to decay within 20 μm of the crystal edge (Farley, 2002; Farley et al., 1996).

3.4. Modelling procedures

Five samples from our dataset contained enough confined tracks for a statistically robust inverse modelling: four from the ATFTB (TU279, TU486, TU488 and TU510) and one from the Khrami Massif (TU515) (Table 1). Modelling was performed using the HeFTy software (Ketcham, 2005). Fission-track length and age data were used as input. For all models, Ketcham et al. (2007) annealing model was employed and the Dpar was chosen as kinetic parameter. For sample TU486 it was possible to model AFT and AHe data together. In that case, two replicates (out of four) have been integrated singularly into the model, choosing the two youngest grains because of their concordance. The RDAAM kinetic model (Flowers et al., 2009) was employed for AHe modelling, with alpha correction according to Ketcham et al. (2011). All relevant geological constraints (intrusion/depositional ages, independent geochronological ages, stratigraphic relationships) were incorporated into the modelling. These constraints are shown as rectangles in the time-temperature plots (Figs. 5, 6, 7 and 8). If no clear-cut information was available, we used broad t-T boxes in order to avoid any forcing. Specific parameters and constraints used for each modelling, compiled according to the protocol of Flowers et al. (2015), are reported in Table S1 (Supplementary Materials).

4. Analytical results

Tables 1 and 2 and Fig. 2 provide a summary of the AFT and AHe dataset. The majority (>86%) of the AFT central ages cluster between 47 and 27 Ma (Middle Eocene-Early Oligocene; Table 1). There are only two outliers with respect to this trend: samples TU481 from the ATFTB and TU354 from the Khrami Massif, which yielded central ages of 15.2 ± 2.7 (Miocene) and 65.2 ± 1.3 Ma (Early Paleocene), respectively. All samples passed the χ^2 statistical test indicating a single population of grains. There is no correlation between sample ages and elevations (Table S3).

Apatite (U-Th)/He data are shown in Table 2, including single-grain ages of the replicates and the error-weighted mean ages. Error-weighted mean ages (henceforth mean ages) are shown in Fig. 2. Clearly, the mean age is representative only if single-grain age dispersion is low.

AHe mean ages range from 9.5 ± 0.2 (Late Miocene) to 3.7 ± 0.02 Ma (Pliocene) and single-grain ages from 17.3 to 2.6 Ma (Middle Miocene to Pliocene). Generally, the dispersion of single-grain ages is low, except for TU486 (~17 to 4 Ma). Single-grain ages of this sample increase with grain radius (although not linearly, Table 1), which could explain the overdispersion. An alternative explanation could be the presence of micro-inclusions of U-rich phases in the oldest crystals which were not recognized during picking. Results from two replicates were discarded: replicate TU486-2 due to a very low eU value coupled with negative count of ^{235}U ppm and replicate TU499-1 due to a negative age. None of the samples analysed showed any clear correlation between crystals age and eU, grain radius (apart from TU486), U or Th content (Table S2a–f). There is no relationship between age and elevation (Table S3).

AFT central ages provide meaningful information from a geological viewpoint if the sample experienced fast cooling through the PAZ but can be misleading if the sample resided within the PAZ for a long time or has experienced moderate reheating at temperatures lower than 120 °C. More complete thermochronological constraints can be obtained through statistical modelling of fission-track length distributions. Similarly, AHe ages can be biased by a long residence time within the PRZ as

Table 1
Results of apatite fission-track analyses (see Fig. 2 for location of samples).

Sample	Rock Type	Age	Location	Elevation (m)	UTM Coordinates	No. crystals	Spontaneous		Induced		P(χ^2)	Dosimeter		Age (Ma) ± s.d.	MCTL (μm) ± standard error	Standard deviation	No. tracks measured	Dpar
							ρ_s	N_s	ρ_i	N_i		ρ_d	N_d					
TU278[a]	Granite	Late Paleozoic	Dzirula Massif	867	38 T 0374158 4658977	14	2.17	36	1.03	879	50.30	14.00	4459	46.9 ± 5.2	–	–	–	–
TU279[a]	Syenite	Middle Eocene	Western ATFTB	334	38 T 0260294 4641212	17	4.99	262	3.27	1716	95.52	13.00	4438	33.1 ± 2.7	13.41 ± 0.12	1.43	50	2.10
TU281[a]	Diorite	Middle Eocene	Western ATFTB	376	37 T 0747431 4607962	8	1.73	37	1.91	409	99.19	10.01	4298	15.2 ± 2.7	–	–	–	–
TU282[a]	Sandstone	Paleocene	Central ATFTB	813	38 T 0368846 4636796	14	1.34	76	0.70	197	58.30	14.00	4432	37.5 ± 5.6	–	–	–	–
TU354[b]	Granitoid	Late Paleozoic	Khrami Massif	1524	38 T 0426185 4599082	21	3.40	175	1.09	540	99.83	9.80	4491	65.2 ± 1.3	–	–	–	–
TU486	Sandstone	latest Paleocene-Early Eocene	Eastern ATFTB	883	38 T 0456357 4599540	49	0.14	290	0.81	1691	99.68	12.22	7638	34.7 ± 2.8	12.05 ± 0.22	1.66	53	2.38
TU487	Sandstone	Late Eocene	Eastern ATFTB	932	38 T 0452684 4611098	38	0.10	107	0.69	725	99.56	12.15	7593	29.3 ± 3.4	–	–	–	2.51
TU488	Sandstone	Late Oligocene	Eastern ATFTB	1391	38 T 0452009 4616299	41	0.14	192	1.05	1393	99.44	12.07	7547	27.3 ± 2.5	12.48 ± 0.31	2.26	53	2.36
TU489	Sandstone	Late Eocene	Eastern ATFTB	1291	38 T 0461429 4612640	13	0.09	36	0.53	224	97.20	12.00	7502	31.9 ± 5.9	–	–	–	2.35
TU490	Sandstone	Late Eocene	Eastern ATFTB	1322	38 T 0472584 4613551	18	0.14	55	0.58	231	99.97	9.73	5046	35.5 ± 5.6	–	–	–	2.46
TU501	Sandstone	Middle Eocene	Eastern ATFTB	561	38 T 0476497 4631400	88	0.16	574	0.64	2320	99.35	11.78	7366	45.3 ± 3.1	–	–	–	2.68
TU504	Sandstone	Oligocene-Early Miocene	Kura Basin	396	38 T 0500933 4602375	61	0.15	333	0.81	1770	99.98	11.64	7276	34.2 ± 2.6	–	–	–	2.56
TU505	Sandstone	Late Eocene	Eastern ATFTB	512	38 T 0500906 4615010	48	0.24	270	1.17	1307	97.99	11.57	7230	37.6 ± 3.1	–	–	–	2.30
TU510	Sandstone	Late Eocene	Central ATFTB	1022	38 T 0343226 4618483	56	0.28	361	1.14	1473	99.80	11.42	7140	46.0 ± 3.5	13.03 ± 0.30	2.29	58	2.50
TU515	Gneiss-diorite	Precambrian-Early Paleozoic	Khrami Massif	985	38 T 0431453 4600622	21	0.55	288	2.37	1242	37.65	11.35	7094	43.6 ± 3.7	13.72 ± 0.21	1.69	65	2.12

ATFTB = Adjara-Trialeti fold-and-thrust belt. MCTL = mean confined tracks length. Central ages are calculated using dosimeter U-free mica CN5 as external detector and $\zeta = 332.68 \pm 16.54$ (analyst T. Gusmeo); ρ_s = spontaneous track densities (x 10^5 cm^{-2}) measured in internal mineral surfaces; Ns = total number of spontaneous tracks; ρ_i and ρ_d = induced and dosimeter track densities (x 10^6 cm^{-2}) on external mica detectors (g = 0.5); N_i and N_d = total number of induced and dosimeter tracks; P(χ^2) = probability of obtaining χ^2-value for n degrees of freedom (n = number of crystals-1): a probability >5% is indicative of a homogeneous population.

[a] Ages from Albino et al. (2014) (analyst I. Albino).

[b] Age from Cavazza et al. (2019) (analyst I. Albino).

Table 2
Results of apatite (U-Th)/He analyses (see Fig. 2 for location of samples).

Sample	Rock Type	Age	Elevation (m)	UTM Coordinates (38 T)	Replicate	Corrected age (Ma)	Error (Ma)	Error Weigthed Age (Ma)	Weighted Error (Ma)	^{4}He (mol)	U 238 (ppm)	U 235 (ppm)	Th 232 (ppm)	Sm 147 (ppm)	eU	Rs (equivalent radius, µm)
TU485	Sandstone	Early Eocene	889	0472357 4609370	TU 485–1	5.37	0.05	3.7	0.02	$8.47*10^{-15}$	8.68	0.07	69.94	39.25	25.12	44.75
					TU 485–2	3.58	0.04			$6.59*10^{-15}$	19.87	0.16	81.87	35.89	39.11	42.75
					TU 485–3	2.58	0.03			$7.95*10^{-15}$	33.50	0.27	288.22	81.36	101.24	38.51
					TU 485–4	8.24	0.09			$1.05*10^{-14}$	14.72	0.12	50.43	15.33	26.58	42.55
					TU 485–5	7.26	0.08			$7.21*10^{-15}$	9.38	0.09	61.75	43.71	23.90	46.95
TU486	Sandstone	latest Paleocene-Early Eocene	883	0456357 4599540	TU 486–1	5.93	0.18	6.1	0.1	$4.96*10^{-15}$	10.16	0.09	23.87	24.08	15.77	46.88
					TU486–2	*9.58*	*0.22*			*$8.89*10^{-15}$*	*2.0*	*−1.3*	*15.6*	*0.9*	*5.7*	*42.10*
					TU 486–3	17.32	0.16			$4.69*10^{-14}$	10.10	0.08	24.19	10.84	15.78	55.53
					TU 486–4	13.62	0.20			$1.58*10^{-14}$	10.16	0.09	40.19	19.82	19.60	47.58
					TU 486–5	4.08	0.06			$4.55*10^{-15}$	10.62	0.09	65.57	43.20	26.03	41.83
TU487	Sandstone	Late Eocene	932	0452684 4611098	TU 487–1	10.81	0.63	6.4	0.1	$4.53*10^{-15}$	6.91	0.08	39.88	29.50	16.28	38.85
					TU 487–2	5.80	0.06			$1.05*10^{-14}$	17.46	0.14	79.57	75.61	36.16	45.53
					TU 487–3	7.31	0.18			$2.67*10^{-15}$	9.20	0.10	37.49	16.87	18.01	36.91
					TU 487–4	5.10	0.13			$3.13*10^{-15}$	16.15	0.15	64.32	54.55	31.27	35.21
					TU 487–5	8.41	0.10			$1.33*10^{-14}$	16.19	0.13	54.02	42.30	28.88	96.94
TU499	Sandstone	Early Eocene	1338	0445544 4631754	*TU 499–1*	*−8.61*	*−0.20*	9.5	0.2	*$-1.22*10^{-15}$*	*2.61*	*0.13*	*21.86*	*1.07*	*7.75*	*37.96*
					TU 499–2	8.85	0.24			$1.02*10^{-15}$	3.46	0.10	20.17	1.87	8.20	37.87
					TU 499–3	10.18	0.24			$1.34*10^{-15}$	6.77	0.15	40.35	11.07	16.25	32.19
TU501	Sandstone	Middle Eocene	561	0476497 4631400	TU 501–1	5.89	0.06	6.5	0.04	$1.13*10^{-14}$	11.67	0.09	44.51	44.45	22.13	53.27
					TU 501–2	9.95	0.16			$5.81*10^{-15}$	8.63	0.08	40.63	29.07	18.17	39.50
					TU 501–3	8.74	0.10			$1.24*10^{-14}$	12.88	0.11	68.94	27.90	29.08	44.97
					TU 501–4	6.86	0.20			$2.08*10^{-15}$	7.30	0.09	34.11	26.01	15.32	37.75
					TU 501–5	5.46	0.07			$3.26*10^{-15}$	11.41	0.11	58.72	32.88	25.21	38.48
TU512	Sandstone	Late Paleocene-Early Eocene	833	0363775 4631968	TU 512–1	11.73	0.16	4.1	0.03	$1.38*10^{-14}$	5.86	0.05	18.99	16.72	10.32	53.21
					TU 512–2	4.37	0.10			$1.61*10^{-15}$	8.17	0.09	43.50	19.42	18.39	36.37
					TU 512–3	9.84	0.17			$1.10*10^{-14}$	7.34	0.06	21.56	19.44	12.40	52.12
					TU 512–4	3.17	0.04			$1.96*10^{-14}$	34.19	0.26	37.23	26.06	42.94	61.11
					TU 512–5	9.56	0.28			$1.64*10^{-14}$	8.13	0.07	24.77	13.85	13.96	57.68

For each sample, corrected ages with relative error of each replicate are shown, and the weighted mean age is also reported. The effective uranium value (eU = [U] + 0.235*[Th]) gives an indication of the goodness of the data: if it is lower than 5, than the uranium content of the apatite crystal was too low to provide a meaningful result. The two discarded replicates (TU486-2 and TU499-1) are in italics.

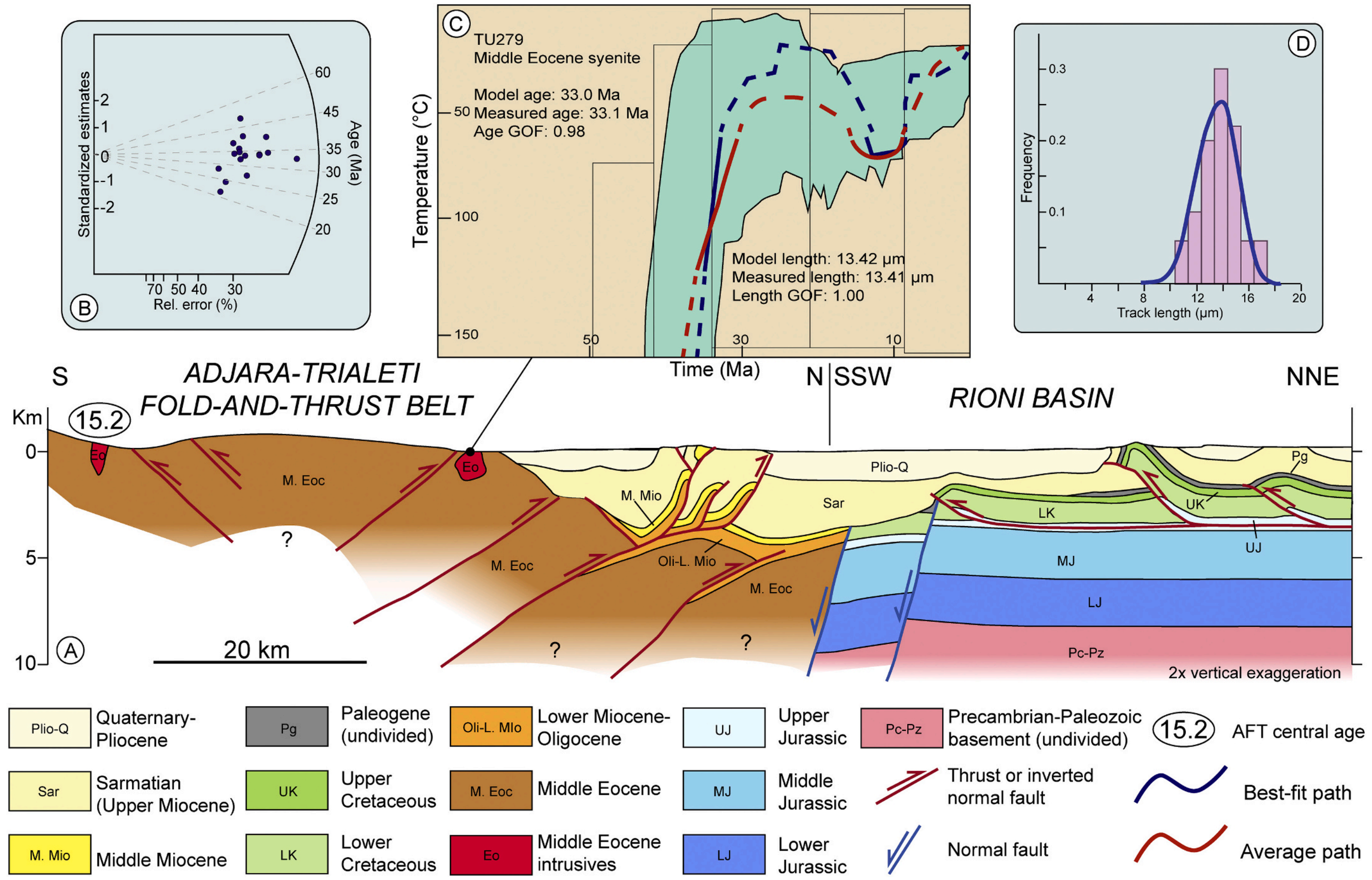

Fig. 5. A) Schematic geological cross-section across the western sector of the Adjara-Trialeti fold-and-thrust belt and the Rioni Basin (after Tari et al., 2018). See Fig. 2 for location. B) Radial plot of single-grain AFT ages; C) Time-temperature paths obtained from inverse modelling of sample TU279. Green area marks the envelope of all thermal histories that have a good (>0.5) fit with the data, red line represents the mean of all good paths, and blue line is the best-fit time-temperature path. Parameters related to inverse modelling are reported: GOF, goodness-of-fit, gives an indication about the fit between observed and predicted data (values closer to 1 are best); D) Confined-track length frequency distribution of apatite grains. (For interpretation of the references to colour in this figure legend, the reader is referred to the web version of this article.)

well as by different He diffusion kinetics. In order to obtain rigorous results, time-temperature modelling was performed integrating all available new and pre-existing data: AFT, (U-Th)/He, other radiometric analyses and stratigraphic relationships. In the following section, the thermochronologic results obtained for the ATFTB and for the Dzirula and Khrami basement salients will be described specifically and interpreted according to their geological context.

5. Data interpretation

5.1. Adjara-Trialeti fold-and-thrust belt

AFT central ages from the ATFTB range from 46 to 15 Ma (Middle Eocene-Middle Miocene). Such a relatively long time span from a geologically coherent tectonic element such as the ATFTB depends on the fact that most sandstone samples were never buried enough to reset completely the AFT system. Apatite grains from sedimentary rocks now incorporated within the ATFTB have thus retained a partial memory of the cooling/exhumation history of the original sediment source area. The high P(χ^2) values (Table 1), corroborated by a check with the binomial peak-fitting program BinomFit (Brandon, 1992), confirm that the samples contain only one population of apatite grains. Partially to non-reset detrital samples containing a single population of grains indicate that they were fed by one thermally coherent source. This point, and its implications for the interpretation of the thermochronologic history of the ATFTB, are discussed below.

AHe ages are consistent, clustering between 10 and 3 Ma, with few outliers. Given the lower closure temperature of the apatite (U-Th)/He thermochronometric system (~70 °C), this implies that the re-heating associated with post-depositional sedimentary burial was enough to reset the helium ages. The Late Miocene-Pliocene He ages suggest fast cooling across the partial retention zone (PRZ) of apatite (ca. 40–70 °C). Following are the low-temperature thermochronology results from the various portions of the ATFTB.

5.1.1. Western Adjara-Trialeti fold-and-thrust belt

Several samples were taken from this area but, after processing, only two of them had enough apatite grains. Sample TU279 is a Middle Eocene (43 Ma; U–Pb on zircons, Okrostsvaridze et al., 2018b) syenite (Figs. 2 and 5). Fission-track analysis yielded a central age of 33.1 ± 2.7 Ma and a mean confined tracks length of 13.41 ± 0.12 μm (Table 1). Track-length distribution is fairly leptokurtic and nearly symmetrical (Fig. 5D). Inverse modelling (Fig. 5C, Table S1a) shows a Middle-to-Late Eocene phase of cooling. This is in line with the commonly held notion that mid-Eocene volcanism and plutonism were largely coeval during the development of the Adjara-Trialeti extensional basin (e.g. Okrostsvaridze et al., 2018a and references therein). The small pluton from which the sample was taken was emplaced at a shallow depth where it cooled quickly, then experienced rather stable temperatures during the Oligocene, minor reheating during the Early-Middle Miocene, and a discrete and fast phase of most likely tectonic cooling/exhumation (see discussion below), starting at around 10 Ma (early Late Miocene).

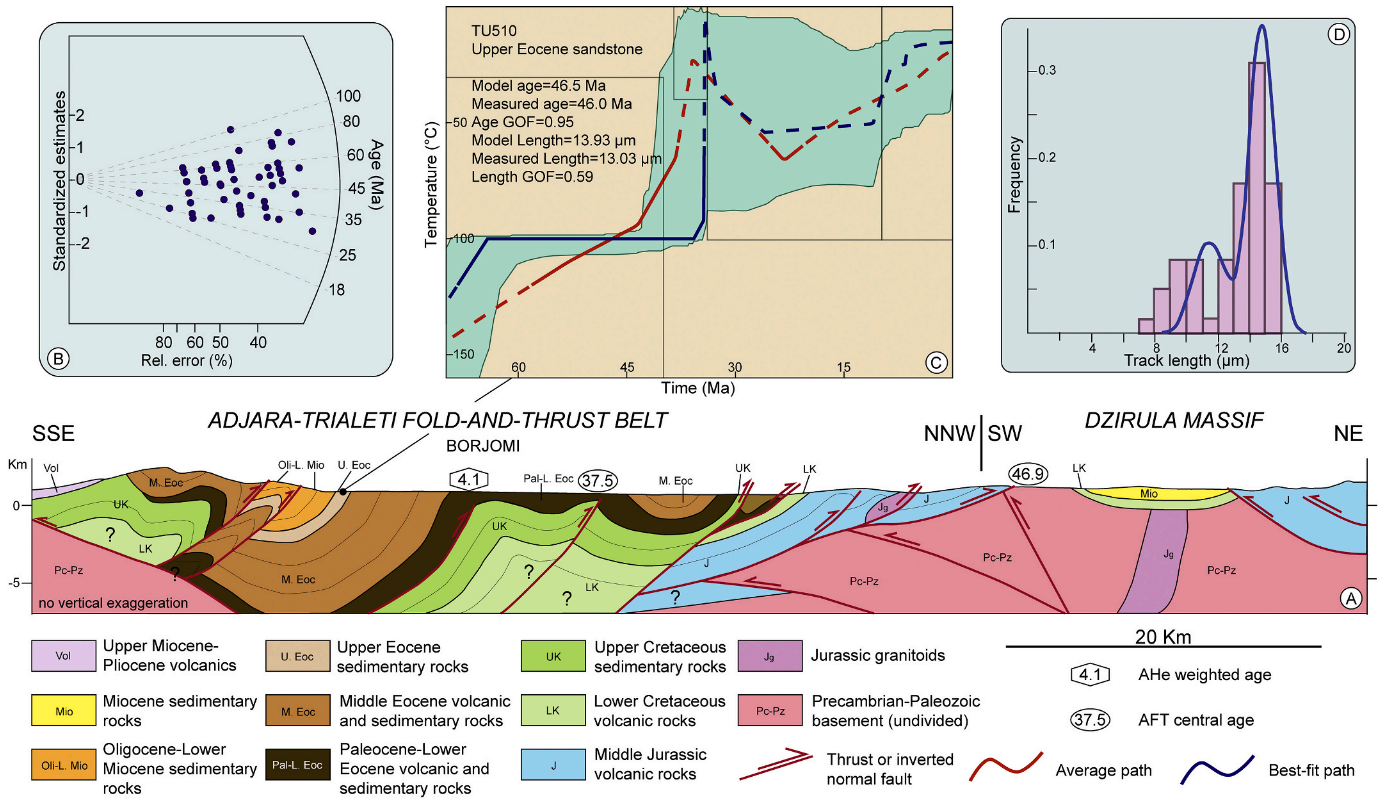

Fig. 6. A) Schematic geological cross-section across the central part of the Adjara-Trialeti fold-and-thrust belt and the Dzirula Massif, modified after Banks et al. (1997). See Fig. 2 for location. B) Radial plot of single-grain AFT ages; C) Time-temperature paths obtained from inverse modelling of sample TU510. Green area marks the envelope of all thermal histories that have a good (>0.5) fit with the data, red line represents the mean of all good paths, and blue line is the best-fit time-temperature path. Parameters related to inverse modelling are reported: GOF, goodness-of-fit, gives an indication about the fit between observed and predicted data (values closer to 1 are best); D) Confined-track length frequency distribution of apatite grains. (For interpretation of the references to colour in this figure legend, the reader is referred to the web version of this article.)

Sample TU281 is a Middle Eocene diorite, ~35 km south of sample TU279, yielding a central age of 15.2 ± 2.7 Ma, by far the youngest central age of the entire dataset. Zircon U–Pb dating provided the same age as sample TU279, about 43 Ma (Okrostsvaridze et al., 2018b). The Middle Miocene AFT central age of sample TU281 is in line with those available nearby for the easternmost Pontides just across the Turkish border, where mid-Miocene shortening exhumed analogous Eocene plutons (e.g. Kackar Mts.) and brought them to elevations up to ca. 4000 m (Cavazza and Zattin, 2015).

5.1.2. *Central Adjara-Trialeti fold-and-thrust belt*

Several samples were collected in the antecedent drainage of the Kura River along the Borjomi Valley and in the adjacent areas. Only three of them yielded enough apatite grains for analysis (Figs. 2 and 6; Tables 1 and 2). Sample TU282 is a Paleocene turbidite sandstone (Borjomi Flysch), collected northeast of the town of Borjomi, which yielded a fission-track central age of 37.5 ± 5.6 Ma. Sample TU512 is a sandstone at the Paleocene-Eocene boundary close to Borjomi. It did not contain enough apatites for fission-track analysis, but it was analysed with the helium method. Five replicates from this samples provided corrected helium ages ranging between 11 and 3 Ma, indicating that this sample cooled across the He partial retention zone of apatite in the Late Miocene-Pliocene.

Sample TU510 is an Upper Eocene sandstone (about 20 km SW of sample TU512). It yielded a central age of 46.0 ± 3.5 Ma and a mean confined tracks length of 13.03 ± 0.30 µm (Table 1). Track-length frequency distribution is bimodal. Inverse modelling, integrating fission-track data and stratigraphic age (Table S1d), indicates some degree of post-depositional reheating (as suggested by the track-length distribution, Fig. 6D). The exact timing of the last episode of cooling is poorly constrained because the sample has not been reheated enough to be reset.

5.1.3. *Eastern Adjara-Trialeti fold-and-thrust belt*

A number of analyses of various samples has provided a fairly detailed picture of the thermochronological evolution of this area. Sample TU499 is a Lower Eocene sandstone from the frontal, northeastern sector of the orogen (Figs. 2 and 7). (U-Th)/He analysis of this sample provided corrected ages of 10 and 8 Ma. The low age dispersion indicates that this sample cooled quickly through the He Partial Retention Zone in the Late Miocene.

Sample TU501 is an Upper Eocene sandstone located at the northeastern border of the ATFTB, close to the town of Mtskheta. It provided an AFT central age of 45.3 ± 3.1 Ma (Middle Eocene; Figs. 2 and 7), older than the depositional age. Corrected helium ages from five replicates range from 10 to 5 Ma, with a mean age of 6.5 ± 0.04 Ma. Helium single-grain ages are relatively well clustered and indicate cooling through the PRZ in the Late Miocene, while the fission-track central age reflects the age of exhumation of the rocks feeding detritus to the Adjara-Trialeti basin.

Sample TU488 is an Upper Oligocene sandstone taken close to the town of Manglisi (Fig. 2). It yielded a central age of 27.3 ± 2.5 Ma and a significant number of measurable confined tracks, with a mean length of 12.48 ± 0.31 µm (Table 1). Track-length frequency distribution is bimodal (Fig. 7D). Inverse modelling integrating depositional age and fission-track data (Table S1c) shows pre-depositional cooling during the Eocene-Early Oligocene, moderate post-depositional heating during progressive burial in the Early Miocene and very fast cooling starting in

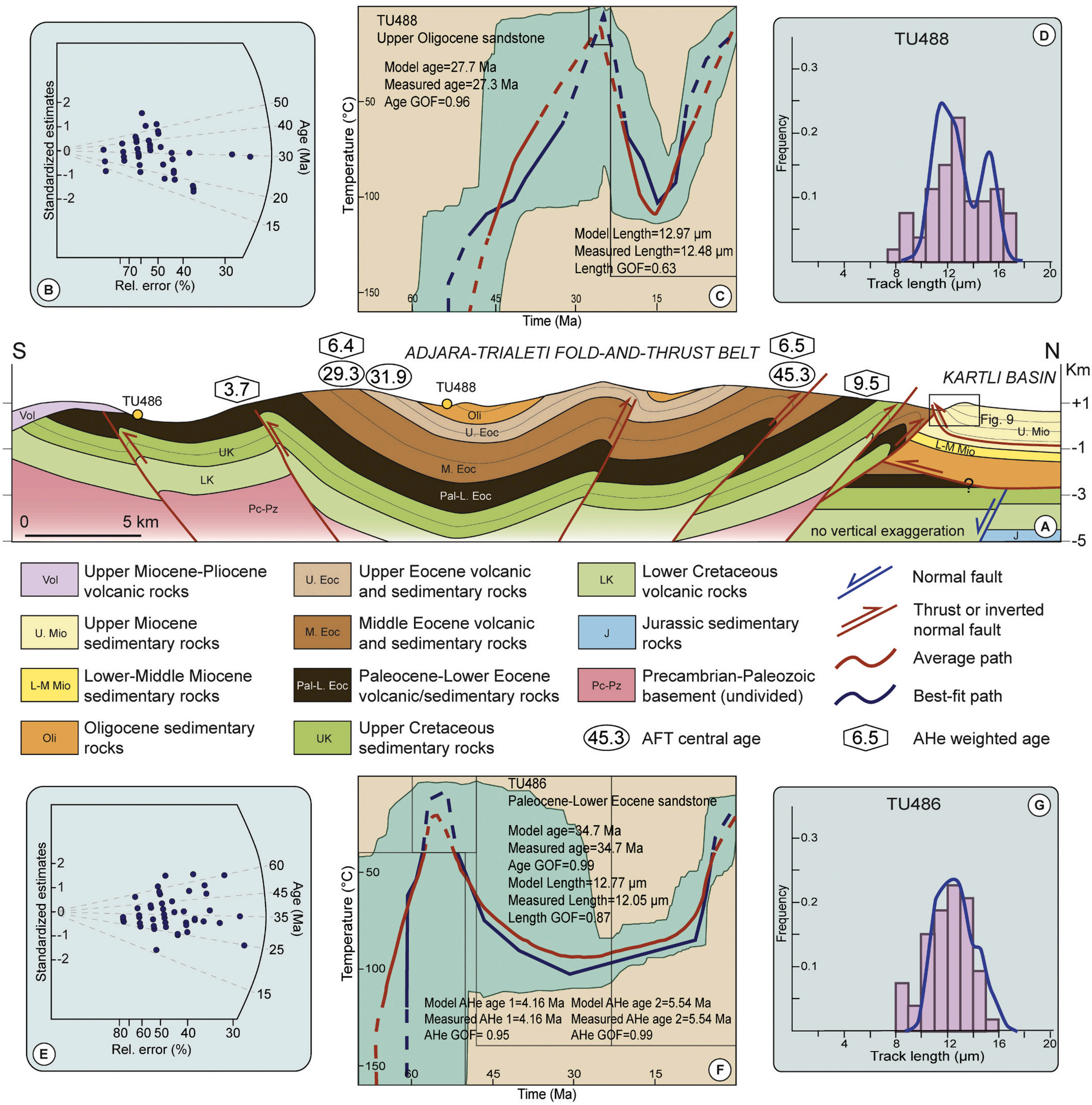

Fig. 7. A) Schematic geological cross-section across the eastern sector of the Adjara-Trialeti fold-and-thrust belt, interpreted from seismic and surface data. See Fig. 2 for location. B) Radial plot of single-grain AFT ages of sample TU488; C) Time-temperature paths obtained from inverse modelling of sample TU488. Green area marks the envelope of all thermal histories that have a good (>0.5) fit with the data, red line represents the mean of all good paths, and blue line is the best-fit time-temperature path. Parameters related to inverse modelling are reported: GOF, goodness-of-fit, gives an indication about the fit between observed and predicted data (values closer to 1 are best). D) Confined-track length frequency distribution of apatite grains of sample TU488; E) Radial plot of single-grain AFT ages of sample TU486; F) Time-temperature paths obtained from inverse modelling of sample TU486; G) Confined-track length frequency distribution of apatite grains of sample TU486. (For interpretation of the references to colour in this figure legend, the reader is referred to the web version of this article.)

the Middle Miocene (14–13 Ma; Fig. 7C).

Five other samples from the eastern ATFTB were analysed but did not yield a sufficient number of confined tracks for inverse modelling. Sample TU487 is an Upper Eocene sandstone which yielded a AFT central age of 29.3 ± 3.4 Ma and AHe corrected ages between 10 and 5 Ma. This rock cooled through the He PRZ of apatite in the Late Miocene and experienced a thermal history similar to the ones of samples TU488 and TU486 (see below and Fig. 7).

Sample TU489 is an Upper Eocene sandstone that yielded a central age of 31.9 ± 5.9 Ma. Sample TU490 is an Upper Eocene sandstone collected at Mount Didgori and yielded a AFT central age of 35.5 ± 5.6 Ma. Sample TU504 is an Oligocene-Lower Miocene sandstone which yielded a fission-track central age of 34.2 ± 2.6 Ma. Sample TU505 provided an apatite fission-track central age of 37.6 ± 3.1 Ma. Samples

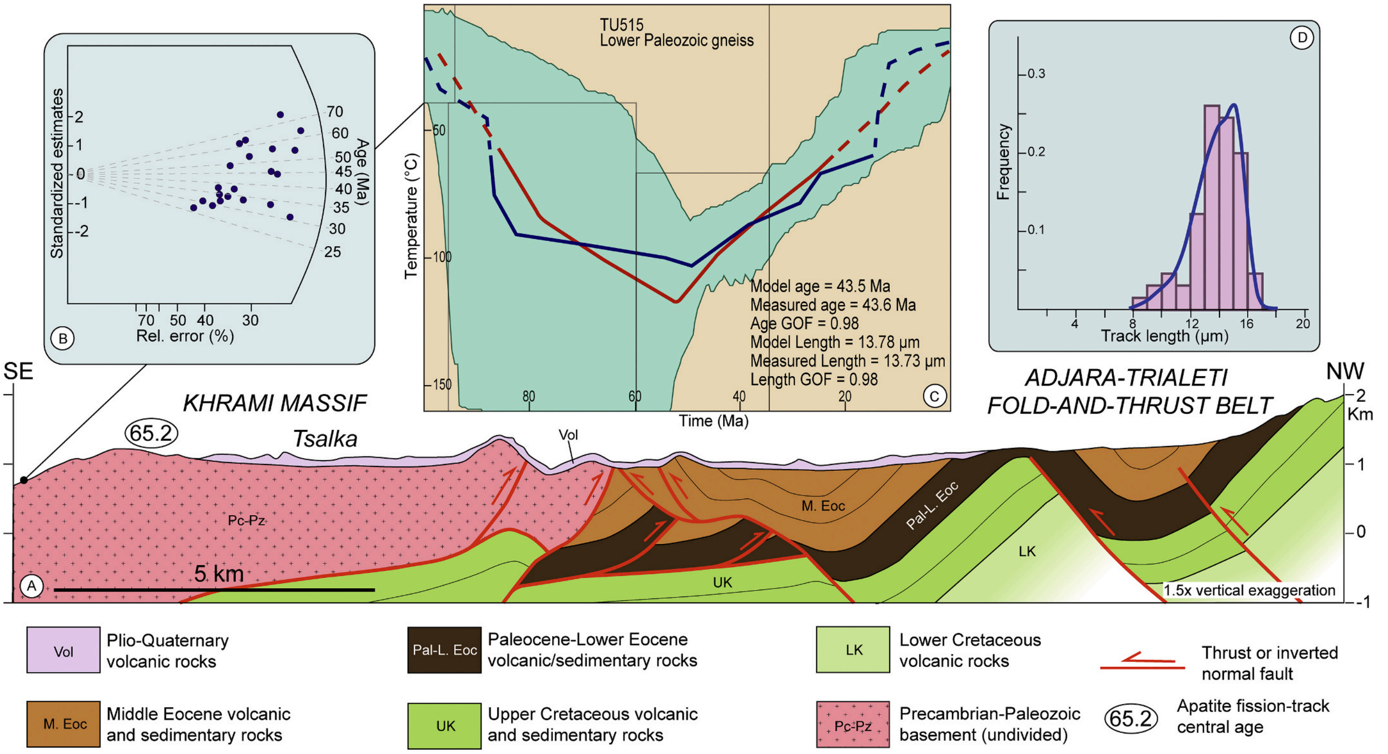

Fig. 8. A) Schematic geological cross-section across the Khrami Massif and the southern Adjara-Trialeti fold-and-thrust belt. See Fig. 2 for location. B) Radial plot of single-grain AFT ages; C) Time-temperature paths obtained from inverse modelling of sample TU515. Green area marks the envelope of all thermal histories that have a good (>0.5) fit with the data, red line represents the mean of all good paths and blue line is the best-fit time-temperature path. Parameters related to inverse modelling are reported: GOF, goodness-of-fit, gives an indication about the fit between observed and predicted data (values closer to 1 are best); D) Confined-track length frequency distribution of apatite grains. (For interpretation of the references to colour in this figure legend, the reader is referred to the web version of this article.)

TU504 and TU505 were collected from the easternmost portion of the ATFTB, east of Tbilisi (Fig. 2).

Sample TU485 is a Lower Eocene sandstone collected close to the town of Asureti (Figs. 2 and 7). Corrected AHe ages obtained from five replicates range from 8 to 2 Ma, indicating that this sample cooled across the PRZ in Late Miocene-Pliocene times.

Sample TU486 is a sandstone dated at the Paleocene-Eocene boundary from the southern border of eastern ATFTB (Figs. 2 and 7). It yielded a central age of 34.7 ± 2.8 Ma and a mean confined tracks length of 12.05 ± 0.22 µm. Track-length frequency distribution is platykurtic (Fig. 7G). Corrected AHe ages from four replicates range from 17 to 4 Ma. The reconstructed t-T path of this sample is similar to that of sample TU488, ca. 20 km to the north (modelling details in Table S1b). Integration of fission-track, helium, and stratigraphic data defines a post-depositional t-T path characterized by moderate burial during the Eocene-Early Oligocene followed by very rapid cooling starting at about 10 Ma (Fig. 7F). The pre-depositional history, although far from clear, points to cooling/exhumation of the sediment source area in the Paleocene-Early Eocene.

5.2. Dzirula Massif

Sample TU278 is a Variscan granite from the eastern side of the Dzirula Massif (Figs. 2 and 6), a Neoproterozoic gneiss-migmatitic complex associated with Lower Paleozoic ophiolites intruded and metamorphosed in the Carboniferous by Variscan granitoids (Adamia et al., 2011; Banks et al., 1997). This sample yielded an AFT central age of 46.9 ± 5.2 Ma. The number of horizontally confined tracks was insufficient to perform inverse modelling, hence we can only make suppositions about the significance of this central age, based on geological constraints and other thermochronological data from the literature.

The Dzirula metamorphic salient had already been at the surface in the Mesozoic, as shown by (i) thin mid-Jurassic volcanics and Lower Cretaceous sedimentary rocks nonconformably overlying the basement complex and unconformably separated one from the other (Adamia et al., 2011; Banks et al., 1997; Mayringer et al., 2011; Rolland et al., 2016) and (ii) the results of AFT thermochronometric modelling indicating that the Dzirula basement rocks cooled at temperatures below 60 °C in the Late Triassic-Late Jurassic (Vincent et al., 2011). The massif was exhumed again during the Paleogene (Vincent et al., 2011). Stratigraphic relationships (Adamia et al., 2011; Banks et al., 1997) indicate that this latter exhumation event occurred sometime between the Middle Paleocene and the Middle Oligocene. The mid-Eocene central age of sample TU278 might be the result of such a cooling event. The presence of a thin (200-400 m) succession of Oligocene-Lower Miocene sandstones and shales unconformably overlying all older units shows that the Dzirula basement complex was exposed at the surface by Late Oligocene time.

5.3. Khrami Massif

Sample TU354 is a Late Paleozoic granitoid from the western border of the massif, yielding an AFT central age of 65.2 ± 1.3 Ma (Figs. 2 and 8). Sample TU515 is a Lower Paleozoic dioritic gneiss (Tedliashvili, 2013) from a migmatitic complex in the central portion of the salient which yielded a central age of 43.6 ± 3.7 Ma and a mean confined tracks length of 13.72 ± 0.21 µm. Its track-length frequency distribution is platykurtic, showing a long tail of short tracks (Fig. 8D). This distribution indicates a long residence in the partial annealing zone and slow cooling. Inverse modelling of this sample integrated fission-track data and stratigraphic data (Fig. 8C, Table S1e). This sample was close to the surface in Cenomanian times, based on Cenomanian sediments onlapping nonconformably the massif. About 2000–2500 m of Upper Cretaceous-Lower Paleocene limestones and volcanics were then deposited on the basement (Adamia et al., 2017b, 2011, 1992). The reconstructed time-temperature path shows such burial heating followed by slow, steady-state cooling starting in the early Eocene at 55–50 Ma (Fig. 8C). Although perfectly in tune with our results in the ATFTB, the pulse of fast cooling in the best-fit path in the Miocene is unreliable because it is outside the partial annealing zone of apatite (60–120 °C), hence beyond the resolution limit of the method.

6. Discussion

6.1. Timing of Adjara-Trialeti structural inversion

The thermochronologic results show that the Adjara-Trialeti back-arc basin underwent cooling related to orogenic exhumation starting from the late Middle Miocene. Independent stratigraphic and structural evidence points consistently to a Middle-Late Miocene inception of deformation: (i) growth-strata geometries, structural relationships, and the overall stratigraphy of the adjacent Rioni, Kartli and Kura basins, both in outcrop and in the subsurface (Alania et al., 2017, 2018; Tari et al., 2018); (ii) deformation in the Gurian fold belt, the offshore equivalent of the Adjara-Trialeti orogenic belt in the Eastern Black Sea (Banks et al., 1997; Robinson et al., 1995b; Tari et al., 2018), and along the Georgia-Armenia border at the contact between the ATFTB and the easternmost Anatolian Plateau (Koçyiğit et al., 2001).

The progressive unconformity west of Mtskheta (Fig. 9), in the Kartli foreland basin, bears witness to syntectonic sedimentation in the Late Miocene. This structure is just north of the frontal surface thrust of the ATFTB, which exposes here overturned Middle Eocene volcaniclastic rocks. At this location, Sarmatian (late Middle-to-Late Miocene) shallow marine sediments show an offlap geometry, with dip of beds becoming progressively gentler moving from south to north, and are overlain in onlap by sub-horizontal Meotian-Pontian (latest Miocene) shallow marine-to-continental sediments. Similar structures are present elsewhere (Alania et al., 2018, 2017) and record the progressive incorporation of the foreland basin proximal portion in the wedge-top depozone (DeCelles and Giles, 1996) in response to the progressive northward advancement of the ATFTB in the Late Miocene.

The vast majority of the Oligocene-to-Middle Miocene sedimentary section of the southern Rioni, Kartli and Kura foreland basins - which have later subsided in response to the progressive growth of the Adjara-Trialeti orogen and have collected the detritus deriving from it - is mostly made of fine-grained siliciclastic rocks. Deposition of coarse-grained syntectonic sandstones and conglomerates, suggesting the proximity of a growing orogenic prism to the south, started from the Late Sarmatian (ca. 10–8 Ma) (Adamia et al., 2010, 2011; Pupp et al., 2018; Sachsenhofer et al., 2018; Tari et al., 2018).

Seismic lines from the Gurian belt offshore western Georgia show a series of northward imbricated blind thrusts flooring into the Maykopian (Oligocene-Lower Miocene) shales and evaporites (Banks et al., 1997). Dramatic thickness variations and synkinematic geometries occur within the Sarmatian section, whereas the overlying Meotian-Pontian section drapes all older structures (Tari and Simmons, 2018).

Further evidence of Miocene tectonism is found along the Georgia-Armenia border. Here, a thick succession dominated by shallow-marine and fluvio-lacustrine sediments of Late Eocene-Early Miocene age is overlain in angular unconformity by a > 500 m thick Late Miocene-Early Pliocene volcano-sedimentary sequence consisting of various volcanic rocks alternating with fluvio-lacustrine deposits, preceded by basal conglomerates (Koçyiğit et al., 2001).

Our results are in agreement with paleoenvironmental reconstructions, based on foraminifera and pollen, which indicate that until the Early Sarmatian the region comprised between the Lesser Caucasus to the south and the Greater Caucasus to the north (commonly referred to as Transcaucasia) was covered by the sea. Since the Middle Sarmatian (ca. 10 Ma) this region became emerged and the connection between the Black Sea and the Caspian Sea was definitely interrupted (Fig. 4), with marine conditions persisting only in the easternmost and westernmost parts of the Kura and Rioni Basin, respectively (Shatilova et al., 2020).

6.2. Cooling history of the Khrami and Dzirula massifs

The thermochronometric histories of the Dzirula and Khrami massifs are significantly different from that of the Adjara-Trialeti back-arc basin. Integrated thermochronological modelling from the Khrami Massif south of the ATFTB indicates prolonged but shallow burial heating at ca. 100–60 Ma due to the deposition of the Late Cretaceous section overlying nonconformably the massif. This phase of burial was followed by cooling/exhumation starting in the Early Eocene (Fig. 8). At the surface, the Khrami Massif is largely concealed by a cover of Pliocene volcanic rocks but industrial seismic lines show that the massif is the surficial expression of an out-of-sequence, north-vergent basement thrust sheet overlying a structural duplex made of Jurassic-Cretaceous rocks (Alania et al., in prep.). Such an out-of-sequence thrust can be related to Paleocene continental accretion along the Erzinçan-Sevan-Akera suture to the south (e.g. Barrier et al., 2018; Okay and Tüysüz, 1999; Sosson et al., 2010, 2016). Early Eocene, shortening-related cooling of the

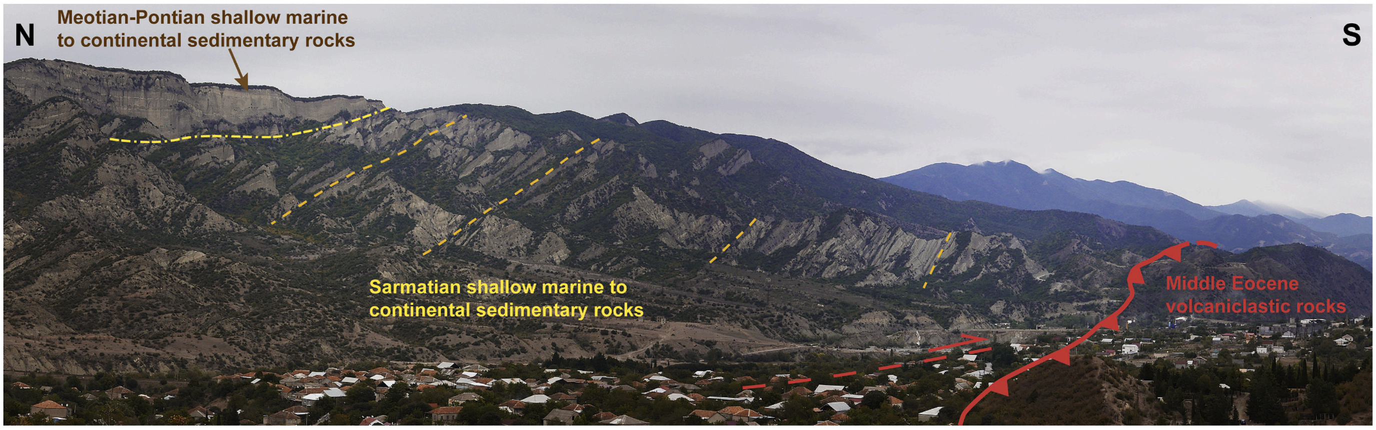

Fig. 9. Progressive unconformity in the Kartli foreland basin, west of Mtskheta (see Figs. 2 and 7 for location). Sarmatian (late Middle Miocene) shallow marine sediments show an offlap geometry and are onlapped by Meotian-Pontian (latest Miocene) mostly continental sediments, indicating active tectonics during the Middle and Late Miocene.

Khrami Massif occurred soon before the main phase of rift-related subsidence and burial heating of the Adjara-Trialeti back-arc basin fill in the Middle Eocene. Such a situation is characteristic of the hinterland of converging continental margins, where phases of orogenic shortening (including thick-skinned tectonics) along the retroarc fold-and-thrust belt and back-arc extension can alternate and partially overlap in space and time (e.g. Horton et al., 2016).

The Dzirula Massif basement complex cooled at temperatures below 60 °C in the Late Triassic-Late Jurassic. The massif was exhumed again between the Middle Paleocene and the Middle Oligocene (Vincent et al., 2011), arguably in the Middle Eocene, as suggested by our data (Table 1; Fig. 6). If this were the case, the basement salient should have been affected by cooling while the basin was experiencing subsidence and burial heating. The Dzirula Massif can be tentatively regarded as a portion of the rift shoulders of the former Adjara-Trialeti back-arc basin, because of its position along the northern margin of the ATFTB and because the reconstructed thermal evolution does not support the notion of an Eocene-Oligocene burial/heating, as one would expect if the massif were involved in rift-related subsidence. Basement rocks exposed as rift shoulders during extension probably represented the main source of detrital apatites to the sedimentary fill of the basin because (i) crystalline rocks have a much higher yield of apatite grains with respect to syn-rift volcanic rocks, the other potential sediment source (Malusà and Garzanti, 2019), (ii) they had been exposed at the surface for a long time, and (iii) their cooling/exhumation history agrees with the partially reset samples of the Adjara-Trialeti. The exact determination of the Adjara-Trialeti syn-rift sediment provenance is worth further investigation as the input of a percentage of penecontemporaneous volcanic apatite grains cannot be ruled out.

6.3. Structural inversion of young rift basins

Due to their geodynamic setting, thermal state, structural configuration, and density distribution, young extensional sedimentary basins are rheologically weak and susceptible to deformation even by episodic stress-field variations (Cloetingh et al., 2005; Hall et al., 2011; Letouzey et al., 1990; Munteanu et al., 2011; Nikishin et al., 2001; Ziegler, 1990; Ziegler et al., 1995, 1998, 2002). Structural inversion of extensional basins can be produced not only by increased convergence rates along subduction zones (e.g. Funiciello et al., 2008; Heuret et al., 2007; Heuret and Lallemand, 2005) but also during continental collisions and the ensuing indentation, when strong mechanical coupling between the collisional orogenic wedge and its forelands promotes far-field stress transfer and the onset and evolution of intraplate compressional features (Cloetingh et al., 1989; Jolivet et al., 1989; Ziegler, 1993).

Numerical and analogue models identify the duration of the post-rift phase as the main factor controlling shortening of a rift basin (Buiter et al., 2009; Ziegler and Cloetingh, 2004) in that structural inversion is facilitated if it occurs within about 25 Ma from the end of the rifting stage, when the lithosphere is still relatively hot. The Adjara-Trialeti back-arc basin underwent a post-rift phase shorter than 25 My, from the Late Eocene to the Middle Miocene (Fig. 4), characterized by the deposition of a post-rift sedimentary cover that blanketed the basin as well as the rift shoulders (Adamia et al., 2011; Banks et al., 1997).

Structural inversion of extensional basins is favoured by a weak lower crust and mainly controlled by the reactivation of pre-existing structural discontinuities (i.e. extensional faults) whereas the inception of new faults that cut through older extensional structures is subordinate (Brun and Nalpas, 1996; Buiter and Pfiffner, 2003; Hooper et al., 1995; Van Wijhe, 1987). The extended continental crust of the Adjara-Trialeti back-arc region was mechanically weaker and hence prone to inversion and reactivation of the extensional faults (Cloetingh et al., 2015, 2003; Munteanu et al., 2013, 2011; Roure, 2008; Ziegler and Cloetingh, 2004) during Miocene compression. Structural inversion was also facilitated by the rheological contrast between the relatively hot and weak rift basin, the strong Dzirula Massif to the north and the more rigid and relatively pristine (quasi)oceanic lithosphere of the adjacent Eastern Black Sea (Munteanu et al., 2013).

Early structural inversion of back-arc rift basins has been recognized in fossil and active orogenic belts, including (i) current inversion of various Miocene rift basins in the eastern margin of the Japan Sea (Kato et al., 2004; Okamura et al., 1995), (ii) Late Paleozoic intra-continental rifting and inversion of the Yamansu belt of NW China (Jiang et al., 2017), (iii) Paleoproterozoic back-arc rifting and inversion of the Kisseynew belt of central Canada (Ansdell et al., 1995), (iv) the Paleogene half-grabens of the eastern Sunda platform in Indonesia (Letouzey et al., 1990), and (v) the Denison Trough in the Bowen Basin of eastern Australia (Buiter et al., 2009). In many cases, far-field stress transmission from continental collision zones has been pointed out as the main cause for compressional reactivation of extensional structures, as in the aforementioned Sunda Platform (Letouzey et al., 1990), the southern North Sea (de Lugt et al., 2003; Nalpas et al., 1995), the Pannonian Basin (Bada et al., 2007a, 2007b; Cloetingh et al., 2006; Horváth et al., 2006), and the Balkanides-Western Black Sea (Munteanu et al., 2013, 2011). In all these examples, the end of extension and the beginning of inversion were separated by a relatively short time span (<25 Ma) and extensional structures perpendicular to stress direction were reactivated as contractional faults. The results of this study indicate that inversion of the Adjara-Trialeti back-arc basin occurred ca. 20 Ma after the cessation of rifting. The E-W-striking normal faults bounding the Adjara-Trialeti basin were broadly perpendicular to the overall convergence direction between the colliding Arabian and Eurasian plates (Barrier et al., 2018; Barrier and Vrielynck, 2008) and thus particularly prone to reactivation by inversion.

6.4. Evolution of the Adjara-Trialeti FTB in the geodynamic context of the Middle East

The opening of the Adjara-Trialeti back-arc basin can be viewed as a late stage development of a wide and largely diachronous Late Cretaceous-Eocene regional extensional domain stretching -west to east- from the Srednogorie rift zone of eastern Bulgaria (Bergerat et al., 2010; Boccaletti et al., 1978; Georgiev et al., 2001), across the Black Sea, to the Adjara-Trialeti basin studied here. This extensional region developed along the southern Eurasian margin during northward subduction of the northern branch of the Neotethys (Barrier et al., 2018; Barrier and Vrielynck, 2008; Stampfli and Hochard, 2009).

Considering the uncertainties on the timing of opening of the eastern Black Sea, it is still unclear whether the Adjara-Trialeti basin (whose volcano-sedimentary fill is now deformed into the ATFTB) is to be considered as (i) the direct eastward onshore prolongation of the Black Sea or (ii) part of an E-W elongate extensional domain right behind the Pontide magmatic arc, as shown in Fig. 4 (cf. Adamia et al., 2017b; Banks et al., 1997; Lordkipanidze et al., 1979; Nikishin et al., 2011; Robinson et al., 1995a, 1995b; Shillington et al., 2008; Spadini et al., 1996). Whatever the exact timing, the Eastern Black Sea and the Adjara-Trialeti basins underwent extension because of the same overall geodynamic process, i.e. rollback during northward subduction of the northern Neotethyan slab (Banks et al., 1997; Barrier et al., 2018). The Eastern Black Sea rift reached a (quasi)oceanic stage (Nikishin et al., 2015b, 2015a; Shillington et al., 2008) whereas Adjara-Trialeti rifting stopped before oceanic crust was formed, despite the emplacement of large volumes of lavas, particularly in the western part of the basin.

In our Danian reconstruction (Fig. 4), the Adjara-Trialeti region is undergoing flexural subsidence due to the continental collision between the Anatolide-Tauride terrane and the Pontide magmatic arc, as previously pointed out in the geological background. Back-arc rifting began in the Eocene (Adamia et al., 2011, 1981, 1977; Okrostsvaridze et al., 2018a, 2018b; Gamkrelidze et al., 2019), when advanced docking of the Anatolide-Tauride-Armenian terrane into the southern Eurasian margin induced roll-back of the northern Neotethyan slab and extension in the upper plate (e.g. Barrier et al., 2018; Barrier and Vrielynck, 2008).

The low-temperature thermochronologic evolution of the Adjara-Trialeti back-arc basin during the Neogene, with particular reference to Miocene cooling, mirrors the results of thermochronometric studies in adjacent regions. An important and discrete phase of cooling/exhumation in the mid-Miocene occurred in the Bitlis-Pütürge collision zone, i.e. the area of maximum indentation between the colliding Arabian and Eurasian plates (Cavazza et al., 2018; Okay et al., 2010). Coevally, the hinterland of this collision zone, particularly the Eastern Pontides of eastern Turkey and the Lesser Caucasus of Armenia and Azerbaijan, was subjected to fault reactivation, shortening, and exhumation (Albino et al., 2014; Cavazza et al., 2019) (Fig. 10). Regional shortening during the Middle Miocene has been reported also in the Alborz, Zagros and Talysh ranges (Axen et al., 2001; Ballato et al., 2016, 2008; Barber et al., 2018; Gavillot et al., 2010; Madanipour et al., 2017) while fast uplift has been recognized in the Greater Caucasus starting at ca. 10 Ma (Avdeev and Niemi, 2011; Mosar et al., 2010; Vasey et al., 2020; Vincent et al., 2020). The late Middle Miocene-Pliocene structural inversion of the Adjara-Trialeti back-arc basin documented in this paper and the coeval synsedimentary deformation within the Kura and Rioni foreland basins (Alania et al., 2017; Tibaldi et al., 2017) can be also interpreted as an effect of far-field stress transmission from the Arabia-Eurasia collision zone into the hinterland.

In this paper, we choose not to elaborate on the evolution of the Greater Caucasus as its timing of uplift is a matter of considerable dispute. Vincent et al. (2016, 2013b, 2013a, 2007) propose an early Oligocene age supported by fossil reworking, paleoaltitude data, paleocurrent vectors, and some thermochronologic data. Other authors (e.g. Lozar and Polino, 1997; Nikishin et al., 2017) reached the same conclusion. On the other hand, Rolland (2017), taking into account the geodynamic context and the thermochronologic constraints on the

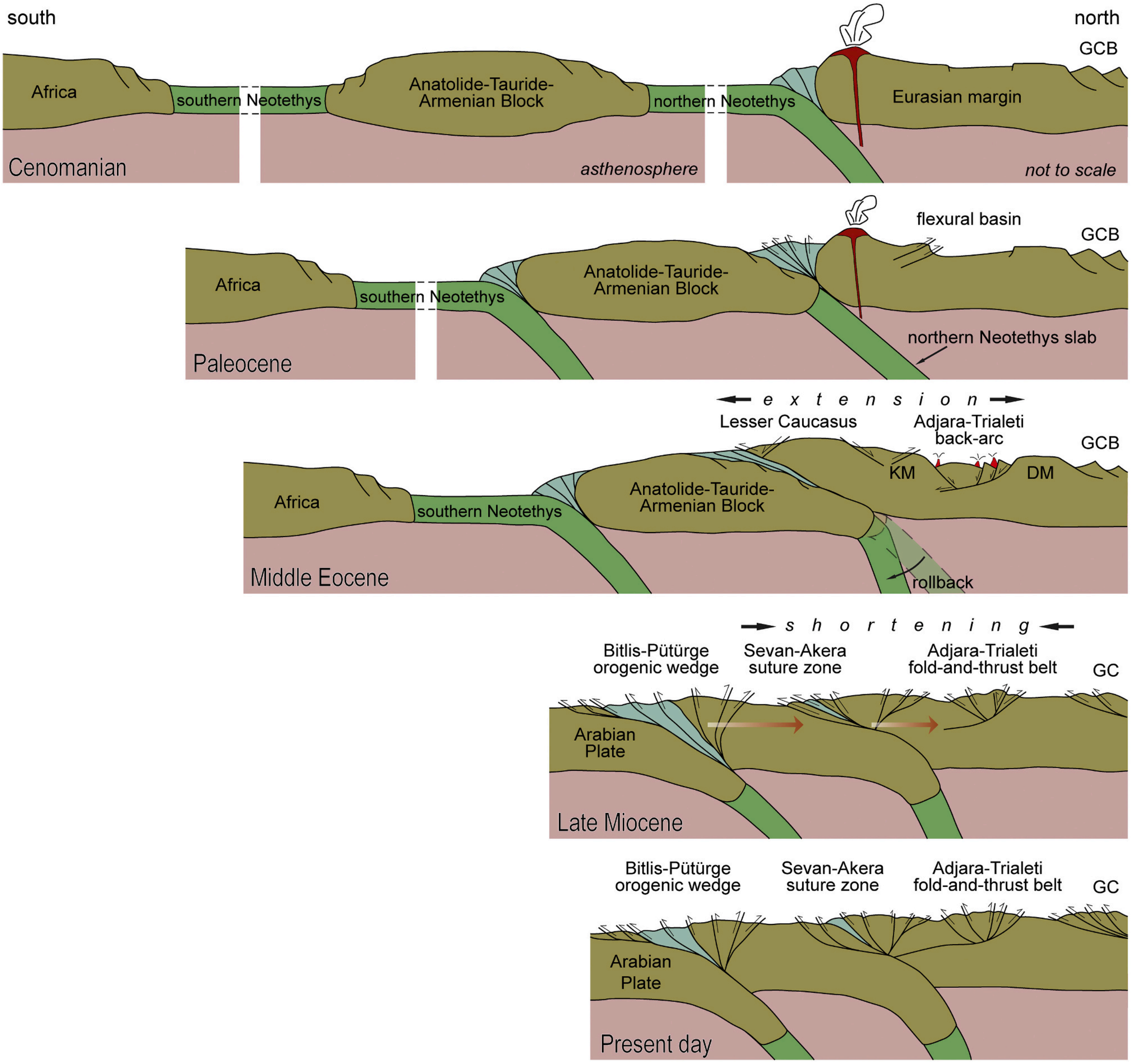

Fig. 10. North-south geodynamic sketch sections across the southern Caucasian - eastern Anatolian domain. Continental accretion along the southern Eurasian margin occurred sequentially with the collision of (i) the Anatolide-Tauride Block (latest Cretaceous – Paleocene) and (ii) the Arabian plate (Miocene). The two episodes of continental accretion were separated by a phase of upper-plate extension resulting from rollback of the subducting northern Neotethyan slab. The Arabia-Eurasia collision caused far-field incremental deformation in the upper plate, with additional shortening in the Lesser Caucasus orogenic wedge and inversion of the Adjara-Trialeti continental back-arc basin. DM = Dzirula Massif; GCB = Greater Caucasus Basin; KM = Khrami Massif.

timing of the Arabia-Eurasia collision (Cavazza et al., 2018; Okay et al., 2010), support a Middle Miocene age for the onset of Caucasus uplift. Lastly, Avdeev and Niemi (2011), Cowgill et al. (2016) and Forte et al. (2014) have proposed that the major phase of uplift occurred no earlier than 5 My ago. Vincent et al. (2020) link the Late Miocene-Pliocene acceleration in exhumation recorded in the Greater Caucasus to a major reorganization of the Arabia-Eurasia collision since ~5 Ma (Allen et al., 2004) and/or to break-off of the hypothesized Greater Caucasus slab (Mumladze et al., 2015). It is evident that more work on the Greater Caucasus is required in order to better constrain its geological evolution and then frame it within the geodynamic context.

7. Conclusions

The main results of this study can be summarized as follows:

- The Paleogene Adjara-Trialeti rift basin, after a short (ca. 20 Ma) post-rift stage, was structurally inverted during the Middle Miocene-Pliocene, starting at 14–10 Ma.
- Basin inversion can be envisioned as a far-field effect of continued stress transfer produced by the Arabia-Eurasia hard collision, which started in the Middle Miocene along the Bitlis-Pütürge suture to the south and affected preexisting structural discontinuities farther away within the hinterland to the north.
- The Khrami Massif is the surficial expression of out-of-sequence, north-vergent basement thrusting possibly related to Paleocene continental accretion along the Erzinçan-Sevan-Akera suture to the south, and started being exhumed in the Early Eocene.
- Back-arc rift basins are sensitive indicators of stress-field variations, not only along subduction zones but also in the hinterland of continental collision zones, where collisional stress can be transmitted and focus along preexisting rheological discontinuities at distances in the order of several hundred kilometres.

Declaration of Competing Interest

The authors declare that they have no known competing financial interests or personal relationships that could have appeared to influence the work reported in this paper.

Acknowledgments

We thank Irene Albino (University of Bologna) and Silvia Cattò (University of Padua) for help during data acquisition and interpretation. Sample preparation and AFT analyses were carried out at the Department of Biological, Geological and Environmental Sciences of the University of Bologna. Helium analyses were performed at the Dept. of Neotectonics and Thermochronology of the Czech Academy of Sciences in Prague. Jon Mosar (University of Fribourg) shared his expertise on the regional tectonic framework of the study area. Anatoly M. Nikishin (Moscow State University) and Randell Stephenson (University of Aberdeen) are thanked for their supportive reviews, Stephen J. Vincent (CASP) provided useful comments on an earlier version of the manuscript. This study was funded by PRIN and RFO funds to W. Cavazza and M. Zattin.

Appendix A. Supplementary data

Supplementary data to this article can be found online at https://doi.org/10.1016/j.tecto.2020.228702.

References

Adamia, S.A., 2004. Geological Map of Georgia, 1: 500 000 Scale.

Adamia, S.A., Lordkipanidze, M.B., Zakariadze, G.S., 1977. Evolution of an active continental margin as exemplified by the Alpine history of the Caucasus. Tectonophysics 40, 183–199. https://doi.org/10.1016/0040-1951(77)90065-8.

Adamia, S.A., Chkhotua, T., Kekelia, M., Lordkipanidze, M., Shavishvili, I., Zakariadze, G., 1981. Tectonics of the Caucasus and adjoining regions: implications for the evolution of the Tethys ocean. J. Struct. Geol. 3, 437–447. https://doi.org/10.1016/0191-8141(81)90043-2.

Adamia, S.A., Akhvlediani, K.T., Kilasonia, V.M., Nairn, A.E.M., Papava, D., Patton, D.K., 1992. Geology of the republic of Georgia: a review. Int. Geol. Rev. 34, 447–476.

Adamia, S.A., Mumladze, T., Sadradze, N., Tsereteli, E., Tsereteli, N., Varazanashvili, O., 2008. Late Cenozoic Tectonics and Geodynamics of Georgia (SW Caucasus). Georg. Int. J. Sci. Technol. 1, 77–107. https://doi.org/10.1111/jbi.12174.

Adamia, S.A., Alania, V., Chabukiani, A., Chichua, G., Enukidze, O., Sadradze, N., 2010. Evolution of the late Cenozoic basins of Georgia (SW Caucasus): a review. In: Sosson, M., Kaymakci, N., Stephenson, R.A., Bergerat, F., Starostenko, V. (Eds.), Sedimentary Basin Tectonics from the Black Sea and Caucasus to the Arabian Platform, 340. Geological Society, London, Special Pubblications, pp. 239–259.

Adamia, S.A., Zakariadze, G., Chkhotua, T., Sadradze, N., Tsereteli, N., Chabukiani, A., Gventsadze, A., 2011. Geology of the Caucasus: a Review. Turk. J. Earth Sci. 20, 489–544. https://doi.org/10.3906/yer-1005-11.

Adamia, S.A., Alania, V., Tsereteli, N., Varazanashvili, O., Sadraze, N., Lursmanashvili, N., Gventsadze, A., 2017a. Postcollisional tectonics and seismicity of Georgia. In: Sorkhabi, R. (Ed.), Tectonic Evolution, Collision, and Seismicity of Southwest Asia: In Honor of Manuel Berberian's Forty-Five Years of Research Contributions, 525. Geological Society of America Special Paper, pp. 1–38.

Adamia, S.A., Chkhotua, T.G., Gavtadze, T.T., Lebanidze, Z.A., Lursmanashvili, N.D., Sadradze, N.G., Zakaraia, D.P., Zakariadze, G.S., 2017b. Tectonic setting of Georgia-Eastern Black Sea: A review. In: Sosson, M., Stephenson, R.A., Adamia, S.A. (Eds.), Tectonic Evolution of the Eastern Black Sea and Caucasus, 428. Geological Society, London, Special Publications, pp. 11–40. https://doi.org/10.1144/SP428.6.

Alania, V., Chabukiani, A.O., Chagelishvili, R.L., Enukidze, O.V., Gogrichiani, K.O., Razmadze, A.N., Tsereteli, N.S., 2017. Growth structures, piggy-back basins and growth strata of the Georgian part of the Kura foreland fold–thrust belt: Implications for late Alpine kinematic evolution. In: Sosson, M., Stephenson, R.A., Adamia, S.A. (Eds.), Tectonic Evolution of the Eastern Black Sea and Caucasus, vol. 428. Geological Society, London, Special Publications, pp. 428–445. https://doi.org/10.1177/1010539510370992.

Alania, V., Enukidze, O., Glonti, N., Razmadze, A., Chabukiani, A., Giorgadze, A., Vakhtang Glonti, B., Koiava, K., Beridze, T., Khutsishvili, S., Chagelishvili, R., 2018. Structural Architecture of the Kura Foreland Fold-and-thrust Belt using Seismic Reflection Profile, Georgia. Univers. J. Geosci. 6, 184–190. https://doi.org/10.13189/ujg.2018.060402.

Albino, I., Cavazza, W., Zattin, M., Okay, A.I., Adamia, S.A., Sadradze, N., 2014. Far-field tectonic effects of the Arabia–Eurasia collision and the inception of the North Anatolian Fault system. Geol. Mag. 151, 372–379. https://doi.org/10.1017/s0016756813000952.

Allen, M., Jackson, J., Walker, R., 2004. Late Cenozoic reorganization of the Arabia-Eurasia collision and the comparison of short-term and long-term deformation rates. Tectonics 23. https://doi.org/10.1029/2003TC001530.

Ansdell, K.M., Lucas, S.B., Connors, K., Stern, R.A., 1995. Kisseynew metasedimentary gneiss belt, Trans-Hudson orogen (Canada): back-arc origin and collisional inversion. Geology 23, 1039–1043. https://doi.org/10.1130/0091-7613(1995)023<1039:KMGBTH>2.3.CO;2.

Avdeev, B., Niemi, N.A., 2011. Rapid Pliocene exhumation of the central Greater Caucasus constrained by low-temperature thermochronometry. Tectonics 30, 1–16. https://doi.org/10.1029/2010TC002808.

Axen, G.J., Lam, P.S., Grove, M., Stockli, D.F., Hassanzadeh, J., 2001. Exhumation of the west-central Alborz Mountains, Iran, Caspian subsidence, and collision-related tectonics. Geology 29, 559–562. https://doi.org/10.1130/0091-7613(2001)029<0559:EOTWCA>2.0.CO;2.

Bada, G., Grenerczy, G., Tóth, L., Horváth, F., Stein, Seth, Cloetingh, S., Windhoffer, G., Fodor, L., Pinter, N., Fejes, I., 2007a. Motion of Adria and ongoing inversion of the Pannonian Basin: Seismicity, GPS velocities, and stress transfer. In: Stein, S., Mazzotti, S. (Eds.), Continental Intraplate Earthquakes: Science, Hazard, and Policy Issues, vol. 425. Geological Society of America Special Paper, pp. 243–262. https://doi.org/10.1130/2007.2425(16).

Bada, G., Horváth, F., Dövényi, P., Szafián, P., Windhoffer, G., Cloetingh, S., 2007b. Present-day stress field and tectonic inversion in the Pannonian basin. Glob. Planet. Chang. 58, 165–180. https://doi.org/10.1016/j.gloplacha.2007.01.007.

Ballato, P., Nowaczyk, N.R., Landgraf, A., Strecker, M.R., Friedrich, A., Tabatabaei, S.H., 2008. Tectonic control on sedimentary facies pattern and sediment accumulation rates in the Miocene foreland basin of the southern Alborz mountains, northern Iran. Tectonics 27, 1–20. https://doi.org/10.1029/2008TC002278.

Ballato, P., Stockli, D.F., Ghassemi, M.R., Landgraf, A., Strecker, M.R., Hassanzadeh, J., Friedrich, A., Tabatabaei, S.H., 2013. Accommodation of transpressional strain in the Arabia-Eurasia collision zone: New constraints from (U-Th)/He thermochronology in the Alborz mountains, North Iran. Tectonics 32, 1–18. https://doi.org/10.1029/2012TC003159.

Ballato, P., Cifelli, F., Heidarzadeh, G., Ghassemi, M.R., Wickert, A.D., Hassanzadeh, J., Dupont-Nivet, G., Balling, P., Sudo, M., Zeilinger, G., Schmitt, A.K., Mattei, M., Strecker, M.R., 2016. Tectono-sedimentary evolution of the northern Iranian Plateau: insights from middle–late Miocene foreland-basin deposits. Basin Res. 29, 417–446. https://doi.org/10.1111/bre.12180.

Banks, C.J., Robinson, A.G., Williams, M.P., 1997. Structure and regional tectonics of the Achara-Trialeti fold belt and the adjacent Rioni and Kartli foreland basins, Republic of Georgia. In: Robinson, A.G. (Ed.), Regional and Petroleum Geology of the Blacks Sea and Surrounding Region: AAPG Memoirs 68. Tulsa, Oklahoma, pp. 331–346.

Barber, D.E., Stockli, D.F., Horton, B.K., Koshnaw, R.I., 2018. Cenozoic exhumation and foreland basin evolution of the Zagros orogen during the Arabia-Eurasia collision, Western Iran. Tectonics 37, 4396–4420. https://doi.org/10.1029/2018TC005328.

Barrier, E., Vrielynck, B., 2008. Palaeotectonic Maps of the Middle East. CCMW/CGMW, Paris.

Barrier, E., Vrielynck, B., Brouillet, J.F., Brunet, M.-F., 2018. Paleotectonic reconstruction of the central Tethyan realm. In: Tectonono-sedimentary-palinspastic maps from late Permian to Pliocene. CCGM/CGMW, Paris (Contributors: Angiolini L., Kaveh F., Poisson A., Pourteau A., Plunder A., Robertson A., Shekawat R., Sosson M., Zanchi, A.).

Bazhenov, M.L., Burtman, V.S., 2002. Eocene paleomagnetism of the Caucasus (Southwest Georgia): Oroclinal bending in the Arabian syntaxis. Tectonophysics 344, 247–259. https://doi.org/10.1016/S0040-1951(01)00189-5.

Bergerat, F., Vangelov, D., Dimov, D., 2010. Brittle deformation, palaeostress field reconstruction and tectonic evolution of the Eastern Balkanides (Bulgaria) during Mesozoic and Cenozoic times. In: Sosson, M., Kaymakci, N., Stephenson, R.A., Bergerat, F., Starostenko, V. (Eds.), Sedimentary Basin Tectonics from the Black Sea and Caucasus to the Arabian Platform, vol. 340. Geological Society, London, Special Pubblications, pp. 70–111.

Boccaletti, M., Manetti, P., Peccerillo, A., Stanisheva-Vassileva, G., 1978. Late Cretaceous high-potassium volcanism in eastern Srednogorie, Bulgaria. Bull. Geol. Soc. Am. 89, 439–447. https://doi.org/10.1130/0016-7606(1978)89<439:LCHVIE>2.0.CO;2.

Brandon, M.T., 1992. Decomposition of fission-track grain-age distributions. Am. J. Sci. 292, 535–564.

Brun, J.P., Nalpas, T., 1996. Graben inversion in nature and experiments. Tectonics 15, 677–687.

Buiter, S.J.H., Pfiffner, O.A., 2003. Numerical models of the inversion of half-graben basins. Tectonics 22, 1057–1073. https://doi.org/10.1029/2002tc001417.

Buiter, S.J.H., Pfiffner, O.A., Beaumont, C., 2009. Inversion of extensional sedimentary basins: a numerical evaluation of the localisation of shortening. Earth Planet. Sci. Lett. 288, 492–504. https://doi.org/10.1016/j.epsl.2009.10.011.

Cavazza, W., Zattin, M., 2015. Exhuming Anatolia: the Italian contribution to the low-temperature thermochronological study of Turkey and the surrounding regions. Acta Vulcanol. 27, 111–122.

Cavazza, W., Albino, I., Zattin, M., Galoyan, G., Imamverdiyev, N., Melkonyan, R., 2015. Thermochronometric evidence for Miocene tectonic reactivation of the Sevan-Akera suture zone (Lesser Caucasus): A far-field tectonic effect of the Arabia-Eurasia collision? In: Sosson, M., Stephenson, R.A., Adamia, S.A. (Eds.), Tectonic Evolution of the Eastern Black Sea and Caucasus, vol. 428. Geological Society, London, Special Publications, pp. 187–198.

Cavazza, W., Cattò, S., Zattin, M., Okay, A.I., Reiners, P., 2018. Thermochronology of the Miocene Arabia-Eurasia collision zone of southeastern Turkey. Geosphere 14, 2277–2293. https://doi.org/10.1130/GES01637.1.

Cavazza, W., Albino, I., Galoyan, G., Zattin, M., Cattò, S., 2019. Continental accretion and incremental deformation in the thermochronologic evolution of the Lesser Caucasus. Geosci. Front. https://doi.org/10.1016/j.gsf.2019.02.007.

Cloetingh, S., Wortel, R., Vlaar, N.J., 1989. On the Initiation of Subduction zones. Pure Appl. Geophys. 129, 7–25.

Cloetingh, S., Spadini, G., Van Wees, J.D., Beekman, F., 2003. Thermo-mechanical modelling of Black Sea Basin (de)formation. Sediment. Geol. 156, 169–184. https://doi.org/10.1016/S0037-0738(02)00287-7.

Cloetingh, S., Ziegler, P.A., Beekman, F., Andriessen, P.A.M., Matenco, L., Bada, G., Garcia-Castellanos, D., Hardebol, N., Dèzes, P., Sokoutis, D., 2005. Lithospheric memory, state of stress and rheology: Neotectonic controls on Europe's intraplate continental topography. Quat. Sci. Rev. 24, 241–304. https://doi.org/10.1016/j.quascirev.2004.06.015.

Cloetingh, S., Bada, G., Matenco, L., Lankreijer, A., Horváth, F., Dinu, C., 2006. Modes of basin (de)formation, lithospheric strength and vertical motions in the Pannonian-Carpathian system: Inferences from thermo-mechanical modelling. In: Gee, D.G., Stephenson, R.A. (Eds.), European Lithosphere Dynamics, vol. 32. Geological Society, London, Memoirs, pp. 207–221. https://doi.org/10.1144/GSL.MEM.2006.032.01.12.

Cloetingh, S., Ziegler, P.A., Beekman, F., Burov, E.B., Garcia-Castellanos, D., Matenco, L., 2015. Tectonic models for the evolution of sedimentary basins. In: Schubert, G. (Ed.), Treatise on Geophysics, Second edition. Elsevier B.V, pp. 513–592. https://doi.org/10.1016/B978-0-444-53802-4.00117-2.

Cowgill, E., Forte, A.M., Niemi, N., Avdeev, B., Tye, A., Trexler, C., Javakhishvili, Z., Elashvili, M., Godoladze, T., 2016. Relict basin closure and crustal shortening budgets during continental collision: an example from Caucasus sediment provenance. Tectonics 35, 2918–2947. https://doi.org/10.1002/2016TC004295.

de Lugt, I.R., van Wees, J.D., Wong, T.E., 2003. The tectonic evolution of the southern Dutch North Sea during the Palaeogene: Basin inversion in distinct pulses. Tectonophysics 373, 141–159. https://doi.org/10.1016/S0040-1951(03)00284-1.

DeCelles, P.G., Giles, K.A., 1996. Foreland basin system. Basin Res. 8, 105–124.

Doglioni, C., Carminati, E., Cuffaro, M., Scrocca, D., 2007. Subduction kinematics and dynamic constraints. Earth-Sci. Rev. 83, 125–175. https://doi.org/10.1016/j.earscirev.2007.04.001.

Donelick, R.A., Ketcham, R.A., Carlson, W.D., 1999. Variability of apatite fission-track annealing kinetics: II. Crystallographic orientation effects. Am. Mineral. 84, 1224–1234. https://doi.org/10.2138/am-1999-0902.

Donelick, R.A., O'Sullivan, P.B., Ketcham, R.A., 2005. Apatite fission-track analysis. Rev. Mineral. Geochem. 58, 49–94. https://doi.org/10.2138/rmg.2005.58.3.

Farley, K.A., 2000. Helium diffusion from apatite: General behavior as illustrated by Durango fluorapatite. J. Geophys. Res. Solid Earth 105, 2903–2914. https://doi.org/10.1029/1999jb900348.

Farley, K.A., 2002. (U-Th)/He dating: techniques, calibrations, and applications. Rev. Mineral. Geochem. 47, 819–844. https://doi.org/10.2138/rmg.2002.47.18.

Farley, K.A., Wolf, R.A., Silver, L.T., 1996. The effects of long alpha-stopping distances on (U-Th)/He ages. Geochim. Cosmochim. Acta 60, 4223–4229. https://doi.org/10.1016/S0016-7037(96)00193-7.

Finetti, I., Bricchi, G., Del Ben, A., Pipan, M., Xuan, Z., 1988. Geophysical study of the Black Sea. Boll. Geofis. Teor. Appl. 30, 197–324.

Flowers, R.M., Ketcham, R.A., Shuster, D.L., Farley, K.A., 2009. Apatite (U-Th)/He thermochronometry using a radiation damage accumulation and annealing model. Geochim. Cosmochim. Acta 73, 2347–2365. https://doi.org/10.1016/j.gca.2009.01.015.

Flowers, R.M., Farley, K.A., Ketcham, R.A., 2015. A reporting protocol for thermochronologic modeling illustrated with data from the Grand Canyon. Earth Planet. Sci. Lett. 432, 425–435. https://doi.org/10.1016/j.epsl.2015.09.053.

Forte, A.M., Cowgill, E., Murtuzayev, I., Kangarli, T., Stoica, M., 2013. Structural geometries and magnitude of shortening in the eastern Kura fold-thrust belt, Azerbaijan: Implications for the development of the Greater Caucasus Mountains. Tectonics 32, 688–717. https://doi.org/10.1002/tect.20032.

Forte, A.M., Cowgill, E., Whipple, K.X., 2014. Transition from a singly vergent to doubly vergent wedge in a young orogen: the Greater Caucasus. Tectonics 33, 2077–2101. https://doi.org/10.1002/2014TC003651.

Funiciello, F., Faccenna, C., Heuret, A., Lallemand, S., Di Giuseppe, E., Becker, T.W., 2008. Trench migration, net rotation and slab-mantle coupling. Earth Planet. Sci. Lett. 271, 233–240. https://doi.org/10.1016/j.epsl.2008.04.006.

Gamkrelidze, P., 1949. Geological Structure of the Adjara-Trialetian Folded System. Acad. Sci. Georgia Press, Tbilisi (378 pp).

Gamkrelidze, I., Koiava, K., Mosar, J., Kvaliashvili, L., Mauvilly, J., 2018. Main features of geological structure and a new tectonic map of Georgia. In: EGU General Assembly, 2018. https://doi.org/10.13140/RG.2.2.26540.56963.

Gamkrelidze, I., Okrostsvaridze, A., Maisadze, F., Basheleishvili, L., Boichenko, G., 2019. Main features of geological structure and geotourism potential of Georgia, the Caucasus. Mod. Environ. Sci. Eng. 5, 422–442. https://doi.org/10.15341/mese(2333-2581)/05.05.2019/010.

Gautheron, C., Tassan-Got, L., Barbarand, J., Pagel, M., 2009. Effect of alpha-damage annealing on apatite (U-Th)/He thermochronology. Chem. Geol. 266, 157–170. https://doi.org/10.1016/j.chemgeo.2009.06.001.

Gavillot, Y., Axen, G.J., Stockli, D.F., Horton, B.K., Fakhari, M.D., 2010. Timing of thrust activity in the High Zagros fold-thrust belt, Iran, from (U-Th)/He thermochronometry. Tectonics 29. https://doi.org/10.1029/2009TC002484.

Georgiev, G., Dabovski, C., Stanisheva-Vassileva, G., 2001. East Srednogorie-Balkan Rift Zone. In: Ziegler, P.A., Cavazza, W., Robertson, A.H.F., Crasquin-Soleau, S. (Eds.), Peri-Thetys Memoir 6: Peri-Tethyan Rift/Wrench Basins and Passive Margins. Mémoires du Muséum National d'Histoire Naturelle, Paris, pp. 259–293.

Gleadow, A.J.W., Duddy, I.R., 1981. A natural long-term track annealing experiment for apatite. Nucl. Tracks 5, 169–174.

Görür, N., 1988. Timing of opening of the Black Sea basin. Tectonophyisics 147, 247–262.

Guest, B., Stockli, D.F., Grove, M., Axen, G.J., Lam, P.S., Hassanzadeh, J., 2006. Thermal histories from the central Alborz Mountains, northern Iran: Implications for the spatial and temporal distribution of deformation in northern Iran. Bull. Geol. Soc. Am. 118, 1507–1521. https://doi.org/10.1130/B25819.1.

Hall, R., Cottam, M.A., Wilson, M.E.J., 2011. The SE Asian gateway: History and tectonics of the Australia-Asia collision. In: Hall, R., Cottam, M.A., Wilson, M.E.J. (Eds.), The SE Asian Gateway: History and Tectonics of the Australia–Asia Collision, vol. 355. Geological Society, London, Special Pubblications, pp. 1–6. https://doi.org/10.1144/SP355.1.

Heuret, A., Lallemand, S., 2005. Plate motions, slab dynamics and back-arc deformation. Phys. Earth Planet. Inter. 149, 31–51. https://doi.org/10.1016/j.pepi.2004.08.022.

Heuret, A., Funiciello, F., Faccenna, C., Lallemand, S., 2007. Plate kinematics, slab shape and back-arc stress: a comparison between laboratory models and current subduction zones. Earth Planet. Sci. Lett. 256, 473–483. https://doi.org/10.1016/j.epsl.2007.02.004.

Hooper, R.J., Goh, L.S., Dewey, F., 1995. The inversion history of the northeastern margin of the Broad Fourteens Basin. In: Buchanan, J.G., Buchanan, P.G. (Eds.), Basin Inversion, vol. 88. Geological Society, London, Special Publications, pp. 307–317. https://doi.org/10.1144/GSL.SP.1995.088.01.17.

Horton, B.K., Fuentes, F., Boll, A., Starck, D., Ramirez, S.G., Stockli, D.F., 2016. Andean stratigraphic record of the transition from backarc extension to orogenic shortening: a case study from the northern Neuquén Basin, Argentina. J. S. Am. Earth Sci. 71, 17–40. https://doi.org/10.1016/j.jsames.2016.06.003.

Horváth, F., Bada, G., Szafián, P., Tari, G., Ádám, A., Cloetingh, S., 2006. Formation and deformation of the Pannonian Basin: Constraints from observational data. Geol. Soc. Mem. 32, 191–206. https://doi.org/10.1144/GSL.MEM.2006.032.01.11.

Hurford, A.J., Green, P.F., 1983. The zeta age calibration of fission-track dating. Chem. Geol. 41, 285–317.

Jiang, H., Han, J., Chen, H., Zheng, Y., Lu, W., Deng, G., Tan, Z., 2017. Intra-continental back-arc basin inversion and late Carboniferous magmatism in Eastern Tianshan, NW China: Constraints from the Shaquanzi magmatic suite. Geosci. Front. 8, 1447–1467. https://doi.org/10.1016/j.gsf.2017.01.008.

Jolivet, L., Huchon, P., Rangin, C., 1989. Tectonic setting of Western Pacific marginal basins. Tectonophysics 160, 23–47. https://doi.org/10.1016/0040-1951(89)90382-X.

Karakhanyan, A., Vernant, P., Doerflinger, E., Avagyan, A., Philip, H., Aslanyan, R., Champollion, C., Arakelyan, S., Collard, P., Baghdasaryan, H., Peyret, M., Davtyan, V., Calais, E., Masson, F., 2013. GPS constraints on continental deformation in the Armenian region and Lesser Caucasus. Tectonophysics 592, 39–45. https://doi.org/10.1016/j.tecto.2013.02.002.

Kato, N., Sato, H., Imaizumi, T., Ikeda, Y., Okada, S., Kagohara, K., Kawanaka, T., Kasahara, K., 2004. Seismic reflection profiling across the source fault of the 2003 Northern Miyagi earthquake (Mj 6.4), NE Japan: Basin inversion of Miocene back-arc rift. Earth, Planets Sp. 56, 1369–1374. https://doi.org/10.1186/BF03353362.

Kazmin, V.G., Schreider, A.A., Bulychev, A.A., 2000. Early stages of evolution of the Black Sea. In: Bozkurt, E., Winchester, J.A., Piper, J.D.A. (Eds.), Tectonics and Magmatism in Turkey and the Surrounding Area, vol. 173. Geological Society of London, Special Publications, pp. 235–249. https://doi.org/10.1144/GSL.SP.2000.173.01.12.

Ketcham, R.A., 2005. Forward and inverse modeling of low-temperature thermochronometry data. Rev. Mineral. Geochem. 58, 275–314. https://doi.org/10.2138/rmg.2005.58.11.

Ketcham, R.A., Donelick, R.A., Carlson, W.D., 1999. Variability of apatite fission-track annealing kinetics: III. Extrapolation to geological time scales. Am. Mineral. 84, 1235–1255. https://doi.org/10.2138/Am.2006.464.

Ketcham, R.A., Carter, A., Donelick, R.A., Barbarand, J., Hurford, A.J., 2007. Improved modeling of fission-track annealing in apatite. Am. Mineral. 92, 799–810. https://doi.org/10.2138/am.2007.2281.

Ketcham, R.A., Gautheron, C., Tassan-Got, L., 2011. Accounting for long alpha-particle stopping distances in (U-Th-Sm)/He geochronology: Refinement of the baseline case. Geochim. Cosmochim. Acta 75, 7779–7791. https://doi.org/10.1016/j.gca.2011.10.011.

Koçyiğit, A., Yılmaz, A., Adamia, S.A., Kuloshvili, S., 2001. Neotectonics of East Anatolian Plateau (Turkey) and Lesser Caucasus: Implication for transition from thrusting to strike-slip faulting. Geodin. Acta 14, 177–195. https://doi.org/10.1080/09853111.2001.11432443.

Letouzey, J., Biju-Duval, B., Dorkel, A., Gonnard, R., Kristchev, K., Montadert, L., Sungurlu, O., 1977. The Black Sea: A marginal basin. Geophysical and geological data. In: Biju-Duval, B., Montadert, L. (Eds.), Structural History of the Mediterranean Basins. Split - Yougoslavie, pp. 363–376.

Letouzey, J., Werner, P., Marty, A., 1990. Fault reactivation and structural inversion. Backarc and intraplate compressive deformations. Example of the eastern Sunda shelf (Indonesia). In: Angelier, J. (Ed.), Geodynamic Evolution of the Eastern Eurasian Margin, pp. 341–362.

Lisker, F., Ventura, B., Glasmacher, U.A., 2009. Apatite thermochronology in modern geology. In: Lisker, F., Ventura, B., Glasmacher, U.A. (Eds.), Thermochronological Methods, vol. 324. Geological Society of London, Special Publications, pp. 1–23. https://doi.org/10.1144/SP324.1.

Lordkipanidze, M.B., Zakariadze, G.S., Popolitov, E.I., 1979. Volcanic evolution of the marginal and interarc basins. Tectonophyiscs 57, 71–83.

Lozar, F., Polino, R., 1997. Early Cenozoic uprising of the Great Caucasus revealed by reworked calcareous nannofossils. In: EUG. Strasbourg, France, p. 141.

Madanipour, S., Ehlers, T.A., Yassaghi, A., Enkelmann, E., 2017. Accelerated middle Miocene exhumation of the Talesh Mountains constrained by U-Th/He thermochronometry: evidence for the Arabia-Eurasia collision in the NW Iranian Plateau. Tectonics 36, 1538–1561. https://doi.org/10.1002/2016TC004291.

Malusà, M.G., Garzanti, E., 2019. The sedimentology of detrital thermochronology. In: Malusà, M.G., Fitzgerald, P.G. (Eds.), Fission-Track Thermochronology and its Application to Geology. Springer, Cham, pp. 123–143. https://doi.org/10.1007/978-3-319-89421-8_7.

Mayringer, F., Treloar, P.J., Gerdes, A., Finger, F., Shengelia, D., 2011. New age data from the Dzirula Massif, Georgia: Implications for the evolution of the Caucasian Variscides. Am. J. Sci. 311, 404–441. https://doi.org/10.2475/05.2011.02.

Miall, A.D., 2013. Principles of Sedimentary Basin Analysis. Springer Science & Business Media. https://doi.org/10.1016/s0037-0738(02)00096-9.

Mosar, J., Kangarli, T., Bochud, M., Glasmacher, U.A., Rast, A., Brunet, M.-F., Sosson, M., 2010. Cenozoic-recent tectonics and uplift in the Greater Caucasus: A perspective from Azerbaijan. In: Sosson, M., Kaymakci, N., Stephenson, R.A., Bergerat, F., Starostenko, V. (Eds.), Sedimentary Basin Tectonics from the Black Sea and Caucasus to the Arabian Platform, vol. 340. Geological Society, London, Special Publications, pp. 261–280. https://doi.org/10.1144/SP340.12.

Motavalli-Anbaran, S.H., Zeyen, H., Jamasb, A., 2016. 3D crustal and lithospheric model of the Arabia-Eurasia collision zone. J. Asian Earth Sci. 122, 158–167. https://doi.org/10.1016/j.jseaes.2016.03.012.

Mumladze, T., Forte, A.M., Cowgill, E.S., Trexler, C.C., Niemi, N.A., Burak Yıkılmaz, M., Kellogg, L.H., 2015. Subducted, detached, and torn slabs beneath the Greater Caucasus. GeoResJ 5, 36–46. https://doi.org/10.1016/j.grj.2014.09.004.

Munteanu, I., Matenco, L., Dinu, C., Cloetingh, S., 2011. Kinematics of back-arc inversion of the Western Black Sea Basin. Tectonics 30, 1–21. https://doi.org/10.1029/2011TC002865.

Munteanu, I., Willingshofer, E., Sokoutis, D., Matenco, L., Dinu, C., Cloetingh, S., 2013. Transfer of deformation in back-arc basins with a laterally variable rheology: Constraints from analogue modelling of the Balkanides-Western Black Sea inversion. Tectonophysics 602, 223–236. https://doi.org/10.1016/j.tecto.2013.03.009.

Nalpas, T., Le Douaran, S., Brun, J.P., Unternehr, P., Richert, J.P., 1995. Inversion of the Broad Fourteens Basin (offshore Netherlands), a small-scale model investigation. Sediment. Geol. 95, 237–250. https://doi.org/10.1016/0037-0738(94)00113-9.

Nemčok, M., Glonti, B., Yukler, A., Marton, B., 2013. Development history of the foreland plate trapped between two converging orogens; Kura Valley, Georgia, case study. In: Nemčok, M., Mora, A., Cosgrove, J.W. (Eds.), Thick-Skin-Dominated Orogens: From Initial Inversion to Full Accretion, vol. 377. Geological Society, London, Special Publications, pp. 159–188. https://doi.org/10.1144/SP377.9.

Nikishin, A.M., Korotaev, M.V., Ershov, A.V., Brunet, M.F., 2003. The Black Sea basin: Tectonic history and Neogene-Quaternary rapid subsidence modelling. Sediment. Geol. 156, 149–168. https://doi.org/10.1016/S0037-0738(02)00286-5.

Nikishin, A.M., Ziegler, P.A., Bolotov, S.N., Fokin, P.A., 2011. Late Palaeozoic to Cenozoic evolution of the Black Sea-Southern Eeastern Europe region: a view from the Russian Platform. Turkish. J. Earth Sci. 21, 571–634. https://doi.org/10.3906/yer-1005-22.

Nikishin, A.M., Okay, A.I., Tüysüz, O., Demirer, A., Wannier, M., Amelin, N., Petrov, E., 2015a. The Black Sea basins structure and history: New model based on new deep penetration regional seismic data. Part 1: Basins structure and fill. Mar. Pet. Geol. 59, 638–655. https://doi.org/10.1016/j.marpetgeo.2014.08.018.

Nikishin, A.M., Okay, A.I., Tüysüz, O., Demirer, A., Wannier, M., Amelin, N., Petrov, E., 2015b. The Black Sea basins structure and history: New model based on new deep penetration regional seismic data. Part 2: Tectonic history and paleogeography. Mar. Pet. Geol. 59, 656–670. https://doi.org/10.1016/j.marpetgeo.2014.08.018.

Nikishin, A.M., Wannier, M., Alekseev, A.S., Almendinger, O.A., Fokin, P.A., Gabdullin, R.R., Khudoley, A.K., Kopaevich, L.F., Mityukov, A.V., Petrov, E.I., Rubtsova, E.V., 2017. Mesozoic to recent geological history of southern Crimea and the Eastern Black Sea region. In: Sosson, M., Stephenson, R.A., Adamia, S.A. (Eds.), Tectonic Evolution of the Eastern Black Sea and Caucasus, vol. 428. Geological Society, London, Special Publications, pp. 241–264. https://doi.org/10.1144/SP428.1.

Nikishin, A.M., Ziegler, P.A., Panov, D.I., Nazarevich, B.P., Brunet, M.F., Stephenson, R.A., Bolotov, S.N., Korotaev, M.V., Tikhomirov, P.L., 2001. Mesozoic and Cenozoic evolution of the Scythian Platform-Black Sea-Caucasus domain. In: Ziegler, P.A., Cavazza, W., Robertson, A.H.F., Crasquin-Soleau, S. (Eds.), Peri-Tethys Memoir 6: Peri-Tethyan Rift/Wrench Basins and Passive Margins. National Museum of Natural History, Paris, pp. 295–346.

Okamura, Y., Watanabe, M., Morijiri, R., Satoh, M., 1995. Rifting and basin inversion in the eastern margin of the Japan Sea. Island Arc 4, 166–181. https://doi.org/10.1111/j.1440-1738.1995.tb00141.x.

Okay, A.I., Tüysüz, O., 1999. Tethyan sutures of northern Turkey. In: Durand, B., Jolivet, L., Horváth, F., Séranne, M. (Eds.), The Mediterranean Basins: Tertiary Extension within the Alpine Orogen, 156. Geological Society of London, Special Publications, pp. 475–515. doi:10.1144/gsl.sp.1999.156.01.22.

Okay, A.I., Şengör, A.M.C., Görür, N., 1994. Kinematic history of the opening of the Black Sea and its effect on the surrounding regions. Geology 22, 267–270. https://doi.org/10.1130/0091-7613(1994)022<0267:KHOTOO>2.3.CO;2.

Okay, A.I., Zattin, M., Cavazza, W., 2010. Apatite fission-track data for the Miocene Arabia-Eurasia collision. Geology 38, 35–38. https://doi.org/10.1130/G30234.1.

Okrostsvaridze, A., Chung, S.L., Chang, Y.H., Gagnidze, N., Bluashvili, D., 2018a. Analysis of magmatic processes of the Paleogene Adjara-Trialeti foldrift zone, Lesser Caucasus: Implication from zircon U-Pb geochronology. In: Neubauer, F., Brendel, U., Friedl, G. (Eds.), Geologica Balcanica (XXI International Congress of the CBGA). Bulgarian Academy of Sciences, p. 298. https://doi.org/10.1017/CBO9781107415324.004.

Okrostsvaridze, A., Chung, S.L., Chang, Y.H., Gagnidze, N., Boichenko, G., Gogoladze, S., 2018b. Zircons U-Pb geochronology of the ore-bearing plutons of Adjara-Trialeti folded zone, Lesser Caucasus and analysis of the magmatic processes. Bull. Georg. Natl. Acad. Sci. 12, 90–99.

Peyton, S.L., Carrapa, B., 2013. An introduction to low-temperature thermochronologic techniques, methodology, and applications. In: Knight, C., Cuzella, J. (Eds.), Application of Structural Methods to Rocky Mountain Hydrocarbon Exploration and Development: AAPG Studies in Geology, 65, pp. 15–36. https://doi.org/10.1306/13381688St653578.

Pupp, M., Bechtel, A., Ćorić, S., Gratzer, R., Rustamov, J., Sachsenhofer, R.F., 2018. Eocene and Oligo-Miocene source rocks in the Rioni and Kura Basins of Georgia: depositional environment and petroleum potential. J. Pet. Geol. 41, 367–392. https://doi.org/10.1111/jpg.12708.

Reilinger, R., McClusky, S., Vernant, P., Lawrence, S., Ergintav, S., Cakmak, R., Ozener, H., Kadirov, F., Guliev, I., Stepanyan, R., Nadariya, M., Hahubia, G., Mahmoud, S., Sakr, K., ArRajehi, A., Paradissis, D., Al-Aydrus, A., Prilepin, M., Guseva, T., Evren, E., Dmitrotsa, A., Filikov, S.V., Gomez, F., Al-Ghazzi, R., Karam, G., 2006. GPS constraints on continental deformation in the Africa-Arabia-Eurasia continental collision zone and implications for the dynamics of plate interactions. J. Geophys. Res. Solid Earth 111, 1–26. https://doi.org/10.1029/2005JB004051.

Reiners, P.W., 2005. Zircon (U-Th)/He thermochronometry. Rev. Mineral. Geochem. 58, 151–179. https://doi.org/10.2138/rmg.2005.58.6.

Reiners, P.W., Spell, T.L., Nicolescu, S., Zanetti, K.A., 2004. Zircon (U-Th)/He thermochronometry: He diffusion and comparisons with $^{40}Ar/^{39}Ar$ dating. Geochim. Cosmochim. Acta 68, 1857–1887. https://doi.org/10.1016/j.gca.2003.10.021.

Robinson, A.G., Banks, C.J., Rutherford, M.M., Hirst, J.P.P., 1995a. Stratigraphic and structural development of the Eastern Pontides, Turkey. J. Geol. Soc. Lond. 152, 861–872. https://doi.org/10.1144/gsjgs.152.5.0861.

Robinson, A.G., Spadini, G., Cloetingh, S., Rudat, J., 1995b. Stratigraphic evolution of the Black Sea: inferences from basin modelling. Mar. Pet. Geol. 12, 821–835. https://doi.org/10.1016/0264-8172(95)98850-5.

Robinson, A.G., Rudat, J.H., Banks, C.J., Wiles, R.L.F., 1996. Petroleum geology of the Black Sea. Mar. Pet. Geol. 13, 195–223. https://doi.org/10.1016/0264-8172(95)00042-9.

Robinson, A.G., Griffith, E.T., Gardiner, A.R., Home, A.K., 1997. Petroleum geology of the georgian fold and thrust belts and foreland basins. In: Robinson, A.G. (Ed.), Regional and Petroleum Geology of the Black Sea and Surrounding Region: AAPG Memoirs, 68, pp. 347–367.

Rolland, Y., 2017. Caucasus collisional history: Review of data from East Anatolia to West Iran. Gondwana Res. 49, 130–146. https://doi.org/10.1016/j.gr.2017.05.005.

Rolland, Y., Hässig, M., Bosch, D., Meijers, M.J.M., Sosson, M., Bruguier, O., Adamia, S. A., Sadradze, N., 2016. A review of the plate convergence history of the East Anatolia-Transcaucasus region during the Variscan: Insights from the Georgian basement and its connection to the Eastern Pontides. J. Geodyn. 96, 131–145. https://doi.org/10.1016/j.jog.2016.03.003.

Roure, F., 2008. Foreland and hinterland basins: what controls their evolution? Swiss J. Geosci. 101, 1–4. https://doi.org/10.1007/s00015-008-1285-x.

Sachsenhofer, R.F., Popov, S.V., Coric, S., Mayer, J., Misch, D., Morton, M.T., Pupp, M., Rauball, J., Tari, G., 2018. Paratethyan petroleum source rocks: an overview. J. Pet. Geol. 41, 219–245. https://doi.org/10.1111/jpg.12702.

Shatilova, I.I., Maissuradze, L.S., Koiava, K.P., Kokolashvili, I.M., Bukhsianidze, M.G., Bruch, A.A., 2020. The Environmental History of Georgia during the Late Miocene Based of Foraminifera and Pollen. Universal, Tbilisi.

Shillington, D.J., White, N., Minshull, T.A., Edwards, G.R.H., Jones, S.M., Edwards, R.A., Scott, C.L., 2008. Cenozoic evolution of the eastern Black Sea: a test of depth-dependent stretching models. Earth Planet. Sci. Lett. 265, 360–378. https://doi.org/10.1016/j.epsl.2007.10.033.

Shuster, D.L., Farley, K.A., 2009. The influence of artificial radiation damage and thermal annealing on helium diffusion kinetics in apatite. Geochim. Cosmochim. Acta 73, 183–196. https://doi.org/10.1016/j.gca.2008.10.013.

Shuster, D.L., Flowers, R.M., Farley, K.A., 2006. The influence of natural radiation damage on helium diffusion kinetics in apatite. Earth Planet. Sci. Lett. 249, 148–161. https://doi.org/10.1016/j.epsl.2006.07.028.

Sokhadze, G., Floyd, M., Godoladze, T., King, R., Cowgill, E.S., Javakhishvili, Z., Hahubia, G., Reilinger, R., 2018. Active convergence between the Lesser and Greater Caucasus in Georgia: Constraints on the tectonic evolution of the Lesser–Greater Caucasus continental collision. Earth Planet. Sci. Lett. 481, 154–161. https://doi.org/10.1016/j.epsl.2017.10.007.

Sosson, M., Rolland, Y., Müller, C., Danelian, T., Melkonyan, R., Kekelia, S., Adamia, S. A., Babazadeh, V., Kangarli, T., Avagyan, A., Galoyan, G., Mosar, J., 2010. Subductions, obduction and collision in the Lesser Caucasus (Armenia, Azerbaijan, Georgia), new insights. In: Sosson, Marc, Kaymakci, N., Stephenson, R.A., Bergerat, F., Starostenko, V. (Eds.), Sedimentary Basin Tectonics from the Black Sea and Caucasus to the Arabian Platform, vol. 340. Geological Society of London, Special Publications, pp. 329–352. https://doi.org/10.1144/SP340.14.

Sosson, M., Stephenson, R., Sheremet, Y., Rolland, Y., Adamia, S.A., Melkonian, R., Kangarli, T., Yegorova, T., Avagyan, A., Galoyan, G., Danelian, T., Hässig, M., Meijers, M., Müller, C., Sahakyan, L., Sadradze, N., Alania, V., Enukidze, O., Mosar, J., 2016. The eastern Black Sea-Caucasus region during the Cretaceous: New evidence to constrain its tectonic evolution. Compt. Rendus Geosci. 348, 23–32. https://doi.org/10.1016/j.crte.2015.11.002.

Spadini, G., Robinson, A., Cloetingh, S., 1996. Western versus Eastern Black Sea tectonic evolution: Pre-rift lithospheric controls on basin formation. Tectonophysics 266, 139–154. https://doi.org/10.1016/S0040-1951(96)00187-4.

Stampfli, G.M., Hochard, C., 2009. Plate tectonics of the Alpine realm. In: Murphy, J.B., Keppie, J.D., Hynes, A.J. (Eds.), Ancient Orogens and Modern Analogues, 327. Geological Society, London, Special Publications, pp. 89–111. https://doi.org/10.1144/SP327.6.

Stephenson, R., Schellart, W.P., 2010. The Black Sea back-arc basin: Insights to its origin from geodynamic models of modern analogues. In: Sosson, M., Kaymakci, N., Stephenson, R.A., Bergerat, F., Starostenko, V. (Eds.), Sedimentary Basin Tectonics from the Black Sea and Caucasus to the Arabian Platform, vol. 340. Geological Society, London, Special Publications, pp. 11–21. https://doi.org/10.1144/SP340.2.

Tari, G.C., Simmons, M.D., 2018. History of deepwater exploration in the Black Sea and an overview of deepwater petroleum play types. In: Simmons, M.D., Tari, G.C., Okay, A.I. (Eds.), Petroleum Geology of the Black Sea, vol. 464. Geological Society, London, Special Pubblications, pp. 439–475. https://doi.org/10.1144/SP464.16.

Tari, G., Vakhania, D., Tatishvili, G., Mikeladze, V., Gogritchiani, K., Vacharadze, S., Mayer, J., Sheya, C., Siedl, W., Banon, J.J.M., Sanchez, J.T., 2018. Stratigraphy, structure and petroleum exploration play types of the Rioni Basin, Georgia. In: Simmons, M.D., Tari, G.C., Okay, A.I. (Eds.), Petroleum Geology of the Black Sea, vol. 464. Geological Society, London, Special Publications, pp. 403–438.

Tedliashvili, K.T., 2013. New data on stages in the formation of the pre-alpine continental crust beneath the Khrami Crystalline Massif (Caucasus). Dokl. Earth Sci. 453, 1188–1192. https://doi.org/10.1134/S1028334X13120179.

Tibaldi, A., Alania, V., Bonali, F.L., Enukidze, O., Tsereteli, N., Kvavadze, N., Varazanashvili, O., 2017. Active inversion tectonics, simple shear folding and back-thrusting at Rioni Basin, Georgia. J. Struct. Geol. 96, 35–53. https://doi.org/10.1016/j.jsg.2017.01.005.

Tsereteli, N., Tibaldi, A., Alania, V., Gventsadse, A., Enukidze, O., Varazanashvili, O., Müller, B.I.R., 2016. Active tectonics of Central-Western Caucasus, Georgia. Tectonophysics 691, 328–344. https://doi.org/10.1016/j.tecto.2016.10.025.

USSR Geological Survey, 1956a. Geological Map of the USSR, 1: 200 000 scale, Sheet K-38-XV.

USSR Geological Survey, 1956b. Geological Map of the USSR, 1: 200 000 scale, Sheet K-38-XIV.

USSR Geological Survey, 1956c. Geological Map of the USSR, 1: 200 000 scale, Sheet K-38-XXII.

USSR Geological Survey, 1957a. Geological Map of the USSR, 1: 200 000 scale, Sheet K-38-XX.

USSR Geological Survey, 1957b. Geological Map of the USSR, 1: 200 000 scale, Sheet K-38-XXI.

Uyeda, S., McCabe, R., 1983. A possible mechanism of episodic spreading of the Philippine Sea. In: Hashimoto, M., Uyeda, S. (Eds.), Accretion Tectonics in the Circum-Pacific Regions. Tokyo, TerraPub, pp. 291–306.

Van Wijhe, D.H., 1987. Structural evolution of inverted basins in the Dutch offshore. In: Ziegler, P.A. (Ed.), Compressional Intra-Plate Deformations in the Alpine Foreland. Tectonophysics, pp. 171–219. https://doi.org/10.1016/0040-1951(87)90320-9.

Vasey, D.A., Cowgill, E., Roeske, S.M., Niemi, N.A., Godoladze, T., Skhirtladze, I., Gogoladze, S., 2020. Evolution of the Greater Caucasus basement and formation of the Main Caucasus Thrust, Georgia. Tectonics 39. https://doi.org/10.1029/2019TC005828.

Vincent, S.J., Morton, A.C., Carter, A., Gibbs, S., Barabadze, T.G., 2007. Oligocene uplift of the Western Greater Caucasus: an effect of initial Arabia-Eurasia collision. Terra Nova 19, 160. https://doi.org/10.1111/j.1365-3121.2007.00731.x.

Vincent, S.J., Carter, A., Lavrishchev, V.A., Rice, S.P., Barabadze, T.G., Hovius, N., 2011. The exhumation of the western Greater Caucasus: a thermochronometric study. Geol. Mag. 148, 1–21. https://doi.org/10.1017/S0016756810000257.

Vincent, S.J., Hyden, F., Braham, W., 2013a. Along-strike variations in the composition of sandstones derived from the uplifting western Greater Caucasus: Causes and implications for reservoir quality prediction in the Eastern Black Sea. In: Scott, R.A., Smyth, H.R., Morton, A.C., Richardson, N. (Eds.), Sediment Provenance Studies in Hydrocarbon Exploration and Production, vol. 386. Geological Society, London, Special Publications, pp. 111–127. https://doi.org/10.1144/SP386.15.

Vincent, S.J., Morton, A.C., Hyden, F., Fanning, M., 2013b. Insights from petrography, mineralogy and U-Pb zircon geochronology into the provenance and reservoir potential of Cenozoic siliciclastic depositional systems supplying the northern margin of the Eastern Black Sea. Mar. Pet. Geol. 45, 331–348. https://doi.org/10.1016/j.marpetgeo.2013.04.002.

Vincent, S.J., Braham, W., Lavrishchev, V.A., Maynard, J.R., Harland, M., 2016. The formation and inversion of the western Greater Caucasus Basin and the uplift of the western Greater Caucasus: Implications for the wider Black Sea region. Tectonics 35, 2948–2962. https://doi.org/10.1002/2016TC004204.

Vincent, S.J., Somin, M.L., Carter, A., Vezzoli, G., Fox, M., Vautravers, B., 2020. Testing models of Cenozoic exhumation in the Western Greater Caucasus. Tectonics 1–27. https://doi.org/10.1029/2018tc005451.

Wolf, R.A., Farley, K.A., Silver, L.T., 1996. Helium diffusion and low-temperature thermochronometry of apatite. Geochim. Cosmochim. Acta 60, 4231–4240. https://doi.org/10.1016/S0016-7037(96)00192-5.

Wolf, R.A., Farley, K.A., Kass, D.M., 1998. Modeling of the temperature sensitivity of the apatite (U-Th)/He thermochronometer. Chem. Geol. 148, 105–114. https://doi.org/10.1016/S0009-2541(98)00024-2.

Yılmaz, A., Adamia, S.A., Chabukiani, A., Chkhotua, T., Erdoğan, K., Tuzcu, S., Karabiyikoğlu, M., 2000. Structural correlation of the southern Transcaucasus (Georgia)-eastern Pontides (Turkey). In: Bozkurt, E., Winchester, J.A., Piper, J.D.A. (Eds.), Tectonics and Magmatism in Turkey and the Surrounding Area, vol. 173. Geological Society of London, Special Publications, pp. 171–182.

Yılmaz, A., Adamia, S.A., Yılmaz, H., 2014. Comparisons of the suture zones along a geotraverse from the Scythian Platform to the Arabian Platform. Geosci. Front. 5, 855–875. https://doi.org/10.1016/j.gsf.2013.10.004.

Ziegler, P.A., 1990. Collision related intra-plate compression deformations in Western and Central Europe. J. Geodyn. 11, 357–388. https://doi.org/10.1016/0264-3707(90)90017-O.

Ziegler, P.A., 1993. Plate-moving mechanisms: their relative importance. J. Geol. Soc. Lond. 150, 927–940.

Ziegler, P.A., Cloetingh, S., 2004. Dynamic processes controlling evolution of rifted basins. Earth-Sci. Rev. 64, 1–50. https://doi.org/10.1016/S0012-8252(03)00041-2.

Ziegler, P.A., Cloetingh, S., van Wees, J.D., 1995. Dynamics of intra-plate compressional deformation: the Alpine foreland and other examples. Tectonophysics 252, 7–59. https://doi.org/10.1016/0040-1951(95)00102-6.

Ziegler, P.A., Van Wees, J.D., Cloetingh, S., 1998. Mechanical controls on collision-related compressional intraplate deformation. Tectonophysics 300, 103–129. https://doi.org/10.1016/S0040-1951(98)00236-4.

Ziegler, P.A., Bertotti, G., Cloetingh, S., 2002. Dynamic processes controlling foreland development – the role of mechanical (de)coupling of orogenic wedges and forelands. Stephan Mueller Spec. Publ. Ser. 1, 17–56. https://doi.org/10.5194/smsps-1-17-2002.

Zoback, M. Lou, 1992. First- and second-order patterns of stress in the lithosphere: the World stress Map Project. J. Geophys. Res. 97, 11703 https://doi.org/10.1029/92jb00132.

Zonenshain, L.P., Le Pichon, X., 1986. Deep basins of the Black Sea and Caspian Sea as remnants of Mesozoic back-arc basins. Tectonophysics 13, 181–121.

SUPPLEMENTARY MATERIALS

Paper: “Structural inversion of back-arc basins–The Neogene Adjara-Trialeti fold-and-thrust belt (SW Georgia) as a far-field effect of the Arabia-Eurasia collision”, Tectonophysics 803

Tables S1a-e: Input and Output details relative to statistical inverse modelling of samples TU279, TU486, TU488, TU510, and TU515.

Tables S2a-f: Age-Rs, Age-eU, Age-U, and Age-Th plots relative to apatite (U-Th)/He single-grain ages for samples TU485, TU486, TU487, TU499, TU501, and TU512. Red dots represent the replicates discarded and not considered in the analyses.

Table S3: Age/elevation plot for AFT results. There is no correlation between samples ages and elevations.

Table S4: Age/elevation plot for AHe results. There is no correlation between samples ages and elevations.

Table S1a: Sample TU279 modelling details

Thermochronologic data

AFT data	*N° grains*	*Central age*	*MCTL*	*N° tracks*	*Mean Dpar*
	17	33.1 ± 2.7 Ma	13.41 ± 0.12 µm	50	2.10 µm

Additional geologic information

Constraint	*Explanation*	*Reference*
900-1000 °C at 45-40 Ma	43.26 ± 0.74 Ma crystallization age obtained through zircon U-Pb LA ICP-MS	Okrostsvaridze et al., 2018b
Five t-T broad boxes	Since no independent geologic constraints are available for this sample, apart from the crystallization age, these boxes have been intentionally put as very broad , allowing the program to search a wide t-T space	
Present-day surface temperature 20 ± 10 °C	Since specific temperature data were not available from the region, we used a standard surface temperature.	

System- and model-specific parameters

AFT	*Annealing model*	*C-axis projection*	*Model c-axis projected lengths?*	*Default initial mean track length*	*Kinetic parameter*	*GOF metod*
	Ketcham et al., 2007	Ketcham et al., 2007, 5.0M	Yes	From Dpar	Dpar	Kuiper's Statistic
Statistical fitting criteria	acceptable paths for GOF values >0.05; good paths for GOF values >0.5					
t-T paths charachteristics	episodic history, halve two times, monotonic consistent between constraints					
Number of paths attempted:	30905					
Number of acceptable paths:	720					
Number of good paths:	300					

Table S1b: Sample TU486 modelling details

Thermochronologic data							
AFT data	*N° grains*	*Central age*	*MCTL*	*N° tracks*	*Mean Dpar*		
	49	34.7 ± 2.8 Ma	12.05 ± 0.22 µm	53	2.38 µm		
AHe data	*Replicate name*	*Uncorrected age*	*eU*	*Grain radius*	*U (ppm)*	*Th (ppm)*	*Sm (ppm)*
	TU486-1	3.93 ± 0.12 Ma	15.8	47 µm	10.3	23.9	24.1
	TU486-5	2.67 ± 0.04 Ma	26.0	42 µm	10.7	65.6	43.2

Additional geologic information		
Constraint	*Explanation*	*Reference*
Near-surface conditions (0-40°C) at 60-48 Ma	Depositional age is Paleocene-Early Eocene	Adamia, 2004
40-160 °C at 70-50 Ma	No data available on the sediment source, hence the pre-depositional history was not stricktly constrained and a broad T-t box was used	
0-140°C at 48-0 Ma	Since we do not have any precise information on the maximum depth/temperatre experienced by the sample after deposition, we decided to put two broad boxes with large T-t borders, allowing the program to search a wide area and avoiding to force it to work in narrower space-time areas.	
Present-day surface temperature 20 ± 10 °C	Since specific temperature data were not available from the region, we used a standard surface temperature.	

System- and model-specific parameters						
AFT	*Annealing model*	*C-axis projection*	*Model c-axis projected lengths?*	*Default initial mean track length*	*Kinetic parameter*	*GOF metod*
	Ketcham et al., 2007	Ketcham et al., 2007, 5.0M	Yes	From Dpar	Dpar	Kuiper's Statistic
AHe	*AHe kinetic model*	*Alpha calculation*	*Age alpha correction*	*Stopping distances*	*Precision*	
	RDAAM (Flowers et al., 2009)	Ejection	Ketcham et al., 2011	Ketcham et al., 2011	Good	
Statistical fitting criteria	acceptable paths for GOF values >0.05; good paths for GOF values >0.5					
t-T paths charachteristics	episodic history, halve two times, monotonic consistent between constraints					
Number of paths attempted:	1234017					
Number of acceptable paths:	2119					
Number of good paths:	300					

Table S1c: Sample TU488 modelling details

Thermochronologic data						
	N° grains	*Central age*	*MCTL*	*N° tracks*	*Mean Dpar*	
AFT data	41	27.3 ± 2.5 Ma	12.48 ± 0.31 µm	53	2.36 µm	
Additional geologic information						
Constraint	*Explanation*					*Reference*
Near surface temperature (0-20 °C) at 27-23 Ma	Depositional age of the sample is Late Oligocene					Adamia, 2004
0-140 °C from 23 to 0 Ma	Since we do not have any precise information on the maximum depth/temperatre experienced by the sample after deposition, we decided to put a broad box with large T-t borders, allowing the program to search a wide area and avoiding to force it to wotk in narrower space-time areas.					
Preset day temperature 20 ± 10 °C	Since specific temperature data were not available from the region, we used a standard surface temperature.					
System- and model-specific parameters						
	Annealing model	*C-axis projection*	*Model c-axis projected lengths?*	*Default initial mean track length*	*Kinetic parameter*	*GOF metod*
AFT	Ketcham et al., 2007	Ketcham et al., 2007, 5.0M	Yes	From Dpar	Dpar	Kuiper's Statistic
Statistical fitting criteria	acceptable paths for GOF values >0.05; good paths for GOF values >0.5					
t-T paths charachteristics	episodic history, halve two times, monotonic consistent between constraints					
Number of paths attempted:	2065996					
Number of acceptable paths:	12674					
Number of good paths:	300					

Table S1d: Sample TU510 modelling details

Thermochronologic data

AFT data	*N° grains*	*Central age*	*MCTL*	*N° tracks*	*Mean Dpar*
	56	46.0 ± 3.5 Ma	13.03 ± 0.30 μm	58	2.50 μm

Additional geologic information

Constraint	*Explanation*	*Reference*
30-160 °C from 70 to 40 Ma	No data available on the sediment source, hence the pre-depositional history was not stricktly constrained	
Near surface temperatures (0-40 °C) from 38 to 34 Ma	Depositional age of the sample is Upper Eocene	Adamia, 2004
0-140°C at 34-0 Ma	Since we do not have any precise information on the maximum depth/temperatre experienced by the sample after deposition, we decided to put two broad boxes with large T-t borders, allowing the program to search a wide area and avoiding to force it to wotk in narrower space-time areas.	
Present-day surface temperature 20 ± 10 °C	Since specific temperature data were not available from the region, we used a standard surface temperature.	

System- and model-specific parameters

AFT	*Annealing model*	*C-axis projection*	*Model c-axis projected lengths?*	*Default initial mean track length*	*Kinetic parameter*	*GOF metod*
	Ketcham et al., 2007	Ketcham et al., 2007, 5.0M	Yes	From Dpar	Dpar	Kuiper's Statistic
Statistical fitting criteria	acceptable paths for GOF values >0.05; good paths for GOF values >0.5					
t-T paths charachteristics	episodic history, halve two times, monotonic consistent between constraints					
Number of paths attempted:	11061878					
Number of acceptable paths:	52834					
Number of good paths:	300					

Table S1e: Sample TU515 modelling details

Thermochronologic data

	N° grains	*Central age*	*MCTL*	*N° tracks*	*Mean Dpar*
AFT data	21	43.6 ± 3.7 Ma	13.72 ± 0.21 µm	65	2.12 µm

Additional geologic information

Constraint	*Explanation*	*References*
Near surface temperatures (0-40°C) at 100-94 Ma	Cenomanian unconformity on the top of the massif, indicating it was exposed or at very shallow levels by that time	Adamia et al, 2011; Yilmaz et al, 2014
40-160 °C between 94 and 60 Ma	1-2 km of lavas, limestones, marls and conglomerates deposited in the area from the Turonian to the Danian. Even being very conservative, thus assuming a very low geothermal gradient (25 °C/km) and an average surface temperature of 20 °C, minimum temperatures of 45-70 °C would have been obtained at the top of the massif at this stage. The upper temperature limit was set to 160 °C in order to let the model search in a wide area.	Adamia et al, 2011; Yilmaz et al, 2014
70-160 °C between 60 and 34 Ma	Additional 1-2 km of sandstones, siltstones, shales and lavas deposited between the Selandian and the Priabonian. Even being very conservative, thus assuming a very low geothermal gradient (25 °C/km) and an average surface temperature of 20 °C, minimum temperatures of 70-120 °C would have been obtained at the top of the massif at this stage. The upper temperature limit was set to 160 °C in order to let the model search in a wide area.	Adamia et al, 2011; Yilmaz et al, 2014
0-160°C between 34 and 0 Ma	Sedimentation in the region stopped at the turn of Oligocene, but we do not have any independent constraints on the exhumation phase, hence we used a broad constraint box.	
Present day temperature 20 ± 10 °C	Since specific temperature data were not available from the region, we used a standard surface temperature.	

System- and model-specific parameters

	Annealing model	*C-axis projection*	*Model c-axis projected lengths?*	*Default initial mean track length*	*Kinetic parameter*	*GOF metod*
AFT	Ketcham et al., 2007	Ketcham et al., 2007, 5.0M	Yes	From Dpar	Dpar	Kuiper's Statistic
Statistical fitting criteria	acceptable paths for GOF values >0.05; good paths for GOF values >0.5					
t-T paths charachteristics	episodic history, halve two times, monotonic consistent between constraints					
Number of paths attempted:	100270					
Number of acceptable paths:	2830					
Number of good paths:	500					

Table S2a: Plots related to apatite (U-Th)/He results of sample TU485.

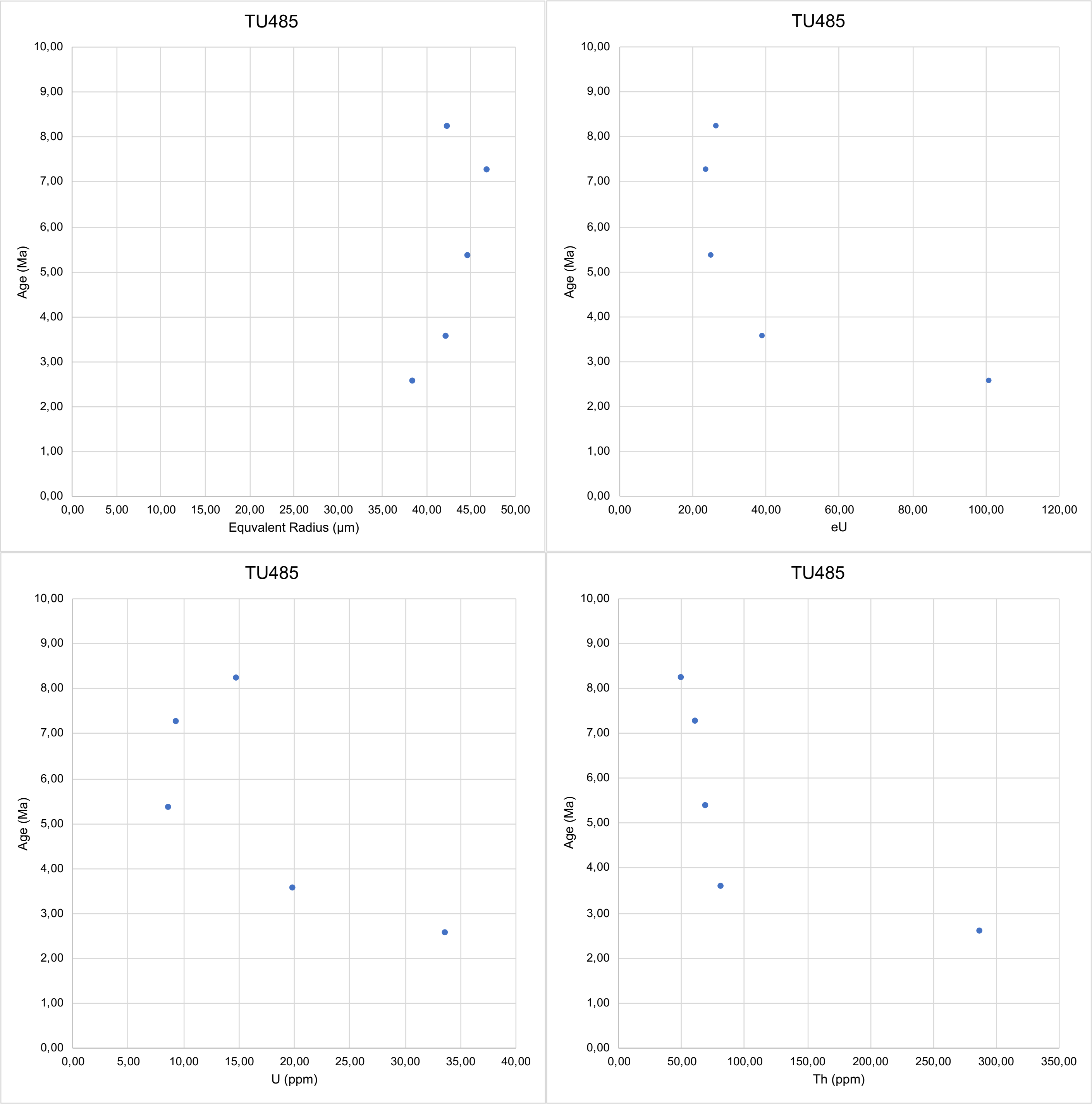

Table S2b: Plots related to apatite (U-Th)/He results of sample TU486. The red point in all plots refers to the replicate discarded and not considered in the analyses.

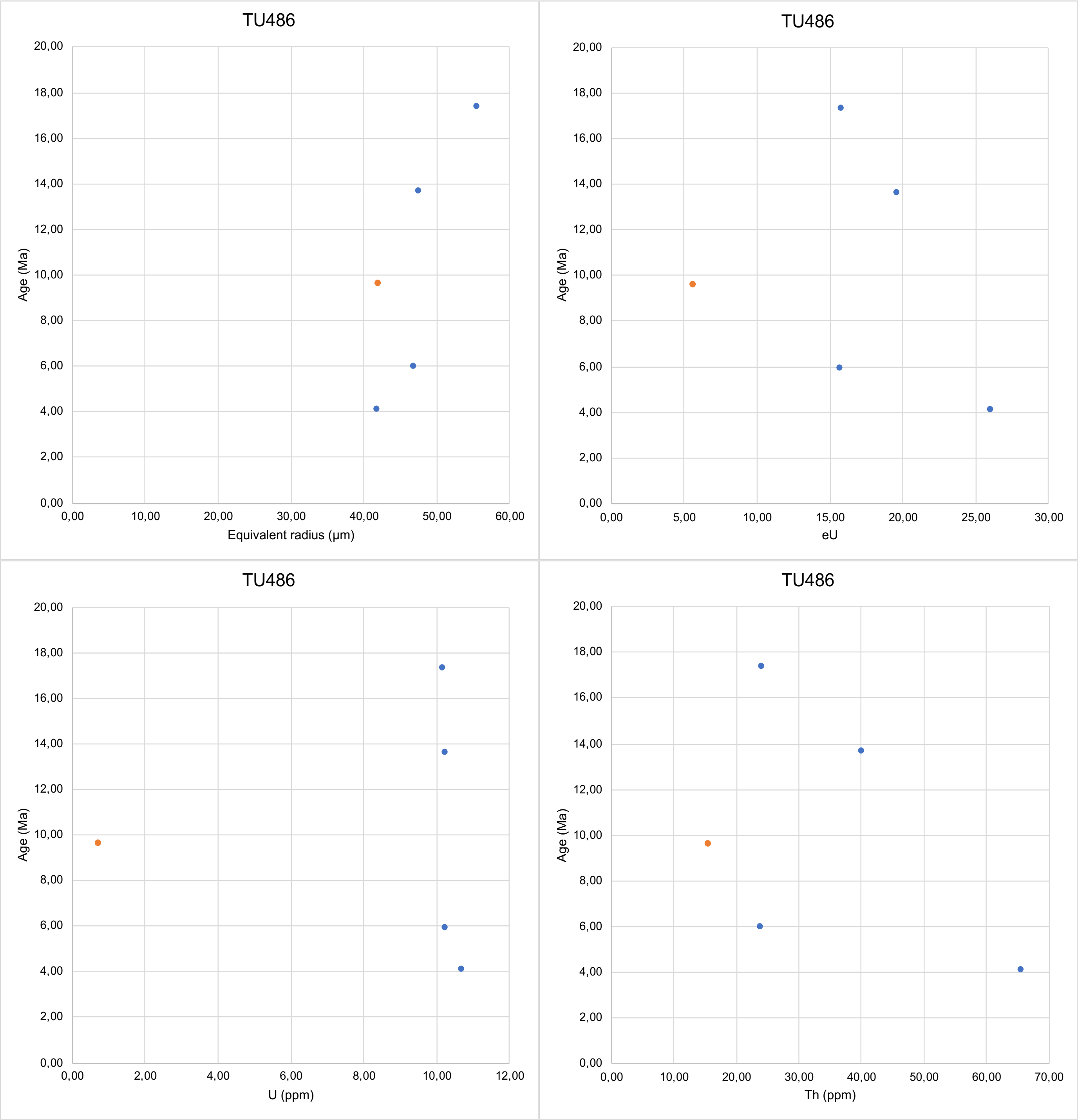

Table S2c: Plots related to apatite (U-Th)/He results of sample TU487.

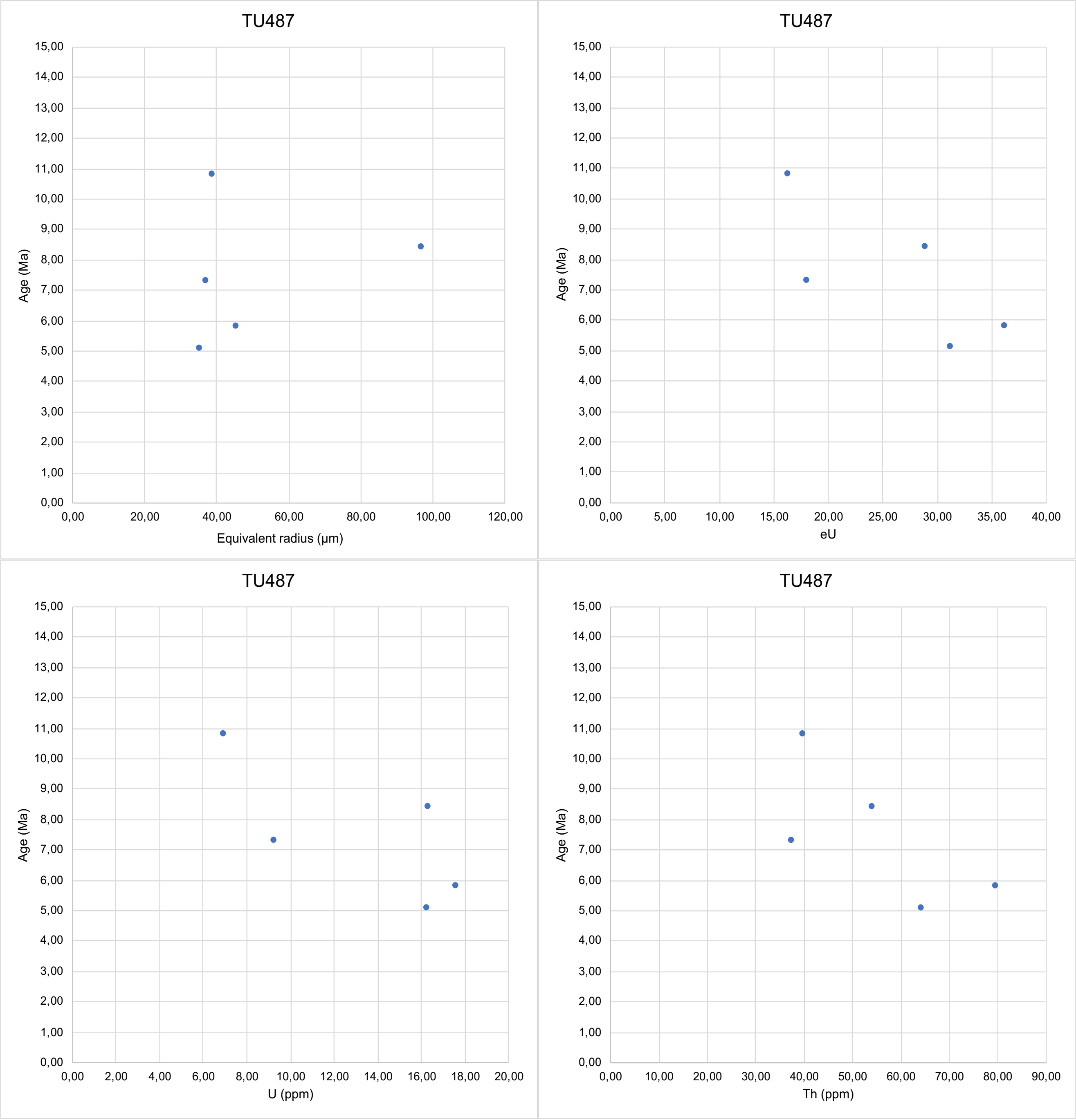

Table S2d: Plots related to apatite (U-Th)/He results of sample TU499. The red point in all plots refers to the replicate discarded and not considered in the analyses.

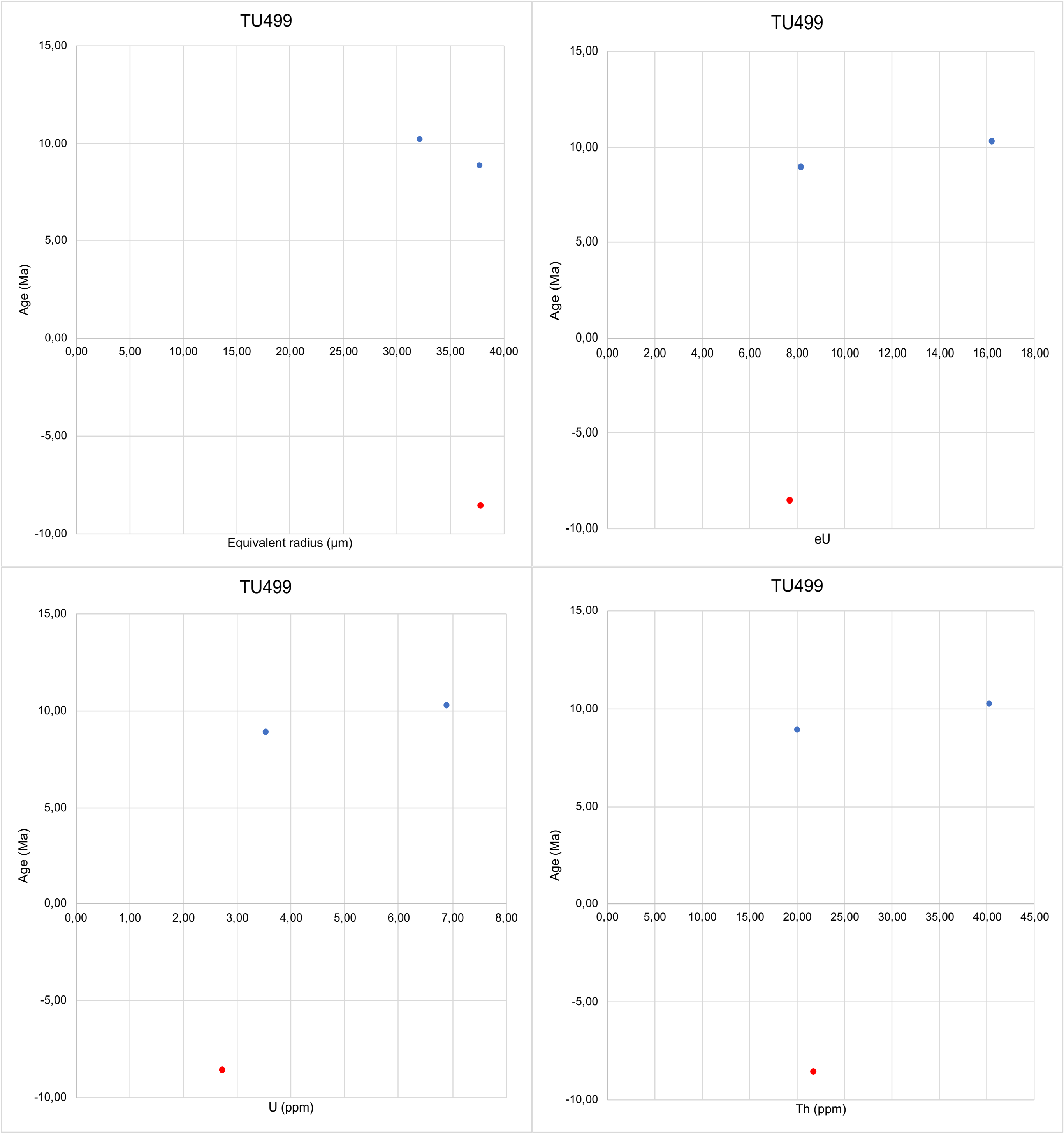

Table S2e: Plots related to apatite (U-Th)/He results of sample TU501.

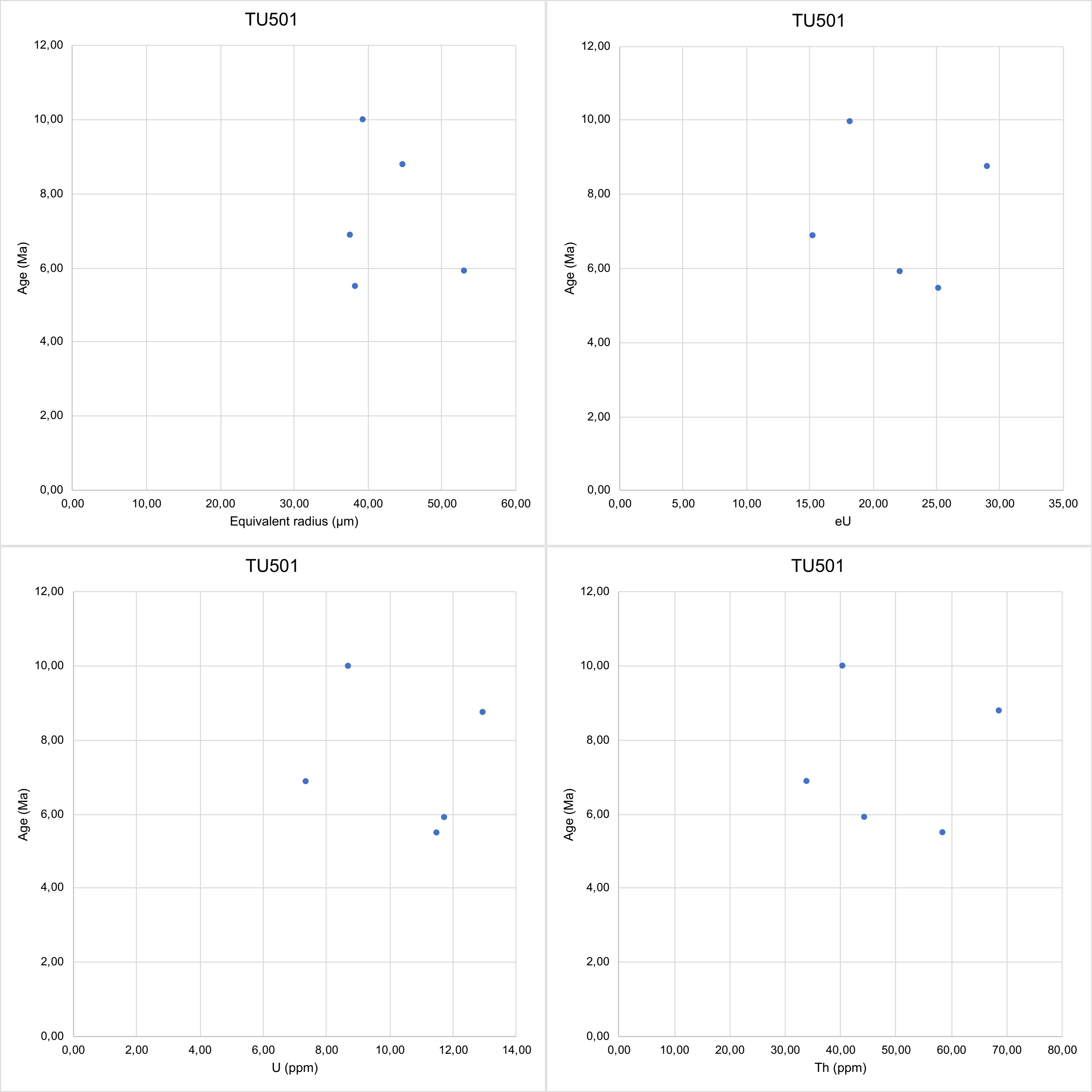

Table S2f: Plots related to apatite (U-Th)/He results of sample TU512.

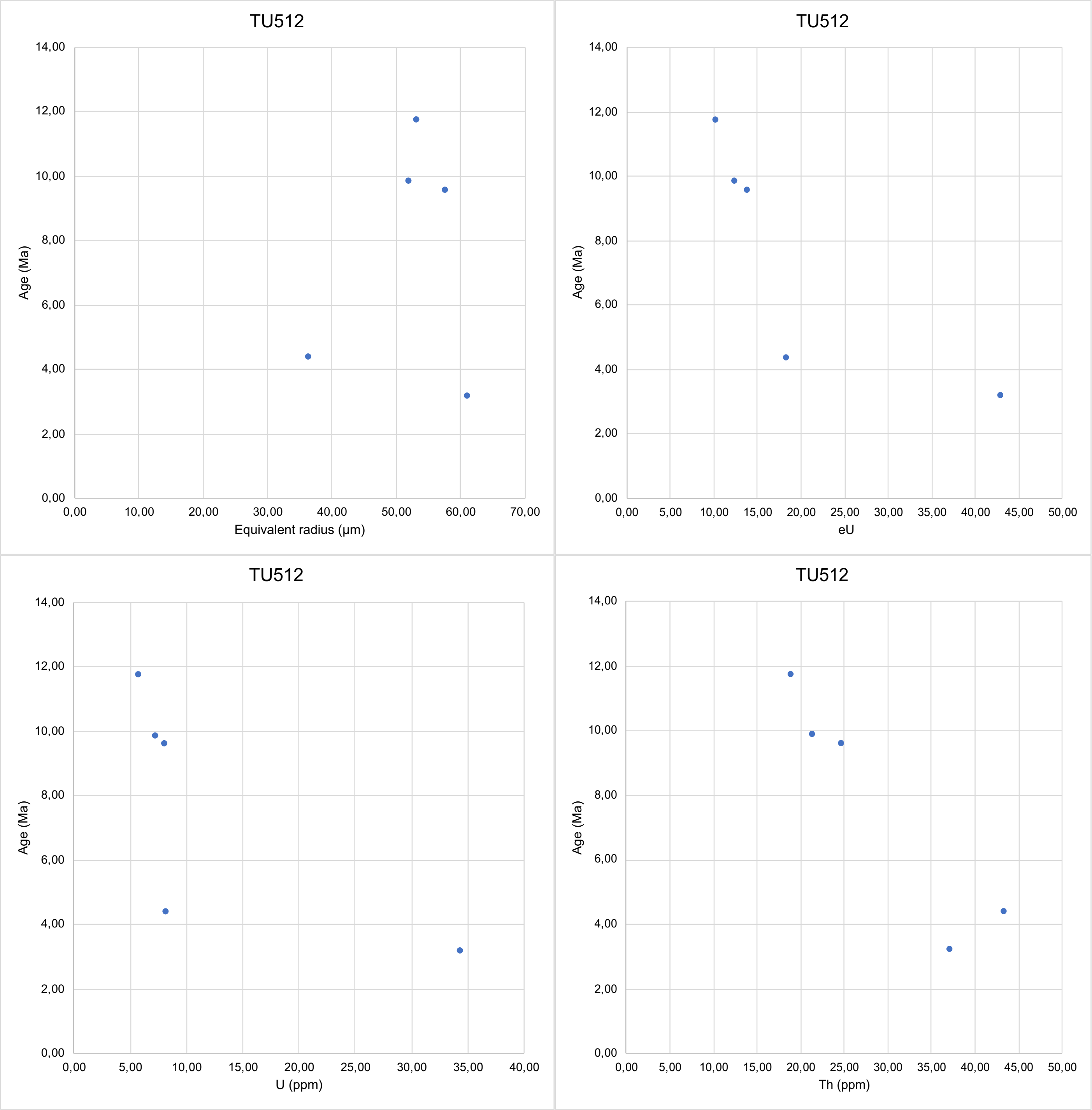

Table S3: Age/elevation plot for AFT results. There is no correlation between samples ages and elevations.

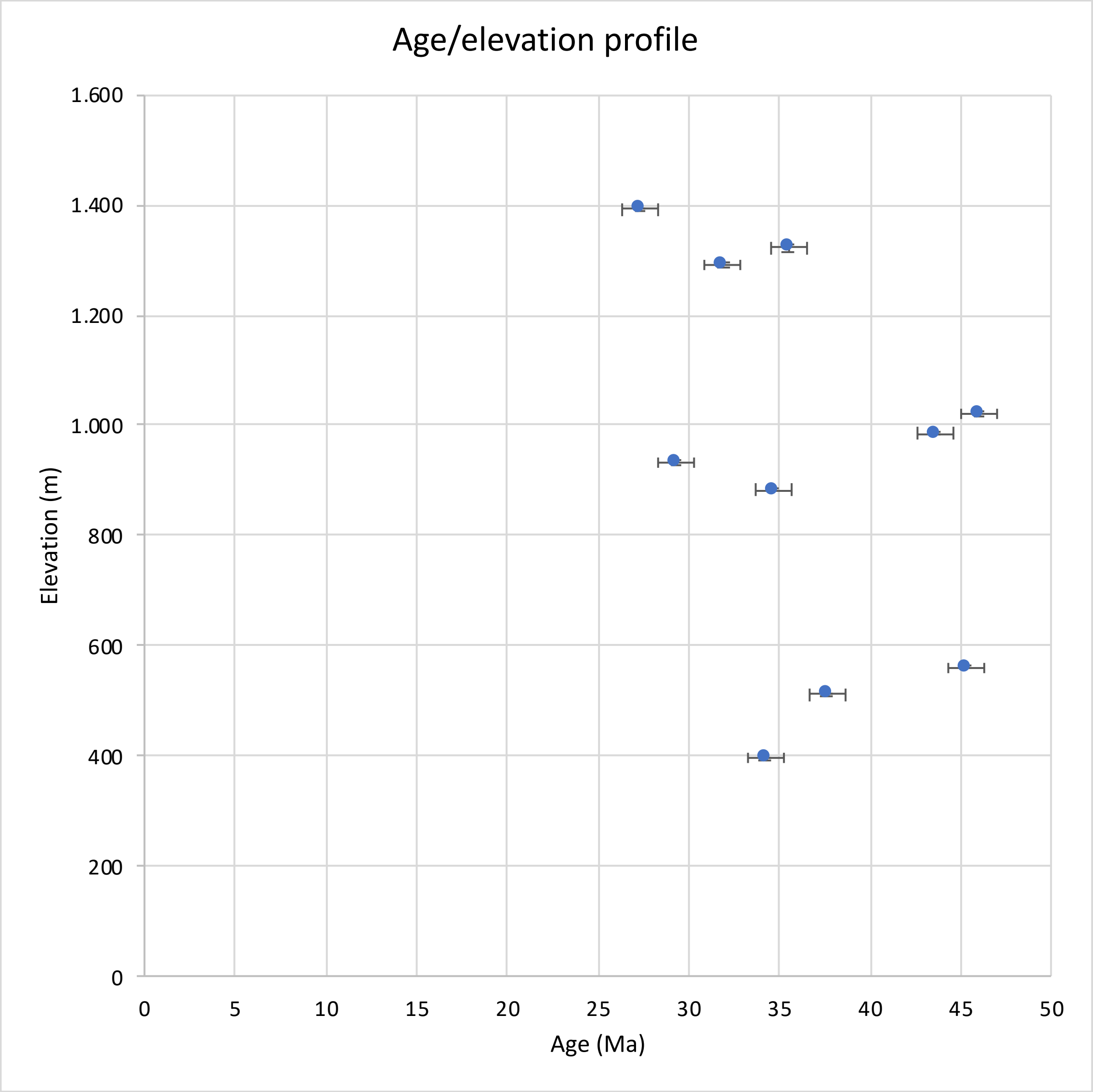

Table S4: Age/elevation plot for AHe results. There is no correlation between samples ages and elevations.

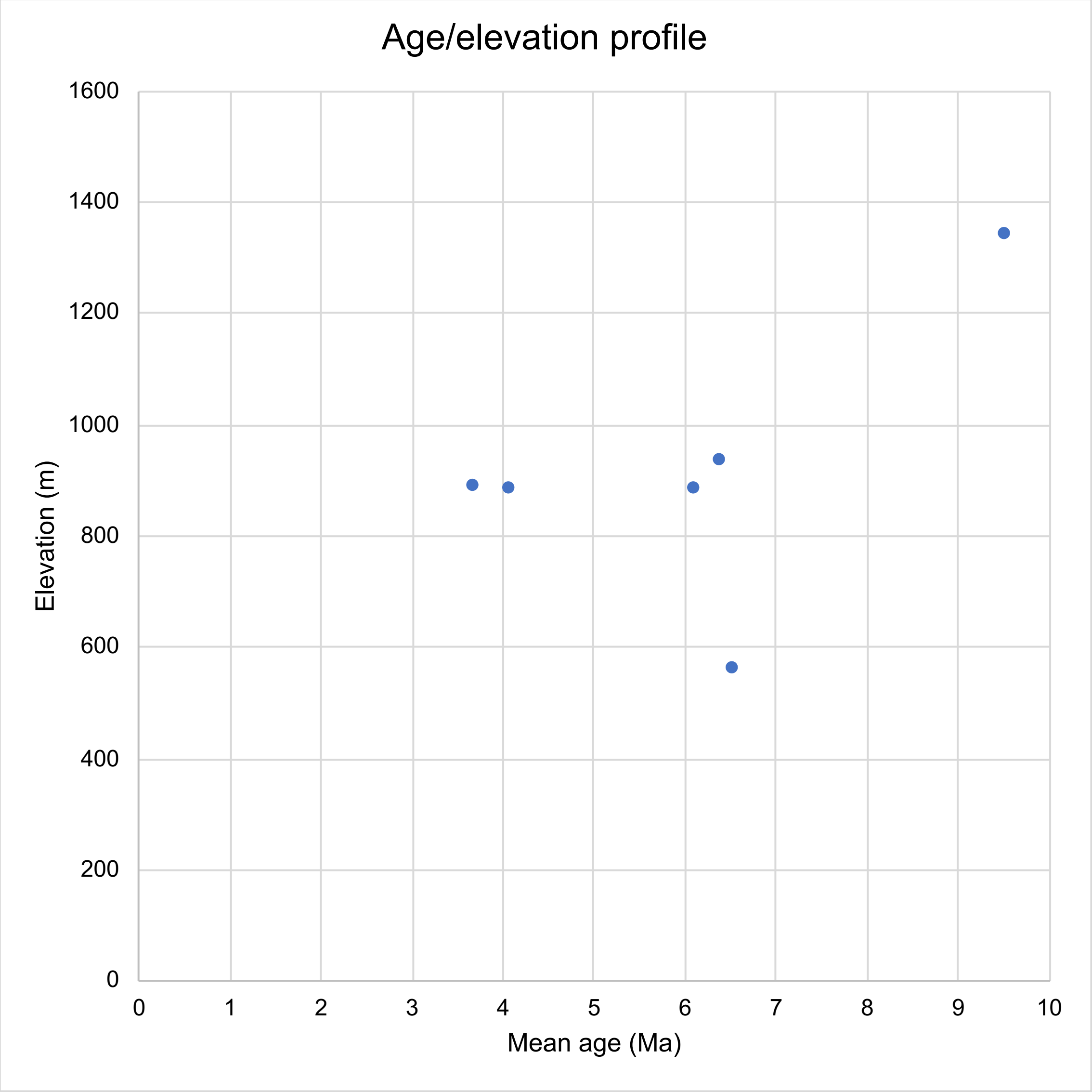

Chapter 3

Manuscript 2:

Validating far-field deformation styles from the Adjara-Trialeti fold-and-thrust belt to the Greater Caucasus (Georgia) through multi-proxy thermal maturity datasets

Manuscript 3

Validating far-field deformation styles from the Adjara-Trialeti fold-and-thrust belt to the Greater Caucasus (Georgia) through multi-proxy thermal maturity datasets

Sveva Corrado, Thomas Gusmeo, Andrea Schito, Victor Alania, Onise Enukidze, Enrico Conventi, and William Cavazza

Submitted to Marine and Petroleum Geology on 5th February 2021, accepted on 15th May 2021, first published online on 20th May 2021.

Marine and Petroleum Geology 130 (2021) 105141

Contents lists available at ScienceDirect

Marine and Petroleum Geology

journal homepage: www.elsevier.com/locate/marpetgeo

Validating far-field deformation styles from the Adjara-Trialeti fold-and-thrust belt to the Greater Caucasus (Georgia) through multi-proxy thermal maturity datasets

Sveva Corrado [a], Thomas Gusmeo [b,*], Andrea Schito [a,c], Victor Alania [d], Onise Enukidze [d], Enrico Conventi [e], William Cavazza [b]

[a] *Dept. of Sciences, Geological Sciences Section, Roma Tre University, Rome, Italy*
[b] *Dept. of Biological, Geological and Environmental Sciences, University of Bologna, Bologna, Italy*
[c] *Dept. of Geology and Petroleum Geology, School of Geosciences, University of Aberdeen, Aberdeen, AB24 3UE, UK*
[d] *Institute of Geophysics, I. Javakhishvili State University, Tbilisi, Georgia*
[e] *Geolog Technologies S.r.l. (GEOTech Research and Laboratory), Viale Ortles 22/4, 20139, Milan, Italy*

ARTICLE INFO

Keywords:
Intra-continental deformation
Alpine orogeny
Maikop
Thermal indicators
Caucasus
Kura basin

ABSTRACT

Thermal history reconstructions can help to better characterise the geological history of areas that experienced a polyphase tectonic evolution. The integration of published stratigraphic/structural data with new and pre-existing data on thermal maturity (clay mineralogy, Raman spectroscopy, vitrinite reflectance, and pyrolysis) of both surface and subsurface sedimentary successions of a wide region of Georgia including -north to south- the southern Greater Caucasus, the western Kura Basin, and the Adjara-Trialeti fold-and-thrust belt (FTB) provides cogent constraints on its late Mesozoic-Cenozoic tectono-sedimentary evolution.

Overall, thermal maturity spans from the low diagenesis (60–80 °C) in the Upper Miocene section of the Kura Basin to anchizone-epizone (about 400 °C) in the central Greater Caucasus axial zone. In more detail, different maturity trends and thermal histories point to the existence of two domains formed by positive tectonic inversion: (i) the Adjara-Trialeti FTB from an Eocene rift basin and (ii) the Greater Caucasus from a Mesozoic rift basin. Multiple thermal indicators, along with stratigraphic/structural evidence, show that the Paleocene section of the Adjara-Trialeti basin fill reached the upper oil window (ca. 115 °C) during maximum sedimentary burial and that the whole basin was then exhumed starting from the late Middle Miocene. A positive correlation between thermal maturity and stratigraphic age points to a limited thermal effect of tectonic loading. In the southern Greater Caucasus, thermal maturity increases progressively with stratigraphic age, from ca. 100 °C (Upper Eocene) to 400 °C (Lower Jurassic), in broad agreement with the reconstructed thickness of the basin-fill succession, thus indicating that most of the thermal maturity was again induced by sedimentary burial.

As to the flexural western Kura Basin, its Maikopian (Oligocene-Early Miocene) section reached the oil window (up to ca. 110 °C) whereas the Middle-Late Miocene one is immature. The Kakheti ridge -a highly tectonised portion of the Kura Basin- reached immature to early mature conditions.

1. Introduction

The use of indicators of maximum paleo-temperatures and thermal maturity from sedimentary successions in orogenic zones is traditionally used for hydrocarbon (HC) exploration (e.g. Aldega et al., 2014; Allen and Allen, 2013; Tozer et al., 2020). Less frequently, it is applied to validate structural styles in deformed orogenic belts (e.g. Aldega et al., 2018; Atouabat et al., 2020; Balestra et al., 2019; Caricchi et al., 2015; Di Paolo et al., 2014; Muirhead et al., 2020; Tozer et al., 2020), either because of lack of constraints on timing of exhumation that can bias thermal modelling, or because such indicators mostly derive from surface outcrops and can allow modelling only of pseudo-well sections, rather than present-day boreholes, introducing an extra degree of uncertainty.

In recent years the frequent integration of classical and cutting-edge indicators of thermal maturity due to burial (either sedimentary or

---

* Corresponding author. Piazza di Porta San Donato 1, 40126, Bologna, Italy.
E-mail address: thomas.gusmeo2@unibo.it (T. Gusmeo).

https://doi.org/10.1016/j.marpetgeo.2021.105141
Received 5 February 2021; Received in revised form 14 May 2021; Accepted 15 May 2021

tectonic) allowed the assessment of maximum paleo-temperatures in sedimentary basins with reduced error bars (Corrado et al., 2005, 2020, 2020; Goodhue and Clayton, 2010; Labeur et al., 2021; Liu et al., 2019; Mangenot et al., 2017, 2019, 2019; Qiu et al., 2020; Spina et al., 2018). For example, pyrolysis parameters (HI, PI, Tmax) (Behar et al., 2001; Tissot et al., 1987), clay-derived geothermometers (such as illite percentage in illite-smectite mixed layers and illite crystallinity index, KI; Aldega et al., 2007a, 2007b; Schito et al., 2016), vitrinite reflectance (Balestra et al., 2019; Burnham and Sweeney, 1989; Corrado et al., 2009; Dow, 1977) in the diagenetic realm and Raman spectroscopy parameters in both the metamorphic and diagenetic realms on organic matter (Beyssac et al., 2002; Lahfid et al., 2010; Lünsdorf and Lünsdorf, 2016; Schito et al., 2017) can lead to significant reduction of admissible paleotemperature ranges in the evolution of compressional areas, especially when they are combined with maximum paleotemperatures derived from low-T thermochronological modelling [fission-track and (U–Th)/He dating on apatite crystals] (Aldega et al., 2011; Corrado et al., 2020; Schito et al., 2018).

Georgia, located in the deformed hinterland of the Arabia-Eurasia collision occurring along the Bitlis-Zagros suture zone, represents a privileged and fascinating natural laboratory to validate structural styles that developed during Arabia-Eurasia convergence using thermal maturity datasets. Here, different orogenic chains crop out with opposite vergences, variable structural styles and shortening degrees, accommodating far-field regional convergence (e.g. Adamia et al., 2010, 2011b; Alania et al., 2017; Nemčok et al., 2013). In the present study we consider three tectonic domains: from south to north they are (i) the Adjara-Trialeti FTB, (ii) the Kura Basin (comprising its northern highly deformed portion, the Kakheti ridge) and (iii) the Georgian Greater Caucasus (Fig. 1). Brittle structures and basin sedimentary fills, due to stretching developed either in Mesozoic or early Cenozoic times, influence the geometry and distribution of the late Cenozoic compressive deformation that brought to minor (Kura Basin and Kakheti ridge), moderate (Adjara-Trialeti FTB) or intense exhumation (Georgian Greater Caucasus), with a peak in Miocene times (Alania et al., 2017; Gusmeo et al., 2021; Vincent et al., 2020).

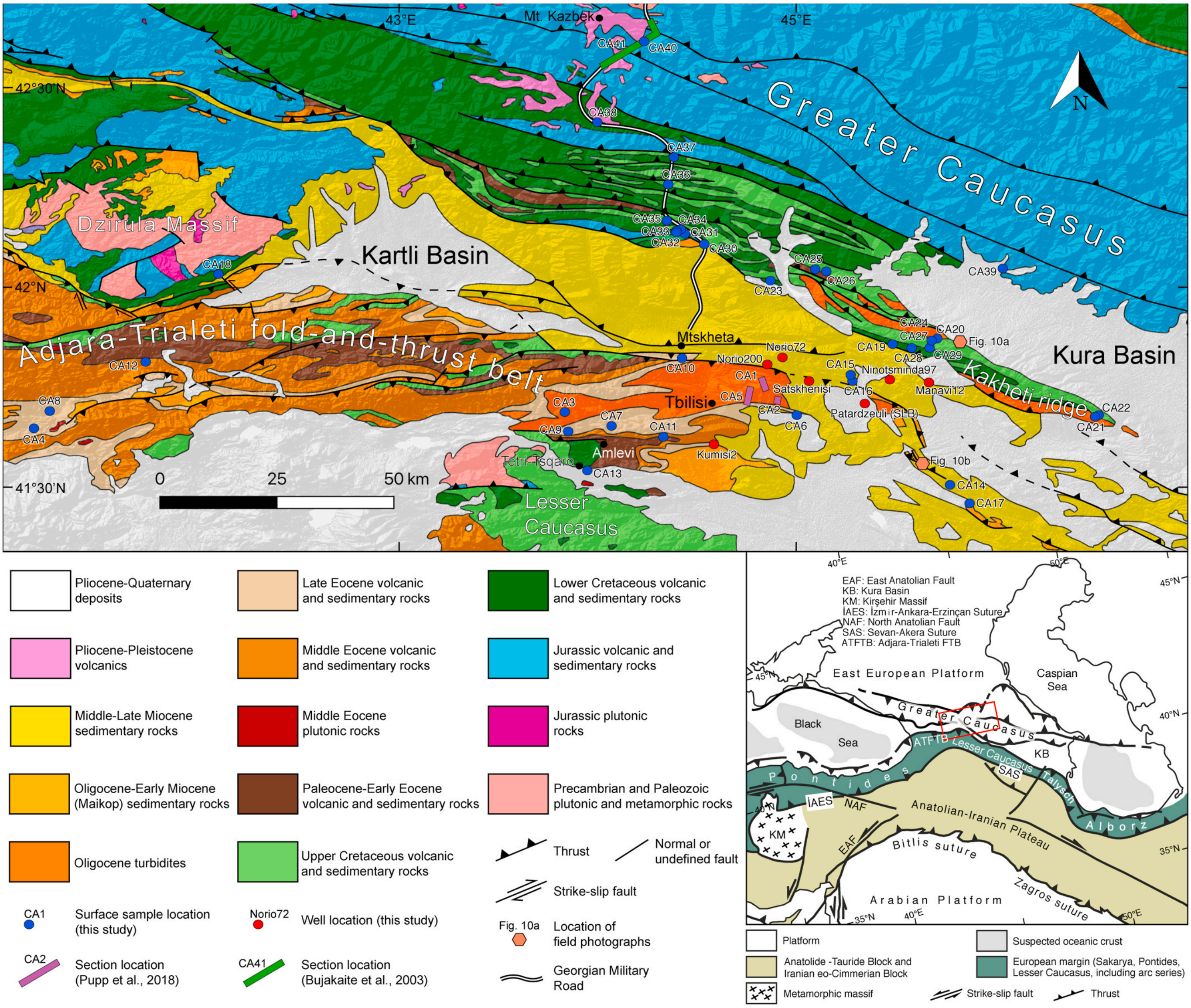

Fig. 1. Geological map of the study area modified after Adamia (2004) and Gusmeo et al. (2021) with discussed sample sites and sections. Sample numbers refer to Tables 1 and 2 Locations of field photographs in Fig. 10 are also shown. Lower-right inbox: geodynamic setting of the collision zone between Eurasia and Arabia (after Cavazza et al., 2019; Sosson et al., 2010). Red rectangle indicates position of Fig. 3. (For interpretation of the references to colour in this figure legend, the reader is referred to the Web version of this article.)

In this region, geometric and genetic relationships between areas affected by positive inversion and moderate to high exhumation, and areas where thin-skinned thrust tectonics develops with higher shortening and less exhumation, are not consistently described (Adamia et al., 2010; Alania et al., 2017, 2018, 2020, 2018; Mosar et al., 2010; Nemčok et al., 2013). Different seismic interpretations and scarcity of detailed structural surveys have led to contrasting structural interpretations (Adamia et al., 2010, 2011b; Alania et al., 2020; Banks et al., 1997; Forte et al., 2010, 2013, 2014; Mosar et al., 2010; Nemčok et al., 2013; Tibaldi et al., 2017, 2018). There is also uncertainty regarding the eastward continuation of the Adjara-Trialeti FTB in easternmost Georgia and Azerbaijan, and its link with the unconstrained retrowedge of the Lesser Caucasus (Alania et al., 2017; Nemčok et al., 2013; Sosson et al., 2010, 2016). Moreover, the geometry of the main structural features within the Greater Caucasus, at least in Georgia, is only shown at a crustal scale (e.g. Mosar et al., 2010; Nemčok et al., 2013; Saintot et al., 2006; Sosson et al., 2016). General agreement exists on the nature of a thin-skinned south-verging thrust system in the western portion of the Kura Basin to the south of the eastern Greater Caucasus, where HC exploration and production are ongoing (Alania et al., 2017, 2018, 2018; Pace et al., 2019; Pupp et al., 2018).

The purpose of this paper is to give new constraints on the structural style in the three domains of continental deformation in Georgia, to the north of the Bitlis-Zagros suture zone, by presenting and integrating two thermal maturity datasets:

- Surface data, derived from clay mineralogy and Raman spectroscopy, petrography and pyrolysis on organic matter, from Jurassic to Upper Miocene lithostratigraphic units. Original data generated during this study have been integrated by published data from the Kura Basin and the Greater Caucasus.
- Subsurface data, including both published and unpublished results from deep wells exploring the Oligocene-Lower Miocene Maikop series, in the western portion of the Kura Basin and in the easternmost Adjara-Trialeti FTB. These data result from the prolonged attention devoted to the Maikop series, recognized as the main source rock in the Kura Basin (Boote et al., 2018; Pupp et al., 2018). Its oil potential is quite low because of low TOC values and prevalence of type III kerogen (rich in terrestrial input) dispersed in sedimentary rocks. These features extend also to the east moving towards the Caspian Sea (Washburn et al., 2019). Nevertheless, the significant burial depth within the Kura Basin allowed source intervals to enter the oil window in the surroundings of Tbilisi (Pupp et al., 2018; Sachsenhofer et al., 2018).

The integration of the two datasets with the tectono-stratigraphic setting of the three main structural domains, derived from original field surveys and pre-existing literature, allowed (i) to constrain the level of thermal maturity acquired through time in the extensional and flexural basins considered, and (ii) to evaluate the relative contribution of sedimentary/tectonic burial to the thermal maturation during extensional phases and intraplate shortening, a few hundred kilometres to the north of the Bitlis-Zagros suture zone of the Arabia-Eurasia collision (Cavazza et al., 2018, 2019).

2. Geological setting

The study area is located in eastern Georgia and covers (i) the easternmost Adjara-Trialeti fold-and-thrust belt, (ii) the southern (Georgian) side of the central Greater Caucasus orogen (GC), (iii) the westernmost Kura Basin (including the Kakheti ridge, a structural culmination developed in its northern sector) (Fig. 1).

The Adjara-Trialeti FTB is an orogen bordered mainly by north-vergent frontal reverse faults (Alania et al., 2018; Banks et al., 1997; Gusmeo et al., 2021; Nemčok et al., 2013) and resulting from the structural inversion of a former back-arc rift basin developed on the upper (Eurasian) plate of the northern Neotethys subduction zone (Adamia et al., 1981, 2011b; Banks et al., 1997; Barrier et al., 2018; Lordkipanidze et al., 1989). The main phase of rifting occurred in the Middle Eocene, characterized by the deposition of a thick volcanic and volcaniclastic succession, accompanied by shallow mafic-to-intermediate intrusions (Adamia et al., 2011b; Banks et al., 1997; Okrostsvaridze et al., 2018; Yılmaz et al., 2000, 2014). The post-rift phase lasted from the Late Eocene/Oligocene to the Early Miocene and was followed by structural inversion since late Middle Miocene times (Gusmeo et al., 2021). The Adjara-Trialeti FTB is often considered as part of the retro-wedge of the Lesser Caucasus orogen *s.l.*, despite having an independent origin (Alania et al., 2017; Mosar et al., 2010; Nemčok et al., 2013; Yılmaz et al., 2014).

The Greater Caucasus orogen is a fold-and-thrust belt resulting from the inversion of a back-arc rift basin (Greater Caucasus Basin) which opened in the Early Jurassic (Adamia et al., 1981, 2011a, 2011b; Dercourt et al., 1986; Mosar et al., 2010; Nikishin et al., 2001; Saintot et al., 2006; Sobornov, 1996; Zonenshain et al., 1990). Rifting is marked by Hettangian-Sinemurian black shales nonconformably overlying the crystalline basement, followed by siliciclastic turbidites, lavas and volcaniclastics deposited until the late Middle Jurassic; volcanic products were mostly deposited from Aalenian to Bajocian times (Adamia et al., 2011a, 2011b; Lordkipanidze et al., 1989; Nikishin et al., 2001; Saintot et al., 2006). From the latest Middle Jurassic until the Late Eocene the basin experienced post-rift thermal subsidence, characterized by the deposition of calcareous and siliciclastic turbidites (Adamia et al., 2011a, 2011b; Saintot et al., 2006; Zonenshain et al., 1990). The Greater Caucasus Basin was probably underlain by thinned continental crust rather than oceanic crust (Ershov et al., 2003).

There is an ongoing debate regarding the timing of structural inversion of the Greater Caucasus Basin and subsequent development of the Greater Caucasus orogen, with hypotheses ranging from the earliest Oligocene (Lozar and Polino, 1997; Nikishin et al., 2017; Vincent et al., 2007, 2013a, 2013b, 2016) to the Middle Miocene (Rolland, 2017) to the Pliocene (Avdeev and Niemi, 2011; Cowgill et al., 2016; Forte et al., 2014; Philip et al., 1989). Low-temperature thermochronology data seem to suggest an earlier growth of the western Greater Caucasus (e.g. Vincent et al., 2011) with respect to the eastern and central parts of the orogen (e.g. Avdeev and Niemi, 2011; Vasey et al., 2020; Vincent et al., 2020). The central and eastern portions of the Greater Caucasus certainly underwent rapid Pliocene to recent uplift. There is no consensus on the causes of such a fast exhumation (see for example the discussion in Vincent et al., 2020). Anyway, most authors agree that at least about 5–8 km of Cenozoic uplift occurred in the Greater Caucasus.

Convergence between the Greater Caucasus and the Lesser Caucasus, namely the Adjara-Trialeti FTB in the study area, caused the development of the so-called Transcaucasian intermontane depression, constituted by the Kura and Rioni flexural foreland basins, plunging to the east and west, respectively, and separated by the Dzirula Massif (Adamia et al., 2010, 2011b; Alania et al., 2017; Banks et al., 1997; Nemčok et al., 2013; Rolland et al., 2011). The two basins developed as a flexural response to both the Greater Caucasus to the north and the Lesser Caucasus *s.l.* to the south, and are filled by Oligocene-to-recent sediments (Fig. 2) (Adamia et al., 2010; Banks et al., 1997; Nemčok et al., 2013). The Kartli Basin (Figs. 1 and 2) is considered as a sub-basin of the Kura foreland basin bordered by the Adjara-Trialeti FTB to the south and the Greater Caucasus to the north. In the Kura Basin, the Maikop series is composed of Oligocene-Lower Miocene clastic (shales, siltstones and fine-grained sandstones) and evaporitic rocks deposited in the anoxic-dysoxic environment of the Paratethys (Pupp et al., 2018; Sachsenhofer et al., 2018). The thickness of the Maikop series can reach 2.5–3.5 km in some parts of the Kura Basin (Adamia et al., 2010). During Middle to early Late Miocene times further 1.5–2.2 km of shales and fine-grained siliciclastics (sandstones), intercalated in the uppermost sections with mainly calcareous units (mudstones, marls and oolitic limestones and locally with coarse-grained rocks), were deposited

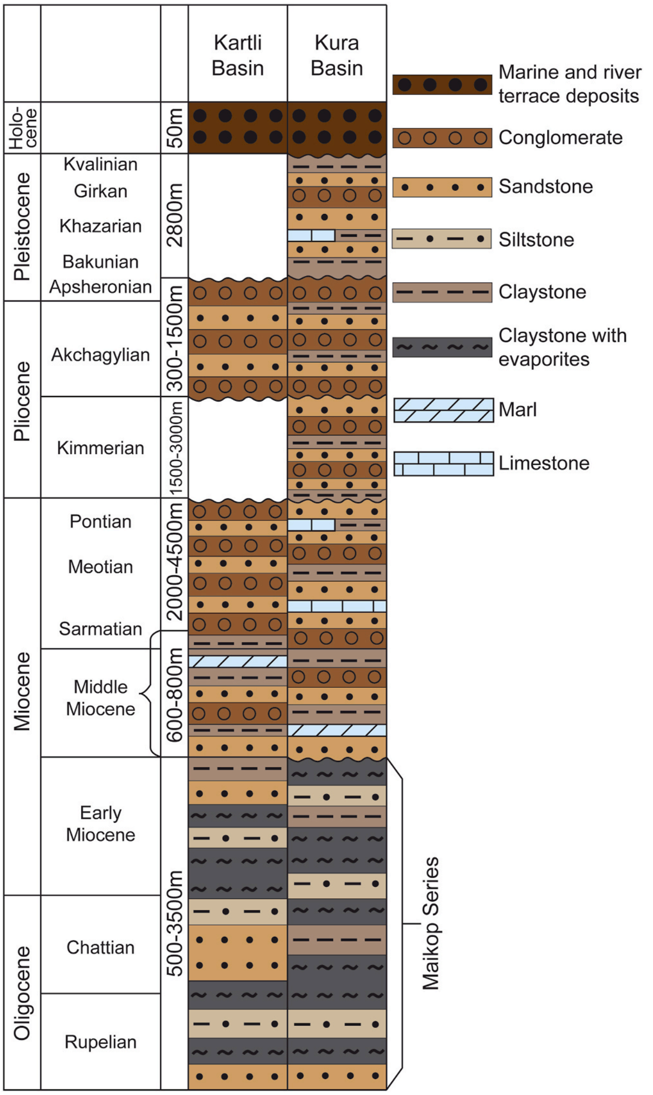

Fig. 2. Schematic chrono-lithostratigraphic columns of the Kartli and Kura basins, after Adamia et al. (2010, 2011b) and Pupp et al. (2018).

within the Kura Basin (Adamia et al., 2010; Alania et al., 2017). Since the Tortonian, the western part of the basin has been under subaerial conditions and marine conditions persisted only in some localities and in the easternmost portion of the basin (Adamia et al., 2010; Barrier et al., 2018). At the same time the widespread deposition of coarse-grained clastic deposits, eroded from the adjacent orogenic belts, started. Continental conditions prevailed from the Late Sarmatian (i.e. Tortonian, Fig. 2; see Adamia et al., 2010; Lazarev et al., 2019; Neubauer et al., 2015 for a review) to the present, interrupted only in the late Pliocene by a short-lived shallow marine environment, probably in response to the rapid growth and advancement of the Greater Caucasus and the ensuing subsidence in the foreland area (Adamia et al., 2010; Avdeev and Niemi, 2011; Nemčok et al., 2013; Sukhishvili et al., 2020).

Nemčok et al. (2013), based on the geometry of the sedimentary wedges, recognized a multi-stage development of the Kura foreland basin. In Oligocene times the depocenter was located along the SW border with the sedimentary fill thinning progressively towards the NE. In Early-Middle Miocene times maximum subsidence switched to the NE, with a clastic wedge progressively thinner and finer grained from NE to SW, indicating that the basin was being flexed in response to the southward advance of the Greater Caucasus. Since the Late Sarmatian (Tortonian) ongoing convergence between the Greater and Lesser Caucasus forced the final uplift of the Dzirula Massif and the Kura Basin started plunging towards the Caspian Sea, as demonstrated by the progressive emergence of the basin from west to east (Adamia et al., 2010; Alania et al., 2017; Nemčok et al., 2013). Symmetrically, the Rioni Basin plunged towards the Black Sea, on the western side of the Dzirula Massif. Thus, the Dzirula Massif basement high separated definitely the Rioni Basin from the Kura Basin (Banks et al., 1997; Barrier et al., 2018; Shatilova et al., 2020).

Continued convergence between the Greater and Lesser Caucasus caused incremental deformation of the Kura foreland basin. Thick-skinned deformation occurred in the Early-Middle Sarmatian (late Serravallian-early Tortonian) followed by thin-skinned deformation from the Late Sarmatian-Meotian (Tortonian) onward (Nemčok et al., 2013). During convergence, the Greater Caucasus deformation propagated into the northern Kura Basin forming the Kura south-vergent thin-skinned foreland FTB (Kakheti ridge), starting from the Middle Miocene, with peak deformation in the Late Miocene-Pliocene (Alania et al., 2017). A Late Pliocene-Pleistocene acceleration of uplift occurred also in this belt (Sukhishvili et al., 2020), probably linked with coeval enhanced uplift in the Greater Caucasus and subsequent propagation of deformation. The south-verging structures due to the southward growth of the frontal Greater Caucasus and the north-verging Adjara-Trialeti FTB structures interfere in the Tbilisi area, creating an outstanding example of incipient collision between two oppositely verging orogenic belts (Alania et al., 2021, Fig. 1).

3. Materials and methods

3.1. Materials

Both outcrop samples and cuttings from wells were analysed to assess thermal maturity and TOC content, when available, in the study area (Tables 1 and 2). Samples were analysed using several techniques and results were integrated with published data available for the study area for the first time in this paper (Figs. 1 and 3). Data from Bujakaite et al. (2003), Pupp et al. (2018) and Samsu (2014) are presented in the Results section (Tables 1 and 2), whereas other published data are integrated in the Discussion section.

More than two hundred subsurface TOC and Tmax data were derived from seven wells drilled in the eastern Adjara-Trialeti FTB and in the western Kura Basin (where HC exploration is concentrated), from which we extrapolated the Oligocene-Early Miocene interval (Maikop series) in order to have a reference section for interpretation. Pyrolysis results and TOC content estimates were made using Rock-Eval technology and ELTRA Elementar Analyser, respectively. Details on the methods are provided in Pupp et al. (2018) and Samsu (2014). From south to north the wells are (Fig. 1):

I. Kumisi 2
II. Patardzeuli (SLB)
III. Satskhenisi 102
IV. Norio 200
V. Norio 72
VI. Ninotsminda 97
VII. Manavi 12

About forty surface samples (Table 1) were analysed or revised in the three geological domains from various stratigraphic intervals: Jurassic (original data and after Bujakaite et al., 2003); Cretaceous (original data); Late Paleocene-Eocene (original data and after Pupp et al., 2018); Oligocene-Early Miocene (original data and after Pupp et al., 2018); Middle-Late Miocene (original data). They were characterised using organic petrography, pyrolysis and micro-Raman analyses on dispersed organic matter, and XRD diffraction on the <2 μm fraction of clay minerals.

Table 1
Thermal maturity data derived from surface samples.

Sample name	Geological domain	Coordinates	Age	Ro% ± sd (measured fragments)	Tmax (with TOC >0.5) (°C)	Hydrogen Index (mgHC/gTOC)	T Raman (°C) ± sd (n° measurements)	XRD <2 μm composition	I% in I–S (R Nr)	Kubler Index	Reference
CA1	Adjara-Trialeti FTB	–	Miocene	–	<437	–	–	–	–	–	Pupp et al. (2018)
CA2	Adjara-Trialeti FTB	–	Late Oligocene-Miocene	–	429–435	–	–	–	–	–	Pupp et al. (2018)
CA3	Adjara-Trialeti FTB	38N 0452009 4616299	Late Oligocene	0.51 ± 0.04 (36)	–	–	–	–	–	–	This study
CA4	Adjara-Trialeti FTB	38N 0325498 4610679	Oligocene	–	430	93	–	–	–	–	This study
CA5	Adjara-Trialeti FTB	–	Late Eocene-Oligocene	–	446–448	–	–	–	–	–	Pupp et al. (2018)
CA6	Adjara-Trialeti FTB	38N 0500906 4615010	Late Eocene	0.47 ± 0.03 (33)	–	–	–	–	–	–	This study
CA7	Adjara-Trialeti FTB	38N 0461429 4612640	Late Eocene	–	–	–	–	$I_{33}I{-}S_{40}C{-}S_{28}$	76 (R1)	–	This study
CA8	Adjara-Trialeti FTB	38N 0343226 4618483	Late Eocene	–	–	–	–	$I_{45}I{-}S_{24}Ch_{31}$	32 (R0)	–	This study
CA9	Adjara-Trialeti FTB	38N 0452684 4611098	early Late Eocene	0.74 ± 0.04 (48)	–	–		$I_{5}I{-}S_{25}C{-}S_{39}Ch_{30}$	27 (R0)	–	This study
CA10	Adjara-Trialeti FTB	38N 0476497 4631400	Middle Eocene	0.50 ± 0.05 (19)	–	–	–	$I_{6}C{-}S_{67}Ch_{28}$	–	–	This study
CA11	Adjara-Trialeti FTB	38N 0472357 4609370	Early Eocene	0.60 ± 0.05 (21)	–	–	–	$I_{30}I{-}S_{24}C{-}S_{16}Ch_{30}$	70 (R1)	–	This study
CA12	Adjara-Trialeti FTB	38N 0363775 4631968	Late Paleocene-Early Eocene	0.60 ± 0.04 (23)	–	–	–	$I_{72}C{-}S_{22}Ch_{6}$	–	–	This study
CA13	Adjara-Trialeti FTB	38N 0456357 4599540	latest Paleocene-Early Eocene	0.77 ± 0.06 (41)	–	–	–	$I_{17}C{-}S_{50}Ch_{33}$	–	–	This study
CA14	Kura Basin	38N 0500909 4595159	Late Miocene	–	–	–	–	$Sm_{85}I_{10}Ch_{5}$	–	–	This study
CA15	Kura Basin	38N 0512307 4625099	Middle-Late Miocene	0.43 ± 0.05 (92)	–	–	–	–	–	–	This study
CA16	Kura Basin	38N 0512536 4624356	late Early Miocene	0.49 ± 0.05 (23)	–	–	–	$I_{47}I{-}S_{19}K_{32}Ch_{2}$	45 (R0)	–	This study
CA17	Kura Basin	38N 0537395 4591009	Oligocene-Early Miocene	0.40 ± 0.03 (31)	–	–	–	–	–	–	This study
CA18	Dzirula Massif/Kura	38N 0379736 4652510	Cretaceous		<437	230	–	–	–		This study
CA19	Kakheti Ridge	38N 0520846 4635330	Oligocene-Early Miocene	–	–	–	–	$I_{54}I{-}S_{26}K_{10}Ch_{10}$	15 (R0)	–	This study
CA20	Kakheti Ridge	38N 0529855 4636895	Oligocene-Early Miocene	0.48 ± 0.03 (46)	–	–	–	$I_{64}I{-}S_{24}K_{10}Ch_{2}$	74 (R1)	–	This study
CA21	Kakheti Ridge	38N 0563536 4615033	Oligocene-Early Miocene	–	427	51	–	–	–	–	This study
CA22	Kakheti Ridge	38N 0563937 4615428	Oligocene-Early Miocene	–	421	99	–	–	–	–	This study
CA23	Kakheti Ridge	38N 0495174 4652984	Late Eocene-Oligocene	–	434	99	–	–	–	–	This study
CA24	Kakheti Ridge	38N 0529177 4636408	Late Eocene-Oligocene	–	–	–	–	$I_{53}I{-}S_{21}K_{15}Ch_{12}$	72 (R1)	–	This study
CA25	Kakheti Ridge	38N 0505210 4652984	Bartonian-Lower Priabonian	–	438	292	–	–	–	–	This study
CA26	Kakheti Ridge	38N 0506810 4656464	Late Eocene	–	442	222	–	–	–	–	This study
CA27	Kakheti Ridge	38N 0529177 4636408	Paleocene	0.66 ± 0.05 (7)	–	–	–	$I_{64}I{-}S_{24}K_{10}Ch_{2}$	72 (R1)	–	This study
CA28	Kakheti Ridge	38N 0524721 4634599	Maastrichtian	0.63 ± 0.06 (40)	–	–	–	$I_{14}I{-}S_{86}$	18 (R0)	–	This study
CA29	Kakheti Ridge	38N 0528762 4634818	Hauterivian-Albian	–	–	–	–	$I_{32}I{-}S_{9}K_{28}Ch_{31}$	75 (R1)	–	This study
CA30	Greater Caucasus	38N 0481457 4663658	Late Eocene	–	454	53	–	–	–	–	This study
CA31	Greater Caucasus	38N 0476888 4666996	Late Eocene	–	451	101	–	–	–	–	This study

(*continued on next page*)

Table 1 (*continued*)

Sample name	Geological domain	Coordinates	Age	Ro% ± sd (measured fragments)	Tmax (with TOC >0.5) (°C)	Hydrogen Index (mgHC/ gTOC)	T Raman (°C) ± sd (n° measurements)	XRD <2 μm composition	I% in I–S (R Nr)	Kubler Index	Reference
CA32	Greater Caucasus	38N 0475448 4667103	Late Eocene	–	459	57	–	–	–	–	This study
CA33	Greater Caucasus	38N 0475448 4667135	Late Eocene	–	455	46	–	–	–	–	This study
CA34	Greater Caucasus	38N 0476401 4667399	Late Eocene	–	467	36	–	–	–	–	This study
CA35	Greater Caucasus	38N 0472854 4669914	Cenomanian	–	445	45	–	–	–	–	This study
CA36	Greater Caucasus	38N 0473963 4680238	Cenomanian	–	–	–	216 ± 13 (7)	$I_1I–S_{28}Ch_{71}$	80 (R3)	–	This study
CA37	Greater Caucasus	38N 0474870 4688016	Aptian-Albian	–	–	–	228 ± 5 (14)	$I_{87}I–S_8Ch_5$	88 (R3)	–	This study
CA38	Greater Caucasus	38N 0459110 4697896	Berriasian-Hauterivian	–	–	–	292 ± 7 (17)	$I_{88}C–S_1Ch_{11}$	86 (R3)	0.29	This study
CA39	Greater Caucasus	38N 0544064 4656874	Oxfordian-Tithonian	–	–	–	235 ± 22 (16)	$I_{82}C–S_{12}Ch_6$	–	0.43	This study
CA40	Greater Caucasus	38N 0469216 4720975	Toarcian-Aalenian	–	–	–	379 ± 9 (15)	$I_{46}Ch_{54}$	–	0.10	This study
CA41	Greater Caucasus	–	Lower-Middle Jurassic	–	–	–	–	–	–	<0.30	Bujakaite et al. (2003)

List of surface original and published data analysed and discussed in the paper with samples name, geological domain, location, age, selected paleo-thermal parameters (VRo%, Tmax with TOC>0.5, HI, TRaman, I% in I–S, KI) and <2 μm XRD composition. Original and published data are indicated from south to north. Pyrolysis data are derived using various editions of IFP Rock-Eval technology (see Behar et al. (2001) and references therein). For <2 μm XRD composition: Ch = Chlorite, C–S = Chlorite-Smectite mixed layers, I = Illite, I–S= Illite-Smectite mixed layers; K = Kaolinite, Sm = Smectite.

3.2. *Methods*

3.2.1. *Organic petrography*

Vitrinite reflectance (VRo%) is generally the best thermal indicator in sedimentary sequences rich in organic matter, and can be correlated with detailed stages of HC generation (Bertrand et al., 2010; Borrego and Cook, 2017; Dow, 1977).

Preparation of the samples for optical microscope analysis of dispersed organic matter and vitrinite reflectance required picking of the visible organic matter particles, that can be easily found in the silty and arenaceous fractions, often as vegetable whips (Barnes et al., 1990; Taylor et al., 1998). Once a few grams of rock containing organic matter were selected, they were smoothly crushed in an agate mortar to a medium sand grain size. Obtained powder was placed on a sample holder and incorporated in a two-component epoxy resin. Then specimens were sanded using a Struers LaboPol 5 automatic sanding/polishing machine, with 320, 500 and 1000 grit carborundum sandpaper, and isopropanol lubricant and water as coolers. Then specimens were finally polished with alumina suspensions, with decreasing grain size (1–0.3 μm) and microfibre cloths. The routine was completed by polishing with 0.12 μm fumed silica suspension.

Vitrinite reflectance analysis was performed at the ALBA (Academic Laboratory of Basin Analysis) of Roma Tre University using a Zeiss Axioskop 40 A microscope equipped with a tungsten halogen lamp (12V, 100W) that produces non-polarized light (λ = 546 nm), Epiplan-Neofluar 50x/1 objective immersed in oil (n = 1.518) at a temperature of 23 °C, photomultiplier MPS 200 (from J & M Analytik AG), short- and long-wave ultraviolet lamps, coupled with a Canon Power Shot G6 digital camera and a dedicated software for reflectance data acquisition.

Before starting measurements, instrument calibration was performed with three reflectance standards. In addition, parasitic light intensity (which varies depending on the intensity of sunlight throughout the day) was measured to allow the software to filter it.

The average vitrinite reflectance (VRo%) values were calculated as the arithmetic mean over a minimum of 20 measurements per sample and considered acceptable with a maximum standard deviation of ±0.06 on the indigenous fragments (Borrego et al., 2006). Each measurement was made on well preserved non-oxidised fragments >5 μm and as far as possible from fractures and pyrite crystals that could decrease or increase true reflectance values, respectively.

3.2.2. *Micro-Raman spectroscopy on dispersed organic matter*

Raman spectroscopy is a non-destructive tool to quantitatively evaluate thermal maturity of organic matter from diagenesis to metamorphism (Beyssac et al., 2002; Ferralis et al., 2016; Guedes et al., 2010, 2012; Henry et al., 2019; Hinrichs et al., 2014; Lahfid et al., 2010; Liu et al., 2013; Lünsdorf and Lünsdorf, 2016; Mumm and Inan, 2016; Quirico et al., 2005; Schito et al., 2017, 2019; Schito and Corrado, 2018; Wilkins et al., 2014; Zhou et al., 2014). Advances in instrumentation and data processing have spurred increased applications, and the technique is now simple, fast and can be performed directly on standard petrographic thin sections or on bulk kerogen.

Raman spectra were acquired at the laboratory of experimental volcanology and petrology (EVPLab) of Roma Tre University on standard petrographic thin sections following the procedure described by Beyssac et al. (2002) and Lünsdorf et al. (2017). The spectrometer used is a Jobin Yvon micro-Raman LabRam with a backscattered geometry in the range of 700–2200 cm^{-1} (1st order Raman spectrum), which uses a grid of 600 meshes per mm and a CCD detector with a maximum magnification of 50×. A Nd-YAG laser with a wavelength of 532 nm (green laser) with a power < 0.4 mW was used as energy source. Raman back scattering was then recorded in six repetitions with 20-s steps for each measurement which, together with the use of green lasers and optical filters, helped to reduce the background noise given by the fluorescence of organic matter within acceptable values (Schito et al., 2017). A total of twenty measurements were made for each sample to

Table 2
Thermal maturity data derived from wells.

Well	UTM Coordinates	Age	Geological domain	Analysed depth (top-bottom, m)	Analysed thickness (m)	Mean Tmax (°C) (Min, Max)	Mean TOC (Min, Max)	Mean HI (Min, Max)	Nr samples	Sample type	Average Ro%	Reference
Kumisi 2	38N 0483141 4607313	Oligocene-Early Miocene	Adjara-Trialeti FTB	1340–1535	195	439 (434, 441)	1.44 (1.05, 1.95)	222 (117–318)	21	cuttings	–	This study
Patardzeuli (SLB)	38N 0515117 4618697	Oligocene-Early Miocene	Adjara-Trialeti FTB	360–1350	990	431 (422, 440)	1.01 (0.64, 1.25)	155 (91–235)	34	cuttings	–	This study
Satskhenisi 102	38N 0507754 4625925	middle Maikop, Late Oligocene	Adjara-Trialeti FTB	200–1200	1000	(437–447)	(0.50, 2.40)	(91–259)	148	cuttings	0.3–0.6	This study
Norio 200	38N 0494735 4629461	Oligocene	Kura Basin	665–1233	568	426 (419–432)	1.77 (1.13, 2.41)	223 (90–318)	18	cuttings	<0.5	This study
Norio 72	38N 0500117 4630132	Oligocene	Kura Basin	3625–4510	885	429 (415–442)	0.80 (0.30, 1.61)	128 (77–208)	64	cuttings	0.5–0.7	Samsu (2014)
Ninotsminda 97	38N 0524029 4624730	lower Maikop, Early Oligocene	Kura Basin	2330–2360	30	422 (421–424)	0.76 (0.63, 0.82)	100 (98–102)	4	cuttings	<0.5	Samsu (2014)
Manavi 12	38N 0535573 4623781	Oligocene-Early Miocene	Kura Basin	3800–3920	120	424 (407–431)	4.20 (3.30, 5.40)	200 (120–279)	32	cuttings	<0.5	Samsu (2014)

List of wells used in this study, with wells name, location, age, thickness and depth of the section considered, Tmax, TOC, HI and VRo% data. Pyrolysis data are derived using various editions of IFP Rock-Eval technology (see Behar et al. (2001) and references therein).

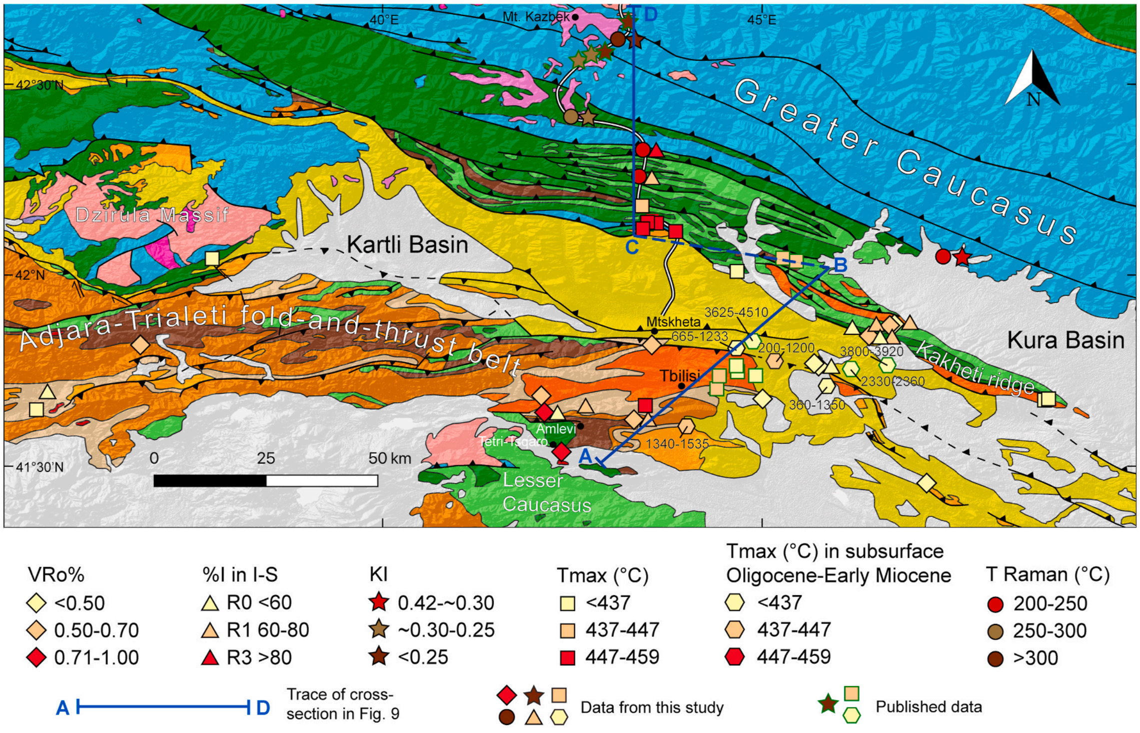

Fig. 3. Geological map with original and published synthetic paleo-thermal maturity datasets. Depths of Tmax data from deep wells are shown. Base map modified after Adamia (2004) and Gusmeo et al. (2021). Colours and symbols of base map as in Fig. 1. (For interpretation of the references to colour in this figure legend, the reader is referred to the Web version of this article.)

ensure reproducibility using a 2 μm diameter spot at 50× magnification.

An automatic approach (Ifors software) was followed for the identification of the number of bands of the Raman spectrum, as illustrated by Lünsdorf et al. (2017) and Lünsdorf and Lünsdorf (2016). The method is based on the STA (Scaled Total Area) parameter, which is a function of the area and maximum intensity of the D and G peaks (Fig. 4). Once this parameter is calculated, using a 532 nm green laser source, it is possible to obtain the maximum burial temperatures by solving the following equation:

$$T_{532\ \mathrm{nm}}\ [^{\circ}\mathrm{C}] = -8,259*10^{-5}*\mathrm{STA}^{3} + 3,733*10^{-2}*\mathrm{STA}^{2} - 6,445*\mathrm{STA} + 6,946*10^{2}.$$

3.2.3. XR diffraction on <2 μm grain-size fraction

Clay minerals in shales and sandstones undergo diagenetic and very low-grade metamorphic reactions in response to sedimentary and/or tectonic burial. In particular, mixed layers illite-smectite (I–S) and the transformation sequence smectite-randomly ordered mixed layers (R0)-ordered mixed layers (R1 and R3)-illite-muscovite (di-octahedral K-mica) can be used as indicators of the thermal evolution of sedimentary successions (Aldega et al., 2007a, 2007b, 2014; Pollastro, 1990).

Illite crystallinity (IC) is the measure of the full width at half maximum (FWHM) of the first illite diffraction peak (1 nm = 10 Å) and is a method suitable to detect the anchizonal and its immediate limits, for which it is most accurate (Kübler and Jaboyedoff, 2000).

Samples were analysed for qualitative and semi-quantitative analyses of the <2 μm grain size fraction at Roma Tre XRD Laboratory. X-Ray diffraction (XRD) analyses were carried out with a Scintag X1 X-ray system (CuKα radiation) at 40 kV and 45 mA. Randomly oriented whole-rock powders were run in the 2–70° 2θ interval with a step size of 0.05° 2θ and a counting time of 3s per step. Oriented air-dried and ethylene-glycol solvated samples of the <2 μm (equivalent spherical diameter) grain-size fraction were scanned from 1 to 48° 2θ and from 1 to 30° 2θ, respectively, with a step size of 0.05° 2θ and a count time of 4s per step.

The illite content in mixed-layers I–S is determined by the delta two-theta method after decomposing the composite peaks between 9 and 10° 2θ and 16–17° 2θ (Moore and Reynolds, 1997) and by modelling XRD patterns using Pearson VII functions. The R ordering of I–S (Reichweite parameter, R; Jagodzinski, 1949) is determined by the position of the I 001–S 001 reflection between 5 and 8.5° 2θ.

'Illite crystallinity' (IC, also called Kübler Index, KI) measurements are made by first subtracting the background from the raw data, and then applying a profile-fitting method (Lanson, 1997). The 10 Å asymmetric illitic multiphase peak was fitted using the Scintag X1 software. Peak shape decomposition was performed on ethylene-glycol preparations using split Pearson VII functions. The peaks identified were rationalized in terms of specific discrete or mixed-layers I–S and/or C–S phases (Lanson, 1997). From fitted data, the crystallinity was determined after calibrating the full width at maximum height (FWHM) of the illite band using Warr and Rice (1994) standards. According to the classification of Kübler (1964), KI values between 0.42 and 0.25 correspond to the anchizone (200–300 °C) while values lower than 0.25 reflect the onset of epizone at temperatures higher than 300 °C.

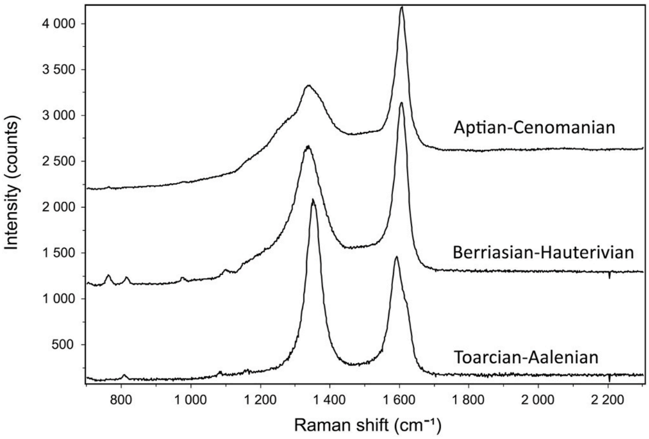

Fig. 4. Selected Raman spectroscopy spectra on dispersed organic matter for samples collected along the Georgian Military Road across the Greater Caucasus. The upper spectrum refers to samples CA36 and CA37 (Aptian-Cenomanian), which are very similar, the central spectrum refers to sample CA38 (Berriasian-Hauterivian), and the lower spectrum refers to sample CA40 (Toarcian-Aalenian). D peak is around 1350 cm^{-1} and G peak is around 1600 cm^{-1}. See text for details.

3.2.4. Correlation among different indicators of maximum temperature exposure

Correlation among different thermal indicators and conversion into temperatures are not straightforward since the different factors that drive maturation in sedimentary basins such as thermal regime, sedimentation rate, tectonic subsidence, mineral availability and fluid circulation dissimilarly affect each analytical parameter. Nevertheless, to provide a broad view of the temperature variation among and within the different basins (Fig. 5), we attempted a conversion of organic indicators using the most accepted equations or correlations, i.e. Barker and Pawlewicz (1986) for vitrinite reflectance and vitrinite reflectance equivalent from Tmax values, and Lünsdorf et al. (2017) for Raman parameters. Tmax values were preliminary converted into vitrinite reflectance equivalent using Barnard et al. (1981). I% in I–S were converted according to Aldega et al. (2007b) and Merryman and Frey (1999). Throughout the paper, we consider the classical temperature range established for the oil window (ca. 90–120 °C, see Hartkopf-Fröder et al. (2015) and references therein). VRo% and I% in I–S were plotted on Hillier et al.'s diagram (1995), where each couple of data can be attributed to different heating rates, that in turn can be ascribed to different geodynamic settings characterised by low (e.g. cratons or foreland basins) to very high (e.g. rift basins) thermal regimes.

4. Results

Results are analytically provided in Tables 1 and 2 and synthesized in Figs. 3 and 5.

4.1. Organic petrography

Vitrinite reflectance and main petrographic observations of new surface samples from the Adjara-Trialeti FTB, the Kura Basin and the Kakheti ridge (Table 1) are described below; no data are provided for the Greater Caucasus because the high maturity levels in this domain prevented accurate VRo% determination.

The Maastrichtian-Danian to Oligocene-Lower Miocene samples collected in the Kakheti ridge show a decrease in thermal maturity from the oil window (VRo about 0.65%) to the immature stage of hydrocarbon generation (VRo 0.48%). Only three out of five samples provided reliable reflectance values, given the scarcity of OM and the diffuse presence of macerals belonging to the inertinite group, useless for maturity studies. Samples CA20 and CA28 show the most reliable results given the high content of in-situ vitrinite (more than 40 fragments) and the low standard deviation. The presence of yellow and UV-fluorescent sporinites confirms the low maturity level.

Three Oligocene-Miocene samples (CA15, CA16 and CA17) from the Kura Basin are characterised by a high content in terrestrial debris with minor amount of inertinite and semifusinite fragments. Vitrinite reflectance measurements indicate as a whole the immature stage of hydrocarbon generation, with VRo values ranging from 0.40 to 0.49% and very low standard deviation values.

Finally, seven Paleogene samples from the Adjara-Trialeti FTB were analysed. Organic facies are mainly composed by huminite-vitrinite group fragments with minor amount of inertinite fragments and some sporinites. Pyrite is frequent in globular aggregates of variable sizes. Measured vitrinite reflectance ranges between 0.50 and 0.77% indicating the early and middle oil window stage.

4.2. New and revised Tmax and TOC data from pyrolysis

Presented Tmax and TOC data generally derive from the Oligocene-

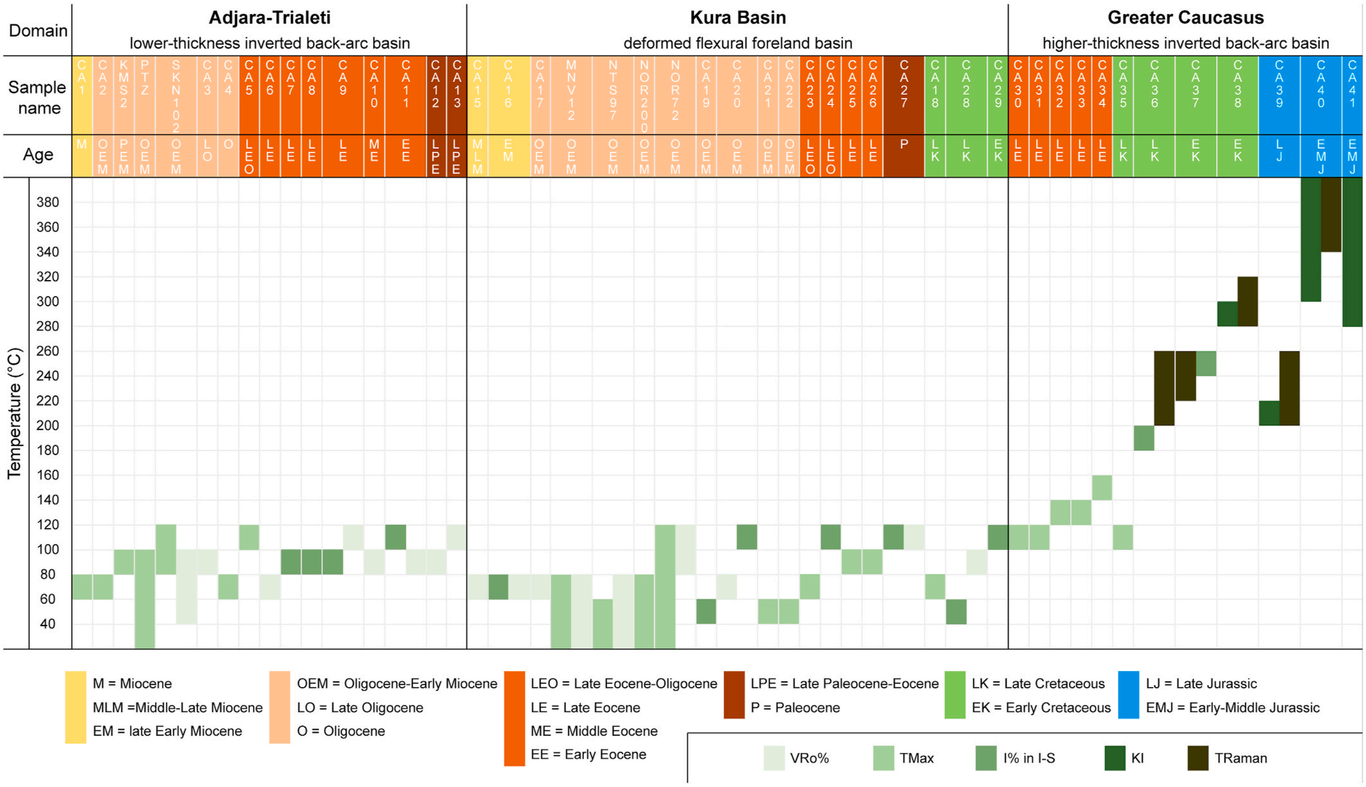

Fig. 5. Correlation scheme of paleotemperatures derived from original and published samples according to VRo%, illite% and R number in illite-smectite mixed layers and Tmax with TOC >0.5%. Paleotemperatures from VRo% are derived after Barker and Pawlewicz (1986) equation; from I–S after Hoffman and Hower (1979) and from Tmax after Barnard et al. (1981). In each domain, samples are listed -from left to right-first in chronological order then in geographical (south to north) order.

Lower Miocene Maikop interval, drilled in seven wells located in the eastern surroundings of Tbilisi (Figs. 1 and 3). They are from unpublished reports produced for the Georgia Oil & Gas Company and from Samsu, 2014.

Further surface data derive from new sampling along the Kakheti ridge, the Dzirula Massif and the more external units of the Greater Caucasus, whereas data from Pupp et al. (2018) come from the easternmost Adjara-Trialeti FTB and the Kura Basin. They have been selected in order to integrate our new maturity data and obtain the maturity distribution shown in the map of Fig. 3.

Tmax values of samples with less than 0.5% TOC were disregarded. Kerogen is mostly type III to type II-III (Fig. 6), with substantial input of terrestrial organic debris. Maturity falls in the diagenetic realm ranging from the immature (<0.5% VRo) to the mid-mature and, rarely, late mature stages of HC generation. Thermal maturity is generally lower in younger (Maikop) with respect to older (Upper Eocene and Cretaceous) stratigraphic intervals (Fig. 6). Analytical data are presented in Tables 1 and 2 and in Fig. 7.

In detail, the sampled Maikop section in the Kumisi 2 well ranges between 1340 and 1535m depth with a Tmax between 434 and 441 °C and a mean value of 439 °C, and with TOC ranging between 1.05 and 1.95% with a mean of 1.44% (Fig. 7).

In the Patarzeuli (SLB) well, sampled between 360 and 1350m depth, Maikop Tmax ranges between 422 and 440 °C with a mean of 431 °C, whereas mean TOC is around 1% with minimum and maximum values of 0.64 and 1.25%, respectively (Fig. 7).

In the Satskhenisi 102 well, sampled between 200 and 1200m depth, over 80% of the Maikop samples have TOC values higher than 1%, with a minimum value of 0.50% and a maximum one of 2.40%. There is no clear TOC trend with depth. Nevertheless, the highest TOC values (>2%) are concentrated towards the bottom half of the section (below 700m of depth) (Fig. 7).

The Oligocene interval in the Norio200 well, between 665 and 1233m depth, shows a Tmax between 423 and 429 °C with a mean of 427 °C, and TOC ranging between 1.75 and 2.19% with a mean of 1.93% (Fig. 7).

In the Norio72 well, the Maikop (3625–4510m) yielded Tmax comprised between 418 and 435 °C with a mean value of 427 °C, and TOC ranging between 0.30 and 1.60% with a mean of 0.80% (Fig. 7).

In the Ninotsminda 97 well the Lower Oligocene interval of the Maikop (2330–2360m) yielded Tmax values between 421 and 424 °C with a mean of 422 °C. TOC ranges between 0.63 and 0.82%, with a mean of 0.76%.

The Manavi 12 well crosses the Maikop between 3800 and 3920m depth with Tmax indicating the immature stage of HC generation (between 407 and 431 °C with a mean of 424 °C), and TOC between 3.30 and 5.40% with a mean of 4.20%.

New surface samples collected along the Kakheti ridge and the frontal tectonic units of the Greater Caucasus show higher Tmax values in the latter ones (mainly >450 °C in Upper Eocene rocks and 445 °C in the Cenomanian sample CA35). In the Kakheti ridge Late Eocene Tmax ranges between 434 and 442 °C and Oligocene-Miocene Tmax ranges between 421 and 427 °C, suggesting a lateral trend of decreasing maturity moving from the WNW to ESE and an increase of maturity from younger to older strata.

Original surface data from the Cretaceous unconformably lying on top of the Dzirula massif indicate a Tmax lower than 437 °C.

Surface sections studied by Pupp et al. (2018) between the Adjara-Trialeti FTB and the Kura Basin provide reliable Tmax data for the Late Eocene-Oligocene (446–448 °C), Late Oligocene-Miocene (429–435 °C) and Miocene (<437 °C) intervals, showing an overall maturity decrease from older to younger units. Oligocene sample CA4, collected in the Akhaltsikhe depression, yielded a Tmax value of 430 °C.

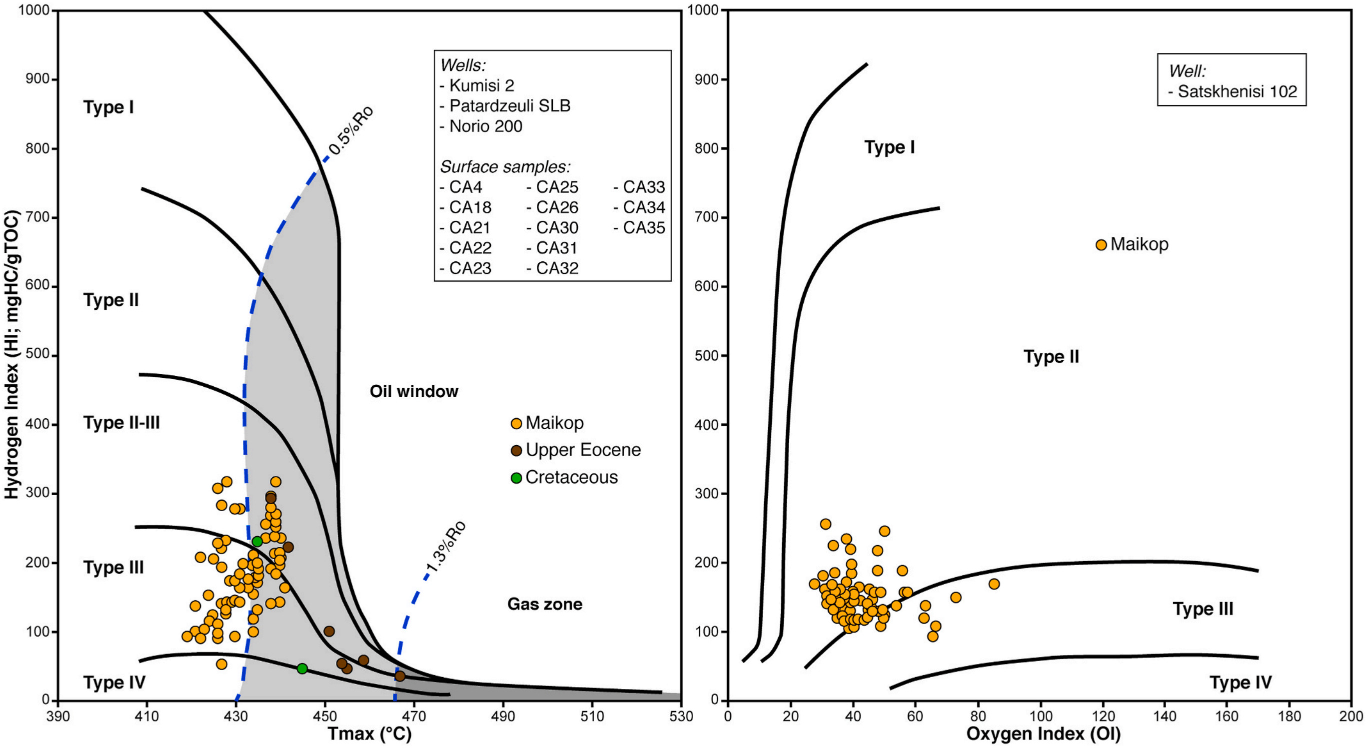

Fig. 6. Tmax vs HI diagram (left) for all new data derived from wells and surface samples, subdivided according to their age, presented in this paper, except for well Satskhenisi 102 (Middle Maikop) for which a OI vs HI diagram is presented (right).

4.3. Raman spectroscopy on dispersed organic matter

Measurements of Raman spectra on dispersed organic matter were focused on samples from the Greater Caucasus, where metamorphic temperatures make vitrinite reflectance data less reliable for thermal maturity assessments. Here, Raman spectra show a clear-cut temperature increase going from the younger to the older chronostratigraphic units as well as toward the axis of the orogen (Table 1). This trend is illustrated in Fig. 4, where spectra from Lower Jurassic to Middle Cretaceous samples collected along a N–S transect running parallel to the Georgian Military Road are shown. Upper Jurassic sample CA39 crops out a few tens of km to the ESE of it and thus its thermal evolution should be considered separately from the other samples; for this reason, the Raman spectrum of this sample is not included in Fig. 4.

Spectra from Aptian to Cenomanian successions (samples CA36 and CA37), as well as in Upper Jurassic sample CA39, are characterised by a broad asymmetric D band at 1350 cm^{-1} with lower intensities with respect to the G band at 1600 cm^{-1}. Such spectra are typical of very low metamorphic conditions, as outlined by the temperature range from the Ifors software (219–235 °C). Moving toward the Berriasian-Hauterivian sample (CA38) the D band shows relatively higher intensities and the bands that underlines the "saddle" between the D and G bands tend to disappear. These changes reflect a temperature increase up to 292 ± 7 °C, near the boundary between anchizone and epizone (~300 °C according to Kübler, 1964). Finally, in the Jurassic sample (Toarcian-Aalenian, CA40) the intensity of the D band is higher than that of the G band, which shows a marked asymmetry at 1620 cm^{-1} due the presence of the D2 band. All these features correspond to an average temperature of 379 ± 9 °C.

4.4. XRD on <2 μm grain-size fraction

Data obtained from clay mineralogy analyses are shown in Table 1. The interpretation of diffractograms on air-dried and glycolated samples are expressed as abundance in percentage to provide the composition of the <2 μm fraction. Moreover, where illite-smectite (I–S) mixed layers are present, the percentage of illite in mixed layers (I% in I–S), which can be interpreted in terms of maximum temperature, and the parameter R (Reichweite index) are provided. IC (illite crystallinity) is provided for samples where only illite (without I–S mixed layers) is present.

In the Greater Caucasus, three samples (CA36, CA37 and CA38) contain 8–28% of I–S mixed layers, together with illite (1–88%) and chlorite (6–71%). These samples have a R3 stacking order of illite-smectite mixed layers and I% in I–S ranging from 80% (Cenomanian, CA36) to 88% (Aptian-Albian, CA37), indicating the late diagenetic realm. The remaining two samples from the Greater Caucasus, CA40 (Toarcian-Aalenian) and CA39 (Oxfordian-Tithonian), contain illite, chlorite and chlorite-smectite mixed layers. According to Kübler's (1964) classification, IC values of the Lower Cretaceous (CA38) and the Lower-Middle Jurassic (CA40) samples indicate respectively anchizone and epizone conditions whereas the Upper Jurassic sample (CA39), located >70 km to the ESE, reached only late diagenetic conditions.

The six samples from the Kakheti ridge of the Kura Basin contain I–S mixed layers (generally >20%), illite (30–65%), chlorite (2–30%) and kaolinite (10–30%), with the exception of the Maastrichtian sample where these last two phases are absent. Kaolinite -indicative of intense weathering-is virtually absent in samples from other domains. I% in I–S mixed layers ranges mainly between 70 and 75%, with R1 stacking order. Two samples (CA28, Maastrichtian, and CA19, Oligocene-Early Miocene), collected near two fault zones, show much lower I% in I–S mixed layers (18 and 15%, respectively) probably due to alteration that could increase the smectite percentage.

Two Miocene samples from other areas of the Kura Basin provided reliable XRD results, indicating low diagenetic conditions. CA14 (Late Miocene) contains mainly smectite (85%) and minor amounts of illite and chlorite (10 and 5%, respectively). CA16 (Early Miocene) contains illite, chlorite, illite-smectite mixed layers (<20%) with a percentage of illite in mixed layers of 45% and R0 stacking order. The abundance of kaolinite (>30%) indicates weathering processes.

Almost all of the eight samples from the Paleogene section of the

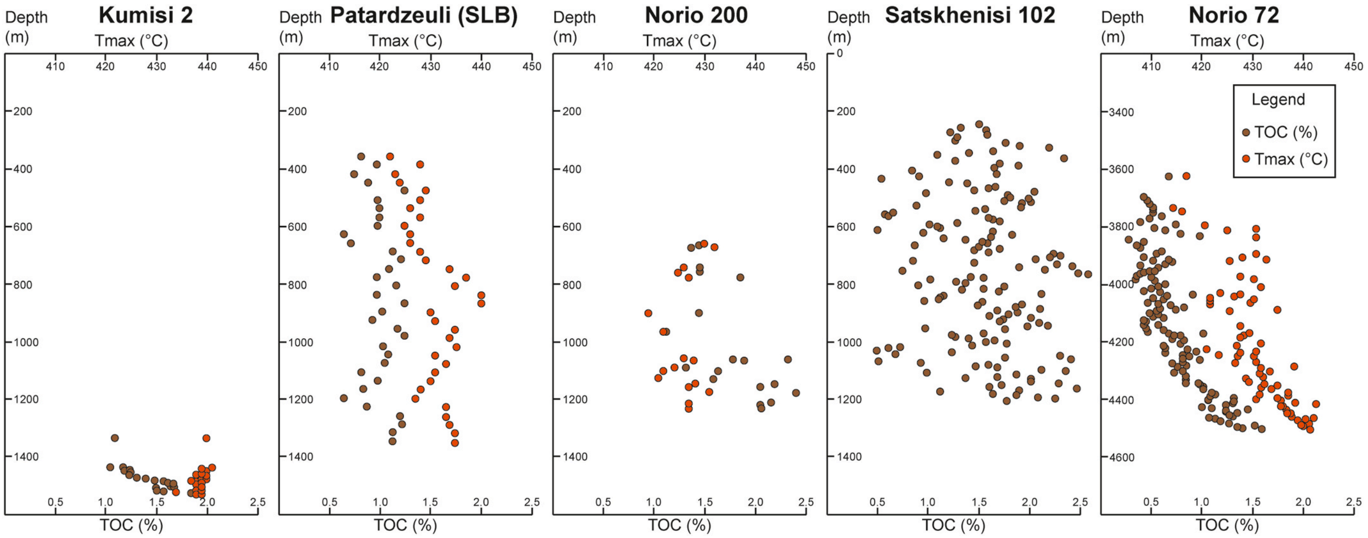

Fig. 7. Depth vs Tmax (orange dots) and depth vs TOC (brown dots) plots (upper and lower x axis, respectively) for the five wells having at least two hundred metres of succession. For Satskhenisi 102 well Tmax data are not available. (For interpretation of the references to colour in this figure legend, the reader is referred to the Web version of this article.)

Adjara-Trialeti FTB contain chlorite-smectite mixed layers, nearly absent in the other domains, with percentages ranging from about 20 to 80%. Illite is ubiquitous with highly variable percentages (5–72%), and chlorite is frequently present, with a lower percentage in the Paleocene-Early Eocene sample (CA13, 6%) than in the Eocene section (28–33%). I–S mixed layers are present only in four samples in the Eocene section, with percentages between 24 and 40%. I% in I–S mixed layers is highly variable, with two samples (CA11 and CA7, Early and Late Eocene, respectively) yielding a percentage between 70 and 76% and R1 stacking order, and two samples (CA10 and CA9, Middle and Late Eocene, respectively) with I% between 27 and 32% and R0 stacking order.

4.5. Extrapolation of paleotemperature ranges and integration with pre-existing datasets

Organic indicators (VRo% and Tmax from pyrolysis) from virtually all of the Paleocene-Miocene samples of the Adjara Trialeti FTB point consistently to the diagenetic realm (early to mid-mature stages of hydrocarbon generation), thus never exceeding about 115 °C. I% in I–S and R ordering show, on the other hand, contrasting values (Table 1). Considering organic results, we suggest that the two samples (CA8 and CA9) with low I% in I–S mixed layers and R0 ordering have probably been affected by alteration processes (hence these two samples were not plotted on Fig. 8). In the Hillier's (1995) diagram (Fig. 8) the correlation between VRo% and I% in I–S for sample CA11 indicates a medium heating rate during back-arc extension in the eastern Adjara-Trialeti basin, before inversion.

The three Oligocene-Miocene samples from the Kura Basin yielded coherent paleotemperatures between 60 and 80 °C, based on VRo% and I% and stacking order of I–S mixed layers (Fig. 5). The correlation between VRo% and I% in I–S for sample CA16 indicates a moderate heating rate typical of relatively cold basins (Fig. 8). This is further confirmed by Tmax values from the Oligocene-Early Miocene Maikop unit, or part of it, in the wells near Tbilisi (Figs. 1, 3 and 6, Table 2), indicating that the maturity trend with depth defines cold conditions, and by Pupp et al. (2018) who define a maturity gradient of 0.08%/km (ΔVRo%) in the Maikop series, typical of cold foreland basins. The new pyrolysis results (Tmax, TOC and HI; Tables 1 and 2, Figs. 6 and 7) also show that the organic matter is mainly of type III to type II-III, thus rich in terrestrial input: this evidence and the maturity level reconstructed are in agreement with published results from wells and outcrop samples in the western Kura Basin (Pupp et al., 2018; Samsu, 2014).

The thermal maturity of the Cretaceous sample (CA18) collected at the surface from the unconformable cover of the Dzirula Massif indicates shallow burial.

As for the Kakheti ridge, all reliable data fall in the diagenetic realm showing a general increase of paleotemperatures derived from organic indicators (Tmax and VRo%) from 40 to 50 °C to about 100 °C moving from younger (Oligocene-Lower Miocene) to older (Lower Cretaceous) lithostratigraphic units (Figs. 5 and 6). XRD analysis of the <2 μm fraction indicates the presence of I–S mixed layers with an illite content of more than 70% and R1 ordering. These results suggest a much higher thermal maturity with respect to VRo% and Tmax that can be interpreted as detrital clay contamination. On the other hand, two samples collected close to thrusts show a much lower illite content in mixed layers (<20%) probably due to post-diagenetic smectite enrichment caused by fluid circulation. Hillier's diagram (Fig. 8) indicates a low to moderate heating rate, typical of relatively cold basins (samples CA27-CA20).

In the Greater Caucasus, Raman spectroscopy and XRD (KI and I% in I–S) in the axial part of the belt, and Tmax in the southern foothills provided new reliable results (Figs. 5 and 9). In the Lower Jurassic section sampled on the highest thrust sheet of the Greater Caucasus close to the Russia-Georgia border, the maximum paleotemperatures derived from XRD and Raman are comprised between 300 and 400 °C, with a more refined range given by Raman spectroscopy (360–400 °C, Figs. 4 and 5). Raman results should be privileged as KI-derived paleotemperatures result from a discontinuous correlation scale (Hoffman and Hower, 1979) whereas the equation used to calculate temperatures from Raman parameters (Lünsdorf et al., 2017) provides a more detailed resolution. Additional KI data (Bujakaite et al. (2003) confirm that maximum paleo-temperatures were higher than 300 °C. These results are further corroborated by thermochronological results from Vasey et al. (2020), indicating that the basement in the axial zone of the Greater Caucasus near Mt. Kazbek (Fig. 1) underwent very fast cooling since about 10–8 Ma from temperatures higher than ~250 °C.

Moving to the footwall of the highest thrust, KI data indicate a decrease in paleotemperatures from more than 300 to about 250 °C going upsection from north (Lower Jurassic) to south (Upper Jurassic) (Bujakaite et al., 2003).

New Raman, KI, Tmax and I% in I–S data from the bottom of the Cretaceous succession indicate a well constrained range between 280 and 300 °C, that decreases to 180–260 °C moving towards the uppermost Lower Cretaceous and Cenomanian units. Here the percentage of

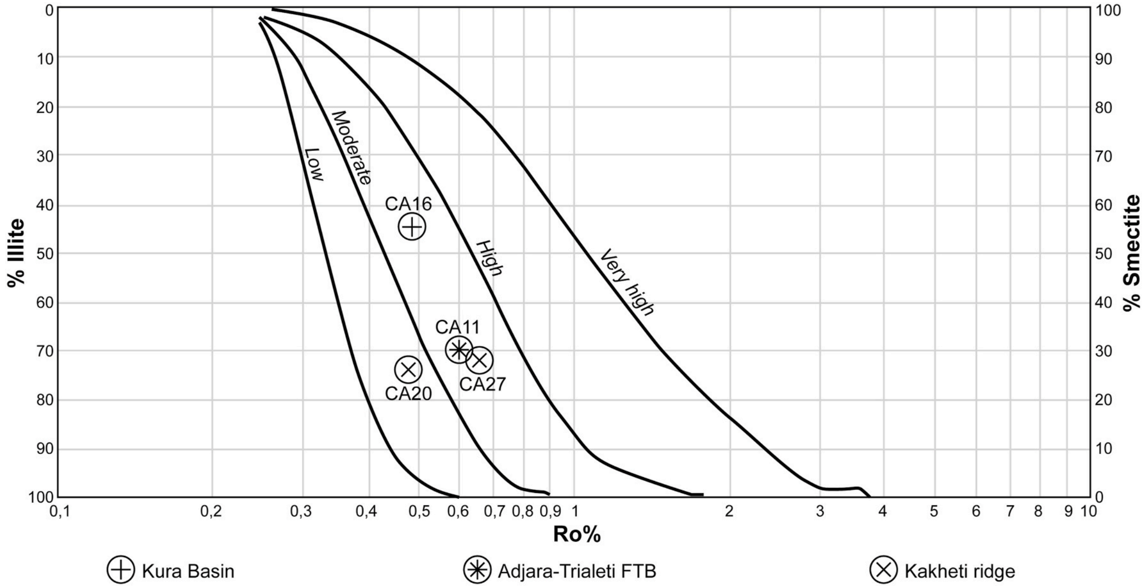

Fig. 8. Correlation of VRo% (x axis) and illite% (left y axis) or smectite% (right y axis) in illite-smectite mixed layers, to derive approximate heating rates. Curves indicating heating rates are redrawn and slightly modified after Hillier et al. (1995).

illite probably slightly underestimates paleotemperatures for lithological reasons (abundant carbonate cement) whereas R3 stacking order suggests paleotemperatures partially superposing with Raman ones.

In the southern foothills of the Greater Caucasus, an area dominated by thin-skinned thrust sheets, Tmax values suggest a paleotemperature range between 100 and 160 °C in the Upper Eocene rocks, corroborated by the Tmax vs HI relationships (Fig. 6) which indicate a late mature to overmature stage of HC generation. These results show that the youngest stratigraphic units in the orogenic belt are characterised by the lowest maturity level.

Overall, the integration of the new data presented here with pre-existing datasets describes a progressive increase of thermal maturity from the southernmost foothills to the highest peaks of Greater Caucasus in Russian territory, i.e. from younger to older strata (Figs. 5 and 9).

5. Discussion

5.1. *Thermal histories*

The thermal maturity distribution for the three geological domains characterising the study area is represented in Fig. 5 and along the profile in Fig. 9. In the Paleocene-Lower Eocene section of the Adjara-Trialeti FTB, thermal maturity decreases from south (Tetri Tsqaro) to north (Mtskheta), from the peak of the oil window to the early mature zone. The difference in thermal maturity is relatively small but could be explained with the possible effect of tectonic thickening due to the inverted E-W fault running in the area of Amlevi, evolving into a low-angle thrust in its present-day eroded portion (Figs. 1, 3 and 9).

The thermal maturity of the Middle-Upper Eocene section does not show significant lateral variations. It ranges from the immature stage of HC generation to the oil window and is slightly lower in comparison with the Paleocene-Eocene section.

The thick Oligocene-Lower Miocene (Maikop) section of the Adjara-Trialeti FTB reached the early mature oil window, whereas it is immature in the central portion of the orogen [samples CA1 and CA2 (Pupp et al., 2018)]. Further to the north, where the Maikop series is overlain by Middle-Upper Miocene sediments in the frontal synform of the Adjara-Trialeti FTB (Figs. 3 and 9), thermal maturity increases again to the early mature stage. The thermal immaturity of the Maikop section in the Kumisi 2 well could be explained with the closure of the former Adjara-Trialeti back-arc basin towards the SE, hence to the lower amount of experienced burial (Fig. 3).

The positive correlation between thermal maturity and stratigraphic age suggests the limited effect of tectonic loading, apart for the southern part of the cross-section in Fig. 9. Maximum temperatures recorded in the Adjara-Trialeti domain are consistent with the thickness of the rift basin fill and hence resulted from sedimentary burial. The thermal maturity trend reconstructed in the Adjara-Trialeti FTB thus provides independent evidence that the dominant deformation style within the orogen is positive inversion of the former extensional faults, as already

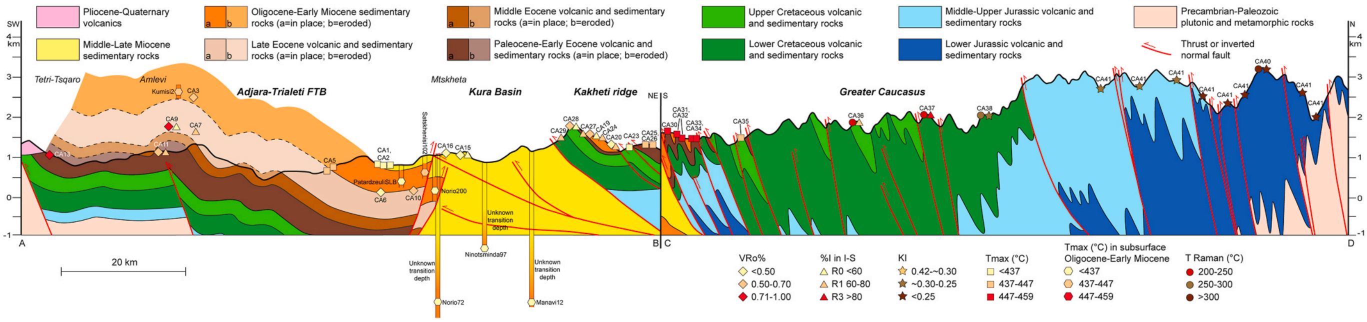

Fig. 9. Composite geological section across the study area with original and published synthetic paleo-thermal maturity datasets. Wells and samples are projected on the cross-section line. Redrawn and modified after Alania et al., 2017, 2018; Gusmeo et al., 2021; Mauvilly et al., 2016.

pointed out in previous works (Alania et al., 2020; Banks et al., 1997; Gusmeo et al., 2021; Sosson et al., 2016), rather than low-angle thrusting, a process which would have resulted in a higher thermal maturity due to tectonic overburden.

Based on our results, suggesting maximum paleotemperatures between about 70 and 120 °C, and assuming an average geothermal gradient of 25–30 °C/km, the total eroded basin fill of the eastern Adjara-Trialeti Basin broadly ranges between 2 and 4.5 km. These rough estimates are in agreement with Pupp et al. (2018), who estimated ~3/3.5 km of eroded Miocene section in the eastern Adjara-Trialeti FTB.

Maturity data from the subsurface of the Kura Basin are available only for the Maikop series and indicate an immature to early mature stage of HC generation (Fig. 6) acquired during progressive burial by the Middle-Late Miocene stratigraphic section (Pupp et al., 2018). Surface samples within the Kura Basin are also characterised by a low maturity level (Fig. 5), with maximum paleotemperatures in the 60–80 °C range. Assuming 25–30 °C/km as average geothermal gradient no more than 2–3 km of basin fill could have been eroded in the deformed Kura Basin. The low maturity of both surface and subsurface samples indicates a cold thermal regime, typical of flexural foreland basins (Fig. 8).

In the Kakheti ridge thermal maturity changes from the early mature to the immature stage of HC generation from the Lower Cretaceous to the Maikop sections, respectively, suggesting that maturity was acquired, as in the Kura Basin, as a consequence of sedimentary burial in a quite cold regime, with limited overthrusting effects on the organic matter indicators, whereas thrust-related fluid circulation may have affected clay mineralogy results (see Section 4.5). The Kakheti ridge was exhumed earlier than the rest of the Kura Basin (Fig. 10) and maturity is generally lower than in the wells drilled to the south of the ridge in the eastern and southern surroundings of Tbilisi, because of the lower amount of burial experienced. Our results indicate maximum paleotemperatures between 40 and 110 °C, which roughly translate into 1–3.5 km of eroded basin fill (assuming 25–30 °C/km of geothermal gradient).

The comparison of the thermal maturity distribution in the Adjara-Trialeti FTB (in its Paleocene-Miocene section), the Kura Basin (in its Oligocene-Miocene section) and the Kakheti ridge (in its Upper Cretaceous-Oligocene section), indicates that:

- Thermal maturity trends in the Adjara-Trialeti FTB and in the Kura Basin/Kakheti ridge are similar, showing an increase in maturity, from younger to older units, from immature to mid-mature oil window. The thickness of the Paleocene-Oligocene sections in the two domains is however different (i.e. 2-3 km thicker in the Adjara-Trialeti FTB), supporting the hypothesis that the final cumulative thermal maturity cannot be due to the same burial/thermal evolution through time. As recognized by Pupp et al. (2018), the maturation of the Oligocene-Lower Miocene source rock in the Kura Basin in the Tbilisi area is due to sedimentation and tectonic thickening of the Neogene basin fill (Nemčok et al., 2013), thus acquired later than in the Adjara-Trialeti inverted basin.
- Peak temperatures in the Adjara-Trialeti basin must have been reached during back-arc basin evolution, probably due to enhanced sediment accumulation driven by subsidence in Paleocene-Early Miocene times when the Kura Basin substratum represented a relative structural high. This is also an indirect proof that in Middle-Late Miocene times the Adjara-Trialeti domain was no longer undergoing subsidence and was being exhumed. At the same time the adjacent Kura Basin was experiencing strong subsidence and sedimentation. This is supported by independent thermochronological data and models (Gusmeo et al., 2021) which define the onset of exhumation in the Adjara-Trialeti FTB at around 14-12 Ma.
- Compared with the Adjara-Trialeti FTB and the rest of the Kura Basin, the Kakheti ridge shows a slightly lower maturity in time-equivalent stratigraphic units (immature stage in the Oligocene section), confirming that pre-Middle Miocene burial did not cause significant maturation of the Maikop section. Furthermore, in Middle-Late Miocene times the fold-and-thrust belt shortened and started exhuming, with scarce accumulation of syn-tectonic sediments, confined in shallow thrust-top basins, later on sutured by Plio-Pleistocene sediments (Fig. 10a; Alania et al., 2017).

The highest paleotemperatures were recorded in the Greater Caucasus, with thermal maturity values spanning from the upper oil/gas generation window up to 200–250 °C in the youngest units (the Upper Cretaceous-Eocene section at the front of the belt), to anchizone and epizone in the Jurassic section in the inner portion of the chain, where recorded maximum paleotemperatures exceed 300 °C. Presently there are no constraints on the timing of acquisition of such a thermal signature; further work has still to be done in order to solve this issue.

These paleotemperatures, if we tentatively assume an average geothermal gradient of 25/30 °C, suggest that a minimum of 3.5 km of basin fill has been removed in the southern foothills of the Greater Caucasus, and up to 12.5 km of section may have been removed in the axial zone. These rough estimates are broadly in agreement with reconstructions of the total basin fill of the former Greater Caucasus Basin, although a contribution due to tectonic nappe emplacement to thermal maturity cannot be excluded (Adamia et al., 2011b; Saintot et al., 2006; Vincent et al., 2016).

Time-equivalent lithostratigraphic units in the Kakheti ridge and the Greater Caucasus (e.g., Oligocene-Late Eocene) underwent a different thermal evolution, suggesting that the Kakheti ridge, though appearing laterally contiguous with the southern Greater Caucasus orogenic edifice (Fig. 1 and 11), is not really akin to it. Thermal maturity trends in this fold-and-thrust belt are much more similar to the ones in the Kura Basin, thus confirming that the Kakheti ridge represents a highly tectonised and more deeply exhumed portion of that basin.

5.2. *Regional geological evolution*

In conclusion, the geological evolution of the sector comprised between the Adjara-Trialeti FTB and the Greater Caucasus can be described as follows (Fig. 11).

In the Late Eocene, both Adjara-Trialeti and Greater Caucasus basins were experiencing extensional subsidence, but with different degrees of extension and thickness of sedimentary fill. The Greater Caucasus Basin was characterized by a thin and intruded continental crust in its axial zone, and by a sedimentary succession at least 7–9 km thick (Adamia et al., 2011a, 2011b; Ershov et al., 2003; Saintot et al., 2006). The Adjara-Trialeti Basin was underlain by a thicker and less intruded continental crust and filled by a thinner sedimentary succession (with thickness variable along-strike) (Adamia et al., 2011b, 2017; Gamkrelidze et al., 2019; Nemčok et al., 2013; Okrostsvaridze et al., 2018; Yılmaz et al., 2000, 2014). Between the two basins, a structural high was located, characterized by a very thin sedimentary succession overlying the basement: this structural high will later crop out as the Dzirula Massif, and more to the east it will represent the basement upon which the Kura Basin and the Kakheti ridge will develop.

The present-day situation witnesses both former basins closed and shortened through positive inversion, with the Kura Basin and the Kakheti ridge trapped between them. Growth of the Adjara-Trialeti FTB started in the late Middle Miocene (Gusmeo et al., 2021), while timing of Greater Caucasus growth is still debated (see section 2; Avdeev and Niemi, 2011; Forte et al., 2014; Vasey et al., 2020; Vincent et al., 2011, 2020). These two orogens are underlain by a thick continental crust, 35–45 km below the Adjara-Trialeti belt and 50–55 km in the Greater Caucasus (Adamia et al., 2017; Brunet et al., 2003; Ershov et al., 2003; Motavalli-Anbaran et al., 2016). The Kura Basin was flexured during convergence, mainly in Miocene times, when a thick pile of sedimentary rocks eroded from both the adjacent orogenic belts was deposited within the basin (Adamia et al., 2010; Pupp et al., 2018), causing maturation of the Maikop series, as evidenced in this study. The Maikop succession in

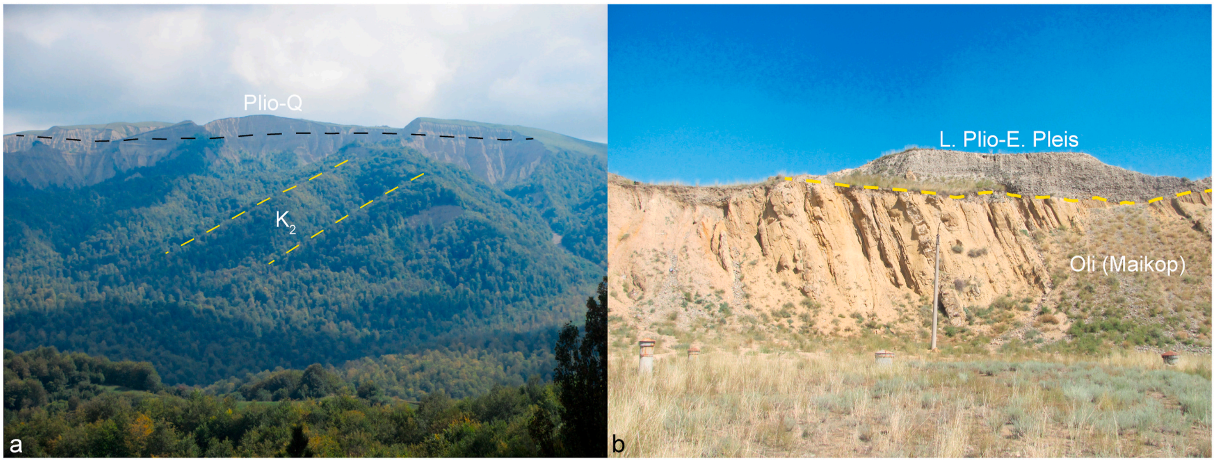

Fig. 10. a) Field photograph from the northern side of the Kakheti ridge showing Pliocene-Quaternary flat-lying strata (see dotted black line) overlying Upper Cretaceous tilted rocks (yellow lines); b) Field photograph from the Kura Basin (near Rustavi town) showing tilted Oligocene (Maikop) sandstones and siltstones unconformably overlain (yellow dotted line) by flat-lying Late Pliocene-Early Pleistocene conglomerates. Both images demonstrate that the main phase of deformation within the Kura Basin/Kakheti ridge ended before the Late Pliocene, but uplift continued without tilting. Locations are indicated in Fig. 1. (For interpretation of the references to colour in this figure legend, the reader is referred to the Web version of this article.)

the Kakheti ridge is characterised by a slightly lower maturity degree because the ridge was experiencing shortening and exhumation while the Kura Basin was still experiencing flexural subsidence and sedimentary burial.

Our thermal maturity results, integrated with published ones and with the structural framework of the study area, can be interpreted in the broader context of the Arabia-Eurasia collision zone. The tectonic evolution reconstructed in this paper, schematically summarised in Fig. 11 and derived from our thermal maturity data and independent stratigraphic and structural constraints, describes a net change in the dominant stress field which occurred in Middle Miocene times, when extensional tectonics was replaced by compression and the Adjara-Trialeti basin was structurally inverted (Alania et al., 2017; Forte et al., 2014; Gusmeo et al., 2021; Sukhishvili et al., 2020; Tari et al., 2018). Miocene shortening occurred also in the Greater Caucasus, although the timing of its inception is a matter of debate (Cowgill et al., 2016; Vasey et al., 2020; Vincent et al., 2020). This compressional geodynamic regime continues to the present day (Reilinger et al., 2006; Sokhadze et al., 2018; Tibaldi et al., 2019).

Inception of compressional tectonics in the study area is coeval with the Arabia-Eurasia hard collision along the Bitlis-Zagros suture zone (Cavazza et al., 2018; Okay et al., 2010). At the same time, wide areas of the suture-zone hinterland, comprising segments of the eastern Pontides, the Caucasus *s.l.*, the Talysh belt, and the Alborz range, were also subjected to deformation (Albino et al., 2014; Axen et al., 2001; Ballato et al., 2011, 2016; Cavazza et al., 2017, 2019; Gavillot et al., 2010; Gusmeo et al., 2021; Koshnaw et al., 2017, 2020; Madanipour et al., 2017; Su and Zhou, 2020; Tibaldi et al., 2017). From this viewpoint, the results shown in this paper further support the hypothesis that the compressional stresses associated to the Arabia-Eurasia hard collision

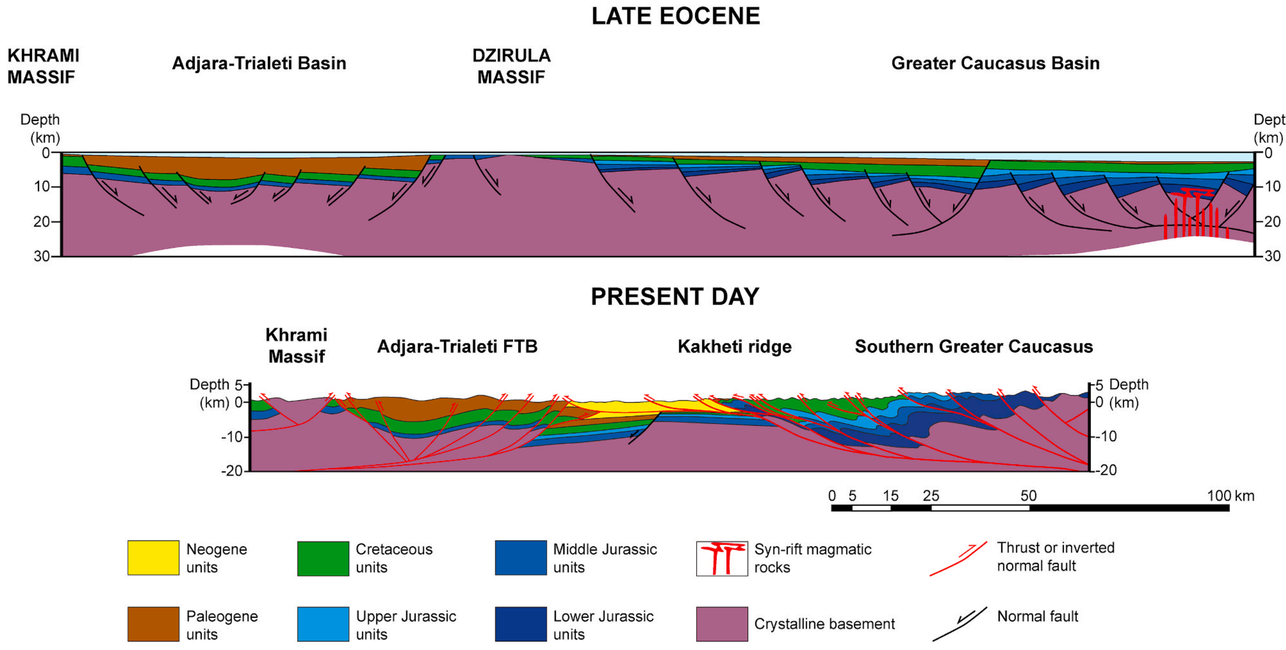

Fig. 11. Schematic cartoon of the structural-stratigraphic setting of the study area across the Dzirula Massif, extending to the south in the Adjara-Trialeti FTB, derived from inversion of a Cenozoic back-arc basin, and to the north across the Greater Caucasus, derived from inversion of a Mesozoic rift basin. Redrawn and modified after Alania et al. (2017); Gusmeo et al. (2021); Mauvilly et al. (2016).

might have been transmitted to the north over long distances, causing far-field deformation in a wide area of the hinterland.

A fundamental unresolved issue is the exact timing of growth and structural evolution of the Greater Caucasus, which according to our results has recorded a range of paleotemperatures much higher than those recorded in the other domains. The high maturity level in the axial zone of the belt and in the Jurassic-Cretaceous stratigraphic successions, characterised by a thick-skinned tectonic style, can be ascribed with confidence mostly to sedimentary burial. Middle Jurassic magmatic activity (Adamia et al., 2011a; Saintot et al., 2006) may have in part contributed to the very high paleotemperatures recorded in the oldest, most mature samples. Both the maturity trend and the structural style of deformation are in agreement with a positive inversion of the former extensional faults (similarly to the Adjara-Trialeti FTB). The fairly high paleotemperatures (100–160 °C) experienced by the Upper Eocene succession of the Greater Caucasus southern foothills require a different explanation. Such maturity level can result from either (i) sedimentary burial underneath a thick succession of younger sedimentary rocks, later almost totally eroded, or (ii) thrust-related tectonic burial. The discrimination of the dominant contribution (sedimentary, tectonic, or both) to the thermal maturity of this part of the belt has crucial implications for a precise reconstruction of the Cenozoic development of the Greater Caucasus.

6. Conclusions

This paper provides new constraints on the thermal evolution and the structural styles of a wide area in eastern Georgia, where three geologic domains can be identified in the hinterland of the Arabia-Eurasia collision zone. Two domains derived from positive inversion of former rift basins (i.e. Adjara-Trialeti FTB and Greater Caucasus), the third is comprised between them and characterised by thin-skinned deformation (i.e. Kura Basin and Kakheti ridge). Integrating newly acquired and published thermal maturity indicators we were able to (i) define the maximum temperatures experienced by the sedimentary successions and (ii) to elucidate the tectonic evolution of the area of study during convergence, including the role played by inherited pre-shortening structures.

The results indicate that the Cretaceous-to-Lower Miocene sedimentary units in the Adjara-Trialeti FTB and in the Kura Basin have a similar thermal maturity degree, comprised in the oil window, whereas time-equivalent successions in the Kakheti ridge are slightly less mature (immature to early mature) and the Middle-Late Miocene section of the Kura Basin is immature. The similar thermal maturity in the same stratigraphic units was acquired during back-arc basin evolution in the Paleogene in the Adjara-Trialeti FTB, and during flexure and sedimentary burial, associated to convergence, in the Miocene in the Kura Basin/Kakheti ridge. The Greater Caucasus is characterised by a much higher maturity level, increasing from the southern foothills to the axial zone, where it reaches the low metamorphic realm. Such a maturity probably represents the cumulative effect of both sedimentary burial during extensional evolution and tectonic overburden during compressional deformation.

Credit roles statement

Sveva Corrado: Conceptualization, Data curation, Investigation, Methodology, Resources, Supervision, Validation, Writing – original draft. Thomas Gusmeo: Conceptualization, Data curation, Investigation, Supervision, Validation, Visualization, Writing – original draft. Andrea Schito: Data acquisition, Methodology, Validation, Writing – review & editing. Victor Alania: Investigation, Resources, Validation. Onise Enukidze: Investigation, Resources, Validation. Enrico Conventi: Data acquisition, Methodology. William Cavazza: Investigation, Resources, Writing – review & editing.

Funding

MUR-PRIN 2017–2021; MUR-Department of Excellence Science Roma Tre; Roma Tre Post-doc grant to A. Schito; ALBA Laboratory funds; MUR PhD grant to T. Gusmeo. Funding sources only provided financial support and did not in any way influence the study design, data interpretation, the writing process or the decision to submit this manuscript.

Declaration of competing interest

The authors declare that they have no known competing financial interests or personal relationships that could have appeared to influence the work reported in this paper.

Acknowledgements

Organic petrography and XRD analyses of fine-grained sediments were performed in ALBA (Academic Laboratory of Basin Analysis) of the Department of Science of “Roma Tre” University. Raman analyses and interpretation have been performed in EVPL (Experimental Volcanology and Petrology Laboratory) of the Department of Science of “Roma Tre” University. Pyrolysis data were kindly provided by Georgia Oil and Gas Company.

Warm acknowledgments to Sergio Lo Mastro for XRD diffractogram acquisition.

Tamar Beridze and Luca Aldega are warmly acknowledged for fruitful discussions on Georgia regional geology and thermal evolution of sedimentary basins.

Constructive comments made by Jocelyn Barbarand and Gabor Tari improved an earlier version of the manuscript. We also thank Associate Editor Johannes Wendebourg for careful handling of the manuscript.

References

Adamia, S.A., 2004. Geological Map of Georgia, 1: 500 000 Scale.

Adamia, S.A., Alania, V., Chabukiani, A., Chichua, G., Enukidze, O., Sadradze, N., 2010. Evolution of the late cenozoic basins of Georgia (SW Caucasus): a review. In: Sosson, M., Kaymakci, N., Stephenson, R.A., Bergerat, F., Starostenko, V. (Eds.), Sedimentary Basin Tectonics from the Black Sea and Caucasus to the Arabian Platform, vol. 340. Geological Society, London, Special Pubblications, pp. 239–259.

Adamia, S.A., Alania, V., Chabukiani, A., Kutelia, Z., Sadradze, N., 2011a. Great Caucasus (cavcasioni): a long-lived north-tethyan back-arc basin. Turk. J. Earth Sci. 20, 611–628. https://doi.org/10.3906/yer-1005-12.

Adamia, S.A., Chkhotua, T., Kekelia, M., Lordkipanidze, M., Shavishvili, I., Zakariadze, G., 1981. Tectonics of the Caucasus and adjoining regions: implications for the evolution of the Tethys ocean. J. Struct. Geol. 3, 437–447. https://doi.org/10.1016/0191-8141(81)90043-2.

Adamia, S.A., Chkhotua, T.G., Gavtadze, T.T., Lebanidze, Z.A., Lursmanashvili, N.D., Sadradze, N.G., Zakaraia, D.P., Zakariadze, G.S., 2017. Tectonic setting of Georgia-eastern Black Sea: a review. In: Sosson, M., Stephenson, R.A., Adamia, S.A. (Eds.), Tectonic Evolution of the Eastern Black Sea and Caucasus, vol. 428. Geological Society, London, Special Publications, pp. 11–40. https://doi.org/10.1144/SP428.6.

Adamia, S.A., Zakariadze, G., Chkhotua, T., Sadradze, N., Tsereteli, N., Chabukiani, A., Gventsadze, A., 2011b. Geology of the Caucasus: a review. Turk. J. Earth Sci. 20, 489–544. https://doi.org/10.3906/yer-1005-11.

Alania, V., Beridze, T., Enukidze, O., Chagelishvili, R., Lebanidze, Z., Maqadze, D., 2021. The Geometry of the two orogens convergence and collision zones in central Georgia: new data from seismic reflection profiles. In: Bonali, F.L., Pasquarè Mariotto, F.A., Tsereteli, N. (Eds.), Building Knowledge for Geohazard Assesment and Management in the Caucasus and Other Regions. Springer, Dordrecht, pp. 73–88.

Alania, V., Beridze, T., Enukidze, O., Lebanidze, Z., Razmadze, A., Sadradze, N., Tevzadze, N., 2020. Structural model of the frontal part of the eastern Achara-Trialeti fold-and-thrust belt: the results of seismic profile interpretation. Bull. Georg. Natl. Acad. Sci. 14, 62–68.

Alania, V., Chabukiani, A.O., Chagelishvili, R.L., Enukidze, O.V., Gogrichiani, K.O., Razmadze, A.N., Tsereteli, N.S., 2017. Growth structures, piggy-back basins and growth strata of the Georgian part of the Kura foreland fold–thrust belt: implications for Late Alpine kinematic evolution. In: Sosson, M., Stephenson, R.A., Adamia, S.A. (Eds.), Tectonic Evolution of the Eastern Black Sea and Caucasus, vol. 428. Geological Society, London, Special Publications, pp. 428–445. https://doi.org/10.1177/1010539510370992.

Alania, V., Enukidze, O., Glonti, N., Razmadze, A., Chabukiani, A., Giorgadze, A., Vakhtang Glonti, B., Koiava, K., Beridze, T., Khutsishvili, S., Chagelishvili, R., 2018.

Structural architecture of the Kura foreland fold-and-thrust belt using seismic reflection profile, Georgia. Univers. J. Geosci. 6, 184–190. https://doi.org/10.13189/ujg.2018.060402.

Albino, I., Cavazza, W., Zattin, M., Okay, A.I., Adamia, S.A., Sadradze, N., 2014. Far-field tectonic effects of the arabia–eurasia collision and the inception of the north anatolian fault system. Geol. Mag. 151, 372–379. https://doi.org/10.1017/s0016756813000952.

Aldega, L., Bigi, S., Carminati, E., Trippetta, F., Corrado, S., Kavoosi, M.A., 2018. The Zagros fold-and-thrust belt in the Fars province (Iran): II. Thermal evolution. Mar. Petrol. Geol. 93, 376–390. https://doi.org/10.1016/j.marpetgeo.2018.03.022.

Aldega, L., Botti, F., Corrado, S., 2007a. Clay mineral assemblages and vitrinite reflectance in the Laga Basin (Central Appenines, Italy): what do they record? Clay Clay Miner. 55, 504–518. https://doi.org/10.1346/CCMN.2007.0550505.

Aldega, L., Corrado, S., Carminati, E., Shaban, A., Sherkati, S., 2014. Thermal evolution of the Kuh-e-Asmari and Sim anticlines in the Zagros fold-and-thrust belt: implications for hydrocarbon generation. Mar. Petrol. Geol. 57, 1–13. https://doi.org/10.1016/j.marpetgeo.2014.04.017.

Aldega, L., Corrado, S., Grasso, M., Maniscalco, R., 2007b. Correlation of diagenetic data from organic and inorganic studies in the apenninic-maghrebian fold-and-thrust belt: a case study from eastern sicily. J. Geol. 115, 335–353. https://doi.org/10.1086/512756.

Aldega, L., Corrado, S., Paolo, L. Di, Somma, R., Maniscalco, R., Balestrieri, M.L., 2011. Shallow burial and exhumation of the Peloritani Mountains (NE Sicily, Italy): insight from paleothermal and structural indicators. Bull. Geol. Soc. Am. 123, 132–149. https://doi.org/10.1130/B30093.1.

Allen, P.A., Allen, J.R., 2013. Basin Analysis: principles and application to petroleum play assessment. Science. https://doi.org/10.1126/science.208.4442.393.

Atouabat, A., Corrado, S., Schito, A., Haissen, F., Gimeno-Vives, O., Mohn, G., Lamotte, D.F. de, 2020. Validating structural styles in the Flysch Basin Northern Rif (Morocco) by means of thermal modeling. Geosci. 10, 1–18. https://doi.org/10.3390/geosciences10090325.

Avdeev, B., Niemi, N.A., 2011. Rapid Pliocene exhumation of the central Greater Caucasus constrained by low-temperature thermochronometry. Tectonics 30, 1–16. https://doi.org/10.1029/2010TC002808.

Axen, G.J., Lam, P.S., Grove, M., Stockli, D.F., Hassanzadeh, J., 2001. Exhumation of the west-central Alborz Mountains, Iran, Caspian subsidence, and collision-related tectonics. Geology 29, 559–562. https://doi.org/10.1130/0091-7613(2001)029<0559:EOTWCA>2.0.CO;2.

Balestra, M., Corrado, S., Aldega, L., Morticelli, M.G., Sulli, A., Rudkiewicz, J.L., Sassi, W., 2019. Thermal and structural modeling of the Scillato wedge-top basin source-to-sink system: insights into the Sicilian fold-and-thrust belt evolution (Italy). Bull. Geol. Soc. Am. 131, 1763–1782. https://doi.org/10.1130/B35078.1.

Ballato, P., Cifelli, F., Heidarzadeh, G., Ghassemi, M.R., Wickert, A.D., Hassanzadeh, J., Dupont-Nivet, G., Balling, P., Sudo, M., Zeilinger, G., Schmitt, A.K., Mattei, M., Strecker, M.R., 2016. Tectono-sedimentary evolution of the northern Iranian Plateau: insights from middle–late Miocene foreland-basin deposits. Basin Res. 29, 417–446. https://doi.org/10.1111/bre.12180.

Ballato, P., Uba, C.E., Landgraf, A., Strecker, M.R., Sudo, M., Stockli, D.F., Friedrich, A., Tabatabaei, S.H., 2011. Arabia-eurasia continental collision: insights from late tertiary foreland-basin evolution in the Alborz mountains, northern Iran. Bull. Geol. Soc. Am. 123, 106–131. https://doi.org/10.1130/B30091.1.

Banks, C.J., Robinson, A.G., Williams, M.P., 1997. Structure and regional tectonics of the Achara-Trialeti fold belt and the adjacent Rioni and Kartli foreland basins, Republic of Georgia. In: Robinson, A.G. (Ed.), Regional and Petroleum Geology of the Blacks Sea and Surrounding Region: AAPG Memoirs 68, pp. 331–346. Tulsa, Oklahoma.

Barker, C.E., Pawlewicz, M.J., 1986. In: Buntebarth, G., Stagena, L. (Eds.), The Correlation of Vitrinite Reflectance with Maximum Temperature in Humic Organic Matter, Paleogeothermics. Springer, Berlin, Heidelberg, pp. 79–93. https://doi.org/10.1007/BFb0012103.

Barnard, P.C., Collins, A.G., Cooper, B.S., 1981. Identification and distribution of kerogen facies in a source rock horizon - examples from the North Sea Basin. In: Brooks, J. (Ed.), Organic Maturation Studies and Fossil Fuel Exploration. Academic Press, London, pp. 271–282.

Barnes, M.A., Barnes, W.C., Bustin, R.M., 1990. Chemistry and diagenesis of organic matter in sediments and fossil fuels. Diagenesis 189–204.

Barrier, E., Vrielynck, B., Brouillet, J.F., Brunet, M.-F., Contributors Angiolini, L., Kaveh, F., Poisson, A., Pourteau, A., Plunder, A., Robertson, A., Shekawat, R., Sosson, M., Zanchi, A., 2018. Paleotectonic Reconstruction of the Central Tethyan Realm. Tectonono-Sedimentary-Palinspastic Maps from Late Permian to Pliocene. CCGM/CGMW, Paris.

Behar, F., Beaumont, V., De, B., Penteado, H.L., 2001. Rock-eval 6 technology: performances and developments. Oil Gas Sci. Technol. 56, 111–134. https://doi.org/10.2516/ogst:2001013.

Bertrand, R., Lavoie, V., Malo, M., 2010. Maturité thermique et potentiel roche-mère des roches ordoviciennes à dévoniennes du secteur Matapédia–Témiscouata du Bas-Saint-Laurent, Québec. Geol. Surv. Canada, Open File 6576 183.

Beyssac, O., Goffe, B., Chopin, C., Rouzaud, J.N., 2002. Raman spectra of carbonaceous material in metasediments: a new geothermometer. J. Metamorph. Geol. J Metamorph Geol 20, 859–871.

Boote, D.R.D., Sachsenhofer, R.F., Tari, G., Arbouille, D., 2018. Petroleum provinces of the paratethyan region. J. Petrol. Geol. 41, 247–298. https://doi.org/10.1111/jpg.12703.

Borrego, A.G., Araujo, C.V., Balke, A., Cardott, B., Cook, A.C., David, P., Flores, D., Hámor-Vidó, M., Hiltmann, W., Kalkreuth, W., Koch, J., Kommeren, C.J., Kus, J., Ligouis, B., Marques, M., Mendonça Filho, J.G., Misz, M., Oliveira, L., Pickel, W., Reimer, K., Ranasinghe, P., Suárez-Ruiz, I., Vieth, A., 2006. Influence of particle and surface quality on the vitrinite reflectance of dispersed organic matter: comparative exercise using data from the qualifying system for reflectance analysis working group of ICCP. Int. J. Coal Geol. 68, 151–170. https://doi.org/10.1016/j.coal.2006.02.002.

Borrego, A.G., Cook, A., 2017. Sampling and sample preparation for reflected light microscopy. In: 10th ICCP Training Course on Dispersed Organic Matter Integrating Transmitted and Reflected Light Microscopy (Instruction Notes), pp. 21–28.

Brunet, F.F., Korotaev, M.V., Ershov, A.V., Nikishin, A.M., 2003. The South Caspian Basin: a review of its evolution from subsidence modelling. Sediment. Geol. 156, 119–148. https://doi.org/10.1016/S0037-0738(02)00285-3.

Bujakaite, M.I., Gavrilov, Y.O., Gertsev, D.O., Golovin, D.I., Panov, D.I., Kushcheva, Y.V., 2003. The K–Ar and Rb–Sr isotopic systems in rocks from the jurassic terrigenous complex of the greater Caucasus. Lithol. Miner. Resour. 38, 522–529. https://doi.org/10.1023/A:1027364527305.

Burnham, A.K., Sweeney, J.J., 1989. A chemical kinetic model of vitrinite maturation and reflectance. Geochem. Cosmochim. Acta 53, 2649–2657. https://doi.org/10.1016/0016-7037(89)90136-1.

Caricchi, C., Aldega, L., Corrado, S., 2015. Reconstruction of maximum burial along the Northern Apennines thrust wedge (Italy) by indicators of thermal exposure and modeling. Bull. Geol. Soc. Am. 127, 428–442. https://doi.org/10.1130/B30947.1.

Cavazza, W., Albino, I., Galoyan, G., Zattin, M., Cattò, S., 2019. Continental accretion and incremental deformation in the thermochronologic evolution of the Lesser Caucasus. Geosci. Front. https://doi.org/10.1016/j.gsf.2019.02.007.

Cavazza, W., Albino, I., Zattin, M., Galoyan, G., Imamverdiyev, N., Melkonyan, R., 2017. Thermochronometric evidence for Miocene tectonic reactivation of the Sevan-Akera suture zone (Lesser Caucasus): a far-field tectonic effect of the Arabia-Eurasia collision?. In: Sosson, M., Stephenson, R.A., Adamia, S.A. (Eds.), Tectonic Evolution of the Eastern Black Sea and Caucasus, vol. 428. Geological Society, London, Special Publications, pp. 187–198. https://doi.org/10.1144/SP428.4.

Cavazza, W., Cattò, S., Zattin, M., Okay, A.I., Reiners, P., 2018. Thermochronology of the Miocene Arabia-Eurasia collision zone of southeastern Turkey. Geosphere 14, 2277–2293. https://doi.org/10.1130/GES01637.1.

Corrado, S., Aldega, L., Balestrieri, M.L., Maniscalco, R., Grasso, M., 2009. Structural evolution of the sedimentary accretionary wedge of the alpine system in Eastern Sicily: thermal and thermochronological constraints. Bull. Geol. Soc. Am. 121, 1475–1490. https://doi.org/10.1130/B26420.1.

Corrado, S., Aldega, L., Di Leo, P., Giampaolo, C., Invernizzi, C., Mazzoli, S., Zattin, M., 2005. Thermal maturity of the axial zone of the southern Apennines fold-and-thrust belt (Italy) from multiple organic and inorganic indicators. Terra. Nova 17, 56–65. https://doi.org/10.1111/j.1365-3121.2004.00584.x.

Corrado, S., Schito, A., Romano, C., Grigo, D., Poe, B.T., Aldega, L., Caricchi, C., Di Paolo, L., Zattin, M., 2020. An integrated platform for thermal maturity assessment of polyphase, long-lasting sedimentary basins, from classical to brand-new thermal parameters and models: an example from the on-shore Baltic Basin (Poland). Mar. Petrol. Geol. 122, 104547. https://doi.org/10.1016/j.marpetgeo.2020.104547.

Cowgill, E., Forte, A.M., Niemi, N., Avdeev, B., Tye, A., Trexler, C., Javakhishvili, Z., Elashvili, M., Godoladze, T., 2016. Relict basin closure and crustal shortening budgets during continental collision: an example from Caucasus sediment provenance. Tectonics 35, 2918–2947. https://doi.org/10.1002/2016TC004295.

Dercourt, J., Zonenshain, L.P., Ricou, L.E., Kazmin, V.G., Le Pichon, X., Knipper, A.L., Grandjacquet, C., Sbortshikov, I.M., Geyssant, J., Lepvrier, C., Pechersky, D.H., Boulin, J., Sibuet, J.C., Savostin, L.A., Sorokhtin, O., Westphal, M., Bazhenov, M.L., Lauer, J.P., Biju-Duval, B., 1986. Geological evolution of the tethys belt from the atlantic to the pamirs since the lias. Tectonophysics 123, 241–315. https://doi.org/10.1016/0040-1951(86)90199-X.

Di Paolo, L., Olivetti, V., Corrado, S., Aldega, L., Balestrieri, M.L., Maniscalco, R., 2014. Detecting the stepwise propagation of the Eastern Sicily thrust belt (Italy): insight from thermal and thermochronological constraints. Terra. Nova 26, 363–371. https://doi.org/10.1111/ter.12106.

Dow, W.G., 1977. Kerogen studies and geological interpretations. J. Geochem. Explor. 7, 79–99.

Ershov, A.V., Brunet, M.F., Nikishin, A.M., Bolotov, S.N., Nazarevich, B.P., Korotaev, M. V., 2003. Northern Caucasus basin: thermal history and synthesis of subsidence models. Sediment. Geol. 156, 95–118. https://doi.org/10.1016/S0037-0738(02)00284-1. None).

Ferralis, N., Matys, E.D., Knoll, A.H., Hallmann, C., Summons, R.E., 2016. Rapid, direct and non-destructive assessment of fossil organic matter via microRaman spectroscopy. Carbon 108, 440–449. https://doi.org/10.1016/j.carbon.2016.07.039.

Forte, A.M., Cowgill, E., Bernardin, T., Kreylos, O., Hamann, B., 2010. Late cenozoic deformation of the Kura fold-thrust belt, southern greater Caucasus. Bull. Geol. Soc. Am. 122, 465–486. https://doi.org/10.1130/B26464.1.

Forte, A.M., Cowgill, E., Murtuzayev, I., Kangarli, T., Stoica, M., 2013. Structural geometries and magnitude of shortening in the eastern Kura fold-thrust belt, Azerbaijan: implications for the development of the Greater Caucasus Mountains. Tectonics 32, 688–717. https://doi.org/10.1002/tect.20032.

Forte, A.M., Cowgill, E., Whipple, K.X., 2014. Transition from a singly vergent to doubly vergent wedge in a young orogen: the Greater Caucasus. Tectonics 33, 2077–2101. https://doi.org/10.1002/2014TC003651.

Gamkrelidze, I., Okrostsvaridze, A., Maisadze, F., Basheleishvili, L., Boichenko, G., 2019. Main features of geological structure and geotourism potential of Georgia, the Caucasus. Mod. Environ. Sci. Eng. 5, 422–442. https://doi.org/10.15341/mese(2333-2581)/05.05.2019/010.

Gavillot, Y., Axen, G.J., Stockli, D.F., Horton, B.K., Fakhari, M.D., 2010. Timing of thrust activity in the High Zagros fold-thrust belt, Iran, from (U-Th)/He thermochronometry. Tectonics 29. https://doi.org/10.1029/2009TC002484.

Goodhue, R., Clayton, G., 2010. Palynomorph darkness index (PDI) - a new technique for assessing thermal maturity. Palynology 34, 147–156. https://doi.org/10.1080/01916121003696932.

Guedes, A., Valentim, B., Prieto, A.C., Noronha, F., 2012. Raman spectroscopy of coal macerals and fluidized bed char morphotypes. Fuel 97, 443–449. https://doi.org/10.1016/j.fuel.2012.02.054.

Guedes, A., Valentim, B., Prieto, A.C., Rodrigues, S., Noronha, F., 2010. Micro-Raman spectroscopy of collotelinite, fusinite and macrinite. Int. J. Coal Geol. 83, 415–422. https://doi.org/10.1016/j.coal.2010.06.002.

Gusmeo, T., Cavazza, W., Alania, V.M., Enukidze, O.V., Zattin, M., Corrado, S., 2021. Structural inversion of back-arc basins – the Neogene Adjara-Trialeti fold-and-thrust belt (SW Georgia) as a far-field effect of the Arabia-Eurasia collision. Tectonophysics 803. https://doi.org/10.1016/j.tecto.2020.228702.

Hartkopf-Fröder, C., Königshof, P., Littke, R., Schwarzbauer, J., 2015. Optical thermal maturity parameters and organic geochemical alteration at low grade diagenesis to anchimetamorphism: a review. Int. J. Coal Geol. 150– 151, 74–119. https://doi.org/10.1016/j.coal.2015.06.005.

Henry, D.G., Jarvis, I., Gillmore, G., Stephenson, M., 2019. Raman spectroscopy as a tool to determine the thermal maturity of organic matter: application to sedimentary, metamorphic and structural geology. Earth Sci. Rev. 198, 102936. https://doi.org/10.1016/j.earscirev.2019.102936.

Hillier, S., Mátyás, J., Matter, A., Vasseur, G., 1995. Illite/smectite diagenesis and its variable correlation with vitrinite reflectance in the pannonian basin. Clay Clay Miner. 43, 174–183.

Hinrichs, R., Brown, M.T., Vasconcellos, M.A.Z., Abrashev, M.V., Kalkreuth, W., 2014. Simple procedure for an estimation of the coal rank using micro-Raman spectroscopy. Int. J. Coal Geol. 136, 52–58. https://doi.org/10.1016/j.coal.2014.10.013.

Hoffman, J., Hower, J., 1979. Clay mineral assemblages as low grade metamorphic geothermometers: application to the thrust faulted disturbed belt of Montana. Soc. Econ. Plaeontologists Mineral. 26, 55–79.

Jagodzinski, H., 1949. Eindimensionale Fehlordnung in Kristallen und ihr Einfluss auf die Röntgeninterferenzen. I. Berechnung des Fehlordnungsgrades aus den Röntgenintensitäten. Acta Crystallogr. 2, 201–207.

Koshnaw, R.I., Horton, B.K., Stockli, D.F., Barber, D.E., Tamar-Agha, M.Y., Kendall, J.J., 2017. Neogene shortening and exhumation of the Zagros fold-thrust belt and foreland basin in the Kurdistan region of northern Iraq. Tectonophysics 694, 332–355. https://doi.org/10.1016/j.tecto.2016.11.016.

Koshnaw, R.I., Stockli, D.F., Horton, B.K., Teixell, A., Barber, D.E., Kendall, J.J., 2020. Late Miocene deformation kinematics along the NW Zagros fold-thrust belt, Kurdistan region of Iraq: constraints from apatite (U-Th)/He thermochronometry and balanced cross sections. Tectonics 1–37. https://doi.org/10.1029/2019tc005865.

Kübler, B., 1964. Les argilles, indicateurs de métamorphisme. Rev. l'Institut Fr. du Pet. 19, 1093–1112.

Kübler, B., Jaboyedoff, M., 2000. Illite crystallinity. Comptes Rendus l'Academie Sci. - Ser. IIa Sci. la Terre des Planetes 331, 75–89. https://doi.org/10.1016/S1251-8050(00)01395-1.

Labeur, A., Beaudoin, N.E., Lacombe, O., Emmanuel, L., Petracchini, L., Daëron, M., Klimowicz, S., Callot, J.-P., 2021. Burial-deformation history of folded rocks unraveled by fracture analysis, stylolite paleopiezometry and vein cement geochemistry: a case study in the Cingoli Anticline (Umbria-Marche, Northern Appennines). Geosciences 11, 135–155. https://doi.org/10.3390/geosciences11030135.

Lahfid, A., Beyssac, O., Deville, E., Negro, F., Chopin, C., Goffé, B., 2010. Evolution of the Raman spectrum of carbonaceous material in low-grade metasediments of the Glarus Alps (Switzerland). Terra. Nova 22, 354–360. https://doi.org/10.1111/j.1365-3121.2010.00956.x.

Lanson, B., 1997. Decomposition of experimental x-ray diffraction patterns (profile fitting): a convenient way to study clay minerals. Clay Clay Miner. 45, 132–146. https://doi.org/10.1346/CCMN.1997.0450202.

Lazarev, S., Jorissen, E.L., van de Velde, S., Rausch, L., Stoica, M., Wesselingh, F.P., Van Baak, C.G.C., Yanina, T.A., Aliyeva, E., Krijgsman, W., 2019. Magneto-biostratigraphic age constraints on the palaeoenvironmental evolution of the South Caspian basin during the Early-Middle Pleistocene (Kura basin, Azerbaijan). Quat. Sci. Rev. 222, 105895. https://doi.org/10.1016/j.quascirev.2019.105895.

Liu, B., Schieber, J., Mastarletz, M., 2019. Petrographic and Micro-FTIR study of organic matter in the Upper Devonian New Albany shale during thermal maturation: implications for kerogen transformation. In: Camp, W.K., Milliken, K.L., Taylor, K., Fishman, N., Hackley, P.C., Macquaker, J.H.S. (Eds.), Mudstone Diagenesis: Research Perspectives for Shale Hydrocarbon Reservoirs, Seals, and Source Rocks, vol. 120. AAPG Memoir, pp. 165–188. https://doi.org/10.1306/13672216M1213380.

Liu, D.H., Xiao, X.M., Tian, H., Min, Y.S., Zhou, Q., Cheng, P., Shen, J.G., 2013. Sample maturation calculated using Raman spectroscopic parameters for solid organics: methodology and geological applications. Chin. Sci. Bull. 58, 1285–1298. https://doi.org/10.1007/s11434-012-5535-y.

Lordkipanidze, M.B., Meliksetian, B., Djarbashian, R., 1989. Meosozic-Cenozoic magmatic evolution of the Pontian-Crimean-Caucasian region. IGCP Proj 198, 103–124.

Lozar, F., Polino, R., 1997. Early Cenozoic uprising of the Great Caucasus revealed by reworked calcareous nannofossils. In: EUG. Strasbourg, p. 141. France.

Lünsdorf, N.K., Dunkl, I., Schmidt, B.C., Rantitsch, G., von Eynatten, H., 2017. Towards a higher comparability of geothermometric data obtained by Raman spectroscopy of carbonaceous material. Part 2: a revised geothermometer. Geostand. Geoanalytical Res. 41, 593–612. https://doi.org/10.1111/ggr.12178.

Lünsdorf, N.K., Lünsdorf, J.O., 2016. Evaluating Raman spectra of carbonaceous matter by automated, iterative curve-fitting. Int. J. Coal Geol. 160–161, 51–62. https://doi.org/10.1016/j.coal.2016.04.008.

Madanipour, S., Ehlers, T.A., Yassaghi, A., Enkelmann, E., 2017. Accelerated middle Miocene exhumation of the talesh mountains constrained by U-Th/He thermochronometry: evidence for the arabia-eurasia collision in the NW Iranian plateau. Tectonics 36, 1538–1561. https://doi.org/10.1002/2016TC004291.

Mangenot, X., Bonifacie, M., Gasparrini, M., Götz, A., Chaduteau, C., Ader, M., Rouchon, V., 2017. Coupling Δ47 and fluid inclusion thermometry on carbonate cements to precisely reconstruct the temperature, salinity and δ18O of paleo-groundwater in sedimentary basins. Chem. Geol. 472, 44–57. https://doi.org/10.1016/j.chemgeo.2017.10.011.

Mangenot, X., Deçoninck, J.F., Bonifacie, M., Rouchon, V., Collin, P.Y., Quesne, D., Gasparrini, M., Sizun, J.P., 2019. Thermal and exhumation histories of the northern subalpine chains (Bauges and Bornes—France): evidence from forward thermal modeling coupling clay mineral diagenesis, organic maturity and carbonate clumped isotope (Δ 47) data. Basin Res. 31, 361–379. https://doi.org/10.1111/bre.12324.

Mauvilly, J., Koiava, K., Gamkrelidze, I., Mosar, J., 2016. Tectonics in the Georgian Greater Caucasus: a structural cross-section in an inverted rifted basin setting. In: 14th Swiss Geoscience Meeting, Geneva, Switzerland. https://doi.org/10.13140/RG.2.2.26540.56963. Geneva, Switzerland.

Merryman, R.J., Frey, M., 1999. Patterns of very low-grade metamorphism in metapelitic rocks. In: Low-Grade Metamorphism. Blackwell Scientific Publications, Oxford, International, pp. 61–107.

Moore, D.M., Reynolds, R.C.J., 1997. X-Ray Diffraction and the Identification and Analysis of Clay Minerals. Oxford Univ Press. https://doi.org/10.1180/claymin.1999.034.1.21.

Mosar, J., Kangarli, T., Bochud, M., Glasmacher, U.A., Rast, A., Brunet, M.-F., Sosson, M., 2010. Cenozoic-Recent tectonics and uplift in the Greater Caucasus: a perspective from Azerbaijan. In: Sosson, M., Kaymakci, N., Stephenson, R.A., Bergerat, F., Starostenko, V. (Eds.), Sedimentary Basin Tectonics from the Black Sea and Caucasus to the Arabian Platform, vol. 340. Geological Society, London, Special Publications, pp. 261–280. https://doi.org/10.1144/SP340.12.

Motavalli-Anbaran, S.H., Zeyen, H., Jamasb, A., 2016. 3D crustal and lithospheric model of the Arabia-Eurasia collision zone. J. Asian Earth Sci. 122, 158–167. https://doi.org/10.1016/j.jseaes.2016.03.012.

Muirhead, D.K., Bond, C.E., Watkins, H., Butler, R.W.H., Schito, A., Crawford, Z., Marpino, A., 2020. Raman Spectroscopy: an effective thermal marker in low temperature carbonaceous fold-thrust belts. In: Hammerstein, J.A., Di Cuia, R., Cottam, M.A., Zamora, G., Butler, R.W.H. (Eds.), Fold and Thrust Belts: Structural Style, Evolution and Exploration, vol. 490. Geological Society, London, Special Publications, pp. 131–151. https://doi.org/10.1144/SP490-2019-27.

Mumm, A.S., Inan, S., 2016. Microscale organic maturity determination of graptolites using Raman spectroscopy. Int. J. Coal Geol. 162, 96–107. https://doi.org/10.1016/j.coal.2016.05.002.

Nemčok, M., Glonti, B., Yukler, A., Marton, B., 2013. Development history of the foreland plate trapped between two converging orogens; Kura Valley, Georgia, case study. In: Nemčok, M., Mora, A., Cosgrove, J.W. (Eds.), Thick-Skin-Dominated Orogens: from Initial Inversion to Full Accretion, vol. 377. Geological Society, London, Special Publications, pp. 159–188. https://doi.org/10.1144/SP377.9.

Neubauer, T.A., Harzhauser, M., Kroh, A., Georgopoulou, E., Mandic, O., 2015. A gastropod-based biogeographic scheme for the European Neogene freshwater systems. Earth Sci. Rev. 143, 98–116. https://doi.org/10.1016/j.earscirev.2015.01.010.

Nikishin, A.M., Wannier, M., Alekseev, A.S., Almendinger, O.A., Fokin, P.A., Gabdullin, R.R., Khudoley, A.K., Kopaevich, L.F., Mityukov, A.V., Petrov, E.I., Rubtsova, E.V., 2017. Mesozoic to recent geological history of southern Crimea and the Eastern Black Sea region. In: Sosson, M., Stephenson, R.A., Adamia, S.A. (Eds.), Tectonic Evolution of the Eastern Black Sea and Caucasus, vol. 428. Geological Society, London, Special Publications, pp. 241–264. https://doi.org/10.1144/SP428.1.

Nikishin, A.M., Ziegler, P.A., Panov, D.I., Nazarevich, B.P., Brunet, M.F., Stephenson, R. A., Bolotov, S.N., Korotaev, M.V., Tikhomirov, P.L., 2001. Mesozoic and cenozoic evolution of the scythian platform-Black Sea-Caucasus domain. In: Ziegler, Peter A., Cavazza, W., Robertson, A.H.F., Crasquin-Soleau, S. (Eds.), Peri-Tethys Memoir 6: Peri-Tethyan Rift/Wrench Basins and Passive Margins. National Museum of Natural History, Paris, pp. 295–346.

Okay, A.I., Zattin, M., Cavazza, W., 2010. Apatite fission-track data for the Miocene Arabia-Eurasia collision. Geology 38, 35–38. https://doi.org/10.1130/G30234.1.

Okrostsvaridze, A., Chung, S.L., Chang, Y.H., Gagnidze, N., Boichenko, G., Gogoladze, S., 2018. Zircons U-Pb geochronology of the ore-bearing plutons of Adjara-Trialeti folded zone, Lesser Caucasus and analysis of the magmatic processes. Bull. Georg. Natl. Acad. Sci. 12, 90–99.

Pace, P., Ricciato, A., Riva, A., Tevzadze, R., Tevzadze, N., Janiashvili, A., Sanishvili, A., Alania, V., Enukidze, O., 2019. Renewed hydrocarbon prospectivity in the kura-kartli foreland basin, onshore Central Georgia. In: AAPG GTW Conference: Exploration and Production in the Black Sea, Caucasus and Caspian Region, 18-19 September 2019. Batumi, Georgia, p. 20.

Philip, H., Cisternas, A., Gvishiani, A., Gorshkov, A., 1989. The Caucasus: an actual example of the initial stages of continental collision. Tectonophysics 161, 1–21.

Pollastro, R.M., 1990. The illite/smectite geothermometer - concepts, methodology, and application to basin history and hydrocarbon generation. In: Nuccio Vito, F., Barker Charles, E., Dyson Sally, J. (Eds.), Applications of Thermal Maturity Studies to Energy Exploration. Eastwood Print. And Publ., pp. 1–18. Denver, CO, United States.

Pupp, M., Bechtel, A., Ćorić, S., Gratzer, R., Rustamov, J., Sachsenhofer, R.F., 2018. Eocene and Oligo-Miocene source rocks in the Rioni and Kura Basins of Georgia:

depositional environment and petroleum potential. J. Petrol. Geol. 41, 367–392. https://doi.org/10.1111/jpg.12708.

Qiu, N., He, L., Chang, J., Zhu, C., 2020. Research progress and challenges of thermal history reconstruction in sedimentary basins. Pet. Geol. Exp. 42, 790–802. https://doi.org/10.11781/sysydz202005790.

Quirico, E., Rouzaud, J.N., Bonal, L., Montagnac, G., 2005. Maturation grade of coals as revealed by Raman spectroscopy: progress and problems. Spectrochim. Acta Part A Mol. Biomol. Spectrosc. 61, 2368–2377. https://doi.org/10.1016/j.saa.2005.02.015.

Reilinger, R., McClusky, S., Vernant, P., Lawrence, S., Ergintav, S., Cakmak, R., Ozener, H., Kadirov, F., Guliev, I., Stepanyan, R., Nadariya, M., Hahubia, G., Mahmoud, S., Sakr, K., ArRajehi, A., Paradissis, D., Al-Aydrus, A., Prilepin, M., Guseva, T., Evren, E., Dmitrotsa, A., Filikov, S.V., Gomez, F., Al-Ghazzi, R., Karam, G., 2006. GPS constraints on continental deformation in the Africa-Arabia-Eurasia continental collision zone and implications for the dynamics of plate interactions. J. Geophys. Res. Solid Earth 111, 1–26. https://doi.org/10.1029/2005JB004051.

Rolland, Y., 2017. Caucasus collisional history: review of data from east anatolia to west Iran. Gondwana Res. 49, 130–146. https://doi.org/10.1016/j.gr.2017.05.005.

Rolland, Y., Sosson, M., Adamia, S.A., Sadradze, N., 2011. Prolonged Variscan to Alpine history of an active Eurasian margin (Georgia, Armenia) revealed by 40Ar/39Ar dating. Gondwana Res. 20, 798–815. https://doi.org/10.1016/j.gr.2011.05.007.

Sachsenhofer, R.F., Popov, S.V., Coric, S., Mayer, J., Misch, D., Morton, M.T., Pupp, M., Rauball, J., Tari, G., 2018. Paratethyan petroleum source rocks: an overview. J. Petrol. Geol. 41, 219–245. https://doi.org/10.1111/jpg.12702.

Saintot, A., Brunet, M.-F.F., Yakovlev, F., Sébrier, M., Stephenson, R., Ershov, A., Chalot-Prat, F., McCann, T., 2006. The mesozoic-cenozoic tectonic evolution of the greater Caucasus. Geol. Soc. Mem. 32, 277–289. https://doi.org/10.1144/gsl.mem.2006.032.01.16.

Samsu, A.S., 2014. Hydrocarbon Source Potential of Upper Eocene and Oligo-Miocene ("Maykop") Rocks in Georgia. MSc thesis. Montanuniversität Leoben.

Schito, A., Andreucci, B., Aldega, L., Corrado, S., Di Paolo, L., Zattin, M., Szaniawski, R., Jankowski, L., Mazzoli, S., 2018. Burial and exhumation of the western border of the Ukrainian Shield (Podolia): a multi-disciplinary approach. Basin Res. 30, 532–549. https://doi.org/10.1111/bre.12235.

Schito, A., Corrado, S., 2018. An automatic approach for characterization of the thermal maturity of dispersed organic matter Raman spectra at low diagenetic stages. In: Dowey, P.J., Osborne, M., Volk, H. (Eds.), Application of Analytical Techniques to Petroleum Systems. Geological Society Special Publication, pp. 107–119. https://doi.org/10.1144/SP484.5.

Schito, A., Corrado, S., Aldega, L., Grigo, D., 2016. Overcoming pitfalls of vitrinite reflectance measurements in the assessment of thermal maturity: the case history of the lower Congo basin. Mar. Petrol. Geol. 74, 59–70. https://doi.org/10.1016/j.marpetgeo.2016.04.002.

Schito, A., Romano, C., Corrado, S., Grigo, D., Poe, B., 2017. Diagenetic thermal evolution of organic matter by Raman spectroscopy. Org. Geochem. 106, 57–67. https://doi.org/10.1016/j.orggeochem.2016.12.006.

Schito, A., Spina, A., Corrado, S., Cirilli, S., Romano, C., 2019. Comparing optical and Raman spectroscopic investigations of phytoclasts and sporomorphs for thermal maturity assessment: the case study of Hettangian continental facies in the Holy cross Mts. (central Poland). Mar. Petrol. Geol. 104, 331–345. https://doi.org/10.1016/j.marpetgeo.2019.03.008.

Shatilova, I.I., Maissuradze, L.S., Koiava, K.P., Kokolashvili, I.M., Bukhsianidze, M.G., Bruch, A.A., 2020. The Environmental History of Georgia during the Late Miocene Based of Foraminifera and Pollen. Universal, Tbilisi.

Sobornov, K.O., 1996. Lateral variations in structural styles of tectonic wedging in the northeastern Caucasus, Russia. Bull. Can. Petrol. Geol. 44, 385–399.

Sokhadze, G., Floyd, M., Godoladze, T., King, R., Cowgill, E.S., Javakhishvili, Z., Hahubia, G., Reilinger, R., 2018. Active convergence between the lesser and greater Caucasus in Georgia: constraints on the tectonic evolution of the lesser–greater Caucasus continental collision. Earth Planet Sci. Lett. 481, 154–161. https://doi.org/10.1016/j.epsl.2017.10.007.

Sosson, M., Rolland, Y., Müller, C., Danelian, T., Melkonyan, R., Kekelia, S., Adamia, S. A., Babazadeh, V., Kangarli, T., Avagyan, A., Galoyan, G., Mosar, J., 2010. Subductions, obduction and collision in the Lesser Caucasus (Armenia, Azerbaijan, Georgia), new insights. In: Sosson, Marc, Kaymakci, N., Stephenson, R.A., Bergerat, F., Starostenko, V. (Eds.), Sedimentary Basin Tectonics from the Black Sea and Caucasus to the Arabian Platform, vol. 340. Geological Society of London, Special Publications, pp. 329–352. https://doi.org/10.1144/SP340.14.

Sosson, M., Stephenson, R., Sheremet, Y., Rolland, Y., Adamia, S.A., Melkonian, R., Kangarli, T., Yegorova, T., Avagyan, A., Galoyan, G., Danelian, T., Hässig, M., Meijers, M., Müller, C., Sahakyan, L., Sadradze, N., Alania, V., Enukidze, O., Mosar, J., 2016. The eastern Black Sea-Caucasus region during the Cretaceous: new evidence to constrain its tectonic evolution. Compt. Rendus Geosci. 348, 23–32. https://doi.org/10.1016/j.crte.2015.11.002.

Spina, A., Vecoli, M., Riboulleau, A., Clayton, G., Cirilli, S., Di Michele, A., Marcogiuseppe, A., Rettori, R., Sassi, P., Servais, T., Riquier, L., 2018. Application of Palynomorph Darkness Index (PDI) to assess the thermal maturity of palynomorphs: a case study from North Africa. Int. J. Coal Geol. 188, 64–78. https://doi.org/10.1016/j.coal.2018.02.001.

Su, H., Zhou, J., 2020. Timing of Arabia-Eurasia collision: constraints from restoration of crustal-scale cross-sections. J. Struct. Geol. 135 https://doi.org/10.1016/j.jsg.2020.104041.

Sukhishvili, L., Forte, A.M., Merebashvili, G., Leonard, J., Whipple, K.X., Javakhishvili, Z., Heimsath, A., Godoladze, T., 2020. Active deformation and Plio-Pleistocene fluvial reorganization of the western Kura fold-thrust belt, Georgia: implications for the evolution of the Greater Caucasus Mountains. Geol. Mag. https://doi.org/10.1017/S0016756820000709.

Tari, G., Vakhania, D., Tatishvili, G., Mikeladze, V., Gogritchiani, K., Vacharadze, S., Mayer, J., Sheya, C., Siedl, W., Banon, J.J.M., Sanchez, J.T., 2018. Stratigraphy, structure and petroleum exploration play types of the Rioni Basin, Georgia. In: Simmons, M.D., Tari, G.C., Okay, A.I. (Eds.), Petroleum Geology of the Black Sea, vol. 464. Geological Society, London, Special Publications, pp. 403–438. https://doi.org/10.1144/SP464.14.

Taylor, G.H., Teichmuller, M., Davis, A., Diessel, C.F.K., Littke, R., Robert, P., Glick, D.C., Smyth, M., Swaine, D.J., Vanderbroucke, M., 1998. Organic petrology: a new handbook incorporating some revised parts of Stach's textbook of coal petrology. Gebruder Borntraeger Verlagsbuchhandlung.

Tibaldi, A., Alania, V., Bonali, F.L., Enukidze, O., Tsereteli, N., Kvavadze, N., Varazanashvili, O., 2017. Active inversion tectonics, simple shear folding and back-thrusting at Rioni Basin, Georgia. J. Struct. Geol. 96, 35–53. https://doi.org/10.1016/j.jsg.2017.01.005.

Tibaldi, A., Bonali, F.L., Russo, E., Pasquarè Mariotto, F.A., 2018. Structural development and stress evolution of an arcuate fold-and-thrust system, southwestern Greater Caucasus, Republic of Georgia. J. Asian Earth Sci. 156, 226–245. https://doi.org/10.1016/j.jseaes.2018.01.025.

Tibaldi, A., Tsereteli, N., Varazanashvili, O., Babayev, G., Barth, A., Mumladze, T., Bonali, F.L., Russo, E., Kadirov, F., Yetirmishli, G., Kazimova, S., 2019. Active stress field and fault kinematics of the Greater Caucasus. J. Asian Earth Sci. 104108 https://doi.org/10.1016/j.jseaes.2019.104108.

Tissot, B.P., Pelet, R., Ungerer, P., 1987. Thermal history of sedimentary basins, maturation indices, and kinetics of oil and gas generation. Am. Assoc. Petrol. Geol. Bull. 71, 1445–1466. https://doi.org/10.1306/703c80e7-1707-11d7-8645000102c1865d.

Tozer, R.S.J., Hertle, M., Petersen, H.I., Zinck-Jørgensen, K., 2020. Quantifying vertical movements in fold and thrust belts: subsidence, uplift and erosion in Kurdistan, northern Iraq. In: Hammerstein, J.A., Di Cuia, R., Cottam, M.A., Zamora, G., Butler, R.W. (Eds.), Fold and Thrist Belts: Structural Style, Evolution and Exploration. Geological Society of London, Special Publications, pp. 397–415. https://doi.org/10.1144/SP490-2019-118.

Vasey, D.A., Cowgill, E., Roeske, S.M., Niemi, N.A., Godoladze, T., Skhirtladze, I., Gogoladze, S., 2020. Evolution of the greater Caucasus basement and formation of the main Caucasus thrust, Georgia. Tectonics 39. https://doi.org/10.1029/2019TC005828.

Vincent, S.J., Braham, W., Lavrishchev, V.A., Maynard, J.R., Harland, M., 2016. The formation and inversion of the western greater Caucasus basin and the uplift of the western greater Caucasus: implications for the wider Black Sea region. Tectonics 35, 2948–2962. https://doi.org/10.1002/2016TC004204.

Vincent, S.J., Carter, A., Lavrishchev, V.A., Rice, S.P., Barabadze, T.G., Hovius, N., 2011. The exhumation of the western Greater Caucasus: a thermochronometric study. Geol. Mag. 148, 1–21. https://doi.org/10.1017/S0016756810000257.

Vincent, S.J., Hyden, F., Braham, W., 2013a. Along-strike variations in the composition of sandstones derived from the uplifting western Greater Caucasus: causes and implications for reservoir quality prediction in the Eastern Black Sea. In: Scott, R.A., Smyth, H.R., Morton, A.C., Richardson, N. (Eds.), Sediment Provenance Studies in Hydrocarbon Exploration and Production, vol. 386. Geological Society, London, Special Publications, pp. 111–127. https://doi.org/10.1144/SP386.15.

Vincent, S.J., Morton, A.C., Carter, A., Gibbs, S., Barabadze, T.G., 2007. Oligocene uplift of the western greater Caucasus: an effect of initial arabia-eurasia collision. Terra. Nova 19, 160. https://doi.org/10.1111/j.1365-3121.2007.00731.x.

Vincent, S.J., Morton, A.C., Hyden, F., Fanning, M., 2013b. Insights from petrography, mineralogy and U-Pb zircon geochronology into the provenance and reservoir potential of Cenozoic siliciclastic depositional systems supplying the northern margin of the Eastern Black Sea. Mar. Petrol. Geol. 45, 331–348. https://doi.org/10.1016/j.marpetgeo.2013.04.002.

Vincent, S.J., Somin, M.L., Carter, A., Vezzoli, G., Fox, M., Vautravers, B., 2020. Testing models of cenozoic exhumation in the western greater Caucasus. Tectonics 1–27. https://doi.org/10.1029/2018tc005451.

Warr, L.N., Rice, A.H.N., 1994. Interlaboratory standardization and calibration of day mineral crystallinity and crystallite size data. J. Metamamorphic Geol. 12, 141–152.

Washburn, A.M., Hudson, S.M., Selby, D., Abdullayev, N., Shiyanova, N., 2019. Constraining the timing and depositional conditions of the Maikop Formation within the Kura Basin, Eastern Azerbaijan, through the application of Re-Os geochronology and chemostratigraphy. J. Petrol. Geol. 42, 281–299. https://doi.org/10.1111/jpg.12734.

Wilkins, R.W.T., Boudou, R., Sherwood, N., Xiao, X., 2014. Thermal maturity evaluation from inertinites by Raman spectroscopy: the "RaMM" technique. Int. J. Coal Geol. 128–129, 143–152. https://doi.org/10.1016/j.coal.2014.03.006.

Yılmaz, A., Adamia, S.A., Chabukiani, A., Chkhotua, T., Erdoğan, K., Tuzcu, S., Karabiyikoğlu, M., 2000. Structural correlation of the southern transcaucasus (Georgia)-eastern Pontides (Turkey). In: Bozkurt, E., Winchester, J.A., Piper, J.D.A. (Eds.), Tectonics and Magmatism in Turkey and the Surrounding Area, vol. 173. Geological Society of London, Special Publications, pp. 171–182.

Yılmaz, A., Adamia, S.A., Yılmaz, H., 2014. Comparisons of the suture zones along a geotraverse from the scythian platform to the arabian platform. Geosci. Front. 5, 855–875. https://doi.org/10.1016/j.gsf.2013.10.004.

Zhou, Q., Xiao, X., Pan, L., Tian, H., 2014. The relationship between micro-Raman spectral parameters and reflectance of solid bitumen. Int. J. Coal Geol. 121, 19–25. https://doi.org/10.1016/j.coal.2013.10.013.

Zonenshain, L.P., Kuzmin, M.I., Natapov, L.M., 1990. Geology of the USSR: A Plate Tectonic Synthesis, Geodynamics Series. American Geophysical Union, Washington, DC, United States.

Chapter 4

Manuscript 3:

Tectono-thermal evolution of central Transcaucasia: Thermal modelling, seismic interpretation, and low-temperature thermochronology of the eastern Adjara-Trialeti and western Kura sedimentary basins (Georgia)

Manuscript 3

Tectono-thermal evolution of central Transcaucasia: Thermal modelling, seismic interpretation, and low-temperature thermochronology of the eastern Adjara-Trialeti and western Kura sedimentary basins (Georgia)

Thomas Gusmeo, Andrea Schito, Sveva Corrado, Victor Alania, Onise Enukidze,
Massimiliano Zattin, Paolo Pace, and William Cavazza

Under revision in Journal of Asian Earth Sciences

Tectono-thermal evolution of central Transcaucasia: Thermal modelling, seismic interpretation, and low-temperature thermochronology of the eastern Adjara-Trialeti and western Kura sedimentary basins (Georgia)

Gusmeo Thomas[a], Schito Andrea[b], Corrado Sveva[c], Alania Victor[d], Enukidze Onise[d], Massimiliano Zattin[e], Pace Paolo[f,g], Cavazza William[a]

[a] Department of Biological, Geological and Environmental Sciences, University of Bologna, Bologna, Italy

[b] Department of Geology and Petroleum Geology, School of Geosciences, University of Aberdeen, Aberdeen AB24 3 UE, UK

[c] Department of Sciences, Geological Sciences Section, Roma Tre University, Rome, Italy

[d] M. Nodia Institute of Geophysics, Ivane Javakhishvili Tbilisi State University, Tbilisi, Georgia

[e] Department of Geosciences, University of Padua, Padua, Italy

[f] Department of Engineering and Geology, "G. d'Annunzio" University of Chieti-Pescara, Chieti, Italy

[g] PACE Geoscience, Chieti, Italy

Abstract:

Structural interference along the boundaries of adjacent tectonic domains generates complex subsidence and exhumation patterns. To focus this topic, in this paper we study a key segment of the convergence zone between the interfering south-verging Greater Caucasus and north-verging Lesser Caucasus. The study area comprises the along-strike transition between the Paleogene Adjara-Trialeti back-arc basin and the Oligocene-Neogene Kura foreland basin of eastern Georgia. During the Neogene, despite their difference in age and subsidence mechanisms, both basins have been progressively inverted to various extent within the overall context of the Arabia-Eurasia continental collision. Thermal modelling of borehole data from the Adjara-Trialeti basin allowed to reconstruct two phases of rapid subsidence, late Paleocene-Early Eocene and Middle-Late Eocene, respectively correlated to flexural loading by the Lesser Caucasus retrowedge and continental rifting. Integration of thermal modelling, apatite fission-track statistical inverse modelling, and seismic interpretation detected a third subsidence phase in the Early Miocene, possibly related to strike-slip tectonics. Thermal maturity data dictate that 1.0-1.3 km of the Adjara-Trialeti sedimentary succession has been eroded since the onset of structural inversion in the mid-Miocene. The burial history of the western Kura Basin outlines intermittent and asymmetrical episodes of flexural subsidence from the Oligocene to the Late Miocene, due to competing loading by the Lesser Caucasus, the Adjara-Trialeti fold-and-thrust belt and the Greater Caucasus. Finally, during latest Miocene times southward propagation of deformation from the Greater Caucasus induced an additional tectonic loading (1.3-1.8 km) due to the emplacement of thin-skinned thrust sheets, mostly eroded during the Plio-Quaternary.

Keywords: *Transcaucasus, Kura Basin, thermal maturity, thermal modelling, fission-track thermochronology, structural interference*

1. Introduction

Tectonic and thermal reconstruction of sedimentary basins evolution during subsidence and structural inversion traditionally refers to clear-cut end-members and ideal models characterised by relatively simple evolutionary patterns, or identify discrete and uniform domains that are then studied more or less independently. Such simplifications can hardly be applied to the boundary zones between adjacent structural domains, where interfering tectonic and subsidence motifs produce complicated temporal-spatial patterns. This is exemplified by the structurally complex Transcaucasian region of central Georgia, an area dominated by the contrasting and partially superposed effects of extension- and compression-driven subsidence, as well as by the structural interference between two oppositely-verging orogenic belts.

The southern Caucasian region is constituted by the Greater and Lesser Caucasus and the intervening Rioni-Kura foreland basins (Fig. 1). This area absorbs a considerable amount (about 15-20%) of the strain associated with the Arabia-Eurasia collision (Reilinger et al., 2006), as testified by GPS vectors indicating an anticlockwise motion relative to stable Eurasia, with northward motion increasing from about 2 mm/yr in the Rioni Basin close to the Black Sea coast to 12 mm/yr in the Kura Basin close to the Caspian Sea coast (Forte et al., 2013; Reilinger et al., 2006). Most deformation in the Caucasian region is accommodated in the domain comprised between the Greater and the Lesser Caucasus (named Transcaucasus; Karakhanyan et al., 2013; Sokhadze et al., 2018).

Transcaucasia (i.e. the region south of the Greater Caucasus) connects the world-class Caspian Basin petroleum province to the east and the underexplored easternmost Black Sea basin to the west, where active hydrocarbon seeps on the seafloor (e.g. Pape et al., 2021) and oil shows in deep-water wells indicate the presence of at least one active petroleum system in the offshore of easternmost Turkey (see Tari et al., 2018, for a review). The oceanographic connection between the Caspian and Black seas closed in the early Late Miocene due to convergence of the facing structural fronts of the south-verging Greater Caucasus and north-verging Lesser Caucasus orogenic prisms (Nemčok et al., 2013). Such a convergence is considered a far-field effect of the collision between the Eurasian and Arabian plates along the

Bitlis-Zagros suture zone, several hundred kilometres to the south (Alavi, 1994; Cavazza et al., 2018; Dewey et al., 1986; Jolivet & Faccenna, 2000; Okay et al., 2010). This deformation has affected a large swath of the Eurasian hinterland, inducing reactivation of older structures (including structural inversion of pre-existing sedimentary basins) and diffuse strike-slip deformation (Albino et al., 2014; Cavazza et al., 2019).

The aim of this work is to provide quantitative constraints on the burial/exhumation history of the eastern portion of the Georgian Transcaucasus, a tectonically complex area featuring the structural interference between two tectonic domains characterised by different pre-deformation history, deformation timing, exhumation degree, and structural styles. These units are: (i) the E-W-trending Adjara-Trialeti fold-and-thrust belt (FTB), a former rift basin now in the retro-wedge of the Lesser Caucasus, and (ii) the western Kura flexural foreland basin, characterised by distinct subsidence pulses and then deformed by the southward advancing Greater Caucasus frontal structures (Figs. 1 and 2). The geological complexity of the along-strike transition from the Adjara-Trialeti to the Kura inverted basins (Fig. 2) has favoured multiple, often contrasting interpretations regarding the structural layout and the tectonic evolution of the eastern termination of the Adjara-Trialeti FTB, where it plunges eastwards and is covered by south-verging thrusts deforming the Kura Basin (Alania et al., 2021a; Gusmeo et al., 2021; Pupp et al., 2018; Tari et al., 2021).

The study area is ideal to investigate the initial phases of collision between two converging orogenic belts: the south-verging Greater Caucasus and the mostly north-verging Adjara-Trialeti FTB (Alania et al., 2021a; Banks et al., 1997; Gusmeo et al., 2021; Nemčok et al., 2013). Tectonic convergence determined progressive exhumation of the intervening Kura Basin sedimentary fill. In this context, the retro-wedge of the Lesser Caucasus may also have played an important role (Alania et al., 2021a; Gusmeo et al., 2021).

During the last few decades, a growing academic and industrial interest has provided structural data and burial models on the western Kura basin (Adamia et al., 1992; Boote et al., 2018; Nemčok et al., 2013; Patton, 1993; Pupp et al., 2018; Robinson et al., 1997; Sachsenhofer et al., 2018, 2021). Recent thermochronologic work has determined the structural inversion of the Adjara-Trialeti FTB as mid-Miocene (Gusmeo et al., 2021). Corrado et al. (2021) obtained thermal maturity data on sedimentary successions across the southern Greater Caucasus - Kura - Adjara-Trialeti system. Building on such datasets, in this paper we integrate new multidisciplinary data in the transitional area between the eastern Adjara-Trialeti inverted rift basin and the thin-skinned western Kura Basin in order to provide quantitative constraints on the burial/exhumation history of the eastern Georgian Transcaucasus. The dataset includes (i) low-temperature thermochronologic inverse models, (ii) thermal models of well data, and (iii) a composite geological cross-section of the transition zone built upon the interpretation of three unpublished seismic reflection profiles.

2. Geological background

The study area covers the region where the north-verging Adjara-Trialeti fold-and-thrust belt (FTB) plunges eastward and is covered by the deformed sedimentary rocks of the western Kura Basin (eastern Georgia). Several wells were drilled for hydrocarbon exploration (Patton, 1993; Sachsenhofer et al., 2021) and six of them are analysed in this work, three in the Adjara-Trialeti FTB and three in the Kura Basin (Figs. 1 and 2).

The Adjara-Trialeti FTB (Figs. 1 and 2) is a W-E-trending orogenic belt formed as a result of the structural inversion of a former back-arc rift basin developed on the upper (Eurasian) plate of the northern Neotethys subduction zone (Adamia et al., 1981, 2011; Alania et al., 2018;

Banks et al., 1997; Barrier et al., 2018; Gusmeo et al., 2021; Lordkipanidze et al., 1989; Nemčok et al., 2013). The pre-rift sedimentary succession features Aptian-Cenomanian volcanic and volcaniclastic rocks, covered by Turonian-to-Early Paleocene limestones and marls (Adamia et al., 1981, 2011; Banks et al., 1997; Yılmaz et al., 2000, 2014). Extension started in the Paleocene, together with the deposition of a thick succession of terrigenous turbidites (the Paleocene-Eocene Borjomi Flysch). The main phase of rifting occurred in the Middle Eocene, characterized by the emplacement of submarine volcanic rocks and shallow mafic-to-intermediate intrusions (Adamia et al., 2011; Banks et al., 1997; Okrostsvaridze et al., 2018; Yılmaz et al., 2000, 2014). In the Late Eocene, mostly epiclastic turbidites with minor marls were deposited in the eastern sector of the Adjara-Trialeti basin. In Oligocene-Early Miocene times shales, siltstones and fine-grained sandstones were deposited in a mainly anoxic/disoxic environment (Pupp et al., 2018; Sachsenhofer et al., 2018, 2021), interbedded with fine-grained terrigenous turbidites. The post-rift phase lasted from the Oligocene to the Early Miocene and was followed by structural inversion since Middle Miocene times (Gusmeo et al., 2021). Despite having an independent origin, the Adjara-Trialeti FTB was then incorporated in the retrowedge of the Lesser Caucasus (Alania et al., 2021a).

The domain comprised between the Greater Caucasus and the Lesser Caucasus (Transcaucasia) is constituted by an intermontane depression extending from the Black Sea to the Caspian Sea (Fig. 1). The depression is divided by the Dzirula Massif, a polymetamorphic basement salient which separates the Kura and Rioni flexural foreland basins (Adamia et al., 2010, 2011; Alania et al., 2017; Banks et al., 1997; Nemčok et al., 2013; Rolland et al., 2011). The two basins plunge to the east and west, respectively, and developed as a flexural response to both the Greater Caucasus to the north and the Lesser Caucasus to the south, being filled by Oligocene-to-Recent sediments (Adamia et al., 2010; Banks et al., 1997; Nemčok et al., 2013).

In the Kura Basin (Figs. 1 and 2) Oligocene-Lower Miocene clastic (shales, siltstones and fine-grained sandstones) and evaporitic rocks deposited in the anoxic-dysoxic environment of the Paratethys, and are locally known as the Maikop series (Pupp et al., 2018; Sachsenhofer et al., 2018). Their thickness can reach up to 2.5-3.5 km in the Georgian sector of the Kura Basin (Adamia et al., 2010).

During Middle to early Late Miocene times (Chokrakian-Sarmatian) further 1.5-2.2 km of shales and fine-grained siliciclastics (sandstones), intercalated in the uppermost sections with mainly calcareous units (mudstones, marls and oolitic limestones and locally with coarse-grained rocks), were deposited within the Kura Basin (Adamia et al., 2010; Alania et al., 2017). Since the Late Sarmatian (Tortonian) ongoing convergence between the Greater and Lesser Caucasus forced the final uplift of the Dzirula Massif and the Kura Basin started plunging towards the Caspian Sea, as demonstrated by the progressive marine regression within the basin from west to east (Adamia et al., 2010; Alania et al., 2017; Barrier et al., 2018; Nemčok et al., 2013; Shatilova et al., 2020). At the same time, within the Kura Basin began the widespread deposition of coarse-grained clastic deposits, eroded from the adjacent orogenic belts.

Continental conditions prevailed from the Late Sarmatian to the present, interrupted only in the Akchagylian-Apsheronian (Late Pliocene-Early Pleistocene) by a short-lived shallow marine transgression, probably in response to the rapid growth and advancement of the Greater Caucasus and the ensuing subsidence in the foreland area (Adamia et al., 2010; Avdeev and Niemi, 2011; Nemčok et al., 2013; Sukhishvili et al., 2020; Trikhunkov et al., 2021).

Continuous convergence between the Greater and Lesser Caucasus caused incremental deformation of the Kura foreland basin. Thick-skinned deformation occurred in the Sarmatian followed by thin-skinned deformation from the Late Sarmatian-Meotian onward (Nemčok et al., 2013). In the final stages of convergence, the Greater Caucasus deformation propagated into the northern Kura Basin forming the Kura south-vergent thin-skinned foreland FTB

(Kakheti ridge, Fig. 2), developed since the Middle Miocene, with peak deformation in the Late Miocene-Pliocene (Alania et al., 2017). A Late Pliocene-Pleistocene acceleration of uplift has also been pointed out in this belt (Sukhishvili et al., 2020), probably linked with coeval enhanced uplift in the Greater Caucasus and subsequent propagation of deformation. The Kakheti ridge and the Adjara-Trialeti structures interfere in the Tbilisi area, creating an outstanding example of incipient collision between two facing orogenic belts (Alania et al., 2021a) (Figs. 1 and 2).

The study area is tectonically active. GPS vectors in the eastern Adjara-Trialeti FTB are N/NNE-oriented and indicate velocities in the order of 4-6 mm/yr, decreasing to the north in the Kura Basin to 2-4 mm/yr (Reilinger et al., 2006; Sokhadze et al., 2018). Historical earthquakes in the study area are of moderate intensity, with the last major event recorded in 2002 in the surroundings of Tbilisi (Fig. 2) yielding a magnitude of 4.5 (Tibaldi et al., 2019). Present-day heat flow is ca. 50 mW/m^2 in the eastern Adjara-Trialeti FTB and ca. 40-45 mW/m^2 in the western Kura Basin (Melikadze et al., 2015; Sangin et al., 2018; Yükler et al., 2000), and crustal thickness ranges between ~ 45 and 50 km in the area of study (Adamia et al., 2017; Motavalli-Anbaran et al., 2016).

2.1 Wells stratigraphy

The six wells analysed in this study are, from south to north, Kumisi 1, Kumisi 2 and Patardzeuli-E1 in the eastern Adjara-Trialeti FTB, and Satskhenisi 102, Satskhenisi 101 and Norio 200 in the western Kura Basin (Figs. 2 and 3).

Wells drilled in the eastern Adjara-Trialeti FTB are generally deeper (ca. 1.8 to 5 km) than the ones in western Kura Basin (ca. 1 km) and the thickest sedimentary succession (5020 m) was drilled in the Patardzeuli-E1 well (Korelskiy et al., 2019).

In the Adjara-Trialeti FTB, the oldest rocks were drilled in the Kumisi 1 well and are Late Cretaceous volcanics and volcaniclastics followed by limestones and marls (Fig. 3). The Paleocene section has similar thickness (ca. 250 m) in both Patardzeuli-E1 and Kumisi 1 wells, but in Patardzeuli-E1 it is entirely made of limestones, whereas in Kumisi 1 it is composed of marls at the base, followed by shales and siltstones. The Early Eocene section is thicker in Patardzeuli-E1 (ca. 1800 m) than in Kumisi 1 (ca. 730 m). In Patardzeuli-E1 the lower portion of the Early Eocene section is mostly characterised by limestones and marls, passing to mostly fine-grained siliciclastic rocks in the upper part; in Kumisi 1 it is made of alternating sandstones and shales (flysch facies). The Middle Eocene is found in all three wells drilled in the eastern Adjara-Trialeti FTB, and it is thicker in Patardzeuli-E1 (ca. 700 m) than in Kumisi 1 and 2 (ca. 250 m). It is mainly composed of tuffs and other volcaniclastic rocks, sporadically interbedded with sandstones and shales (Fig. 3). The thickness (700-900 m) and composition of the Late Eocene section are similar in all three wells. The lower portion (ca. 230 m) in Kumisi 1 is entirely made of shales and siltstones, whereas the upper part (Tbilisi Suite) is composed of alternating shales, sandstones, and siltstones with marls interlayers. In Patardzeuli-E1 and Kumisi 2 the Late Eocene is lithologically similar to the Tbilisi Suite of Kumisi 1 (Fig. 3).

The Maikop Series is the only succession found in all six wells and it is composed by shales, siltstones, and fine-grained sandstones. The thickness of the succession ranges from ca. 550 m (Kumisi 1) to >1200 m (Satskhenisi 102). The Maikop Series is probably incomplete in all wells except for Norio 200. In Satskhenisi 101 and 102 wells the lower part of the succession (representing the Lower Maikop, hence the Lower Oligocene section) is missing, whereas in

Kumisi 1, Kumisi 2 and Patardzeuli-E1 at least part of the uppermost section was eroded away, as demonstrated by unconformable surfaces detected during drilling.

Middle Miocene rocks (Chokrakian, Karaganian and Konkian) are found almost exclusively in the Norio 200 well, where they are entirely made of shales and siltstones. The same well is topped by Sarmatian (late Middle-early Late Miocene) shales and siltstones, with frequent alternations of sandstones and conglomerates in the uppermost portion. Chokrakian shales are found also in the Satskhenisi 101well (Fig. 3).

Finally, Akchagylian-Quaternary conglomerates are present in the Patardzeuli-E1 well, whereas very thin Quaternary deposits constitute the top of the Kumisi 1 well (Fig. 3).

3. Materials and methods

3.1 Apatite fission-track analysis and modelling

Fission tracks are linear radiation damages within the crystal lattice, caused by the nuclear fission of radioactive isotope ^{238}U, which can be etched and counted with an optical microscope (Donelick et al., 2005). Concurrently, neutron irradiation is used to induce the decay of ^{235}U, generating radiation damages on the surface of an external detector. Grain-by-grain determination of both spontaneous and induced fission-track densities yields a single-grain age representing the cooling of the grain below a closure temperature of ~100°C. Apatite grains are concentrated through crushing and sieving, followed by hydrodynamic, magnetic, and heavy-liquids separation. Then apatites are embedded in epoxy resin, polished, and etched in 5N HNO_3 at 20°C for 20s. The external detector method was applied: following irradiation at the Radiation Center of Oregon State University (Donelick et al., 2005) and etching of the mica detector in 40% HF at 20°C for 45 min, spontaneous and induced fission tracks were counted under a Zeiss Axioscope optical microscope at x1250 magnification. Central ages (Fig. 2, Table 1) were obtained using the Radial Plotter software (Vermeesch, 2009).

Fission tracks in apatites have the same initial length of about 16 μm (Donelick et al., 1999; Ketcham et al., 1999) but at about 60°C they start to anneal at a rate that is proportional to temperature. Over geological time periods, partial annealing of fission tracks occurs at temperatures between about 60 and 120°C (the Partial Annealing Zone or PAZ; Gleadow & Duddy, 1981). Since track shortening is a function of the intensity and duration of heating, the measurement of fission-track lengths and the numerical modelling of their frequency distribution give quantitative information on the thermal evolution in the PAZ temperature range. Modelling procedures find a range of cooling paths compatible with the fission-track length frequency distribution (Ketcham, 2005).

In this work, we provide additional constraints on the thermal history of two samples (TU504 and TU505) already included in the dataset of Gusmeo et al. (2021). These two samples were selected because of their peculiar positions within the study area. Since only their central ages were available, further mounts of apatite grains for each sample were produced, etched and analysed under a Zeiss Axioscope optical microscope in order to measure enough horizontally confined tracks for statistical inverse modelling. Inverse modelling of track length data was performed using the HeFTy program (Ketcham, 2005), which generates a number of possible T-t paths by running a Monte Carlo algorithm using fission-track lengths and ages as input data. Predicted AFT data were calculated according to the Ketcham et al. (2007) annealing model for fission tracks revealed by etching. Dpar values (i.e. the etch pit length) were used to define the annealing kinetics. Broad T-t boxes were used for the pre- and post-depositional history of the analysed samples in order to limit any user-dependent forcing on the program. Details on parameters and constraints used for both models, compiled following the protocol of Flowers et al. (2015), can be found in the Supplementary Materials (Tables ST6 and ST7).

3.2 Thermal Modelling

3.2.1 Calibration data from Rock-Eval Pyrolysis and optical analyses

Thermal model calibration is generally based on the assumption that thermal maturity at different depths of a stratigraphic section allows to fit a maturity curve, giving an insight on the maximum thermal exposure and heating regimes experienced by the sediments during burial. For this purpose, $VR_o\%$ data are generally used, given their high sensitivity to thermal perturbations. However, when such data are absent they can be replaced by other thermal maturity indicators (e.g. Tmax, biomarkers, illite % in illite-smectite mixed layers, Raman and FTIR parameters) properly converted into $VR_o\%$ (see Corrado et al., 2020; Schito et al., 2016).

Calibration data for thermal models were provided by the Georgian Oil & Gas Company. They were obtained from five wells drilled for hydrocarbon exploration in the western portion of the Kura Basin and in the eastern Adjara-Trialeti FTB (Fig. 2, Table 2). From south to north the wells are: Kumisi 1, Kumisi 2, Patardzeuli-E1, Satskhenisi 102, Norio 200. Calibration data were acquired in different laboratories and are described in industrial reports and published papers: Stratochem Egypt (2014) for Kumisi 1 well; Sachsenhofer et al. (2021) for Kumisi 2, Patardzeuli-E1 and Norio 200 wells; DIG (2014) for Satskhenisi 102 well. Part of the dataset (relative only to the Maikop sections) was also reported by Corrado et al. (2021).

Most of the thermal maturity data derive from Rock-Eval Pyrolysis, except for the Satskhenisi 102 well where additional vitrinite reflectance measurements are available (Table

2). In detail, more than two hundred Rock-Eval Pyrolysis data and ten vitrinite reflectance measurements are available, acquired from cuttings representative of the Eocene-Early Miocene interval (Table 2, Suppl. Mat. Tables ST1, ST2, ST3, ST4, ST5). The Satskhenisi 101 well was not modelled as no thermal maturity data were available.

Rock-Eval Pyrolysis is the most used quantitative method for kerogen characterization. It is based on the relative intensity and distribution of three peaks (S1, S2 and S3), artificially generated at different lab temperatures from a whole rock specimen containing kerogen. The S2 peak relates to the hydrocarbon residual potential of a source rock, whereas S1 records the amount of already generated hydrocarbons. Tmax is calculated from the temperature corresponding to the maximum of the S2 envelope (e.g. Behar et al., 2001) and can be used as a thermal maturity indicator, at least when Total Organic Carbon (TOC) is higher than 0.5% (Hunt, 1996). The TOC refers to the weight percentage (wt %) of the organic carbon present in the rock (e.g. Langford and Blanc-Velleron, 1990). The Hydrogen Index (HI) is defined as the ratio between the area of the S2 peak and the TOC. The most used diagram for kerogen classification is the modified Van Krevelen's one, which is based on the Hydrogen Index (HI) and the Oxygen Index (OI) (Abdullah et al., 2017; Tissot and Welte, 1978).

Pseudo-Van Krevelen diagrams (OI vs HI, Tmax vs HI, and TOC vs S2) were used to assess the type of kerogen for each data (Fig. 4; Suppl. Mat. Figs. S1, S2, S3, S4, S5).

Vitrinite reflectance (VR_o%) measures the reflectivity under incident light of huminite-vitrinite group macerals that derive from upper plants (Type III kerogen). VR_o% is known to be well correlated with the stages of hydrocarbon generation and is by far the most known and used thermal maturity indicator (Bertrand et al., 2010; Borrego and Cook, 2017; Corrado et al., 2020; Dow, 1977).

3.2.2 Modelling procedures

Five wells have been modelled matching Tmax and $VR_o\%$ data with calculated maturity curves at different depths using the Basin Mod 2-D software package. For models' calibration Tmax data were first converted into $VR_o\%$ values. No single equation exists for such conversion, since it depends on kerogen type. According to the most recent review (Yang and Horsfield, 2020) and considering a prevalent type III (or II/III) kerogen (Fig. 4), the onset of the oil window ($VR_o\% = 0.55$) can be set at a Tmax value of 430 °C, whereas the immature stage at a Tmax value of 420 °C roughly coincides with a $VR_o\%$ value of 0.4 and the onset of the wet gas stage ($VR_o\% = 1.3$) is set at a Tmax value of 460 °C. These values are then correlated by a least squared curve.

Tmax data can have a large spread, as outlined in the dataset presented in this study. The causes of such spread are multiple and cannot be resolved with the available data. In general, data indicating higher maturity (with respect to the mean maturity trend) can be ascribed to the presence of reworked organic matter, whereas relatively low values can be due to carryover effects (i.e. presence of heavy hydrocarbons) or to high H or S content (Yang and Horsfield, 2020). Given the higher uncertainties (with respect to $VR_o\%$) derived from the use of Tmax data for thermal models calibration, different scenarios have been tested and framed according to the geological evolution of the two studied areas: the eastern Adjara-Trialeti FTB and the western Kura Basin (Figs. 5 and 6; see below and Discussion).

Mixed lithologies were reproduced from the relative abundance of sandstones, limestones and shales as shown in Table 3 and rock decompaction follows Sclater and Christie (1980). Seawater depth variations were not taken into account given that the long-term thermal evolution of a sedimentary basin is mainly affected by sediment thickness rather than by water depth (Butler, 1991). A surface temperature of 12°C and a sediment-water interface temperature of 5°C were adopted, and vitrinite reflectance maturation through time was modelled according to the Easy %Ro method (Burnham and Sweeney, 1989; Sweeney and Burnham, 1990).

Present day heat flow HF data for the Adjara-Trialeti FTB derive from Melikadze et al. (2010), Sangin et al. (2018) and Yükler et al. (2000), who indicate a value of ~ 50 mW/m^2 in the eastern Adjara-Trialeti FTB, whereas for the Kura Basin they derive from Kutas (2010), who indicate values between 40 and 45 mW/m^2 in the studied sector of the western Kura Basin. Since direct constraints on the HF evolution through time in the two geologic domains analysed are not available, two scenarios were assumed and tested in the two domains to allow a systematic comparison. In the first scenario, the HF was set at the present day value of 50 mW/m^2 in the Adjara-Trialeti FTB and 45 mW/m^2 in the Kura Basin (Kutas, 2010; Melikadze et al., 2015; Sangin et al., 2018; Yükler et al., 2000) and kept constant through time. In the second scenario, a HF peak of around 70 mW/m^2 was assumed at about 45 Ma (i.e. during the main phase of Adjara-Trialeti rifting, see Section 2), followed by a gradual decrease in HF up to the present-day value according to the McKenzie model (McKenzie, 1978).

In all the studied wells an additional overburden was required in order to fit thermal maturity data. A sensitivity analysis was then performed, showing (for each HF scenario and each well) different maturity curves assuming different amounts of additional burial (Figs. 5 and 6). See Section 4.2.2 for further discussion on this topic and the results of the sensitivity analyses.

3.3 Seismic interpretation

Three broadly N-S trending depth-migrated seismic reflection profiles (from north to south, lines 3004, 13 and 1401; Figs. 2 and 7) were obtained from the Georgian Oil & Gas Company.

Lines 3004 and 13 cross the frontal part of the eastern Adjara-Trialeti FTB and the southernmost Kura Basin, passing through the location of the Norio 200 well; Line 1401 crosses the south-eastern Adjara-Trialeti FTB, passing through the location of the Kumisi 1 well and close to the Kumisi 2 well (Fig. 2).

Seismic interpretation is constrained by surface geology, exploration wells and the application of fault-related folding models (Butler et al., 2018; Shaw et al., 2006). Line 1401 was interpreted alone, whereas lines 13 and 3004 were combined and interpreted together (Fig. 7). Linking together the three interpreted seismic profiles a geological cross-section was then built, showing the structural relationships between the eastern Adjara-Trialeti FTB and western Kura Basin tectonic domains (Fig. 7).

4. Results

4.1 Apatite fission-track analysis and modelling

Analytical results of apatite fission-track analysis are reported in Table 1. The χ^2 statistical test (Galbraith, 1981) indicates that a single population of grains is present in the analysed samples. AFT central ages provide meaningful information from a geological viewpoint if the sample experienced fast cooling through the PAZ but can be misleading if the sample resided within the PAZ for a long time or experienced moderate reheating at temperatures lower than 120°C (Gleadow et al., 1986). To avoid such potential issues, more complete thermochronological constraints were obtained through statistical modelling of fission-track length distributions.

Sample TU504 is a sandstone collected north of the town of Rustavi in the eastern Adjara-Trialeti FTB (Fig. 2). Its depositional age, in the local Paratethyan stratigraphy, is Sakaraulian (USSR Geological Survey, 1971), which corresponds to the base of the Burdigalian (Adamia et al., 2010): hence an age of 20-18 Ma was assigned to this sample. Sample TU504 yielded an AFT central age of 36.3 ± 2.8 Ma (Fig. 2, Table 1), older than its stratigraphic age, which indicates that this sample was not buried enough to completely reset the AFT system. The very high $P(\chi^2)$ value of 99.98% (Table 1) and the absence of dispersion (0%) (Fig. 8) indicates the presence of only one population of grains. Partially to non-reset detrital samples containing a single population of grains may suggest that they were fed by one thermally coherent sediment source-area. The mean confined tracks length, on a total number of 83 horizontally confined tracks, is 13.34 ± 0.17 μm (Table 1) and the track-length frequency distribution is bimodal, with two peaks centred at ~12 and 15 μm (Fig. 8). Inverse modelling, integrating fission-track data and stratigraphic age (Fig. 8, Table ST6), shows a phase of heating due to sedimentary burial after deposition (20-15 Ma), followed by rapid cooling since 15 Ma. Although with the available data we cannot be certain that the apatite grains derived from a thermally coherent source, since a number of assumptions have to be verified (see a comprehensive review in Malusà and Fitzgerald, 2020), the very high $P(\chi^2)$ value, the absence of dispersion and other independent geologic evidence (see Sections 2 and 5.2) allow us to be reasonably confident regarding the inverse modelling results which suggest an Early Eocene cooling (best-fit curve; Fig. 8) in the original sediment source area.

Sample TU505 is a middle-late Oligocene (30-23 Ma) (USSR Geological Survey, 1971) sandstone (Fig. 2), collected ~15 km north of sample TU504, yielding an apatite fission-track central age of 39.6 ± 3.6 Ma (Fig. 2, Table 1) which is older that its stratigraphic age, indicating that burial was not enough to completely reset the AFT system. The very high $P(\chi^2)$ value of 97.99% (Table 1) and the absence of dispersion (0%) (Fig. 9) confirm that this sample contains only one population of grains, thus suggesting a thermally coherent source. The mean confined tracks length, based on 67 horizontally confined tracks, is 13.41 ± 0.18 μm (Table 1) and the track-length frequency distribution is bimodal, with two peaks centred at ~12 and 15 μm (Fig. 9). TU505 modelling results are broadly in agreement with the ones of sample TU504. Inverse modelling, integrating fission-track data and stratigraphic age, (Fig. 9, Table ST7) shows fast burial/heating from about 28-25 to 20-19 Ma, followed by relatively rapid cooling since 20-19 Ma. Under the same assumptions explained for sample TU505 (Malusà and Fitzgerald, 2020), the very high P(χ^2) value and other independent geologic evidence (see Section 5.2) allow us to be reasonably confident about the best-fit t-T path in the statistical inverse modelling results suggesting late Paleocene-Early Eocene rapid cooling in the original source of detritus (Fig. 9).

4.2 Thermal modelling

4.2.1 Calibration data

Maturity data used for modelling calibration consist in Tmax and VR_o% (only for Satskhenisi 102 well) data which were provided by the Georgian Oil & Gas Company. Only Tmax data from samples with TOC >0.5% were used as input data for modelling calibration.

Analytical details of calibration data are summarised in Table 2, where the minimum, maximum and average values of each parameter are reported, whereas the complete list of single analytical data is enclosed in the Supplementary Materials (Tables ST1, ST2, ST3, ST4 and ST5). Further details are reported in Corrado et al. (2021), DIG (2014), Sachsenhofer et al. (2021) and Stratochem Egypt (2014).

4.2.2 Thermal models calibration

In this study, Tmax data are able to depict a maturity trend in three out of five wells (i.e. Kumisi 1, Patardzeuli-E1 and Satskhenisi 102), whereas in Kumisi 2 and Norio 200 wells they only provide information on the thermal maturity along restricted stratigraphic sections (Late Eocene and Early Oligocene, respectively; Figs. 5 and 6; Table 2).

In the three wells (Kumisi 1, Kumisi 2 and Patardzeuli-E1) from the eastern Adjara-Trialeti FTB, two main constraints derive from Tmax data: the top of the Maikop section shows values generally lower than the onset of the oil window (i.e. below 430 °C), whereas the bottom of the Late Eocene section is close to the peak of oil generation (around 440 °C). The Late Eocene section yields a higher degree of uncertainty, due to the high data spread in Patardzeuli-E1 well and to the few data available in the Kumisi 1 well, although a better constrain on the maturity level is given for this section by the clear cluster at the bottom of the Late Eocene section in the Kumisi 2 well. To fit such maturity trends, depending on the assumed HF scenario (see Section 3.2.2), different amounts of additional burial were required (Fig. 5). In the constant HF scenario, maturity data are best fitted with 2000m of additional burial in the Kumisi 1 well and 1500m of additional burial in the Kumisi 2 and Patardzeuli-E1 wells (Fig. 5a, c, e). On the other hand, in the rifting HF model (the scenario with a HF peak around 45 Ma) the additional burial required to fit thermal maturity data is of 1300m and 1000m, respectively (Fig. 5b, d, f).

Figure 10 shows the results of thermal modelling for the wells in the eastern Adjara-Trialeti FTB (Kumisi 1, Kumisi 2 and Patardzeuli-E1), produced assuming the HF model with a peak around 45 Ma (Fig. 10d), that is the most realistic one taking into account the geological evolution of the Adjara-Trialeti back-arc rift basin (Adamia et al., 1981, 2011; Banks et al., 1997). See Section 5.1.1 for further discussion on the thermal modelling results.

In the two wells (Norio 200 and Satskhenisi 102) from the western Kura Basin a high spread characterises the Tmax data distribution. Nonetheless, a Tmax trend can be recognised along the Maikopian section in the Satskhenisi 102 well; in this well, thermal maturity can be further constrained by means of ten VR_o% data (Fig. 6c, d). Combining Tmax and VR_o% data in the Satskhenisi 102 well, thermal maturity ranges between about 0.4 (at the top of the Maikop section) to about 0.6 (at the bottom of the Maikop section) of equivalent VR_o%. Such trend can be fitted with an additional burial comprised between 800 and 2000 m assuming a constant HF similar to the present-day value, and between 0 and 1300 m assuming the HF model with a peak at around 45 Ma (Fig. 6c and d, respectively). The additional burial considered do not comprise 500m of shales that we assume were deposited during the Sarmatian since they are present in the nearby Norio 200 well (Fig. 3; Table 3). For what concerns the Norio 200 well, the additional burial required to fit thermal maturity data varies between 1000 and 2500 m assuming a constant HF, and between 800 and 2000 m assuming the rifting model with a peak at ~ 45 Ma (Fig. 6a, c).

Figure 11 shows the results of thermal modelling for the wells in the western Kura Basin (Norio 200 and Satskhenisi 102), produced assuming a constant HF of 45 mW/m^2 (Fig. 11c), which is the more realistic scenario given the flexural nature of the Kura foreland basin (Adamia et al., 2010; Nemčok et al., 2013; Patton, 1993). See Section 5.1.2 for further discussion on the thermal modelling results.

4.3 Structural cross-section

The geological cross-section shown in Figure 7 was created linking together three interpreted depth-migrated seismic reflection profiles (lines 1401, 13 and 3004) provided by the Georgian Oil & Gas Company. The cross-section, oriented NE-SW, covers the eastern Adjara-Trialeti FTB and the southernmost western Kura Basin, and depicts the overall structural layout of the study area.

The Adjara-Trialeti FTB is characterised at depth by mostly north-verging and subordinately south-verging duplex systems made of Cretaceous-Paleogene rocks, which accommodate considerable shortening (Fig. 7). The Teleti and Varketili anticlines, separated by a broad syncline, are fault-propagation folds developed upon south- and north-directed thrusts, respectively, involving the Cretaceous-to-Eocene sequence. Structural interpretation at shallow crustal levels (0-4 km) is consistent with those shown in other published cross-sections and interpreted seismic lines in the study area (cf. Alania et al., 2021a). As seismic resolution decreases at deeper levels, different models can be applied to reconstruct the structural style. For example, Alania et al. (2021a, 2021b) propose an interpretation implying a higher degree of shortening than Tari et al. (2021).

The overall geometry of the Adjara-Trialeti FTB can be interpreted as the result of the structural inversion of the former extensional faults of the Adjara-Trialeti back-arc rift. The complex fault pattern at depth was formed during the progressive northward progradation of the retro-wedge of the Lesser Caucasus (Alania et al., 2021a; Gusmeo et al., 2021). The Ormoiani syncline is mainly made of Maikopian (Oligocene-Early Miocene) rocks, topped by thin Middle and Upper Miocene rocks.

Since Maikopian rocks are involved in the deformation (Fig. 7), the cross-section indicates that inception of deformation postdates the Early Miocene, a timing in agreement with the Middle Miocene inception of inversion of the Adjara-Trialeti FTB, based on seismic interpretation (Pace et al., 2019) and low-temperature thermochronology results (Gusmeo et al., 2021; this study).

The northern segment of the section shows a series of shallow, thin-skinned south-verging thrusts involving Miocene rocks, which overlie the frontal part of the Adjara-Trialeti FTB (Fig. 7). In this sector, a triangle zone is formed by the interference between the north-verging structures related to the Adjara-Trialeti FTB and the south-directed thrusts deforming the Kura Basin. Further to the west, published seismic lines show a very similar structure in the triangle zone (Alania et al., 2018, 2020, 2021a; Pace et al., 2019; Tari et al., 2021), but there the south-verging thrusts deforming the Kura Basin do not overthrust yet the Adjara-Trialeti FTB (Fig. 12). Since Upper Miocene rocks are clearly involved in the south-verging thrusts, the onset of thin-skinned deformation is not older than Late Miocene (Fig. 7).

5. **Discussion**

5.1 Thermal and burial histories

The integration of organic thermal indicators, thermochronology and structural data is key in basin analysis and has been successfully applied in a number of studies focused on the burial and erosion history of sedimentary successions (Balestra et al., 2019; Corrado et al., 2020; Di Paolo et al., 2012; Schito et al., 2018) and/or on the deformation style within an orogenic wedge (Andreucci et al., 2014; Caricchi et al., 2015; Corrado et al., 2021; Curzi et al., 2020; Di Paolo et al., 2012).

The overall evolution of the Adjara-Trialeti FTB and the western Kura Basin has involved different subsidence mechanisms (rifting vs. lithospheric flexure) and complex patterns of structural interference between the facing Greater Caucasus and Adjara-Trialeti fold-and-thrust belt, to the point that only an integrated approach can unravel with sufficient detail the timing and magnitude of maximum burial and exhumation, as well as the paleo-heat flows during basin evolution.

5.1.1 Adjara-Trialeti FTB

In the Adjara-Trialeti FTB low-temperature thermochronologic analyses and inverse modelling of the two surface samples analysed provide an insight into the post-Oligocene thermal history of the basin, while thermal models calibrated by means of wells stratigraphy and thermal maturity data also constrain the oldest phases of burial. Despite the uncertainties related to the high spread of Tmax well data (Fig. 5), the results suggest thermal maturity at the onset and at the peak of the oil window in the Maikop and Late Eocene sections, respectively. In the Patardzeuli-E1 and Kumisi 2 wells, hydrocarbon generation by Eocene and, in minor account, Maikop sources has been confirmed by gas chromatography-mass spectrometry (GC-MS) data (Sachsenhofer et al., 2021), strengthening the reliability of our dataset. Among the two HF scenarios tested in the sensitivity analysis (Fig. 5), the one which best suits the geological evolution of the Adjara-Trialeti Basin is in our view the one involving a peak of HF during Middle Eocene (around 45 Ma; Fig. 10d) back-arc rifting (Adamia et al., 1977, 1981, 2011; Okrostsvaridze et al., 2018). Additional support to the tested HF model is provided by the high present-day heat flow in the western sector of the fold-and-thrust belt (Melikadze et al., 2015). In this area, rifting was more pronounced and arguably decreased at a slower pace, thus suggesting that also the easternmost Adjara-Trialeti Basin experienced in the past higher HF values than the present-day value of 50 mW/m^2.

Given that rifting did not lead to continental break-up and oceanization, HF values in the Adjara-Trialeti Basin probably never exceeded 100 mW/m^2, as shown in typical continental rift basins such as the Rhine Graben, Lake Tanganika, Gulf of Suez and Rio Grande Rift (Allen

& Allen, 2013; Ebinger et al., 1989; Evans, 1988; Friedmann & Burbank, 1995; Jackson & McKenzie, 1988; Morley et al., 1990; Patton et al., 1994). Considering that our study area in the easternmost Adjara-Trialeti FTB was likely a marginal portion of the basin, a value of 70 mW/m^2 can be reasonably assumed as adequate to represent the maximum HF peak during rifting. Nonetheless, also higher values were tested in a trial-and-error approach, and the results show significant changes only in the deeper part of the maturity curve, which increases its slope and loses fit with the data.

Even with the HF model involving a peak around 45 Ma, an additional burial of about 1 km was still required to fit thermal maturity data (Fig. 5a, c and e). In the Kumisi 1 well such additional burial is slightly higher (1.3 km) to compensate for the missing uppermost part of the Maikop section, which is instead present in the Kumisi 2 well. This 1.0-1.3 km of additional burial can reasonably be attributed a sedimentary load deposited in the Early Miocene, between about 20 and 15 Ma (Table 3), i.e. after the most recent sedimentary units preserved in the wells and before the cooling event accompanying erosion, that could represent the persistence of marine conditions in the Adjara-Trialeti basin during Burdigalian-Langhian times. Such sedimentary burial matches the fast increase of temperatures detected by statistical inverse modelling of AFT data between Burdigalian and Langhian times (Figs. 8 and 9). Conversely, tectonic loading at that time is unrealistic, since the main phase of deformation in the nearby advancing thrust front affecting the Kura Basin occurred in the Late Miocene (Sarmatian-Pontian; Alania et al., 2017; Nemčok et al., 2013). Finally, the thickness of the Lower Miocene section (1-2 km) shown in the cross-section of Figure 7 supports the interpretation of such additional loading as due to sedimentary burial.

Based on the assumptions described above on the thermal history (i.e. the HF model applied) and the additional sedimentary burial required to fit thermal maturity data, the isotherms derived from thermal modelling of the Adjara-Trialeti wells predicts that maximum paleotemperatures experienced by the Maikop section (Oligocene-Early Miocene) in all three wells were comprised between about 90 and 110 °C (Suppl. Mat. Fig. S6), in agreement with (i) statistical inverse modelling of AFT data (e.g. Figs. 8 and 9), which indicate that Maikop samples from the Adjara-Trialeti FTB are partially reset and hence experienced maximum paleotemperature within the Partial Annealing Zone of apatite, i.e. between 60 and 120 °C (this study; Gusmeo et al., 2021), and (ii) maximum paleotemperatures estimated on Maikop samples from multiple thermal maturity proxies within the Adjara-Trialeti FTB (Corrado et al., 2021).

The only other thermal model available for the study area (Pupp et al., 2018) estimates a total amount of eroded section of ca. 3.5 km, different from our estimates of 1.0-1.3 km. This value results from the very low heat-flow value used as input data: Pupp et al. (2018) used a constant value of 40 mW/m^2 to model a pseudo-well built upon surface data from the Tbilisi area, considered as part of the Kura Basin. Conversely, based on geological and geophysical data (see for example Figs. 2 and 7), the section analysed by Pupp et al. (2018) is actually part of the Adjara-Trialeti domain, hence the higher amount of burial derived from an underestimation of the heat flow values. On the other hand, the modelling of Pupp et al. (2018), based on stratigraphy, sets the beginning of exhumation of the studied section at 15 Ma, which perfectly agrees with our timing of deformation based on thermochronological data. Furthermore, their model shows an increase in subsidence rates in the Early Miocene, as postulated in our models (Fig. 10).

According to our thermal modelling results (Fig. 10), the three wells in the eastern Adjara-Trialeti FTB show a similar burial pattern, despite some minor differences in the thickness of equivalent stratigraphic units, in the age range of the sampled sections (e.g. Late Cretaceous-Miocene in Kumisi 1 versus Late Eocene-Miocene in Kumisi 2), and in the maximum depths estimated by the models. The burial history of the Kumisi 1 and Patardzeuli-E1 wells is characterised by rapid subsidence starting in the late Paleocene and continuing, with varying intensity, until the mid-Miocene (Fig. 10). The Eocene-Miocene burial history of the Kumisi 2 well is virtually identical but this borehole did not penetrate the older chronostratigraphic units. Sedimentation rates were higher during the late Paleocene-Early Eocene in the Kumisi 1 and Patardzeuli-E1 wells, and during the Middle-Late Eocene and Early Miocene in all three wells (Fig. 10a, b and c). Timing of inception of cooling/exhumation was set at 15 Ma for all three wells, based on thermochronological data on the beginning of tectonic inversion of the Adjara-Trialeti back-arc basin (Figs. 8 and 10; see Section 4.1; Gusmeo et al., 2021).

5.1.2 Kura Basin

In the western sector of the Kura Basin, the Oligocene portion of the Maikop section was sampled and studied within the Norio 200 and Satskhenisi 102 wells. Despite a large data spread, thermal maturity at the onset of the oil window is also confirmed by GC-MS data (DIG, 2014) and by the datasets reported in Corrado et al. (2021), Pupp et al. (2018) and Sachsenhofer et al. (2021).

The western sector of the Kura basin acted as a foreland basin in front of the northward advancing Lesser Caucasus - Adjara-Trialeti system (Nemčok et al., 2013) during the Oligocene. Given the relatively thick and rigid crust upon which the Kura foreland basin developed (Adamia et al., 2010; Alania et al., 2017; Banks et al., 1997; Nemčok et al., 2013), it could be argued that the heat flow has been relatively low throughout the entire evolution of the basin, as already suggested by Corrado et al. (2021). Thus, even if for the sake of comparison the scenario involving a HF peak around 45 Ma (as in the adjacent Adjara-Trialeti domain) has been tested too (Fig. 6), the constant HF scenario is in our view the most appropriate to apply. Based on the heat flow map of the Black-Caspian seas region (Kutas,

2010) the present-day heat-flow value in the studied sector of the western Kura Basin is around 45 mW/m^2, a slightly lower value than in the adjacent, relatively hotter, Adjara-Trialeti FTB. Such value agrees with the low geothermal gradient of the area (28 °C/km; Patton, 1993), and is in the range of other foreland basins worldwide (20-60 mW/m^2) (Allen and Allen, 2013; Sachsenhofer, 2001; Weides and Majorowicz, 2014).

Using a steady-state heat-flow model, both wells in the Kura Basin required an additional burial after the deposition of the Sarmatian section (the latest sedimentary succession preserved within the two wells) which ended at about 8 Ma in the Norio 200 well. Given the large spread of Tmax data in both wells, it is not an easy task to accurately determinate the amount of additional burial (Fig. 6a and c). Nevertheless, the maturity curves built assuming 1800 m and 1300 m of additional burial for Norio 200 and Satskhenisi 102, respectively, seem to fit at best the data. Such estimations are just below the range given by Corrado et al. (2021) who, based on surface and subsurface thermal maturity data, calculated 2-3 km of Kura basin fill erosion. It is worth noting that these values can sensibly change depending on the lithologies assumed for the additional loading. In our models, we used a mixed lithology composed by shales and sandstones, which is the same one characterising the Sarmatian sections (Fig. 3, Table 3) and best represents the Miocene sedimentary fill of the Kura Basin.

Thermal modelling of the two wells from the western Kura Basin produced a broadly similar subsidence pattern (Fig. 11). Relatively fast subsidence during the Oligocene was followed by slower rates in the Early-Middle Miocene and very fast burial in the Late Miocene, especially after 8 Ma. This means that the additional burial required to fit thermal maturity data was emplaced very rapidly, suggesting a tectonic origin rather than sedimentary burial: the most probable cause of such tectonic loading is the emplacement of south-verging thrusts (Figs. 1, 2, 7 and 12) related to southward propagation of deformation from the Greater Caucasus.

Since precise constraints on the beginning of cooling/exhumation in this sector are not available, such timing was tentatively set at 6 Ma, i.e. after the most recent deposits within the Norio 200 well (8 Ma; Fig. 11, Table 3). However, after several simulations (with such timing varying between 7 and 3 Ma), we found that differences in the timing of inception of erosion did not affect significatively the results. A latest Miocene-Early Pliocene age of inception of erosion/cooling is also in agreement with the Late Miocene age of the youngest rock units within the thrust sheets imaged in the seismic lines across the southern Kura basin (e.g. Fig. 7) and with previous estimates on the inception of deformation in the Kura Basin (Alania et al., 2017; Nemčok et al., 2013).

According to modelling results, the base of the Oligocene section in both wells experienced maximum paleotemperatures in excess of 80 °C (Fig. 11).

5.2 Tectonic implications

The integration of our new AFT inverse modelling and thermal modelling results constrains the burial/exhumation history of the structurally complex transition zone between two adjacent geologic domains, the Adjara-Trialeti FTB to the south and the Kura Basin to the north, which differ in age, origin, subsidence mechanisms and evolution.

A rift model best describes the HF evolution in the eastern Adjara-Trialeti back-arc basin, with a peak at ca. 70mW/m^2 around 45 Ma followed by gradual reduction down to the present-day value of 50 mW/m^2 (Fig. 10d). Applying such HF model, the Adjara-Trialeti basin experienced continuous subsidence from the Paleocene to the middle Miocene, punctuated by three main pulses of increased subsidence (Fig. 10). High subsidence rates were first registered in the Kumisi 1 and Patardzeuli-E1 wells in the late Paleocene-Early Eocene. During this time a thick succession, including the terrigenous turbidites of the Borjomi Flysch (Adamia et al., 2011; Banks et al., 1997; Yılmaz et al., 2000, 2014), was deposited in the Adjara-Trialeti basin in the northern foreland of the Erzinçan-Sevan-Akera orogen, which was experiencing a gradient of increasing flexural subsidence from west to east (Gusmeo et al., 2021), as confirmed by the progressive eastward thickening of the Borjomi Flysch (Gamkrelidze, 1949; Yılmaz et al., 2000). Interpreting the pre-depositional history of detrital samples as derived from inverse modelling must be done with great care, because of the intrinsic assumptions that are hardly verifiable (Malusà and Fitzgerald, 2020). Nevertheless, our thermochronologic inverse modelling results (Gusmeo et al., 2021; this study) are supported by very high chi-square values (close to 100%) and describe a thermal history (i.e. fast cooling/exhumation of the sediment source area during Paleocene-Eocene times; Figs. 8 and 9) that is compatible with the reconstructed geologic evolution of the region during that time span, when the Northern Neotethys finally closed along the Izmir-Ankara-Erzinçan suture zone due to the oblique collision between the Anatolide-Tauride terrane and the southern Eurasian margin (Barrier et al., 2018; Rolland et al., 2019; Stampfli and Hochard, 2009). As a result, the building-up of the Lesser Caucasus was most likely the source of the sediments deposited in the Adjara-Trialeti basin, that was forming under lithospheric flexure due to loading by the Lesser Caucasus retro-wedge (Gamkrelidze, 1949; Gusmeo et al., 2021). During the final stages of closure of the Northern Neotethys, slab roll-back brought, in the Lutetian, to the main phase of continental rifting within the Adjara-Trialeti basin, as testified by the intrusion of plutonic/hypabyssal bodies and by the deposition of volcanic and volcaniclastic rocks (Adamia et al., 2011; Gamkrelidze et al., 2019; Okrostsvaridze et al., 2018). The second phase of increased subsidence rate (Middle-Late Eocene) is likely a consequence of such continental rifting. Furthermore, the presence of volcanic and plutonic rocks, most abundant in the western sector of the basin towards the Black Sea coast, corroborates the hypothesis of high heat-flow at that time (Fig. 10).

The third phase of fast burial (Early Miocene), previously unrecognised, is evident in the thermal models (Fig. 10) and confirmed by the fast heating phase outlined by inverse modelling of AFT data (Figs. 8 and 9). At this time the area was characterized by the convergence between the Greater and Lesser Caucasus (Nemčok et al., 2013). The structures imaged in seismic profiles in the eastern Adjara-Trialeti fold-and-thrust belt (see cross-section of Fig. 7 and Tari et al., 2021) show high complexity including evidence of strike-slip tectonics, as also supported by earthquake focal mechanisms in the surroundings of the study area (Ismail-Zadeh et al., 2020; Sokhadze et al., 2018; Tibaldi et al., 2019). We argue that strike-slip tectonics could have been the cause for a such subsidence pulse just before the uplift of the area.

Early to Middle Miocene (20-15 Ma) Adjara-Trialeti basin inversion is constrained by inverse modelling of thermochronologic data (Figs. 8 and 9; Table 1) and confirms previous results obtained more to the west along the orogenic belt (Gusmeo et al., 2021). Exhumation can be framed in the context of the Middle Miocene hard collision between the Arabian and Eurasian plates along the Bitlis-Zagros suture zone (Cavazza et al., 2018; Okay et al., 2010) that caused reactivation of tectonic structures, basin inversion, and strike-slip deformation in the hinterland of the collision zone, from the eastern Pontides and the East Anatolian-Iranian Plateau, to the Lesser and Greater Caucasus, to the Talysh and Alborz ranges (Albino et al., 2014; Avdeev and Niemi, 2011; Axen et al., 2001; Ballato et al., 2008, 2016; Barber et al., 2018; Cavazza et al., 2017, 2019; Corrado et al., 2021; Gavillot et al., 2010; Gusmeo et al., 2021; Madanipour et al., 2017; Mosar et al., 2010; Paknia et al., 2021; Vasey et al., 2020; Vincent et al., 2020).

Our preferred model describing the HF evolution in the western Kura Basin assumes a constant HF of 45 mW/m^2 (Fig. 11c) throughout the Oligocene-to-Present basin history.

Applying such model, in the western Kura basin the subsidence curves derived from the burial histories of the two analysed wells (Fig. 11) mostly describe the evolution during Maikop deposition and show continuous burial since the Oligocene, with two main pulses of enhanced subsidence in the Oligocene and in the Middle-Late Miocene, respectively.

A first phase of relatively fast subsidence (higher in Satskhenisi 102 than in Norio 200) occurred during the Oligocene (Fig. 11), when the western Kura foreland basin behaved as a flexural basin, reacting by prominent fill asymmetry to loading by the northward advancing Lesser Caucasus - Adjara-Trialeti system (Nemčok et al., 2013). It was only in the Middle-Late Miocene that the flexural wave induced by the south-verging advancement of the Greater Caucasus structural front reached the southern margin of the Kura Basin (Figs. 11 and 12). The sedimentation pattern at that time is typical of foreland basins, characterized by convex-upward subsidence curves (e.g. Allen and Allen, 2013; Fig. 11).

Competing and asymmetrical episodes of flexural subsidence within the western Kura Basin have been envisioned by Nemčok et al. (2013), who interpreted the marked southward thickening of the Oligocene section and the northward thickening of the Early-Middle Miocene one as effects of flexural loading by the advancing Lesser Caucasus and Greater Caucasus, respectively.

Finally, in Late Miocene times (late Sarmatian-Pontian; Alania et al., 2017; Nemčok et al., 2013) the southward propagation of deformation from the Greater Caucasus affected the Kura Basin in the area of the Norio 200 and Satskhenisi 102 wells (Fig. 12). This resulted in the emplacement of a complex system of thin-skinned south-verging thrusts, arguably responsible for the additional 1.3-1.8 km of tectonic loading required to fit thermal maturity data (Figs. 11 and 12). After this fast burial, which led to maximum paleo-temperatures of more than 80°C at the bottom of the succession, the area was ultimately exhumed and experienced significant erosion. The complex deformation that took place in the southern part of the Kura foreland basin is represented by deformation and uplift of Miocene strata by thin-skinned thrusting at the top of the triangle zone (Fig. 7). Such a structural thickening induced the erosion of a ca. 1.3-1.8 km thick section since latest Miocene-Pliocene times.

The overall tectonic evolution and burial-exhumation history reconstructed for the Adjara-Trialeti and Kura basins, in the central Transcaucasian sector, can be framed in the context of the broad Arabia-Eurasia collision zone. Initial flexural subsidence and subsequent back-arc rifting in the Adjara-Trialeti Basin can be interpreted as a consequence of continental collision along the Erzinçan-Sevan-Akera suture during Paleocene-Early Eocene times and roll-back during the Middle Eocene, respectively. During the Oligocene, thermal subsidence was affecting the Adjara-Trialeti basin (Fig. 10), whereas the Kura Basin was flexured by the advance of the Lesser Caucasus system (Fig.11). The Middle Miocene inception of inversion of the Adjara-Trialeti basin defined in this study and in Gusmeo et al. (2021), as well as the timing of renewal of flexural behaviour in the Kura Basin highlighted by thermal modelling results (Fig. 11), can both be ascribed to far-field stress propagation from the Bitlis-Zagros suture zone, hundreds of kilometres to the south, where the Middle Miocene hard collision between the Arabian and Eurasian plates took place (Cavazza et al., 2018; Okay et al., 2010). Furthermore, continued northward stress transmission may have been also responsible for shortening/uplift in the Greater Caucasus. Given that in its central sector this orogen is mainly south-verging (Forte et al., 2014), far-field stress transmission from the Bitlis-Zagros suture zone could ultimately be responsible for southward propagation of deformation from the Greater Caucasus, affecting also the Kura Basin (Fig. 12). Such a stress field is active also at present in the Transcaucasus, as demonstrated by GPS and earthquakes data (Karakhanyan et al., 2013; Reilinger et al., 2006; Sokhadze et al., 2018; Tsereteli et al., 2016).

6. Conclusions

In this paper we show the successful application of an integrated approach to the study of the complex transition zone between the eastern Adjara-Trialeti FTB and the western Kura Basin (central Georgia). The integration of AFT inverse modelling, well thermal modelling and seismic interpretation has elucidated the pattern of subsidence/exhumation and provided new constraints on the overall tectonic evolution of the eastern Georgian sector of the Transcaucasus.

New AFT inverse modelling results from the eastern Adjara-Trialeti FTB indicate latest Paleocene-Early Eocene fast cooling/exhumation, arguably linked with final closure of the Northern Neotethys ocean and subsequent building of the Lesser Caucasus. A previously unrecognized and localized Early Miocene phase of fast subsidence and heating can be attributed to strike-slip motion components between the Greater and Lesser Caucasus orogenic systems. AFT modelling results also confirms the mid-Miocene inception of structural inversion of the Adjara-Trialeti basin.

Thermal modelling of the Adjara-Trialeti inverted back-arc basin delineates three pulses of enhanced subsidence in Late Paleocene-Early Eocene, Middle-Late Eocene and Early Miocene times in the Adjara-Trialeti basin, associated respectively to flexural subsidence, rifting and strike-slip tectonics. Modelling results also predict that about 1.0-1.3 km of sedimentary rocks have been eroded since inversion started.

Our preferred thermal models from the Kura Basin describes a complex subsidence pattern during Oligocene-Miocene times, resulting from the interference between the competing and oppositely advancing Lesser and Greater Caucasus orogenic systems. During the Late Miocene the southwestern Kura Basin experienced rapid tectonic burial (ca. 1.3-1.8 km), related to south-verging thrusts linked to southward propagation of deformation from the Greater Caucasus, ultimately followed by exhumation and erosion.

On a larger scale, the tectonic evolution and burial/exhumation history of central Transcaucasia can be correlated with episodic continental accretion along the Eurasian plate margin related to (i) collision of the Anatolide-Tauride terrane and the ensuing development of the Erzinçan-Sevan-Akera suture in the Late Cretaceous - Eocene, and (ii) the hard collision of Arabia along the Bitlis-Zagros suture zone in the Miocene.

Acknowledgements

We thank GOGC (Georgian Oil & Gas company) for kindly providing part of the lithological and thermal maturity data used in this study. Platte River Associates, Inc. is acknowledged for providing an academic licence for the Basin Mod 2-D software package. Reinhard Sachsenhofer (Montanuniversität Leoben) provided useful comments on an earlier version of the manuscript. Irene Albino assisted in sample preparation for fission-track analysis. This research was funded by the PRIN Program of the Italian Ministry of University and Research 2017-2020.

References

Abdullah, W.H., Togunwa, O.S., Makeen, Y.M., Hakimi, M.H., Mustapha, K.A., Baharuddin, M.H., Sia, S.G., Tongkul, F., 2017. Hydrocarbon source potential of Eocene-Miocene sequence of Western Sabah, Malaysia. Mar. Pet. Geol. 83, 345–361.

https://doi.org/10.1016/j.marpetgeo.2017.02.031

Adamia, S.A., Akhvlediani, K.T., Kilasonia, V.M., Nairn, A.E.M., Papava, D., Patton, D.K., 1992. Geology of the republic of Georgia: a review. Int. Geol. Rev. 34, 447–476.

Adamia, S.A., Alania, V., Chabukiani, A., Chichua, G., Enukidze, O., Sadradze, N., 2010. Evolution of the Late Cenozoic basins of Georgia (SW Caucasus): a review, in: Sosson, M., Kaymakci, N., Stephenson, R.A., Bergerat, F., Starostenko, V. (Eds.), Sedimentary Basin Tectonics from the Black Sea and Caucasus to the Arabian Platform. Geological Society, London, Special Pubblications, 340, pp. 239–259.

Adamia, S.A., Chkhotua, T., Kekelia, M., Lordkipanidze, M., Shavishvili, I., Zakariadze, G., 1981. Tectonics of the Caucasus and adjoining regions: implications for the evolution of the Tethys ocean. J. Struct. Geol. 3, 437–447. https://doi.org/https://doi.org/10.1016/0191-8141(81)90043-2

Adamia, S.A., Chkhotua, T.G., Gavtadze, T.T., Lebanidze, Z.A., Lursmanashvili, N.D., Sadradze, N.G., Zakaraia, D.P., Zakariadze, G.S., 2017. Tectonic setting of Georgia-Eastern Black Sea: A review, in: Sosson, M., Stephenson, R.A., Adamia, S.A. (Eds.), Tectonic Evolution of the Eastern Black Sea and Caucasus. Geological Society, London, Special Publications 428, pp. 11–40. https://doi.org/10.1144/SP428.6

Adamia, S.A., Lordkipanidze, M.B., Zakariadze, G.S., 1977. Evolution of an active continental margin as exemplified by the Alpine history of the Caucasus. Tectonophysics 40, 183–199. https://doi.org/https://doi.org/10.1016/0040-1951(77)90065-8

Adamia, S.A., Zakariadze, G., Chkhotua, T., Sadradze, N., Tsereteli, N., Chabukiani, A., Gventsadze, A., 2011. Geology of the Caucasus: A Review. Turkish J. Earth Sci. 20, 489–544. https://doi.org/10.3906/yer-1005-11

Alania, V., Beridze, T., Enukidze, O., Chagelishvili, R., Lebanidze, Z., Maqadze, D., 2021a.

The Geometry of the two orogens convergence and collision zones in central Georgia: new data from seismic reflection profiles, in: Bonali, F.L., Pasquarè Mariotto, F.A., Tsereteli, N. (Eds.), Building Knowledge for Geohazard Assesment and Management in the Caucasus and Other Regions. Springer, Dordrecht, pp. 73–88.

Alania, V., Beridze, T., Enukidze, O., Lebanidze, Z., Razmadze, A., Sadradze, N., Tevzadze, N., 2020. Structural model of the frontal part of the eastern Achara-Trialeti fold-and-thrust belt: The results of seismic profile interpretation. Bull. Georg. Natl. Acad. Sci. 14, 62–68.

Alania, V., Chabukiani, A.O., Chagelishvili, R.L., Enukidze, O. V., Gogrichiani, K.O., Razmadze, A.N., Tsereteli, N.S., 2017. Growth structures, piggy-back basins and growth strata of the Georgian part of the Kura foreland fold–thrust belt: implications for Late Alpine kinematic evolution, in: Sosson, M., Stephenson, R.A., Adamia, S.A. (Eds.), Tectonic Evolution of the Eastern Black Sea and Caucasus. Geological Society, London, Special Publications 428, pp. 428–445. https://doi.org/10.1177/1010539510370992

Alania, V., Enukidze, O., Glonti, N., Razmadze, A., Chabukiani, A., Giorgadze, A., Vakhtang Glonti, B., Koiava, K., Beridze, T., Khutsishvili, S., Chagelishvili, R., 2018. Structural Architecture of the Kura Foreland Fold-and-thrust Belt Using Seismic Reflection Profile, Georgia. Univers. J. Geosci. 6, 184–190. https://doi.org/10.13189/ujg.2018.060402

Alania, V., Kvavadze, N., Enukidze, O., Beridze, T., Gventsadze, A., Tevzadze, N., 2021b. Seismic interpretation of southern part of the eastern Achara-Trialeti fold-and-thrust belt, Georgia. Bull. Georg. Natl. Acad. Sci. 15, 57–62.

Alavi, M., 1994. Tectonics of the Zagros orogenic belt of Iran: new data and interpretations. Tectonophysics 229, 211–238.

Albino, I., Cavazza, W., Zattin, M., Okay, A.I., Adamia, S.A., Sadradze, N., 2014. Far-field tectonic effects of the Arabia–Eurasia collision and the inception of the North Anatolian Fault system. Geol. Mag. 151, 372–379. https://doi.org/10.1017/s0016756813000952

Allen, P.A., Allen, J.R., 2013. Basin Analysis: Principles and Application to Petroleum Play Assessment, Science. https://doi.org/10.1126/science.208.4442.393

Andreucci, B., Castelluccio, A., Corrado, S., Jankowski, L., Mazzoli, S., Szaniawski, R., Zattin, M., 2014. Interplay between the thermal evolution of an orogenic wedge and its retro-wedge basin: An example from the Ukrainian Carpathians. Bull. Geol. Soc. Am. 127, 410–427. https://doi.org/10.1130/B31067.1

Avdeev, B., Niemi, N.A., 2011. Rapid Pliocene exhumation of the central Greater Caucasus constrained by low-temperature thermochronometry. Tectonics 30, 1–16. https://doi.org/10.1029/2010TC002808

Axen, G.J., Lam, P.S., Grove, M., Stockli, D.F., Hassanzadeh, J., 2001. Exhumation of the west-central Alborz Mountains, Iran, Caspian subsidence, and collision-related tectonics. Geology 29, 559–562. https://doi.org/10.1130/0091-7613(2001)029<0559:EOTWCA>2.0.CO;2

Balestra, M., Corrado, S., Aldega, L., Morticelli, M.G., Sulli, A., Rudkiewicz, J.L., Sassi, W., 2019. Thermal and structural modeling of the Scillato wedge-top basin source-to-sink system: Insights into the Sicilian fold-and-thrust belt evolution (Italy). Bull. Geol. Soc. Am. 131, 1763–1782. https://doi.org/10.1130/B35078.1

Ballato, P., Cifelli, F., Heidarzadeh, G., Ghassemi, M.R., Wickert, A.D., Hassanzadeh, J., Dupont-Nivet, G., Balling, P., Sudo, M., Zeilinger, G., Schmitt, A.K., Mattei, M., Strecker, M.R., 2016. Tectono-sedimentary evolution of the northern Iranian Plateau: insights from middle–late Miocene foreland-basin deposits. Basin Res. 29, 417–446. https://doi.org/10.1111/bre.12180

Ballato, P., Nowaczyk, N.R., Landgraf, A., Strecker, M.R., Friedrich, A., Tabatabaei, S.H.,

2008. Tectonic control on sedimentary facies pattern and sediment accumulation rates in the Miocene foreland basin of the southern Alborz mountains, northern Iran. Tectonics 27, 1–20. https://doi.org/10.1029/2008TC002278

Banks, C.J., Robinson, A.G., Williams, M.P., 1997. Structure and regional tectonics of the Achara-Trialeti fold belt and the adjacent Rioni and Kartli foreland basins, Republic of Georgia, in: Robinson, A.G. (Ed.), Regional and Petroleum Geology of the Blacks Sea and Surrounding Region: AAPG Memoirs 68. Tulsa, Oklahoma, pp. 331–346.

Barber, D.E., Stockli, D.F., Horton, B.K., Koshnaw, R.I., 2018. Cenozoic exhumation and foreland basin evolution of the Zagros orogen during the Arabia-Eurasia collision, Western Iran. Tectonics 37, 4396–4420. https://doi.org/10.1029/2018TC005328

Barrier, E., Vrielynck, B., Brouillet, J.F., Brunet, M.-F., (Contributors: Angiolini L., Kaveh F., Poisson A., Pourteau A., Plunder A., Robertson A., Shekawat R., Sosson M., Zanchi, A.., 2018. Paleotectonic reconstruction of the central Tethyan realm. Tectonono-sedimentary-palinspastic maps from late Permian to Pliocene. CCGM/CGMW, Paris.

Behar, F., Beaumont, V., De B. Penteado, H.L., 2001. Rock-Eval 6 Technology: Performances and Developments. Oil Gas Sci. Technol. 56, 111–134. https://doi.org/10.2516/ogst:2001013

Bertrand, R., Lavoie, V., Malo, M., 2010. Maturité thermique et potentiel roche-mère des roches ordoviciennes à dévoniennes du secteur Matapédia–Témiscouata du Bas-Saint-Laurent, Québec. Geol. Surv. Canada, Open File 6576 183.

Boote, D.R.D., Sachsenhofer, R.F., Tari, G., Arbouille, D., 2018. Petroleum Provinces of the Paratethyan Region. J. Pet. Geol. 41, 247–297. https://doi.org/10.1111/jpg.12703

Borrego, A.G., Cook, A., 2017. Sampling and Sample Preparation for Reflected Light Microscopy, in: 10th ICCP Training Course on Dispersed Organic Matter Integrating Transmitted and Reflected Light Microscopy (Instruction Notes). pp. 21–28.

Burnham, A.K., Sweeney, J.J., 1989. A chemical kinetic model of vitrinite maturation and reflectance. Geochim. Cosmochim. Acta 53, 2649–2657. https://doi.org/10.1016/0016-7037(89)90136-1

Butler, R.W.H., 1991. Hydrocarbon maturation, migration and tectonic loading in the Western Alpine foreland thrust belt, in: England, W.A., Fleet, A.J. (Eds.), Petroleum Migration. Geological Society, London, Special Publications 59, pp. 227–244.

Butler, R.W.H., Bond, C.E., Cooper, M.A., Watkins, H., 2018. Interpreting structural geometry in fold-thrust belts: Why style matters. J. Struct. Geol. 114, 251–273. https://doi.org/10.1016/j.jsg.2018.06.019

Caricchi, C., Aldega, L., Corrado, S., 2015. Reconstruction of maximum burial along the Northern Apennines thrust wedge (Italy) by indicators of thermal exposure and modeling. Bull. Geol. Soc. Am. 127, 428–442. https://doi.org/10.1130/B30947.1

Cavazza, W., Albino, I., Galoyan, G., Zattin, M., Cattò, S., 2019. Continental accretion and incremental deformation in the thermochronologic evolution of the Lesser Caucasus. Geosci. Front. 10, 2189–2202. https://doi.org/10.1016/j.gsf.2019.02.007

Cavazza, W., Albino, I., Zattin, M., Galoyan, G., Imamverdiyev, N., Melkonyan, R., 2017. Thermochronometric evidence for Miocene tectonic reactivation of the Sevan-Akera suture zone (Lesser Caucasus): A far-field tectonic effect of the Arabia-Eurasia collision?, in: Sosson, M., Stephenson, R.A., Adamia, S.A. (Eds.), Tectonic Evolution of the Eastern Black Sea and Caucasus. Geological Society, London, Special Publications 428, pp. 187–198. https://doi.org/10.1144/SP428.4

Cavazza, W., Cattò, S., Zattin, M., Okay, A.I., Reiners, P., 2018. Thermochronology of the Miocene Arabia-Eurasia collision zone of southeastern Turkey. Geosphere 14, 2277–2293. https://doi.org/10.1130/GES01637.1

Cohen, K.M., Finney, S.C., Gibbard, P.L., Fan, J.-X., 2021. The ICS International

Chronostratigraphic Chart. Episodes 36, 199–204.

Corrado, S., Gusmeo, T., Schito, A., Alania, V., Enukidze, O., Conventi, E., Cavazza, W., 2021. Validating far-field deformation styles from the Adjara-Trialeti fold-and-thrust belt to the Greater Caucasus (Georgia) through multi-proxy thermal maturity datasets. Mar. Pet. Geol. 130. https://doi.org/10.1016/j.marpetgeo.2021.105141

Corrado, S., Schito, A., Romano, C., Grigo, D., Poe, B.T., Aldega, L., Caricchi, C., Di Paolo, L., Zattin, M., 2020. An integrated platform for thermal maturity assessment of polyphase, long-lasting sedimentary basins, from classical to brand-new thermal parameters and models: An example from the on-shore Baltic Basin (Poland). Mar. Pet. Geol. 122, 104547. https://doi.org/10.1016/j.marpetgeo.2020.104547

Curzi, M., Aldega, L., Bernasconi, S.M., Berra, F., Billi, A., Boschi, C., Franchini, S., Van der Lelij, R., Viola, G., Carminati, E., 2020. Architecture and evolution of an extensionally-inverted thrust (Mt. Tancia Thrust, Central Apennines): Geological, structural, geochemical, and K–Ar geochronological constraints. J. Struct. Geol. 136. https://doi.org/10.1016/j.jsg.2020.104059

Dewey, J.F., Hempton, M.R., Kidd, W.S.F., Saroglu, F., Şengör, A.M.C., 1986. Shortening of continental lithosphere: the neotectonics of Eastern Anatolia — a young collision zone, in: Coward, M.P., Ries, A.C. (Eds.), Collision. Geological Society, London, Special Publications 19, pp. 1–36. https://doi.org/10.1144/GSL.SP.1986.019.01.01

Di Paolo, L., Aldega, L., Corrado, S., Mastalerz, M., 2012. Maximum burial and unroofing of Mt. Judica recess area in Sicily: ®mplication for the Apenninic-Maghrebian wedge dynamics. Tectonophysics 530–531, 193–207. https://doi.org/10.1016/j.tecto.2011.12.020

DIG, 2014. Sackhenisi #102 Geochemical Analysis. Boulder, CO, United States.

Donelick, R.A., Ketcham, R.A., Carlson, W.D., 1999. Variability of apatite fission-track annealing kinetics: II. Crystallographic orientation effects. Am. Mineral. 84, 1224–1234. https://doi.org/10.2138/am-1999-0902

Donelick, R.A., O'Sullivan, P.B., Ketcham, R.A., 2005. Apatite Fission-Track Analysis. Rev. Mineral. Geochemistry 58, 49–94. https://doi.org/10.2138/rmg.2005.58.3

Dow, W.G., 1977. Kerogen studies and geological interpretations. J. Geochemical Explor. 7, 79–99.

Ebinger, C.J., Bechtel, T.D., Forsyth, D.W., Bow, C.O., 1989. Effective elastic plate thickness beneath the East African and Afar plateaus and dynamic compensation of the uplifts. J. Geophys. Res. B Solid Earth 94, 2883–2901.

Evans, A.L., 1988. Neogene tectonic and stratigraphic events in the Gulf of Suez rift area, Egypt. Tectonophysics 153, 235–247. https://doi.org/10.1016/0040-1951(88)90018-2

Flowers, R.M., Farley, K.A., Ketcham, R.A., 2015. A reporting protocol for thermochronologic modeling illustrated with data from the Grand Canyon. Earth Planet. Sci. Lett. 432, 425–435. https://doi.org/10.1016/j.epsl.2015.09.053

Forte, A.M., Cowgill, E., Murtuzayev, I., Kangarli, T., Stoica, M., 2013. Structural geometries and magnitude of shortening in the eastern Kura fold-thrust belt, Azerbaijan: Implications for the development of the Greater Caucasus Mountains. Tectonics 32, 688–717. https://doi.org/10.1002/tect.20032

Forte, A.M., Cowgill, E., Whipple, K.X., 2014. Transition from a singly vergent to doubly vergent wedge in a young orogen: The Greater Caucasus. Tectonics 33, 2077–2101. https://doi.org/10.1002/2014TC003651

Friedmann, S.J., Burbank, D.W., 1995. Rift basins and supradetachment basins: Intracontinental extensional end-members. Basin Res. 7, 109–127. https://doi.org/10.1111/j.1365-2117.1995.tb00099.x

Galbraith, R.F., 1981. On statistical models for fission track counts. J. Int. Assoc. Math. Geol.

13, 471–478. https://doi.org/10.1007/BF01034498

Gamkrelidze, I., Okrostsvaridze, A., Maisadze, F., Basheleishvili, L., Boichenko, G., 2019. Main features of geological structure and geotourism potential of Georgia, the Caucasus. Mod. Environ. Sci. Eng. 5, 422–442. https://doi.org/10.15341/mese(2333-2581)/05.05.2019/010

Gamkrelidze, P., 1949. Geological structure of the Adjara-Trialetian folded system. Academy of Sciences of Georgia Press, Tbilisi.

Gavillot, Y., Axen, G.J., Stockli, D.F., Horton, B.K., Fakhari, M.D., 2010. Timing of thrust activity in the High Zagros fold-thrust belt, Iran, from (U-Th)/He thermochronometry. Tectonics 29. https://doi.org/10.1029/2009TC002484

Gleadow, A.J.W., Duddy, I.R., 1981. A natural long-term track annealing experiment for apatite. Nucl. Tracks 5, 169–174.

Gleadow, A.J.W., Duddy, I.R., Green, P.F., Lovering, J.F., 1986. Confined fission track lengths in apatite: a diagnostic tool for thermal history analysis. Contrib. to Mineral. Petrol. 94, 405–415.

Gusmeo, T., Cavazza, W., Alania, V.M., Enukidze, O. V, Zattin, M., Corrado, S., 2021. Structural inversion of back-arc basins – The Neogene Adjara-Trialeti fold-and-thrust belt (SW Georgia) as a far-field effect of the Arabia-Eurasia collision. Tectonophysics 803. https://doi.org/10.1016/j.tecto.2020.228702

Hunt, J.M., 1996. Petroleum Geochemistry and Geology. W. H. Freeman and Company, New York.

Ismail-Zadeh, A., Adamia, S.A., Chabukiani, A., Chelidze, T., Cloetingh, S., Floyd, M., Gorshkov, A., Gvishiani, A., Ismail-Zadeh, T., Kaban, M.K., Kadirov, F., Karapetyan, J., Kangarli, T., Kiria, J., Koulakov, I., Mosar, J., Mumladze, T., Müller, B., Sadradze, N., Safarov, R., Schilling, F., Soloviev, A., 2020. Geodynamics, seismicity, and seismic hazards of the Caucasus. Earth-Science Rev. 207. https://doi.org/10.1016/j.earscirev.2020.103222

Jackson, J., McKenzie, D., 1988. The relationship between plate motions and seismic moment tensors, and the rates of active deformation in the Mediterranean and Middle East. Geophys. J. 93, 45–73. https://doi.org/10.1111/j.1365-246X.1988.tb01387.x

Jarvie, D.M., Claxton, B.L., Henk, F., Breyer, J.T., 2001. Oil and shale gas from the Barnett Shale, Ft . Worth Basin, Texas, in: AAPG National Convention. AAPG Bulletin, Denver, CO, United States.

Jolivet, L., Faccenna, C., 2000. Mediterranean extension and the Africa-Eurasia collision Laurent. Tectonics 19, 1095–1106. https://doi.org/10.1029/2000TC900018

Karakhanyan, A., Vernant, P., Doerflinger, E., Avagyan, A., Philip, H., Aslanyan, R., Champollion, C., Arakelyan, S., Collard, P., Baghdasaryan, H., Peyret, M., Davtyan, V., Calais, E., Masson, F., 2013. GPS constraints on continental deformation in the Armenian region and Lesser Caucasus. Tectonophysics 592, 39–45. https://doi.org/10.1016/j.tecto.2013.02.002

Ketcham, R.A., 2005. Forward and inverse modeling of low-temperature thermochronometry data. Rev. Mineral. Geochemistry 58, 275–314. https://doi.org/10.2138/rmg.2005.58.11

Ketcham, R.A., Carter, A., Donelick, R.A., Barbarand, J., Hurford, A.J., 2007. Improved modeling of fission-track annealing in apatite. Am. Mineral. 92, 799–810. https://doi.org/10.2138/am.2007.2281

Ketcham, R.A., Donelick, R.A., Carlson, W.D., 1999. Variability of apatite fission-track annealing kinetics: III. Extrapolation to geological time scales. Am. Mineral. 84, 1235–1255. https://doi.org/Doi 10.2138/Am.2006.464

Korelskiy, E., Yildiz, T.T., Urazaliev, J., Goloborodko, A., Orlov, A., Tirumanapali, S., Savinov, R., Akhmetov, M., Ivanov, R., 2019. Multidisciplinary engineering approach and proper planning enables successful drilling of one of the deepest exploration HPHT well in the Samgori-Patardzeuli area, Georgia, in: Society of Petroleum Engineers - SPE Russian Petroleum Technology Conference. Moscow, Russia, October 2019. Moscow, Russia, pp. 1–21. https://doi.org/10.2118/196806-ru

Kutas, R.I., 2010. Heat Flow in the Caspian – Black Sea Region and its Tectonic Implications, in: AAPG European Region Annual Conference. Kiev, Ukraine, October 17-19, 2010.

Langford, F.F., Blanc-Velleron, M.M., 1990. Interpreting Rock-Eval Pyrolysis data using graphs of pyrolizable hydrocarbons vs Total Organic Carbon. Am. Assoc. Pet. Geol. Bullettin 74, 799–804.

Lazarev, S., Jorissen, E.L., van de Velde, S., Rausch, L., Stoica, M., Wesselingh, F.P., Van Baak, C.G.C., Yanina, T.A., Aliyeva, E., Krijgsman, W., 2019. Magneto-biostratigraphic age constraints on the palaeoenvironmental evolution of the South Caspian basin during the Early-Middle Pleistocene (Kura basin, Azerbaijan). Quat. Sci. Rev. 222, 105895. https://doi.org/10.1016/j.quascirev.2019.105895

Lordkipanidze, M.B., Meliksetian, B., Djarbashian, R., 1989. Meosozic-Cenozoic magmatic evolution of the Pontian-Crimean-Caucasian region. IGCP Proj. 198 103–124.

Madanipour, S., Ehlers, T.A., Yassaghi, A., Enkelmann, E., 2017. Accelerated middle Miocene exhumation of the Talesh Mountains constrained by U-Th/He thermochronometry: Evidence for the Arabia-Eurasia collision in the NW Iranian Plateau. Tectonics 36, 1538–1561. https://doi.org/10.1002/2016TC004291

Malusà, M.G., Fitzgerald, P.G., 2020. The geologic interpretation of the detrital thermochronology record within a stratigraphic framework, with examples from the European Alps, Taiwan and the Himalayas. Earth-Science Rev. 201. https://doi.org/10.1016/j.earscirev.2019.103074

McKenzie, D., 1978. Some remarks on the development of sedimentary basins. Earth Planet. Sci. Lett. 40, 25–32.

Melikadze, G., Vardigoreli, O., Kapandze, N., 2015. Country Update from Georgia, in: Proceeding World Geothermal Congress 2015. Melbourne, Australia, pp. 1015–1018.

Morley, C.K., Nelson, R.A., Patton, T.L., Munn, S.G., 1990. Transfer Zones in the East African Rift System and their relevance to hydrocarbon exploration in rifts. Am. Assoc. Pet. Geol. Bull. 74, 1234–1253.

Mosar, J., Kangarli, T., Bochud, M., Glasmacher, U.A., Rast, A., Brunet, M.-F., Sosson, M., 2010. Cenozoic-Recent tectonics and uplift in the Greater Caucasus: a perspective from Azerbaijan, in: Sosson, M., Kaymakci, N., Stephenson, R.A., Bergerat, F., Starostenko, V. (Eds.), Sedimentary Basin Tectonics from the Black Sea and Caucasus to the Arabian Platform. Geological Society, London, Special Publications 340, pp. 261–280. https://doi.org/10.1144/SP340.12

Motavalli-Anbaran, S.H., Zeyen, H., Jamasb, A., 2016. 3D crustal and lithospheric model of the Arabia-Eurasia collision zone. J. Asian Earth Sci. 122, 158–167. https://doi.org/10.1016/j.jseaes.2016.03.012

Nemčok, M., Glonti, B., Yukler, A., Marton, B., 2013. Development history of the foreland plate trapped between two converging orogens; Kura Valley, Georgia, case study, in: Nemčok, M., Mora, A., Cosgrove, J.W. (Eds.), Thick-Skin-Dominated Orogens: From Initial Inversion to Full Accretion. Geological Society, London, Special Publications 377, pp. 159–188. https://doi.org/10.1144/SP377.9

Neubauer, T.A., Harzhauser, M., Kroh, A., Georgopoulou, E., Mandic, O., 2015. A gastropod-based biogeographic scheme for the European Neogene freshwater systems. Earth Sci. Rev. 143, 98–116. https://doi.org/10.1016/j.earscirev.2015.01.010

Okay, A.I., Zattin, M., Cavazza, W., 2010. Apatite fission-track data for the Miocene Arabia-

Eurasia collision. Geology 38, 35–38. https://doi.org/10.1130/G30234.1

Okrostsvaridze, A., Chung, S.L., Chang, Y.H., Gagnidze, N., Boichenko, G., Gogoladze, S., 2018. Zircons U-Pb geochronology of the ore-bearing plutons of Adjara-Trialeti folded zone, Lesser Caucasus and analysis of the magmatic processes. Bull. Georg. Natl. Acad. Sci. 12, 90–99.

Pace, P., Riva, A., Ricciato, A., Tevzadze, R., Janiashvili, A., Sanishvili, A., Alania, V., Enikidze, O., 2019. The Control of Pre-Existing Faults on the Development of Thrust-Related Folds in the Kura Foreland Fold-and-Thrust Belt (Norio License Block, Onshore Georgia), in: AAPG European Region Annual Conference, Paratethys Petroleum Systems Between Central Europe and the Caspian Region. Vienna, Austria, p. March 26-27.

Paknia, M., Ballato, P., Heidarzadeh, G., Cifelli, F., Hassanzadeh, J., Vezzoli, G., Mirzaie Ataabadi, M., Ghassemi, M.R., Mattei, M., 2021. Neogene Tectono-Stratigraphic Evolution of the Intermontane Tarom Basin: Insights Into Basin Filling and Plateau Building Processes Along the Northern Margin of the Iranian Plateau (Arabia-Eurasia Collision Zone). Tectonics 40, 1–36. https://doi.org/10.1029/2020TC006254

Pape, T., Blumenberg, M., Reitz, A., Scheeder, G., Schmidt, M., Haeckel, M., Blinova, V.N., Ivanov, M.K., Sahling, H., Wallmann, K., Bohrmann, G., 2021. Oil and gas seepage offshore Georgia (Black Sea) – Geochemical evidences for a Paleogene-Neogene hydrocarbon source rock. Mar. Pet. Geol. 128. https://doi.org/10.1016/j.marpetgeo.2021.104995

Patton, D.K., 1993. Samgori Field, Republic of Georgia: Critical Review of Island-Arc Oil and Gas. J. Pet. Geol. 16, 153–167. https://doi.org/10.1111/j.1747-5457.1993.tb00103.x

Patton, T.L., Moustafa, A.R., Nelson, R.A., Abdine, S.A., 1994. Tectonic Evolution and Structural Setting of the Suez Rift: Chapter 1: Part I. Type Basin: Gulf of Suez, in:

Landon, S.M., Coury, A.B. (Eds.), Interior Rift Basins. AAPG Memoir 59, pp. 9–55. https://doi.org/10.1306/M59582

Pupp, M., Bechtel, A., Ćorić, S., Gratzer, R., Rustamov, J., Sachsenhofer, R.F., 2018. Eocene and Oligo-Miocene source rocks in the Rioni and Kura Basins of Georgia: depositional environment and petroleum potential. J. Pet. Geol. 41, 367–392. https://doi.org/10.1111/jpg.12708

Reilinger, R., McClusky, S., Vernant, P., Lawrence, S., Ergintav, S., Cakmak, R., Ozener, H., Kadirov, F., Guliev, I., Stepanyan, R., Nadariya, M., Hahubia, G., Mahmoud, S., Sakr, K., ArRajehi, A., Paradissis, D., Al-Aydrus, A., Prilepin, M., Guseva, T., Evren, E., Dmitrotsa, A., Filikov, S. V., Gomez, F., Al-Ghazzi, R., Karam, G., 2006. GPS constraints on continental deformation in the Africa-Arabia-Eurasia continental collision zone and implications for the dynamics of plate interactions. J. Geophys. Res. Solid Earth 111, 1–26. https://doi.org/10.1029/2005JB004051

Robinson, A.G., Griffith, E.T., Gardiner, A.R., Home, A.K., 1997. Petroleum geology of the georgian fold and thrust belts and foreland basins, in: Robinson, A.G. (Ed.), Regional and Petroleum Geology of the Black Sea and Surrounding Region: AAPG Memoirs 68. pp. 347–367.

Rolland, Y., Hässig, M., Bosch, D., Bruguier, O., Melis, R., Galoyan, G., Topuz, G., Sahakyan, L., Avagyan, A., Sosson, M., 2019. The East Anatolia–Lesser Caucasus ophiolite: An exceptional case of large-scale obduction, synthesis of data and numerical modelling. Geosci. Front. 11, 83–108. https://doi.org/10.1016/j.gsf.2018.12.009

Rolland, Y., Sosson, M., Adamia, S.A., Sadradze, N., 2011. Prolonged Variscan to Alpine history of an active Eurasian margin (Georgia, Armenia) revealed by 40Ar/39Ar dating. Gondwana Res. 20, 798–815. https://doi.org/10.1016/j.gr.2011.05.007

Sachsenhofer, R.F., 2001. Syn- and post-collisional heat flow in the cenozoic Eastern Alps.

Int. J. Earth Sci. 90, 579–592. https://doi.org/10.1007/s005310000179

Sachsenhofer, R.F., Bechtel, A., Gratzer, R., Enukidze, O., Janiashvili, A., Nachtmann, W., Sanishvili, A., Tevzadze, N., Yukler, M.A., 2021. Petroleum Systems in the Rioni and Kura Basins of Georgia. J. Pet. Geol. 44, 287–316. https://doi.org/10.1111/jpg.12794

Sachsenhofer, R.F., Popov, S. V., Coric, S., Mayer, J., Misch, D., Morton, M.T., Pupp, M., Rauball, J., Tari, G., 2018. Paratethyan petroleum source rocks: an overview. J. Pet. Geol. 41, 219–245. https://doi.org/10.1111/jpg.12702

Sangin, S., Buntebarth, G., Weller, A., Melikadze, G., 2018. Temperature Gradient Measurements in Hydrothermal Areas of Georgia. Int. J. Terr. Heat Flow Appl. 1, 14–17. https://doi.org/10.31214/ijthfa.v1i1.7

Schito, A., Andreucci, B., Aldega, L., Corrado, S., Di Paolo, L., Zattin, M., Szaniawski, R., Jankowski, L., Mazzoli, S., 2018. Burial and exhumation of the western border of the Ukrainian Shield (Podolia): a multi-disciplinary approach. Basin Res. 30, 532–549. https://doi.org/10.1111/bre.12235

Schito, A., Corrado, S., Aldega, L., Grigo, D., 2016. Overcoming pitfalls of vitrinite reflectance measurements in the assessment of thermal maturity: The case history of the lower Congo basin. Mar. Pet. Geol. 74, 59–70. https://doi.org/10.1016/j.marpetgeo.2016.04.002

Sclater, J.G., Christie, P.A.F., 1980. Continental stretching: an explanation of the post-mid-Cretaceous subsidence of the Central North Sea Basin. J. Geophys. Res. 85, 3711–3739.

Shatilova, I.I., Maissuradze, L.S., Koiava, K.P., Kokolashvili, I.M., Bukhsianidze, M.G., Bruch, A.A., 2020. The environmental history of Georgia during the Late Miocene based of foraminifera and pollen. Universal, Tbilisi.

Shaw, J.H., Connors, C., Suppe, J., 2006. Seismic interpretation of contractional fault-related folds. AAPG Studies in Geology, Volume 53. https://doi.org/10.1306/St531003

Sokhadze, G., Floyd, M., Godoladze, T., King, R., Cowgill, E.S., Javakhishvili, Z., Hahubia, G., Reilinger, R., 2018. Active convergence between the Lesser and Greater Caucasus in Georgia: Constraints on the tectonic evolution of the Lesser–Greater Caucasus continental collision. Earth Planet. Sci. Lett. 481, 154–161. https://doi.org/10.1016/j.epsl.2017.10.007

Stampfli, G.M., Hochard, C., 2009. Plate tectonics of the Alpine realm, in: Murphy, J.B., Keppie, J.D., Hynes, A.J. (Eds.), Ancient Orogens and Modern Analogues. Geological Society, London, Special Publications 327, pp. 89–111. https://doi.org/10.1144/SP327.6

Stratochem Egypt, 2014. Cuttings & Outcrop Samples_TOC% & Pyrolysis Data.

Sukhishvili, L., Forte, A.M., Merebashvili, G., Leonard, J., Whipple, K.X., Javakhishvili, Z., Heimsath, A., Godoladze, T., 2020. Active deformation and Plio-Pleistocene fluvial reorganization of the western Kura fold-thrust belt, Georgia: Implications for the evolution of the Greater Caucasus Mountains. Geol. Mag. https://doi.org/10.1017/S0016756820000709

Sweeney, J.J., Burnham, A.K., 1990. Evaluation of a Simple Model of Vitrinite Reflectance Based on Chemical Kinetics. Am. Assoc. Pet. Geol. Bull. 74, 1559–1570.

Tari, G., Vakhania, D., Tatishvili, G., Mikeladze, V., Gogritchiani, K., Vacharadze, S., Mayer, J., Sheya, C., Siedl, W., Banon, J.J.M., Sanchez, J.T., 2018. Stratigraphy, structure and petroleum exploration play types of the Rioni Basin, Georgia, in: Simmons, M.D., Tari, G.C., Okay, A.I. (Eds.), Petroleum Geology of the Black Sea. Geological Society, London, Special Publications 464, pp. 403–438. https://doi.org/https://doi.org/10.1144/SP464.14

Tari, G., Vrsic, A., Gumpenberger, T., Mekonnen, E., Hujer, W., Fallah, M., Tevzadze, N., Janiashvili, A., Pace, P., Ricciato, A., Alania, V., Enukidze, O., 2021. Eocene volcaniclastics in the Kartli Basin, Georgia: a fractured reservoir sequence. J. Pet. Geol.

44, 413–433. https://doi.org/10.1111/jpg.12795

Tibaldi, A., Tsereteli, N., Varazanashvili, O., Babayev, G., Barth, A., Mumladze, T., Bonali, F.L., Russo, E., Kadirov, F., Yetirmishli, G., Kazimova, S., 2019. Active stress field and fault kinematics of the Greater Caucasus. J. Asian Earth Sci. 104108. https://doi.org/10.1016/j.jseaes.2019.104108

Tissot, B.P., Welte, D.H., 1978. Petroleum formation and occurrence; a new approach to oil and gas exploration. Springer-Verlag, Berlin, Heidelberg, New York.

Trikhunkov, Y., Kangarli, T.N., Bachmanov, D.M., Frolov, P.D., Shalaeva, E.A., Latyshev, A.V., Simakova, A.N., Popov, S.V., Bylinskaya, M.E., Aliyev, F.A., 2021. Evaluation of Plio-Quaternary uplift of the South-Eastern Caucasus based on the study of the Akchagylian marine deposits and continental molasses. Quat. Int. https://doi.org/10.1016/j.quaint.2021.04.043

Tsereteli, N., Tibaldi, A., Alania, V., Gventsadse, A., Enukidze, O., Varazanashvili, O., Müller, B.I.R., 2016. Active tectonics of central-western Caucasus, Georgia. Tectonophysics 691, 328–344. https://doi.org/10.1016/j.tecto.2016.10.025

USSR Geological Survey, 1971. 1 : 25.000 geological maps of Georgia, Sheet K38.

Vasey, D.A., Cowgill, E., Roeske, S.M., Niemi, N.A., Godoladze, T., Skhirtladze, I., Gogoladze, S., 2020. Evolution of the Greater Caucasus basement and formation of the Main Caucasus Thrust, Georgia. Tectonics 39. https://doi.org/10.1029/2019TC005828

Vermeesch, P., 2009. RadialPlotter: A Java application for fission track, luminescence and other radial plots. Radiat. Meas. 44, 409–410. https://doi.org/10.1016/j.radmeas.2009.05.003

Vincent, S.J., Somin, M.L., Carter, A., Vezzoli, G., Fox, M., Vautravers, B., 2020. Testing models of Cenozoic exhumation in the Western Greater Caucasus. Tectonics 1–27. https://doi.org/10.1029/2018tc005451

Weides, S., Majorowicz, J., 2014. Implications of spatial variability in heat flow for geothermal resource evaluation in large foreland basins: The case of the Western Canada sedimentary basin. Energies 7, 2573–2594. https://doi.org/10.3390/en7042573

Yang, S., Horsfield, B., 2020. Critical review of the uncertainty of Tmax in revealing the thermal maturity of organic matter in sedimentary rocks. Int. J. Coal Geol. 225. https://doi.org/10.1016/j.coal.2020.103500

Yılmaz, A., Adamia, S.A., Chabukiani, A., Chkhotua, T., Erdoğan, K., Tuzcu, S., Karabiyikoğlu, M., 2000. Structural correlation of the southern Transcaucasus (Georgia)-eastern Pontides (Turkey), in: Bozkurt, E., Winchester, J.A., Piper, J.D.A. (Eds.), Tectonics and Magmatism in Turkey and the Surrounding Area. Geological Society of London, Special Publications 173, pp. 171–182.

Yılmaz, A., Adamia, S.A., Yılmaz, H., 2014. Comparisons of the suture zones along a geotraverse from the Scythian Platform to the Arabian Platform. Geosci. Front. 5, 855–875. https://doi.org/10.1016/j.gsf.2013.10.004

Yükler, A., Djavadova, A., Siradze, N., Spiller, R., 2000. The geology, geochemistry and basin modeling of the western Kura Basin depression, Georgia, in: AAPG Regional International Conference. Instanbul, Turkey, July 9-12, 2000.

Figure 1: Main tectonic units and structures of the Eastern Anatolia-Caucasus region superimposed on an ASTER GDEM shaded relief map (source: USGS) (modified after Gusmeo et al., 2021). ASASZ = Amasia-Sevan-Akera suture zone; D = Dzirula Massif; IAESZ = Izmir-Ankara-Erzinçan suture zone; K = Khrami Massif; L = Loki Massif; MCT = Main Caucasian Thrust. Red lines with triangles indicate thrusts; red lines are normal, strike-slip or unknown kinematics faults. Dashed rectangle indicates location of Figures 2 and 12. Inset: Tectonic sketch map of the Arabia-Eurasia collision zone. Red arrows represent selected GPS vectors after Reilinger et al. (2006); numbers indicate relative displacement with respect to stable Eurasia (in mm/yr). EAF = East Anatolian Fault; NAF = North Anatolian Fault.

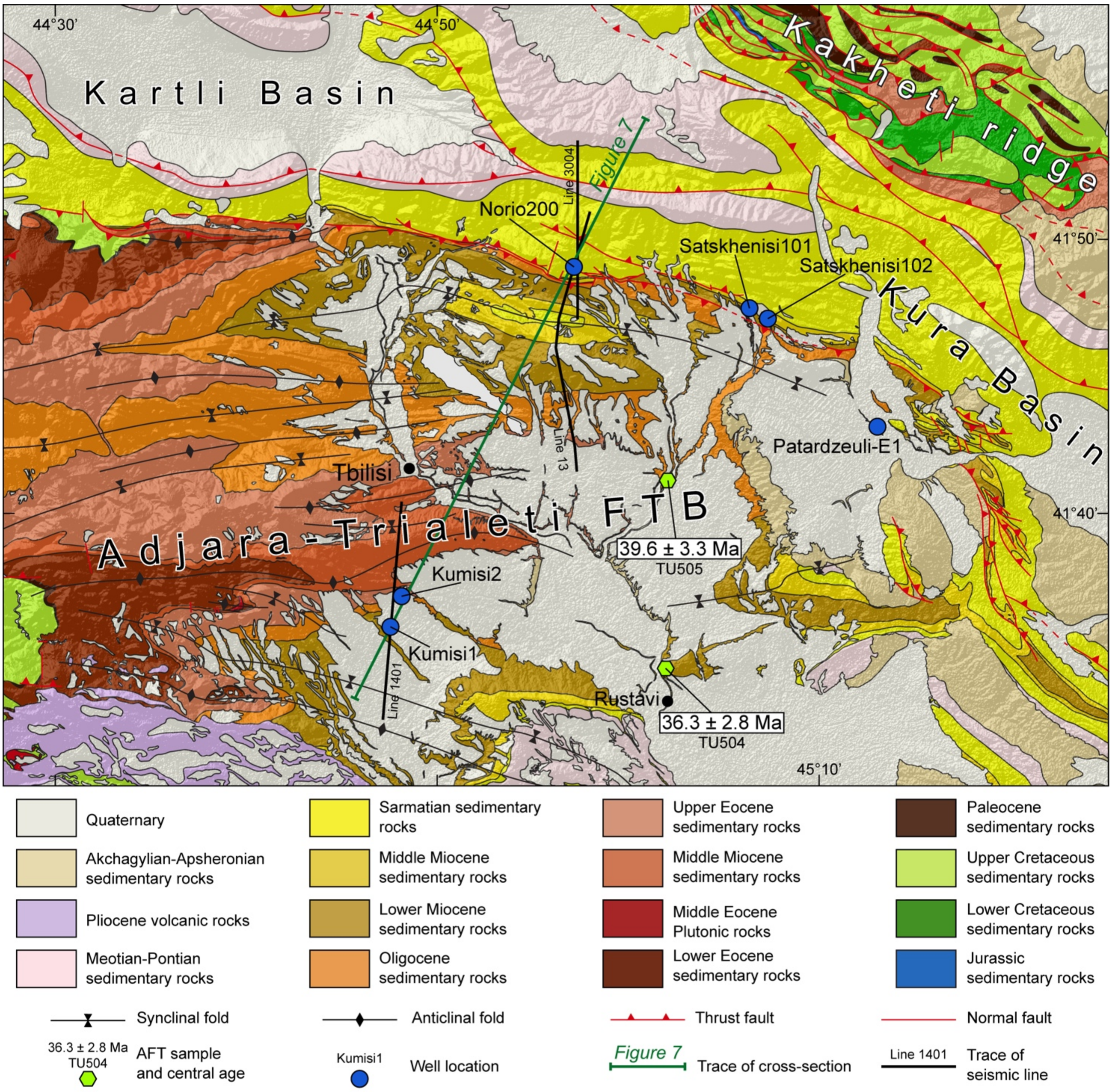

Figure 2: Geological map of the study area (USSR Geological Survey, 1971), with location of the six wells considered in this study, the two samples analysed for AFT inverse modelling, and the three seismic reflection profiles interpreted to build the cross-section in Figure 7. The trace of the cross-section in Figure 7 is also shown. Map location is indicated in Figure 1. See Figure 3 for regional stratigraphic stages.

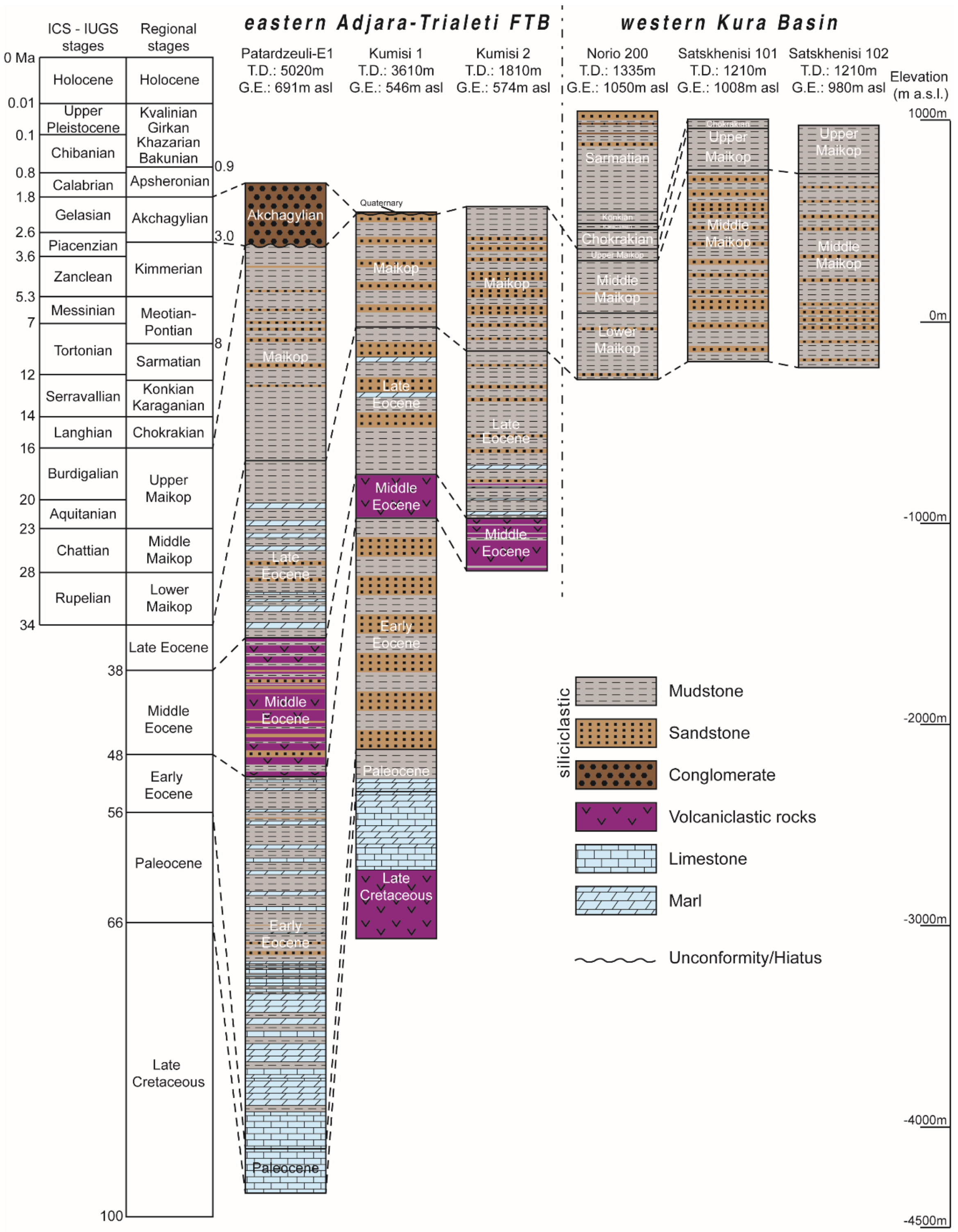

Figure 3: Detailed stratigraphy of the six wells analysed in this study, with total depth (T.D.) and ground elevation (G.E.) of the opening pit reported for each well. The chronostratigraphic chart at the left side is after Adamia et al. (2010), Lazarev et al. (2019) and Neubauer et al. (2015). Numerical ages after Cohen et al. (2021).

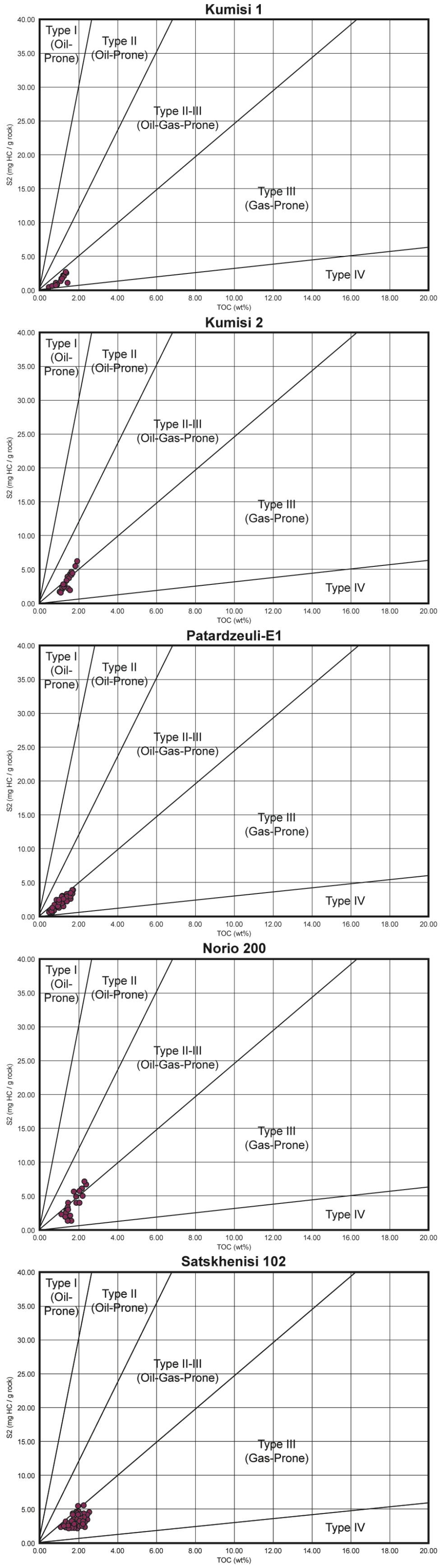

Figure 4: TOC vs S2 plots for the five wells for which thermal maturity data are available, showing the kerogen type of each data (prevailing Type III, alternatively Type II-III). Data from DIG (2014), Sachsenhofer et al. (2021), Stratochem Egypt (2014). See Supplementary Materials Figs. S1, S2, S3, S4, S5 for additional diagrams showing kerogen types with greater detail.

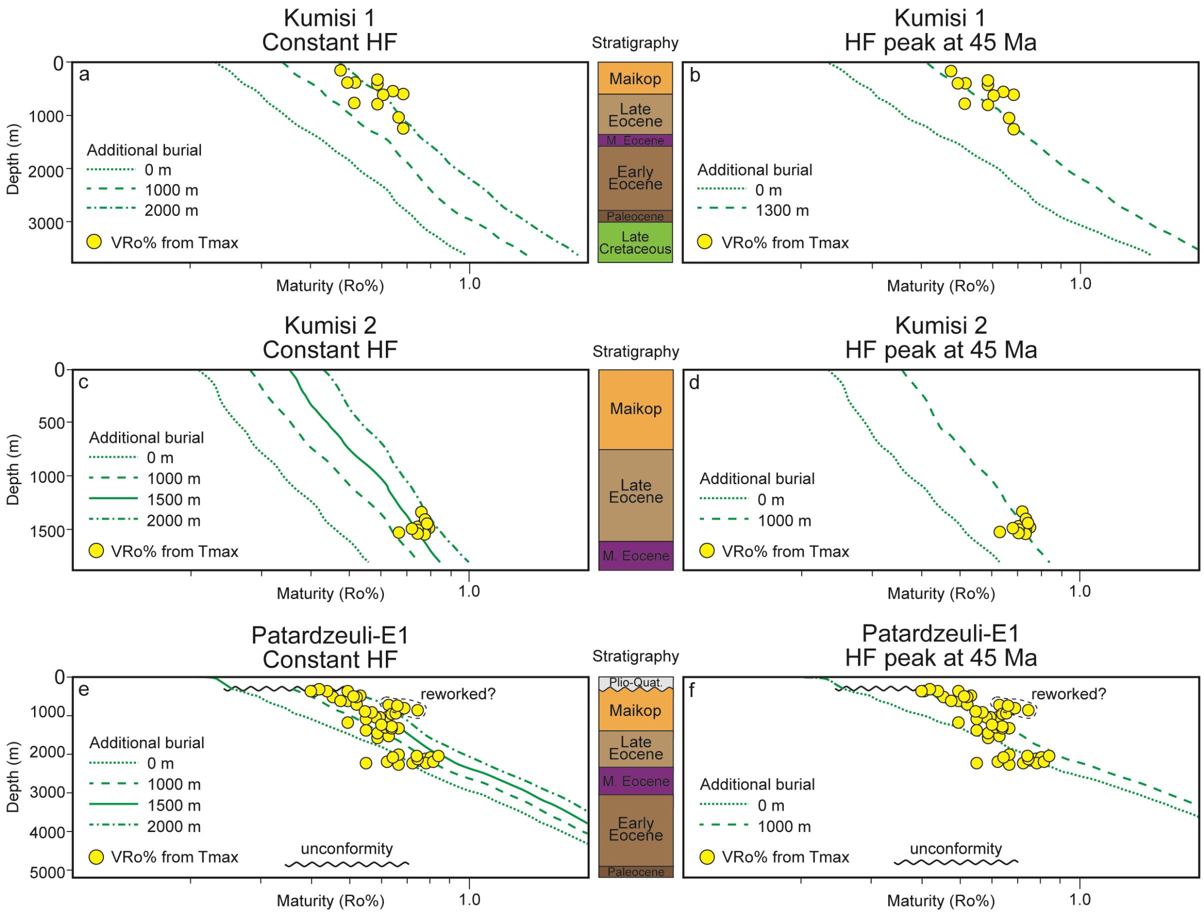

Figure 5: Sensitivity analysis for the three wells located in eastern Adjara-Trialeti FTB (see Fig. 2 for location), showing the different fitting of thermal maturity data with various amounts of additional burial, assuming a constant heat flow (a, c, and e) or a rifting model with an HF peak around 45 Ma (b, d and f). Data from Sachsenhofer et al. (2021), Stratochem Egypt (2014).

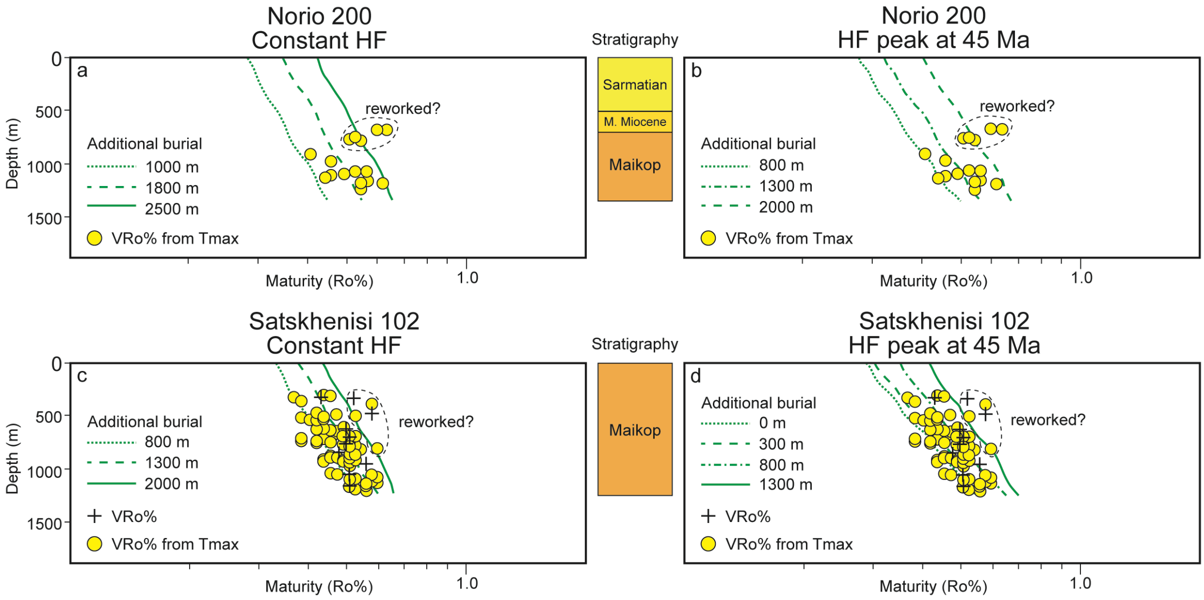

Figure 6: Sensitivity analysis for two of the wells located in the western Kura Basin (see Fig. 2 for location), showing the different fitting of thermal maturity data with various amounts of additional burial, assuming a constant heat flow (a, c) or a rifting model with an HF peak around 45 Ma (b and d). Data from DIG (2014), Sachsenhofer et al. (2021).

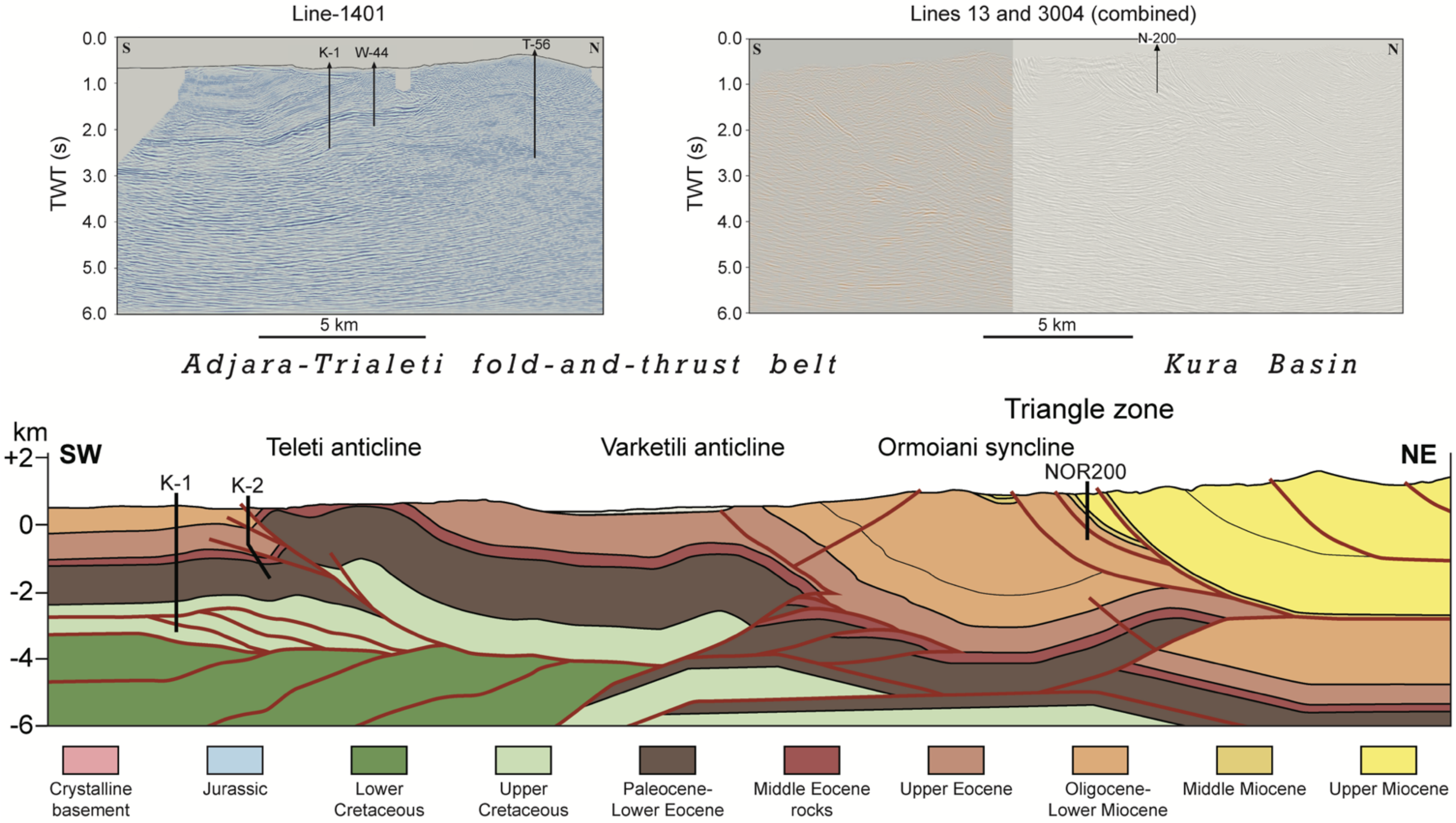

Figure 7: Geological cross-section based on the interpretation of three depth-migrated seismic reflection profiles (lines 1401, 13 and 3004) across the eastern Adjara-Trialeti FTB and the western Kura Basin. Uninterpreted seismic profiles are reported on top. Seismic interpretation by V. Alania and P. Pace. Wells are projected on the section (K-1 = Kumisi 1; K-2 = Kumisi 2; NOR200 = Norio 200). Original seismic data courtesy of Georgia Oil & Gas Limited. No vertical exaggeration. See Figure 2 for location of cross-section and seismic profiles.

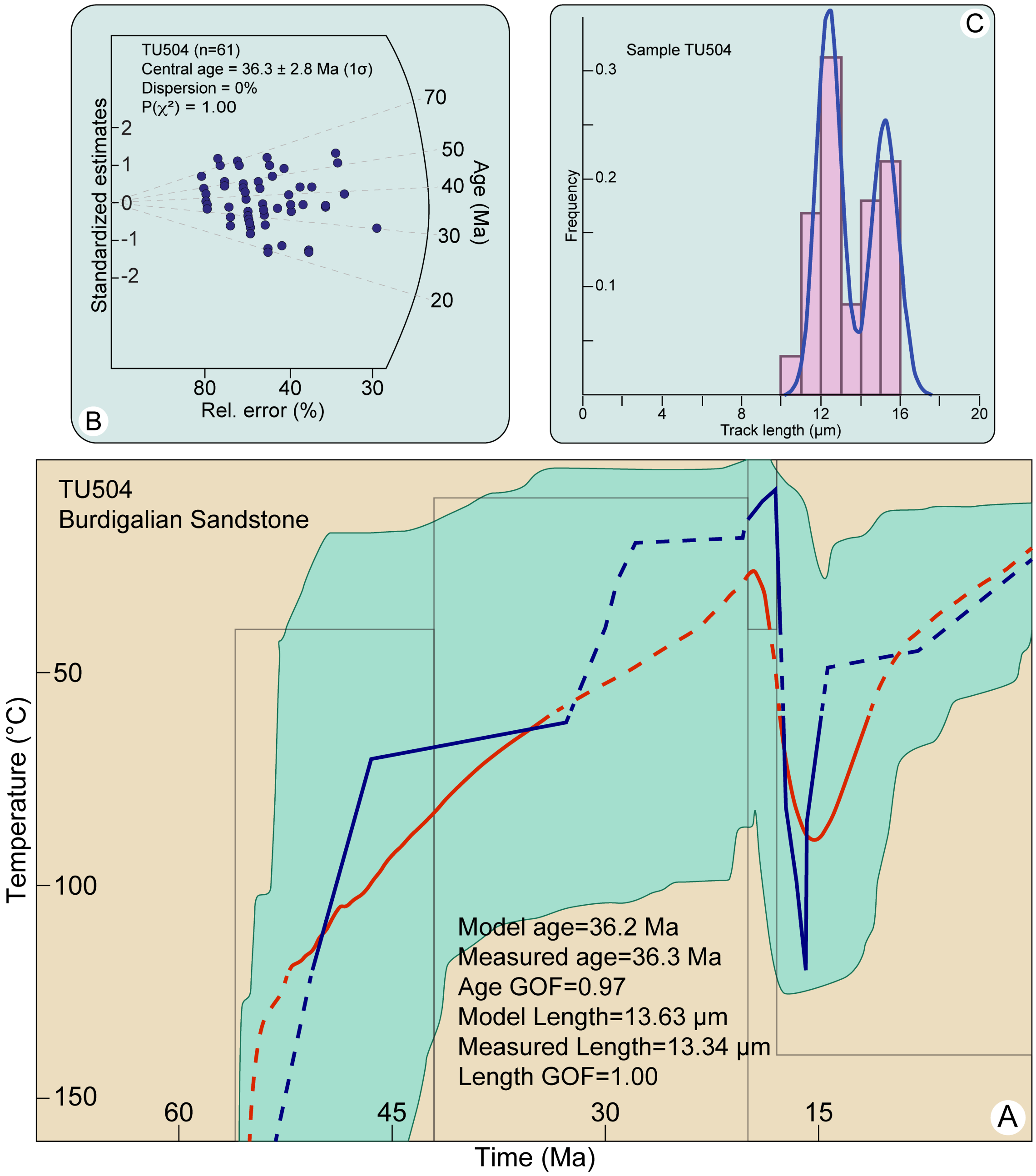

Figure 8: A) Time-temperature path obtained from inverse modelling of sample TU504. See Fig. 2 for sample location. Green area marks the envelope of all thermal histories that have a good (>0.5) fit with the data, red line represents the mean of all good paths, and the blue line is the best-fit time-temperature path. Parameters related to inverse modelling are reported: GOF, goodness-of-fit, gives an indication about the fit between observed and predicted data (values closer to 1 are best). B) Radial plot of single-grain AFT ages. C) D) Confined-track length frequency distribution.

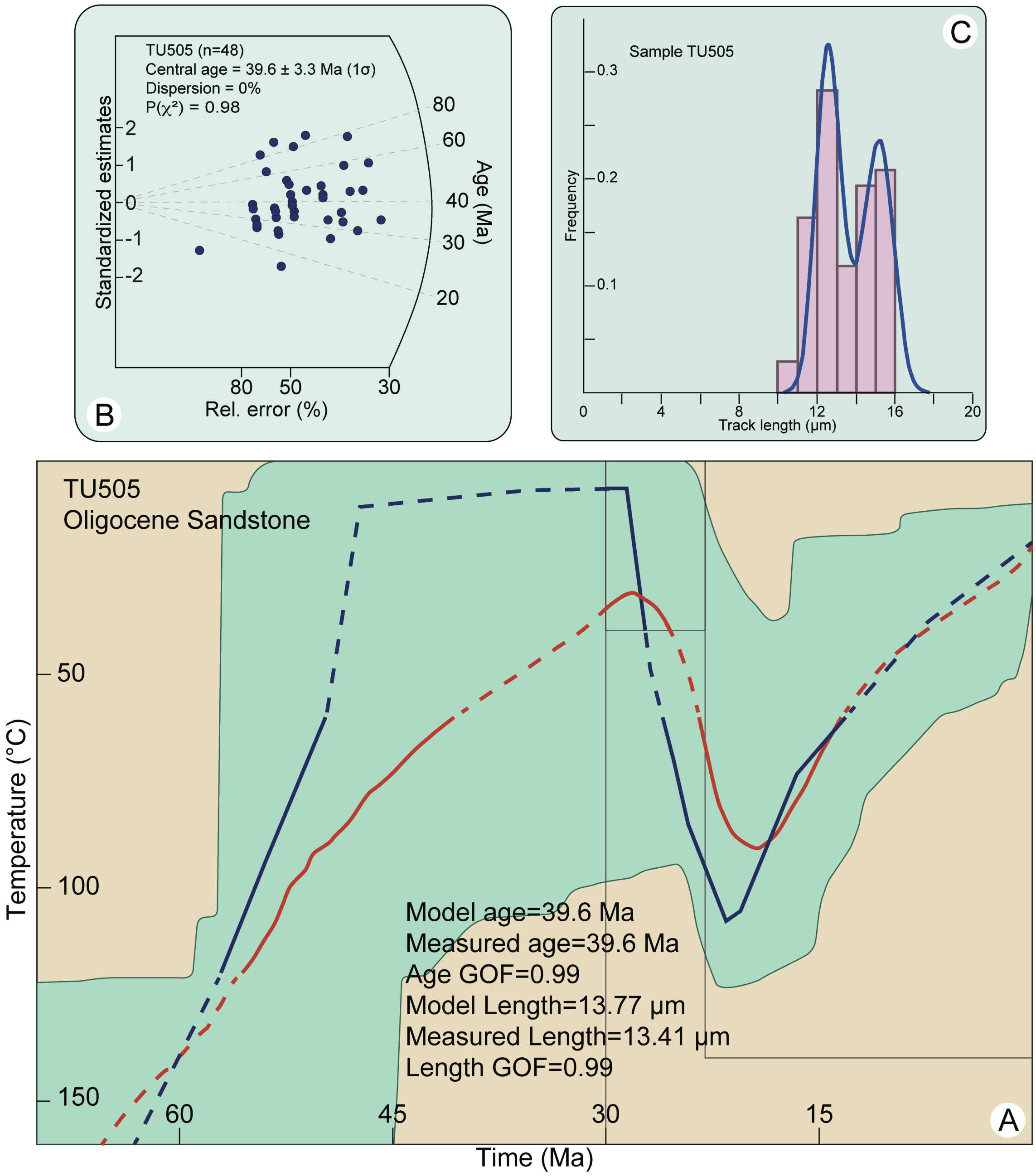

Figure 9: A) Time-temperature path obtained from inverse modelling of sample TU505. See Fig. 2 for sample location. Green area marks the envelope of all thermal histories that have a good (>0.5) fit with the data, red line represents the mean of all good paths, and the blue line is the best-fit time-temperature path. Parameters related to inverse modelling are reported: GOF, goodness-of-fit, gives an indication about the fit between observed and predicted data (values closer to 1 are best). B) Radial plot of single-grain AFT ages. C) Confined-track length frequency distribution.

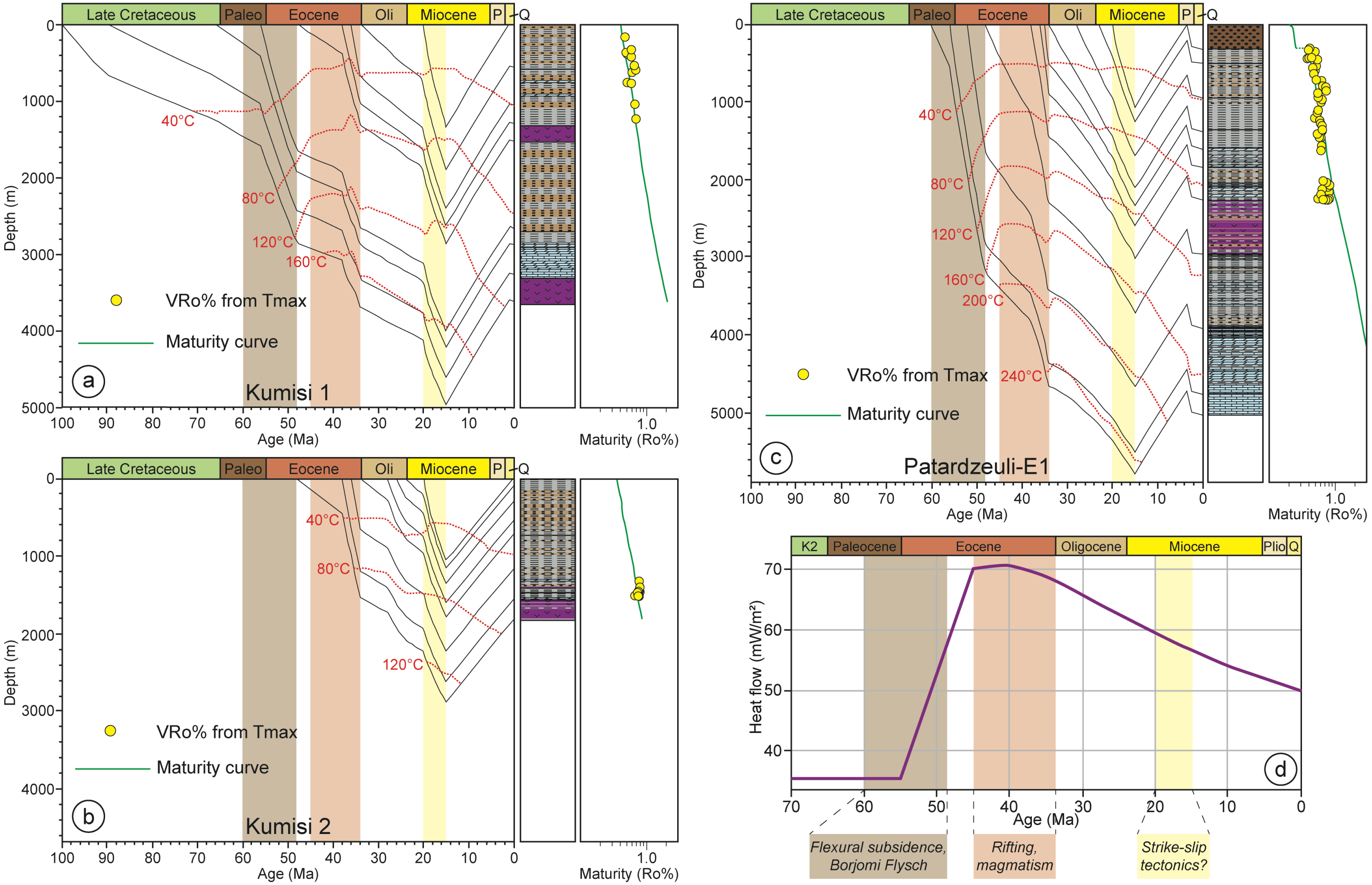

Figure 10: 1D burial and thermal history for the Kumisi 1 (a), Kumisi 2 (b) and Patardzeuli-E1 (c) wells, located in the eastern Adjara-Trialeti fold-and-thrust belt. See Fig. 2 for location. The models are calibrated against Tmax data. A rifting heat-flow model, with a peak around 45 Ma, was used for modelling (d). Vertical bars highlight the main subsidence pulses and the related tectonic events (see text for further discussion).

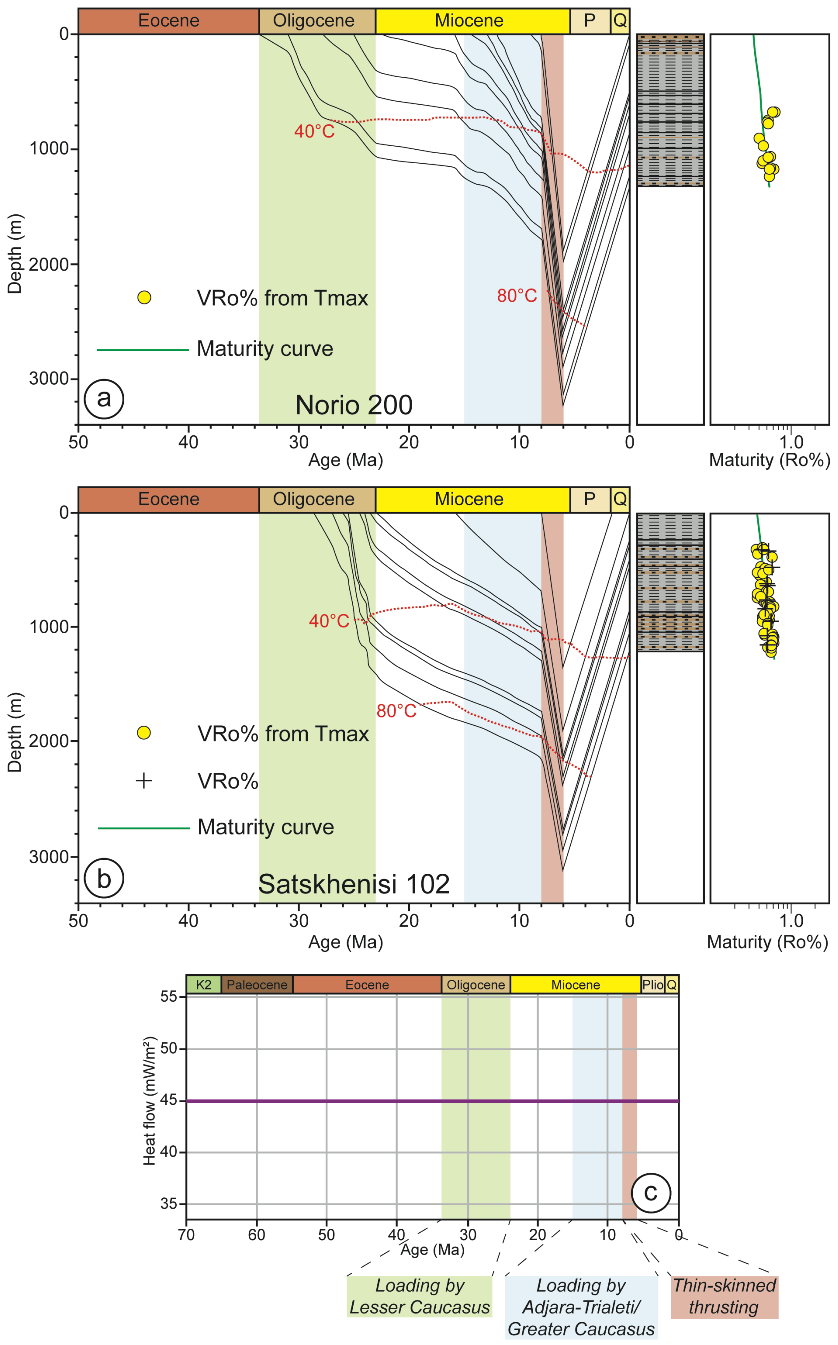

Figure 11: 1D burial and thermal history for the Norio 200 (a) and Satskhenisi 102 (b) wells, located in the western Kura Basin. See Fig. 2 for location. The models are calibrated against Tmax data (Norio 200) and Tmax and vitrinite reflectance data (Satskhenisi 102). A steady-state heat flow of 45 mW/m^2 was adopted (c). Vertical bars highlight the main subsidence pulses and the related tectonic events (see text for further discussion).

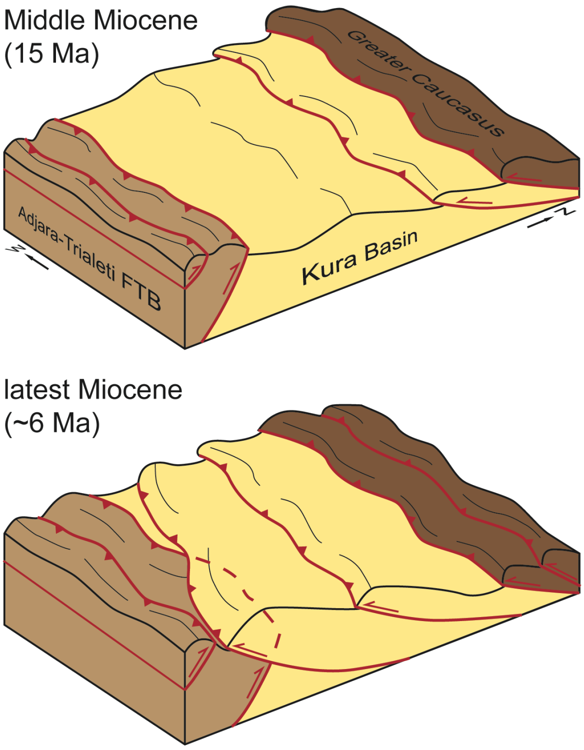
Middle Miocene
(15 Ma)

latest Miocene
(~6 Ma)

Figure 12: Block diagrams showing the Cenozoic tectonic evolution of the eastern Adjara-Trialeti FTB-western Kura Basin system (see Fig. 1 for location) as reconstructed in this paper. During the Middle Miocene the Kura Basin experienced cumulative subsidence due to structural inversion of the Adjara-Trialeti basin and southward propagation of the Greater Caucasus deformation front. In the latest Miocene south-directed thrusts reached the southern margin of the Kura Basin and covered the eastern Adjara-Trialeti FTB, forcing its eastward plunge. To the west the south-directed thrusts affecting the Kura Basin and the north-directed structures of the Adjara-Trialeti FTB were not yet interfering.

Table 1: Results of apatite fission-track analyses (see Fig. 2 for location of samples).

Sample	Rock Type	Age	Location	Elevation (m)	UTM Coordinates	No. crystals	Spontaneous		Induced		$P(\chi^2)$	Dosimeter		Age (Ma) ± 1s	MCTL (µm) ± standard error	Standard deviation	No. tracks measured	Mean D-par
							ρ_s	N_s	ρ_i	N_i		ρ_d	N_d					
TU504	Sandstone	Early Miocene (Burdigalian)	Eastern ATFTB	396	38T 0500933 4602375	61	0.15	333	0.81	1770	99.98	11.64	7276	36.3 ± 2.8	13.34 ± 0.17	1.57	83	2.75
TU505	Sandstone	middle-late Oligocene	Eastern ATFTB	512	38T 0500906 4615010	48	0.24	270	1.17	1307	97.99	11.57	7230	39.6 ± 3.3	13.41 ± 0.18	1.47	67	2.31

ATFTB = Adjara-Trialeti fold-and-thrust belt. MCTL = mean confined tracks length. Central ages are calculated using dosimeter U-free mica CN5 as external detector and $\zeta = 332.68 \pm 16.54$ (analyst T. Gusmeo); ρ_s= spontaneous track densities (x 10^5 cm^{-2}) measured in internal mineral surfaces; Ns= total number of spontaneous tracks; ρ_i and ρ_d= induced and dosimeter track densities (x 10^6 cm^{-2}) on external mica detectors (g= 0.5); N_i and N_d= total number of induced and dosimeter tracks; $P(\chi^2)$= probability of obtaining χ^2-value for n degrees of freedom (n= number of crystals-1): a probability >5% is indicative of a homogeneous population.

Table 2: Summary of thermal maturity data used as input for wells modelling. Average, minimum and maximum values of TOC (>0.5%), Rock-Eval Pyrolysis data (S1, S2, S3, Tmax, HI, OI) and vitrinite reflectance data (either measured in situ or calculated from Tmax) are provided, subdivided for age interval in each well analysed. Equivalent VR_o% in the Satskhenisi 102 well was calculated from Tmax using the equation by Jarvie et al. (2001). Data derive from DIG (2014), Sachsenhofer et al. (2021) and Stratochem Egypt (2014), and were kindly provided by the GOGC.

Well name	**GPS Coordinates (UTM Zone 38N)**	**Samples depth interval (m)**	**Age of interval**	**N° samples**	**TOC (>0.5) (%)** **Average** **min, max**	**S1 (mg/g)** **Average** **min, max**	**S2 (mg/g)** **Average** **min, max**	**S3 (mg/g)** **Average** **min, max**	**Tmax (°C)** **Average** **min, max**	**HI (mgHC/gTOC)** **Average** **min, max**	**OI (mgCO2/gTOC)** **Average** **min, max**	**VR_o% (measured)** **Average** **min, max**	**VR_o% (calculated from Tmax)** **Average** **min, max**
Kumisi 1	0482387 4605231	165-425	Maikop (Oligocene)	5	1.09 0.82, 1.46	0.08 0.05, 0.11	1.17 0.74, 1.72	1.17 0.75, 1.52	429 426, 432	107 73, 146	117 51, 185	- -	- -
		555-1245	Late Eocene	9	1.01 0.52, 1.36	0.08 0.05, 0.10	1.47 0.38, 2.67	0.92 0.66, 1.34	434 428, 437	136 74, 196	102 53,196	- -	- -
Kumisi 2	0483141 4607313	1340-1535	Late Eocene	21	1.44 1.05, 1.95	0.16 0.05, 0.27	3.30 1.55, 6.20	- -	439 434, 441	222 117, 318	- -	- -	- -
Patardzeuli	0515117 4618697	330-1350	Maikop (Oligocene-Early Miocene)	35	1.01 0.64, 1.26	0.15 0.08, 0.27	1.63 0.64, 2.92	- -	430 422, 440	158 96, 238	- -	- -	- -
		1380-2260	Late Eocene	45	1.18 0.59, 1.77	0.24 0.06, 0.55	1.98 0.57, 3.75	- -	436 430, 445	160 97, 212	- -	- -	- -
Norio 200	0494735 4629461	665-675	Chokrakian	2	1.42 1.37, 1.46	0.16 0.14, 0.18	3.38 2.71, 4.04	- -	431 430, 432	238 198, 277	- -	- -	- -
		745-966	Middle Maikop (Late Oligocene)	5	1.47 1.13, 2.51	0.20 0.12, 0.24	2.83 1.36, 4.09	- -	424 419, 427	191 93, 228	- -	- -	- -
		1062-1233	Lower Maikop (Early Oligocene)	12	1.96 1.32, 2.93	0.28 0.06, 0.46	4.75 1.48, 7.13	- -	426 421, 431	234 90, 318	- -	- -	- -
Satskhenisi 101	0506512 4626657	-	-	-	-	-	-	-	-	-	-	-	-
Satskhenisi 102	0507754 4625925	309-1205	Middle Maikop (Late Oligocene)	78	1.88 0.50, 2.58	- -	2.85 2.05, 5.43	- -	424 417, 430	175 90, 260	55 25, 85	0.51 0.43, 0.56	0.48 0.35, 0.58

Table 3: Lithological data used as input for wells modelling, subdivided for each well. Keys for abbreviations are: mds = mudstone; sds = sandstone; cng = conglomerate; lms = limestone; tff = tuff.

Kumisi 1

Event name	Type	End Age (Ma)	Top depth (m)	Present thickness (m)	Eroded thickness (m)	Lithology				
						mds (%)	sds (%)	cng (%)	lms (%)	tff (%)
Quaternary	Formation	0.1	0	10	-	-	-	100	-	-
Erosion	Erosion	1	-	-	-1.300	-	-	-	-	-
Deposition (Maikop)	Deposit	15	-	-	1.300	100	-	-	-	-
Maikop	Formation	20	10	560	-	70	30	-	-	-
Late Eocene	Formation	34	570	500	-	45	45	-	10	-
	Formation	36	1.070	233	-	100	-	-	-	-
Middle Eocene	Formation	38	1.303	217	-	-	-	-	-	100
Early Eocene	Formation	48	1.520	1.150	-	50	50	-	-	-
Paleocene	Formation	56	2.670	210	-	70	-	-	30	-
Late Cretaceous	Formation	66	2.880	390	-	-	-	-	100	-
	Formation	90	3.270	339	-	-	-	-	-	100

Kumisi 2

Event name	Type	End Age (Ma)	Top depth (m)	Present thickness (m)	Eroded thickness (m)	Lithology				
						mds (%)	sds (%)	cng (%)	lms (%)	tff (%)
Erosion	Erosion	1	-	-	-1.000	-	-	-	-	-
Deposition (Maikop)	Deposit	15	-	-	1.000	100	-	-	-	-
Maikop	Formation	20	0	100	-	100	-	-	-	-
	Formation	24	100	190	-	60	40	-	-	-
	Formation	26	290	250	-	40	60	-	-	-
	Formation	28	540	180	-	90	10	-	-	-
Late Eocene	Formation	34	720	440	-	90	10	-	-	-
	Formation	36	1.160	390	-	80	10	-	10	-
Middle Eocene	Formation	38	1.550	260	-	-	-	-	-	100

Patardzeuli-E1

Event name	Type	End Age (Ma)	Top depth (m)	Present thickness (m)	Eroded thickness (m)	Lithology				
						mds (%)	sds (%)	cng (%)	lms (%)	tff (%)
Quaternary	Formation	0.1	0	40	-	-	-	100	-	-
Akchagylian	Formation	2.5	40	270	-	-	-	100	-	-
Erosion	Erosion	3.5	-	-	-1.000	-	-	-	-	-
Deposition (Maikop)	Deposit	15	-	-	1.000	100	-	-	-	-
Maikop	Formation	20	310	195	-	100	-	-	-	-
	Formation	23	505	445	-	80	20	-	-	-
	Formation	28	950	415	-	90	10	-	-	-
Late Eocene	Formation	34	1.365	225	-	100	-	-	-	-
	Formation	35	1.590	260	-	60	-	-	40	-
	Formation	36	1.850	410	-	80	20	-	-	-
Middle Eocene	Formation	38	2.260	690	-	-	-	-	-	100
Early Eocene	Formation	48	2.950	960	-	70	-	-	30	-
	Formation	52	3.910	840	-	20	-	-	80	-
Paleocene	Formation	56	4.750	270	-	-	-	-	100	-

Norio 200

Event name	Type	End Age (Ma)	Top depth (m)	Present thickness (m)	Eroded thickness (m)	Lithology				
						mds (%)	sds (%)	cng (%)	lms (%)	tff (%)
Erosion	Erosion	0.1	-	-	-1.800	50	50	-	-	-
Deposition (Late Miocene)	Deposit	6	-	-	1.800	50	50	-	-	-
Sarmatian	Formation	8	0	85	-	50	50	-	-	-
	Formation	9	85	415	-	80	20	-	-	-
Konkian	Formation	12	500	60	-	100	-	-	-	-
Karaganian	Formation	13	560	30	-	100	-	-	-	-
Chokrakian	Formation	14.5	590	95	-	100	-	-	-	-
Upper Maikop (Early Miocene)	Formation	16	685	55	-	100	-	-	-	-
Middle Maikop (Late Oligocene)	Formation	23	740	130	-	100	-	-	-	-
	Formation	25	870	132	-	90	10	-	-	-
Lower Maikop (Early Oligocene)	Formation	28	1.002	250	-	100	-	-	-	-
	Formation	31	1.252	83	-	90	10	-	-	-

Satskhenisi 102

Event name	Type	End Age (Ma)	Top depth (m)	Present thickness (m)	Eroded thickness (m)	Lithology				
						mds (%)	sds (%)	cng (%)	lms (%)	tff (%)
Erosion	Erosion	0.1	-	-	-1.800	50	50	-	-	-
Deposition (Middle-Late Miocene)	Deposit	6	-	-	1.300	50	50	-	-	-
Deposition (Middle-Late Miocene)	Deposit	8	-	-	500	50	50	-	-	-
Upper Maikop (Early Miocene)	Formation	16	0	240	-	100	-	-	-	-
Middle Maikop (Late Oligocene)	Formation	23	240	30	-	100	-	-	-	-
	Formation	23.5	270	135	-	90	10	-	-	-
	Formation	24	405	60	-	60	40	-	-	-
	Formation	24.5	465	390	-	80	20	-	-	-
	Formation	25.5	855	45	-	60	40	-	-	-
	Formation	26	900	140	-	50	50	-	-	-
	Formation	27	1040	170	-	90	10	-	-	-

Supplementary Materials

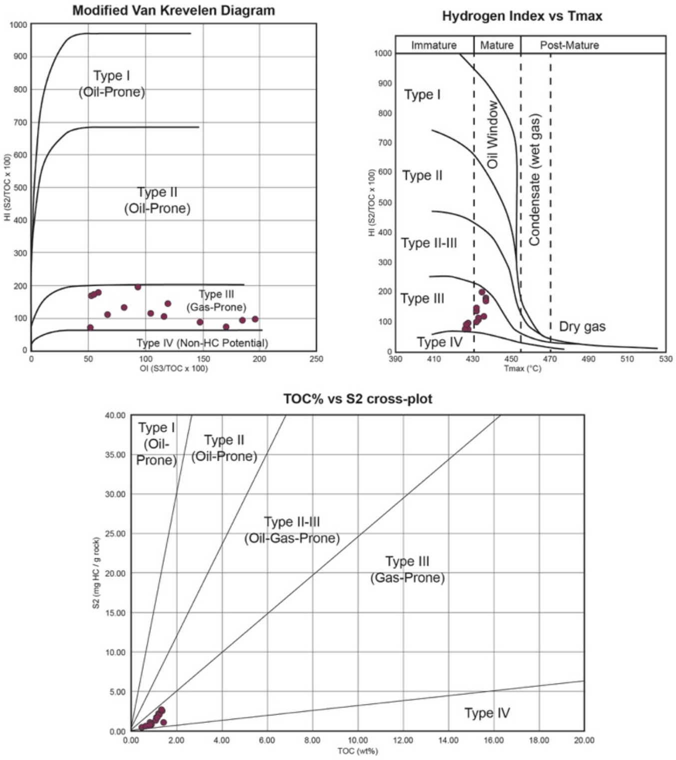

Figure 1: Diagrams showing the kerogen type of the samples analysed from the Kumisi 1 well.

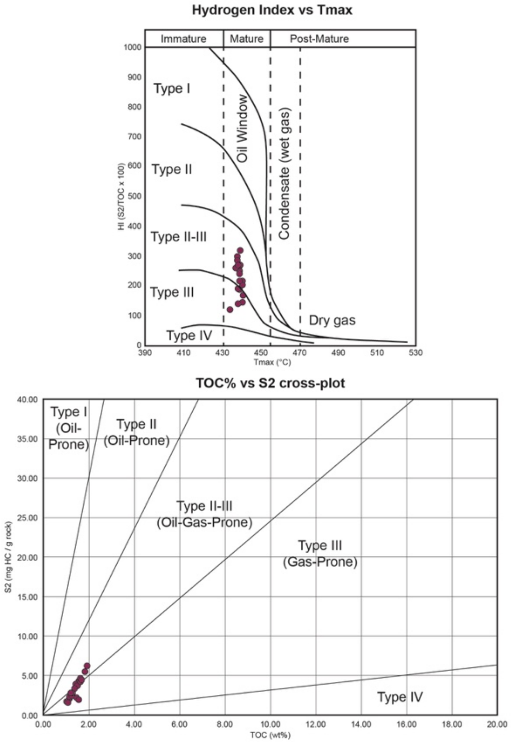

Figure 2: Diagrams showing the kerogen type of the samples analysed from the Kumisi 2 well.

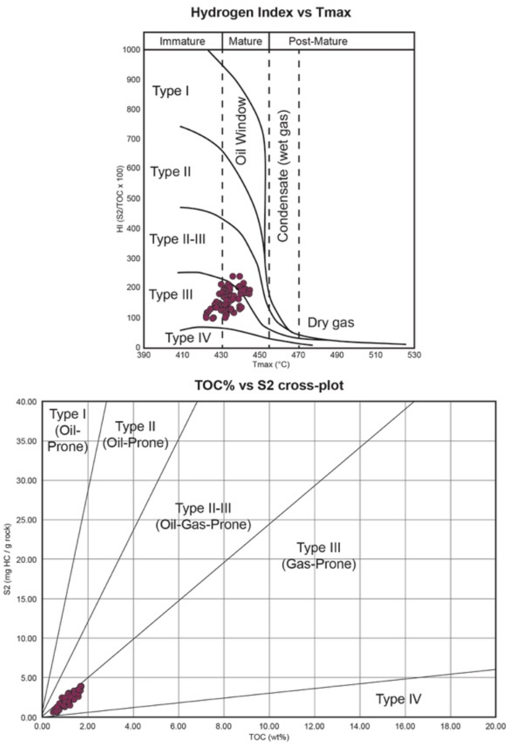

Figure 3: Diagrams showing the kerogen type of the samples analysed from the Patardzeuli-E1 well.

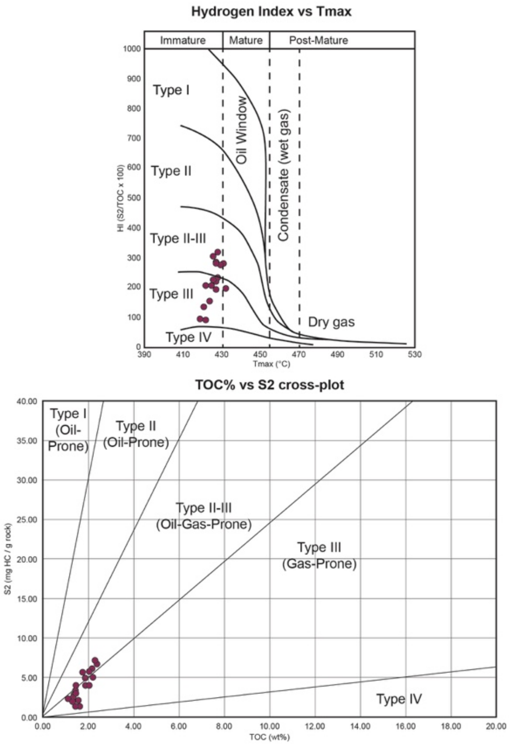

Figure 4: Diagrams showing the kerogen type of the samples analysed from the Norio 200 well.

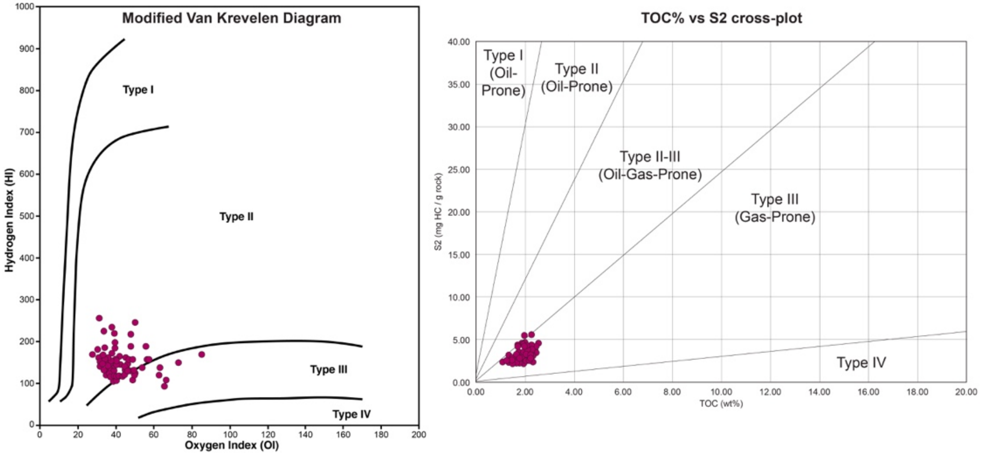

Figure 6: Diagrams showing the kerogen type of the samples analysed from the Satskhenisi 102 well.

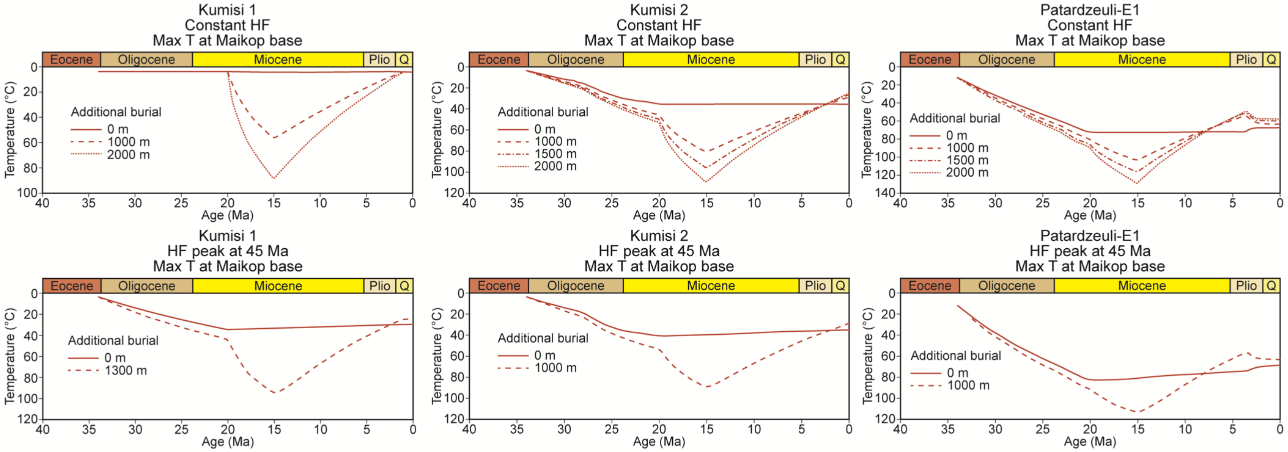

Figure 5: Calculated temperature at the base of the Maikop Group rocks, according to the modelling results, computed using the two different HF scenarios and assuming different amounts of additional burial.

Depth interval (m)	**Sample Depth [m]**	**Sample type**	**S_1 [mgHC/g]**	**S_2 [mgHC/g]**	**S_3 [mgHC/g]**	**T_{max} [°C]**	**TOC [%]**	**PI [-]**	**HI [mgHC/gTOC]**	**OI [mgCO2/gTOC]**	**Interval age**
0-10	-	-	-	-	-	-	-	-	-	-	Quaternary
10-570	165	cutting	0.05	1.06	0.75	426	1.46	0.05	73	51	Maikop (Oligocene)
	335	cutting	0.08	1.55	0.94	432	1.16	0.05	134	81	
	378	cutting	0.10	0.77	1.52	428	0.82	0.11	94	185	
	385	cutting	0.08	0.74	1.23	427	0.83	0.10	89	147	
	425	cutting	0.11	1.72	1.41	432	1.18	0.06	146	119	
570-1303	555	cutting	0.10	2.67	1.27	435	1.36	0.04	196	93	Late Eocene
	595	cutting	0.07	2.20	0.72	437	1.23	0.03	179	59	
	605	cutting	0.06	2.11	0.67	437	1.22	0.03	173	55	
	615	cutting	0.08	0.90	1.01	433	0.87	0.08	104	116	
	625	cutting	0.06	0.95	0.57	433	0.85	0.06	112	67	
	765	cutting	0.05	0.38	0.88	428	0.52	0.12	74	171	
	785	cutting	0.07	0.67	1.34	432	0.68	0.09	98	196	
	795	cutting	0.05	0.26	1.43	425	0.36	0.16	73	402	
	815	cutting	0.04	0.28	1.26	431	0.44	0.13	64	286	
	825	cutting	0.06	0.30	1.05	432	0.47	0.17	65	226	
	845	cutting	0.05	0.31	1.30	433	0.47	0.14	66	278	
	855	cutting	0.05	0.27	1.28	430	0.44	0.16	62	294	
	1005	cutting	0.04	0.28	0.65	438	0.48	0.13	58	136	
	1055	cutting	0.10	1.26	1.13	436	1.08	0.07	117	105	
	1245	cutting	0.16	2.11	0.66	437	1.25	0.07	169	53	
1303-1520	1353	cutting	0.09	0.39	0.74	435	0.44	0.19	89	169	Middle Eocene
1520-2670	1523	cutting	-	-	-	-	0.20	-	-	-	Early Eocene
	1558	cutting	-	-	-	-	0.21	-	-	-	
	1563	cutting	0.05	0.25	0.89	433	0.31	0.17	82	292	
	1593	cutting	-	-	-	-	0.26	-	-	-	
	1608	cutting	0.04	0.21	0.76	436	0.34	0.16	62	223	
	1633	cutting	0.08	0.29	0.85	434	0.35	0.22	83	244	
	1638	cutting	0.08	0.31	1.16	433	0.37	0.21	85	317	
	1643	cutting	0.09	0.30	1.22	433	0.38	0.23	80	325	
	1818	cutting	0.09	0.32	0.53	441	0.46	0.22	70	115	
	2053	cutting	0.07	0.20	1.14	444	0.30	0.26	66	376	
	2063	cutting	-	-	-	-	0.14	-	-	-	
	2083	cutting	-	-	-	-	0.26	-	-	-	
	2093	cutting	0.08	0.20	0.60	439	0.30	0.29	67	201	
	2098	cutting	-	-	-	-	0.28	-	-	-	
	2103	cutting	0.12	0.26	1.10	439	0.38	0.32	69	293	
	2158	cutting	0.26	0.77	1.31	336	0.39	0.25	196	333	
	2563	cutting	0.13	0.31	0.63	438	0.40	0.30	77	157	
	2593	cutting	0.25	0.36	0.83	318	0.35	0.41	103	236	
	2603	cutting	0.28	0.37	1.12	320	0.38	0.43	98	296	
	2673	cutting	-	-	-	-	0.15	-	-	-	
	2678	cutting	-	-	-	-	0.12	-	-	-	
2670-2880	2728	cutting	-	-	-	-	0.07	-	-	-	Paleocene
	2733	cutting	-	-	-	-	0.23	-	-	-	
2880-3609	2903	cutting	-	-	-	-	0.06	-	-	-	Late Cretaceous
	3003	cutting	-	-	-	-	0.08	-	-	-	
	3053	cutting	-	-	-	-	0.04	-	-	-	
	3203	cutting	-	-	-	-	0.03	-	-	-	

Table S1: Thermal maturity data derived from the analyses of the Kumisi 1 well samples. Data from Stratochem Egypt (2014).

Depth interval (m)	**Sample Depth [m]**	**Sample type**	**S_1 [mgHC/g]**	**S_2 [mgHC/g]**	**T_{max} [°C]**	**TOC [%]**	**S [%]**	**PI [-]**	**HI [mgHC/gTOC]**	**TIC [%]**	**TOC/S [-]**	**Calcite Equivalent [%]**	**Interval age**
0-720	-	cutting	-	-	-	-	-	-	-	-	-	-	Maikop (Oligocene-Early Miocene)
720-1550	1340	cutting	0.05	1.55	440	1.09	2.07	0.05	142	1.95	0.53	16.24	Late Eocene
	1440	cutting	0.09	1.72	441	1.05	3.04	0.06	163	1.14	0.35	9.50	
	1445	cutting	0.12	2.17	439	1.18	2.94	0.06	184	1.08	0.40	9.00	
	1450	cutting	0.13	2.34	440	1.19	2.91	0.06	196	1.37	0.41	11.43	
	1455	cutting	0.13	2.58	440	1.24	2.98	0.07	208	1.51	0.42	12.58	
	1460	cutting	0.14	2.68	439	1.25	2.82	0.08	214	1.65	0.44	13.79	
	1465	cutting	0.11	2.37	438	1.24	2.84	0.06	191	1.60	0.44	13.31	
	1470	cutting	0.12	2.48	440	1.24	2.85	0.07	200	1.69	0.43	14.09	
	1475	cutting	0.11	2.80	440	1.31	2.81	0.05	214	1.66	0.46	13.82	
	1480	cutting	0.18	3.34	439	1.40	2.73	0.08	238	1.93	0.51	16.07	
	1485	cutting	0.18	3.83	437	1.49	2.72	0.07	257	2.17	0.55	18.04	
	1490	cutting	0.24	4.23	438	1.58	2.84	0.07	268	2.05	0.56	17.05	
	1495	cutting	0.27	4.36	439	1.62	2.75	0.08	270	2.27	0.59	18.88	
	1500	cutting	0.25	4.68	438	1.67	2.84	0.07	280	2.09	0.59	17.43	
	1505	cutting	0.23	4.30	439	1.65	2.94	0.06	260	1.96	0.56	16.34	
	1510	cutting	0.23	4.43	439	1.68	2.90	0.06	263	1.95	0.58	16.27	
	1515	cutting	0.14	3.74	439	1.50	2.80	0.04	250	2.06	0.54	17.19	
	1520	cutting	0.07	2.11	438	1.51	2.78	0.05	139	2.27	0.55	18.89	
	1525	cutting	0.07	1.85	434	1.58	2.70	0.04	117	2.35	0.58	19.59	
	1530	cutting	0.21	5.46	438	1.85	2.71	0.04	296	2.32	0.68	19.30	
	1535	cutting	0.26	6.20	439	1.95	2.78	0.05	318	2.05	0.70	17.11	
	1550	cutting	-	-	-	0.52	0.81	-	-	1.33	0.64	11.09	
1550-1810	1570	cutting	-	-	-	0.56	1.03	-	-	1.27	0.54	10.62	Middle Eocene
	1585	cutting	-	-	-	0.12	0.36	-	-	1.29	0.34	10.72	
	1625	cutting	-	-	-	0.15	0.08	-	-	3.12	1.81	26.00	
	1650	cutting	-	-	-	0.68	1.24	-	-	1.12	0.55	9.37	
	1685	cutting	-	-	-	0.17	0.15	-	-	4.46	1.14	37.20	
	1730	cutting	-	-	-	0.07	0.05	-	-	1.97	1.52	16.38	
	1770	cutting	-	-	-	0.09	0.14	-	-	0.88	0.64	7.36	
	1790	cutting	-	-	-	0.15	0.08	-	-	7.50	1.76	62.51	
	1810	cutting	-	-	-	0.05	0.01	-	-	3.44	4.30	28.68	

Table S2: Thermal maturity data derived from the analyses of the Kumisi 2 well samples. Data from Sachsenhofer et al., 2021.

Depth interval (m)	Sample Depth [m]	Sample type	S_1 [mgHC/g]	S_2 [mgHC/g]	T_{max} [°C]	TOC [%]	S [%]	PI [-]	HI [mgHC/gTOC]	TIC [%]	TOC/S [-]	Calcite Equivalent [%]	Interval age
0-310	-	-	-	-	-	-	-	-	-	-	-	-	Akchagylian-Quaternary
310-1365	330	cutting	0.12	1.46	423	1.26	2.00	0.08	116	0.61	0.63	5.08	Maikop (Oligocene-Early Miocene)
	360	cutting	0.08	0.80	422	0.82	1.49	0.09	98	0.64	0.55	5.34	
	390	cutting	0.09	1.30	427	0.97	1.85	0.06	134	1.00	0.53	8.35	
	420	cutting	0.08	0.79	422	0.75	1.72	0.09	105	1.23	0.43	10.27	
	450	cutting	0.08	1.06	424	0.89	1.81	0.07	120	1.15	0.49	9.58	
	480	cutting	0.11	1.80	429	1.25	2.28	0.06	143	0.80	0.55	6.63	
	510	cutting	0.10	1.38	428	0.98	1.96	0.07	140	1.12	0.50	9.34	
	540	cutting	0.08	1.36	428	1.00	1.95	0.06	136	1.02	0.51	8.52	
	570	cutting	0.10	1.42	428	1.00	1.88	0.06	142	0.64	0.53	5.37	
	600	cutting	0.14	1.24	425	0.99	1.88	0.10	124	0.40	0.53	3.32	
	630	cutting	0.08	0.64	427	0.65	1.10	0.11	98	0.47	0.59	3.92	
	660	cutting	0.08	0.70	426	0.72	1.06	0.10	96	0.72	0.68	5.99	
	690	cutting	0.14	1.49	428	1.14	1.91	0.08	131	0.28	0.60	2.33	
	720	cutting	0.12	1.83	428	1.21	1.99	0.06	151	0.38	0.61	3.19	
	750	cutting	0.11	1.70	434	1.09	1.52	0.06	155	0.59	0.72	4.89	
	780	cutting	0.19	2.30	436	0.97	0.81	0.07	238	2.33	1.20	19.39	
	810	cutting	0.14	2.01	437	1.16	0.98	0.07	173	0.96	1,18	8.01	
	840	cutting	0.12	1.96	440	0.97	0.51	0.06	203	0.95	1.18	7.90	
	870	cutting	0.16	2.92	440	1.24	0.82	0.05	235	0.67	1.51	5.55	
	900	cutting	0.20	1.48	430	1.03	1.45	0.12	144	0.92	0.71	7.67	
	930	cutting	0.14	1.33	431	0.93	1.53	0.09	142	1.21	0.61	10.08	
	960	cutting	0.17	2.34	435	1.18	1.20	0.07	198	0.80	0.98	6.67	
	990	cutting	0.27	2.52	434	1.25	1.68	0.10	202	0.88	0.74	7.35	
	1020	cutting	0.22	1.98	434	1.04	1.32	0.10	191	0.76	0.79	6.32	
	1050	cutting	0.22	1.84	432	1.09	1.59	0.11	168	0.47	0.68	3.90	
	1080	cutting	0.21	1.78	433	1.05	1.60	0.11	170	0.66	0.65	5.54	
	1110	cutting	0.17	1.56	431	0.82	1.55	0.10	190	1.40	0.53	11.63	
	1140	cutting	0.25	1.76	430	0.99	1.56	0.12	178	1.30	0.63	10.84	
	1170	cutting	0.15	1.22	427	0.84	1.56	0.11	145	1.91	0.54	15.94	
	1200	cutting	0.11	0.91	427	0.64	1.34	0.10	142	1.83	0.48	15.28	
	1230	cutting	0.13	1.56	433	0.88	1.78	0.08	177	1.77	0.49	14.75	
	1260	cutting	0.16	1.97	433	1.21	1.90	0.07	163	1.06	0.64	8.85	
	1290	cutting	0.24	2.56	434	1.22	1.97	0.08	209	1.65	0.62	13.74	
	1320	cutting	0.22	2.16	435	1.13	1.60	0.09	192	1.21	0.70	10.06	
	1350	cutting	0.22	1.92	436	1.13	1.71	0.10	171	0.79	0.66	6.56	
1365-2260	1380	cutting	0.17	1.73	435	1.10	1.97	0.09	158	1.45	0.56	12.11	Late Eocene
	1410	cutting	0.16	1.12	430	0.91	1.52	0.12	122	1.40	0.60	11.65	
	1440	cutting	0.21	1.58	433	0.98	1.49	0.12	161	1.27	0.66	10.55	
	1470	cutting	0.31	2.70	432	1.44	1.86	0.10	187	1.27	0.77	10.61	
	1500	cutting	0.24	2.07	434	1.14	1.87	0.10	181	1.30	0.61	10.86	
	1530	cutting	0.16	1.60	434	0.86	1.71	0.09	185	1.77	0.50	14.71	
	1560	cutting	0.16	1.29	434	0.89	1.48	0.11	145	1.89	0.60	15.72	
	1590	cutting	0.28	2.43	434	1.15	2.04	0.10	212	1.82	0.56	15.17	
	1620	cutting	0.21	1.93	432	1.16	1.18	0.10	166	2.10	0.98	17.46	
	1650	cutting	0.11	1.07	433	0.78	0.99	0.09	137	1.45	0.79	12.04	
	1680	cutting	0.14	1.03	433	0.74	1.00	0.12	139	1.43	0.74	11.96	
	1710	cutting	0.08	0.73	432	0.65	1.03	0.09	112	1.51	0.63	12.54	
	1740	cutting	0.14	0.77	437	0.68	0.91	0.15	113	1.32	0.75	10.99	
	1770	cutting	0.10	0.91	432	0.75	1.00	0.10	120	1.46	0.75	12.13	
	1800	cutting	0.10	0.79	434	0.64	0.96	0.11	123	1.68	0.67	14.00	
	1830	cutting	0.19	1.99	431	1.09	1.56	0.09	182	1.05	0.70	8.72	
	1860	cutting	0.14	1.20	432	0.84	1.30	0.10	144	1.33	0.64	11.08	
	1890	cutting	0.10	0.96	432	0.79	1.19	0.09	121	1.49	0.66	12.38	
	1920	cutting	0.06	0.57	432	0.59	0.91	0.10	97	2.16	0.65	18.01	
	1950	cutting	0.09	0.75	433	0.68	1.01	0.11	109	2.36	0.68	19.63	
	1980	cutting	0.21	1.02	435	0.83	1.23	0.17	123	2.25	0.67	18.71	
	2010	cutting	0.19	1.08	435	0.84	1.33	0.15	128	2.14	0.63	17.79	
	2040	cutting	0.20	2.22	436	1.43	1.90	0.08	155	1.68	0.75	13.96	
	2070	cutting	0.18	1.28	440	1.02	1.50	0.12	125	2.17	0.68	18.08	
	2080	cutting	0.17	1.33	441	0.99	1.66	0.11	135	2.29	0.60	19.04	
	2090	cutting	0.37	3.03	445	1.61	2.62	0.11	188	2.02	0.61	16.79	

	2100	cutting	0.19	1.42	440	1.02	1.71	0.12	139	2.24	0.60	18.67	
	2110	cutting	0.37	2.62	443	1.47	2.52	0.12	178	1.98	0.58	16.50	
	2120	cutting	0.36	2.55	442	1.43	2.46	0.12	178	1.83	0.58	15.12	
	2130	cutting	0.22	2.49	435	1.51	2.30	0.08	165	1.57	0.66	13.08	
	2140	cutting	0.47	3.75	442	1.77	2.47	0.11	212	2.08	0.72	17.29	
	2150	cutting	0.34	2.93	441	1.63	2.22	0.10	180	1.68	0.73	13.96	
	2160	cutting	0.54	2.97	440	1.58	2.54	0.15	188	2.29	0.62	19.08	
	2170	cutting	0.45	2.72	441	1.43	2.43	0.14	190	2.10	0.59	17.46	
	2180	cutting	0.55	2.65	440	1.38	2.49	0.17	192	2.20	0.55	18.37	
	2190	cutting	0.23	2.55	434	1.50	2.23	0.08	170	1.50	0.67	12.46	
	2200	cutting	0.43	2.87	440	1.62	2.51	0.13	178	2.06	0.64	17.17	
	2210	cutting	0.45	2.52	440	1.38	2.31	0.15	183	1.60	0.60	13.33	
	2220	cutting	0.49	2.84	444	1.61	2.61	0.15	176	2.35	0.62	19.54	
	2230	cutting	0.50	2.74	444	1.54	2.33	0.15	178	2.52	0.66	20.96	
	2235	cutting	0.23	2.60	439	1.62	2.53	0.08	160	2.33	0.64	19.42	
	2245	cutting	0.07	3.13	430	1.51	2.06	0.02	208	4.89	0.73	40.76	
	2250	cutting	0.11	3.39	439	1.73	2.20	0.03	197	1.57	0.79	13.08	
	2255	cutting	0.18	2.88	442	1.50	2.00	0.06	193	1.55	0.75	12.88	
	2260	cutting	0.07	2.17	436	1.33	1.85	0.03	164	1.24	0.71	10.36	

Table S3: Thermal maturity data derived from the analyses of the Patardzeuli-E1 well samples. Data from Sachsenhofer et al., 2021.

Depth interval (m)	Sample Depth [m]	Sample type	S_1 [mgHC/g]	S_2 [mgHC/g]	T_{max} [°C]	TOC [%]	S [%]	PI [-]	HI [mgHC/gTOC]	TIC [%]	TOC/S [-]	Calcite Equivalent [%]	Interval age
0-500	450	cutting	-	-	-	0.81	-	-	-	-	-	-	Sarmatian
500-560	525	cutting	-	-	-	1.25	-	-	-	-	-	-	Konkian
	556	cutting	-	-	-	0.92	-	-	-	-	-	-	
560-590	580	cutting	-	-	-	1.06	-	-	-	-	-	-	Karaganian
590-685	635	cutting	-	-	-	0.73	-	-	-	-	-	-	Chokrakian
	665	cutting	0.18	4.04	430	1.46	1.72	0.04	277	0.31	0.85	2.57	
	670	cutting	-	-	-	1.49	-	-	-	-	-	-	
	675	cutting	0.14	2.71	432	1.37	1.39	0.05	198	0.46	0.98	3.79	
685-740	700	cutting	-	-	-	2.23	-	-	-	-	-	-	Upper Maikop (Early Miocene)
	715	cutting	-	-	-	1.54	-	-	-	-	-	-	
	735	cutting	-	-	-	1.81	-	-	-	-	-	-	
740-1002	745	cutting	0.22	3.32	426	1.46	1.72	0.06	228	0.31	0.85	2.57	Middle Maikop (Late Oligocene)
	760	cutting	0.21	3.02	425	1.46	1.95	0.07	206	0.48	0.75	3.98	
	765	cutting	-	-	-	1.95	-	-	-	-	-	-	
	780	cutting	-	-	-	1.81	-	-	-	-	-	-	
	780	cutting	0.23	4.09	427	1.86	2.17	0.05	220	0.45	0.86	3.75	
	795	cutting	-	-	-	1.81	-	-	-	-	-	-	
	810	cutting	-	-	-	2.43	-	-	-	-	-	-	
	825	cutting	-	-	-	2.51	-	-	-	-	-	-	
	905	cutting	0.12	1.36	419	1.45	2.28	0.08	93	0.26	0.64	2.20	
	910	cutting	-	-	-	2.08	-	-	-	-	-	-	
	966	cutting	0.24	2.35	422	1.13	1.97	0.09	208	0.64	0.57	5.33	
1002-1335	1038	cutting	-	-	-	2.65	-	-	-	-	-	-	Lower Maikop (Early Oligocene)
	1062	cutting	0.46	7.13	426	2.33	2.81	0.06	306	1.07	0.83	8.92	
	1065	cutting	0.35	5.68	428	1.79	2.47	0.06	318	1.25	0.72	10.41	
	1068	cutting	0.38	4.83		1.90	2.03	0.07	254	0.69	0.94	5.78	
	1080	cutting	-	-	-	2.79	-	-	-	-	-	-	
	1092	cutting	0.13	2.02	424	1.32	1.69	0.06	153	0.70	0.78	5.86	
	1095	cutting	-	-	-	2.09	-	-	-	-	-	-	
	1104	cutting	0.06	1.48	422	1.64	2.40	0.04	90	0.39	0.68	3.23	
	1113	cutting	-	-	-	2.43	-	-	-	-	-	-	
	1131	cutting	-	-	-	1.95	-	-	-	-	-	-	
	1131	cutting	0.13	2.17	421	1.60	2.60	0.06	136	0.60	0.61	4.97	
	1149	cutting	-	-	-	2.93	-			-	-	-	
	1149	cutting	0.31	5.11	428	2.20	2.57	0.06	232	1.00	0.86	8.33	
	1161	cutting	0.38	5.84	427	2.06	2.77	0.06	283	1,74	0.74	14.49	
	1167	cutting	-	-	-	2.93	-			-	-	-	
	1179	cutting	0.37	6.7	431	2.41	2.52	0.05	278	0.81	0.95	6.78	
	1185	cutting	-	-	-	2.72	-	-	-	-	-	-	
	1197	cutting	-	-	-	2.57	-	-	-	-	-	-	
	1215	cutting	-	-	-	2.57	-	-	-	-	-	-	
	1215	cutting	0.33	6.16	427	2.17	3.31	0.05	284	1.55	0.66	12.95	
	1221	cutting	0.12	3.98	427	2.06	2.69	0.03	194	0.91	0.76	7.55	
	1233	cutting	0.29	5.84	427	2.07	2.26	0.05	282	0.53	0.92	4.40	

Table S4: Thermal maturity data derived from the analyses of the Norio 200 well samples. Data from Sachsenhofer et al., 2021.

Depth interval (m)	Sample Depth [m]	Sample type	S_2 [mgHC/g]	TOC [%]	Ro% indigenous	Ro% all	VRE (Tmax)%	HI [mgHC/gTOC]	OI [mgCO2/gTOC]	Interval age
0-240	-	cutting	-	-	-	-	-	-	-	Upper Maikop (Early Miocene)
240-1210	246	cutting	-	1.51	-	-	-	90-260	25-85	Middle Maikop (Late Oligocene)
	255	cutting	-	1.33	-	-	-			
	264	cutting	-	1.58	-	-	-			
	273	cutting	-	1.23	-	-	-			
	282	cutting	-	1.59	-	-	-			
	291	cutting	-	1.28	-	-	-			
	300	cutting	-	1.27	-	-	-			
	309	cutting	2.1	1.77	-	-	0.42			
	317	cutting	2.05	1.91	-	-	0.44			
	326	cutting	2.96	2.19	0.55	0.43	0.35			
	336	cutting	-	1.64	-	-	-			
	344	cutting	-	1.4	-	-	-			
	354	cutting	-	1.09	-	-	-			
	362	cutting	2.21	2.34	0.55	0.52	0.36			
	371	cutting	-	1.27	-	-	-			
	381	cutting	-	1.7	-	-	-			
	390	cutting	2.21	1.9	-	-	0.56			
	399	cutting	-	1.65	-	-	-			
	407	cutting	-	0.84	-	-	-			
	416	cutting	-	1.68	-	-	-			
	425	cutting	-	0.91	-	-	-			
	434	cutting	-	0.54	-	-	-			
	443	cutting	-	1.21	-	-	-			
	450	cutting	-	1.39	-	-	-			
	461	cutting	-	1.66	-	-	-			
	467	cutting	-	1.6	-	-	-			
	474	cutting	-	1.46	-	-	-			
	480	cutting	2.56	2.05	0.58	0.58	0.40			
	485	cutting	-	0.98	-	-	-			
	492	cutting	2.14	1.79	-	-	0.45			
	498	cutting	-	1.81	-	-	-			
	503	cutting	2.13	2	-	-	0.51			
	510	cutting	2.47	1.75	-	-	0.42			
	516	cutting	2.37	2.01	-	-	0.42			
	521	cutting	2.1	1.93	-	-	0.36			
	528	cutting	-	0.88	-	-	-			
	534	cutting	2.32	1.91	-	-	0.42			
	540	cutting	2.07	1.56	-	-	0.38			
	546	cutting	2.12	1.47	-	-	0.40			
	552	cutting	-	0.65	-	-	-			
	558	cutting	-	0.58	-	-	-			
	563	cutting	-	0.61	-	-	-			
	569	cutting	-	1.6	-	-	-			
	576	cutting	-	1.64	-	-	-			
	581	cutting	-	1.7	-	-	-			
	587	cutting	-	1.29	-	-	-			
	594	cutting	-	1.01	-	-	-			
	598	cutting	-	1.1	-	-	-			
	605	cutting	2.12	1.12	-	-	0.47			
	611	cutting	-	0.50	-	-	-			
	618	cutting	2.05	1.64	-	-	0.42			
	623	cutting	-	0.96	-	-	-			
	629	cutting	2.42	1.83	0.54	0.5	0.42			
	635	cutting	2.1	1.63	-	-	0.40			
	641	cutting	-	1.15	-	-	-			
	648	cutting	2.12	1.37	-	-	0.44			
	654	cutting	-	1.54	-	-	-			
	659	cutting	2.64	1.59	-	-	0.45			

	665	cutting	-	0.87	-	-	-			
	672	cutting	2.08	1.5	-	-	0.45			
	677	cutting	-	1.71	-	-	-			
	683	cutting	-	1.46	-	-	-			
	690	cutting	-	1.6	-	-	-			
	696	cutting	2.97	2.24	-	-	0.49			
	701	cutting	3.11	2.31	0.56	0.51	0.47			
	707	cutting	3.18	2.2	-	-	0.51			
	713	cutting	3.34	2.07	-	-	0.36			
	719	cutting	-	0.85	-	-				
	725	cutting	2.39	1.46	-	-	0.42			
	731	cutting	4.14	2.27	-	-	0.44			
	738	cutting	3.23	2.43	-	-	0.40			
	743	cutting	3.3	1.9	-	-	0.49			
	749	cutting	3.37	2.16	-	-	0.36			
	755	cutting	-	0.75	-	-				
	761	cutting	3.27	2.48	-	-	0.40			
	766	cutting	4.34	2.58	0.54	0.5	0.44			
	773	cutting	2.28	1.43	-	-	0.47			
	779	cutting	2.56	1.55	-	-	0.51			
	786	cutting	-	1.03	-	-	-			
	792	cutting	-	1.28	-	-	-			
	799	cutting	2.34	1.37	-	-	0.49			
	804	cutting	-	0.9	-	-	-			
	809	cutting	2.42	1.75	-	-	0.58			
	815	cutting	2.27	1.55	-	-	0.53			
	821	cutting	2.19	1.34	-	-	0.51			
	827	cutting	2.07	1.7	-	-	0.53			
	833	cutting	2.55	2.12	0.53	0.48	0.51			
	839	cutting	-	1.15	-	-	-			
	846	cutting	-	1.13	-	-	-			
	852	cutting	-	1.11	-	-	-			
	859	cutting	-	0.97	-	-	-			
	864	cutting	-	1.54	-	-	-			
	869	cutting	2.12	1.93	-	-	0.49			
	875	cutting	2.57	1.5	-	-	0.44			
	881	cutting	2.96	1.87	-	-	0.44			
	887	cutting	3.2	2.11	-	-	0.51			
	893	cutting	2.05	1.69	-	-	0.45			
	899	cutting	2.49	1.89	-	-	0.44			
	905	cutting	2.16	1.8	-	-	0.49			
	911	cutting	2.14	1.61	-	-	0.49			
	916	cutting	3.23	2.01	-	-	0.42			
	923	cutting	2.53	1.74	-	-	0.51			
	929	cutting	2.72	1.71	-	-	0.47			
	935	cutting	3.02	2.09	-	-	0.42			
	941	cutting	3.38	2.19	0.56	0.56	0.47			
	947	cutting	2.9	1.99	-	-	0.49			
	953	cutting	-	0.97	-	-	-			
	959	cutting	2.39	1.76	-	-	0.49			
	971	cutting	2.37	1.55	-	-	0.49			
	978	cutting	-	1.24	-	-	-			
	984	cutting	-	1.27	-	-	-			
	990	cutting	-	1.4	-	-	-			
	995	cutting	-	1.66	-	-	-			
	1002	cutting	-	1.57	-	-	-			
	1008	cutting	-	1.78	-	-	-			
	1013	cutting	-	1.44	-	-	-			
	1020	cutting	-	0.72	-	-	-			
	1025	cutting	-	0.61	-	-	-			
	1032	cutting	-	0.5	-	-	-			
	1037	cutting	-	1.24	-	-	-			
	1044	cutting	-	0.68	-	-	-			
	1049	cutting	3.05	2.31	-	-	0.44			

	1056	cutting	2.99	1.76	-	-	0.56			
	1061	cutting	3.54	2.41	0.62	0.51	0.45			
	1069	cutting	-	0.51	-	-	-			
	1074	cutting	-	0.92	-	-	-			
	1080	cutting	2.54	1.6	-	-	0.58			
	1086	cutting	2.3	1.47	-	-	0.56			
	1091	cutting	3.16	1.69	-	-	0.58			
	1098	cutting	4.03	2.12	-	-	0.51			
	1104	cutting	3.56	2.36	-	-	0.49			
	1109	cutting	-	0.99	-	-	-			
	1115	cutting	3.74	1.88	-	-	0.56			
	1122	cutting	4.19	1.69	-	-	0.56			
	1127	cutting	3	1.37	-	-	0.56			
	1033	cutting	4.48	2.01	-	-	0.58			
	1140	cutting	5.21	2.01	-	-	0.54			
	1146	cutting	5.43	2.29	-	-	0.54			
	1151	cutting	2.48	1.72	-	-	0.54			
	1158	cutting	-	1.61	-	-	-			
	1163	cutting	4.03	2.46	0.62	0.51	0.49			
	1170	cutting	4.34	1.9	-	-	0.54			
	1176	cutting	-	1.12	-	-	-			
	1182	cutting	2.56	1.64	-	-	0.51			
	1187	cutting	2.7	1.88	-	-	0.51			
	1193	cutting	2.68	2.09	-	-	0.51			
	1199	cutting	3.34	2.26	-	-	0.54			
	1205	cutting	3.33	1.78	-	-	0.54			

Table S5: Thermal maturity data derived from the analyses of the Satskhenisi 102 well samples. Data from DIG, 2014.

Thermochronologic data

	N° grains	*Central age*	*MCTL*	*N° tracks*	*Mean Dpar*
AFT data	61	36.3 ± 2.8 Ma	13.34 ± 0.17 µm	83	2.75 µm

Additional geologic information

Constraint	*Explanation*	*References*
40-160°C from 56 to 42 Ma	Since we do not have any constraint on the pre-depositional history of the sample, we used a broad T-t box in order to avoid forcing.	
10-160 °C from 42 to 20 Ma	Since we do not have any constraint on the pre-depositional history of the sample, we used a broad T-t box in order to avoid forcing.	
0-40 °C at 20-18 Ma	The stratigraphic age of the sample is Sakaraulian, which in the local (Paratethyan) stratigraphy coresponds to the lower part of the Burdigalian.	Adamia et al, 2004; USSR gelogical maps 1: 25.000 scale
0-140°C from 20 to 0 Ma	Since we do not have any constraint on the post-depositional history of the sample, we used a broad T-t box in order to avoid forcing.	

System- and model-specific parameters

	Annealing model	*C-axis projection*	*Model c-axis projected lengths?*	*Default initial mean track length*	*Kinetic parameter*	*GOF metod*
AFT	Ketcham et al., 2007	Ketcham et al., 2007, 5.0M	Yes	From Dpar	Dpar	Kuiper's Statistic

Statistical fitting criteria	acceptable paths for GOF values >0.05; good paths for GOF values >0.5
t-T paths charachteristics	episodic history, halve two times, monotonic consistent between constraints, except for the post-deposition segment which was set to gradual history, halve two times, monotonic consistent
Number of paths attempted:	175440
Number of acceptable paths:	1315
Number of good paths:	300

Table S6: Thermochronological inverse modelling details relative to sample TU504.

Thermochronologic data

	N° grains	*Central age*	*MCTL*	*N° tracks*	*Mean Dpar*
AFT data	48	39.6 ± 3.3 Ma	13.41 ± 0.18 µm	67	2.31 µm

Additional geologic information

Constraint	*Explanation*	*References*
0-160° between 70 and 30 Ma	No constraints are available on the pre-depositional history of the smple, hence this broad T-t box has been put in order to avoid any forcing on the program.	
0-40 °C between 30 and 23 Ma	The depositional age of the sample is middle-upper Oligocene, which we translated into 30-23 Ma.	Adamia et al, 2010; USSR geological maps 1:25000 scale
0-140°C between 23 and 0 Ma	No constraints are available for the post-depositional history of the sample, henace a broad T-t box has been put in order to avoid any forcing on the program.	
Present day temperature 20 ± 10 °C	Since specific temperature data were not available from the region, we used a standard surface temperature.	

System- and model-specific parameters

	Annealing model	*C-axis projection*	*Model c-axis projected lengths?*	*Default initial mean track length*	*Kinetic parameter*	*GOF metod*
AFT	Ketcham et al., 2007	Ketcham et al., 2007, 5.0M	Yes	From Dpar	Dpar	Kuiper's Statistic
Statistical fitting criteria	acceptable paths for GOF values >0.05; good paths for GOF values >0.5					
t-T paths charachteristics	episodic history, halve two times, monotonic consistent between constraints, except for the post-deposition segment for which a gradual history, halve two times, monotonic consistent path was chosen.					
Number of paths attempted:	218520					
Number of acceptable paths:	1842					
Number of good paths:	300					

Table S7: Thermochronological inverse modelling details relative to sample TU505.

Chapter 5

THERMOCHRONOLOGICAL EVOLUTION OF THE GREATER CAUCASUS

The Greater Caucasus results from the structural inversion of a back-arc rift basin that opened in Early Jurassic times along the southern Eurasian margin, genetically linked with the northward subduction of the Northern Neotethys ocean (Saintot et al., 2006; Adamia et al., 2011a, 2011b; Vincent et al., 2016; Vasey et al., 2021). Much debate regards the exact size and structure of the former Greater Caucasus Basin (Cowgill et al., 2016; Vincent et al., 2016), the nature of the underlying crust (Ershov et al., 2003; Mosar et al., 2010; Cowgill et al., 2016; Vincent et al., 2016), and especially the timing and mechanisms of its closure (Philip et al., 1989; Nikishin et al., 2001; Saintot et al., 2006; Vincent et al., 2007; Mosar et al., 2010; Avdeev and Niemi, 2011; Vincent et al., 2011, 2013b, 2013a; Mumladze et al., 2015; Cowgill et al., 2016; Vincent et al., 2016; Vasey et al., 2020; Trexler et al., 2022).

The two end-member models regarding the mechanisms of closure of the Greater Caucasus Basin are (i) the *collisional model* which predicts that the basin closed after consumption of a wide (minimum 230-280 km) marine basin floored by oceanic or highly extended continental crust (Avdeev and Niemi, 2011; Mumladze et al., 2015; Cowgill et al., 2016, 2018; Tye et al., 2020; Trexler et al., 2022), and (ii) the *rift inversion model* which predicts that initial basin closure and deformation/uplift occurred through structural inversion of the former extensional faults and then propagated towards the northern and southern forelands in a thin-skinned fashion (Nikishin et al., 2001, 2011; Mosar et al., 2010, 2022; Vincent et al., 2016, 2018). Discrimination between these two models is hampered by the absence of a sufficiently detailed knowledge of the structural architecture of the Greater Caucasus, because structural and tectonic studies are mostly localised and often lack regional correlations (Sobornov, 1994, 1996, 2021; Somin et al., 2006; Tibaldi et al., 2017, 2019; Alania et al., 2020; Trexler et al., 2020, 2022; Mosar et al., 2022).

The current state-of-the-art in thermochronologic studies along the Greater Caucasus does not allow a thorough understanding of the cooling/exhumation history of the orogen. Despite this, many authors claimed to derive the thermal evolution of the whole orogen starting from very limited (both spatially and numerically) datasets, which is hardly possible given the extraordinary complexity of the belt and the extreme limitation of available data.

In this work we present a brand-new dataset of thermochronological data, featuring apatite fission-track and apatite and zircon (U-Th)/He ages, acquired along a transect through the southern slope of the central Greater Caucasus. Our results, supported by statistical inverse modelling and combined with published stratigraphic, structural and thermal maturity data, constrain the subsidence and exhumation history of the analysed transect. Furthermore, they contribute to fill the gap in thermochronological data along the Greater Caucasus and represent a step forward the comprehensive understanding of its tectonic evolution. In the following sections, the existing thermochronologic data from the Greater Caucasus are described and discussed together with the newly acquired ones.

5.1 Summary of available thermochronologic data for the Greater Caucasus

The thermochronometric data currently available are not uniformly distributed along the >1200 km-long Greater Caucasus (Fig. 5.1) but are most concentrated in the western sector of the orogen, with very few and sparse data in the central and eastern sectors. For the purposes of the present study, we define as Western Greater Caucasus the portion of the orogen west of 44° of E longitude (Vincent et al., 2020), as Central Greater Caucasus the portion between 44° and 46° E and as Eastern Greater Caucasus the portion east of 46° E (Fig. 5.1). Table 5.1 summarises all thermochronologic data available for the Greater Caucasus. However, many of the results published either (i) do not report all the analytical details necessary for an independent assessment of the robustness of the data, or (ii) show a high age dispersion (for ZHe or AHe ages) or a very low $P(\chi^2)$ (for ZFT or AFT ages) which make the relative ages not useful for the assessment of the cooling/exhumation history, or (iii) suffer from reset from adjacent magmatic centres. These problems may lead to errors in the interpretation of the cooling history, because for example fission-track central ages with $P(\chi^2)$ values < 5 % and He mean ages deriving from highly dispersed single-grain ages do not represent the real cooling

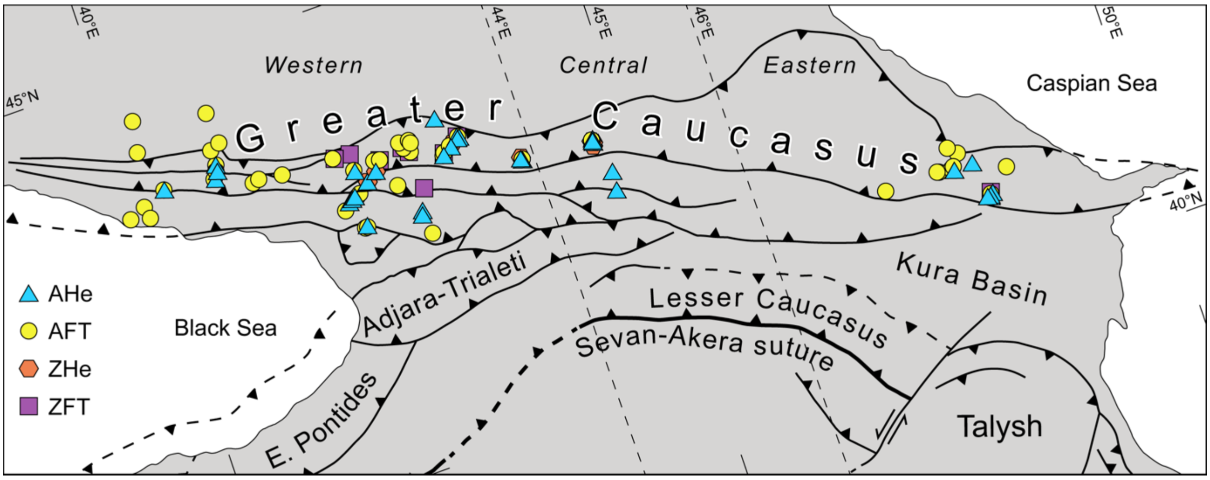

Figure 5.1: Tectonic sketch map of the Caucasian region with location of the available low-temperature thermochronologic results along the Greater Caucasus orogenic belt, subdivided according to the respective thermochronometric system (see details in the text).

time of the relative sample below the closure temperature, thus they may be misleading if one takes in consideration only the numerical age. If we do not consider such problematic results the already low number of thermochronometric data further decreases, leaving in particular the central and eastern sector of the Greater Caucasus with very few reliable data (Fig. 5.2).

The first thermochronological dataset produced in the Greater Caucasus is composed of forty-four apatite fission-track results from the crystalline basement outcropping in the western sector of the orogen (Kral and Gurbanov, 1996) (Table 5.1). The AFT central ages range from 68 to 1 Ma, and the authors subdivided their dataset into two groups: the first one comprises all data to the west of the supposed Elbrus fault system, characterised by ages between 12 and 68 Ma which increase progressively towards the west, and the second one comprises all data to the east of the supposed fault system, characterised by ages generally younger than 10 Ma. The authors interpreted such difference to reflect different uplift histories in the two regions. It must be stressed that in their work the authors do not report the $P(\chi^2)$ value and use an old, not standard method for fission-track counting, hence their results must be considered with care.

Domain	System	Age range (Ma)	N° samples	Reference
Western Greater Caucasus	AHe	25.4	1	Vincent et al., 2007
		39.9 - 49.5	2	Vincent et al., 2011
		1.7 - 19.0	10	Avdeev and Niemi, 2011
		5.6 - 24.5	5	Vincent et al., 2020
		3.3 - 6.2	3	Vasey et al., 2020
		1.9 – 4.2	3	Trexler et al., 2022
	AFT	1 - 68	44	Kral and Gurbanov, 1996
		57 - 176.4	9	Vincent et al., 2007
		2.5 - 264.2	21	Vincent et al., 2011
		3.6 - 21.8	6	Avdeev and Niemi, 2011
		1.4 - 48.2	19	Vincent et al., 2020
		4.6	1	Vasey et al., 2020
		4.2 – 136.6	4	Trexler et al., 2022
	ZHe	20.4 - 188.5	5	Avdeev and Niemi, 2011
		19.1 - 115.0	4	Vasey et al., 2020
	ZFT	139.6 -271.5	4	Vincent et al., 2011
		230.4 - 433.0	3	Avdeev and Niemi, 2011
		1.7 - 231.6	4	Vincent et al., 2020
Central Greater Caucasus	AHe	5.1 - 7-0	2	Trexler et al., 2022
		2.2 - 3.2	3	Vasey et al., 2020
	AFT	2.7	1	Vasey et al., 2020
	ZHe	7.1 - 8.2	3	Vasey et al., 2020
Eastern Greater Caucasus	AHe	1.7 - 92.7	8	Avdeev, 2011
	AFT	12.5 - 89.8	10	Bochud, 2011
		14 - 88.4	3	Avdeev, 2011
	ZFT	102.8	1	Avdeev, 2011

Table 5.1: Summary of the thermochronologic data available for the Greater Caucasus, subdivided according to the domain (western, central or eastern), the thermochronometric system and the reference study.

Vincent et al. (2007) provide nine apatite fission-track and one apatite (U-Th)/He results from Maikopian (Oligocene-Lower Miocene) sandstones collected in the westernmost Greater Caucasus (Table 5.1). AFT central ages range between about 57 and 176 Ma, older than the depositional ages, and only three of them yield $P(\chi^2) > 5$ % with AFT central ages much older than the depositional ages (78.5, 124.6 and 176.4 Ma). The authors recognised, in two samples with very low $P(\chi^2)$ values, two populations of grains, the younger of which yielded ages of 31 and 34 Ma in the two samples. One of these sample provided also the only AHe result of the dataset, yielding a mean age (25.4 Ma) almost identical to its depositional age. The authors interpret the thermochronologic dataset, together with stratigraphic and heavy mineral data, to reflect initial uplift/exhumation of the western Greater Caucasus in Early Oligocene times, which they link to initial collision of Arabia with the southern margin of Eurasia.

Further thermochronologic data, consisting in twenty-one AFT, four ZFT and two AHe ages, are provided by Vincent et al. (2011) for Paleozoic bedrock and Mesozoic-Cenozoic detrital samples from the western Greater Caucasus (Table 5.1). AFT central ages of detrital samples are all older than the depositional ages. Also in this case, most of the samples yielded very low $P(\chi^2)$ values, indicating very high age dispersion. In four samples, though, two populations of grains have been recognised by the authors: in three samples the younger population yields ages comprised between 52 and 59 Ma, in the fourth sample the younger population has an age of 41 Ma. The two AHe ages reported are 49.5 and 39.9 Ma, and are all older than the depositional ages. Statistical inverse modelling of thermochronologic data was performed on six samples, three from the basement core of the orogen and three from Cenozoic sedimentary rocks. The thermochronologic data reported in this study, according to the authors, are compatible with Cimmerian and Alpine cooling events, during Triassic-to-Middle Jurassic and Oligocene-Miocene times, respectively. The authors also note an inverse relationship between AFT age and depositional age in many Oligo-Miocene sedimentary rocks, attributing this to some degree of Eocene intermediate sediment storage. The thermochronologic dataset is also used to limit the amount of Cenozoic exhumation west of Mt. Elbrus to about 2.5 km. The results of this study are somewhat indeterminate. As admitted by the authors *"…the thermochronometric data are not sufficiently detailed to be able to better constrain time-temperature pathways during the Alpine transpressional evolution of the range, other than to confirm Oligo-Miocene cooling and identify a number of pulsed events during the evolution"*.

A new thermochronologic dataset for the western Greater Caucasus, east of Mt. Elbrus, was provided by Avdeev and Niemi (2011), comprising ten AHe, six AFT, five ZHe and three ZFT results obtained from basement samples (Table 5.1). AHe mean ages range between about 1.7

and 19.0 Ma, AFT central ages between about 3.6 and 21.8 Ma, ZHe mean ages between about 20.4 and 188.5 Ma, and ZFT central ages between about 230.4 and 433.0 Ma. These thermochronologic results, and the statistical inverse modelling of five samples, are used to infer a two-phase exhumation of the Greater Caucasus, starting with slow cooling since Oligocene times followed by inception of fast cooling since ~ 5 Ma. Such cooling/exhumation event is interpreted to represent the final closure of the Greater Caucasus Basin and collision between the Lesser and Greater Caucasus terranes, and is linked to the coeval reorganisation of the Arabia-Eurasia collision zone envisioned by Allen et al. (2004). Such interpretation is recalled by Cowgill et al. (2016), but is not supported by any sedimentological, provenance, structural or geochemical data (Cowgill et al., 2018; Vincent et al., 2018).

Additional results for the western Greater Caucasus are reported by Vincent et al. (2020), who provides five AHe, nineteen AFT and four ZFT results (Table 5.1). AHe mean ages range between 5.6 and 24.5 Ma, AFT central ages between 1.4 and 48.2 Ma and ZFT central ages between 1.7 and 231.6 Ma. The authors, based on such dataset integrated with statistical inverse modelling of some samples, suggest that the Greater Caucasus experienced no more than ~ 5-7 km of Cenozoic exhumation, with low rates during Oligo-Miocene times followed by acceleration during Late Miocene-Pliocene times. Furthermore, they divide the greater Caucasus basement in two regions, respectively to the east and west of Mt. Elbrus, which experienced different late Cenozoic cooling/exhumation histories: in their reconstruction the eastern region experienced more rapid uplift since about 5 Ma, whereas the western region experienced less rapid uplift starting at about 10-8 Ma.

Vasey et al. (2020) provides three AHe, one AFT and four ZHe results from the western Greater Caucasus, yielding AHe mean ages between 3.3 and 6.2 Ma, a 4.6 Ma AFT central age and ZHe mean ages between 19.1 and 115.0 Ma (Table 5.1). These authors also provide results for the easternmost outcrop of the Greater Caucasus basement (Dariali Massif), in the central sector of the orogen. Samples from the Dariali Massif (central Greater Caucasus) provide AHe mean ages comprised between 2.2 and 3.2 Ma, an AFT central age of 2.7 Ma and ZHe mean ages between 7.1 and 8.2 Ma (Table 5.1). The two AFT results do not report the relative the P(χ^2) value. The authors use their thermochronologic dataset, together with other geochronologic and microstructural data, and statistical inverse modelling of some thermochronologic results, to conclude that the Greater Caucasus experienced ~ 5-8 km of exhumation since about 10 Ma in response to Arabia-Eurasia collision.

Recently, Trexler et al. (2022) provided four AFT and three AHe results from the western Greater Caucasus, and two AHe results along a traverse in the central Greater Caucasus. AHe mean ages along a traverse in the western Greater Caucasus are comprised between about 1.9 and 4.2 Ma, whereas in the north of the traverse two samples yield AFT central ages of about 5.5 and 4.2 Ma, and to the south of the same traverse one sample yields an AFT central age of about 104 Ma. Another sample in the western Greater Caucasus provided an AFT central age of about 137 Ma. Along the traverse in the central Greater Caucasus, the two AHe results yield 5.1 and 7.0 Ma mean ages (Table 5.1).

The only available thermochronologic results for the eastern Greater Caucasus are reported in two PhD Dissertations (Avdeev, 2011; Bochud, 2011), which together provide thirteen AFT, eight AHe and one ZFT results (Table 5.1). Avdeev (2011) reports three AFT central ages ranging between about 14 and 88.4 Ma, one ZHe mean age of 102.8 Ma and eight AHe mean ages mostly ranging between 1.7 and 4.0 Ma, with one outlier yielding a 92.7 Ma mean age. The author does not report the $P(\chi^2)$ for their AFT results. Bochud (2011) provides ten AFT central ages ranging between about 12.5 and 89.8 Ma, but only one of them yields a $P(\chi^2) > 5$ %: this sample has a central age of 12.5 ± 2.4 Ma.

The compilation of Fig 5.2, which incorporates all reliable thermochronological results, attests that at least some portions of the axial zone of the central-western Greater Caucasus experienced fast cooling below 100-120 °C in the last 10 My. Assuming an average geothermal gradient of 30 °C/km this would translate into less than 4 km of exhumation. Looking more in detail, the easternmost outcrop of crystalline basement in the orogen (Dariali Massif) has undergone quick cooling from about 180 °C since about 10-8 Ma (indicating about 6 km of exhumation) and at least some sectors of the eastern Greater Caucasus experienced cooling in the last ~ 5 Ma (Fig. 5.2). The axial zone of the westernmost Greater Caucasus yields cooling ages older than 10 Ma, implying that this sector did not register the late Cenozoic pulse of cooling/exhumation recorded more to the east.

Contrary to many authors (Kral and Gurbanov, 1996; Vincent et al., 2011, 2020) which identify in Mt. Elbrus the border between two portions of the basement core of the orogen (the eastern recently cooled/exhumed one versus the western more elderly cooled/exhumed one), Figure 5.2 shows very well that the divide between the two portions coincides indeed with the eastern Black Sea coastline to the south. Thermochronologic ages in the Greater Caucasus become older just west of the Black Sea coastline in western Georgia. Timing of opening of the eastern Black Sea basin is disputed, but occurred somewhere between the latest Cretaceous and the Eocene (Robinson et al., 1995; Spadini et al., 1996; Kazmin et al., 2000; Stephenson and Schellart, 2010; Nikishin et al., 2015), thus during late Cenozoic times it was a relatively old deep marine basin underlain by a rigid, quasi-oceanic crust (Shillington et al., 2008, 2009;

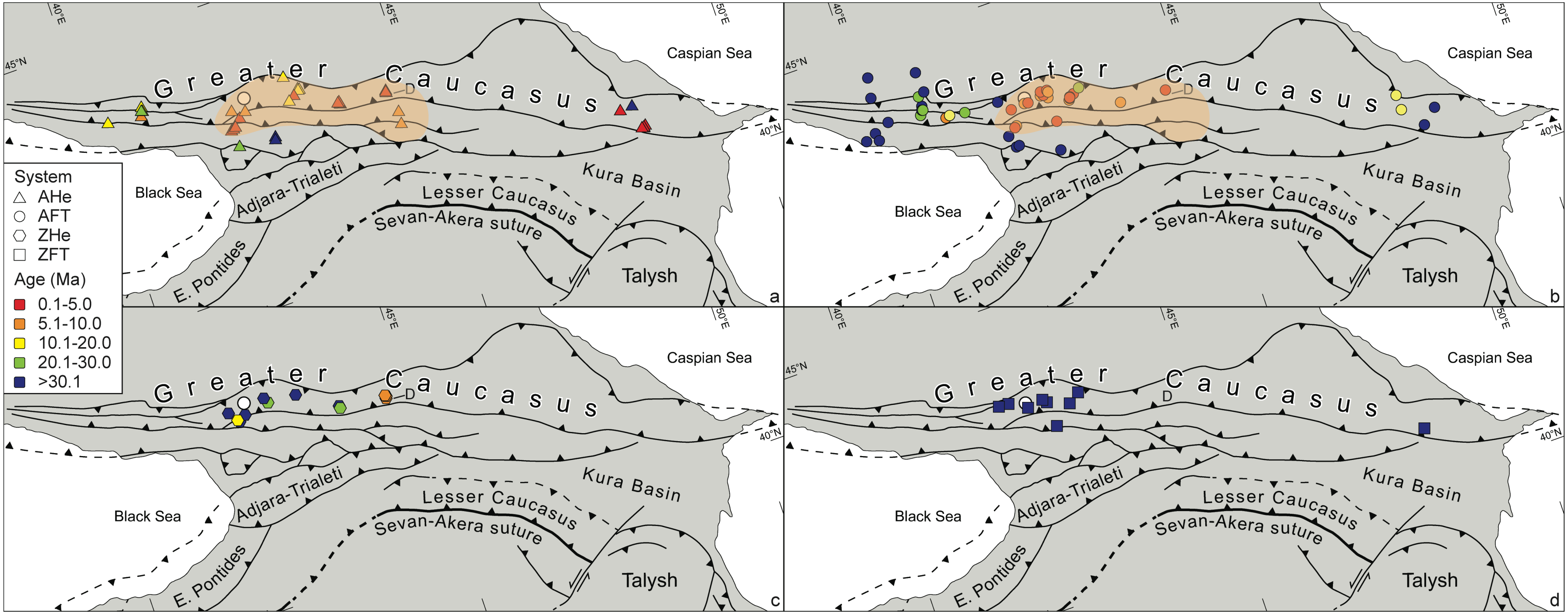

Figure 5.2: Compilation of the reliable thermochronological data available to date for the Greater Caucasus, subdivided according to the thermochronometric system and coloured according to determined cooling age ranges (see legend). a) apatite (U-Th)/He mean ages; b) apatite fission-track central ages; c) zircon (U-Th)/He mean ages; d) zircon fission-track central ages. See text for details and references. Orange overlay identifies the area which experienced fast cooling below 120-100 °C in the last 10 My. White dot indicates the location of Mt. Elbrus. D identifies the location of the Dariali Massif.

Edwards et al., 2009), hence representing a strong rheological backstop. Such backstop can thus have forced the stress propagated from the Bitlis suture to focus preferentially along the eastern Pontides, at the southern margin of the basin, as demonstrated by Albino et al. (2014) and Cavazza et al. (2019). This would favour the interpretation of the Greater Caucasus exhumation as driven by far-field stress transmission from the Arabia-Eurasia collision zone, as suggested by many authors (Avdeev and Niemi, 2011; Vincent et al., 2011; Cavazza et al., 2018, 2019; Vasey et al., 2020): to the east of the Black Sea coast, the absence of such a rheological barrier would have allowed far-field stresses to be efficiently transmitted northward promoting fast exhumation in the Greater Caucasus core, whereas to the west such stresses would have been mostly absorbed along the eastern Pontides, fostering their fast exhumation and thus inhibiting the same in the western Greater Caucasus.

Further discussion regarding this point and the tectonic evolution of the Greater Caucasus can be found in Section 5.3 and in Chapter 6.

5.2 New thermochronological constraints on the exhumation history of the southern sector of the central Greater Caucasus

As explained in the previous section, most of the thermochronological data available for the Greater Caucasus are concentrated in the western sector of the orogenic belt, whereas the central and eastern sectors are only covered by very few and sparse data. In this section, in an attempt to partially fill these gaps, a thermochronological dataset along a transect in the central Greater Caucasus is presented (Fig. 5.3), integrating newly acquired results with the very limited and sparse existing data from the area. Such dataset includes nine zircon (U-Th)/He, four apatite fission track and nine apatite (U-Th)/He ages derived from samples collected along the Georgian Military Road crossing the southern slope of the central Greater Caucasus (Fig. 5.4; Tables 5.2, 5.3 and 5.4). The samples analysed are Variscan metamorphic rocks from the easternmost outcrop of the Greater Caucasus basement, the Dariali Massif (Vasey et al., 2020), and Jurassic-to-Eocene detrital rocks representing the sedimentary fill of the Greater Caucasus basin, which experienced considerable heating during burial (up to about 380°C, under anchizone-epizone conditions; Corrado et al., 2021). In addition to the new results along the southern central Greater Caucasus, new low-temperature thermochronological results obtained from the eastern Adjara-Trialeti FTB and the Khrami Massif will be presented, providing further constraints on their tectonic evolution. In the following, all the results will be presented and discussed from north to south.

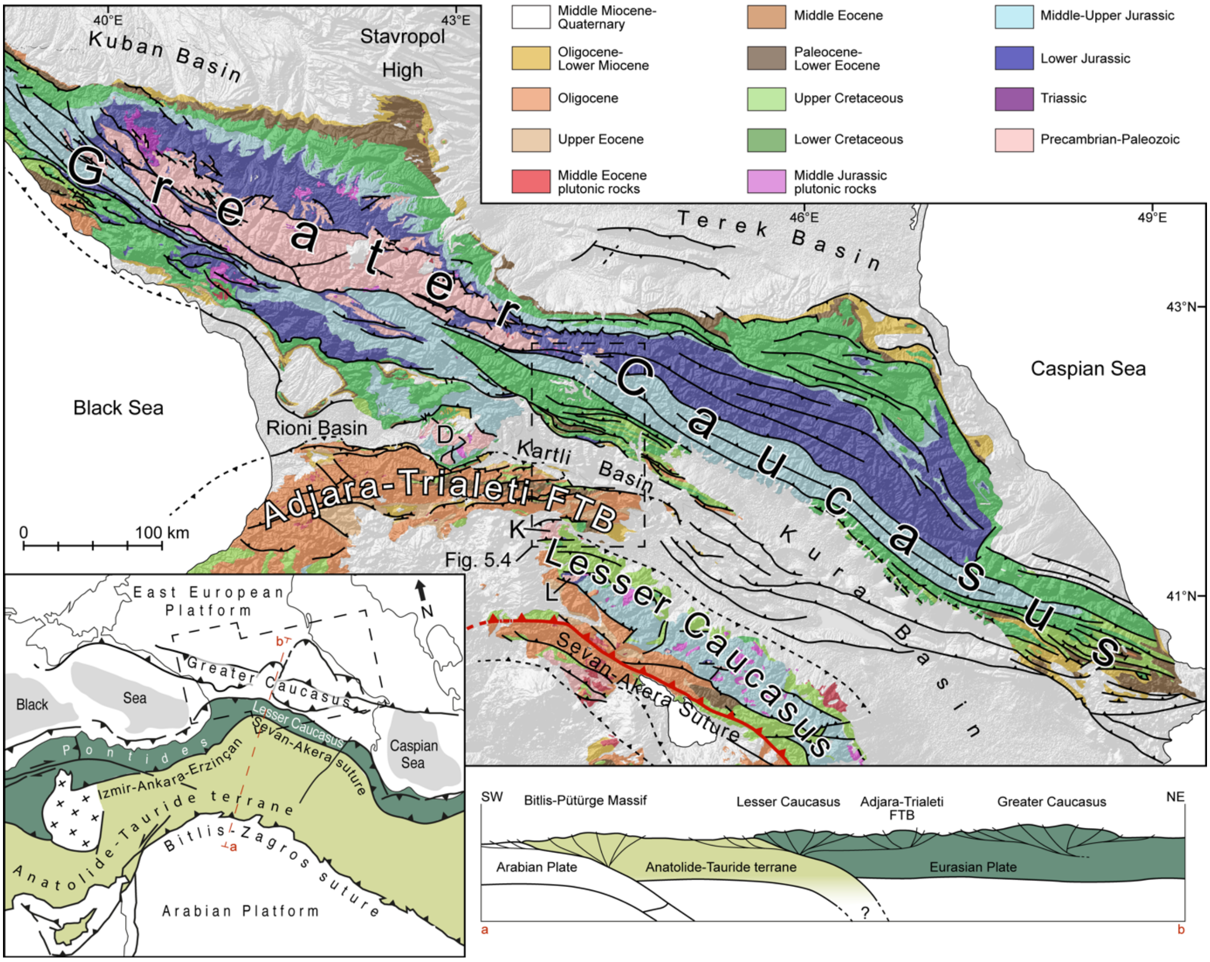

Figure 5.3: Geological sketch map of the Caucasian region with indication of the main tectonic domains and lineaments. Dashed rectangle indicates location of Figure 5.4. D = Dzirula Massif, K = Khrami Massif, L = Loki Massif. Lower-left inset shows location of geological map and cross section a-b within the context of the Arabia Eurasia collision zone (modified after Cavazza et al., 2019). Cross-section a-b schematically represents the geodynamic setting and the tectonic relationships among the various domains.

In the northernmost sector of the analysed transect, the Dariali Massif is made of gneissic rocks metamorphosed at 330-310 Ma during the Variscan orogeny (Vasey et al., 2020). Samples from the Dariali Massif yielded zircon (U-Th)/He mean ages around 7-8 Ma (Fig. 5.4) and ZHe single-grain ages comprised between about 10 and 6 Ma (Table 5.4). The same samples yielded apatite (U-Th)/He mean ages around 2-3 Ma, with single-grain ages comprised between about 5 and 2 Ma (Fig. 5.4; Table 5.2), and two of them yielded apatite fission-track central ages around 3-4 Ma (Fig. 5.4; Table 5.3). The low dispersion of He ages and the very high P(χ^2) value of the AFT results indicate that the samples experienced rapid cooling across the closure temperature of the respective thermochronometric systems, thus pointing to very

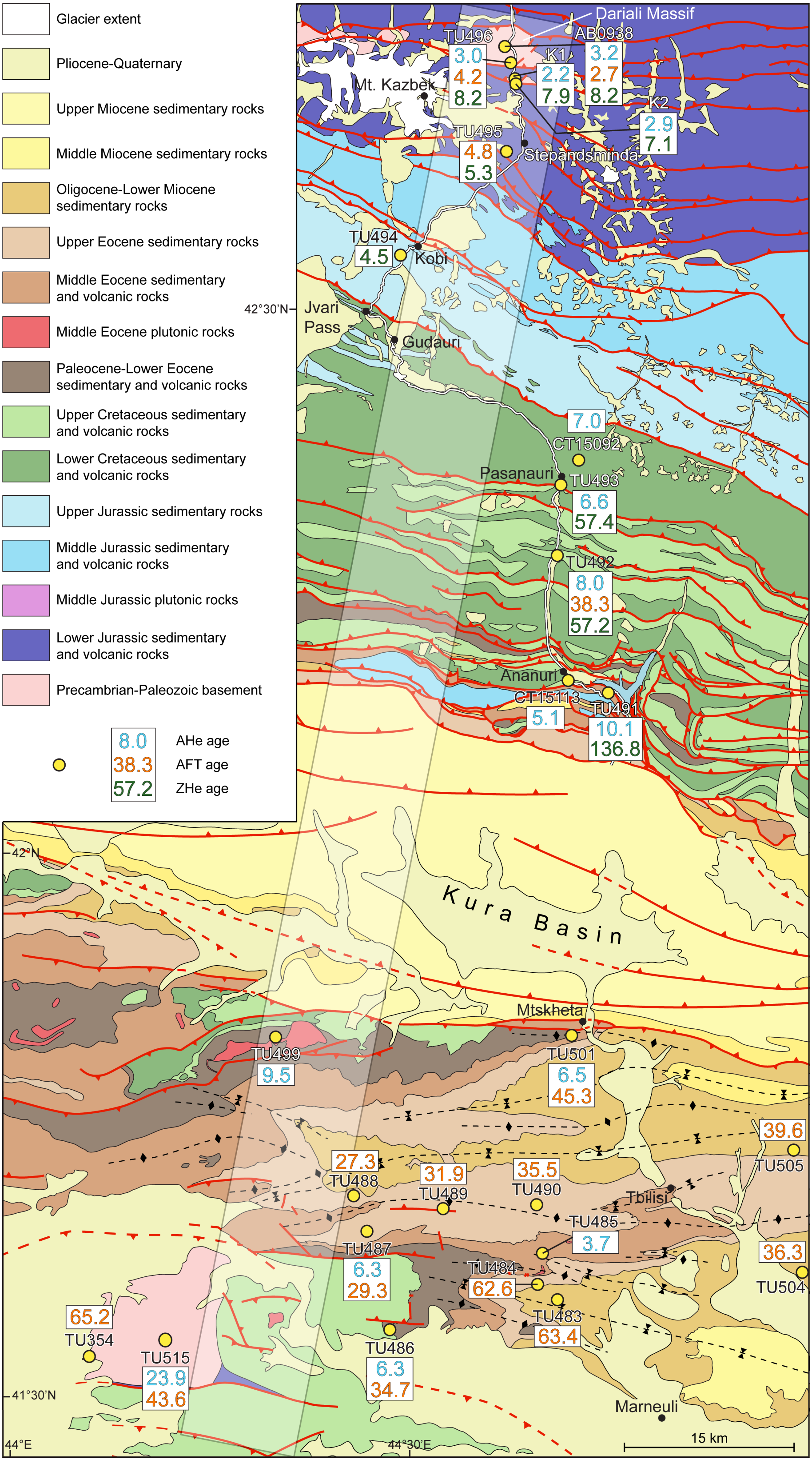

Figure 5.4: Geological map of the transect analysed across the southern central Greater Caucasus, the eastern Adjara-Trialeti FTB and the Khrami Massif to the retro-wedge of the Lesser Caucasus, showing results of low-temperature thermochronological analyses and the respective samples location. Shaded rectangle identifies the approximate trace of cross-section in Fig. 5.5. MCT locates the Main Caucasus Thrust according to Mosar et al. (2010, 2022); Vasey et al. (2020) and Trexler et al. (2022).

fast cooling from > 180 °C to < 40 °C during Late Miocene-Pliocene times (10-2 Ma). This is supported by the statistical inverse modelling result reported by Vasey et al. (2020) which also shows fast cooling of sample K1 since about 10 Ma. Statistical inverse modelling of thermochronologic data was performed for the Variscan gneiss of sample TU496, integrating ZHe, AFT and AHe with all other available geochronologic and stratigraphic data: the results indicate fast cooling/exhumation from temperatures > 250 °C since about 10-12 Ma (Figs. 5.5). South of the Dariali Massif, two Jurassic sandstones yield ZHe single-grain ages comprised between about 6 and 4 Ma (Fig. 5.4; Table 5.4), and one of them yield an AFT central age of 4.8 ± 0.8 Ma (Fig. 5.4; Table 5.3). Thermal maturity analyses (Corrado et al., 2021) on the same samples (Raman spectroscopy, I% in I-S mixed layers and KI) indicate that they have experienced maximum temperatures above 300 °C (anchizone-epizone conditions). The results hence suggest that also this sector was exhumed very quickly, coevally with the Dariali Massif. Statistical inverse modelling of sample TU495, a Toarcian-Aalenian sandstone (Fig. 5.4), integrating ZHe and AFT results with thermal maturity and stratigraphic data, indicates fast cooling/exhumation from temperatures between 250 and 350 °C since about 8 Ma (Figs. 5.5), in agreement with sample TU496 and Vasey et al. (2020).

Moving further south, three sandstone samples from the Early-to-early Late Cretaceous succession yield AHe single-grain ages comprised between about 5 and 9 Ma. Two samples yield ZHe ages around 57 Ma and one of them yields an AFT central age of 38.3 ± 5.0 Ma (Fig. 5.4; Tables 5.2, 5.3, and 5.4). Thermal maturity analyses indicate that the sedimentary rocks analysed experienced maximum burial temperatures > 200 °C (Corrado et al., 2021), hence these samples are fully reset for their respective thermochronometric system. The young AHe ages are coeval with those found more to the north along the transect, whereas AFT and ZHe ages indicate that these samples cooled from more than ~ 180 °C to less than ~ 110°C during Paleocene-Eocene times. In order to obtain more quantitative information on the cooling history of this sector, statistical inverse modelling have been performed for two Cretaceous sandstones samples (TU492 and TU493; Fig. 5.4), integrating ZHe, AFT and AHe results with thermal maturity and stratigraphic data: the modelling results indicate a first phase of cooling/exhumation during Late Cretaceous/early Paleogene times, followed by nearly isothermal holding during the Eocene, the Oligocene and the Early Miocene, and by a final episode of fast cooling/exhumation starting at about 15-10 Ma (Figs. 5.5).

In the southernmost part of the transect, two conglomeratic units were sampled and analysed. One of them (CT15113; Trexler et al., 2022) is a Lower Cretaceous conglomerate, and the other one (TU491) is a group of granitoid clasts from a Upper Eocene conglomerate.

Table 5.1: Results of new and published apatite (U-Th)/He analyses on the samples collected along the Georgian Military Road in the southern central Greater Caucasus, in the eastern Adjara-Trialeti FTB, and in the Khrami Massif (see Fig. 5.4 for location of samples).

Sample	Rock Type	Age	Location	Elevation (m)	UTM Coordinates (38T)	Replicate	Ft	Corrected age (Ma)	Error (Ma)	Mean Age (Ma)	Mean error (Ma)	^{4}He (mol)	U 238 (ppm)	U 235 (ppm)	Th 232 (ppm)	Sm 147 (ppm)	eU	Rs (Equivalent radius, µm)
AB0938[a]	Ortogneiss	Late Paleozoic	Greater Caucasus	1300	0469790 4731455	AB0938b		3.50	0.04	3.2	0.5	-	41.0		46.9	296.7		56.1
						AB0938c		2.01	0.02			-	36.6		30.2	271.3		66.3
						AB0938d		3.42	0.03			-	23.8		43.1	361.0		42.9
						AB0938e		2.73	0.03			-	49.6		56.0	321.7		80.7
						AB0938f		2.27	0.03			-	32.2		31.5	230.7		52.0
						AB0938g		5.09	0.05			-	32.7		24.5	217.1		62.2
CT15092[b]	Sandstone	Early Cretaceous	Greater Caucasus	1130	0475989 4689034	-	-	-	-	7.0	0.1	-	-	-	-	-	-	-
CT15113[b]	Conglomerate	Early Cretaceous	Greater Caucasus	850	0475379 4667692	-	-	-	-	5.1	0.8	-	-	-	-	-	-	-
K1[a]	Granodiorite	Late Paleozoic	Greater Caucasus	1434	0469520 4728642	V16046Db		1.96	0.03	2.2	0.1	-	33.4		50.0	350.1		40.4
						V16046Dc		1.98	0.03			-	21.7		23.5	198.0		47.9
						V16046Dd		2.51	0.04			-	15.7		22.3	175.8		55.4
						V16046De		2.18	0.02			-	64.4		94.0	578.3		48.6
K2[a]	Mylonitic gneiss	Late Paleozoic	Greater Caucasus	1522	0469793 4728308	V16052Bc		3.35	0.05	2.9	0.3	-	10.8		20.6	141.9		56.3
						V16052Be		3.53	0.05			-	14.3		28.2	212.9		44.0
						V16052Bg		2.38	0.03			-	17.9		39.4	250.9		45.7
						V16052Bh		2.20	0.03			-	24.5		54.1	309.9		46.4
TU485[c]	Sandstone	Early Eocene	Eastern ATFTB	889	0472357 4609370	TU485-1	0.66	5.37	0.05	3.7*	0.02*	$8.47*10^{-15}$	8.68	0.07	69.94	39.25	25.12	44.75
						TU485-2	0.64	3.58	0.04			$6.59*10^{-15}$	19.87	0.16	81.87	35.89	39.11	42.75
						TU485-3	0.62	2.58	0.03			$7.95*10^{-15}$	33.50	0.27	288.22	81.36	101.24	38.51
						TU485-4	0.65	8.24	0.09			$1.05*10^{-14}$	14.72	0.12	50.43	15.33	26.58	42.55
						TU485-5	0.65	7.26	0.08			$7.21*10^{-15}$	9.38	0.09	61.75	43.71	23.90	46.95
TU486[c]	Sandstone	latest Paleocene-Early Eocene	Eastern ATFTB	883	0456357 4599540	TU486-1	0.66	5.93	0.18	6.1*	0.1*	$4.96*10^{-15}$	10.16	0.09	23.87	24.08	15.77	46.88
						TU486-3	0.73	17.32	0.16			$4.69*10^{-14}$	10.10	0.08	24.19	10.84	15.78	55.53
						TU486-4	0.68	13.62	0.20			$1.58*10^{-14}$	10.16	0.09	40.19	19.82	19.60	47.58
						TU486-5	0.66	4.08	0.06			$4.55*10^{-15}$	10.62	0.09	65.57	43.20	26.03	41.83
TU487[c]	Sandstone	Late Eocene	Eastern ATFTB	932	0452684 4611098	TU487-1	0.62	10.81	0.63	6.4*	0.1*	$4.53*10^{-15}$	6.91	0.08	39.88	29.50	16.28	38.85
						TU487-2	0.66	5.80	0.06			$1.05*10^{-14}$	17.46	0.14	79.57	75.61	36.16	45.53
						TU487-3	0.59	7.31	0.18			$2.67*10^{-15}$	9.20	0.10	37.49	16.87	18.01	36.91
						TU487-4	0.59	5.10	0.13			$3.13*10^{-15}$	16.15	0.15	64.32	54.55	31.27	35.21
						TU487-5	0.68	8.41	0.10			$1.33*10^{-14}$	16.19	0.13	54.02	42.30	28.88	96.94
TU491	Granitoid clasts in conglomerate	Late Eocene (conglomerate)	Greater Caucasus	772	0479248 4666600	TU491-1	0.69	13.66	0.23	10.1	3.4	$5.50*10^{-15}$	37.08		140.68	718.09	73.38	39.87
						TU491-2	0.73	9.72	0.17			$8.94*10^{-15}$	85.54		133.10	673.11	119.85	46.19
						TU491-3	0.65	6.97	0.31			$9.96*10^{-16}$	21.99		62.51	449.09	38.73	35.24
TU492	Sandstone	Cenomanian	Greater Caucasus	922	0473963 4680238	TU492_1	0.68	7.58	0.78	8.0	1.1	$3.44*10^{-16}$	5.23		25.13	198.65	12.04	38.96
						TU492_2	0.75	7.23	0.36			$9.98*10^{-16}$	6.16		35.42	189.89	15.34	51.52
						TU492_3	0.61	9.22	0.53			$4.75*10^{-16}$	13.19		86.17	353.23	35.02	30.83
TU493	Sandstone	Aptian-Albian	Greater Caucasus	1057	0474870 4688016	TU493-2	0.70	6.47	0.17	6.6	1.8	$0.55*10^{-15}$	18.71		17.75	123.09	22.88	42.18
						TU493-3	0.71	9.02	0.18			$0.72*10^{-15}$	13.90		33.53	101.85	21.78	42.63
						TU493-4	0.71	6.38	0.18			$0.44*10^{-15}$	28.46		6.66	116.43	30.02	43.34
						TU493-5	0.70	4.66	0.10			$0.59*10^{-15}$	33.75		66.92	401.64	49.47	42.05
TU496	Gneiss	Late Paleozoic	Greater Caucasus	1320	0469676 4730334	TU496-2	0.71	3.19	0.06	3.0	0.9	$1.16*10^{-15}$	44.30		53.39	295.89	56.85	42.93
						TU496-3	0.75	4.05	0.07			$0.74*10^{-15}$	20.51		27.70	201.34	27.02	50.20
						TU496-4	0.76	2.87	0.05			$0.56*10^{-15}$	23.20		24.83	198.45	29.04	53.60
						TU496-5	0.78	1.82	0.02			$1.40*10^{-15}$	67.49		134.62	442.35	99.12	58.43
TU499[c]	Sandstone	Early Eocene	Eastern ATFTB	1338	0445544 4631754	TU499-2	0.62	8.85	0.24	9.5*	0.9*	$1.02*10^{-15}$	3.46	0.10	20.17	1.87	8.20	37.87
						TU499-3	0.55	10.18	0.24			$1.34*10^{-15}$	6.77	0.15	40.35	11.07	16.25	32.19
TU501[c]	Sandstone	Middle Eocene	Eastern ATFTB	561	0476497 4631400	TU501-1	0.71	5.89	0.06	6.5*	0.04*	$1.13*10^{-14}$	11.67	0.09	44.51	44.45	22.13	53.27
						TU501-2	0.62	9.95	0.16			$5.81*10^{-15}$	8.63	0.08	40.63	29.07	18.17	39.50
						TU501-3	0.67	8.74	0.10			$1.24*10^{-14}$	12.88	0.11	68.94	27.90	29.08	44.97
						TU501-4	0.60	6.86	0.20			$2.08*10^{-15}$	7.30	0.09	34.11	26.01	15.32	37.75
						TU501-5	0.61	5.46	0.07			$3.26*10^{-15}$	11.41	0.11	58.72	32.88	25.21	38.48
TU515	Gneiss-diorite	Precambrian-Early Paleozoic	Khrami Massif	985	0431453 4600622	TU515-2	0.79	26.20	0.35	23.9	5.7	$1.15*10^{-14}$	20.70		2.34	444.91	21.25	60.18
						TU515-3	0.82	28.08	0.36			$3.75*10^{-14}$	28.31		7.65	559.26	30.10	71.52
						TU515-4	0.77	17.44	0.26			$1.44*10^{-15}$	31.56		12.66	333.18	34.54	54.66

For each sample, corrected ages with relative error of each replicate are shown, and the weighted mean age is also reported. The effective uranium value (eU = [U] + 0.235*[Th]) gives an indication of the goodness of the data: if it is lower than 5, than the uranium content of the apatite crystal was too low to provide a meaningful result. All replicates considered in the discussion have eU>5. a = results from Vasey et al., 2020; b = results from Trexler et al., 2022; c = results from Gusmeo et al., 2021. * mark weighted mean ages and errors (Gusmeo et al., 2021).

Table 5.3: Results of new and published apatite fission-track results from the samples collected along the Georgian Military Road in the southern central Greater Caucasus, in the eastern Adjara-Trialeti FTB, and in the Khrami Massif (see Fig. 5.4 for location of samples).

Sample	**Rock Type**	**Age**	**Location**	**Elevation (m)**	**UTM Coordinates (38T)**	**No. crystals**	**Spontaneous**		**Induced**		**P(χ^2)**	**Dosimeter**		**Age (Ma) ± 1s**	**MCTL (µm) ± standard error**	**Standard deviation**	**No. tracks measured**	**D-par**
							ρ_s	**N_s**	**ρ_i**	**N_i**		**ρ_d**	**N_d**					
AB0938[a]	Ortogneiss	Late Paleozoic	Greater Caucasus	1300	0469790 4731455	-	-	-	-	-	-	-	-	2.7 ± 0.4	-	-	-	-
TU354[b]	Granitoid	Late Paleozoic	Khrami Massif	1524	0426185 4599082	21	3.40	175	1.09	540	99.83	9.80	4491	65.2 ± 1.3	-	-	-	-
TU483	Sandstone	Late Oligocene	Eastern ATFTB	684	0473006 4604652	42	0.18	222	0.71	871	94.18	14.5	7498	63.4 ± 5.8	14.10 ± 0.22	1.59	50	2.91
TU486[c]	Sandstone	latest Paleocene-Early Eocene	Eastern ATFTB	883	0456357 4599540	49	0.14	290	0.81	1691	99.68	12.22	7638	34.7 ± 2.8	12.05 ± 0.22	1.66	53	2.38
TU487[c]	Sandstone	Late Eocene	Eastern ATFTB	932	0452684 4611098	38	0.10	107	0.69	725	99.56	12.15	7593	29.3 ± 3.4	-	-	-	2.51
TU488[c]	Sandstone	Late Oligocene	Eastern ATFTB	1391	0452009 4616299	41	0.14	192	1.05	1393	99.44	12.07	7547	27.3 ± 2.5	12.48 ± 0.31	2.26	53	2.36
TU489[c]	Sandstone	Late Eocene	Eastern ATFTB	1291	0461429 4612640	13	0.09	36	0.53	224	97.20	12.00	7502	31.9 ± 5.9	-	-	-	2.35
TU490[c]	Sandstone	Late Eocene	Eastern ATFTB	1322	0472584 4613551	18	0.14	55	0.58	231	99.97	9.73	5046	35.5 ± 5.6	-	-	-	2.46
TU492	Sandstone	Cenomanian	Greater Caucasus	922	0473963 4680238	29	0.12	75	0.61	371	86.52	11.93	7457	38.3 ± 5.0	13.45 ± 0.20	1.54	62	2.86
TU495	Sandstone	Toarcian-Aalenian	Greater Caucasus	1754	0469216 4720975	24	0.67	41	27.97	1696	100.00	11.86	7411	4.8 ± 0.8	15.04 ± 0.13	1.20	85	2.61
TU496	Gneiss	Late Paleozoic	Greater Caucasus	1320	0469676 4730334	20	0.61	39	24.26	1563	100.00	9.65	5010	4.2 ± 0.7	15.19 ± 0.09	0.92	97	2.13
TU501[c]	Sandstone	Middle Eocene	Eastern ATFTB	561	0476497 4631400	88	0.16	574	0.64	2320	99.35	11.78	7366	45.3 ± 3.1	-	-	-	2.68
TU515[c]	Gneiss-diorite	Precambrian-Early Paleozoic	Khrami Massif	985	0431453 4600622	21	0.55	288	2.37	1242	37.65	11.35	7094	43.6 ± 3.7	13.72 ± 0.21	1.69	65	2.12

ATFTB = Adjara-Trialeti fold-and-thrust belt. MCTL= mean confined tracks length. Central ages are calculated using dosimeter U-free mica CN5 as external detector and ζ = 332.68 ± 16.54 (analyst T. Gusmeo); ρs= spontaneous track densities (x 105 cm-2) measured in internal mineral surfaces; Ns= total number of spontaneous tracks; ρi and ρd= induced and dosimeter track densities (x 106 cm-2) on external mica detectors (g= 0.5); Ni and Nd= total number of induced and dosimeter tracks; P(χ2)= probability of obtaining χ2-value for n degrees of freedom (n= number of crystals-1): a probability >5% is indicative of a homogeneous population. A = results from Vasey et al., 2020; b = results from Cavazza et al., 2019; c = results from Gusmeo et al., 2021.

Table 5.4: Results of new and published zircon (U-Th)/He analyses on the samples collected along the Georgian Military Road in the southern central Greater Caucasus.

Sample	**Rock Type**	**Age**	**Location**	**Elevation (m)**	**UTM Coordinates (38T)**	**Replicate**	**Ft**	**Corrected age (Ma)**	**Error (Ma)**	**Mean Age (Ma)**	**Mean error (Ma)**	**^{4}He (mol)**	**U 238 (ppm)**	**Th 232 (ppm)**	**eU**	**Rs (Equivalent radius, µm)**
AB0938[a]	Ortogneiss	Late Paleozoic	Greater Caucasus	1300	0469790 4731455	AB0938Zra	0.77	7.43	0.08	8.2	1.0	-	2746.5	659.6	2901.5	48.8
						AB0938Zrb	0.76	6.88	0.07			-	1701.3	748.2	1877.1	46.6
						AB0938Zrc	0.75	10.24	0.10			-	1912.6	591.8	2051.7	44.2
K1[a]	Granodiorite	Late Paleozoic	Greater Caucasus	1434	0469520 4728642	V16046DZra	0.74	7.44	0.08	7.9	0.3	-	1048.1	334.1	1126.6	45.3
						V16046DZrb	0.73	8.30	0.09			-	479.4	163.5	517.8	42.0
						V16046DZrc	0.77	8.00	0.08			-	1135.7	362.1	1220.8	49.5
K2[a]	Mylonitic gneiss	Late Paleozoic	Greater Caucasus	1522	0469793 4728308	V16052BZra	0.75	5.86	0.06	7.1	0.7	-	1087.4	355.4	1170.9	44.8
						V16052BZrb	0.71	8.10	0.08			-	1159.7	503.8	1278.1	41.1
						V16052BZrc	0.73	7.28	0.08			-	1143.1	409.3	1239.3	42.0
TU491	Granitoid clasts in conglomerate	Late Eocene (conglomerate)	Greater Caucasus	772	0479248 4666600	TU491-1	0.84	135.71	1.82	136.8	1.1	$1.44*10^{-12}$	297.2	231.0	351.5	68.0
						TU491-2	0.84	136.73	1.93			$1.25*10^{-12}$	264.6	142.0	298.0	71.6
						TU491-3	0.86	137.99	1.97			$1.70*10^{-12}$	252.9	115.9	280.1	78.2
TU492	Sandstone	Cenomanian	Greater Caucasus	922	0473963 4680238	*TU492_1*	*0.77*	*33.11*	*0.47*	57.2	0.8	$3.79*10^{-12}$	*747.2*	*403.6*	*842.0*	*45.9*
						TU492_2	0.75	57.21	0.76			$2.22*10^{-13}$	407.8	303.9	479.3	43.1
						TU492_3	*0.81*	*17.67*	*0.24*			$1.42*10^{-13}$	*429.6*	*180.2*	*471.9*	*58.3*
TU493	Sandstone	Aptian-Albian	Greater Caucasus	1057	0474870 4688016	*TU493-1*	*0.71*	*14.21*	*0.21*	57.4	0.8	$3.34*10^{-14}$	*862.9*	*200.9*	*910.2*	*36.0*
						TU493-2	*0.71*	*7.55*	*0.11*			$1.28*10^{-14}$	*1299.9*	*387.5*	*1391.0*	*36.2*
						TU493-3	0.72	57.42	0.79			$4.88*10^{-14}$	217.7	190.2	262.4	37.7
TU494	Sandstone	Oxfordian-Tithonian	Greater Caucasus	2021	0458552 4711144	TU494-1	0.70	5.31	0.08	4.5	0.7	$8.00*10^{-15}$	517.0	83.39	536.6	34.9
						TU494-2	0.69	3.95	0.06			$7.13*10^{-15}$	752.1	132.1	783.1	33.3
						TU494-3	0.66	4.32	0.06			$2.64*10^{-15}$	433.7	287.0	501.1	29.9
TU495	Sandstone	Toarcian-Aalenian	Greater Caucasus	1754	0469216 4720975	TU495-1	0.78	5.05	0.07	5.3	0.5	$4.70*10^{-14}$	675.4	226.9	728.8	49.6
						TU495-2	0.76	5.86	0.08			$2.08*10^{-14}$	397.7	254.3	457.5	44.6
						TU495-3	0.74	4.99	0.07			$1.59*10^{-14}$	491.6	296.8	561.3	41.1
TU496	Gneiss	Late Paleozoic	Greater Caucasus	1320	0469676 4730334	TU496-1	0.84	9.34	0.12	8.2	1.2	$5.82*10^{-13}$	1834.8	840.1	2032.2	70.3
						TU496-2	0.87	7.03	0.09			$6.88*10^{-13}$	1533.1	653.9	1686.7	83.2
						TU496-3	0.80	8.23	0.12			$1.18*10^{-13}$	926.7	152.6	962.6	53.7

For each sample, corrected ages with relative error of each replicate are shown, and the weighted mean age is also reported. The effective uranium value (eU = [U] + 0.235*[Th]) gives an indication of the goodness of the data. The replicates in italics (Samples TU492 and TU493) were discarded and are not considered in the discussion, since they yield ages lower than the AFT age from Sample TU492. Sample TU492 has a negative age-eU correlation, hence suffered from radiation damage. Sample a = results from Vasey et al., 2020.

The Early Cretaceous conglomerate yields an AHe age of about 5 Ma, whereas the granitoid clasts in the Late Eocene conglomerate yield a ZHe age of about 137 Ma and AHe single-grain ages between about 7 and 14 Ma (Fig. 5.4; Tables 5.2 and 5.4). Thermal maturity analyses on the sedimentary rocks in this sector indicate that they experienced maximum burial temperatures never exceeding about 100-150 °C (Corrado et al., 2021); these results indicate that the AHe system is fully reset, whereas the ZHe system is not reset, hence the obtained ZHe ages record an older cooling/exhumation history registered by the granitoid clasts.

In the eastern Adjara-Trialeti FTB, new apatite fission-track results have been obtained from three Oligocene-Miocene sandstones (TU483, TU504, and TU505; Fig. 5.4; Table 5.3). The three samples have high $P(\chi^2)$ values, indicating a single population of grains, and yield AFT central ages of 36.3, 39.6, and 63.4 Ma, respectively. Thermal maturity analyses on the same samples, or in nearby sedimentary rocks, indicate that these samples are partially-to-not reset (Corrado et al., 2021). All three samples contained enough confined tracks to perform inverse statistical modelling (Chapter 4; Fig. 5.5). Modelling results for samples TU504 and TU505 indicate fast cooling/exhumation since Early-Middle Miocene times, starting between about 20 and 15 Ma, whereas sample TU483 was not buried enough to provide truly reliable constraints on the post-depositional history: nevertheless, the modelling results point to Middle Miocene inception of cooling/exhumation also for this sample (Figs. 5.5).

New apatite (U-Th)/He results were obtained from sample TU515, a Precambrian-Early Paleozoic gneiss from the Khrami Massif which already provided an AFT central age and robust statistical inverse modelling results (Gusmeo et al., 2021) (Chapter 2; Fig. 5.4; Tables 5.2 and 5.3). Such analyses have been performed in order to try to better constrain the cooling history in the shallowest crustal levels, at the lowest temperatures. AHe single-grain ages range between about 17 and 28 Ma (Table 5.2). The updated statistical inverse modelling, integrating also AHe data together with the other thermochronological, geochronological and stratigraphic constraints already used previously, confirms Paleocene-Early Eocene inception of slow cooling. A possible increment of fast cooling/exhumation in the Early-Middle Miocene since about 20-15 Ma (Fig. 5.6) is suggested by modelling, although at the limit of the resolution of the dataset.

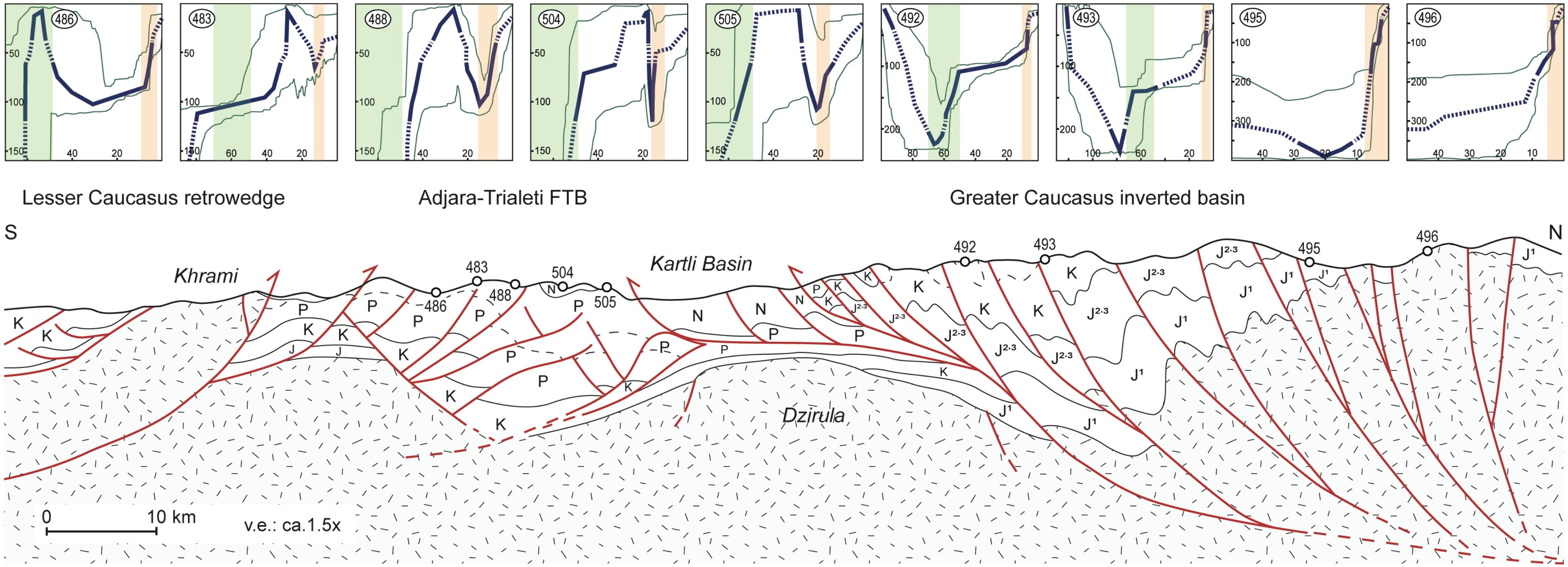

Figure 5.5: Schematic geological cross-section across the southern pro-wedge of the central Greater Caucasus, the western Kura Basin, and the eastern Adjara-Trialeti FTB to the northern tip of the Lesser Caucasus retro-wedge (modified after Alania et al., pers. comm.; Nemčok et al., 2013; Mosar et al., 2022; Tan et al., 2021). Note the 1.5x vertical exaggeration. Statistical inverse modelling results of nine samples, projected along the profile (white dots), are shown with time on the x-axis and temperature on the y-axis (note the non-uniform vertical and horizontal scales across the models). The pale green areas mark the envelope of all t-T paths having a good (GOF > 0.5) fit with the data; the blue lines indicate the best-fit paths, and are dashed when not constrained by data. Green and orange vertical stripes indicate the Paleocene-Early Eocene and Middle-Late Miocene cooling events, in response to Sevan-Akera and Bitlis continental collisions, respectively. See Appendix II for more detailed modelling results.

Figure 5.6: Thermochronologic statistical inverse modelling results for sample TU515. Green area marks the envelope of all t-T paths having a good (GOF > 0.5) fit with the data; red line is the mean t-T path; blue line is the best-fit path. Parameters related to inverse modelling are reported: GOF (goodness-of-fit) gives an indication of the fit between observed and predicted data (values close to 1 are best). Upper left square: Histogram showing the distribution of horizontally confined fission-track lengths. Upper right square: Radial plot of single-grain AFT ages.

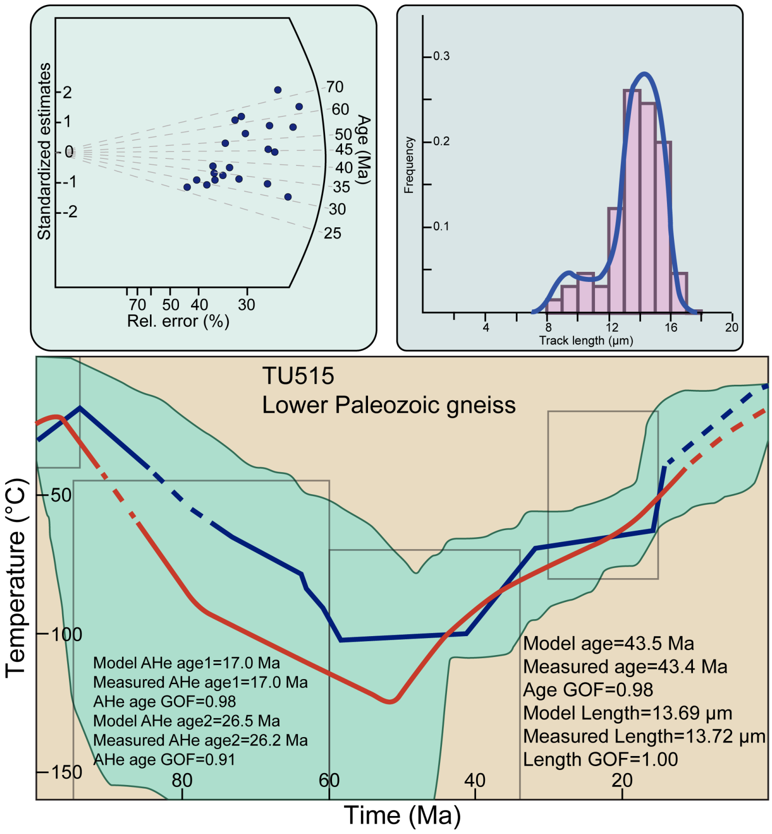

5.3 Integration of new and published data

The new low-temperature thermochronological results presented in Section 5.2 provide compelling constraints on the cooling/exhumation history of the southern side of the central Greater Caucasus, and contribute to partially fill the gap in thermochronologic data along the orogenic belt, which indeed still needs much more data to be considered comprehensive (Fig. 5.1). Statistical inverse modelling results performed on several samples along the studied transect quantitatively define their time-temperature evolution and allows comparison with other thermochronologic studies in other sectors of the Greater Caucasus.

New ZHe, AFT and AHe results from the axial zone of the orogen (samples TU494, TU495 and TU496) are in general agreement with previously published results from the same area (Fig. 5.4). Their statistical inverse modelling (Fig. 5.5) indicates fast cooling/exhumation of this sector of the Greater Caucasus since about 12-10 Ma, a result very similar to the inverse modelling result obtained by Vasey et al. (2020) in the same area and shown in Figure 5.7.

Such rapid cooling/exhumation phase, beginning slightly earlier at about 15 Ma, is evidenced also in the statistical inverse modelling results from the central part of the transect crossing the southern central Greater Caucasus (samples TU492 and TU493; Fig. 5.5). These results are in agreement with the single AHe mean age obtained by Trexler et al. (2022) in the same area (Fig. 5.4) In this sector, though, modelling results clearly evidence a previous cooling/exhumation phase during latest Cretaceous-early Paleogene times which was not recognised before in this sector of the Greater Caucasus.

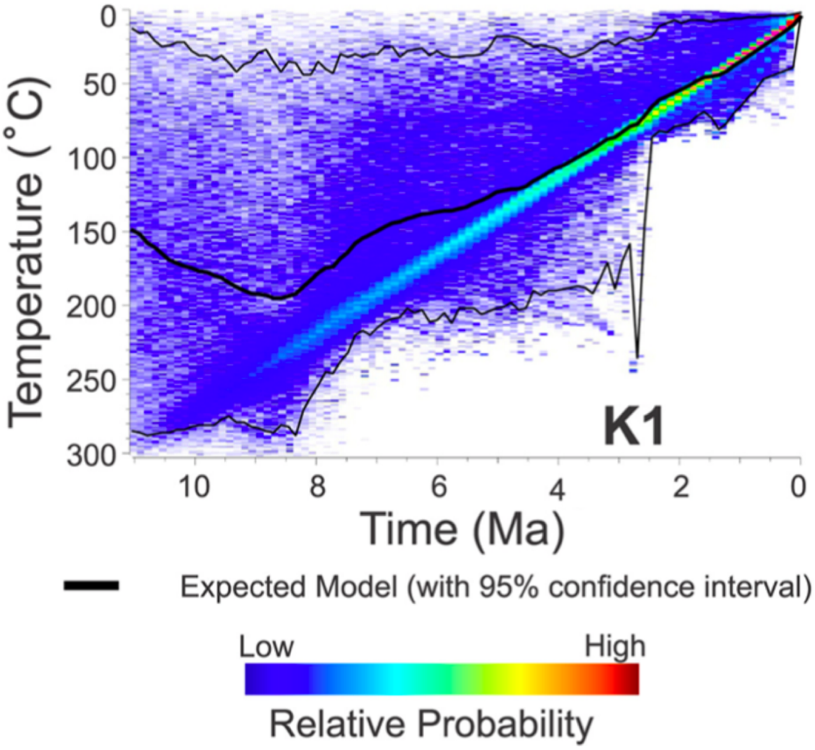

Figure 5.7: Thermochronologic statistical inverse modelling result for sample K1 (Vasey et al., 2020).

Moving further south, the newly acquired AHe results (TU491), supported by the mean age reported by Trexler et al. (2022), confirm that also the southernmost sector of the analysed transect experienced cooling/exhumation since about 15-10 Ma (Fig. 5.4; Table 5.2). In this area, the old and unreset ZHe age (~ 137 Ma, sample TU491) yielded by the granitoid clasts within the Upper Eocene conglomerate analysed is very similar to a ~ 134 Ma Ar-Ar muscovite age found in the western Greater Caucasus close to the Main Caucasus Thrust (MCT) shear zone (Vasey et al., 2020). These authors interpret the Ar-Ar muscovite age to reflect formation of the MCT during partial inversion of the Greater Caucasus basin at the Jurassic-Cretaceous boundary or partial resetting (hence younging of an originally older age) due to post-Jurassic cooling (Nikishin et al., 2011; Vasey et al., 2020). Given the very low dispersion of our single-grain ages, a rapid cooling across the ZHe closure temperature seems more probable.

Overall, our dataset describes a progressive increase of ZHe, AFT and AHe ages moving towards the south along the analysed traverse. For example, ZHe ages are around 8 Ma in the axial zone, increasing to around 137 Ma at the southern end, although to the very south of the Dariali Massif they decrease to around 5 Ma. The span in AHe ages is much more limited, since they range from around 2-3 Ma in the axial zone and increase up to around 10 Ma at the southern end. Both maximum paleotemperatures (Corrado et al., 2021) and degree of metamorphism (Trexler et al., 2022) decrease from north to south. Our thermochronologic data and inverse modelling results indicate that the whole transect experienced cooling/exhumation from shallow depths (corresponding to temperatures between about 70 and 100 °C, i.e. higher than the closure temperature of the AHe system and lower than the one of the AFT system) in the last ~ 10 Ma, whereas only the axial zone of the orogen experienced very rapid cooling/exhumation from greater crustal depths (corresponding to > 180 °C, i.e. the closure temperature of the ZHe system) to surface in the same time span (Figs. 5.5).

Such late Middle Miocene-Pliocene phase of rapid cooling/exhumation revealed by our dataset in the southern central Greater Caucasus is consistent with the Middle Miocene timing of Arabia-Eurasia hard collision along the Bitlis suture (Okay et al., 2010; Cavazza et al., 2018) and the coeval widespread deformation in a wide swath of the hinterland, that is interpreted as a far-field effect of the same continental collision (Axen et al., 2001; Guest et al., 2006, 2007; Ballato et al., 2008, 2016; Albino et al., 2014; Madanipour et al., 2017; Cavazza et al., 2017, 2019; Barber et al., 2018; Gusmeo et al., 2021). The uplift of the studied sector of the Greater Caucasus, probably caused by the final structural inversion of the Greater Caucasus basin, may also be placed within the general framework of northward transmission of far-field collisional stress from the Bitlis suture following Arabia-Eurasia continental collision (see Chapters 2, 3 and 4 for details on such mechanism).

The older ZHe and AFT ages and the related thermochronologic inverse modelling results from samples TU492 and TU493 (Figs. 5.5), in the southern half of the analysed transect, clearly indicate that this sector experienced an older (Late Cretaceous-early Paleogene) cooling event which may have caused exhumation from deeper to shallower crustal depths (corresponding to temperatures between about 70 and 100 °C, see above). Such Late Cretaceous-early Paleogene phase of cooling/exhumation is coeval with the continental collision between the Anatolide-Tauride-Armenian block and the Eurasian margin along the Erzinçan-Sevan-Akera suture zone (Okay and Tüysüz, 1999; Stampfli et al., 2001; Cavazza et al., 2004; Rolland et al., 2009; Sosson et al., 2010). It would be tempting to interpret such cooling/exhumation phase as due to partial inversion of the central Greater Caucasus basin in response to the Sevan-Akera suturing.

If examined carefully, previous results from the western Greater Caucasus (Vincent et al., 2011, 2020; Vasey et al., 2020) indicate that a wide sector of its axial zone (particularly its basement core) experienced rapid cooling/exhumation during Middle-Late Miocene times (Fig. 5.2), in agreement with our data. Statistical inverse modelling results reported by Vincent et al. (2011) for three samples from the western Greater Caucasus crystalline basement indicate a sharp increase of cooling rates since Early-Middle Miocene times (Fig. 5.8). Thus, a wide sector of the Greater Caucasus was affected by deformation and uplift since Middle Miocene times. Nevertheless, looking at the distribution of the AFT and AHe cooling ages, it appears that they generally increase abruptly west of the longitude of the Black Sea coastline, in western Georgia (Fig. 5.2). This may suggest that the rigid, quasi-oceanic crust of the eastern Black Sea (Shillington et al., 2008, 2009; Edwards et al., 2009) prevented efficient transmission of far-field compressional stresses towards the westernmost portion of the orogen from the Bitlis suture, that instead focused preferentially along the Eastern Pontides promoting their fast exhumation (Albino et al., 2014).

Interestingly, the statistical inverse modelling results reported by Vincent et al. (2011) on two basement samples clearly indicate initial rapid cooling during Late Cretaceous-Eocene times, followed by a nearly flat thermochronologic evolution during Eocene, Oligocene and Early Miocene times prior to the final Middle-Late Miocene fast cooling phase (Fig. 5.8d, e): this evolution resembles the one found in samples TU492 and TU493 in the southern central Greater Caucasus, thus suggesting that also some sectors of the western Greater Caucasus experienced a cooling/exhumation event (partial basin inversion?) in the Late Cretaceous-early Paleogene, i.e. during the Sevan-Akera continental collision.

Moving to the eastern Greater Caucasus, the few (unpublished) thermochronologic data available indicate that at least some portions of this sector experienced fast cooling/exhumation during Miocene-Pliocene times (Avdeev, 2011; Bochud, 2011) (Fig. 5.2). Only one AFT result from this region provides a reliable indication of cooling below the ~ 110 °C closure temperature (sample AZ109 of Bochud, 2011): such sample yields a central age of 12.5 Ma and contained enough confined tracks for statistical inverse modelling (Fig. 5.9). Modelling results do not provide clear information on the older time-temperature history, but clearly indicate fast cooling/exhumation since at least Late Miocene times (Fig. 5.9D), in agreement with the other results obtained in the central and western Greater Caucasus (this study; Avdeev and Niemi, 2011; Vincent et al., 2011, 2020; Vasey et al., 2020). Bochud (2011) provide statistical inverse modelling results from other three samples (AZ083, AZ091 and AZ093; Fig.

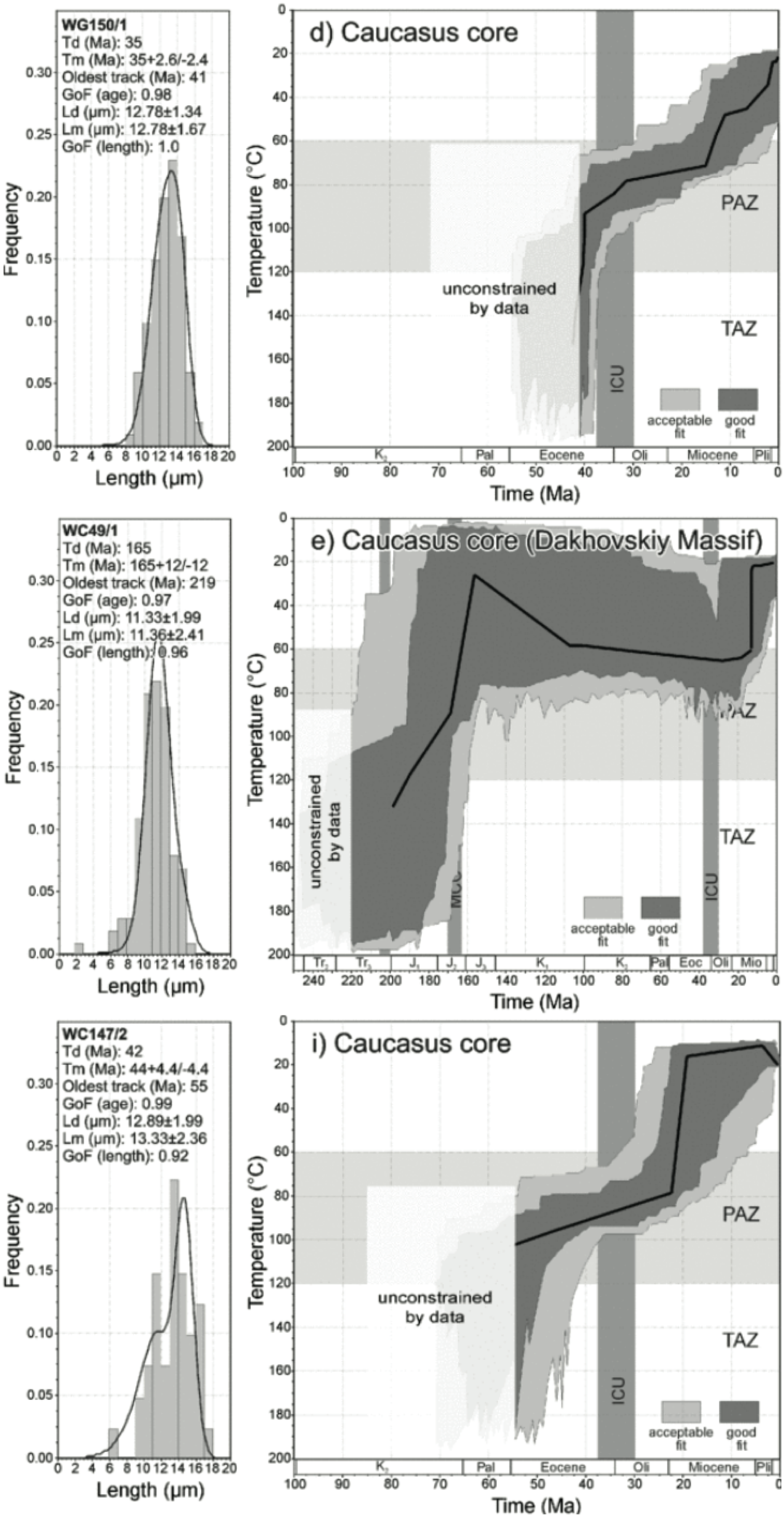

Figure 5.8: Time-Temperature paths obtained from statistical inverse modelling of three samples derived from the western Greater Caucasus basement core (Vincent et al., 2011). For all three graphs, the dark area marks the envelope of all t-T paths which have a good (GOF > 0.5) fit with the data, and the black line represents the best-fit path. ICU is the Initial Caucasus Uplift, which the authors assign to the Late Eocene-Early Oligocene. Further details are reported in Vincent et al. (2011).

5.9 A, B, and C) which yield AFT results with very low P(χ^2). Two modelling results indicate inception of fast cooling since the Late Miocene, whereas sample AZ091 (Fig. 5.9B) suggest an earlier inception of slower cooling since Oligocene times.

In conclusion, the few AFT and AHe results available in the eastern Greater Caucasus (Fig. 5.2) and the statistical inverse modelling results shown in Figure 5.9 suggest that this sector of the orogen was affected by cooling/uplift since at least Late Miocene times, suggesting continued stress transfer from the Bitlis suture towards the north after Middle Miocene Arabia-Eurasia continental collision. Miocene-Pliocene deformation and uplift is also attested by structural and stratigraphic data obtained both on the northern and southern sides of the eastern Greater Caucasus (Sobornov, 1996, 2021; Mosar et al., 2010; Trikhunkov et al., 2021).

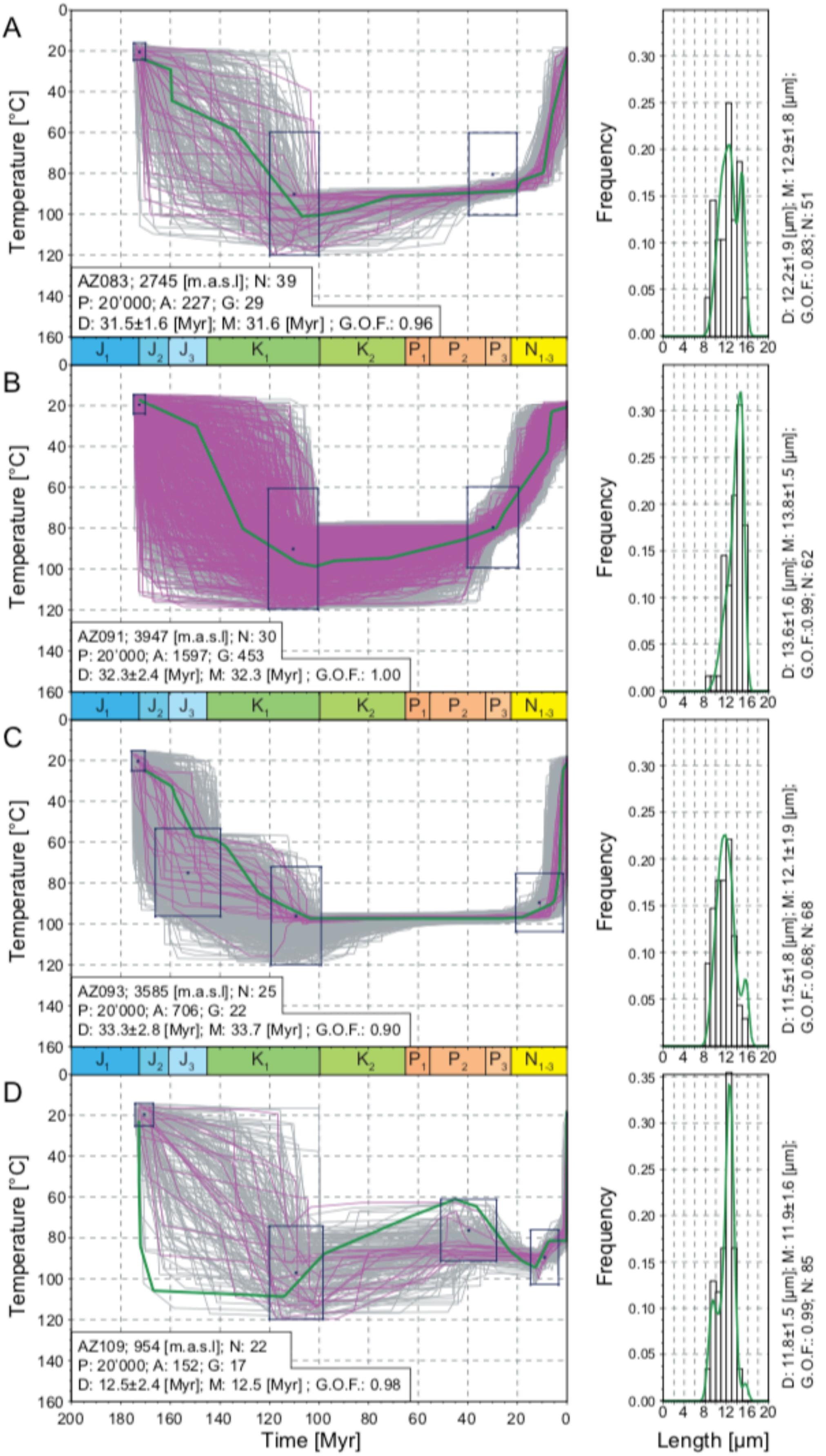

Figure 5.9: Time-Temperature paths obtained from statistical inverse modelling of samples AZ083, AZ091, AZ093 and AZ109 from the eastern Greater Caucasus (Bochud, 2011). Gray lines are acceptable paths (GOF > 0.05), purple lines are good paths (GOF > 0.5) and the green line is the best-fit path. GOF (goodness-of-fit) provides an indication on the fit between modelled and measured data (values close to 1 are best). To the right of each plot is the frequency histogram of the measured confined track lengths, fitted by statistical inverse modelling (green line).

Chapter 6

DISCUSSION AND CONCLUSIONS

The integration of low-temperature thermochronology (apatite fission-track and apatite and zircon (U-Th)/He), thermal maturity analyses on both organic matter and clay minerals, and thermal modelling of borehole data can successfully elucidate the entire thermo-tectonic (burial-exhumation) evolution of regions that experienced a complex geological history. The results of this Dissertation provide compelling constraints on the subsidence history and timing of orogenic exhumation of the former Adjara-Trialeti basin and of the western Kura Basin, and on the thermo-tectonic evolution of the southern central Greater Caucasus, which in turn have implications for the whole Caucasian region and, at a greater scale, mirror the tectonic evolution of the region which currently represents the Arabia-Eurasia collision zone. Chapter 5 provides an overview of all thermochronological data currently available for the Greater Caucasus, highlighting their limitation and what objective conclusions can be drawn from such compilation, and then provides new thermochronological results obtained in a transect along the southern central Greater Caucasus, the eastern Adjara-Trialeti FTB and the Khrami Massif.

The two main sutures that characterise the modern Arabia-Eurasia collision zone (i.e. the Erzinçan-Sevan-Akera suture zone to the north and the Bitlis-Zagros suture zone to the south) and the relative orogenic belts (i.e. the Pontides-Lesser Caucasus and the Bitlis-Zagros orogens, respectively) record the progressive history of convergence between the African and Eurasian plates throughout Mesozoic and Cenozoic times, related to the consumption of the intervening Northern and Southern Neotethyan oceans and the ensuing continental collisions (Dewey et al., 1986; Okay and Tüysüz, 1999; Stampfli et al., 2001; Barrier et al., 2018).

In the following sections, the results obtained in this study, and reported in the previous chapters, will be explained and integrated in the context of the tectonic/geodynamic events that affected the southern margin of Eurasia since Late Cretaceous times, with reference to incremental hinterland deformation related to the development of the Erzinçan-Sevan-Akera and Bitlis suture zones.

6.1 The Caucasian response to the Sevan-Akera collision

The Northern Neotethys ocean closed during the Maastrichtian-Ypresian diachronous collision between the irregular margins of the Anatolide-Tauride-Armenian block and the Eurasian plate (Figs. 6.1, 6.2), forming the Izmir-Ankara-Erzinçan-Sevan-Akera suture zone (Stampfli et al., 2001; Cavazza et al., 2004; Barrier and Vrielynck, 2008; Rolland et al., 2009; Barrier et al., 2018). Such continental collision amalgamated Variscan terranes of Eurasian affinity and Panafrican terranes of Gondwanan affinity, respectively to the north and south of the suture, and created the Pontides-Lesser Caucasus orogenic belt (Khain, 1994; Okay and Tüysüz, 1999; Rolland et al., 2012, 2016; Hässig et al., 2013). In the northern foreland of this orogenic belt, during Paleocene-Early Eocene times in the Adjara-Trialeti area a deep east-west-trending marine elongate basin formed where thick terrigenous turbidites were deposited (Borjomi Flysch). The Adjara-Trialeti area at that time was likely a flexural basin (Fig. 6.1), as supported by the progressive eastward thickening of the Borjomi Flysch induced by the oblique collision (Gamkrelidze, 1949; Banks et al., 1997; Yılmaz et al., 2000, 2014; Adamia et al., 2011). Rapid increase of subsidence in the eastern Adjara-Trialeti basin during Paleocene-Early Eocene times is also attested by thermal modelling results derived from borehole data and showing an eastward thickening of Paleocene-Early Eocene strata (see Chapter 4).

The continental collision between the Anatolide-Tauride-Armenian block and the Eurasian plate induced a decrease in plates convergence rates, which in turn caused rollback of the Northern Neotethys slab triggering upper plate extension and back-arc opening of the Adjara-Trialeti basin during the Middle Eocene (Fig. 6.1). Middle Eocene rifting is testified by coeval thick volcaniclastic turbidites interbedded with submarine lavas and shallow plutonic/hypabyssal intrusions (Adamia et al., 1977, 1981, 2011; Okrostsvaridze et al., 2018, 2021). The Middle Eocene section thickens towards the Black Sea, reaching more than 5,000 m, and plutonic rocks are most abundant in the central/western sector of the Adjara-Trialeti FTB. Volcanic and volcaniclastic rocks associated to rifting have been recognised in the stratigraphy of the eastern Adjara-Trialeti wells and indicate a second pulse of increased subsidence within the basin during Middle-Late Eocene times (Chapter 4).

Thermochronological and stratigraphic data indicate that the Dzirula Massif, to the north of the Adjara-Trialeti FTB, was exhumed during Paleocene-Eocene times (Vincent et al., 2011; Gusmeo et al., 2021). Such exhumation may have been directly triggered by the coeval Sevan-Akera continental collision, or alternatively be interpreted as due to uplift during the Adjara-

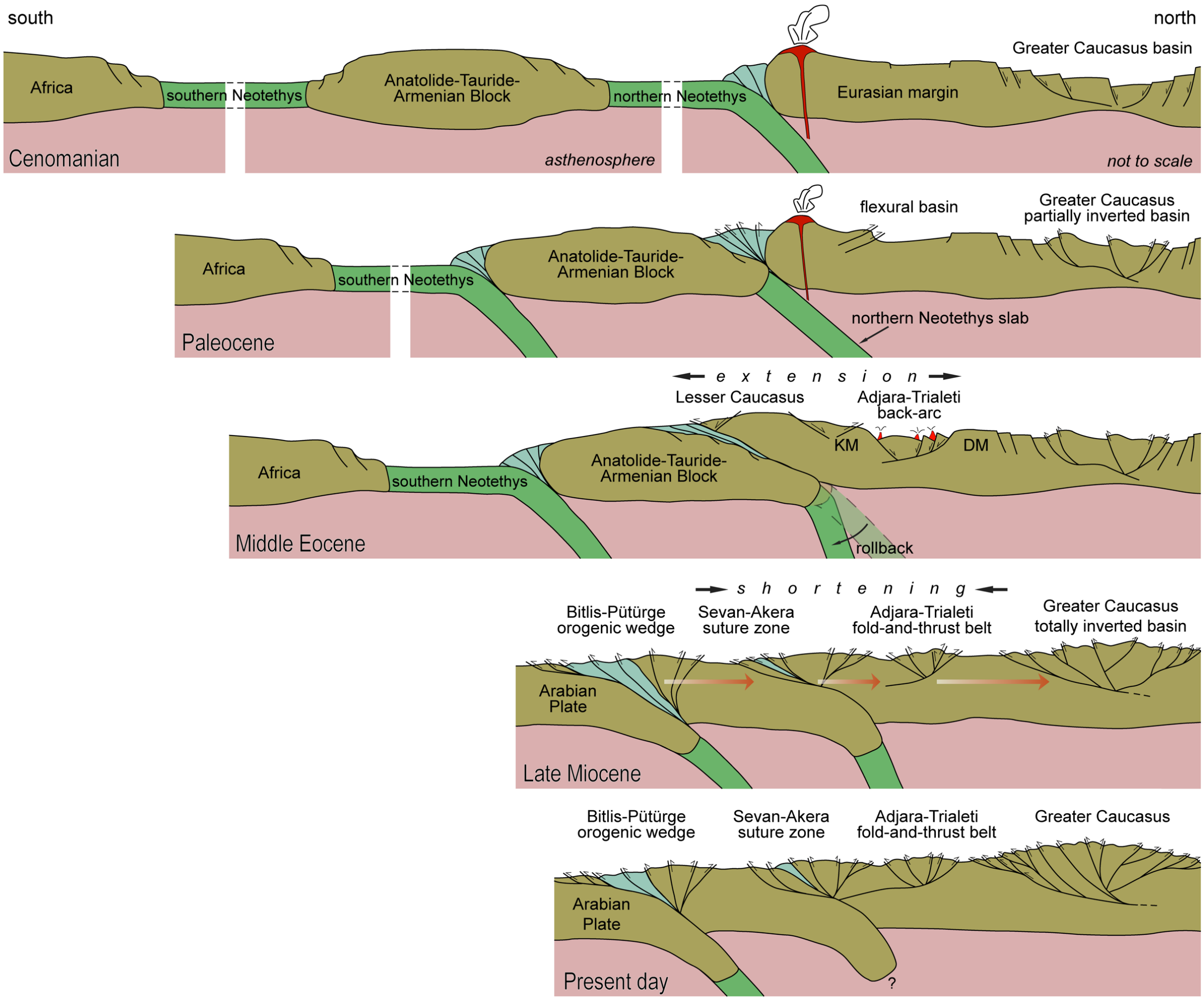

Figure 6.1: North-south geodynamic sketch sections across the eastern Anatolian-Caucasian domain. Continental accretion along the southern Eurasian margin occurred with the collision of (i) the Anatolide-Tauride-Armenian Block (Maastrichtian-Ypresian) and (ii) the Arabian Plate (Middle Miocene). The two episodes of continental collision were separated by a phase of upper plate extension resulting from rollback of the subducting northern Neotethyan slab. The Arabia-Eurasia collision caused far-field incremental deformation in the upper plate, with additional shortening in the Lesser Caucasus and inversion of the Adjara-Trialeti, Kura and Greater Caucasus basins. DM = Dzirula Massif; KM = Khrami Massif.

Trialeti rifting (i.e. the Dzirula Massif would have been part of the rift shoulders), thus as an indirect consequence of the same continental collision (Chapter 2).

The results of apatite fission-track analysis and statistical inverse modelling from the Khrami Massif (Cavazza et al., 2019; Gusmeo et al., 2021) point to inception of slow cooling/exhumation during Paleocene-Early Eocene times, which again can have been caused by continental collision along the Sevan-Akera suture (Chapter 2). This interpretation is supported by industrial seismic lines which indicate that the massif is the surficial expression of a north-vergent basement thrust sheet, overlying a structural duplex made of Jurassic-Cretaceous rocks, within the retro-wedge of the Lesser Caucasus (Gusmeo et al., 2021; Alania, pers. comm.) (Fig. 6.1).

The growing Erzinçan-Sevan-Akera orogen likely represented an important sediment source for the detritus accumulated in the Adjara-Trialeti basin. Hints to this derive from the thermochronologic statistical inverse modelling performed on the samples representing the sedimentary fill of the inverted basin. These samples are partially reset (Corrado et al., 2021; Gusmeo et al., 2021), and inverse modelling provided useful information on their pre-depositional t-T history. Such history consistently indicates fast cooling/exhumation of the source of the apatite grains (i.e. of the detritus) during Paleocene-Early Eocene times (Chapters 2, 4 and 5), a timing in agreement with the Erzinçan-Sevan-Akera orogen growth. The Dzirula Massif, which was exhumed in a similar time span, could represent an additional sediment source from the north (Chapter 2).

Our low-temperature thermochronological data (ZHe, AFT and AHe analyses) from the southern central Greater Caucasus (Chapter 5), indicate that also the Greater Caucasus basin was affected by deformation (partial inversion?) in the latest Cretaceous-early Paleogene, possibly in response to the Erzinçan-Sevan-Akera collision. This is suggested by statistical inverse modelling of two Cretaceous sandstones samples (TU492 and TU493) from the central sector of the former Greater Caucasus basin (Fig. 6.1, 6.2). Thermochronologic statistical inverse modelling results from two basement samples reported from the western Greater Caucasus by Vincent et al. (2011) also show a Late Cretaceous-Eocene cooling which agrees well with our results (Chapter 5). Furthermore, stratigraphic and structural data (growth strata geometries and regional unconformities) and interpretation of seismic sections from the central-western Greater Caucasus and the Rioni Basin also indicate a Paleocene-Eocene compressional event (Saintot and Angelier, 2002; Candaux, 2021), which has been interpreted by Candaux (2021) as a response to coeval Sevan-Akera collision.

In summary, the Late Cretaceous-Paleocene continental collision along the Erzinçan-Sevan-Akera suture was responsible for the building of the Pontides-Lesser Caucasus orogen and triggered diffuse deformation in the Caucasian region (Fig. 6.2), including (i) growth of the Lesser Caucasus retro-wedge and inception of cooling/exhumation in the Khrami Massif (Paleocene-Early Eocene), (ii) flexural subsidence in the Adjara-Trialeti area and deposition of the Borjomi Flysch (Paleocene-Early Eocene), (iii) Paleocene-Eocene cooling/exhumation of the Dzirula Massif (either directly or indirectly linked to continental collision), and, according to our new thermochronologic results and other published data, (iv) Late Cretaceous-Paleogene partial inversion of the central and at least of some sectors of the western Greater Caucasus basin (Chapter 5), and (v) Middle Eocene rifting of the Adjara-Trialeti back-arc basin arguably

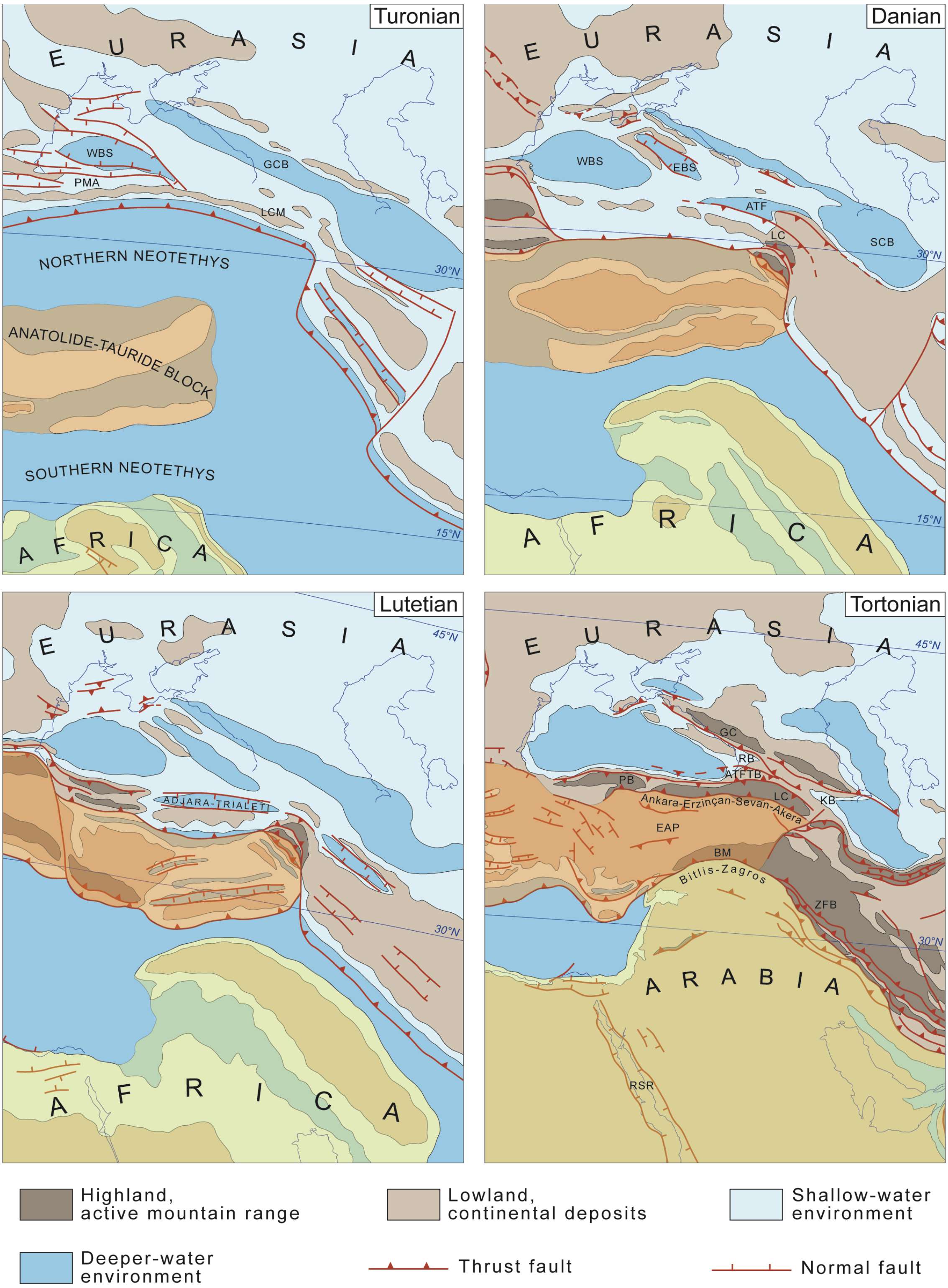

Figure 6.2: Paleogeographic sketch maps showing the evolution of the Arabia-Eurasia convergence zone since Late Cretaceous times, modified after Barrier et al. (2018). During the Turonian, both the northern and southern branches of the Neotethys were open, with the northern branch actively subducting below the southern Eurasian margin to form the Pontides-Lesser Caucasus magmatic arc. The Danian map shows the continental collision between the Anatolide-Tauride Block and Eurasia, forming the Lesser Caucasus orogenic wedge and causing partial inversion of at least the southern central Greater Caucasus basin. In Middle Eocene times rollback of the northern Neotethyan slab triggered opening of the Adjara-Trialeti back-arc basin. Finally, during Tortonian times compressional tectonics was active in the Caucasian region following Middle Miocene continental collision along the Bitlis suture, that caused deformation in a wide region of the hinterland structural inversion of the Adjara-Trialeti and Greater Caucasus back-arc basins, and southward propagation of deformation in the Kura Basin. ATF = Adjara-Trialeti foreland basin; ATFTB = Adjara-Trialeti fold-and-thrust belt; BM = Bitlis Massif; EAP = East Anatolian Plateau; EBS = Eastern Black Sea; GC = Greater Caucasus orogen; GCB = Greater Caucasus Basin; KB = Kura Basin; LC = Lesser Caucasus orogen; LCM = Lesser Caucasus magmatic arc; PB = Pontides Belt; PMA = Pontides magmatic arc; RB = Rioni Basin; RSR = Red Sea rift; SCB = South Caspian Basin; WBS = Western Black Sea; ZFB = Zagros fold-and-thrust belt.

due to Northern Neotethys slab rollback, in turn a consequence of the slower convergence rates following continental collision.

6.2 The Caucasian response to the Bitlis collision

Timing of closure of the Southern Neotethys ocean and collision between the Arabian and Eurasian plates along the Bitlis-Zagros suture zone has long been debated, with proposed Late Cretaceous (Hall, 1976; Berberian and King, 1981; Alavi, 1994), Late Eocene-Oligocene (Jolivet and Faccenna, 2000; Agard et al., 2005; Vincent et al., 2007; Allen and Armstrong, 2008), Miocene (Şengör et al., 1985; Dewey et al., 1989; Robertson et al., 2007) and even Pliocene (Philip et al., 1989; Avdeev and Niemi, 2011) ages. Thermochronologic data, supported by stratigraphic and structural constraints, indicate a discrete Middle Miocene phase of growth of the Bitlis-Pütürge Massif along the Bitlis suture zone, which is interpreted to reflect the inception of continental collision during mid-Miocene times (Okay et al., 2010; Cavazza et al., 2018). The exact timing of continental collision along the Zagros segment of the Arabia-Eurasia suture is still controversial.

Coeval Middle Miocene deformation is registered in a large swath of the Arabia-Eurasia northern hinterland, comprising the Eastern Pontides (Albino et al., 2014), selected portions of the Lesser Caucasus (Cavazza et al., 2017, 2019), the Talysh Mountains (Madanipour et al., 2013, 2017) and the Alborz Mountains (Axen et al., 2001; Guest et al., 2007; Ballato et al., 2008, 2016), indicating that stress from the Bitlis-Zagros suture zone was transmitted efficiently across the East Anatolian-northern Iranian Plateau focusing along rheological discontinuities (Fig. 6.2).

The results of apatite fission-track and (U-Th)/He analyses performed on syn-rift plutonic rocks and on the sedimentary basin fill, together with statistical inverse modelling results (Chapters 2, 4 and 5), constrain the Middle Miocene inception of structural inversion of the Adjara-Trialeti back-arc basin (Gusmeo et al., 2021). Middle-Late Miocene development of the Adjara-Trialeti FTB is confirmed by growth strata geometries in the adjacent Kura and Rioni foreland basins (Banks et al., 1997; Alania et al., 2017; Tibaldi et al., 2017a; Gusmeo et al., 2021), coeval growth of the Gurian fold-belt, the offshore prolongation of the ATFTB in the eastern Black Sea (Tari and Simmons, 2018), and by the stratigraphy of the East Anatolian

Plateau at the southern border of the Adjara-Trialeti FTB (Koçyiğit et al., 2001). The coeval timing of deformation suggests that northward transmission of far-field compressional stresses from the Middle Miocene Arabia-Eurasia collision along the Bitlis suture was responsible for the structural inversion of the Adjara-Trialeti back-arc basin (Gusmeo et al., 2021; Fig. 6.1).

Thermal maturity analyses on the sedimentary successions within the western Kura Basin indicate that its northern sector, called Kura foreland fold-and-thrust belt or Kakheti Ridge or Gombori range, experienced lower maximum paleotemperatures, hence lower burial, than the remaining basin to the south (Chapter 3). Other structural and stratigraphic data suggest that this sector was affected by deformation and uplift since Middle-Late Miocene times (Adamia et al., 2010; Nemčok et al., 2013; Alania et al., 2017, 2018) as a result of southward propagation of deformation from the Greater Caucasus. The difference in thermal maturity between the Kakheti Ridge and the remaining western Kura Basin is attributed to the fact that the former was already being exhumed while the latter was still experiencing subsidence and burial (Chapter 3; Corrado et al., 2021). Thermal modelling of borehole data from wells at the southern margin of the western Kura Basin (Chapter 4) indicate that such region was affected first by flexural subsidence from the northward growing Adjara-Trialeti FTB during the Middle-Late Miocene, and later by deformation by south-directed thin-skinned thrusts since latest Miocene times, consistently with southward propagation of deformation from the Greater Caucasus. Thus, the western Kura flexural foreland basin experienced incremental deformation in response to far-field stress transmission from the Arabia-Eurasia continental collision: (i) during the Middle Miocene initial deformation affected the southern and northern margins in response to Adjara-Trialeti and Greater Caucasus uplift, respectively, and (ii) continued stress transmission from the Bitlis suture caused southward propagation of deformation from the Greater Caucasus, in the form of thin-skinned thrusts which affected the southern margin in latest Miocene times (Chapter 4).

The new thermochronological dataset obtained along the southern central Greater Caucasus and exposed in Chapter 5 consistently points to fast cooling/exhumation of this sector of the orogen since at least late Middle Miocene times (12-10 Ma), slightly later than the inception of deformation registered more to the south. Nevertheless, this pulse of cooling/exhumation associated to the complete structural inversion of the studied sector of the Greater Caucasus basin fits well the timing of Arabia-Eurasia collision (and hinterland deformation), hence can be considered as a result of the northward transmission of far-field compressional stresses from the Bitlis suture (Fig. 6.1). Other thermochronological data obtained more to the west (Avdeev and Niemi, 2011; Vincent et al., 2011, 2020; Vasey et al., 2020) and to the east (Avdeev, 2011;

Bochud, 2011) along the Greater Caucasus are in agreement with the new results (Chapter 5), suggesting that since late Middle Miocene times fast uplift/exhumation affected a wide region of the orogen (Fig. 6.2), probably in a diachronous and not uniform fashion.

Other structural and stratigraphic data obtained on both sides of the orogenic belt and in the adjacent Rioni, Kura, Kuban and Terek foreland basins indicate growth of the Greater Caucasus since Middle Miocene times. For example, Sarmatian (late Middle-early Late Miocene) marine sediments are now found at high altitudes (3700-4000 m a.s.l.) in the eastern Greater Caucasus, indicating very fast uplift in the last ~ 10 Ma (Mosar et al., 2010). Inception of deformation in the Kura foreland fold-and-thrust belt, to the south of the central-eastern Greater Caucasus and resulting form propagation of deformation southward from the latter, also started growing during Middle-Late Miocene times, as attested by growth strata geometries and thermal maturity data (Alania et al., 2017; Corrado et al., 2021). The results of wells thermal modelling from the Kura Basin shown in Chapter 4 indicate that the southern margin of the basin was affected by deformation since the latest Miocene, consistently with southward propagation of deformation from the Greater Caucasus which then must have been started shortly before. Growth strata geometries in the Rioni Basin also indicate that south-directed deformation in response to the western Greater Caucasus uplift since Middle Miocene times (Tibaldi et al., 2017b, 2017a, 2018). On the northern side of the orogen, seismic lines interpretation, subsidence studies from boreholes data and stratigraphic analyses all indicate important deformation/uplift in the Greater Caucasus since Middle Miocene times (Sobornov, 1996, 2021; Mikhailov et al., 1999; Ershov et al., 2003; Mosar et al., 2010).

(U-Th)/He data recently acquired from the Khrami Massif (Chapter 5), in addition to the apatite fission-track data already exposed in Chapter 2, suggest that after initial slow cooling/exhumation since Paleocene-Early Eocene times the massif experienced a pulse of fast cooling/exhumation during Miocene times, which can be considered further evidence of efficient far-field stress transmission from the Bitlis suture towards the north.

In conclusion, the Middle Miocene Arabia-Eurasia continental collision along the Bitlis suture was responsible for coeval deformation of a large area of the hinterland, as already pointed out in several works, caused by efficient far-field stress transmission towards the north from the main locus of Arabian indentation (Axen et al., 2001; Guest et al., 2007; Ballato et al., 2008; Albino et al., 2014; Madanipour et al., 2017; Cavazza et al., 2019). Such stresses also focused in the Caucasus region, causing (i) Middle Miocene structural inversion of the Adjara-Trialeti back-arc basin (Chapters 2, 3, 4 and 5), (ii) Middle-Late Miocene deformation in the Rioni and Kura foreland basins (Banks et al., 1997; Alania et al., 2017; Tibaldi et al., 2017a;

Corrado et al., 2021; Gusmeo et al., 2021), in the eastern Black Sea offshore (Tari and Simmons, 2018) and in the East Anatolian Plateau (Koçyiğit et al., 2001), (iii) Middle-Late Miocene uplift of the northern Kura Basin (Kakheti Ridge) propagating southward and affecting the southern margin of the basin since the latest Miocene, (iv) a Miocene pulse of fast cooling/exhumation in the Khrami Massif (Chapter 5), and (v) fast cooling/exhumation of the southern central Greater Caucasus (Chapter 5) and at least of selected portions of the western and easter sectors of the orogen (Mosar et al., 2010; Avdeev and Niemi, 2011; Vasey et al., 2020; Vincent et al., 2020; Sobornov, 2021).

6.3 Tectonic evolution of the Greater Caucasus

Current GPS data indicate that the Caucasian region absorbs about 15-20 % of the strain associated to the Arabia-Eurasia collision. Vectors magnitude increases progressively from about 2 mm/yr close to the Black Sea coast in the west, up to about 14 mm/yr (relative to Eurasia fixed) close to the Caspian Sea coast in the east (Reilinger et al., 2006; Forte et al., 2010; Ismail-Zadeh et al., 2020), consistent with the anticlockwise rotation of the Arabian Plate (Reilinger et al., 2006). However, the magnitude of horizontal movements dramatically drops north of the southern margin of the Greater Caucasus (Karakhanyan et al., 2013; Sokhadze et al., 2018). This is particularly evident in the central-eastern sectors of the belt, indicating that most of the strain associated to the Arabia-Eurasia post-collisional convergence is absorbed, in the Caucasian region, within the Kura Basin and/or along the southern margin of the Greater Caucasus (Reilinger et al., 2006; Forte et al., 2010, 2013; Ismail-Zadeh et al., 2020).

Such pattern is confirmed by the record of seismicity, which focuses particularly along the southern margin of the Greater Caucasus (Tibaldi et al., 2019; Ismail-Zadeh et al., 2020; Gunnels et al., 2021), with a general decrease in seismicity towards the west (Tsereteli et al., 2016). Focal mechanisms are mostly transpressional in the Kura Basin along the southern border of the eastern Greater Caucasus, whereas they are mostly indicative of thrust faulting in the central and western sectors (Tibaldi et al., 2019). Geodetic and seismic data together indicate that the Greater Caucasus is mainly deforming in an aseismic way and with prevailing vertical movements in its interior, where geomorphologic data indicate fast uplift rates (Mosar et al., 2010; Forte et al., 2014, 2016), whereas horizontal, seismically active shortening occurs preferentially at the margins (in particular along the southern margin) (Forte et al., 2014).

Along the southeastern margin of the Greater Caucasus, the Kura fold-and-thrust belt shows an eastward along-strike decrease in elevation, width, structural complexity, exposure depth, age of the rocks involved into thrusting, and total shortening (Forte et al., 2010, 2013), thus suggesting that inception of deformation becomes progressively younger toward the east. Indeed, age of initial deformation/uplift in the Kura fold-and-thrust belt is attributed to the Middle-Late Miocene in the westernmost portion (Alania et al., 2017, 2018) and to the Pliocene more to the east (Forte et al., 2010, 2013). The eastward increase in horizontal movements and widening of the Kura Basin are in agreement with a progressive eastward younging of deformation, which has begun earlier to the west, where incipient collision between the facing Greater and Lesser Caucasus is occurring (Alania et al., 2021), and has propagated towards the east. Such conclusion is also supported by the Sarmatian (late Middle-early Late Miocene) inception of structural inversion in the Rioni Basin (Tibaldi et al., 2017a, 2017b, 2018).

Diachronous inception of fast cooling/exhumation along the strike of the Greater Caucasus is also attested by thermochronological data (Chapter 5), which record a progressive younging of cooling ages from west to east (Trexler et al., 2022) supported by the age of inception of fast cooling in the axial zone of the orogen revealed by thermochronologic statistical inverse modelling, which begins in the Early-Middle Miocene in the western Greater Caucasus (Vincent et al., 2011), in the Middle-Late Miocene in the central Greater Caucasus (this study; Vasey et al., 2020; Vincent et al., 2020), and in the latest Miocene in the eastern Greater Caucasus (Bochud, 2011) (see discussion in Chapter 5). Detrital zircon U-Pb analyses in the Caucasian region reveal changes in sediment provenance and in the Greater Caucasus structure between the Middle Miocene and the Pliocene, also suggesting acceleration of exhumation/uplift rates since the latest Miocene (Cowgill et al., 2016; Tye et al., 2020). Structural data and subsidence analyses in the northern foreland of the central-eastern Greater Caucasus also consistently suggest Middle-Late Miocene inception of deformation and growth of the Greater Caucasus (Sobornov, 1994, 1996, 2021; Mikhailov et al., 1999; Ershov et al., 2003; Mosar et al., 2010).

The above mentioned geological, geomorphological, structural and thermochronological data suggest that inception of deformation and uplift occurred first in the western sector of the Caucasus and migrated in time towards the east, mirroring the present-day anticlockwise rotation of the Arabian Plate and favouring the interpretation that the Greater Caucasus growth is due to continued far-field stress transmission from the Arabian-Eurasia collision zone.

Mumladze et al. (2015) recognised a north-dipping stripe of seismicity below the central-eastern Greater Caucasus, with increasing earthquake depths, which they interpret to represent an active northward subducting slab. The western sector of the orogen instead lacks deep earthquakes, hence the authors suggest that the slab is already detached in this sector and propose an eastward propagation of slab-tear. In this model, collision would occur progressively later moving from west to east. Slab detachment in the western Greater Caucasus is used to explain the high topography despite very low modern convergence rates (Forte et al., 2016) and the presence of recent/active volcanoes only in the central and western sectors of the orogen, but mantle upwelling following slab break-off would have caused the recent uplift in a much wider region than the narrow one evidenced by low-temperature thermochronologic data (Avdeev and Niemi, 2011; Vincent et al., 2011, 2020; Trexler et al., 2022). Furthermore, the available seismic tomography studies did not image high velocity bodies, which could represent detached slabs, below the western Greater Caucasus (e.g. Koulakov et al., 2012; Zabelina et al., 2016). Additionally, to date no ophiolitic rocks of “Alpine” age have been reported for the entire Greater Caucasus, which questions the idea of continental collision in the Greater Caucasus following closure of an intervening oceanic basin.

Many authors, based on thermochronological and sedimentological data, suggest that the western Greater Caucasus started uplifting since early Oligocene times, with very low rates (Lozar and Polino, 1997; Vincent et al., 2007, 2011, 2013b, 2013a; Avdeev and Niemi, 2011). Such Oligocene inception of slow exhumation has variably been interpreted as reflecting initial “soft” Late Eocene/Early Oligocene Arabia-Eurasia collision (e.g. Vincent et al., 2007) or beginning of northward subduction of the Greater Caucasus Basin (e.g. Avdeev and Niemi, 2011) or both (e.g. Cowgill et al., 2016). On the other hand, new and published thermochronological data and inverse modelling results reported in this study do not show any initial Oligocene inception of slow cooling in the central Greater Caucasus, but instead indicate a rather flat Oligocene thermochronologic history (see Chapter 5; Avdeev and Niemi, 2011; Vasey et al., 2020). In the western Greater Caucasus, the authors mentioned above attribute the Late Miocene/Pliocene acceleration of cooling/exhumation to “hard” collision between the Greater and Lesser Caucasus and/or to a reorganisation of the Arabia-Eurasia collision zone occurring at ~ 5 Ma (Allen et al., 2004; Avdeev and Niemi, 2011; Cowgill et al., 2016; Vincent et al., 2020). It is clear that more work in needed to unravel the exact mechanisms and timing of growth and uplift in the Greater Caucasus.

6.4 Conclusions

This study provides evidence of incremental deformation in the Caucasian region during the tectonic/geodynamic events that affected the southern margin of Eurasia since Late Cretaceous times, in response to the closure of the northern and southern branches of the Neotethys ocean and the subsequent continental collisions. In particular, it provides new constraints on the tectonic evolution of the Adjara-Trialeti fold-and-thrust belt, the Khrami and Dzirula massifs, the western Kura Basin and the southern central Greater Caucasus.

The integration of thermal maturity analyses, thermal modelling of borehole data and low-temperature thermochronological analyses and inverse modelling was applied to unravel the subsidence-exhumation history of the Adjara-Trialeti back-arc basin. Such basin experienced initial flexure during the Paleocene-Early Eocene because of Lesser Caucasus loading from the south, in turn caused by continental collision along the Sevan-Akera suture. Back-arc rifting occurred during the Middle Eocene, the sedimentary fill accumulated within the basin never exceeded ~ 110-115 °C, and basin structural inversion began in the Middle Miocene triggered by far-field transmission of compressional stresses from the Bitlis suture.

The Khrami Massif experienced initial slow cooling/exhumation during Paleocene-Early Eocene times, following continental collision between the Anatolide-Tauride-Armenian block and the southern Eurasia margin along the Sevan-Akera suture, as a north-directed basement thrust sheet in the retrowedge of the Lesser Caucasus. It then experienced a pulse of cooling/exhumation during Miocene times following Arabia-Eurasia continental collision. The Dzirula Massif was exhumed during Paleocene-Eocene times, either because of stress transmission from the Sevan-Akera suture or as part of the rift shoulders of the Adjara-Trialeti back-arc basin.

The western Kura Basin, according to thermal maturity data and wells thermal modelling, was initially flexured from the south during Oligocene times because of loading by the growing retro-wedge of the Lesser Caucasus, then since Middle-Late Miocene times its northern sector experienced deformation and uplift during southward propagation of the Greater Caucasus and its southern sector was flexured by the northward growing Adjara-Trialeti FTB. Southern propagation of deformation from the Greater Caucasus continued and during latest Miocene times the southern margin of the basin was affected by thin-skinned tectonics.

The southern side of the central Greater Caucasus, according to new thermochronologic data and statistical inverse modelling results, experienced cooling/exhumation as a result of partial structural inversion during the Late Cretaceous-early Paleogene: a timing which suggests that it was caused by the coeval continental collision along the Sevan-Akera suture. Complete structural inversion of the Greater Caucasus basin, in the sector studied (and according to previous results also in other sectors to the east and west), occurred since late Middle Miocene times probably in response to northward transmission of far-field compressional stresses from the Bitlis suture.

REFERENCES

(Chapters 1, 5 and 6)

Adamia, S.A., Alania, V., Chabukiani, A., Chichua, G., Enukidze, O., and Sadradze, N., 2010, Evolution of the Late Cenozoic basins of Georgia (SW Caucasus): a review, *in* Sosson, M., Kaymakci, N., Stephenson, R.A., Bergerat, F., and Starostenko, V. eds., Sedimentary Basin Tectonics from the Black Sea and Caucasus to the Arabian Platform, Geological Society, London, Special Pubblications, 340, p. 239–259.

Adamia, S.A., Alania, V., Chabukiani, A., Kutelia, Z., and Sadradze, N., 2011a, Great Caucasus (Cavcasioni): A Long-lived North-Tethyan Back-Arc Basin: Turkish Journal of Earth Sciences, v. 20, p. 611–628, doi:10.3906/yer-1005-12.

Adamia, S.A., Chkhotua, T.G., Gavtadze, T.T., Lebanidze, Z.A., Lursmanashvili, N.D., Sadradze, N.G., Zakaraia, D.P., and Zakariadze, G.S., 2017, Tectonic setting of Georgia-Eastern Black Sea: A review, *in* Sosson, M., Stephenson, R.A., and Adamia, S.A. eds., Tectonic Evolution of the Eastern Black Sea and Caucasus, Geological Society, London, Special Publications 428, v. 428, p. 11–40, doi:10.1144/SP428.6.

Adamia, S.A., Chkhotua, T., Kekelia, M., Lordkipanidze, M., Shavishvili, I., and Zakariadze, G., 1981, Tectonics of the Caucasus and adjoining regions: implications for the evolution of the Tethys ocean: Journal of Structural Geology, v. 3, p. 437–447, doi:https://doi.org/10.1016/0191-8141(81)90043-2.

Adamia, S.A., Gamkrelidze, I., Zakariadze, G.S., and Lordkipanidze, M.B., 1974, Achara-Trialeti trough and problem of origin of the deep marine trough of the Black Sea: Geotectonics, v. 1, p. 78–94.

Adamia, S.A., Lordkipanidze, M.B., and Zakariadze, G.S., 1977, Evolution of an active continental margin as exemplified by the Alpine history of the Caucasus: Tectonophysics, v. 40, p. 183–199, doi:https://doi.org/10.1016/0040-1951(77)90065-8.

Adamia, S.A., Zakariadze, G., Chkhotua, T., Sadradze, N., Tsereteli, N., Chabukiani, A., and Gventsadze, A., 2011b, Geology of the Caucasus: A Review: Turkish Journal of Earth Sciences, v. 20, p. 489–544, doi:10.3906/yer-1005-11.

Agard, P., Omrani, J., Jolivet, L., and Mouthereau, F., 2005, Convergence history across Zagros (Iran): Constraints from collisional and earlier deformation: International Journal of Earth Sciences, v. 94, p. 401–419, doi:10.1007/s00531-005-0481-4.

Alania, V. et al., 2018, Structural Architecture of the Kura Foreland Fold-and-thrust Belt Using Seismic Reflection Profile, Georgia: Universal Journal of Geoscience, v. 6, p. 184–190, doi:10.13189/ujg.2018.060402.

Alania, V., Beridze, T., Enukidze, O., Chagelishvili, R., Lebanidze, Z., and Maqadze, D., 2021, The Geometry of the two orogens convergence and collision zones in central

Georgia: new data from seismic reflection profiles, *in* Bonali, F.L., Pasquarè Mariotto, F.A., and Tsereteli, N. eds., Building knowledge for geohazard assesment and management in the Caucasus and other regions, Springer, Dordrecht, p. 73–88, https://doi.org/10.1007/978-94-024-2046-3_6.

Alania, V., Chabukiani, A.O., Chagelishvili, R.L., Enukidze, O. V., Gogrichiani, K.O., Razmadze, A.N., and Tsereteli, N.S., 2017, Growth structures, piggy-back basins and growth strata of the Georgian part of the Kura foreland fold–thrust belt: implications for Late Alpine kinematic evolution, *in* Sosson, M., Stephenson, R.A., and Adamia, S.A. eds., Tectonic Evolution of the Eastern Black Sea and Caucasus, Geological Society, London, Special Publications 428, p. 428–445, doi:10.1177/1010539510370992.

Alania, V., Enukidze, O., Sadradze, N., Boichenko, G., Sadradze, G., Chabukiani, A., Kiria, T., Kvavadze, N., and Gventsadze, A., 2020, 3D structural model of the Bitsmendi anticline using seismic profiles, Georgia: Bulletin of the Georgian National Academy of Sciences, v. 14, p. 90–96.

Alavi, M., 1994, Tectonics of the Zagros orogenic belt of Iran: new data and interpretations: Tectonophysics, v. 229, p. 211–238.

Albino, I., Cavazza, W., Zattin, M., Okay, A.I., Adamia, S.A., and Sadradze, N., 2014, Far-field tectonic effects of the Arabia–Eurasia collision and the inception of the North Anatolian Fault system: Geological Magazine, v. 151, p. 372–379, doi:10.1017/s0016756813000952.

Allen, P.A., and Allen, J.R., 2013, Basin Analysis: Principles and Application to Petroleum Play Assessment:, doi:10.1126/science.208.4442.393.

Allen, M.B., and Armstrong, H.A., 2008, Arabia-Eurasia collision and the forcing of mid-Cenozoic global cooling: Palaeogeography, Palaeoclimatology, Palaeoecology, v. 265, p. 52–58, doi:10.1016/j.palaeo.2008.04.021.

Allen, M., Jackson, J., and Walker, R., 2004, Late Cenozoic reorganization of the Arabia-Eurasia collision and the comparison of short-term and long-term deformation rates: Tectonics, v. 23, doi:10.1029/2003TC001530.

Avdeev, B., 2011, Tectonics of Greater Caucasus and the Arabia-Eurasia orogen: University of Michigan, 1–147 p.

Avdeev, B., and Niemi, N.A., 2011, Rapid Pliocene exhumation of the central Greater Caucasus constrained by low-temperature thermochronometry: Tectonics, v. 30, p. 1–16, doi:10.1029/2010TC002808.

Axen, G.J., Lam, P.S., Grove, M., Stockli, D.F., and Hassanzadeh, J., 2001, Exhumation of the west-central Alborz Mountains, Iran, Caspian subsidence, and collision-related tectonics: Geology, v. 29, p. 559–562, doi:10.1130/0091-7613(2001)029<0559:EOTWCA>2.0.CO;2.

Ballato, P. et al., 2016, Tectono-sedimentary evolution of the northern Iranian Plateau: insights from middle–late Miocene foreland-basin deposits: Basin Research, v. 29, p. 417–446, doi:10.1111/bre.12180.

Ballato, P., Nowaczyk, N.R., Landgraf, A., Strecker, M.R., Friedrich, A., and Tabatabaei, S.H., 2008, Tectonic control on sedimentary facies pattern and sediment accumulation rates in the Miocene foreland basin of the southern Alborz mountains, northern Iran: Tectonics, v. 27, p. 1–20, doi:10.1029/2008TC002278.

Banks, C.J., Robinson, A.G., and Williams, M.P., 1997, Structure and regional tectonics of the Achara-Trialeti fold belt and the adjacent Rioni and Kartli foreland basins, Republic of Georgia, *in* Robinson, A.G. ed., Regional and petroleum geology of the Blacks Sea and surrounding region: AAPG Memoirs 68, Tulsa, Oklahoma, p. 331–346.

Barber, D.E., Stockli, D.F., Horton, B.K., and Koshnaw, R.I., 2018, Cenozoic exhumation and foreland basin evolution of the Zagros orogen during the Arabia-Eurasia collision, Western Iran: Tectonics, v. 37, p. 4396–4420, doi:10.1029/2018TC005328.

Barrier, E., and Vrielynck, B., 2008, Palaeotectonic maps of the Middle East, *in* Paris, CCMW/CGMW.

Barrier, E., Vrielynck, B., Brouillet, J.F., Brunet, M.-F., and (Contributors: Angiolini L., Kaveh F., Poisson A., Pourteau A., Plunder A., Robertson A., Shekawat R., Sosson M., Zanchi, A.., 2018, Paleotectonic reconstruction of the central Tethyan realm. Tectonono-sedimentary-palinspastic maps from late Permian to Pliocene, *in* Paris, CCGM/CGMW, http://www.ccgm.org.

Berberian, M., and King, G.C.P., 1981, Towards a paleogeography and tectonic evolution of Iran: Canadian Journal of Earth Sciences, v. 18, p. 210–265.

Bochud, M., 2011, Tectonics of the Eastern Greater Caucasus in Azerbaijan: 207 p.

Boote, D.R.D., Sachsenhofer, R.F., Tari, G., and Arbouille, D., 2018, Petroleum Provinces of the Paratethyan Region: Journal of Petroleum Geology, v. 41, p. 247–297, doi:10.1111/jpg.12703.

Brun, J.P., and Nalpas, T., 1996, Graben inversion in nature and experiments: Tectonics, v. 15, p. 677–687.

Buiter, S.J.H., and Pfiffner, O.A., 2003, Numerical models of the inversion of half-graben basins: Tectonics, v. 22, p. 1057–1073, doi:10.1029/2002tc001417.

Buiter, S.J.H., Pfiffner, O.A., and Beaumont, C., 2009, Inversion of extensional sedimentary basins: A numerical evaluation of the localisation of shortening: Earth and Planetary Science Letters, v. 288, p. 492–504, doi:10.1016/j.epsl.2009.10.011.

Candaux, Z.C., 2021, Surface and subsurface structures of the Greater Caucasus flexural basin in Georgia, reconstruction of its tectonic inversion since the Early Cretaceous: Université Cote d'Azur, https://tel.archives-ouvertes.fr/tel-03426246.

Cavazza, W., Albino, I., Galoyan, G., Zattin, M., and Cattò, S., 2019, Continental accretion and incremental deformation in the thermochronologic evolution of the Lesser Caucasus: Geoscience Frontiers, v. 10, p. 2189–2202, doi:10.1016/j.gsf.2019.02.007.

Cavazza, W., Albino, I., Zattin, M., Galoyan, G., Imamverdiyev, N., and Melkonyan, R., 2017, Thermochronometric evidence for Miocene tectonic reactivation of the Sevan-Akera suture zone (Lesser Caucasus): A far-field tectonic effect of the Arabia-Eurasia collision?, *in* Sosson, M., Stephenson, R.A., and Adamia, S.A. eds., Tectonic Evolution of the Eastern Black Sea and Caucasus, Geological Society, London, Special Publications 428, v. 428, p. 187–198, doi:10.1144/SP428.4.

Cavazza, W., Cattò, S., Zattin, M., Okay, A.I., and Reiners, P., 2018, Thermochronology of the Miocene Arabia-Eurasia collision zone of southeastern Turkey: Geosphere, v. 14, p. 2277–2293, doi:10.1130/GES01637.1.

Cavazza, W., Roure, F., Spakman, W., Stampfli, G.M., and Ziegler, P.A., 2004, The TRANSMED Atlas: The Mediterranean Region from Crust to Mantle: , p. 141 + CD-ROM.

Cloetingh, S., Wortel, R., and Vlaar, N.J., 1989, On the Initiation of Subduction Zones: Pure and Applied Geophysics, v. 129, p. 7–25.

Cloetingh, S.A.P.L., Wortel, M.J.R., and Vlaar, N.J., 1982, State of stress at passive margins and initiation of subduction zones: Studies in Continental Margin Geology, v. 34, p. 717–723.

Cloetingh, S., Ziegler, P.A., Beekman, F., Andriessen, P.A.M., Matenco, L., Bada, G., Garcia-Castellanos, D., Hardebol, N., Dèzes, P., and Sokoutis, D., 2005, Lithospheric memory, state of stress and rheology: Neotectonic controls on Europe's intraplate continental topography: Quaternary Science Reviews, v. 24, p. 241–304, doi:10.1016/j.quascirev.2004.06.015.

Corrado, S., Gusmeo, T., Schito, A., Alania, V., Enukidze, O., Conventi, E., and Cavazza, W., 2021, Validating far-field deformation styles from the Adjara-Trialeti fold-and-thrust belt to the Greater Caucasus (Georgia) through multi-proxy thermal maturity datasets: Marine and Petroleum Geology, v. 130, doi:10.1016/j.marpetgeo.2021.105141.

Cowgill, E., Forte, A.M., Niemi, N., Avdeev, B., Tye, A., Trexler, C., Javakhishvili, Z., Elashvili, M., and Godoladze, T., 2016, Relict basin closure and crustal shortening budgets during continental collision: An example from Caucasus sediment provenance: Tectonics, v. 35, p. 2918–2947, doi:10.1002/2016TC004295.

Cowgill, E., Niemi, N.A., Forte, A.M., and Trexler, C.C., 2018, Reply to Comment by Vincent et al.: Tectonics, v. 37, p. 1017–1028, doi:10.1002/2017TC004793.

Dewey, J.F., Helman, M.L., Turco, E., Hutton, D.H.W., and Knott, S.D., 1989, Kinematics of the western Mediterranean, *in* COWARD, M.P., DIETRICH, D., and PARK, R.G. eds., Alpine tectonics, Geol. Soc. Spec. Publ., p. 421–443.

Dewey, J.F., Hempton, M.R., Kidd, W.S.F., Saroglu, F., and Şengör, A.M.C., 1986, Shortening of continental lithosphere: the neotectonics of Eastern Anatolia — a young collision zone, *in* Coward, M.P. and Ries, A.C. eds., Collision, Geological Society, London, Special Publications 19, v. 19, p. 1–36, doi:10.1144/GSL.SP.1986.019.01.01.

Dewey, J.F., Pitman III, W.C., Ryan, W.B.F., and Bonnin, J., 1973, Plate tectonics and the evolution of the Alpine system: Geol. Soc. Am. Bull., v. 84, p. 3137–3180.

Dickinson, W.R., and Seely, D.R., 1979, Structure and stratigraphy of forearc regions: Bulletin of American Association of Petroleum Geologists, v. 63, p. 2–31.

Doglioni, C., Carminati, E., Cuffaro, M., and Scrocca, D., 2007, Subduction kinematics and dynamic constraints: Earth-Science Reviews, v. 83, p. 125–175, doi:10.1016/j.earscirev.2007.04.001.

Edwards, R.A., Scott, C.L., Shillington, D.J., Minshull, T.A., and Brown, P.J., 2009, Wide-angle seismic data reveal sedimentary and crustal structure of the Eastern Black Sea: The Leading Edge, v. 28, p. 1056–1065.

Ershov, A. V., Brunet, M.F., Nikishin, A.M., Bolotov, S.N., Nazarevich, B.P., and Korotaev, M. V., 2003, Northern Caucasus basin: Thermal history and synthesis of subsidence models: Sedimentary Geology, v. 156, p. 95–118, doi:10.1016/S0037-0738(02)00284-1.

Faccenda, M., Gerya, T. V., and Chakraborty, S., 2008, Styles of post-subduction collisional orogeny: Influence of convergence velocity, crustal rheology and radiogenic heat production: Lithos, v. 103, p. 257–287, doi:10.1016/j.lithos.2007.09.009.

Faccenda, M., Minelli, G., and Gerya, T. V., 2009, Coupled and decoupled regimes of continental collision: Numerical modeling: Earth and Planetary Science Letters, v. 278, p. 337–349, doi:10.1016/j.epsl.2008.12.021.

Forte, A.M., Cowgill, E., Bernardin, T., Kreylos, O., and Hamann, B., 2010, Late Cenozoic deformation of the Kura fold-thrust belt, southern Greater Caucasus: Bulletin of the Geological Society of America, v. 122, p. 465–486, doi:10.1130/B26464.1.

Forte, A.M., Cowgill, E., Murtuzayev, I., Kangarli, T., and Stoica, M., 2013, Structural geometries and magnitude of shortening in the eastern Kura fold-thrust belt, Azerbaijan: Implications for the development of the Greater Caucasus Mountains: Tectonics, v. 32, p. 688–717, doi:10.1002/tect.20032.

Forte, A.M., Cowgill, E., and Whipple, K.X., 2014, Transition from a singly vergent to doubly vergent wedge in a young orogen: The Greater Caucasus: Tectonics, v. 33, p. 2077–2101, doi:10.1002/2014TC003651.

Forte, A.M., Whipple, K.X., Bookhagen, B., and Rossi, M.W., 2016, Decoupling of modern shortening rates, climate, and topography in the Caucasus: Earth and Planetary Science Letters, v. 449, p. 282–294, doi:10.1016/j.epsl.2016.06.013.

Gamkrelidze, P., 1949, Geological structure of the Adjara-Trialetian folded system: Academy of Sciences of Georgia Press, Tbilisi, 378 p.

Gamkrelidze, I., Okrostsvaridze, A., Maisadze, F., Basheleishvili, L., and Boichenko, G., 2019, Main features of geological structure and geotourism potential of Georgia, the Caucasus: Modern Environmental Science and Engineering, v. 5, p. 422–442, doi:10.15341/mese(2333-2581)/05.05.2019/010.

Gavillot, Y., Axen, G.J., Stockli, D.F., Horton, B.K., and Fakhari, M.D., 2010, Timing of thrust activity in the High Zagros fold-thrust belt, Iran, from (U-Th)/He thermochronometry: Tectonics, v. 29, doi:10.1029/2009TC002484.

Granado, P., and Ruh, J.B., 2019, Numerical modelling of inversion tectonics in fold-and-thrust belts: Tectonophysics, v. 763, p. 14–29, doi:10.1016/j.tecto.2019.04.033.

Guest, B., Guest, A., and Axen, G., 2007, Late Tertiary tectonic evolution of northern Iran: A case for simple crustal folding: Global and Planetary Change, v. 58, p. 435–436, doi:10.1016/j.gloplacha.2007.02.014.

Guest, B., Stockli, D.F., Grove, M., Axen, G.J., Lam, P.S., and Hassanzadeh, J., 2006, Thermal histories from the central Alborz Mountains, northern Iran: Implications for the spatial and temporal distribution of deformation in northern Iran: Bulletin of the Geological Society of America, v. 118, p. 1507–1521, doi:10.1130/B25819.1.

Gunnels, M., Yetrimishli, G., Kazimova, S., and Sandvol, E., 2021, Seismotectonic evidence for subduction beneath the Eastern Greater Caucasus: Geophysical Journal International, v. 224, p. 1825–1834, doi:10.1093/gji/ggaa522.

Gusmeo, T., Cavazza, W., Alania, V.M., Enukidze, O. V, Zattin, M., and Corrado, S., 2021, Structural inversion of back-arc basins – The Neogene Adjara-Trialeti fold-and-thrust belt (SW Georgia) as a far-field effect of the Arabia-Eurasia collision: Tectonophysics, v. 803, doi:10.1016/j.tecto.2020.228702.

Hall, R., 1976, Ophiolite emplacement and the evolution of the Taurus suture zone, southeastern Turkey: Bulletin of the Geological Society of America, v. 87, p. 1078–1088, doi:10.1130/0016-7606(1976)87<1078:OEATEO>2.0.CO;2.

Hall, R., Cottam, M.A., and Wilson, M.E.J., 2011, The SE Asian gateway: History and tectonics of the Australia-Asia collision, *in* Hall, R., Cottam, M.A., and Wilson, M.E.J. eds., The SE Asian Gateway: History and Tectonics of the Australia–Asia Collision, Geological Society, London, Special Pubblications 355, v. 355, p. 1–6, doi:10.1144/SP355.1.

Hässig, M., Rolland, Y., Sosson, M., Galoyan, G., Sahakyan, L., Topuz, G., Çelik, Ö.F., Avagyan, A., and Müller, C., 2013, Linking the NE Anatolian and Lesser Caucasus ophiolites: Evidence for large-scale obduction of oceanic crust and implications for the formation of the Lesser Caucasus-Pontides Arc: Geodinamica Acta, v. 26, p. 311–330, doi:10.1080/09853111.2013.877236.

Hooper, R.J., Goh, L.S., and Dewey, F., 1995, The inversion history of the northeastern margin of the Broad Fourteens Basin, *in* Buchanan, J.G. and Buchanan, P.G. eds., Basin Inversion, Geological Society, London, Special Publications 88, v. 88, p. 307–317, doi:10.1144/GSL.SP.1995.088.01.17.

Ismail-Zadeh, A. et al., 2020, Geodynamics, seismicity, and seismic hazards of the Caucasus: Earth-Science Reviews, v. 207, doi:10.1016/j.earscirev.2020.103222.

Jolivet, L., and Faccenna, C., 2000, Mediterranean extension and the Africa-Eurasia collision Laurent: Tectonics, v. 19, p. 1095–1106, doi:10.1029/2000TC900018.

Jolivet, L., Huchon, P., and Rangin, C., 1989, Tectonic setting of Western Pacific marginal basins: Tectonophysics, v. 160, p. 23–47, doi:https://doi.org/10.1016/0040-1951(89)90382-X.

Karakhanyan, A. et al., 2013, GPS constraints on continental deformation in the Armenian region and Lesser Caucasus: Tectonophysics, v. 592, p. 39–45, doi:10.1016/j.tecto.2013.02.002.

Kazmin, V.G., Schreider, A.A., and Bulychev, A.A., 2000, Early stages of evolution of the Black Sea, *in* Bozkurt, E., Winchester, J.A., and Piper, J.D.A. eds., Tectonics and Magmatism in Turkey and the Surrounding Area, Geological Society of London, Special Publications 173, v. 173, p. 235–249, doi:10.1144/GSL.SP.2000.173.01.12.

Khain, V.E., 1994, Geology of northern Eurasia (Ex-USSR): Berlin, Gebruder Borntraeger, 404 p.

Koçyiğit, A., Yılmaz, A., Adamia, S.A., and Kuloshvili, S., 2001, Neotectonics of East Anatolian Plateau (Turkey) and Lesser Caucasus: Implication for transition from thrusting to strike-slip faulting: Geodinamica Acta, v. 14, p. 177–195, doi:10.1080/09853111.2001.11432443.

Koulakov, I., Zabelina, I., Amanatashvili, I., and Meskhia, V., 2012, Nature of orogenesis and volcanism in the Caucasus region based on results of regional tomography: Solid Earth, v. 3, p. 327–337, doi:10.5194/se-3-327-2012.

Kral, J., and Gurbanov, A.G., 1996, Apatite Fission Track Data from the Great Caucasus pre-Alpine Basement: Chemie Der Erde-Geochemistry, v. 56, p. 177- 192 ST- Apatite fission track data from the.

Letouzey, J., Werner, P., and Marty, A., 1990, Fault reactivation and structural inversion. Backarc and intraplate compressive deformations. Example of the eastern Sunda shelf (Indonesia), *in* Angelier, J. ed., Geodynamic evolution of the Eastern Eurasian Margin, v. 183, p. 341–362, papers3://publication/uuid/51B6DA9F-C4C2-4248-B7D0-B8459AA28F11.

Lordkipanidze, M.B., Meliksetian, B., and Djarbashian, R., 1989, Meosozic-Cenozoic magmatic evolution of the Pontian-Crimean-Caucasian region: IGCP Project 198, p. 103–124.

Lozar, F., and Polino, R., 1997, Early Cenozoic uprising of the Great Caucasus revealed by reworked calcareous nannofossils, *in* EUG, Strasbourg, France, v. 9, p. 141.

Madanipour, S., Ehlers, T.A., Yassaghi, A., and Enkelmann, E., 2017, Accelerated middle Miocene exhumation of the Talesh Mountains constrained by U-Th/He thermochronometry: Evidence for the Arabia-Eurasia collision in the NW Iranian Plateau: Tectonics, v. 36, p. 1538–1561, doi:10.1002/2016TC004291.

Madanipour, S., Ehlers, T.A., Yassaghi, A., Rezaeian, M., Enkelmann, E., and Bahroudi, A., 2013, Synchronous deformation on orogenic plateau margins: Insights from the Arabia-Eurasia collision: Tectonophysics, v. 608, p. 440–451, doi:10.1016/j.tecto.2013.09.003.

McCann, T., Chalot-Prat, F., and Saintot, A., 2010, The Early Mesozoic evolution of the Western Greater Caucasus (Russia): Triassic-Jurassic sedimentary and magmatic history, *in* Sosson, M., Kaymakci, N., Stephenson, R.A., Bergerat, F., and Starostenko, V. eds., Sedimentary Basin Tectonics from the Black Sea and Caucasus to the Arabian Platform, Geological Society, London, Special Publications, v. 340, p. 181–238, doi:10.1144/SP340.10.

Miall, A.D., 2013, Principles of Sedimentary Basin Analysis: Springer Science & Business Media, 615 p., doi:10.1016/s0037-0738(02)00096-9.

Mikhailov, V.O., V. Panina, L., Polino, R., Koronovsky, N. V., Kiseleva, E.A., Klavdieva, N. V., and Smolyaninova, E.I., 1999, Evolution of the North Caucasus foredeep: Constraints based on the analysis of subsidence curves: Tectonophysics, v. 307, p. 361–379, doi:10.1016/S0040-1951(99)00053-0.

Mosar, J., Kangarli, T., Bochud, M., Glasmacher, U.A., Rast, A., Brunet, M.-F., and Sosson, M., 2010, Cenozoic-Recent tectonics and uplift in the Greater Caucasus: a perspective from Azerbaijan, *in* Sosson, M., Kaymakci, N., Stephenson, R.A., Bergerat, F., and Starostenko, V. eds., Sedimentary Basin Tectonics from the Black Sea and Caucasus to the Arabian Platform, Geological Society, London, Special Publications 340, v. 340, p. 261–280, doi:10.1144/SP340.12.

Mosar, J., Mauvilly, J., Koiava, K., Gamkrelidze, I., Enna, N., Lavrishev, V., and Kalberguenova, V., 2022, Tectonics in the Greater Caucasus (Georgia – Russia): From an intracontinental rifted basin to a doubly verging fold-and-thrust belt: Marine and Petroleum Geology, v. 140, doi:10.1016/j.marpetgeo.2022.105630.

Mumladze, T., Forte, A.M., Cowgill, E.S., Trexler, C.C., Niemi, N.A., Burak Yıkılmaz, M., and Kellogg, L.H., 2015, Subducted, detached, and torn slabs beneath the Greater Caucasus: GeoResJ, v. 5, p. 36–46, doi:10.1016/j.grj.2014.09.004.

Munteanu, I., Matenco, L., Dinu, C., and Cloetingh, S., 2011, Kinematics of back-arc inversion of the Western Black Sea Basin: Tectonics, v. 30, p. 1–21, doi:10.1029/2011TC002865.

Nalpas, T., Le Douaran, S., Brun, J.P., Unternehr, P., and Richert, J.P., 1995, Inversion of the Broad Fourteens Basin (offshore Netherlands), a small-scale model investigation: Sedimentary Geology, v. 95, p. 237–250, doi:10.1016/0037-0738(94)00113-9.

Nemčok, M., Glonti, B., Yukler, A., and Marton, B., 2013, Development history of the foreland plate trapped between two converging orogens; Kura Valley, Georgia, case study, *in* Nemčok, M., Mora, A., and Cosgrove, J.W. eds., Thick-Skin-Dominated Orogens: From Initial Inversion to Full Accretion, Geological Society, London, Special Publications 377, v. 377, p. 159–188, doi:10.1144/SP377.9.

Nikishin, A.M., Ziegler, P.A., Panov, D.I., Nazarevich, B.P., Brunet, M.F., Stephenson, R.A., Bolotov, S.N., Korotaev, M. V., and Tikhomirov, P.L., 2001, Mesozoic and Cenozoic evolution of the Scythian Platform-Black Sea-Caucasus domain, *in* Ziegler, P.A., Cavazza, W., Robertson, A.H.F., and Crasquin-Soleau, S. eds., Peri-Tethys Memoir 6: Peri-Tethyan Rift/Wrench Basins and Passive Margins, Paris, National Museum of Natural History, p. 295–346.

Nikishin, A.M., Ziegler, P.A., Bolotov, S.N., and Fokin, P.A., 2011, Late Palaeozoic to Cenozoic evolution of the Black Sea-Southern Eeastern Europe region: A view from the Russian Platform: Turkish Journal of Earth Sciences, v. 21, p. 571–634, doi:10.3906/yer-1005-22.

Nikishin, A.M., Okay, A.I., Tüysüz, O., Demirer, A., Wannier, M., Amelin, N., and Petrov, E., 2015, The Black Sea basins structure and history: New model based on new deep penetration regional seismic data. Part 2: Tectonic history and paleogeography: Marine and Petroleum Geology, v. 59, p. 656–670, doi:10.1016/j.marpetgeo.2014.08.018.

Okay, A.I., and Tüysüz, O., 1999, Tethyan sutures of northern Turkey, *in* Durand, B., Jolivet, L., Horváth, F., and Séranne, Mi. eds., The Mediterranean Basins: Tertiary Extension within the Alpine Orogen, Geological Society of London, Special Publications 156, v. 156, p. 475–515, doi:10.1144/gsl.sp.1999.156.01.22.

Okay, A.I., Zattin, M., and Cavazza, W., 2010, Apatite fission-track data for the Miocene Arabia-Eurasia collision: Geology, v. 38, p. 35–38, doi:10.1130/G30234.1.

Okrostsvaridze, A., Chang, Y.-H., Chung, S.-L., Rabayrol, F., Boichenko, G., and Gogoladze, S., 2021, Paleozoic Xenoliths in Eocene Plutons: the Evidence for the Destruction of Pre-Jurassic Crystalline Basement Beneath Adjara–Trialeti Belt, Lesser Caucasus: Geologica Carpathica, v. 72, p. 299–314, doi:10.31577/geolcarp.72.4.2.

Okrostsvaridze, A., Chung, S.L., Chang, Y.H., Gagnidze, N., Boichenko, G., and Gogoladze, S., 2018, Zircons U-Pb geochronology of the ore-bearing plutons of Adjara-Trialeti folded zone, Lesser Caucasus and analysis of the magmatic processes: Bulletin of the Georgian National Academy of Sciences, v. 12, p. 90–99.

Pape, T. et al., 2021, Oil and gas seepage offshore Georgia (Black Sea) – Geochemical evidences for a Paleogene-Neogene hydrocarbon source rock: Marine and Petroleum Geology, v. 128, doi:10.1016/j.marpetgeo.2021.104995.

Philip, H., Cisternas, A., Gvishiani, A., and Gorshkov, A., 1989, The Caucasus: an actual example of the initial stages of continental collision: Tectonophysics, v. 161, p. 1–21.

Pupp, M., Bechtel, A., Ćorić, S., Gratzer, R., Rustamov, J., and Sachsenhofer, R.F., 2018, Eocene and Oligo-Miocene source rocks in the Rioni and Kura Basins of Georgia: depositional environment and petroleum potential: Journal of Petroleum Geology, v. 41, p. 367–392, doi:10.1111/jpg.12708.

Reilinger, R. et al., 2006, GPS constraints on continental deformation in the Africa-Arabia-Eurasia continental collision zone and implications for the dynamics of plate interactions: Journal of Geophysical Research: Solid Earth, v. 111, p. 1–26, doi:10.1029/2005JB004051.

Robertson, A.H.F., Parlak, O., Rízaoğlu, T., Ünlügenç, Ü., İnan, N., Tasli, K., and Ustaömer, T., 2007, Tectonic evolution of the South Tethyan ocean: Evidence from the Eastern Taurus Mountains (Elaziğ region, SE Turkey), *in* Ries, A.C., Butler, R.W.H., and Graham, R.H. eds., Deformation of the Continental Crust: Geol. Soc., London, Spec. Pub., p. 231–272.

Robinson, A.G., Spadini, G., Cloetingh, S., and Rudat, J., 1995, Stratigraphic evolution of the Black Sea: inferences from basin modelling: Marine and Petroleum Geology, v. 12, p. 821–835, doi:10.1016/0264-8172(95)98850-5.

Rolland, Y., Billo, S., Corsini, M., Sosson, M., and Galoyan, G., 2009, Blueschists of the amassia-stepanavan suture zone (Armenia): Linking tethys subduction history from E-Turkey to W-Iran: International Journal of Earth Sciences, v. 98, p. 533–550, doi:10.1007/s00531-007-0286-8.

Rolland, Y., Hässig, M., Bosch, D., Meijers, M.J.M., Sosson, M., Bruguier, O., Adamia, S.A., and Sadradze, N., 2016, A review of the plate convergence history of the East Anatolia-Transcaucasus region during the Variscan: Insights from the Georgian basement and its connection to the Eastern Pontides: Journal of Geodynamics, v. 96, p. 131–145, doi:10.1016/j.jog.2016.03.003.

Rolland, Y., Perincek, D., Kaymakci, N., Sosson, M., Barrier, E., and Avagyan, A., 2012, Evidence for ~80-75Ma subduction jump during Anatolide-Tauride-Armenian block accretion and ~48Ma Arabia-Eurasia collision in Lesser Caucasus-East Anatolia: Journal of Geodynamics, v. 56–57, p. 76–85, doi:10.1016/j.jog.2011.08.006.

Sachsenhofer, R.F., Bechtel, A., Gratzer, R., Enukidze, O., Janiashvili, A., Nachtmann, W., Sanishvili, A., Tevzadze, N., and Yukler, M.A., 2021, Petroleum Systems in the Rioni and Kura Basins of Georgia: Journal of Petroleum Geology, v. 44, p. 287–316, doi:10.1111/jpg.12794.

Sachsenhofer, R.F., Popov, S. V., Coric, S., Mayer, J., Misch, D., Morton, M.T., Pupp, M., Rauball, J., and Tari, G., 2018, Paratethyan petroleum source rocks: an overview: Journal of Petroleum Geology, v. 41, p. 219–245, doi:10.1111/jpg.12702.

Saintot, A., and Angelier, J., 2002, Tectonic paleostress fields and structural evolution of the NW-Caucasus fold-and-thrust belt from Late Cretaceous to Quaternary: Tectonophysics,

v. 357, p. 1–31, doi:10.1016/S0040-1951(02)00360-8.

Saintot, A., Brunet, M.-F.F., Yakovlev, F., Sébrier, M., Stephenson, R., Ershov, A., Chalot-Prat, F., and McCann, T., 2006, The Mesozoic-Cenozoic tectonic evolution of the Greater Caucasus: Geological Society Memoir, v. 32, p. 277–289, doi:10.1144/gsl.mem.2006.032.01.16.

Şengör, A.M.C., Gorur, N., Saroglu, F., Sengor, A.M.C., Gorur, N., and Saroglu, F., 1985, Strike-slip faulting and related basin formation in zones of tectonic escape: Turkey as a case study: Strike-slip deformation, basin formation, and sedimentation, p. 227–264.

Sharkov, E., Lebedev, V., Chugaev, A., Zabarinskaya, L., Rodnikov, A., Sergeeva, N., and Safonova, I., 2015, The Caucasian-Arabian segment of the Alpine-Himalayan collisional belt: Geology, volcanism and neotectonics: Geoscience Frontiers, v. 6, p. 513–522, doi:10.1016/j.gsf.2014.07.001.

Shatilova, I., Kokolashvili, I., Bukhsianidze, M., Koiava, K., Maissuradze, L., and Bruch, A.A., 2021, Late Cenozoic Bioevents on the Territory of Georgia (Foraminifera and Pollen) (D. Lordkipanidze, Ed.): Tbilisi, Georgia, Universal.

Shatilova, I.I., Maissuradze, L.S., Koiava, K.P., Kokolashvili, I.M., Bukhsianidze, M.G., and Bruch, A.A., 2020, The environmental history of Georgia during the Late Miocene based of foraminifera and pollen (D. Lordkipanidze, Ed.): Tbilisi, Universal, 86 p.

Shillington, D.J., Scott, C.L., Minshull, T.A., Edwards, R.A., Brown, P.J., and White, N., 2009, Abrupt transition from magma-starved to magma-rich rifting in the eastern Black Sea: Geology, v. 37, p. 7–10, doi:10.1130/G25302A.1.

Shillington, D.J., White, N., Minshull, T.A., Edwards, G.R.H., Jones, S.M., Edwards, R.A., and Scott, C.L., 2008, Cenozoic evolution of the eastern Black Sea: A test of depth-dependent stretching models: Earth and Planetary Science Letters, v. 265, p. 360–378, doi:10.1016/j.epsl.2007.10.033.

Sobornov, K.O., 1996, Lateral variations in structural styles of tectonic wedging in the northeastern Caucasus, Russia: Bulletin of Canadian Petroleum Geology, v. 44, p. 385–399.

Sobornov, K.O., 2021, Structure and evolution of the Terek-Caspian fold-and-thrust belt: new insights from regional seismic data: Journal of Petroleum Geology, v. 44, p. 259–286, doi:10.1111/jpg.12793.

Sobornov, K.O., 1994, Structure and petroleum potential of the Dagestan thrust belt, northeastern Caucasus, Russia: Bulletin of Canadian Petroleum Geology, v. 42, p. 352–364.

Sokhadze, G., Floyd, M., Godoladze, T., King, R., Cowgill, E.S., Javakhishvili, Z., Hahubia, G., and Reilinger, R., 2018, Active convergence between the Lesser and Greater Caucasus in Georgia: Constraints on the tectonic evolution of the Lesser–Greater Caucasus continental collision: Earth and Planetary Science Letters, v. 481, p. 154–161, doi:10.1016/j.epsl.2017.10.007.

Sokoutis, D., and Willingshofer, E., 2011, Decoupling during continental collision and intra-plate deformation: Earth and Planetary Science Letters, v. 305, p. 435–444, doi:10.1016/j.epsl.2011.03.028.

Somin, M.L., 2011, Pre-Jurassic Basement of the Greater Caucasus: Brief Overview: Turkish Journal of Earth Sciences, v. 20, p. 545–610, doi:10.3906/yer-1008-6.

Somin, M.L., Kotov, A.B., Sal’nikova, E.B., Levchenkov, O.A., Pis’mennyi, A.N., and Yakovleva, S.Z., 2006, Paleozoic rocks in infrastructure of the metamorphic core, the Greater Caucasus Main Range zone: Stratigraphy and Geological Correlation, v. 14, p. 475–485, doi:10.1134/S0869593806050029.

Sosson, M. et al., 2010, Subductions, obduction and collision in the Lesser Caucasus (Armenia, Azerbaijan, Georgia), new insights, *in* Sosson, M., Kaymakci, N., Stephenson, R.A., Bergerat, F., and Starostenko, V. eds., Sedimentary Basin Tectonics from the Black Sea and Caucasus to the Arabian Platform, Geological Society of London, Special Publications 340, v. 340, p. 329–352, doi:10.1144/SP340.14.

Spadini, G., Robinson, A., and Cloetingh, S., 1996, Western versus Eastern Black Sea tectonic evolution: Pre-rift lithospheric controls on basin formation: Tectonophysics, v. 266, p. 139–154, doi:10.1016/S0040-1951(96)00187-4.

Stampfli, G.M., Borel, G., Cavazza, W., Mosar, J., and Ziegler, P.A., 2001, The Paleotectonic Atlas of the PeriTethyan Domain: , p. CD-ROM.

Stampfli, G.M., and Hochard, C., 2009, Plate tectonics of the Alpine realm, *in* Murphy, J.B., Keppie, J.D., and Hynes, A.J. eds., Ancient Orogens and Modern Analogues, Geological Society, London, Special Publications 327, v. 327, p. 89–111, doi:10.1144/SP327.6.

Stephenson, R., and Schellart, W.P., 2010, The Black Sea back-arc basin: insights to its origin from geodynamic models of modern analogues, *in* Sosson, M., Kaymakci, N., Stephenson, R.A., Bergerat, F., and Starostenko, V. eds., Sedimentary Basin Tectonics from the Black Sea and Caucasus to the Arabian Platform, Geological Society, London, Special Publications 340, v. 340, p. 11–21, doi:10.1144/SP340.2.

Tari, G. et al., 2018, Stratigraphy, structure and petroleum exploration play types of the Rioni Basin, Georgia, *in* Simmons, M.D., Tari, G.C., and Okay, A.I. eds., Petroleum Geology of the Black Sea, Geological Society, London, Special Publications 464, p. 403–438, doi:https://doi.org/10.1144/SP464.14.

Tari, G., Blackbourn, G., Boote, D.R.D., Sachsenhofer, R.F., and Yukler, A., 2021, Exploration Plays in the Caucasus Region: Journal of Petroleum Geology, v. 44, p. 213–236, doi:10.1111/jpg.12791.

Tari, G.C., and Simmons, M.D., 2018, History of deepwater exploration in the Black Sea and an overview of deepwater petroleum play types, *in* Simmons, M.D., Tari, G.C., and Okay, A.I. eds., Petroleum Geology of the Black Sea, Geological Society, London, Special Pubblications 464, v. 464, p. 439–475, doi:10.1144/SP464.16.

Tibaldi, A. et al., 2019, Active stress field and fault kinematics of the Greater Caucasus: Journal of Asian Earth Sciences, p. 104108, doi:10.1016/j.jseaes.2019.104108.

Tibaldi, A., Alania, V., Bonali, F.L., Enukidze, O., Tsereteli, N., Kvavadze, N., and Varazanashvili, O., 2017a, Active inversion tectonics, simple shear folding and back-thrusting at Rioni Basin, Georgia: Journal of Structural Geology, v. 96, p. 35–53, doi:10.1016/j.jsg.2017.01.005.

Tibaldi, A., Bonali, F.L., Russo, E., and Pasquarè Mariotto, F.A., 2018, Structural development and stress evolution of an arcuate fold-and-thrust system, southwestern Greater Caucasus, Republic of Georgia: Journal of Asian Earth Sciences, v. 156, p. 226–245, doi:10.1016/j.jseaes.2018.01.025.

Tibaldi, A., Russo, E., Bonali, F.L., Alania, V., Chabukiani, A., Enukidze, O., and Tsereteli, N., 2017b, 3-D anatomy of an active fault-propagation fold: A multidisciplinary case study from Tsaishi, western Caucasus (Georgia): Tectonophysics, v. 717, p. 253–269, doi:10.1016/j.tecto.2017.08.006.

Trexler, C.C., 2018, Structural Investigations of the Tectonic History of the Western Greater Caucasus Mountains , Republic of Georgia: University of California Davis, 260 p.

Trexler, C.C., Cowgill, E., Niemi, N.A., Vasey, D.A., and Godoladze, T., 2022, Tectonostratigraphy and major structures of the Georgian Greater Caucasus: Implications for structural architecture, along-strike continuity, and orogen evolution: Geosph, v. 17, p. 1–30, doi:10.1130/GES02385.1.

Trexler, C.C., Cowgill, E., Spencer, J.Q.G., and Godoladze, T., 2020, Rate of active shortening across the southern thrust front of the Greater Caucasus in western Georgia from kinematic modeling of folded river terraces above a listric thrust: Earth and Planetary Science Letters, v. 544, p. 116362, doi:10.1016/j.epsl.2020.116362.

Trikhunkov, Y., Kangarli, T.N., Bachmanov, D.M., Frolov, P.D., Shalaeva, E.A., Latyshev, A.V., Simakova, A.N., Popov, S.V., Bylinskaya, M.E., and Aliyev, F.A., 2021, Evaluation of Plio-Quaternary uplift of the South-Eastern Caucasus based on the study of the Akchagylian marine deposits and continental molasses: Quaternary International, doi:10.1016/j.quaint.2021.04.043.

Tsereteli, N., Tibaldi, A., Alania, V., Gventsadse, A., Enukidze, O., Varazanashvili, O., and Müller, B.I.R., 2016, Active tectonics of central-western Caucasus, Georgia: Tectonophysics, v. 691, p. 328–344, doi:10.1016/j.tecto.2016.10.025.

Tye, A.R., Niemi, N.A., Safarov, R.T., Kadirov, F.A., and Babayev, G.R., 2020, Sedimentary response to a collision orogeny recorded in detrital zircon provenance of Greater Caucasus foreland basin sediments: Basin Research, p. 1–35, doi:10.1111/bre.12499.

Uyeda, S., and Kanamori, H., 1979, Back-arc opening and the mode of subduction: Journal of Geophysical Research, v. 84, p. 1049–1061.

Uyeda, S., and McCabe, R., 1983, A possible mechanism of episodic spreading of the Philippine Sea, *in* Hashimoto, M. and Uyeda, S. eds., Accretion Tectonics in the Circum-Pacific Regions, Tokyo: TerraPub., p. 291–306.

Vasey, D.A., Cowgill, E., and Cooper, K.M., 2021, A Preliminary Framework for Magmatism in Modern Continental Back-Arc Basins and Its Application to the Triassic-Jurassic Tectonic Evolution of the Caucasus: Geochemistry, Geophysics, Geosystems, v. 22, p. 1–38, doi:10.1029/2020gc009490.

Vasey, D.A., Cowgill, E., Roeske, S.M., Niemi, N.A., Godoladze, T., Skhirtladze, I., and Gogoladze, S., 2020, Evolution of the Greater Caucasus basement and formation of the Main Caucasus Thrust, Georgia: Tectonics, v. 39, doi:10.1029/2019TC005828.

Vincent, S.J., Braham, W., Lavrishchev, V.A., Maynard, J.R., and Harland, M., 2016, The formation and inversion of the western Greater Caucasus Basin and the uplift of the western Greater Caucasus: Implications for the wider Black Sea region: Tectonics, v. 35, p. 2948–2962, doi:10.1002/2016TC004204.

Vincent, S.J., Carter, A., Lavrishchev, V.A., Rice, S.P., Barabadze, T.G., and Hovius, N., 2011, The exhumation of the western Greater Caucasus: A thermochronometric study: Geological Magazine, v. 148, p. 1–21, doi:10.1017/S0016756810000257.

Vincent, S.J., Hyden, F., and Braham, W., 2013a, Along-strike variations in the composition of sandstones derived from the uplifting western Greater Caucasus: Causes and implications for reservoir quality prediction in the Eastern Black Sea, *in* Scott, R.A., Smyth, H.R., Morton, A.C., and Richardson, N. eds., Sediment Provenance Studies in Hydrocarbon Exploration and Production, Geological Society, London, Special

Publications 386, v. 386, p. 111–127, doi:10.1144/SP386.15.

Vincent, S.J., Morton, A.C., Carter, A., Gibbs, S., and Barabadze, T.G., 2007, Oligocene uplift of the Western Greater Caucasus: An effect of initial Arabia-Eurasia collision: Terra Nova, v. 19, p. 160, doi:10.1111/j.1365-3121.2007.00731.x.

Vincent, S.J., Morton, A.C., Hyden, F., and Fanning, M., 2013b, Insights from petrography, mineralogy and U-Pb zircon geochronology into the provenance and reservoir potential of Cenozoic siliciclastic depositional systems supplying the northern margin of the Eastern Black Sea: Marine and Petroleum Geology, v. 45, p. 331–348, doi:10.1016/j.marpetgeo.2013.04.002.

Vincent, S.J., Saintot, A., Mosar, J., Okay, A.I., and Nikishin, A.M., 2018, Comment on “Relict Basin Closure and Crustal Shortening Budgets During Continental Collision: An Example From Caucasus Sediment Provenance” by Cowgill et al. (2016): Tectonics, v. 37, p. 1006–1016, doi:10.1002/2017TC004515.

Vincent, S.J., Somin, M.L., Carter, A., Vezzoli, G., Fox, M., and Vautravers, B., 2020, Testing models of Cenozoic exhumation in the Western Greater Caucasus: Tectonics, p. 1–27, doi:10.1029/2018tc005451.

Vogt, K., Matenco, L., and Cloetingh, S., 2017, Crustal mechanics control the geometry of mountain belts. Insights from numerical modelling: Earth and Planetary Science Letters, v. 460, p. 12–21, doi:10.1016/j.epsl.2016.11.016.

Van Wijhe, D.H., 1987, Structural evolution of inverted basins in the Dutch offshore, *in* Ziegler, P.A. ed., Compressional intra-plate deformations in the Alpine foreland, Tectonophysics, v. 137, p. 171–219, doi:10.1016/0040-1951(87)90320-9.

Yılmaz, A., Adamia, S.A., Chabukiani, A., Chkhotua, T., Erdoğan, K., Tuzcu, S., and Karabiyikoğlu, M., 2000, Structural correlation of the southern Transcaucasus (Georgia)-eastern Pontides (Turkey), *in* Bozkurt, E., Winchester, J.A., and Piper, J.D.A. eds., Tectonics and Magmatism in Turkey and the Surrounding Area, Geological Society of London, Special Publications 173, p. 171–182.

Yılmaz, A., Adamia, S.A., and Yılmaz, H., 2014, Comparisons of the suture zones along a geotraverse from the Scythian Platform to the Arabian Platform: Geoscience Frontiers, v. 5, p. 855–875, doi:10.1016/j.gsf.2013.10.004.

Zabelina, I., Koulakov, I., Amanatashvili, I., El Khrepy, S., and Al-Arifi, N., 2016, Seismic structure of the crust and uppermost mantle beneath Caucasus based on regional earthquake tomography: Journal of Asian Earth Sciences, v. 119, p. 87–99, doi:10.1016/j.jseaes.2016.01.010.

Ziegler, P.A., 1990, Collision related intra-plate compression deformations in Western and Central Europe: Journal of Geodynamics, v. 11, p. 357–388, doi:10.1016/0264-3707(90)90017-O.

Ziegler, P.A., 1993, Plate-moving mechanisms: their relative importance: Journal of the Geological Society of London, v. 150, p. 927–940.

Ziegler, P.A., Bertotti, G., and Cloetingh, S., 2002, Dynamic processes controlling foreland development – the role of mechanical (de)coupling of orogenic wedges and forelands: Stephan Mueller Special Publication Series, v. 1, p. 17–56, doi:10.5194/smsps-1-17-2002.

Ziegler, P.A., and Cloetingh, S., 2004, Dynamic processes controlling evolution of rifted basins: Earth-Science Reviews, v. 64, p. 1–50, doi:10.1016/S0012-8252(03)00041-2.

Ziegler, P.A., Cloetingh, S., and van Wees, J.D., 1995, Dynamics of intra-plate compressional deformation: the Alpine foreland and other examples: Tectonophysics, v. 252, p. 7–59, doi:10.1016/0040-1951(95)00102-6.

Ziegler, P.A., Van Wees, J.D., and Cloetingh, S., 1998, Mechanical controls on collision-related compressional intraplate deformation: Tectonophysics, v. 300, p. 103–129, doi:10.1016/S0040-1951(98)00236-4.

Zoback, M. Lou, 1992, First- and second-order patterns of stress in the lithosphere: The World Stress Map Project: Journal of Geophysical Research, v. 97, p. 11703, doi:10.1029/92jb00132.

Zonenshain, L.P., Kuzmin, M.I., and Natapov, L.M., 1990, Geology of the USSR: A plate tectonic synthesis (B. M. Page, Ed.): American Geophysical Union, Washington, DC, United States, v. 21, 242 p.

APPENDIX I

ANALYTICAL METHODS

The following section provides a thorough description of the methodologies applied during the course of this Ph.D. project, the specific methods applied in each study is synthetically reported in the relative Chapters 2, 3, and 4. They can be distinguished into two groups: low-temperature thermochronology methods and methods for thermal maturity analysis of sediments. The former have been employed on apatite and zircon minerals, and comprehend apatite and zircon (U-Th)/He (AHe) and apatite fission-track (AFT) analyses, while the latter were applied on organic matter and clay minerals. Among them, vitrinite reflectance (Ro%), Total Organic Carbon (TOC), Rock-Eval Pyrolysis and Raman analyses were performed on organic matter, while X-Ray Diffraction (XRD) and X-Ray Fluorescence (XRF) analyses were used for clay minerals.

Low-temperature thermochronology is aimed at the reconstruction of the cooling/exhumation history of samples, thus constraining the main tectonic and evolutionary phases experienced by a certain area. Thermal maturity analyses of sediments allow the determination of the maximum temperature experienced by sediments, hence their maximum burial once linked to the geothermal gradient.

The methods hereafter described, including sampling, analysis and interpretation, follow the same routine currently adopted in most of the centres where these studies are carried on. Main references for the thermochronometric methods are found in Donelick et al. (2005), Reiners (2005), Reiners and Brandon (2006), Peyton and Carrapa (2013), and Malusà and Garzanti (2019). For organic matter analysis, instead, they can be found in Durand (1980), Barnes et al. (1990) and Taylor et al. (1998), while as concerns clay minerals the reader is referred to Moore and Reynolds (1997) and Giampaolo and Lo Mastro (2000).

I.1 THERMOCHRONOLOGICAL METHODS

I.1.1 The theory of thermochronometry

Thermochronometry can be defined as the quantitative study of the thermal histories of rocks using temperature-sensitive radiometric dating methods, which are based on the comparison between the observed abundance of a naturally occurring radioactive isotope and its decay products. The dating is achieved through well-known decay rates equations, and the calibration on a vertical succession of strata previously recognized with basic geologic principles.

The term “thermochronometer” defines an isotopic system consisting of (i) radioactive parent, (ii) radiogenic daughter or crystallographic feature, and (iii) the mineral in which they are found (Reiners, 2005). Several isotopic systems can be evaluated, each one is characterized by a particular precision and, most importantly, a particular thermal sensitivity and closure temperature (Fig. I-1). The thermal sensitivity of a thermochronometer describes its tendency to turn from an open to a closed system with decreasing temperatures. The closure temperature (Tc) can be defined as the temperature of a system at the

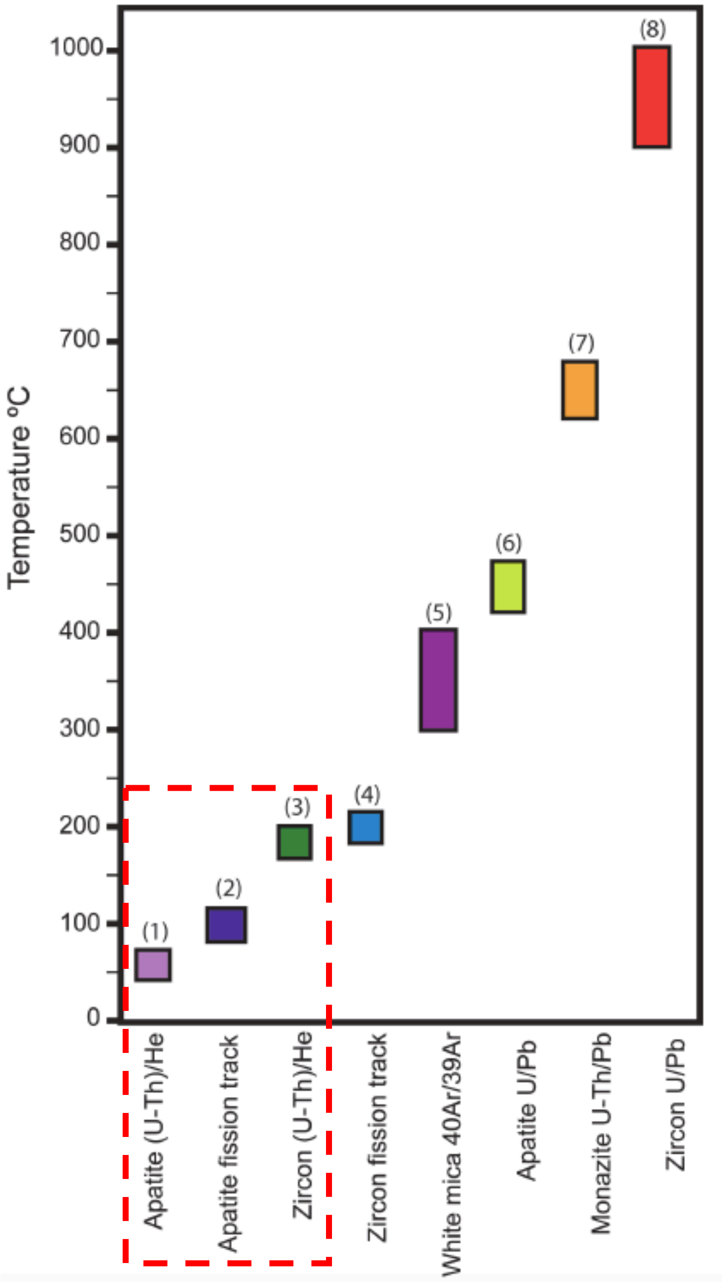

Figure I-1: Closure temperature windows of thermochronometers and geochronometers. Modified from Carrapa (2010). Red rectangle identifies the low-temperature thermochronometers used in this study. (1) Farley (2000); (2) Green et al. *(1989); (3) Reiners* et al. *(2004); (4) Zaun & Wagner (1985); (5) Purdy & Jager (1976); (6) Chamberlain & Bowring (2001); (7) Dahl (1997); (8) Dahl (1997) and Mezger & Krogstad (1997).*

time of its thermochronometric cooling age, assuming a steady monotonic cooling history. The closure temperature concept can be seen as an oversimplification of the actual behaviour of the natural system. In fact, the closure of a thermochronometer occurs through a range of temperatures for which the retention of daughter products within the system (and hence the capability of registering thermochronometric ages) varies from 0% at the top (maximum temperature) to 100% to the bottom (minimum temperature). This interval is called Partial Retention Zone (PRZ) for (U/Th)/He dating and Partial Annealing Zone (PAZ) for fission-track dating, and strictly speaking depends on a number of factors, i.e. the chemical composition, morphology and internal integrity of the mineral, the hold time and the cooling rate (Peyton and Carrapa, 2013) (Fig. I-2, I-3). Closure temperatures and Partial Retention Zones/Partial Annealing Zones for AFT and AHe are discussed in their respective paragraphs (Sections I.1.1.1 and I.1.1.2). The thermochronometric age given by a particular thermochronometer represents the latest time of cooling of a sample under the Tc (or above the top of the PRZ/PAZ). Conversely, when a sample is heated above the Tc (or under the base of the PRZ/PAZ) the system re-opens and the previous thermochronometric age is obliterated; this process is called reset of the sample.

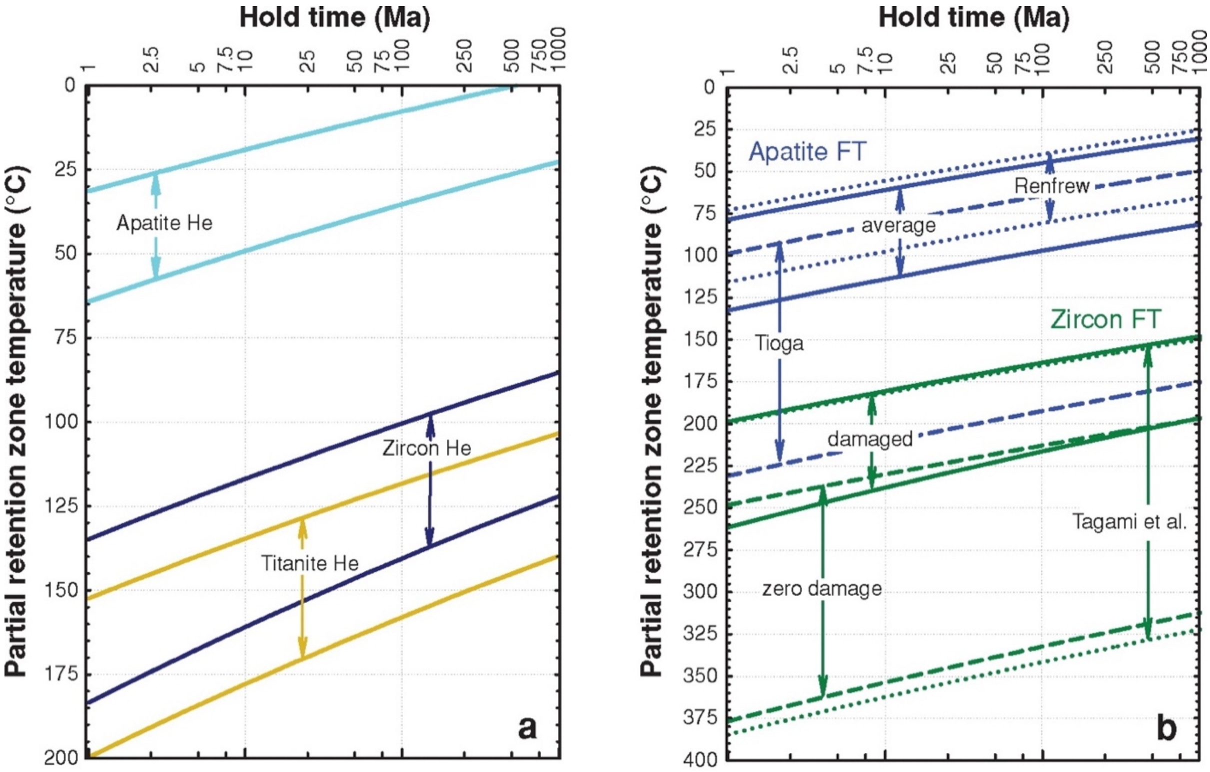

Figure I-2: Partial Retention Zones for He and FT thermochronometers as function of hold time (Reiners & Brandon, 2006). The upper and lower boundaries indicate respectively 90% and 10% retention; estimates were determined using the CLOSURE program with parameters in Tba 1 and 3 of Reiners & Brandon (2006).

A vast array of thermochronometers are known nowadays; the ones we mostly used are most sensitive to low temperatures (Fig. I-1, red-dashed rectangle), typically between 40°C and 120 °C (for durations of heating and cooling in excess of 10^6 years), and are used to investigate the thermal evolution within the upper (< ~5km) part of the Earth's crust.

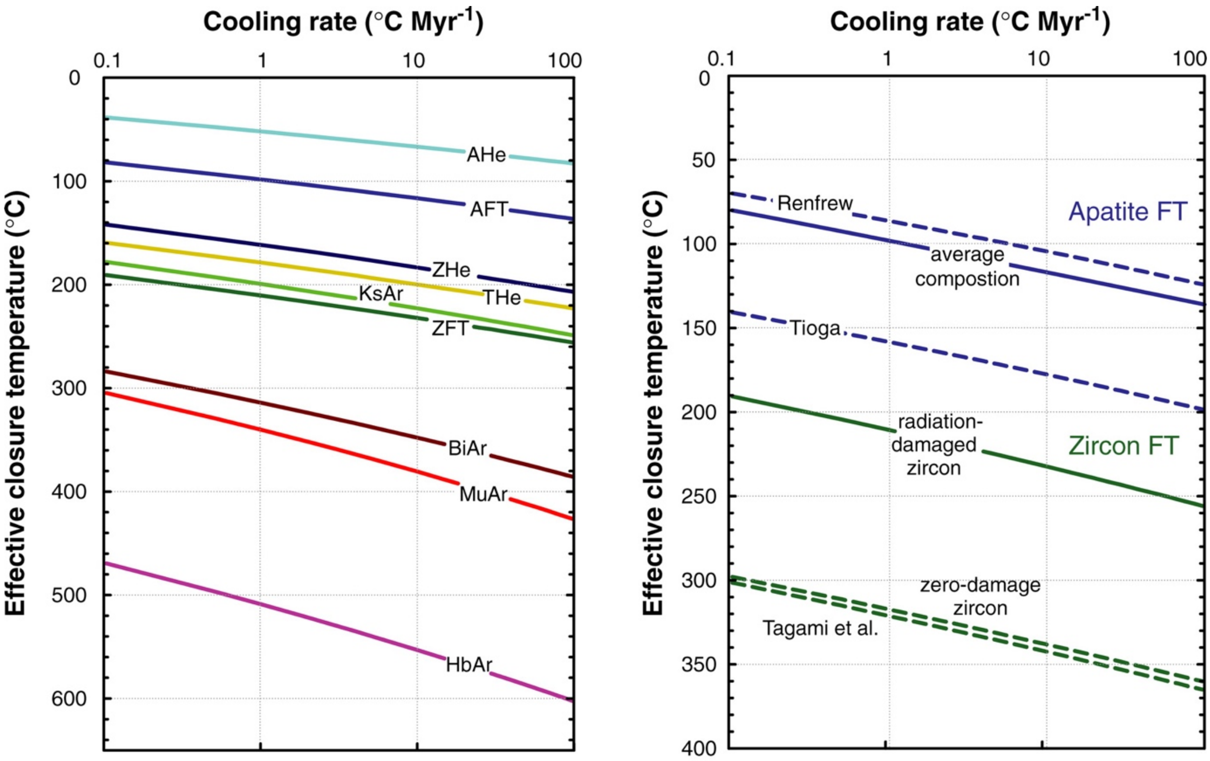

Figure I-3: Effective closure temperature (Tc) as a function of cooling rate for common He and FT Thermochronometers, (Reiners & Brandon, 2006).

I.1.1.1 Fission-track thermochronology

Fission-track dating is very similar to the other isotopic dating methods based on the decay of an unstable parent to a stable daughter atom. The age is function of the proportion between the abundance of the new stable isotope and the parent unstable atom. In fact, fission-track thermochronology is not based on the analysis of the amount of parent and daughter products *per se*, which would be a very expensive task involving spectrometer techniques, rather it takes in account the amount of uranium (U) present in the sample and the evidence of the radioactive decay, namely the “fission tracks” (FT): damage trails produced by the spontaneous fission of U. Nuclear fission is one of the several modes of disintegration which occur among heavy nuclides that have atomic mass ≥ 230 and atomic number ≥ 90. These nuclides are isotopes of elements of the actinides series (Th, Pa, U, Np, Pu, etc.), most of which also disintegrate by other processes, such as α-decay. Among them, only ^{232}Th and the two isotopes of U (^{238}U and ^{235}U) occur in appreciable concentrations in natural substances. The most abundant isotope in U series is ^{238}U, which is also the one that produces most of the fission tracks in apatites and zircons. Moreover, its half-life for fission and α-decay is relatively short, with respect to the other isotopes ($8.2 * 10^{15}$ years). Most of the fission reactions produce two fragments, which can have different atomic masses.

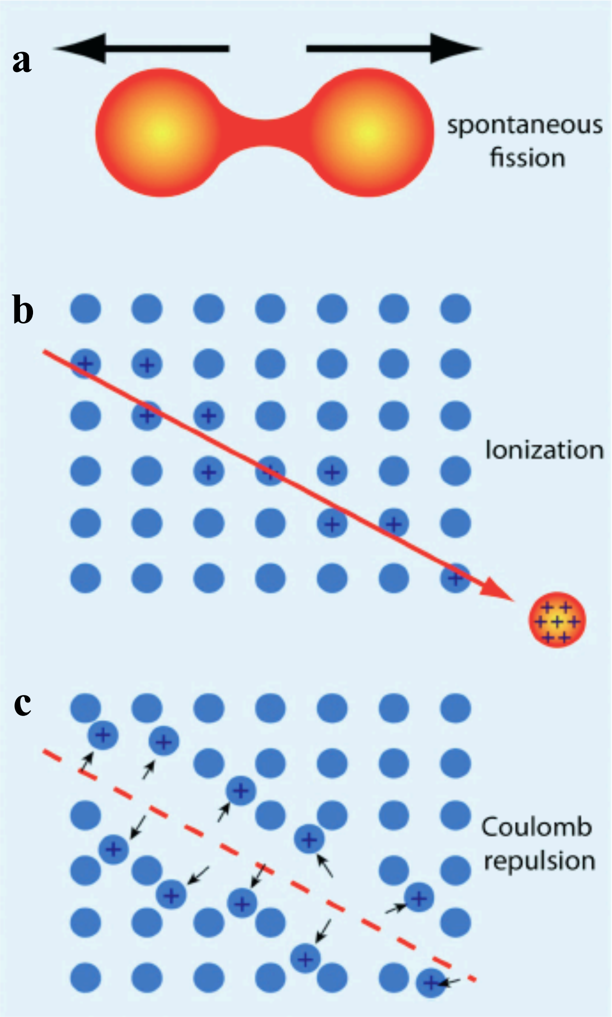

Figure I-4: The "Ion Explosion Spike" model for FT formation (after Fleischer et al., *1975). (a) The heavy nucleus splits in two nuclear fragments; (b) the two positively charged fragments are pushed away from each other and along their tracks they tear off electrons from the atoms of the lattice; (c) the positively charged atoms along the track dislocate from their lattice position due to repulsive electrostatic forces.*

Nuclear fission is an exoenergetic process that can occur both spontaneously and artificially, in the latter case through bombardment with neutrons, protons or other particles. Each reaction produces a large amount of energy (~210 MeV). The spontaneous fission decay of ^{238}U produces linear defects (latent fission tracks) in the lattice of U-bearing minerals (Fleischer et al., 1975), which are enlarged using a chemical etching process that enables their observation under an optical microscope.

A heavy, unstable ^{238}U nucleus decays spontaneously and splits into two positively charged nuclear fragments, which are pushed away from each other by both strong Coulomb repulsion forces and the energy released by the nuclear fission (~170 MeV in the form of kinetic energy), and then travel through the crystal affecting the electrostatic charge of the region they cross.

Electrons are ripped off from the atoms of the lattice and the ionized particles dislocate themselves from their original positions due to repulsive forces, then the stressed region relaxes elastically, straining the undamaged matrix (“Ion Explosion Spike” model for FT formation from Fleischer *et al.* (1975), Fig. I-4).

The length of newly formed fission tracks is specific for the mineral involved; in apatite grains fission-tracks have an initial width of approximately 10 nm and a length of ca. 16 µm (Reiners and Brandon, 2006).

The determination of FT age is made using the same general equation of any radioactive decay scheme, modified considering that ^{238}U decays not only by spontaneous fission but also by α-decay (Tagami and O’ Sullivan, 2005). The technique can be applied to minerals which contain sufficient U (typically >10 ppm) to generate a statistically useful quantity of spontaneous fission tracks over geological time. In this work apatite has been the only mineral dated by FT, so the following equations are specific for this thermochronometer.

Unlike other radioactive systems, AFT thermochronology measures the effect - rather than the product - of the radioactive decay scheme:
where

Ns = number of spontaneous fission tracks per unit volume;

$$N_s = \frac{\lambda_f}{\lambda_\alpha} {}^{238}N\left(e^{\lambda_\alpha t} - 1\right)$$

λ_f= spontaneous fission decay constant (8.5 $*10^{-17}$ yr^{-1});

λ_α= α-decay constant (1.5 $*10^{-10}$ yr^{-1});

^{238}N = number of ^{238}U atoms per unit volume;

t = time.

The most common technique adopted in order to infer AFT single grain ages is the External Detector Method (EDM), which main stages are schematically indicated in Figure I-5. A detailed description of the method can be found in Gleadow & Duddy (1981); Hurford & Green (1982, 1983); Green *et al.* (1985); Gleadow *et al.* (1986); Hurford (1990); Donelick (2005); Peyton & Carrapa (2013).

After crushing and sieving of about 1.5 kg of sample, apatites are separated using hydrodynamic, magnetic and heavy liquid density procedures (Donelick et al., 2005). The mineral grains to be dated are mounted in epoxy resin, polished and chemically etched. By doing so, latent fission tracks are revealed and can be counted under an optical microscope, thus determining the spontaneous tracks density of the single mineral grain.

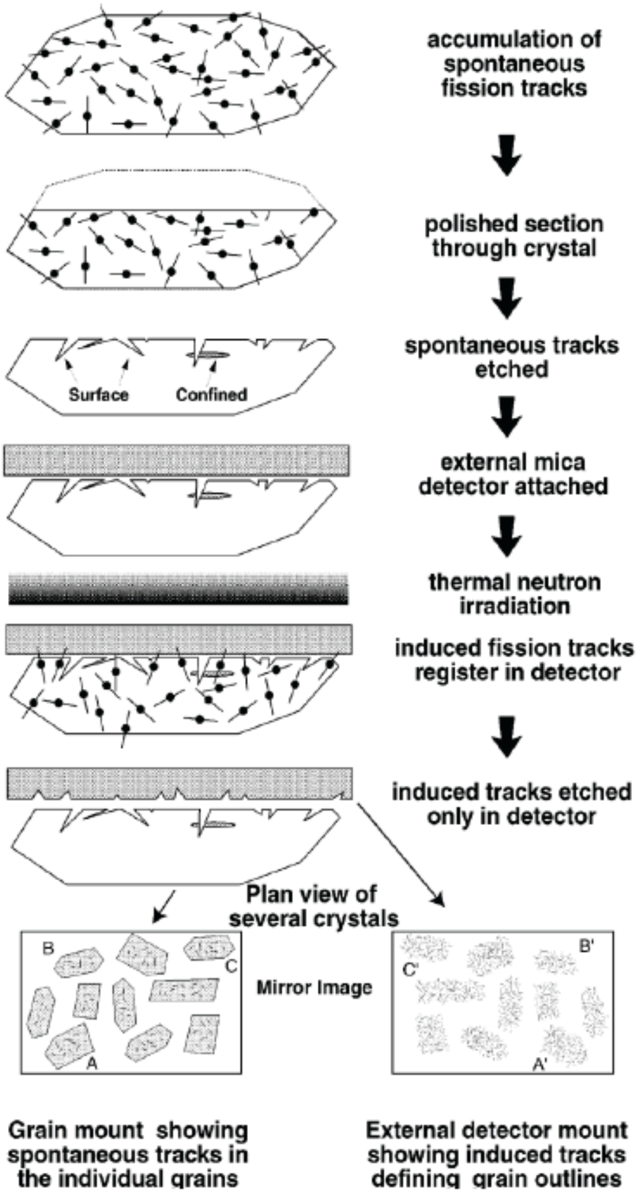

Figure I-5: Schematic procedure for FT analysis with the EDM method (from Gallagher et al., 1998).

Visible tracks considered for track-length investigations can be divided into two groups. The first one is given by tracks which directly intersect the crystal surface and which are also counted for age determinations. The second one represented by the confined tracks which are entirely localized in the interior of the crystal, and that can be revealed by the etchant only if they intersect another track, a cleavage or a fracture that emerge at the crystal surface. These tracks are also called with the acronyms TINT (Tracks IN Tracks) and TINCLE (Tracks IN CLEavage) (Fig. I-6; Bhandari et al., 1971). In order to determine the ^{238}U initial concentration, a sheet of U-free mica is placed over the polished mount, then the mount-mica package is sent for neutron irradiation in a nuclear reactor. The mica records the fission tracks produced by the ^{235}U decay and, when properly etched, provides the number of induced fission tracks (N_i) (Fig. I-5). The spontaneous and induced track densities are counted with an optical microscope implemented with a sliding table and a dedicated software; then knowing the natural ^{235}U/^{238}U ratio (a constant value of $7.252*10^{-3}$), the initial ^{238}U content can be determined.

The equation used to date the single apatite grains is:

where

$$t_i = \frac{1}{\lambda_D} \ln\left(1 + \lambda_D \zeta g \, \rho_d \, \frac{\rho_{s,i}}{\rho_{i,i}}\right)$$

t_i = fission track age of the grain *i;*

λ_D = total decay constant of ^{238}U;

ζ = calibration factor, different for each counting operator (Hurford and Green, 1982, 1983);

g = geometry factor for spontaneous fission tracks registration;

ρ_d = induced fission track density for a uranium standard corresponding to the sample position during neutron irradiation;

$\rho_{s,i}$ = spontaneous track density for grain *i;*

$\rho_{i,i}$ = induced track density for grain *i.*

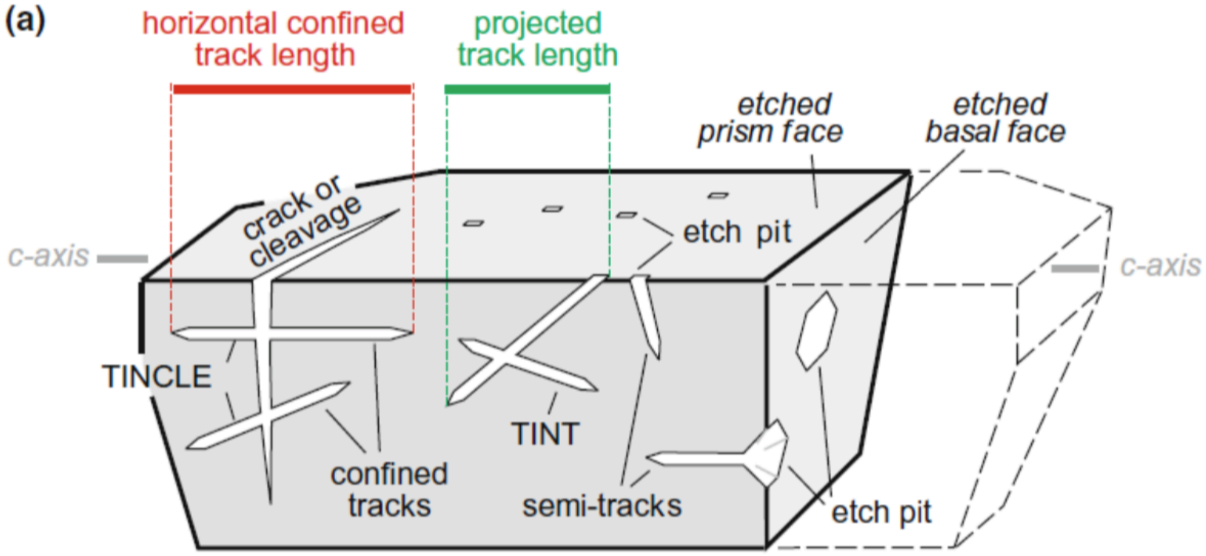

Figure I-6: Schematic cross-section illustrating the revelation of fission tracks by chemical etching. Only latent tracks in communication with the surface exposed to the etchant are revealed. These include tracks-in-tracks (TINTs) and tracks-in-cleavage (TINCLEs) (Hurford, 2019).

The calibration of the ζ-factor has to be repeated for more than 5 analyses, preferably using more than one standard, each of them included in different irradiations (Hurford, 1990). The obtained values are specific to each scientist, because the counting procedure can be different for each person, and for the mineral phase (Green et al., 1985). Results obtained for 13 different analysts who have used the same microscope, the same standards and the same counting approach, are reported in Figure I-7. Variation of the mean value arise from factors such as small differences in the size of the cut-off point for acceptance of a track, the crystal selection criteria and the precision of locating an induce image on the mica detector (Hurford, 1990). According to Hurford and Green, 1983, age standards should have the following requisites:

- The sample should come from a very well-documented horizon, readily accessible and which contains reasonable amounts of the standard;
- The sample should be homogeneous in age (the mineral separate should consist of a single population);
- The independent K/Ar and Rb/Sr ages should be unambiguous and compatible with the known stratigraphy;

- The fission-track age must relate to the independent age and neither to the age of an inherited age nor to an overprinting event or post-formational slow cooling.

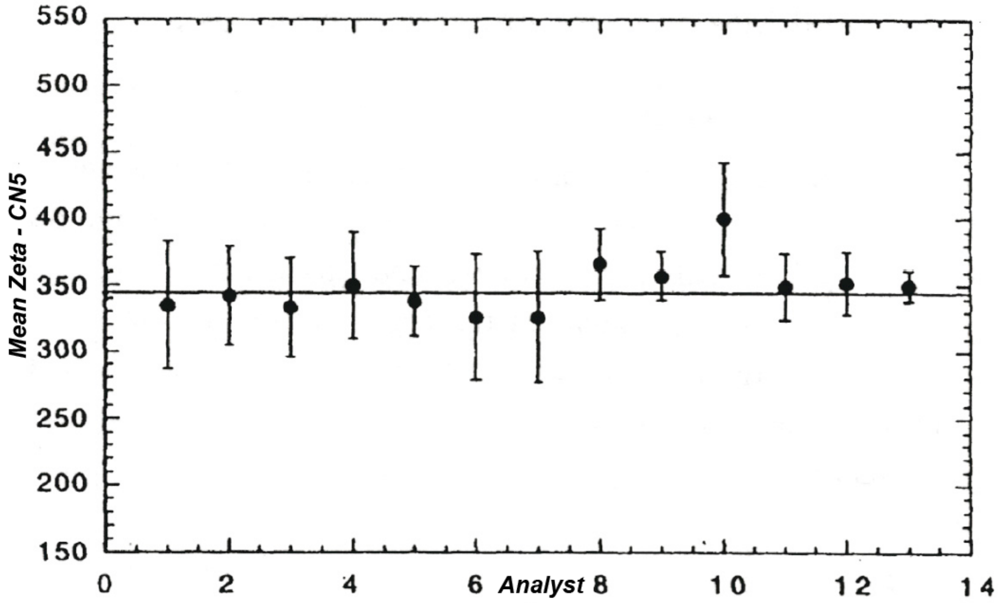

Figure I-7: Comparison of mean zeta values measured by 13 analysts on the same Fish Canyon Tuff and Durango apatite standards. Each mean value represents >15 determination; error bars are ± 1s (Hurford, 1984).

The ideal standard should come from sub-volcanic rocks rapidly cooled and which are not affected by heating events. Current most used standards for apatites are Fish Canyon Tuff (Colorado, 28.8 ± 0.2 ^{40}Ar/^{39}Ar age), Durango ore body (Cerro de Mercado, Mexico; 31.4 ± 0.6 K/Ar age) and Mount Dromedary intrusives (New South Wales, Australia; 98.8 ± 0.6 Rb/Sr age). There is no accepted physical model for fission-track annealing processes at the atomic level, since the process of fission-track annealing is much more complicated than the diffusion of a single atomic species out of a mineral lattice, and still poorly known (Braun et al., 2006). Fission tracks annealing models have thus been developed using a completely empirical approach, looking at what form of the annealing relationship best fits the data statistically (Braun et al., 2006). Fission tracks are characterized by a semi-stable nature: all newly formed tracks in apatites have a length of approximately 16 μm but they significantly shorten when heated within a particular interval of temperatures called Partial Annealing Zone (PAZ). Above the upper limit of the PAZ (~120 °C) fission tracks are immediately annealed, while below its lower limit they remain stable and are ideally not annealed. FT annealing behaviour is independent on grain size, but it is demonstrated to vary with apatite chemistry, with retention increasing with increasing Cl/(F+Cl) ratio (Green et al., 1985), although other cations and anions substitutions also play a role (Donelick et al., 1999; Ketcham et al., 1999, 2007).

Moreover, the annealing behaviour also depends on the crystallographic orientation of the tracks, with higher annealing rate for tracks orthogonal with respect to tracks parallel to the c-axis of the crystal (Gleadow et al., 1986; Donelick et al., 2005; Ketcham et al., 2007). The D_{par}, i.e. the mean width of fission-track etch pits, is a commonly used proxy for track retentivity of single crystals, first proposed by Ketcham *et al.* (1999). The effects of annealing can be quantified by measuring the lengths of horizontal confined tracks (Gleadow et al., 1986). This depends on the fact that tracks form continuously, and thus each track experiences a different portion of the integrated thermal history (Braun et al., 2006). Therefore, the tracks length distribution obtained by measuring a sufficient number of horizontal confined tracks (usually at least 50) contains information on the thermal history experienced by the sample (Braun *et al.,* 2006; Fig I-7).

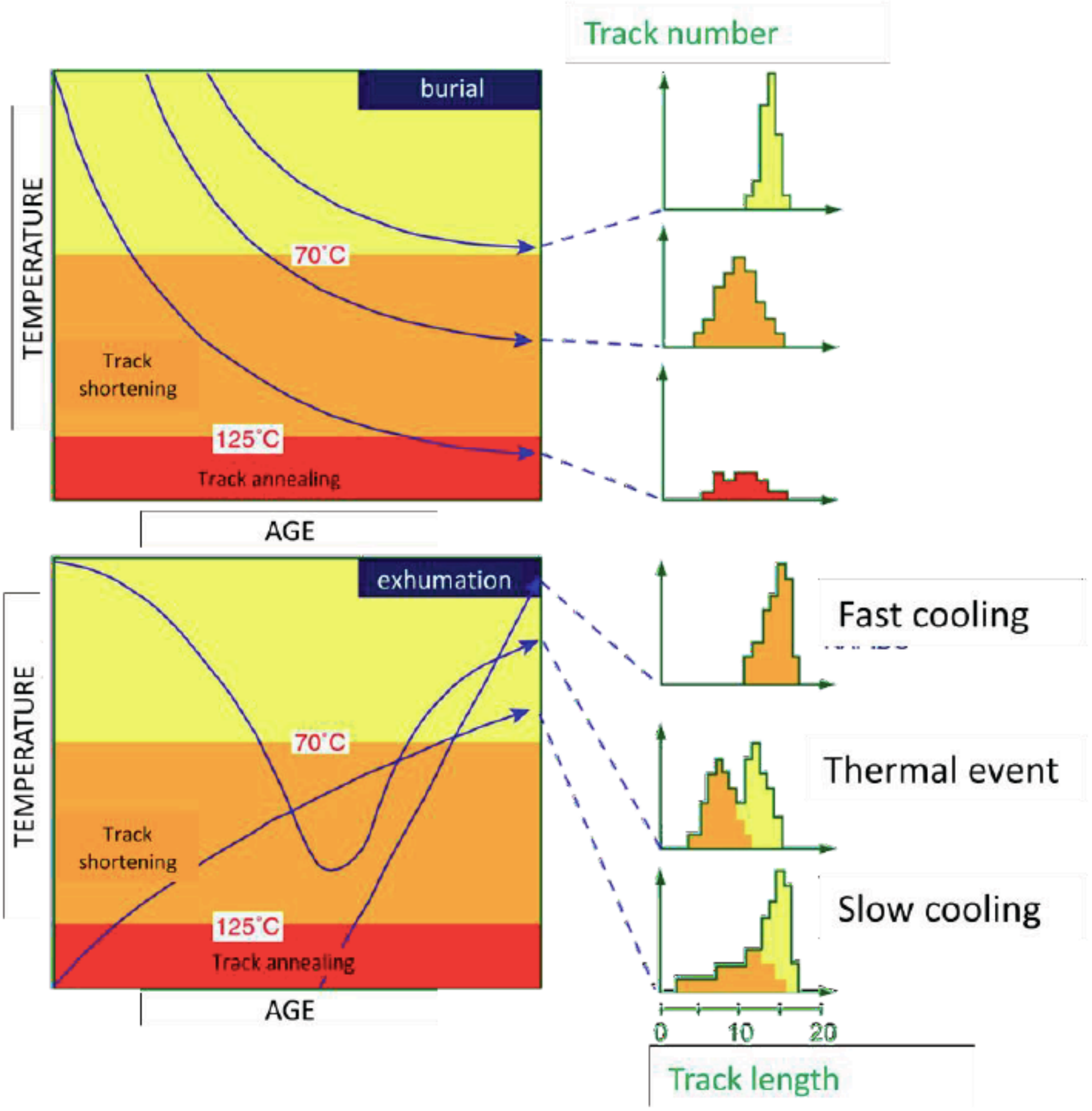

Figure I-8: Relationship between track length distribution and thermal history (modified from Gleadow et al., 1983).

The lower and upper temperature limits of AFT PAZ are usually comprised between 60 and 120°C (that are found between ~2 and 4 km below Earth's surface, assuming a 30 °C/km geothermal gradient), but can be significantly different depending on cooling rate and apatite chemistry (Figs. I-2, I-3); AFT closure temperatures generally vary between ca. 80 and 120°C but are largely affected by apatite composition; an apatite of "average" composition (Ketcham et al., 1999) has Tc=116°C for cooling rates of 10 °C/Ma.

I.1.1.2 (U-Th)/He thermochronology

(U-Th)/He dating is based on the detection by mass spectrometry of both the parent (^{238}U, ^{235}U, ^{232}Th) and daughter (^{234}U,^{230}Th, ^{147}Sm) products of decay, through the emission of an alpha particle (^{4}He nucleus), as part of the much longer decay series beginning in ^{238}U and ending in ^{206}Pb (Reiners, 2005; Lisker et al., 2009). The decay equation, used to infer the He ingrowth through time in apatite crystals, is:

$$^{4}He = 8^{238}U\left(e^{\lambda_{238}t} - 1\right) + 7^{235}U\left(e^{\lambda_{235}t} - 1\right) + {}^{232}UTh\left(e^{\lambda_{232}t} - 1\right)$$

where λ_{238} is the decay constant of ^{238}U, λ_{235} is the decay constant of ^{235}U and so forth (λ_{238} = 1.551*10^{-10}yr^{-1}; λ_{235} = 9.849*10^{-10}yr^{-1}; λ_{232} =4.948*10^{-11}yr^{-1}); U, Th and He are the number of atoms of each isotope; and t is the (U-Th)/He age. He thermochronology relies on the accumulation of ^{4}He during the α-disintegration of ^{238}U, ^{235}U, ^{232}Th and their daughter products. The T_c of mineral grains is dependent on activation energy, a geometry factor for the crystal shape, the thermal diffusivity (D_0), the length of the average diffusion pathway from the interior to the surface of the grain and the cooling rate at T_c.

The He ingrowth equation assumes absence of both initial ^{4}He and the one produced by sources extraneous to the crystal, and secular equilibrium among all daughter products in the decay chain. Considering the normally high content of U and Th in apatites and zircons, these assumptions can be considered valid in most cases. A careful selection of the crystals is however required, in order to avoid grains affected by pervasive inclusions or broad coating.

Below the closure temperature of He thermochronology in crystalline apatite and zircon, which are ~70 ºC and 180 °C, respectively, He is largely retained in a crystal, and calculated AHe and ZHe ages will record a cooling age. Above this closure temperature, He escapes from crystals through diffusion and the calculated AHe or ZHe age will be zero (Peyton & Carrapa, 2013 and refs. therein).

Similar to the fission-track technique, there is a PRZ of He between ~40 and 70 ºC in apatite and between ~130 and 180 °C in zircon (Fig. I-2). If a crystal resides in the PRZ for a sufficient time, some He will diffuse out of the crystal. AHe ages should typically be younger than AFT ages because the closure temperature and PRZ temperature range for AHe dating are lower (i.e., shallower in the upper crust) than for AFT dating. Conversely, ZHe ages should be older than AFT ages given the higher closure temperature and PRZ range. Assuming a geothermal gradient of 25 ºC/km, rocks ~3 km below Earth's surface will have a zero AHe age until they are exhumed to shallower depths, whereas rocks below 6-7 km of Earth's surface will have zero ZHe age. Thus, integrating ZHe, AFT, and AHe dating should record uplift and exhumation in regions that have experienced burial in excess of about 6-7 km.

For AHe dating, a binocular microscope is used to select clear, inclusion-free apatite crystals with widths >60 µm. Crystals are photographed and measured before being wrapped in either a platinum or niobium tube. They are then degassed by laser-heating using Nd-YAG or CO_2 lasers, and after cryogenic purification the ^{4}He is measured by quadrupole mass spectrometry. Standard procedures are described in Reiners *et al.* (2004). The degassed crystals (and the tube) are then dissolved in nitric acid and the concentrations of U, Th and Sm are measured using an inductively coupled plasma mass spectrometer (ICP-MS).

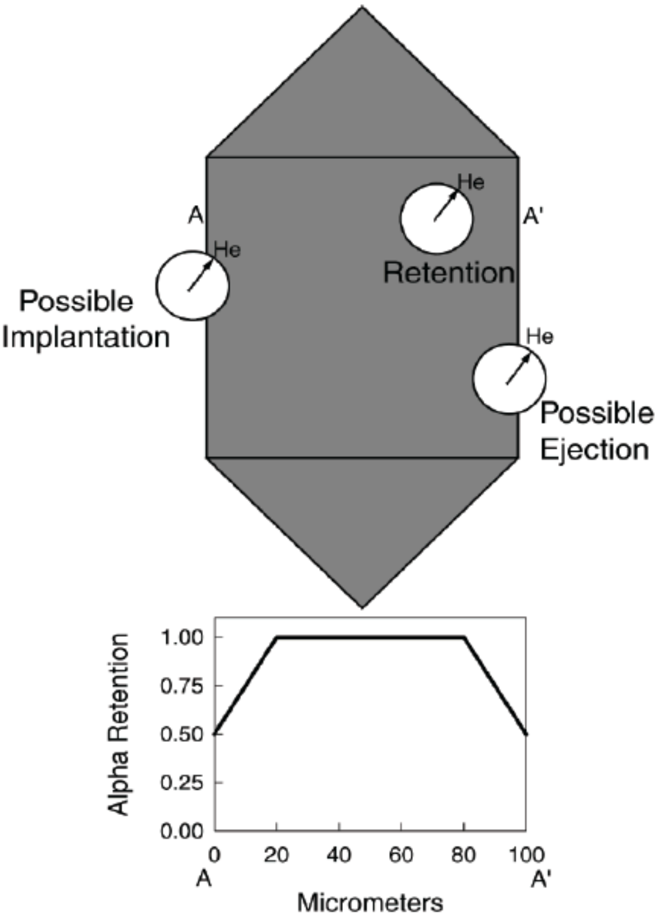

Figure I-9: The effects of long α-stopping distances on He retention (from Farley, 2002). The upper figure illustrates the three possibilities within a schematic crystal: α retention, possible α-ejection, and possible α-implantation. The center of the circle denotes the site of the parent U or Th nuclide, and the edge of the white circle labelled He indicates the locus of points where the α particle may come to rest; the arrow indicates one possible trajectory. The lower plot shows schematically how α retention changes from rim to core to rim along the path AA'; exact equations defining the shape of this curve as a function of grain size were given by Farley et al. (1996).

For the present work, single grains were loaded into 0.8 mm Nb tubes and degassed under vacuum by heating with a Nd-YAG laser. The concentration of ^{4}He was determined by ^{3}He itotope diluition and measurement of the ^{4}He/^{3}He ratio through a quadrupole mass spectrometer. U, Th and Sm concentrations were obtained by isotope diluition using an inductively coupled plasma mass spectrometer (ICP-MS) (Reiners et al., 2004; Reiners, 2007).

During the decay process, He nuclei have sufficient energy to travel ~20 μm through an apatite crystal lattice before stopping. When the decay occurs within 20 μm of the crystal edge, some He nuclei will be ejected from the apatite crystal (Fig. I-9). Therefore, for a given concentration of parent nuclides, there will be less He than expected within the crystal, and calculated AHe ages will be too young. A correction to account for this loss of He, called the alpha ejection correction, must be applied to the calculated AHe age, taking into account the geometric dimensions of the crystal (Farley et al., 1996; Farley, 2000, 2002; Peyton and Carrapa, 2013).

I.1.1.3 Helium diffusion

A consistent body of studies have demonstrated that a number of factors affect He diffusivity in apatites: these include grain size, composition, crystallographic features, microvoids, vacancy damage, radiation damage and strain-induced dislocation traps (e.g. Farley, 2002; Ehlers and Farley, 2003).

Factors such as the size of a crystal may affect how much He is lost to diffusion, with larger crystals losing proportionally less He than smaller crystals. When cooling through the PRZ has been slow enough for He diffusion to occur, larger apatite crystals will have older AHe ages than smaller apatite crystals from the same sample.

Furthermore, radiation damage of apatites may have a significant effect on He diffusion. Radiation damage is caused by the recoil of a parent nuclide (U or Th) as it decays by ejecting an alpha particle (α-decay). In apatites, these radiation-induced damages in the crystal lattice affect the diffusion parameters, particularly theirs effect is that helium diffusivity is impeded. Thus, the closure temperature (Tc) results to be higher the than normally assumed 70 °C for apatite, and it also evolves through time: hence one must be careful when dealing with slowly cooled and old (>50 Ma) samples (Green and Duddy, 2006; Green et al., 2006; Flowers et al., 2009; Gautheron et al., 2009; McDannell et al., 2019).

These damage sites may form traps for He and result in a range of AHe ages from the same sample that are proportional to the effective U concentration of the apatite crystals, defined as eU = [U] + 0.235[Th]. Apatites with higher eU will accumulate more damage traps and so will develop a higher closure temperature that apatites with lower eU, that accumulate fewer damage traps (Peyton & Carrapa, 2013 and refs. therein).

The effect of radiation damage on He diffusivity is quite large, corresponding to a variation of up to tens of degrees in Tc, across the range of typical apatite eU. Radiation damages evolve as a function of time, temperature and eU concentration (Flowers et al., 2009; Gautheron et al., 2009; McDannell et al., 2019).

I.1.2 Apatite fission-track data analysis

AFT thermochronometric age is achieved measuring the number of spontaneous and induced tracks, the relative areas and the mean D_{par} for usually 20-30 apatite grains from the same rock sample. The grain mounts and the external detectors (mica sheets) are affixed to a microscope slide and counted. The counting procedure was carried on using a Zeiss AxioSkope 40, equipped with a Ludl MAC6000 sliding plate and a DeltaPix camera. Dates were calculated using the external-detector and the zeta(ζ)-calibration methods (Hurford and Green, 1983) with IUGS age standards (above-mentioned Durando, Fish Canyon Tuff and Mount Dromedary apatites) and a value of 0.5 for the $4\pi/2\pi$ geometry correction factor (Hurford, 1990). Measured data were put into the specific TrackKey software (Dunkl, 2002), which calculates the central age, tests the homogeneity of age populations and generates radial plots for every analyzed sample. The Y axis of a radial plot (Fig. I-10) represents the standard error $((a_g-a_c)/\ \sigma)$ of the single grain age (a_g) with respect to the central age of the whole population (a_c) and the X axis represents the relative error ($1/\sigma$), decreasing towards the radial scale. Single grain ages are read on the intercept with the radial axis (plotted on a logarithmic scale) of the line drawn through the single grain point and the origin. The χ^2 statistical test (Galbraith, 1981) is used to define the probability that all the grains counted belong to a single population of ages. A probability ($P\chi^2$) of less than 5% is evidence of an asymmetric spread of single grain ages, and thus it indicates the presence of several age populations either due to inheritance of detrital grains from mixed detrital source areas, or to differential annealing in grains of different compositions (Green et al., 1989). If a sample passes the χ^2 test ($P\chi^2 >5\%$) the central age, which is essentially a weighted mean of the grain ages, reliably describes the AFT age of the sample.

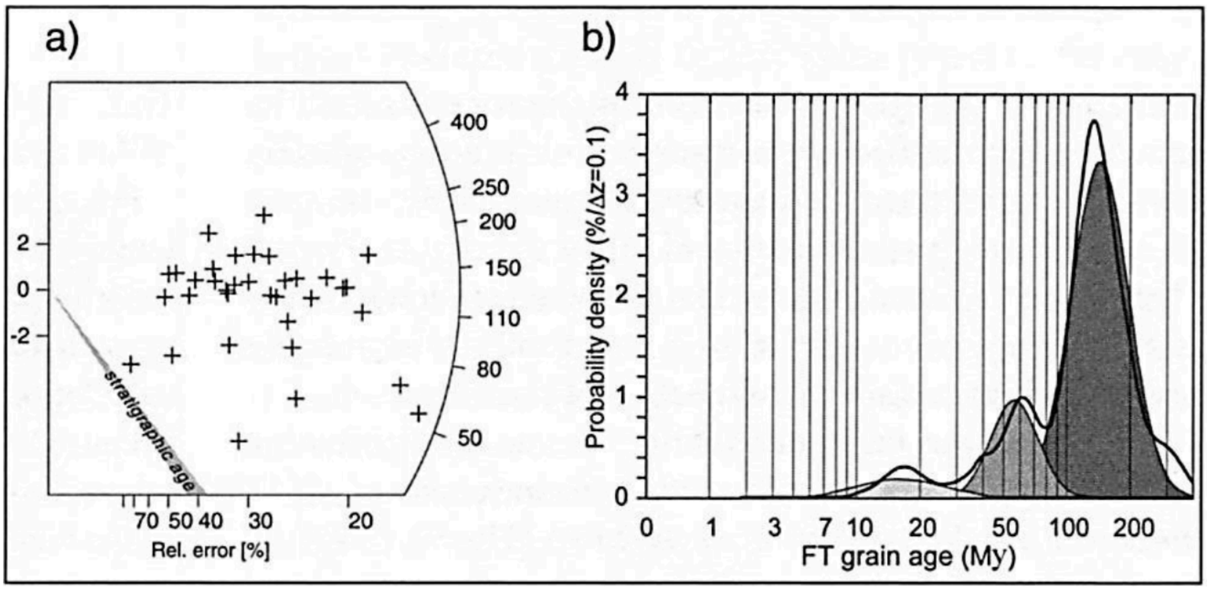

Figure I-10: Graphical methods for visualization of FT data. a) Radial plot: each single cross represents a crystal; age can be read on the intersection between the line linking the origin with the point and the arc; the x coordinate is the precision of the age, which increases towards the arc; the error ± 2, represented by the bar on the origin, is easily detected superimposing the bar on the selected point. b) Probability density plot: the thicker line represents the observed distribution whereas different tones of grey are assigned to the individual peaks obtained by the binomial peak-fitting method (Zattin, 2003).

When possible, confined fission tracks are also measured for thermal modeling. A large number of confined FT (preferably > 50) is necessary to have enough statistical confidence, thus hindering this procedure for most of the samples. In suitable samples confined FT lengths are measured along with their orientation in respect to *c*-axis and mean D_{par}. More information about this process will be provided in the t-T Modelling paragraph (I.1.5).

I.1.3 Apatite (U-Th)/He data analysis

Usually, three to five grains from the same sample (called replicates) are analysed. The comparison between single grain ages of the replicates gives information about the thermal history of the sample. Age reproducibility is firstly checked: if the age dispersion is low and the single grain ages cluster tightly, then the weighted mean of ages can be used for interpretation and the Tc concept can generally be applied (Fitzgerald et al., 2006), whereas high age dispersion is usually related to a somehow complex thermal history i.e. slow cooling and a long permanence within the PRZ. The magnitude of the effect on cooling age of subtle factors controlling He diffusion (like zonation, crystal size, kinetic parameters) increases with decreasing cooling rates (Ehlers and Farley, 2003), and these parameters tend to correlate with age. The correlation between grain age and crystal size (radius) is particularly evident in case of slow cooling, since crystal size affects both α-ejection and He diffusion kinetics; in this case age dispersion adds further information on the evolution of the samples and can be used to model the thermal history.

The correlation between grain age and eU indicates that the zircons where affected by radiation damages; also in this case dispersion do not preclude to use dates for reconstructing thermal histories, provided the RDAAM (Radiation Damage Accumulation and Annealing Model) model of Flowers *et al.* 2009.

I.1.4 Samples preparation

In order to perform low-temperature thermochronological analyses, about 2 kg of each rock sample have been collected during field trips. In this study, samples analysed are mainly constituted by medium-grained polygenic sandstones, but some granitoids and gneisses were collected too. Apatites had to be separated from the rest of the rock through successive stages, in the laboratory. Separations were performed at the Laboratory of Sedimentary Petrography of the University of Bologna (Italy).

Figure I-11: The jaw crusher in the Laboratory of Sedimentary Petrography of the University of Bologna.

The first phase consisted in the crushing of ~1.4/1.5kg of rock using a jaw crusher (Fig. I-11) first, and a roller mill (Fig. I-12) successively. Then the crushed samples were sieved in order to obtain a rock powder of <250 μm grain size. During the second phase, heavy and light minerals were separated from the <250 μm powder through hydrodynamic separation, using a Wilfley water table (Fig. I-13). The heavy minerals fraction was then passed in the magnetic separator (Fig. I-14), to eliminate ferromagnetic minerals and maintain only diamagnetic ones. Then, the diamagnetic fraction was further separated with two heavy-liquid density methods under a fume hood, involving Tetrabromoethane and Methylene

Figure I-12: The roller mill in the Laboratory of Sedimentary Petrography of the University of Bologna.

Iodide, which have the function of separating zircons and apatites from other minerals in first instance, and then zircons from apatites (Fig. I-15). The whole processing procedure up to this point is summarized in Figure I-16.

Separated apatites have then be seen in both reflected and transmitted light microscopy, to select sample which had the best yield of apatites, in terms of grain-size, shape and quantity. Apatites of the selected samples have then been mounted in epoxy resin (10:3 proportion), making one mount for each sample; every mount was first hand-ground using 800 and 1200 μm alumina powders and then polished with 2 different polishing laps having decreasing grain-size of diamond crystals (6 μm and 1 μm respectively), in order to expose grain surfaces. Each lapping cycle consisted in 5min at 250 r.p.m. in a Buhler machine. Polished mounts were then etched in nitric acid (HNO_3 5M) for 20s. Etched mounts were then cut into thin (~1.3/1.4 mm thick) discs and again lapped to obtain little squares of about 1.2 cm^2.

In the end, a square of U-free muscovite mica sheet was attached to every mount containing the apatites etched, and all the so-constructed packages were put into appropriate holders (Fig. I-17), together with dosimeters (standard glass CN-5) which have the function of controlling the

Figure I-13: The Wilfley shacking water table in the Laboratory of Sedimentary Petrography of the University of Bologna.

Figure I-14: *The magnetic separator (so-called "Frantz") in the Laboratory of Sedimentary Petrography of the University of Bologna.*

neutron fluence during irradiation. These holders were then sent to the nuclear reactor at Radiation Center of Oregon State University, where mounts were irradiated with a nominal neutron fluence of 9 $*10^{15}$ n/cm^2. After irradiation, induced fission tracks in the U-free muscovite sheets that covered apatite grain mounts were etched in 40% HF at 20 °C for 1 hour.

For AHe analyses, apatites were not mounted in epoxy resin. Instead, 3 to 5 grains of apatites for each sample were selected at a transmitted light microscope. Selection was based on the shape, size and condition of the grains: only the most beautiful, big (>60 μm), euhedral, not fractured nor too much abraded, with no inclusions or too much coating apatites were chosen. Every grain was then measured (noting both width and length in two different faces of the crystal), photographed and put into a Nb or Pt tube, that was in the end closed at both extremities (Fig. I-18).

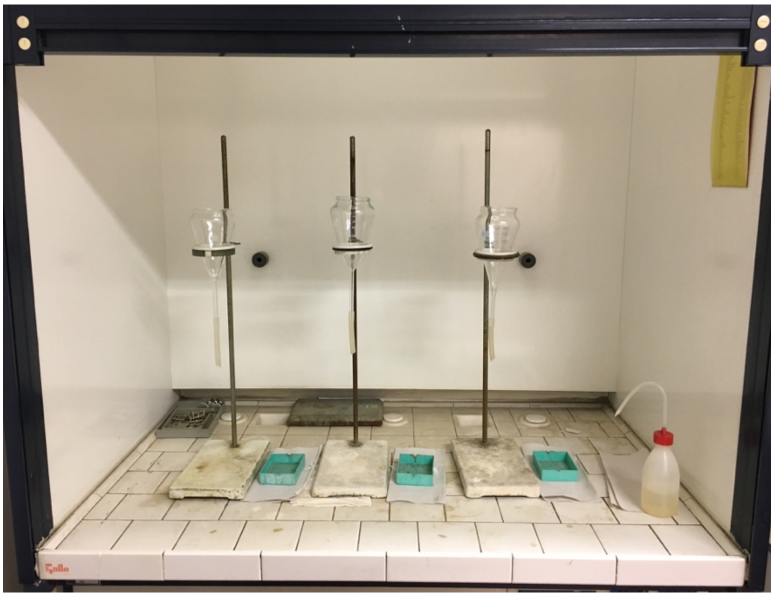

Figure I-15: The fume hood used for heavy-liquid density separation in the Laboratory of Sedimentary Petrography of the University of Bologna.

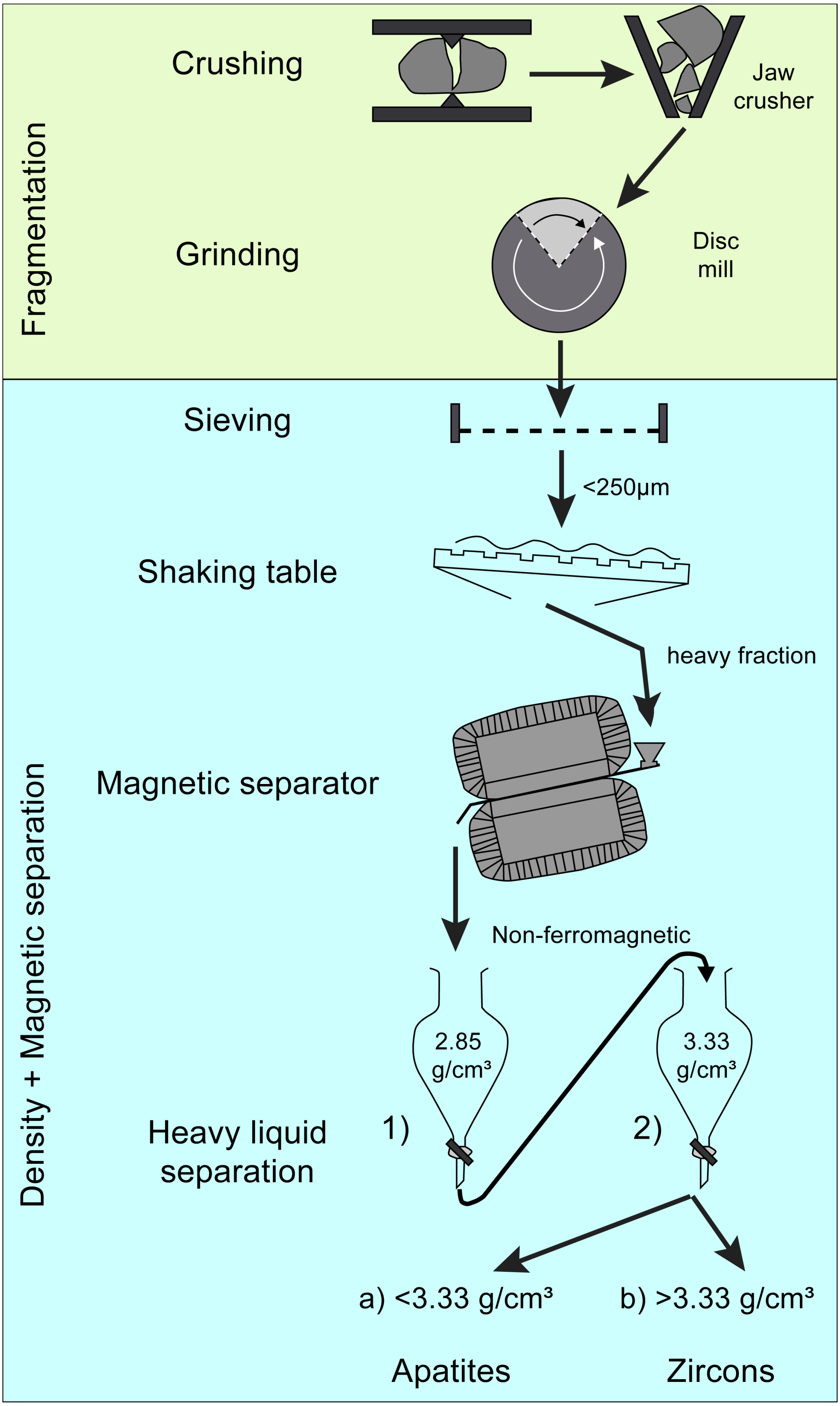

Figure I-16: Flow chart showing a general sequence of steps and conditions for the separation of minerals suitable for FT and He analysis (modified after Kohn et al., 2019).

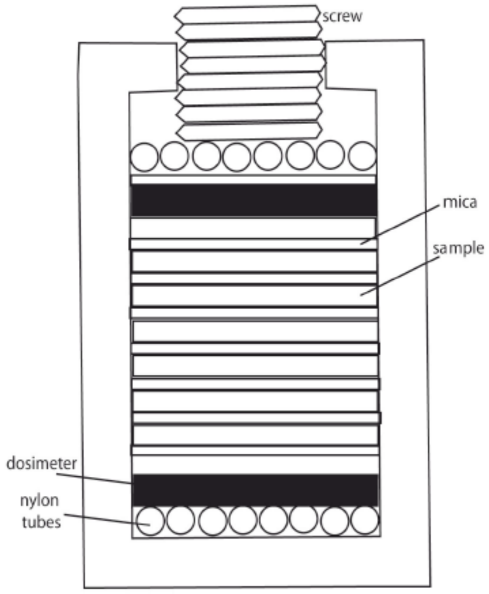

Figure I-17: Scheme of a holder for irradiation and position of mounts, micas and dosimeters.

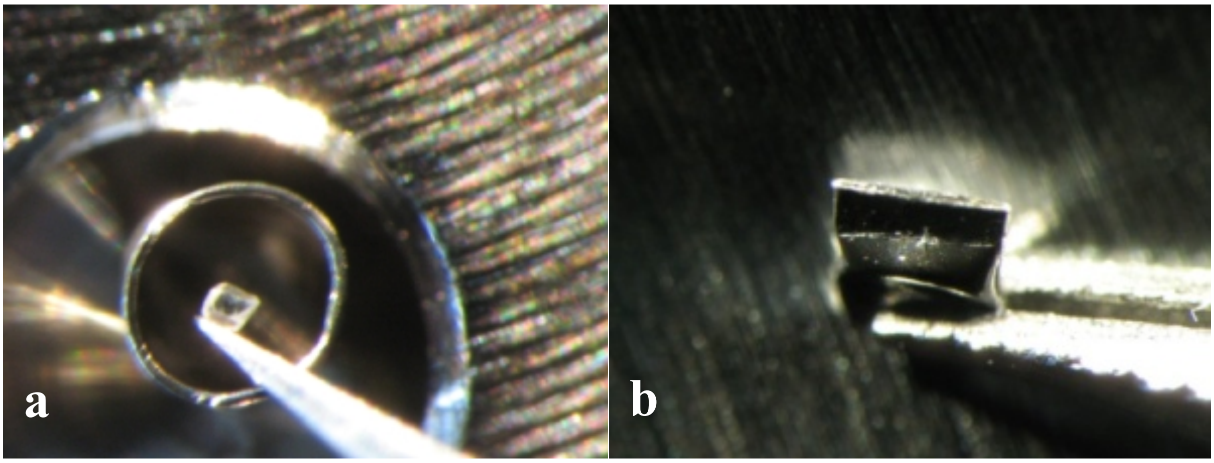

Figure I-18: a) Apatite grain put into a Nb tube; b) Nb tube closed at both extremities.

I.1.5 t-T modelling

There are two types of time-Temperature modeling that can be performed when there is avaiability of AFT and/or AHe data: forward and inverse modeling. Forward modeling involves calculating a thermo-chronometric age from a proposed time-temperature path, using diffusion or annealing kinetics derived from laboratory experiments. This kind of modeling is thus used to check if a time-temperature path provides a plausible explanation for measured thermochronometric ages, and it's also a useful tool for predicting and understanding the effect of a certain thermal history on ages and track-length distributions. Instead, inverse modeling is used to calculate time-temperature paths that match certain thermochronometric data and ages, within a specified amount of statistical error, assuming a starting time and temperature. Track-length distribution, AFT ages, AHe ages and a kinetic parameter such as D_{par} represent the entire thermal history of an apatite crystal from cooling through the PAZ to the present-day temperature, and provide significant constraints on possible thermal histories. As already stated in section I.1.1.1, a broad or bimodal distribution of fission-track legths indicates that a sample has resided longtime at temperatures within the PAZ. In the same way, a correlation of AHe age with eU concentration indicates that a sample has resided long time within the PRZ. Modeling is thus the only way to gain understanding of the thermal histories of slowly cooled samples, or of samples that have experienced complex t-T paths, residing in the PAZ or PRZ for a significant time (relative to their age) and so being partially reset (Peyton and Carrapa, 2013 and refs. therein).

In this dissertation, inverse modelling of track-length data was performed using the HeFTy software (Ketcham, 2005; Fig. I-19), in order to achieve realistic thermal modellings for the analysed samples. The software allows to integrate AFT and AHe data, as well as other constrains inferred from stratigraphic relationships between strata, pre-existing radiometric ages and/or maximum temperatures derived from organic matter (OM) and clay minerals analyses. Time-temperature paths (T–t paths) are generated using a constrained Monte Carlo algorithm that allows the user to specify time-temperature regions through which each path is forced to pass. Each path must also pass some statystical criteria, accepting some of them that have a "good" or "acceptable" fit with the data and rejecting the others (Ketcham, 2009). In general, all time-temperature histories should begin at a sufficiently high temperature to ensure that there is total annealing as an initial condition. Thus, the earliest T-t constraint should have a minimum temperature above the total annealing temperature of the most resistant apatite being modelled. An exception to this principle might be the modelling of rapidly cooled volcanic rocks where it is known *a priori* that the initial condition is represented by zero tracks present at some temperature below the total annealing temperature. The input parameters for AFT are single grain ages and confined fission tracks length, orientation and mean D_{par}. Modelling was based on the fission-track annealing model of Ketcham *et al.* (2007), and the diffusion kinetics of apatites after Ehlers & Farley (2003) and Flowers *et al.* (2009). For apatites, a homogeneous distribution of U and Th was assumed. The gauge of the match between the modelled thermal history and the experimental data is given by the goodness-of-fit parameter (GOF), which indicates the probability of failing the null hypothesis that the

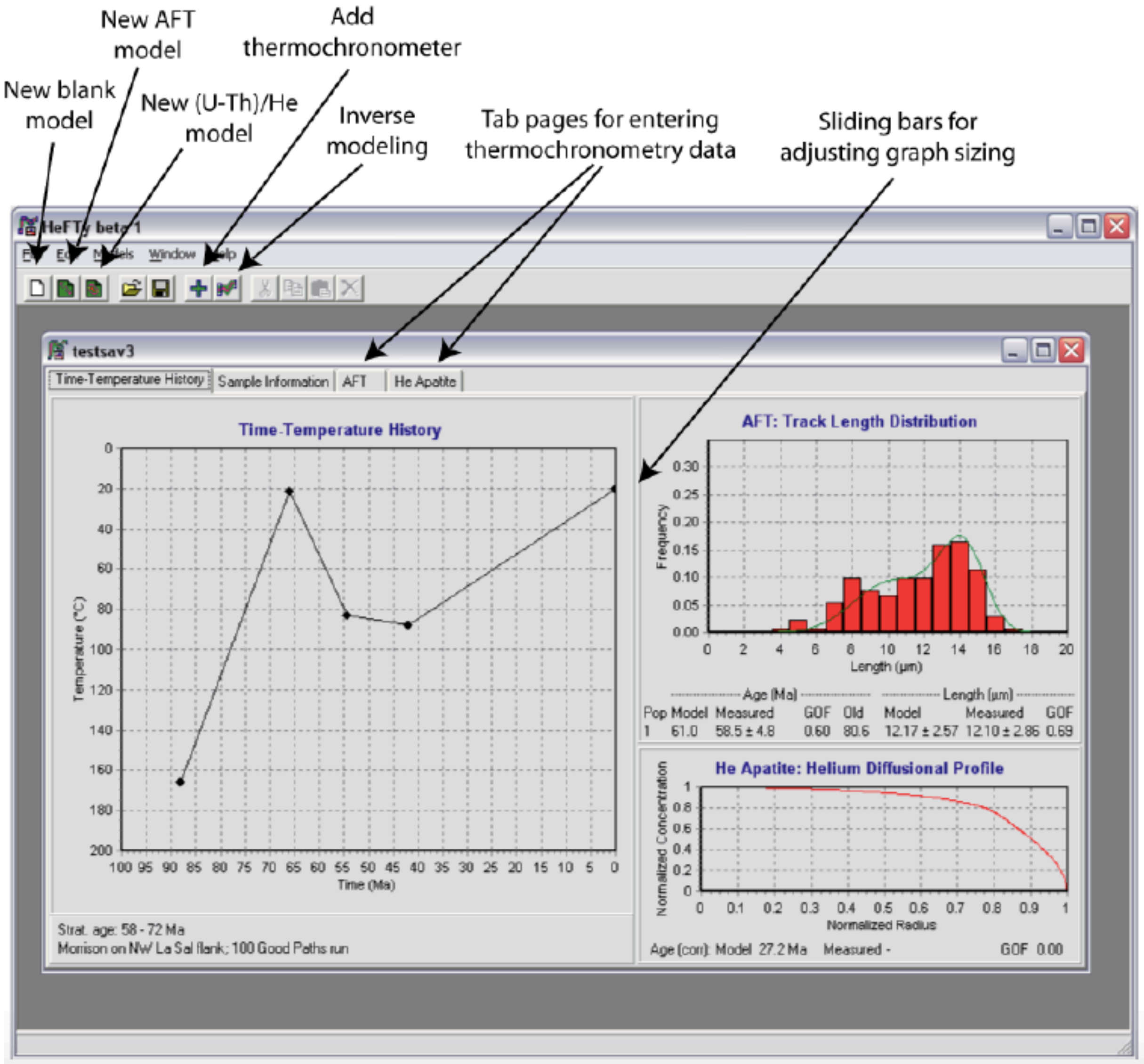

Strat. age: 58 - 72 Ma
Morrison on NW La Sal flank; 100 Good Paths run

	Age (Ma)				Length (µm)		
Pop	Model	Measured	GOF	Old	Model	Measured	GOF
1	61.0	58.5 ± 4.8	0.60	80.6	12.17 ± 2.57	12.10 ± 2.86	0.69

Age (cor): Model 27.2 Ma Measured - GOF 0.00

Figure I-19: The HeFTy program user interface (Ketcham, 2005).

model and data are different. In general, a value of 0.05 or higher is considered not to fail the null hypothesis, and thus reflects an acceptable fit between model and data (Ketcham, 2009). Furthermore, GOF values give an indication about the fit between observed and predicted data (values close to 1 indicate a high degree of fit, while on the contrary values close to 0 indicate a poor degree of fit). GOF values higher than 0.5 are considered good and the closer the GOF gets to 1, the more the modelled T–t paths fit the data. In figure I-20 is shown an example of an inverse modeling of track lengths, using the HeFTy program.

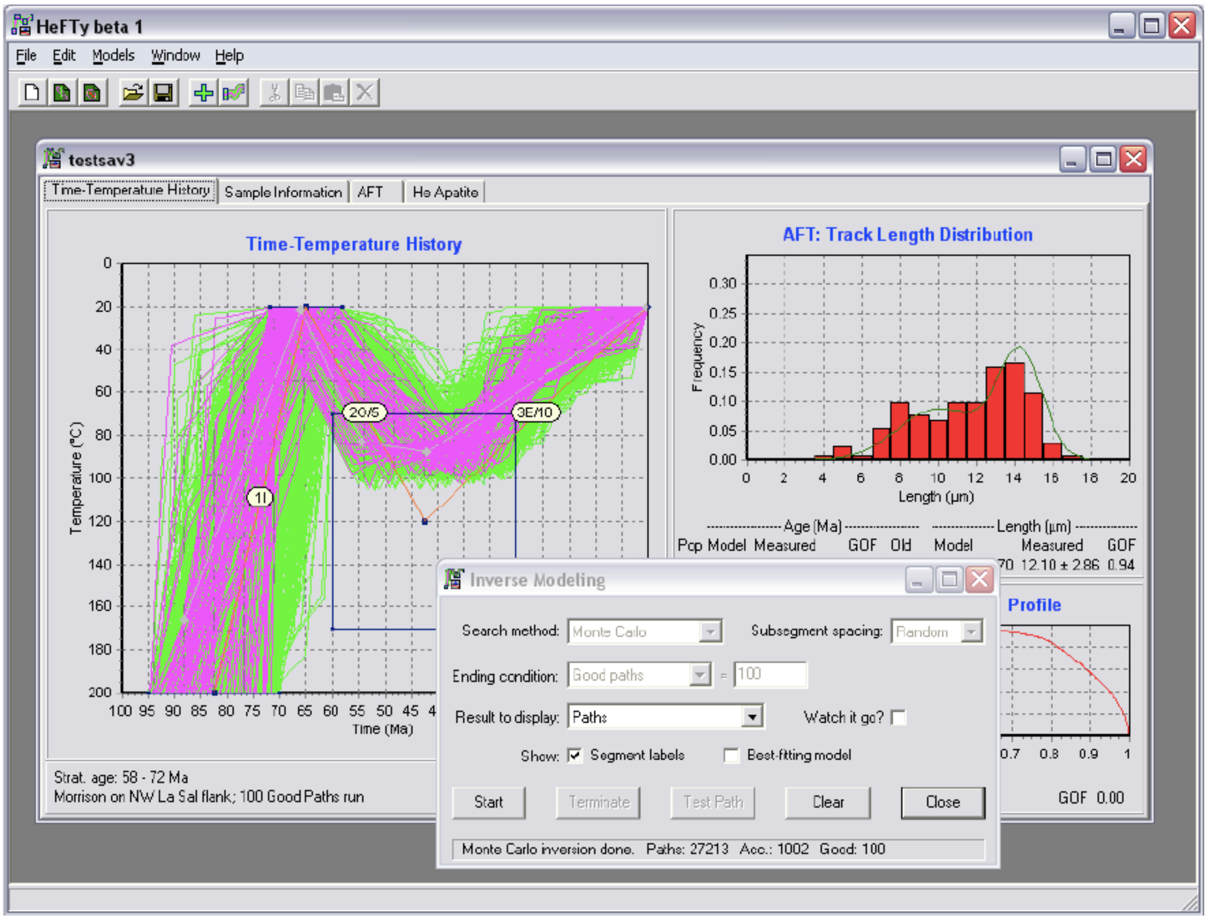

Strat. age: 58 - 72 Ma
Morrison on NW La Sal flank; 100 Good Paths run

---------- Age (Ma) ----------				---------- Length (µm) ----------		
Pop Model	Measured	GOF	Old	Model	Measured	GOF
				70	12.10 ± 2.86	0.94

Search method: Monte Carlo
Subsegment spacing: Random
Ending condition: Good paths = 100
Result to display: Paths
Watch it go? ☐
Show: ☑ Segment labels ☐ Best-fitting model

Monte Carlo inversion done. Paths: 27213 Acc.: 1002 Good: 100

Figure I-20: HeFTy inverse modelling mode (Ketcham, 2005).

I.2 ORGANIC MATTER CHARACTERIZATION

Most organic matter (OM) in rocks represents the solid, usually dark coloured, remains of plants or animals which lived at the time of deposition (Taylor et al., 1998). Many rocks contain only a little amount of OM, while others, such as coals, are made up almost totally of organic matter.

At the time of deposition the organic matter dispersed in sediments is composed of a mixture of organic compounds of various origin and composition. In particular, aquatic organisms contribute mainly proteins, lipids and carbohydrates while higher plants contribute resins, waxes, lignins and carbohydrates in the form of cellulose (Barnes et al., 1990). These basic chemical constituent or their hydrolysis product (aminoacids, long-chain fatty acids and sugars) are mostly microbially degraded in the water column and in the upper part of the sedimentary column. The principal processes involving the degradation of OM are aerobic respiration, bacterial sulphate reduction and methanogenesis as well as the reduction of manganes oxides, nitrates and iron oxides (Henrichs, 1993). An exception to this rules is lignin, a complex, partly aromatic macromolecule, concentrated in the inner cell walls of vascular plants, that can hardly be degraded by microorganisms, with the exception of some aerobic fungi acting in the soil (Taylor et al., 1998).

OM that is not degraded in these processes is incorporated in sediments and the insoluble part of these materials is called kerogen (Durand, 1980). Starting from this point, further degradation will be primarily associated with temperature changes. In particular, it is usual to distinguish three zones that with increase in temperatures are called: diagenesis, catagenesis and metagensis. In these zones, kerogen progressively converts into hydrocarbons (primary oil in catagenesis and gas in metagenesis) leading to the formation of new constituents such as bitumen, pyrobitumen, exsudatinite and micrinite (Taylor et al., 1998). A first kerogen classification can be made by the use of bulk parameters, such as the H/C and O/C atomic

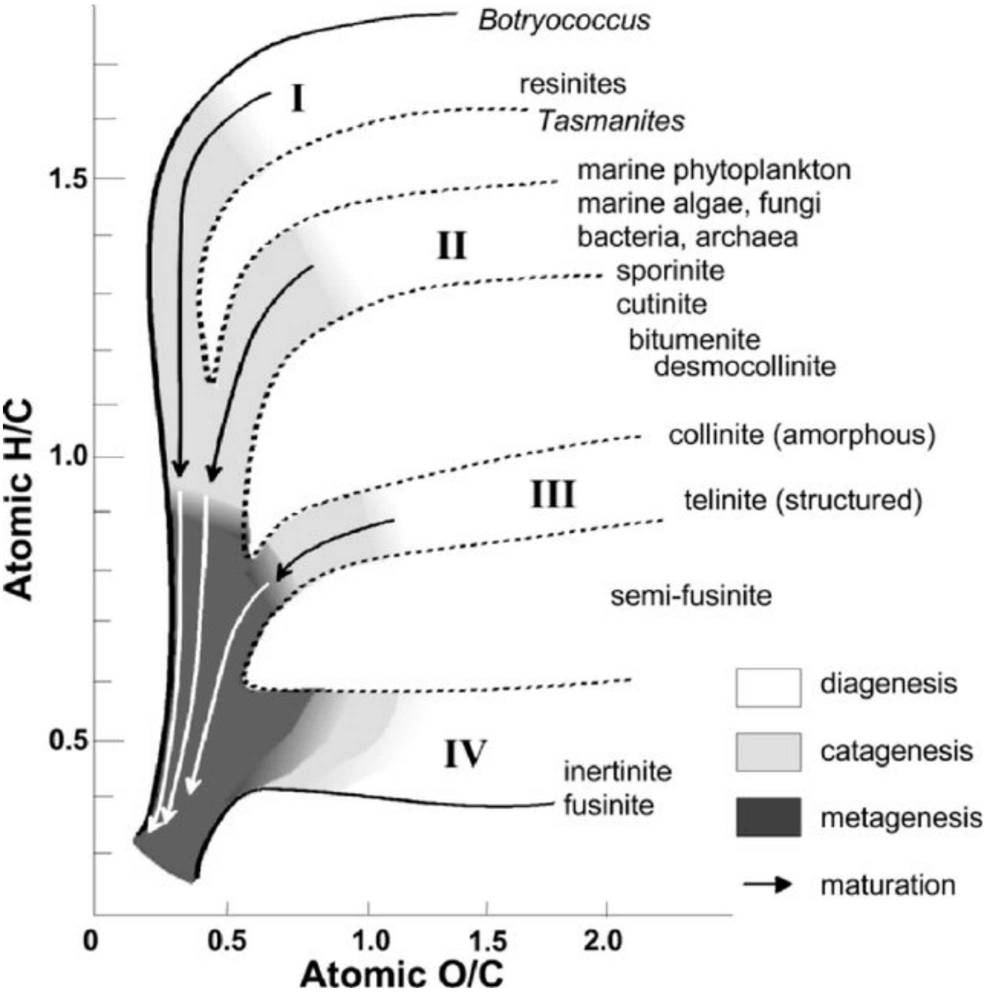

Figure I-21: Van Krevelen diagram showing maturation pathways for types I to IV of kerogen as traced by changes in atomic H/C and O/C ratios. The progressively darker shaded areas approximately represent diagenesis, catagenesis and metagenesis stages, respectively (Walters, 2007).

ratios, obtained from elemental analyses (Fig. I-21). On the basis of these ratios, four types of kerogen have been defined which follow distinct diagenetic pathways.

Type I kerogen has high initial H/C and low O/C ratios. The source material is mainly algal, or a combination of algal lipids and waxes from higher plants (Fig. I-22). It forms part of the liptinite macerals in coal.

Type II kerogen has intermediate initial H/C and O/C ratios, and larger contributions by aromatic and carboxylic acid groups than type I kerogen. Ester bonds are abundant, as are medium-length aliphatic hydrocarbon chains and naphthenic rings. Both algal and higher plant sources appear to contribute to type II kerogens (liptinite macerals).

Type III kerogen has an initial H/C ratio less than 1, an initial O/C ratio of 0.2 to 0.3, and is derived dominantly from terrestrial plants. It consists mainly of aromatic groups formed from lignins and humic compounds, and represents the huminite/vitrinite fractions of coal petrography. Oxygen is present as carboxylic acids, ketones and ethers rather than in ester bonds.

Type IV kerogen has <0.5 H/C ratio and contains mostly decomposed organic matter and highly oxidized material of various origins; it represents the inertinite group (Fig. I-21).

A palynological classification on the base of transmitted light analysis for a rapid assessment of hydrocarbon potential can be performed according to Tyson (2012). This classification is primarily designed for routine source rock 'kerogen typing' with the aim of identifying the relative proportions of inert, gas-prone, oil-prone and very oil-prone material within the total kerogen assemblage (Tyson, 2012).

In general, more detailed characterizations are needed, which can be performed by means of optical and chemical indicators related to the changes in kerogen composition. With increasing maturity, kerogen looses first preferentially O to produce CO_2 and H_2O, then H to produce hydrocarbons. Changes in the molecular structure have effect in the:

1) maximum temperature of the S2 band registered by Pyrolysis Rock Eval (Tmax, section 2.1);

2) petrographic detection of the constituents that can be observed in reflected and transmitted light;

3) molecular changes, reflected mainly in the decrease of aliphatic chains with respect to aromatic rings and changes in the spatial distribution of the aromatic rings. All these variations can be measured through Fourier Transform Infrared Spectroscopy (FT-IR) and Raman spectroscopy (section 2.5).

These are the thermal maturity indicators used in this work, whose principles and applications will be discussed in the text below.

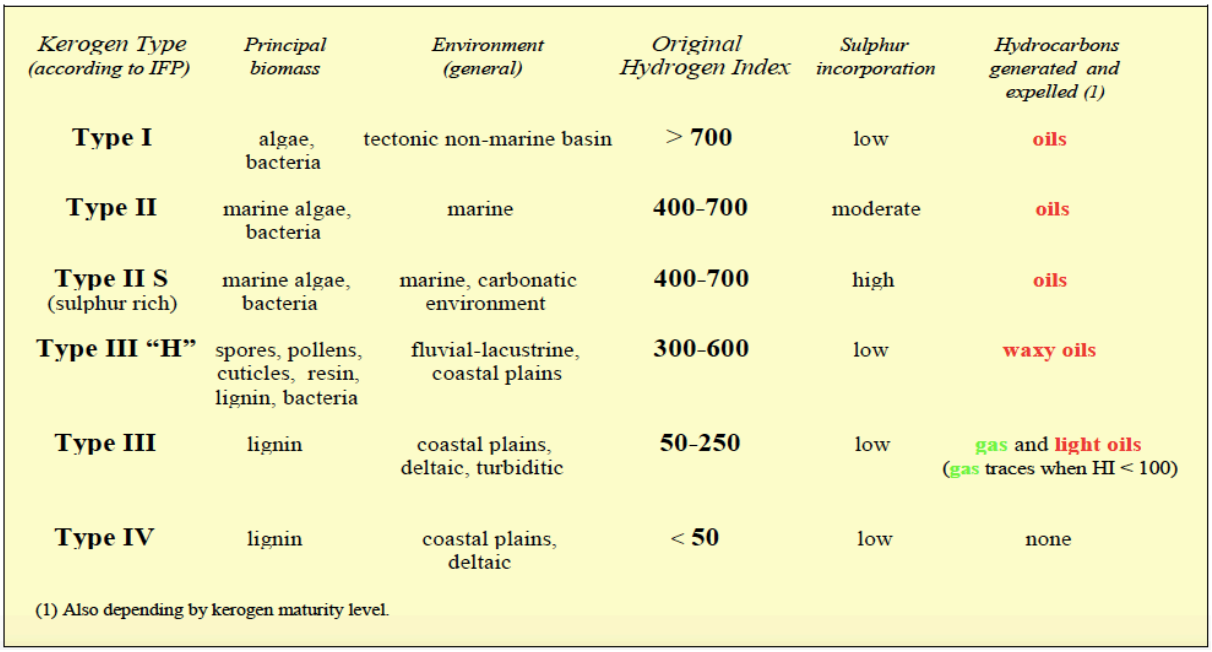

Kerogen Type (according to IFP)	*Principal biomass*	*Environment (general)*	*Original Hydrogen Index*	*Sulphur incorporation*	*Hydrocarbons generated and expelled (1)*
Type I	algae, bacteria	tectonic non-marine basin	> **700**	low	**oils**
Type II	marine algae, bacteria	marine	**400-700**	moderate	**oils**
Type II S (sulphur rich)	marine algae, bacteria	marine, carbonatic environment	**400-700**	high	**oils**
Type III "H"	spores, pollens, cuticles, resin, lignin, bacteria	fluvial-lacustrine, coastal plains	**300-600**	low	**waxy oils**
Type III	lignin	coastal plains, deltaic, turbiditic	**50-250**	low	**gas** and **light oils** (gas traces when HI < 100)
Type IV	lignin	coastal plains, deltaic	< **50**	low	none

(1) Also depending by kerogen maturity level.

Figure I-22: The main kerogen types, origin and pyrolysis indexes (Scotti, 2003).

I.2.1 Rock-Eval Pyrolysis and TOC

Pyrolysis Rock Eval and TOC measurements were performed at ENI laboratory (Milan - Italy) using Rock Eval 6 equipment. Total Organic Carbon (TOC) refers to the weight percentage (wt%) of the organic carbon present in 100g of rock (Langford and Blanc-Velleron, 1990).

Total Organic Carbon is measured from 1g sample of ground rock that is combusted and converted to CO or CO_2. According to Hunt et al. (2002) a value of approximately 0.5% TOC by weight percent is considered the minimum for an effective source rock.

Rock Eval Pyrolysis is a widely used degradation technique that allows breaking a complex substance into fragments, by heating it under an inert gas atmosphere (Vandenbroucke, 2003). In this technique, a sample is firstly heated at 300°C and the free hydrocarbons (HC) are volatilized and measured as the S1 peak. In general a S1 higher than 1 mg/g (mg of HC on g of sample) may be indicative of oil (Fig. I-23).

Then the temperature is increased from 300° to 550°C (at a rate of 25 °C/min) and leads to the volatilization of the very heavy hydrocarbon compounds as well as the cracking of the nonvolatile organic matter. The hydrocarbons released from this thermal cracking are measured as the S2 peak that, thus, is an indication of the quantity of hydrocarbons that the rock has the potential of producing, should burial and maturation continue (Fig. I-23).

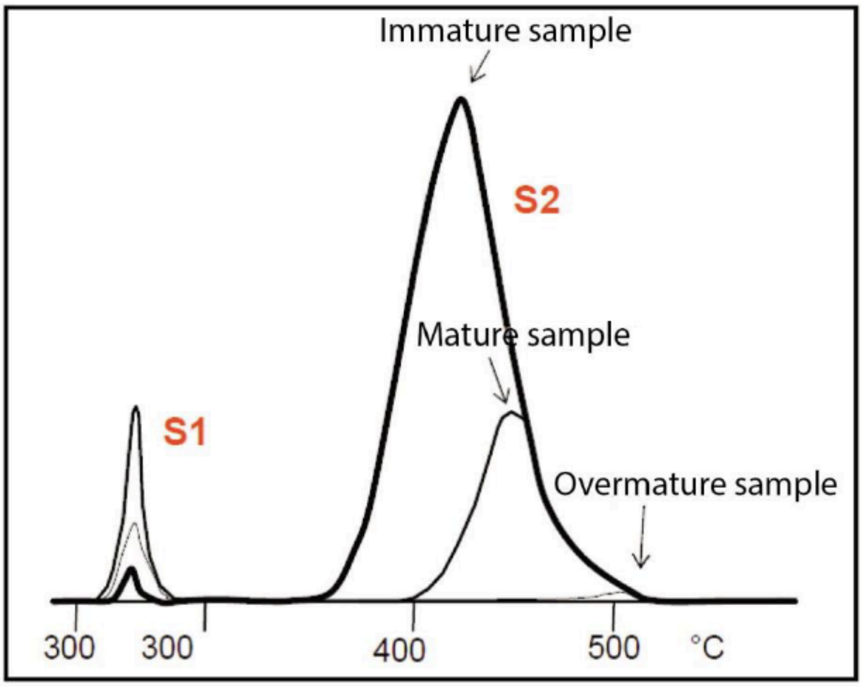

Figure I-23: S1 and S2 peaks after Pyrolysis Rock-Eval heating, for samples with different starting thermal maturity (from Scotti, 2003).

The temperature at which S2 reaches its maximum depends on the nature and maturity of the kerogen and is called Tmax. Tmax is directly related to the stage of maturation of the organic matter.

The CO_2 issued from kerogen cracking is trapped in the 300°-390°C range. The trap is heated, and CO_2 is released and detected on a TCD during the cooling of the pyrolysis oven (S3 peak). This peak is an indication of the amount of oxygen in the kerogen and is used to calculate the oxygen index.

The type and maturity of organic matter in petroleum source rocks can be characterized from Rock Eval Pyrolysis data using the following parameters:

- HI = hydrogen index (HI = [100xS2]/TOC). HI is a parameter used to characterize the origin of organic matter. Marine organisms and algae, in general, are composed of lipid- and protein-rich organic matter, where the ratio of H to C is higher than in the carbohydrate-rich constituents of land plants. HI typically ranges from ~100 to 600 in geological samples.
- OI = oxygen index (OI = [100xS3]/TOC). OI is a parameter that correlates with the ratio of O to C, which is high for polysacharide-rich remains of land plants and inert organic

material (residual organic matter) encountered as background in marine sediments. OI values range from near 0 to ~150.

- PI = production index (PI = S1/[S1+ S2]). PI is used to characterize the evolution level of the organic matter.

I.2.2 Organic petrography

OM in coals or dispersed in sedimentary rocks is usually highly heterogeneous, firstly because it has various origins (from plant, plant organs and less commonly animals), and also because its components suffered modifications of various degree and in different ways before and after deposition (Taylor et al., 1998). The best way to describe the OM heterogeneity is using a reflection light or, even better, an electron microscope. Through these techniques it is possible to classify qualitatively and quantitatively the components of the OM on the basis on their origin, nature and properties.

The base of this classification is the "maceral concept" that, according to Taylor et al. (1998), defines macerals as the microscopically recognized individual constituents of OM (through the use of light, especially reflected light, microscopy). The word 'maceral' refers to the selective oxidative treatment of OM used in paleobotany and is derived from the latin verb "macerare" which means "to soften".

Macerals represent, at least partly, the remains of plants whose form and/or structure have been preserved in coal and other rocks, while other macerals are degradation products which are so altered that their plant origin cannot be determined.

All macerals have the suffix '-inite', and are classified into three main groups (Fig. I-24):

1) vitrinites: are the coalification products of humic substances, which essentially originate from the lignin and cellulose of plants cell walls. They are characterized by high oxygen and aromatic fraction content;

2) liptinites: they derive from relatively hydrogen-rich plant remains such as sporopollenin, resins, waxes and fats. They differ from vitrinites for a higher aliphatic (paraffin) fraction and a correspondingly higher hydrogen content;

3) inertinites: are characterized by relatively high carbon content, low hydrogen content and a much increased level of aromatization. Most inertinites have the same origin of vitrinite and liptinite but they experienced different primary transformations due to various processes (e.g. charring, oxidation or fungal attack).

Vitrinite is the standard reference material for reflectance measurements, in order to determine the level of organic maturation. This technique is well known and widely used as it provides consistent and reliable thermal maturity assessments, with high resolution degree.

In the same sample, the three groups can coexist but showing different reflectance values, as shown in the histograms in Figure I-24.

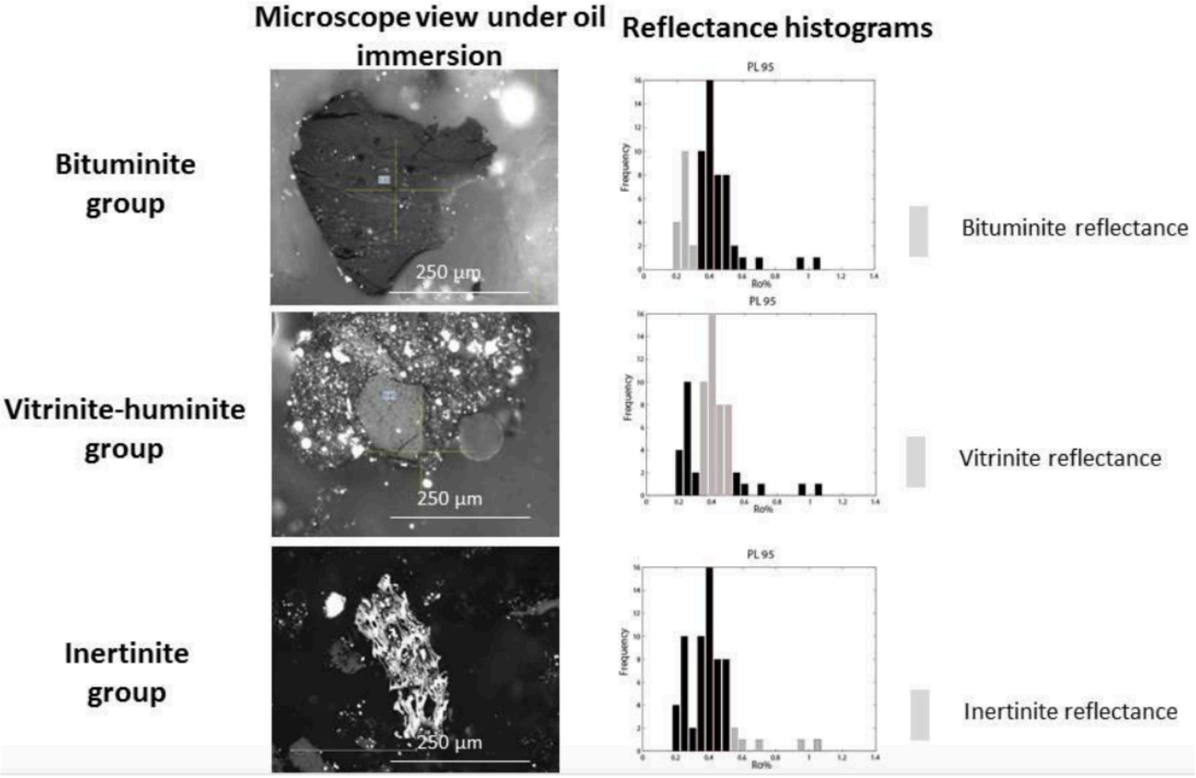

Figure I-24: Microphotographs of different macerals at the same thermal maturity level. On the right are reflectance random histograms, where grey bins indicate the reflectance for the corresponding macerals on the left. Photos are taken from microscope, with 50x magnification, under oi immersion.

To avoid as much ambiguity as possible among different macerals, the International Committee for Coal and Organic Petrology (ICCP) has established standard rules for petrographic microscopy, which state that the description of macerals should be in terms of their appearance in reflected light using oil immersion objectives with 25-50X magnification.

Fluorescence microscopy can be seen as a complementary method of examination that can help to reveal details, not otherwise visible, of the internal make-up of macerals and some of their chemical and physical properties.

I.2.2.1 Samples preparation

Sample preparation was performed at the Academic Laboratory of Basin Analysis (ALBA) of "Roma Tre" University (Italy).

Analyses were performed on concentrated kerogen using acid attack and on dispersed OM fragments in the bulk rock. When analyses were performed on the bulk rock, samples were grounded in a mortar and were hand-picked under an optical microscope (Leica zoom 2000).

For optical analyses both bulk kerogen and bulk rock were mounted on epoxy resin blocks (Serefix resin + hardening with a 1:20 ratio – Fig. I-25). Samples were polished using an automated polishing system (Struers Labopol 5), three sheets of 250, 500, 1000 carborundum paper and isopropanol lubricant. After washing samples in order to remove debris, three polishing laps were used with alumina powders of decreasing grain size (1.00, 0.30, 0.01 μm) and samples where polished for a few minutes with each lap (Fig. I-26).

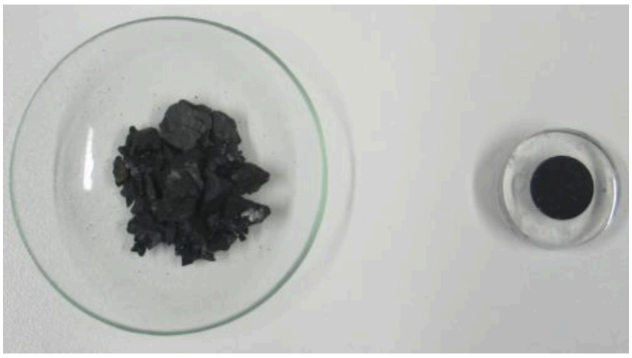

Figure I-25: Extracted kerogen particles (on the left) and kerogen embedded in an epoxy resin block (on the right).

In this thesis kerogen was extracted using wet-chemical acid demineralization according to Robl & Davis (1993) and Schimmelmann et al. (1999). Samples were crushed using the mixer ball mill. Removal of carbonates was done adding HCl on the dried samples. The HCl was added in small increments to prevent excessive foaming. The acid digestion process was done at 50-60°C in a water bath to facilitate removal of carbonates.

The acid was removed with pipette and disposed in plastic containers with neutralizing limestone gravel under a fume hood. Digestion of inorganic matter was done by hydrofluoric acid (HF). For every 5 g of powder sample a mixture of 50% distilled water and 50% HF was added (45 ml). Samples were placed on a shaker table for 2 hours at regular intervals. The samples were finally washed 5-6 times with distilled water.

Figure I-26: Automated polishing system.

I.2.3 Analysis in reflected light and reflectance measurements

Optical analyses were performed at the Academic Laboratory of Basin Analysis (ALBA) of "Roma Tre" University (Italy). The microscope used was a Zeiss Axioskop 40 A, equipped with a tungsten-halogen lamp (12V, 100w) and an Epiplan-Neofluar 50x/1.0 oil objective; the analyses were made in incident filtered (λ = 546 nm) non-polarized light under oil immersion (n = 1.518) at about 23°C (Figure I-27). The microscope is equipped with the MPS 200 detection system by J & M Analytik AG (website: http://www.j-m.de).

On each sample measurements were performed on unaltered fragments. Mean reflectance values (Ro%) were calculated from the arithmetic mean of these measurements with a standard deviation, identifying the indigenous population. Microphotographs of specimens fragments were taken using a microscope-mounted Canon Power Shot G6.

In most cases a population of a few tens of readings per sample was collected on fragments only slightly fractured and/or altered (Borrego et al., 2006).

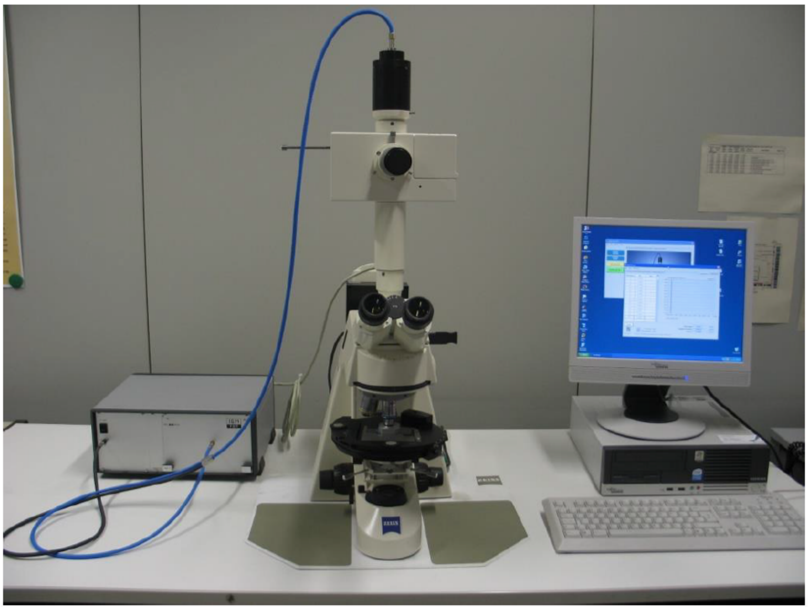

Figure I-27: Zeiss Axioskop 40 A microscope, equipped with MPS detection system.

I.2.3.1 Vitrinite reflectance

Mean vitrinite reflectance (VRo%) is measured as the percentage of the incident light intensity which is reflected from the polished surface of vitrinite macerals fragments relative to a standard substance (e.g., glass, sapphire, etc.). This measurement uses immersion oil and is related to the refractive index and absorptive index of immersion oil and standards which follows the Fresnel-Beer equation:

$$R_o = (\mu - \mu_o)^2 + \mu^2 k^2/(\mu + \mu_o)^2 + \mu^2 k_o^2$$

where: μ, μ_o = refractive index of vitrinite and immersion oil, respectively; k, k_o = absorption index of vitrinite and immersion oil, respectively.

These indexes are wavelength dependent, thus a green monochromatic non-polarised light (λ = 546 nm) is chosen for Ro% measurements.

In diagenesis and in the first stages of catagenesis (Ro% <1.5), vitrinite is optically isotropic and the aromatic clusters present in the organic structure have no preferred orientations. In metagenesis instead, vitrinite behaves like an anisotropic material because of the orientation of aromatic clusters (Oberlin et al., 1980). When tectonic stress affects the thermal maturity of sediments, vitrinite macerals can turn out to be biaxial (Levine and Davis, 1989) (Fig. I-28).

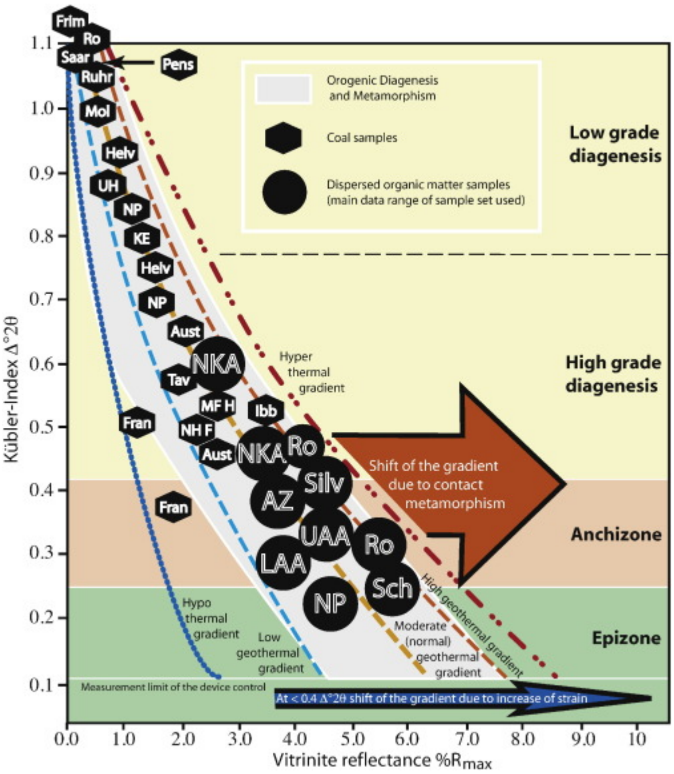

Figure I-28: Increase od vitrinite reflectance (%Rmax, Rm and Rmin) with depth (connected to the increase of metamorphic degree), as shown by coal (diamonds) and OM (circles). Deepening is associated with a divergent trend for Ro%, that relates to the biaxial nature of vitrinite when Ro% becomes >1.5 (Ferreiro Mählmann and Le Bayon, 2016).

I.2.4 Organic matter analysis in transmitted light

Another approach to the study of OM in sedimentary rocks is the use of microscope in transmitted light using kerogen concentrate (Teichmuller, 1986), whose advantage is a better identification of palynomorphs with respect to incident light techniques. In particular, the use of fluorescence-light techniques allows liptinite occurrences to be distinguished from the less fluorescent components of kerogen, and the individual liptinite macerals to be differentiated one from another (Fig. I-29). Applied to hydrocarbon exploration, transmitted light analysis has the advantage of estimating directly all factors which are decisive for oil and gas proneness: like type, abundance distribution and substance.

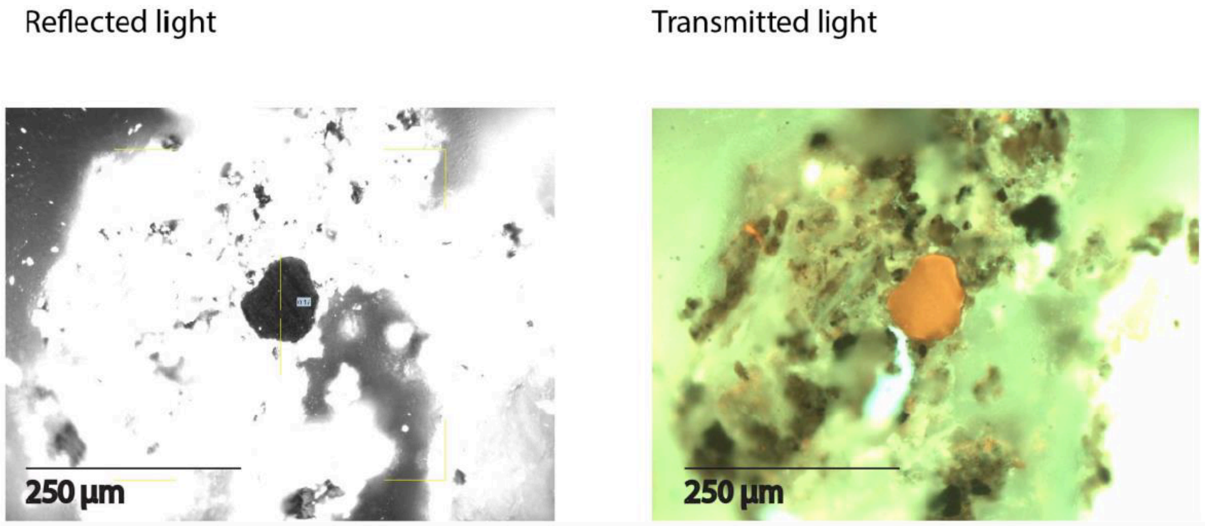

Figure I-29: Two microphotographs showing the same liptinite fragment observed under a) reflected light and b) transmitted light.

This analysis has been used to quantitatively assess the kerogen composition according to the ENI classification, that proposes four classes:

1) AOM: amorphous organic matter;
2) MPH: marine phytoplankton;
3) CWF: continental wooden organic matter;
4) CHF: continental herbaceous fragments.

I.2.5 Raman spectroscopy

I.2.5.1 Theory

When radiation passes through a transparent medium, the species present scatters a fraction of the beam in all directions. Nevertheless, in 1928 it was found by an Indian physicist, C. Raman, that a small fraction of the radiation scattered by certain molecules differs from that of the incident beam, and the shifts in wavelength depend on the chemical structure of the molecules responsible for scattering.

Raman spectra are obtained by irradiating a sample with a powerful laser source of monochromatic radiation. During irradiation, the spectrum of the scattered radiation is measured. The scattered radiation is of three types, namely Stokes, anti-Stokes and Rayleigh (Fig. I-30). The wavelength of Rayleigh radiation is the same of the incident radiation, while a shift toward higher and lower wavenumbers is observed for the anti-Stokes and Stokes radiations respectively.

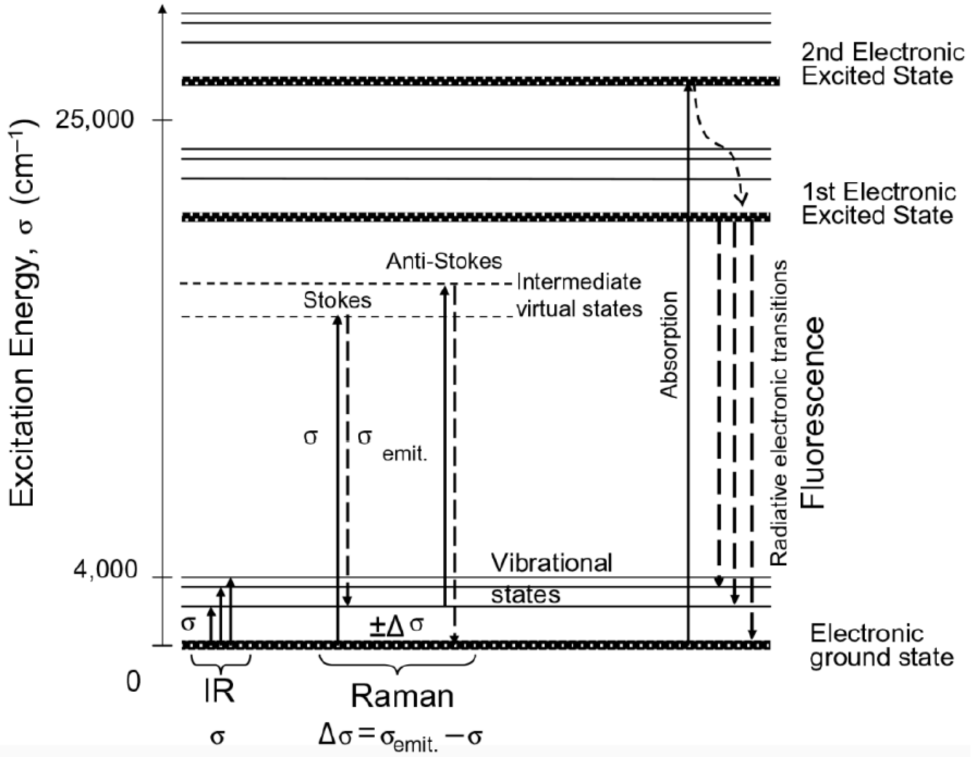

Figure I-30: Jablonski energy-level diagram representing the virtual vibrational states involved in Raman inelastic diffusion and the real electronic excited states involved in fluorescence (modified from Schwartz, 2011).

The Raman effect can be described in terms of transitions between vibrational energy levels. When an energetic photon strikes a molecule in its ground state, it may raise the molecule to a higher virtual state. As this is not a stable energy state for the molecule, three things can occur.

The firtst one and most probable, is that the molecule will return to its ground vibrational state and emit a photon with the same energy and frequency as the exciting photon (i.e. Rayleigh scattering). However, some of the excited molecules will not return to the ground state, but to some excited vibrational state. Such a molecule emits a photon, which has a lower energy than the exciting photon, the energy difference being equal to the difference between the initial and final vibrational states. This is Stokes-type Raman scattering.

If a molecule, which is in the first excited vibrational state, absorbs the photon, then the molecule is again raised to some higher, non-stable energy state. This molecule will probably then return to the ground state, and doing so, emits a photon, which has a higher energy than the exciting photon. The difference in energy between the exciting photon and the emitted photon is equal to the energy difference between the two excited vibrational states of the molecule. This is anti-Stokes-type Raman scattering.

The relative populations of the two energy states are such that Stokes Raman is much favoured over anti-Stokes. The quantum theory of Raman scattering shows that the phenomenon results from the same type of vibrational changes that are associated with infrared (IR) absorption. Thus, the difference in wavelength between the incident and scattered radiation corresponds to wavelengths in the mid-IR region.

There are, however, notable differences between the kinds of groups that are IR active and those that are Raman active. The IR absorption requires that a vibrational mode of the molecule have a change in dipole or charge distribution associated with it. Only then can radiation of the same frequency interact with the molecule and promote it to an excited vibrational state. In contrast, scattering involves a momentary distortion of the electron distribution around a bond in a molecule, followed by re-emission of the radiation as the bond returns to its ground state. In its distorted form, the molecule is temporarily polarized, i.e. momentarily develops an induced dipole, which disappears upon relaxation and re-emission.

Each band in a Raman spectrum represents the interaction of the incident light with certain atomic vibrations. Atomic vibrations, in turn, are controlled by the sizes, valences and masses of the atomic species of which the sample is composed, the bond forces between these atoms, and the symmetry of their arrangement in the crystal structure. These factors affect not only the frequencies of atomic vibrations and the observed Raman shifts, but also the number of observed Raman bands, their relative intensities, their widths and their polarization. Therefore, Raman spectra are highly specific for a certain type of sample and can be used for the identification and structural characterization of unknowns.

I.2.5.2 The Raman spectrometer

Micro-Raman spectroscopic analyses, were performed at the Laboratory of Experimental Volcanology and Petrology (EVPLab) of "Roma Tre" University (Italy).

At EVPLab laboratory a Jobin Yvon micro-Raman LabRam system was used in a backscattering geometry, in the range of 700-2300 cm^{-1} (first order Raman spectrum) using a 600 grooves/mm spectrometer gratings and CCD detector under a maximum of 50X optical power (Fig. I-31).

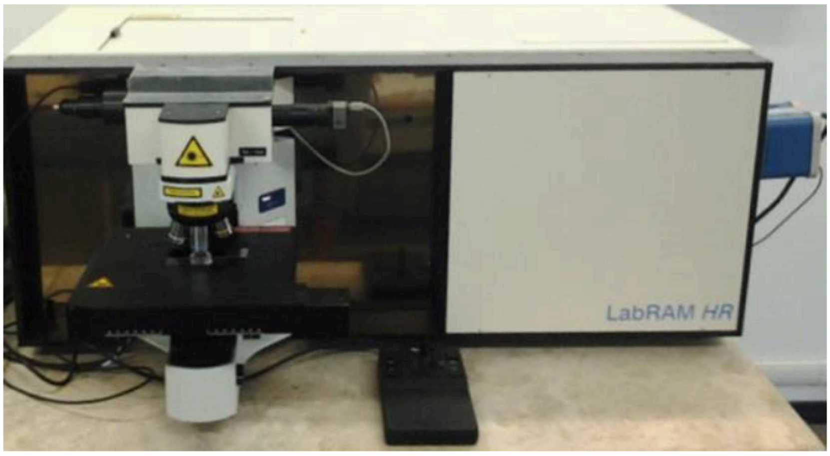

Figure I-31: Jobin Yvon micro-Raman LabRam system from EVPLab laboratory (Roma Tre University, Italy).

A laser source Neodimium-Yag at 532 nm (green laser) was used as the light source and optical filters adjusted the power of the laser (<6mW). The Raman backscattering was recorded after an integration time of 20s for 6 repetitions for each measurement. This, together with the use of green laser and optical filters, allowed to reduce the fluorescence background to optimal values. Between ten to fifteen measurements were performed for each sample to ensure reproducibility of the measurements.

Each organic grain was analysed with a 2 µm diameter spot and a 50× objective lens.

I.2.5.3 Band assignment for Raman spectra in dispersed organic matter

Raman spectral signal of kerogen is concentrated in a "first order" region between 1000 and 2000 cm^{-1} and "second order " region between 2000 and 3500 cm^{-1}. Bands in the second order region are visible only in higher thermal maturity samples (Beyssac et al., 2003).

The first order Raman spectra for carbon materials consist of two main bands, known as D and G bands (Tuinstra and Koenig, 1970; Friedel and Carlson, 1972), and in other less defined bands that can vary depending on the kind of material and rank degree (Li, 2007; Potgieter-Vermaak et al., 2011).

D and G bands correspond respectively to breathing and stretching mode in sp^2 bonded carbon clusters (Ferrari and Robertson, 2000). In graphite, the G band is related to E_{2g} vibration mode of a crystal with D^4_{6h} symmetry, i.e. to in-plane vibration of aromatic carbons at 1580-1600 cm^{-1}. The D band was originally observed at 1355 cm^{-1} with a 488 Ar-ion laser and was related to the in-plane A_{1g} mode that is active only in the presence of lattice defect of polycrystalline graphite (Pócsik et al., 1998). It's worth to note that D mode is dispersive and vary with photon excitation energy, while G peak is not dispersive (Pócsik et al., 1998; Ferrari and Robertson, 2000, 2004; Nestler et al., 2003; Castiglioni et al., 2004).

Dealing with very disordered materials, the contribution of other features at 1100-1200 and 1400-1500 cm^{-1} cannot be neglected and even the assignment of the G and D bands to specific vibrational modes is questioned. Unfortunately, very few works exist that attempt to explain the origin of these bands and the results are often contradictory. For this reason, assignment of Raman bands for disordered material is still matter of debate.

In high-rank coals, Beyssac et al. 2002, based on literature work (Tuinstra and Koenig, 1970; Nemanich and Solin, 1979; Beny-Bassez and Rouzard, 1985) (Fig. I-32) proposes the presence

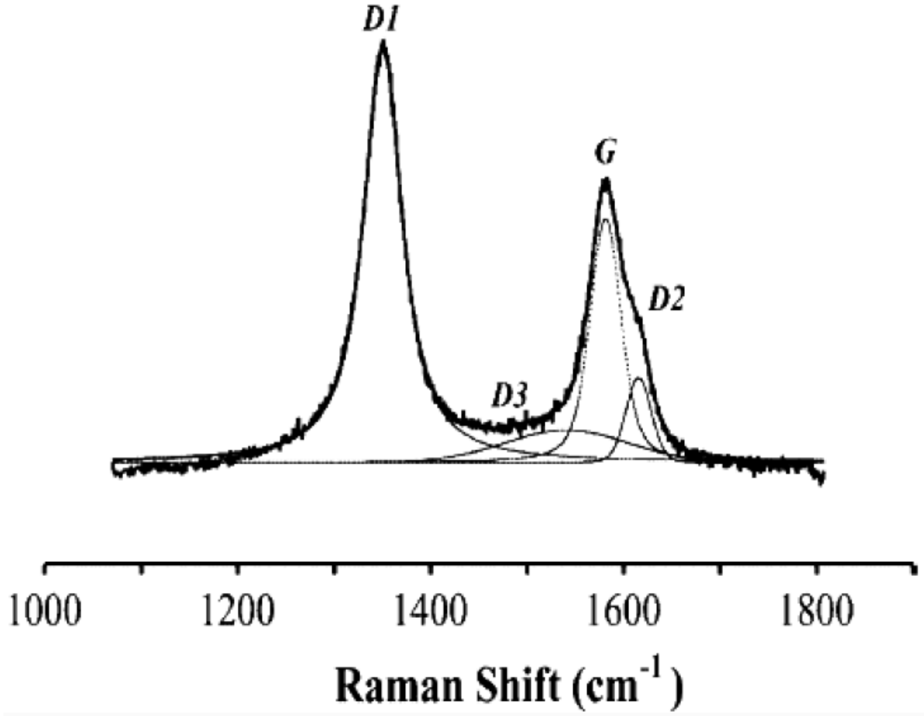

Figure I-32: Raman spectra deconvolution in the first order region according to Beyssac et al. *2002.*

of two additional bands: the D2 band, that appear as a right ned shoulder of the G band at approximately 1620 cm^{-1} and the D3 band, which is a wide band at approximately 1500 cm^{-1}. The band has been attributed to out-plane defects like tetrahedral carbons (Beny-Bassez and Rouzard, 1985), or to small crystallite sizes (Nemanich and Solin, 1979).

Working on carbon material matured at lower temperatures (about 200-320°C), Sadezky et al. (2005) and Lahfid et al. (2010) proposed the presence of an additional band called D4 at about 1200 cm^{-1}, attributed to sp^3-sp^2 bonds or C–C and C=C stretching vibrations of polyene-like structures (Fig. I-33).

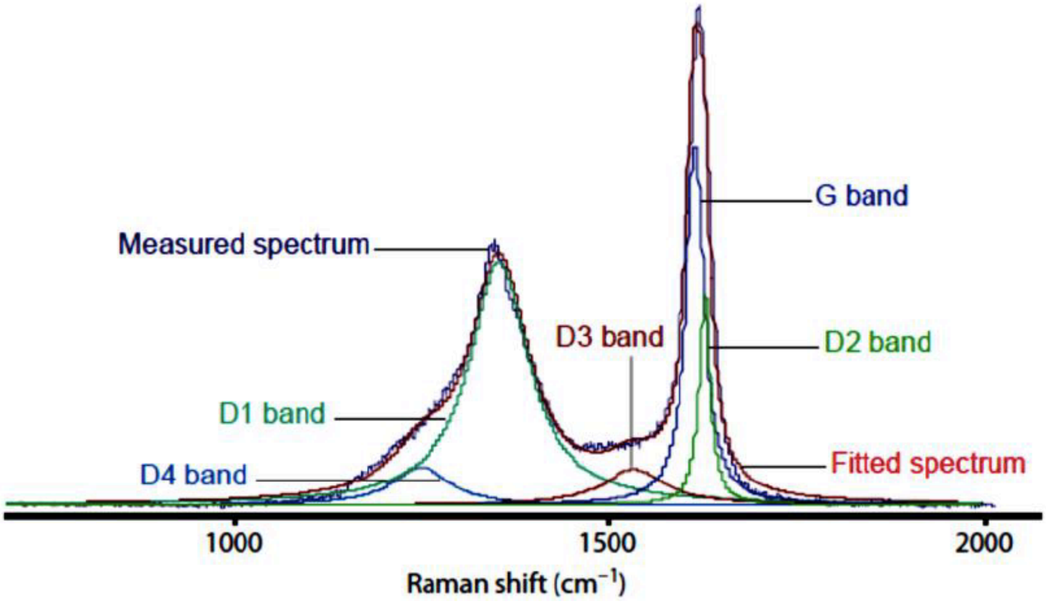

Figure I-33: Raman spectra deconvolution in the first order region, according to Lahfid et al. *2010.*

In low maturity coal, the Raman spectra of very disordered carbonaceous matter are significantly different and more complex than the spectra of highly ordered carbon materials such as those investigated by Beyssac et al. (2002) and Lahfid et al. (2010). One of the first order band assignment for disordered materials, based on analyses on Victorian brown coal, is provided by Li et al. (2006) and Li (2007). In their work the Raman spectrum was deconvoluted into 10 bands, as illustrated in Fig. I-34.

In the above mentioned papers, the authors proposed the assignment of the G band (1580-1600 cm^{-1}) to aromatic quadrant ring-breathing mode with little contribution from graphitic structures and the D band (1300 cm^{-1}), not to defects, as previously proposed for highly ordered carbonaceous matter, but to disordered of fused benzene rings having more than six rings, but less than graphite. Li (2007) attributed the band at about 1700 cm^{-1} (Gl band) to carbonyl group C=O, while the Gr (1540 cm^{-1}), Vl (1465 cm^{-1}) and Vr band (1380 cm^{-1}) that represent the "overlap" between D and G are assigned to semi-circle breathing of 3-5 membered aromatic

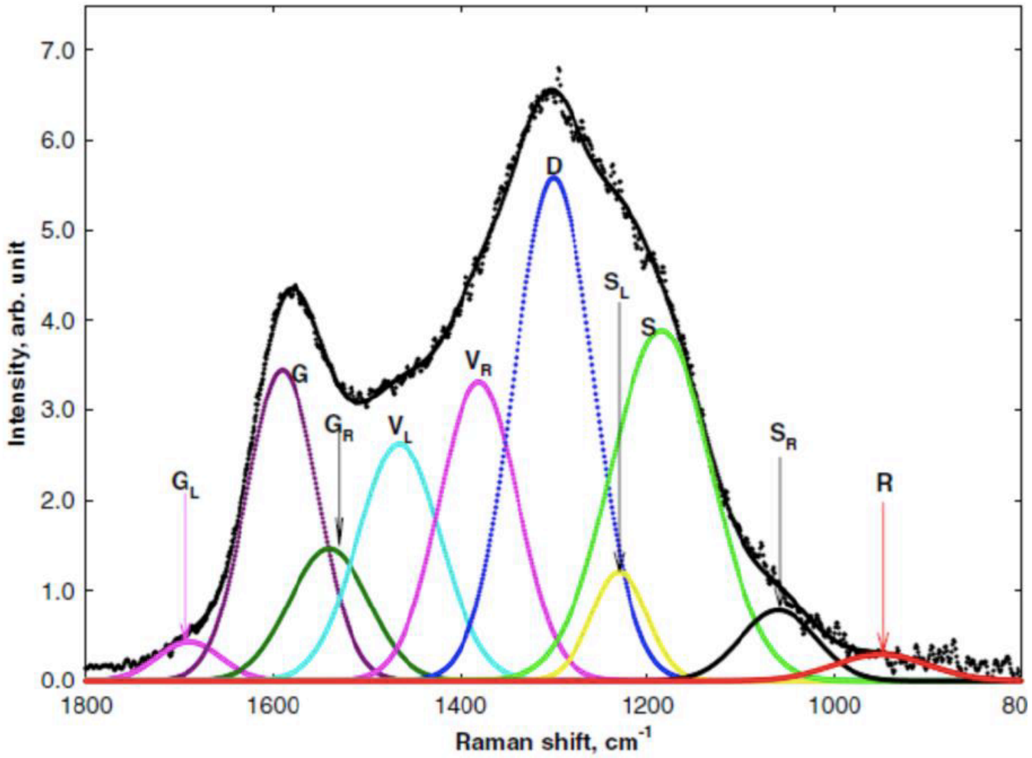

Figure I-34: Raman spectra deconvolution in the first order region, according to Li 2007.

rings and methylene or methyl aromatic rings with mixed sp^2- sp^3 structures. At lower wavenumbers they found that the S band (1185 cm-1) band together with Sl band (~1220 cm^{-1}) act as the shoulder of the D band (1230 cm^{-1}= aryl-alkyl ether; para-aromatics) and mainly representing Caromatic–Calkyl, aromatic (aliphatic) ethers, C–C on hydroaromatic rings, hexagonal diamond carbon sp3 and C–H on aromatic rings. Finally SR band (1060 cm^{-1}) is assigned to C-H on aromatic rings and benzene ring and the R band (960-800 cm^{-1}) C-C to alkanes and cyclic alkanes and/or C-H on aromatic rings.

More recently, based on analyses on carbon nanotubes, Rebelo et al. (2016) proposed new assignments on the first order deconvoluted peaks in which the "D region" is deconvoluted with a central Lorentzian D band at 1350 cm^{-1} and two satellites Gaussian bands called Dl and Dr (left and right) at ~1250 and ~1400 cm^{-1} respectively (Fig. I-35).

D band corresponds to vibration with A_{1g} symmetry associated with interlayer arrangement. Dl and Dr are assigned to identical vibration of the D band, but in low size aromatic domains. For higher Raman shift values the G band is fitted with a Lorentzian shape at ~1580 cm^{-1} surrounded by a Lorentzian Gr peak at ~1610 cm^{-1} and a Gaussian Gl peak near 1500 cm^{-1} (Heise et al., 2009).

The G band corresponds to vibrations with E_{2g} symmetry from in-plane aromatic graphene sheets and Gr band to the same vibration in low size aromatic domains. A further band, called

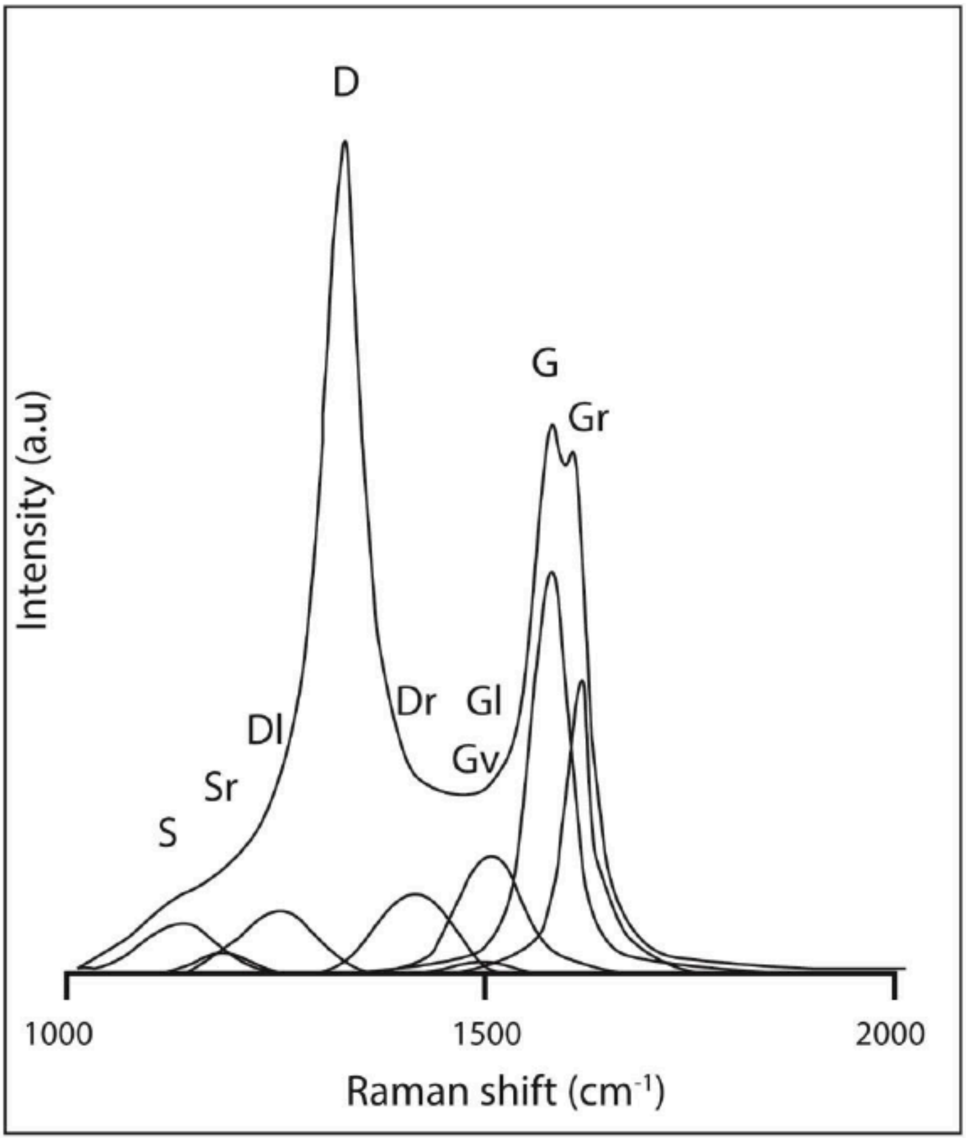

Figure I-35: Raman spectra deconvolution in the first and second order region. Redrawn after Rebelo et al. *2016.*

S band, was used to fit a relative small feature in the left side of the spectra, at ca. 1120 cm^{-1}. Bands S and Gl were assigned to a fingerprint of polyacetylene like structures or areas of conjugated double bonds mainly present in the border of structures were aromaticity has been broken upon functionalization (Shirakawa et al., 1973). For highly functionalized materials, other bands can arise at 1180 cm^{-1} (Sr) and at 1480 cm^{-1} (Gv).

For a further understanding of disorder, it is important to obtain appropriate correlations between the spectral features and effects arising from covalent functionalization (transformation of sp^2 aromatic carbon into sp^3 carbon), and to distinguish them from other structural effects and deviations from the perfect graphite structure: namely, the curvature in carbon nanotubes or nanofibers, the reduction of the graphitic crystals size in few layer graphene and edge structures, or the presence of amorphous carbon.

I.3 INORGANIC FRACTION OF SEDIMENTS

I.3.1 X-Ray diffraction of clay minerals

I.3.1.1 Samples preparation

In the Academic Laboratory of Basin Analysis (ALBA) of "Roma Tre" University, the procedure described by Moore & Reynolds (1997) and modified by Giampaolo & Lo Mastro (2000) was adopted to analyze the <2 μm grain size fraction of sediments (equivalent spherical diameter).

About 20 g of the whole-rock sample were slightly crushed by hand in an agate mortar and put in a flask with 150 ml of distilled water (Fig. I-36). Samples were disaggregated in distilled water by swinging the clay-rich mixture at 200 oscillation/min (Fig. I-37).

Figure I-36: Crushed rock samples in distilled water.

Then, 50 ml of the suspension was put in a plastic tube and centrifuged to separate the <2 μm fraction according to standard procedures, which take into account water temperature and the centrifuge radius (Figure 37).

After centrifugation, the suspension containing <2 μm was separated, pipetted, and dried at room temperature on glass slides to produce a thin highly oriented aggregate (Fig. I-39) (Giampaolo and Lo Mastro, 2000).

Figure I-37: Clay-rich mixture swinging at 200 oscillations/min.

Qualitative and semi-quantitative analyses were performed with a Scintag X1 X-ray system (CuKα radiation) at 40 kV and 45 mA (Figure I-40). Oriented mounts were analyzed in air-dried and ethylene glycol solvated forms (saturation in ethylene-glycol atmosphere at room

Figure I-38: Centrifuge up to 4000 rpm.

temperature for 24 h) in the 1 to 48°2θ and 1 to 30°2θ ranges respectively with a step size of 0.05°2θ and a counting time of 4 s per step.

The illite content in mixed-layer I–S was determined by the delta two-theta method after decomposing the composite peaks between 9–10°2θ and 16–17°2θ (Moore and Reynolds, 1997) and by modeling X-ray diffraction patterns using Pearson VII functions and the DMSNT Scintag associated program.

The I–S stacking order (Reichweite parameter, R; Jagodzinski, 1949) was determined by the position of the I 001–S 001 reflection between 5 and 8.5°2θ. Kübler index (KI)

Figure I-39: Air-dried oriented slides.

measurements were made by first subtracting the background from the raw data, and then applying a profile fitting method (Lanson, 1997). From the fitted data, KI was measured by the FWHM (full-with-half-maximum) parameter of the program. Half-peak widths were calibrated using standards by Warr & Rice (1994). Peaks in relative close position were selected for clay mineral quantitative analysis in order to minimize the angle-dependent intensity effect. Integrated peak areas were transformed into mineral concentrations by using mineral intensity factors as a calibration constant (for a review, see Moore & Reynolds, 1997). Non-clay minerals were not taken in account in the <2 μm grain-size fraction quantitative analysis.

Figure I-40: Scintag X1 X-ray system.

I.3.2 Thermal maturity interpretation

The study of clay mineralogy has provided several useful tools for studies on diagenesis and very low-grade metamorphism, by providing information on the burial and thermal history of sedimentary sequences (Corrado et al., 2005; Aldega et al., 2007b, 2007a, 2011; Botti et al., 2007; Di Paolo et al., 2012). Clay minerals in shales and sandstones undergo diagenetic and very low-grade metamorphic reactions in response to sedimentary and/or tectonic burial.

Reactions in clay minerals are irreversible under normal diagenetic and anchizonal conditions, so that exhumed sequences generally retain indices and fabrics indicative of their maximum maturity and burial (Merryman and Frey, 1999).

An important reaction occurring in shales during burial diagenesis and in hydrothermal settings is the gradual conversion of smectite to illite through I-S mixed layers as intermediate phases. The progressive trend ranging from early diagenesis to epizone includes the following series: dioctahedral smectite - disordered mixed layers (R0) - ordered mixed layers (R1 and R3) - illite - dioctahedral white K-mica (muscovite). This prograde series is characterized by various crystal structural changes as the decrease of proportions of swelling phases and the increase of ordering in mixed layers. The layers are stacked along a direction parallel to the c-axis in random, partially regular, or regular sequences. The layers are stacked along a direction parallel to the c-axis in random, partially regular, or regular sequences. The classical terminology for the stacking order is based on the term R (Reichweite; Jagodzinski, 1949) that expresses the probability, given a layer A, of finding the next layer to be B. The R parameter may range from 0 to 3. R=0 means that there is no stacking order and illite and smectite layers are stacked randomly along the c-axis, R=1 indicates that a smectite layer is followed by an illite layer and a stacking order appears in the interstratification sequence, R=3 means that each smectite layer is surrounded by at least three illite layers on each side (Pollastro, 1990).

In this report, I-S structures will be described by means of the Reichweite nomenclature using R1 to mean R=1, R3 for R=3, etc. (Figure I-41).

The most common approaches utilizing I-S “geothermometer” in diagenetic studies are vertical profiles from wells and outcrops and thermal maturity mapping at local and regional scale. In the first case, illitization reaction profiles are generally produced. They are compared to the present-day geothermal gradient profile and to organic matter maturity profiles, in order to determine the temperature range in a particular point of the well, correlating them to hydrocarbon generation phases (Pollastro, 1993; Merryman and Frey, 1999) (Fig. I-42).

Although the conversion to paleotemperatures depends on more than one factor (e.g., heating rate, protolith, fluid composition, permeability, fluid flow), Pollastro (1990, 1993) summarized the application of two simple time-temperature models for I-S geothermometry studies, based primarily on the duration of heating (or residence time) at critical I-S reaction temperatures. The first model was developed (Hoffman and Hower, 1979) for long-term, burial diagenetic settings that can be applied to most geologic and petroleum studies of sedimentary rocks and basins of Miocene age or older. In this model, the major changes from R0 to R1 and from R1 to R3 occur in the temperature range of about 100-110 °C and of 170 °C-180 °C

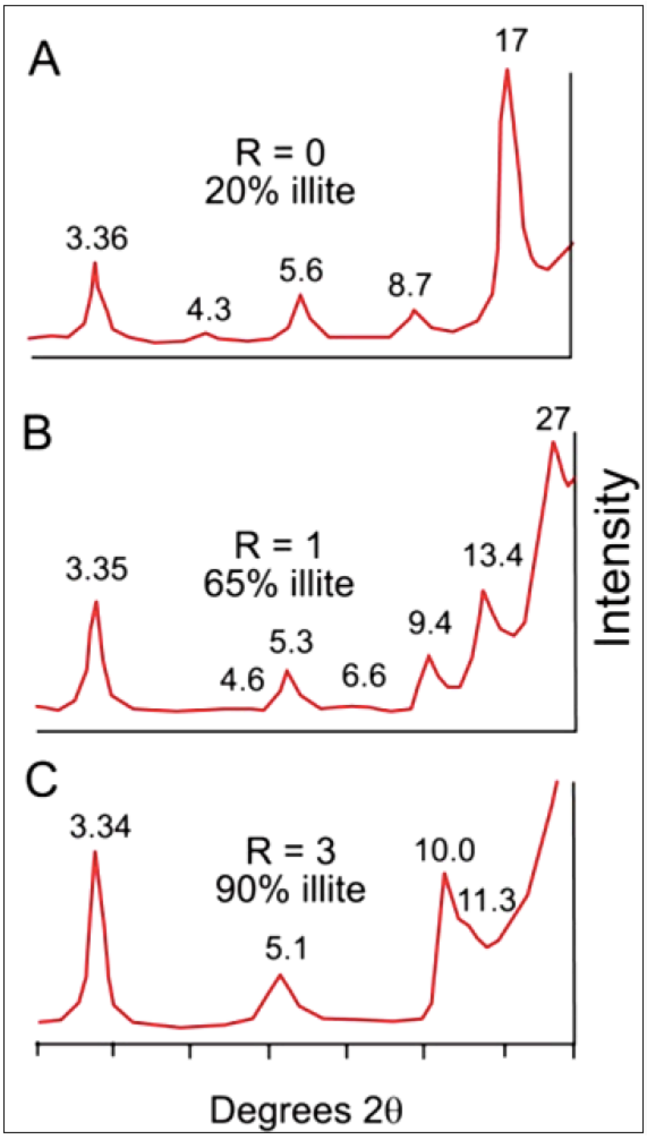

Figure I-41: Calculated XRD patterns of illite-smectite mixed layers with different content and stacking order: A) random ordered I-S; B) short range ordered I-S; C) long range ordered I-S (Pollastro, 1990).

respectively, and a minimum heating duration of 2 My is generally required (Hoffman and Hower, 1979). The second model, which was developed for short-lived heating events, applies to young basins or areas characterized by relatively recent thermal activity with high geothermal gradients, or to recent hydrothermal environments.

Such settings are those where relatively young rocks were subject to burial temperatures in excess of 100 °C for <2 My. In this model the conversion from R0 to R1 and from R1 to R3 ordering occurs at about 130-140 °C and 170-180 °C respectively (Jennings and Thompson, 1986). Many authors have studied the use of illite-smectite reaction as a measure of temperature. Bibliographic data of approximate temperatures for changes in mixed layer illite/smectite, relative to different geological settings, are reported in Table I-1.

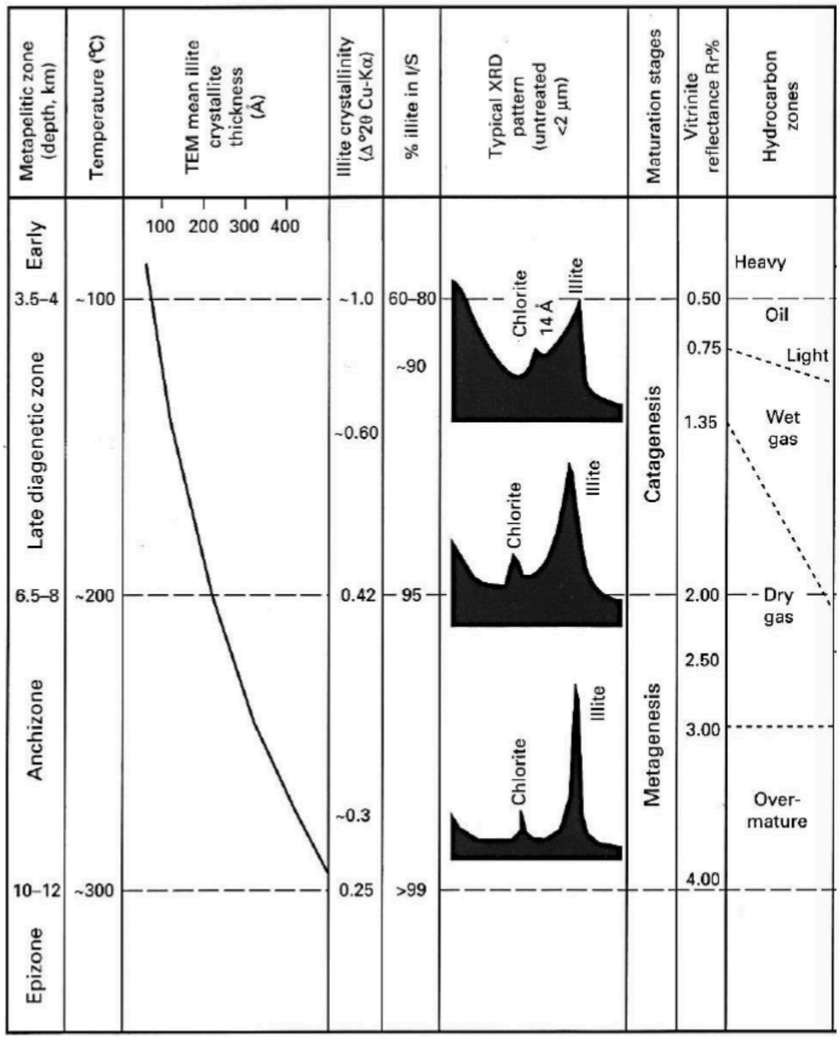

Figure I-42: Correlation scheme among clay mineral geothermometers, vitrinite reflectance data, hydrocarbon zones, metapelitic zones and paleo-temperature (Merriman & Frey, 1999).

%I in I-S (R number)	**0-20% (smectite to R0)**	**30-60% (R0)**	**60-80% (R0 to R1)**	**80-90% (R1 to R3)**	**90-95% (R3)**	**100% (illite)**
Hoffman & Hower 1979	50-60°C		100-110°C	170-180°C		210°C
Jennings & Thompson 1986			130-140°C	170-180°C		
Weaver & Broekstra 1984		90-130°C (only 40% I)		200°C	250-280°C	
Merriman & Frey 1999	<100°C		100°C		200°C	300°C
Jaboyedoff & Thelin 1999	<100°C		100-130°C		200-250°C	
Uysal et al. 2000			115-120°			

Table I-1: Approximate temperature ranges derived from mixed layer illite/smectite composition and stacking order (according to different authors, listed in the left column).

I.4 REFERENCES

Aldega, L., Botti, F., and Corrado, S., 2007a, Clay mineral assemblages and vitrinite reflectance in the Laga Basin (Central Appenines, Italy): What do they record? Clays and Clay Minerals, v. 55, p. 504–518, doi:10.1346/CCMN.2007.0550505.

Aldega, L., Corrado, S., Grasso, M., and Maniscalco, R., 2007b, Correlation of Diagenetic Data from Organic and Inorganic Studies in the Apenninic-Maghrebian Fold-and-Thrust Belt: A Case Study from Eastern Sicily: The Journal of Geology, v. 115, p. 335–353, doi:10.1086/512756.

Aldega, L., Corrado, S., Paolo, L. Di, Somma, R., Maniscalco, R., and Balestrieri, M.L., 2011, Shallow burial and exhumation of the Peloritani Mountains (NE Sicily, Italy): Insight from paleothermal and structural indicators: Bulletin of the Geological Society of America, v. 123, p. 132–149, doi:10.1130/B30093.1.

Andreucci, B., 2013, Thermochronology of the Polish and Ukrainian Carpathians: Alma mater Studiorum Università di Bologna, doi:DOI 10.6092/unibo/amsdottorato/5505.

Barnes, M.A., Barnes, W.C., and Bustin, R.M., 1990, Chemistry and diagenesis of organic matter in sediments and fossil fuels: Diagenesis, p. 189–204.

Beny-Bassez, C., and Rouzard, J.N., 1985, Characterization of carbonaceous materials by correlated electron and optical microscopy and Raman microspectroscopy: Scanning Electron Microscopy, v. 1, p. 119–182.

Beyssac, O., Goffe, B., Chopin, C., and Rouzaud, J.N., 2002, Raman spectra of carbonaceous material in metasediments: a new geothermometer: Journal of Metamorphic Geology J Metamorph Geol, v. 20, p. 859–871.

Beyssac, O., Goffé, B., Petitet, J.P., Froigneux, E., Moreau, M., and Rouzaud, J.N., 2003, On the characterization of disordered and heterogeneous carbonaceous materials by Raman spectroscopy: Spectrochimica Acta - Part A: Molecular and Biomolecular Spectroscopy, v. 59, p. 2267–2276, doi:10.1016/S1386-1425(03)00070-2.

Bhandari, N., Bhat, S.G., Lal, D., Rajagopalan, G., Tamhane, A.S., and Venkatavaradan, V.S., 1971, Fission fragment tracks in apatite: recordable track lengths: Earth and Planetary Science Letters, v. 13, p. 191–199.

Borrego, A.G. et al., 2006, Influence of particle and surface quality on the vitrinite reflectance of dispersed organic matter: Comparative exercise using data from the qualifying system for reflectance analysis working group of ICCP: International Journal of Coal Geology, v. 68, p. 151–170, doi:10.1016/j.coal.2006.02.002.

Botti, F., Aldega, L., and Corrado, S., 2007, Sedimentary and tectonic burial evolution of the Northern Apennines in the Modena-Bologna area: constraints from combined stratigraphic, structural, organic matter and clay mineral data of Neogene thrust-top basins: Geodinamica Acta, v. 17, p. 185–203, doi:10.3166/ga.17.185-203.

Braun, J., Van Der Beek, P., and Batt, G., 2006, Quantitative thermochronology: numerical methods for the interpretation of thermochronological data: 1–258 p.

Carrapa, B., 2010, Resolving tectonic problems by dating detrital minerals: Geology, v. 38, p. 191–192, doi:10.1016/j.

Castiglioni, C., Tommasini, M., and Zebri, G., 2004, Raman Spectroscopy of Polyconjugated Molecules and Materials: Confinement Effect in One and Two Dimensions: Philosophical Transactions of the Royal Society of London A: Mathematical, Physical and Engineering Sciences, v. 362, p. 2425–2459.

Chamberlain, K.R., and Bowring, S.A., 2001, Apatite – feldspar U – Pb thermochronometer : a reliable , mid-range (~450 °C), diffusion-controlled system: Chemical Geology, v. 172, p. 173–200.

Corrado, S., Aldega, L., Di Leo, P., Giampaolo, C., Invernizzi, C., Mazzoli, S., and Zattin, M., 2005, Thermal maturity of the axial zone of the southern Apennines fold-and-thrust belt (Italy) from multiple organic and inorganic indicators: Terra Nova, v. 17, p. 56–65, doi:10.1111/j.1365-3121.2004.00584.x.

Crowley, K.D., Naeser, C.W., and Naeser, N.D., 1989, Fission-track Analysis: Theory and Applications: 297 p.

Dahl, P.S., 1997, A crystal-chemical basis for Pb retention and fission-track annealing systematics in U-bearing minerals, with implications for geochronology: Earth and Planetary Science Letters, v. 150, p. 277–290, doi:10.1016/s0012-821x(97)00108-8.

Donelick, R.A., Ketcham, R.A., and Carlson, W.D., 1999, Variability of apatite fission-track annealing kinetics: II. Crystallographic orientation effects: American Mineralogist, v. 84, p. 1224–1234, doi:10.2138/am-1999-0902.

Donelick, R.A., O'Sullivan, P.B., and Ketcham, R.A., 2005, Apatite Fission-Track Analysis:

Reviews in Mineralogy and Geochemistry, v. 58, p. 49–94, doi:10.2138/rmg.2005.58.3.

Dunkl, I., 2002, Trackkey: A windows program for calculation and graphical presentation of fission track data: Computers and Geosciences, v. 28, p. 3–12, doi:10.1016/S0098-3004(01)00024-3.

Durand, B., 1980, Kerogen: Insoluble organic matter from sedimentary rocks: 1–520 p.

Ehlers, T.A., and Farley, K.A., 2003, Apatite (U–Th)/He thermochronometry: methods and applications to problems in tectonic and surface processes: Earth and Planetary Science Letters, v. 206, p. 1–14, http://www.sciencedirect.com/science/article/pii/S0012821X02010695.

Farley, K.A., 2002, (U-Th)/He Dating: Techniques, Calibrations, and Applications: Reviews in Mineralogy and Geochemistry, v. 47, p. 819–844, doi:10.2138/rmg.2002.47.18.

Farley, K.A., 2000, Helium diffusion from apatite: General behavior as illustrated by Durango fluorapatite: Journal of Geophysical Research: Solid Earth, v. 105, p. 2903–2914, doi:10.1029/1999jb900348.

Farley, K.A., Wolf, R.A., and Silver, L.T., 1996, The effects of long alpha-stopping distances on (U-Th)/He ages: Geochimica et Cosmochimica Acta, v. 60, p. 4223–4229, doi:10.1016/S0016-7037(96)00193-7.

Ferrari, A.C., and Robertson, J., 2000, Interpretation of Raman spectra of disordered and amorphous carbon: Physical Review B, v. 61, p. 14095–14107, doi:10.1136/ip.2010.029215.730.

Ferrari, A.C., and Robertson, J., 2004, Raman spectroscopy of amorphous, nanostructured, diamond–like carbon, and nanodiamond: Philosophical Transactions of the Royal Society of London A: Mathematical, Physical and Engineering Sciences, v. 362, p. 2477–2512, doi:10.1038/161375b0.

Ferreiro Mählmann, R., and Le Bayon, R., 2016, Vitrinite and vitrinite like solid bitumen reflectance in thermal maturity studies: Correlations from diagenesis to incipient metamorphism in different geodynamic settings: International Journal of Coal Geology, v. 157, p. 52–73, doi:10.1016/j.coal.2015.12.008.

Fitzgerald, P.G., Baldwin, S.L., Webb, L.E., and O'Sullivan, P.B., 2006, Interpretation of (U-Th)/He single grain ages from slowly cooled crustal terranes: A case study from the Transantarctic Mountains of southern Victoria Land: Chemical Geology, v. 225, p. 91–

120, doi:10.1016/j.chemgeo.2005.09.001.

Fleischer, R.L., Price, P.B., and Walker, R.M., 1975, Nuclear tracks in solids: principles and applications: University of California Press.

Flowers, R.M., Ketcham, R.A., Shuster, D.L., and Farley, K.A., 2009, Apatite (U-Th)/He thermochronometry using a radiation damage accumulation and annealing model: Geochimica et Cosmochimica Acta, v. 73, p. 2347–2365, doi:10.1016/j.gca.2009.01.015.

Friedel, R.A., and Carlson, G.L., 1972, Difficult carbonaceous materials and their infra-red and Raman spectra. Reassignments for coal spectra: Fuel, v. 51, p. 194–198.

Galbraith, R.F., 1981, On statistical models for fission track counts: Journal of the International Association for Mathematical Geology, v. 13, p. 471–478, doi:10.1007/BF01034498.

Gautheron, C., Tassan-Got, L., Barbarand, J., and Pagel, M., 2009, Effect of alpha-damage annealing on apatite (U-Th)/He thermochronology: Chemical Geology, v. 266, p. 157–170, doi:10.1016/j.chemgeo.2009.06.001.

Giampaolo, C., and Lo Mastro, S., 2000, Analisi (semi) quantitativa delle argille mediante diffrazione a raggi x: Incontri Scientifici, v. 2, p. 109–146.

Gleadow, A.J.W., and Duddy, I.R., 1981, A natural long-term track annealing experiment for apatite: Nuclear Tracks, v. 5, p. 169–174.

Gleadow, A.J.W., Duddy, I.R., Green, P.F., and Lovering, J.F., 1986, Confined fission track lengths in apatite: a diagnostic tool for thermal history analysis: Contribution to Mineralogy and Petrology, v. 94, p. 405–415.

Green, P.F., Crowhurst, P. V., Duddy, I.R., Japsen, P., and Holford, S.P., 2006, Conflicting (U-Th)/He and fission track ages in apatite: Enhanced He retention, not anomalous annealing behaviour: Earth and Planetary Science Letters, v. 250, p. 407–427, doi:10.1016/j.epsl.2006.08.022.

Green, P.F., and Duddy, I.R., 2006, Interpretation of apatite (U-Th)/He ages and fission track ages from cratons: Earth and Planetary Science Letters, v. 244, p. 541–547, doi:10.1016/j.epsl.2006.02.024.

Green, P.F., Duddy, I.R., Gleadow, A.J.W., Tingate, P.R., and Laslett, G.M., 1985, Fission-track annealing in apatite: track length measurements and the form of the Arrhenius plot: Nuclear Tracks and Radiation Measurements, v. 10, p. 323–328.

Green, P.F., Duddy, I.R., Laslett, G.M., Hegarty, K.A., Gleadow, A.J.W., and Lovering, J.F., 1989, Thermal annealing of fission tracks in apatite 4. Quantitative modelling techniques and extension to geological timescales: Chemical Geology, v. 79, p. 155–182.

Heise, H.M., Kuckuk, R., Ojha, A.K., Srivastava, A., Srivastava, V., and Asthana, B.P., 2009, Characterisation of carbonaceous materials using Raman spectroscopy: A comparison of carbon nanotube filters, single- And multi-walled nanotubes, graphitised porous carbon and graphite: Journal of Raman Spectroscopy, v. 40, p. 344–353, doi:10.1002/jrs.2120.

Henrichs, S.M., 1993, Early diagenesis of organic matter: the dynamics (rates) of cycling of organic compounds: Organic Geochemistry, p. 101–117.

Hoffman, J., and Hower, J., 1979, Clay mineral assemblages as low grade metamorphic geothermometers: application to the thrust faulted disturbed belt of Montana: The Society of Economic Plaeontologists and Mineralogists, v. 26, p. 55–79.

Hunt, J.M., Philp, R.P., and Kvenvolden, K.A., 2002, Early developments in petroleum geochemistry: Organic Geochemistry, v. 33, p. 1025–1052, doi:10.1016/S0146-6380(02)00056-6.

Hurford, A.J., 2019, An Historical Perspective on Fission-Track Thermochronology, *in* Malusà, M.G. and Fitzgerald, P.G. eds., Fission-Track Thermochronology and its Application to Geology, Springer Berlin Heidelberg, p. 3–23, doi:10.1007/978-3-319-89421-8_1.

Hurford, A.J., 1990, Standardization of fission track dating calibration: Recommendation by the Fission Track Working Group of the I.U.G.S. Subcommission on Geochronology: Chemical Geology, v. 80, p. 171–178.

Hurford, A.J., and Green, P.F., 1982, A users' guide to fission track dating calibration: Earth and Planetary Science Letters, v. 59, p. 343–354.

Hurford, A.J., and Green, P.F., 1983, The zeta age calibration of fission-track dating: Chemical Geology, v. 1, p. 285–317.

Jaboyedoff, M., Kübler, B., and Thélin, P., 1999, An empirical Scherrer equation for weakly swelling mixed-layer minerals, especially illite-smectite: Clay Minerals, v. 34, p. 601–

617, doi:10.1180/000985599546479.

Jagodzinski, H., 1949, Eindimensionale Fehlordnung in Kristallen und ihr Einfluss auf die Röntgeninterferenzen. I. Berechnung des Fehlordnungsgrades aus den Röntgenintensitäten: Acta Crystallographica, v. 2, p. 201–207.

Jennings, S., and Thompson, G.R., 1986, Diagenesis of Plio-Pleistocene Sediments of the Colorado River Delta, Southern California: Journal of Sedimentary Petrology, v. 56, p. 89–98, doi:10.1306/212f8891-2b24-11d7-8648000102c1865d.

Ketcham, R.A., 2005, Forward and inverse modeling of low-temperature thermochronometry data: Reviews in Mineralogy and Geochemistry, v. 58, p. 275–314, doi:10.2138/rmg.2005.58.11.

Ketcham, R.A., 2009, HeFTy version 1.6.7 Manual:

Ketcham, R.A., Carter, A., Donelick, R.A., Barbarand, J., and Hurford, A.J., 2007, Improved modeling of fission-track annealing in apatite: American Mineralogist, v. 92, p. 799–810, doi:10.2138/am.2007.2281.

Ketcham, R.A., Donelick, R.A., and Carlson, W.D., 1999, Variability of apatite fission-track annealing kinetics: III. Extrapolation to geological time scales: American Mineralogist, v. 84, p. 1235–1255, doi:Doi 10.2138/Am.2006.464.

Kohn, B., Chung, L., and Gleadow, A., 2019, Fission-Track Analysis: Filed Collection, Sample Preparation and Data Acquisition, *in* Malusà, M.G. and Fitzgerald, P.G. eds., Fission-Track Thermochronology and its Application to Geology, Springer International Publishing, p. 25–48, doi:10.1007/978-3-319-89421-8_3.

Lahfid, A., Beyssac, O., Deville, E., Negro, F., Chopin, C., and Goffé, B., 2010, Evolution of the Raman spectrum of carbonaceous material in low-grade metasediments of the Glarus Alps (Switzerland): Terra Nova, v. 22, p. 354–360, doi:10.1111/j.1365-3121.2010.00956.x.

Langford, F.F., and Blanc-Velleron, M.M., 1990, Interpreting Rock-Eval Pyrolysis data using graphs of pyrolizable hydrocarbons vs Total Organic Carbon: The American Association of Petrolrum Geologists Bullettin, v. 74, p. 799–804.

Lanson, B., 1997, Decomposition of experimental x-ray diffraction patterns (profile fitting): A convenient way to study clay minerals: Clays and Clay Minerals, v. 45, p. 132–146, doi:10.1346/CCMN.1997.0450202.

Levine, J.R., and Davis, A., 1989, Reflectance anisotropy of Upper Carboniferous coals in the Appalachian foreland basin, Pennsylvania, USA: International Journal of Coal Geology, v. 13, p. 341–373.

Li, C.Z., 2007, Some recent advances in the understanding of the pyrolysis and gasification behaviour of Victorian brown coal: Fuel, v. 86, p. 1664–1683, doi:10.1016/j.fuel.2007.01.008.

Li, X., Hayashi, J. ichiro, and Li, C.Z., 2006, FT-Raman spectroscopic study of the evolution of char structure during the pyrolysis of a Victorian brown coal: Fuel, v. 85, p. 1700–1707, doi:10.1016/j.fuel.2006.03.008.

Lisker, F., Ventura, B., and Glasmacher, U.A., 2009, Apatite thermochronology in modern geology, *in* Lisker, F., Ventura, B., and Glasmacher, U.A. eds., Thermochronological Methods, Geological Society of London, Special Publications 324, v. 324, p. 1–23, doi:10.1144/SP324.1.

Malusà, M.G., and Garzanti, E., 2019, The Sedimentology of Detrital Thermochronology, *in* Malusà, M.G. and Fitzgerald, P.G. eds., Fission-Track Thermochronology and its Application to Geology, Springer, Cham, p. 123–143, doi:https://doi.org/10.1007/978-3-319-89421-8_7.

McDannell, K.T., Issler, D.R., and O’Sullivan, P.B., 2019, Radiation-enhanced fission track annealing revisited and consequences for apatite thermochronometry: Geochimica et Cosmochimica Acta, v. 252, p. 213–239, doi:10.1016/j.gca.2019.03.006.

Merryman, R.J., and Frey, M., 1999, Patterns of very low-grade metamorphism in metapelitic rocks, *in* Low-grade metamorphism, Blackwell Scientific Publications, Oxford, International, p. 61–107.

Mezger, K., and Krogstad, E.J., 1997, Interpretation of discordant U-Pb zircon ages: An evaluation: Journal of Metamorphic Geology, v. 15, p. 127–140, doi:10.1111/j.1525-1314.1997.00008.x.

Moore, D.M., and Reynolds, R.C.J., 1997, X-Ray Diffraction and the Identification and Analysis of Clay Minerals: Oxford Univ Press, 392 p., doi:10.1180/claymin.1999.034.1.21.

Nemanich, R., and Solin, S., 1979, First-and second-order Raman scattering from finite-size crystals of graphite: Physical Review B, v. 2, p. 392.

Nestler, K., Dietrich, D., Witke, K., Rößler, R., and Marx, G., 2003, Thermogravimetric and Raman spectroscopic investigations on different coals in comparison to dispersed anthracite found in permineralized tree fern Psaronius sp.: Journal of Molecular Structure, v. 661–662, p. 357–362, doi:10.1016/j.molstruc.2003.09.020.

Oberlin, A., Boulmier, J., and Villey, M., 1980, Electron microscopy study of kerogen microtexture: Selected criteria for determining the evolution path and evolution stage of kerogen, *in* Kerogen: Insoluble organic matter from sedimentary rocks, p. 191–241.

Di Paolo, L., Aldega, L., Corrado, S., and Mastalerz, M., 2012, Maximum burial and unroofing of Mt. Judica recess area in Sicily: ®mplication for the Apenninic-Maghrebian wedge dynamics: Tectonophysics, v. 530–531, p. 193–207, doi:10.1016/j.tecto.2011.12.020.

Peyton, S.L., and Carrapa, B., 2013, An introduction to low-temperature thermochronologic techniques, methodology, and applications, *in* Knight, C. and Cuzella, J. eds., Application of structural methods to Rocky Mountain hydrocarbon exploration and development: AAPG Studies in Geology 65, p. 15–36, doi:10.1306/13381688St653578.

Pócsik, I., Hundhausen, M., Koós, M., and Ley, L., 1998, Origin of the D peak in the Raman spectrum of microcrystalline graphite: Journal of Non-Crystalline Solids, v. 227–230, p. 1083–1086, doi:10.1016/S0022-3093(98)00349-4.

Pollastro, R.M., 1993, Considerations and applications of the illite/smectite geothermometer in hydrocarbon-bearing rocks of miocene to Mississippian age: Clays and Clay Minerals, v. 41, p. 119–133, doi:10.1346/CCMN.1993.0410202.

Pollastro, R.M., 1990, The illite/smectite geothermometer - concepts, methodology, and application to basin history and hydrocarbon generation, *in* Nuccio Vito, F., Barker Charles, E., and Dyson Sally, J. eds., Applications of thermal maturity studies to energy exploration., Denver, CO, United States, Eastwood Print. and Publ., p. 1–18.

Potgieter-Vermaak, S., Maledi, N., Wagner, N., Van Heerden, J.H.P., Van Grieken, R., and Potgieter, J.H., 2011, Raman spectroscopy for the analysis of coal: A review: Journal of Raman Spectroscopy, v. 42, p. 123–129, doi:10.1002/jrs.2636.

Purdy, J.W., and Jager, E., 1976, K-Ar ages on rock-forming minerals from the central Alps: Memoirs of the Institute of Geology and Mineralogy, University of Padova, v. 30, p. 3–31.

Rebelo, S.L.H., Guedes, A., Szefczyk, M.E., Pereira, A.M., Araújo, J.P., and Freire, C., 2016, Progress in the Raman spectra analysis of covalently functionalized multiwalled carbon nanotubes: Unraveling disorder in graphitic materials: Physical Chemistry Chemical Physics, v. 18, p. 12784–12796, doi:10.1039/c5cp06519d.

Reiners, P.W., 2007, Thermochronologic Approaches to Paleotopography: Reviews in Mineralogy and Geochemistry, v. 66, p. 243–267, doi:10.2138/rmg.2007.66.10.

Reiners, P.W., 2005, Zircon (U-Th)/He thermochronometry: Reviews in Mineralogy and Geochemistry, v. 58, p. 151–179, doi:10.2138/rmg.2005.58.6.

Reiners, P.W., and Brandon, M.T., 2006, Using Thermochronology To Understand Orogenic Erosion: Annual Review of Earth and Planetary Sciences, v. 34, p. 419–466, doi:10.1146/annurev.earth.34.031405.125202.

Reiners, P.W., Spell, T.L., Nicolescu, S., and Zanetti, K.A., 2004, Zircon (U-Th)/He thermochronometry: He diffusion and comparisons with 40Ar/39Ar dating: Geochimica et Cosmochimica Acta, v. 68, p. 1857–1887, doi:10.1016/j.gca.2003.10.021.

Robl, T.L., and Davis, B.H., 1993, Comparison of the HF-HCl and HF-BF3 maceration techniques and the chemistry of resultant organic concentrates: Organic Geochemistry, v. 20, p. 249–255.

Sadezky, A., Muckenhuber, H., Grothe, H., Niessner, R., and Pöschl, U., 2005, Raman microspectroscopy of soot and related carbonaceous materials: Spectral analysis and structural information: Carbon, v. 43, p. 1731–1742, doi:10.1016/j.carbon.2005.02.018.

Schimmelmann, A., Lewan, M.D., and Wintsch, R.P., 1999, D/H isotope ratios of kerogen, bitumen, oil, and water in hydrous pyrolysis of source rocks containing kerogen types I, II, IIS, and III: Geochimica et Cosmochimica Acta, v. 63, p. 3751–3766, doi:10.1016/0002-9343(80)90516-1.

Schito, A., Spina, A., Corrado, S., Cirilli, S., and Romano, C., 2019, Comparing optical and Raman spectroscopic investigations of phytoclasts and sporomorphs for thermal maturity assessment: the case study of Hettangian continental facies in the Holy cross Mts. (central Poland): Marine and Petroleum Geology, v. 104, p. 331–345, doi:10.1016/j.marpetgeo.2019.03.008.

Scotti, P., 2003, Thermal constraints from the organic matter: Atti Ticinesi di Scienze della Terra, v. 9, p. 23–32.

Tagami, T., and O' Sullivan, P., 2005, Fundamentals of Fission-Track Thermochronology: Reviews in Mineralogy and Geochemistry, v. 58, p. 19–47, doi:10.2138/rmg.2005.58.2.

Taylor, G.H., Teichmuller, M., Davis, A., Diessel, C.F.K., Littke, R., Robert, P., Glick, D.C., Smyth, M., Swaine, D.J., and Vanderbroucke, M., 1998, Organic petrology: A new handbook incorporating some revised parts of Stach's textbook of coal petrology: Gebruder Borntraeger Verlagsbuchhandlung, 1–720 p.

Teichmuller, M., 1986, Organic petrology of source rocks, history and state of the art: Organic Geochemistry, v. 10, p. 581–599.

Tuinstra, F., and Koenig, J.L., 1970, Raman spectrum of graphite: The Journal of Chemcal Physics, v. 53, p. 1280–1281.

Tyson, R. V., 2012, Sedimentary organic matter: organic facies and palynofacies:

Vandenbroucke, M., 2003, Kerogen: From types to models of chemical structure: Oil and Gas Science and Technology, v. 58, p. 243–269, doi:10.2516/ogst:2003016.

Walters, C.C., 2007, The Origin of Petroleum, *in* Practical Advances in Petroleum Processing, p. 79–101, doi:10.1007/978-0-387-25789-1.

Warr, L.N., and Rice, A.H.N., 1994, Interlaboratory standardization and calibration of day mineral crystallinity and crystallite size data: Journal of Metamamorphic Geology, v. 12, p. 141–152.

Zattin, M., 2003, Apatite Fission-Track Analysis and the Thermochronology of Sedimentary Successions: Atti Ticinesi di Scienze della Terra, v. 9, p. 33–42.

Zattin, M., Stefani, C., and Martin, S., 2003, Detrital Fission-Track Analysis and Sedimentary Petrofacies as Keys of Alpine Exhumation: The Example of the Venetian Foreland (European Southern Alps, Italy): Journal of Sedimentary Research, v. 73, p. 1051–1061, doi:10.1306/051403731051.

Zaun, P.E., and Wagner, G.A., 1985, No TitleFission-track stability in zircons under geological conditions: Nuclear tracks and radiation measurements: Nuclear Tracks and Radiation Measurements, v. 10, p. 303–307.

APPENDIX II

THERMOCHRONOLOGICAL ANALYSES

Within this appendix, all the analytical details of the low-temperature thermochronological analyses performed during the course of my Ph.D. project will be presented, with particular reference to the ones that are not reported elsewhere in this dissertation. Forty-one rock samples were collected during fieldwork and sampling in Georgia in September-October 2018 (Fig. II-1; Table II-1), and they were processed following standard procedures in order to separate apatite and zircon grains from the other minerals (see details in Appendix I). Among the total number of collected samples, only the ones which contained enough apatite grains, or apatite grains of sufficient quality, for fission-track and/or (U-Th)/He analysis were selected at the end of the processing procedures. Only samples from the southern central Greater Caucasus were selected for zircon (U-Th)/He analyses, since they experienced paleotemperatures high enough to reset the ZHe system (Corrado et al., 2021). In Table II-1 are reported the details of all the samples collected, and the analytical details of the AFT results. In Tables II-2 and II-3 are reported the analytical details of the (U-Th)/He analyses performed on apatites and zircons, respectively, within the framework of my Ph.D. project.

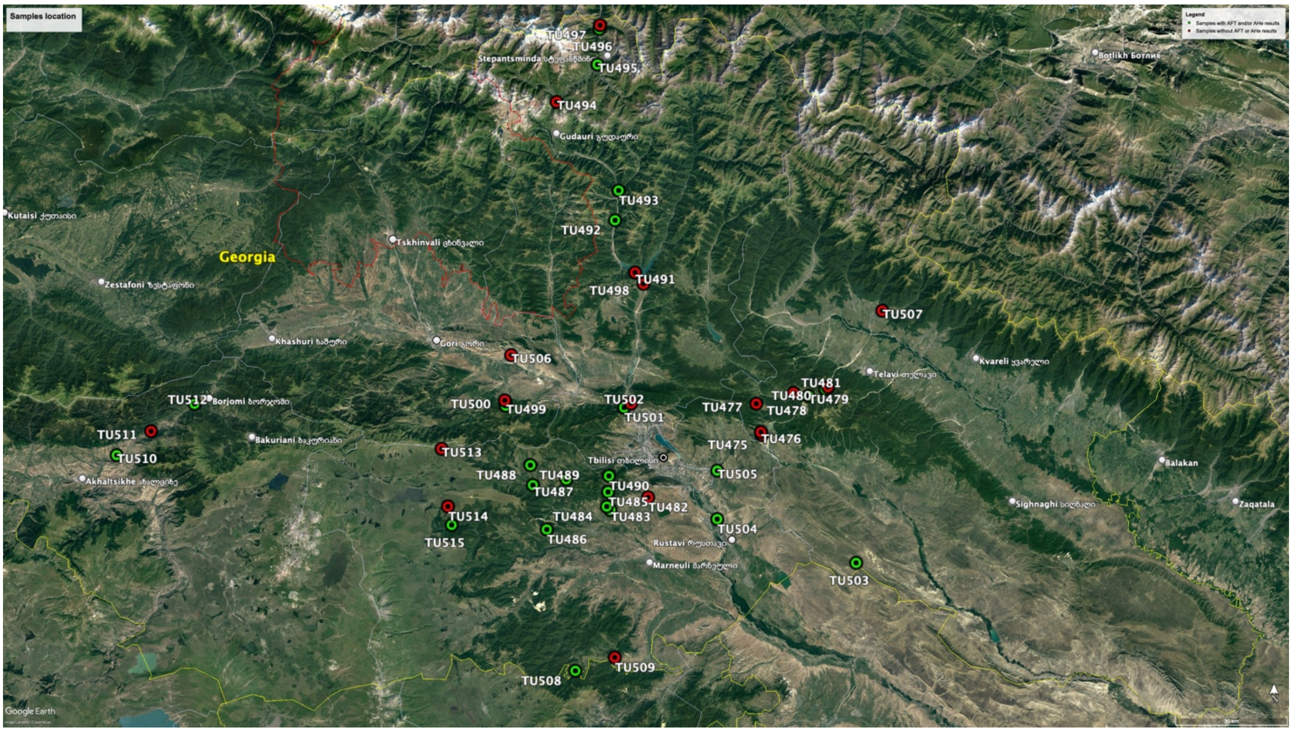

Figure II-1: Satellite map showing location of the forty-one samples collected for thermochronological analyses within the framework of my Ph.D. project. Green circles represent samples which yielded AFT and/or AHe results, whereas red circles represent samples which did not provide any AFT or AHe result (Google, 2022).

Figure II-2 shows the radial plots of single-grain ages, resulting from AFT analyses, obtained within my Ph.D. project but which are not reported elsewhere in this Dissertation.

Figures II-3 to II-7 show the radial plots of AFT single-grain ages, the frequency histogram of the confined fission-track lengths, and the statistical inverse modelling results for the samples analysed along the southern slope of the central Greater Caucasus and in the eastern Adjara-Trialeti FTB, providing additional details to the same results reported schematically in Figure 5.5 of Chapter 5.

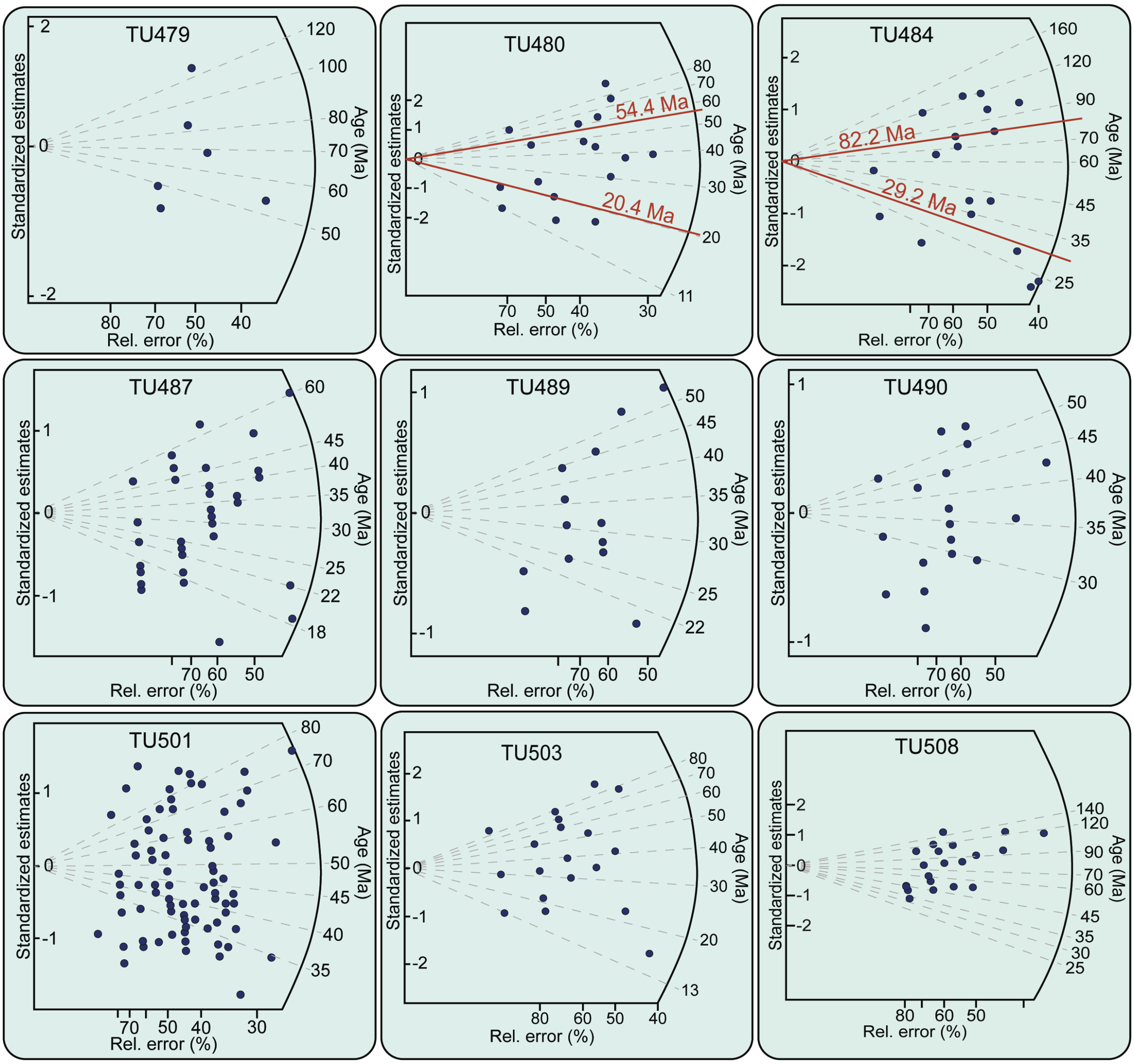

Figure II-1: Radial plots resulting from apatite fission-track analyses, obtained within the framework of this study and not reported elsewhere, showing the distribution of individual grain ages on the right y axis and the relative percentage error on the x axis. Samples TU480 and TU484 contain two population of grains, identified by the red lines which report the relative mean ages as resulting from analysis with the Binomfit software (Brandon, 1992). See Table II-1 for samples details.

Finally, Figures II-8 and II-9 show the radial plots of AFT single-grain ages, the frequency histograms of the confined fission-track lengths, and the statistical inverse modelling results for two samples (TU508 and TU284) which are not reported elsewhere in this Dissertation. Sample TU508 is a Jurassic granitoid collected in the retro-wedge if the Lesser Caucasus, and its statistical inverse modelling show initial slow cooling since Paleocene-Early Eocene times and a possible acceleration of cooling/exhumation during the Middle Miocene (see best-fit line), resembling the modelling results from sample TU515 (Chapter 5). Sample TU284 is an Early-Middle Paleozoic gneiss sample from the Loki Massif originally reported by Albino et al. (2014), which have been further enriched in order to obtain enough confided track lengths for modelling. Statistical inverse modelling results from this sample show a two-phase cooling history, characterised by a first increment of cooling/exhumation

Table II-1: Analytical details of all apatite fission-track analyses.

Sample	Rock Type	Age	Region	Notes	Elevation (m)	UTM Coordinates	No. crystals	Spontaneous		Induced		$P(\chi)^2$	Dosimeter		Age (Ma) ± 1s	Mean confined track length (mm) ± standard error	Standard deviation	No. tracks measured	D-par
								ρ_s	N_s	ρ_i	N_i		ρ_d	N_d					
TU475	Sandstone	late Early Miocene	Georgia	Kakheti-Gombori Ridge	817	38N 0512536 4624356	-	-	-	-	-	-	-	-	-	-	-	-	-
TU476	Sandstone	Middle-Late Miocene	Georgia	Kakheti-Gombori Ridge	851	38N 0512307 4625099	-	-	-	-	-	-	-	-	-	-	-	-	-
TU477	Granitoid clasts	Paleozoic? (in Late Sarmatian conglomerate)	Georgia	Kakheti-Gombori Ridge	869	38N 0511072 4632508	-	-	-	-	-	-	-	-	-	-	-	-	-
TU478	Sandstone	Oligocene-Early Miocene	Georgia	Kakheti-Gombori Ridge	1321	38N 0520846 4635330	-	-	-	-	-	-	-	-	-	-	-	-	-
TU479	Sandstone	Maastrichtian	Georgia	Kakheti-Gombori Ridge	1468	38N 0524721 4634599	6	0,001	33	0,01	122	66,71	14,42	7457	66.9 ± 13.6	-	-	-	-
TU480	Sandstone	Late Eocene-Oligocene	Georgia	Kakheti-Gombori Ridge	1015	38N 0529177 4636408	17	0,40	129	2,11	683	0,14	12,36	7729	40.2 ± 6.1	-	-	-	-
TU481	Sandstone	Oligocene-Early Miocene	Georgia	Kakheti-Gombori Ridge	999	38N 0529855 4636895	-	-	-	-	-	-	-	-	-	-	-	-	-
TU482	Tuffitic Sandstone	Middle Eocene	Georgia	Eastern Adjara-Trialeti FTB	608	38N 0482826 4608005	-	-	-	-	-	-	-	-	-	-	-	-	-
TU483	Sandstone	Middle-Late Oligocene	Georgia	Eastern Adjara-Trialeti FTB	684	38N 0473006 4604652	42	0,18	222	0,71	871	94,18	14,50	7498	63.4 ± 5.8	14.10 ± 0.22	1.59	50	2.91
TU484	Granitoid clasts	Mesozoic? (in Late Eocene conglomerate)	Georgia	Eastern Adjara-Trialeti FTB	754	38N 0472044 4605562	20	0,25	90	1,21	426	2,89	12,29	7683	62.6 ± 6.3	-	-	-	-
TU485	Sandstone	Early Eocene	Georgia	Eastern Adjara-Trialeti FTB	889	38N 0472357 4609370	-	-	-	-	-	-	-	-	-	-	-	-	-
TU486	Sandstone	latest Paleocene-Early Eocene	Georgia	Eastern Adjara-Trialeti FTB	883	38N 0456357 4599540	49	0,14	290	0,81	1691	99,68	12,22	7638	34.7 ± 2.8	12.05 ± 0.22	1.66	53	2.38
TU487	Sandstone	early Late Eocene	Georgia	Eastern Adjara-Trialeti FTB	932	38N 0452684 4611098	38	0,10	107	0,69	725	99,56	12,15	7593	29.3 ± 3.4	-	-	4	-
TU488	Sandstone	Late Oligocene	Georgia	Eastern Adjara-Trialeti FTB	1391	38N 0452009 4616299	41	0,14	192	1,05	1393	99,44	12,07	7547	27.3 ± 2.5	12.48 ± 0.31	2.26	53	2.36
TU489	Sandstone	Late Eocene	Georgia	Eastern Adjara-Trialeti FTB	1291	38N 0461429 4612640	13	0,09	36	0,53	224	97,2	12,00	7502	31.9 ± 5.9	-	-	1	-
TU490	Sandstone	Late Eocene	Georgia	Eastern Adjara-Trialeti FTB	1322	38N 0472584 4613551	18	0,14	55	0,58	231	99,97	9,73	5046	35.5 ± 5.6	-	-	6	-
TU491	Granitoid	Late Eocene	Georgia	Central Greater Caucasus	772	38N 0479248 4666600	-	-	-	-	-	-	-	-	-	-	-	-	-
TU492	Sandstone	Cenomanian	Georgia	Central Greater Caucasus	922	38N 0473963 4680238	29	0,12	75	0,61	371	86,52	11,93	7457	36.8 ± 5.0	13.45 ± 0.20	1.54	62	2.86
TU493	Sandstone	Aptian-Albian	Georgia	Central Greater Caucasus	1057	38N 0474870 4688016	-												-
TU494	Sandstone	Late Jurassic (Oxfordian-Tithonian)	Georgia	Central Greater Caucasus	2021	38N 0458552 4711144	-	-	-	-	-	-	-	-	-	-	-	-	-
TU495	Sandstone	Early Jurassic (Toarcian-Aalenian)	Georgia	Central Greater Caucasus	1754	38N 0469216 4720975	24	0.67	41	27.97	1696	100.00	11,86	7411	4.8 ± 0.8	15.04 ± 0.13	1.20	85	2.61
TU496	Gneiss	late Carboniferous	Georgia	Central Greater Caucasus	1320	38N 0469676 4730334	20	0.61	39	24.26	1563	100.00	9,65	5010	4.1 ± 0.7	15.19 ± 0.09	0.92	97	2.13
TU497	Gneiss	late Carboniferous	Georgia	Central Greater Caucasus	1311	38N 0469864 4731299	-	-	-	-	-	-	-	-	-	-	-	-	-
TU498	Sandstone	Late Eocene	Georgia	Central Greater Caucasus	756	38N 0481455 4663670	-	-	-	-	-	-	-	-	-	-	-	-	-
TU499	Sandstone	Early Eocene	Georgia	Eastern Adjara-Trialeti FTB	1338	38N 0445544 4631754	-	-	-	-	-	-	-	-	-	-	-	-	-
TU500	Sandstone	Late Cretaceous (Maastrichtian)	Georgia	Eastern Adjara-Trialeti FTB	1124	38N 0445282 4633129	-	-	-	-	-	-	-	-	-	-	-	-	-
TU501	Sandstone	Middle Eocene	Georgia	Eastern Adjara-Trialeti FTB	561	38N 0476497 4631400	88	0,16	574	0,64	2320	99,35	11,78	7366	45.3 ± 3.1	-	-	-	-
TU502	Sandstone	Early Miocene (Aquitanian)	Georgia	Kartli Basin	555	38N 0478316 4632430	-	-	-	-	-	-	-	-	-	-	-	-	-
TU503	Sandstone	Oligocene-Early Miocene	Georgia	Kura Basin	643	38N 0537395 4591009	19	0,14	61	0,77	325	44,79	11,71	7321	35.6 ± 5.6	-	-	-	-
TU504	Sandstone	Burdigalian (Sakaraulian; Early Miocene)	Georgia	Kura Basin	396	38N 0500933 4602375	61	0,15	333	0,81	1770	99,98	11,64	7276	36.3 ± 2.8	13.34 ± 0.17	1.57	83	2.75
TU505	Sandstone	middle-late Oligocene	Georgia	Eastern Adjara-Trialeti FTB	512	38N 0500906 4615010	48	0,24	270	1,17	1307	97,99	11,57	7230	39.6 ± 3.3	13.41 ± 0.18	1.47	67	2.31
TU506	Sandstone	Early Miocene	Georgia	Kartli Basin	603	38N 0446892 4644975	-	-	-	-	-	-	-	-	-	-	-	-	-
TU507	Sandstone	Late Jurassic (Oxfordian-Tithonian)	Georgia	South-eastern Greater Caucasus	486	38N 0544064 4656874	-	-	-	-	-	-	-	-	-	-	-	-	-
TU508	Granitoid	Middle Jurassic	Georgia	Lesser Caucasus	1004	38N 0463940 4562655	28	0,23	116	0,55	278	98,8	11,50	7185	79.2 ± 9.6	13.20 ± 0.25	1.76	51	2.23
TU509	Andesite/Dacite	Middle Jurassic (Callovian)	Georgia	Lesser Caucasus	858	38N 0474254 4566173	-	-	-	-	-	-	-	-	-	-	-	-	-
TU510	Sandstone	Late Eocene	Georgia	Central Adjara-Trialeti FTB	1022	38N 0343226 4618483	56	0,28	361	1,14	1473	99,8	11,42	7140	46.0 ± 3.5	13.03 ± 0.30	2.29	58	2.50
TU511	Sandstone	Middle Eocene	Georgia	Central Adjara-Trialeti FTB	905	38N 0352309 4624800	-	-	-	-	-	-	-	-	-	-	-	-	-
TU512	Sandstone	Late Paleocene-Early Eocene	Georgia	Central Adjara-Trialeti FTB	833	38N 0363775 4631968	-	-	-	-	-	-	-	-	-	-	-	-	-
TU513	Sandstone	Late Paleocene-Early Eocene	Georgia	Eastern Adjara-Trialeti FTB	1824	38N 0428773 4620487	-	-	-	-	-	-	-	-	-	-	-	-	-
TU514	Porphyritic Granitoid	Late Paleozoic (Variscan)	Georgia	Khrami Massif	1607	38N 0430457 4605450	-	-	-	-	-	-	-	-	-	-	-	-	-
TU515	Gneiss-diorite	Precambrian-Early Paleozoic	Georgia	Khrami Massif	985	38N 0431453 4600622	21	0,55	288	2,37	1242	37,65	11,35	7094	43.6 ± 3.7	13.72 ± 0.21	1.69	65	2.12

Table II-2: Analytical details of all apatite (U-Th)/He analyses.

Sample Name	Raw age (Ma)	Raw 1s error (Ma)	FT	Corrected age (Ma)	Corrected 1s error (Ma)	Mean age (Ma)	Mean error (Ma)	Th/U	U238 (ppm)	U235 (ppm)	Th232 (ppm)	Sm147 (ppm)	eU (ppm)	Rs (µm)
TU 479-1	89,48	5,33	0,74	121,08	7,21	45,3	1,8	0,45	33,44	0,25	15,20	92,87	37,02	60,00
TU 479-2	6,83	0,10	0,69	9,91	0,15			3,05	10,32	0,08	31,47	19,13	17,71	46,46
TU 479-3	30,33	0,35	0,70	43,64	0,50			3,61	20,60	0,16	74,31	55,68	38,06	48,92
TU 479-4	19,65	0,24	0,61	32,11	0,40			4,11	25,94	0,21	106,72	53,83	51,02	43,26
TU 479-5	12,45	0,39	0,62	19,95	0,63			6,54	3,61	0,06	23,62	1,11	9,16	40,26
TU 485-1	3,54	0,04	0,66	5,37	0,05	5,4	0,1	8,06	8,68	0,07	69,94	39,25	25,12	44,75
TU 485-2	2,29	0,03	0,64	3,58	0,04			4,12	19,87	0,16	81,87	35,89	39,11	42,33
TU 485-3	1,61	0,02	0,62	2,58	0,03			8,60	33,50	0,27	288,22	81,36	101,24	38,51
TU 485-4	5,34	0,06	0,65	8,24	0,09			3,43	14,72	0,12	50,43	16,33	26,58	42,55
TU 485-5	4,75	0,05	0,65	7,26	0,08			6,58	9,38	0,09	61,75	43,71	23,90	46,95
TU 486-1	3,93	0,12	0,66	5,93	0,18	10,1	0,2	2,35	10,16	0,09	23,87	24,08	15,77	46,88
TU 486-2	6,23	0,14	0,65	9,58	0,22			7,83	2,00	-1,27	15,63	0,91	5,67	42,10
TU 486-3	12,68	0,12	0,73	17,32	0,16			2,40	10,10	0,08	24,19	10,84	15,78	55,53
TU 486-4	9,22	0,13	0,68	13,62	0,20			3,96	10,16	0,09	40,19	19,82	19,60	47,58
TU 486-5	2,67	0,04	0,66	4,08	0,06			6,18	10,62	0,09	65,57	43,20	26,03	41,83
TU 487-1	6,72	0,39	0,62	10,81	0,63	7,5	0,2	5,77	6,91	0,08	39,88	29,50	16,28	38,85
TU 487-2	3,82	0,04	0,66	5,80	0,06			4,56	17,46	0,14	79,57	75,61	36,16	45,53
TU 487-3	4,33	0,10	0,59	7,31	0,18			4,07	9,20	0,10	37,49	16,87	18,01	36,91
TU 487-4	2,98	0,07	0,59	5,10	0,13			3,98	16,15	0,15	64,32	54,44	31,27	35,21
TU 487-5	5,73	0,07	0,68	8,41	0,10			3,34	16,19	0,13	54,02	42,30	28,88	96,94
TU 491 -1	8,65	0,14	0,69	13,66	0,23	10,1	0,2	3,89	37,08		140,68	718,09	70,14	39,87
TU 491 -2	6,66	0,11	0,73	9,72	0,17			1,60	85,54		133,10	673,11	116,82	46,19
TU 491 -3	4,15	0,18	0,65	6,97	0,31			2,92	21,99		62,51	449,09	36,68	35,24
TU 492 -1	4,74	0,49	0,68	7,58	0,78	8,0	0,6	4,93	5,23		25,13	198,65	11,13	38,96
TU 492 -2	5,10	0,25	0,75	7,23	0,36			5,90	6,16		35,42	189,89	14,48	51,52
TU 492 -3	4,94	0,27	0,61	9,22	0,53			6,70	13,19		86,17	353,23	33,44	30,83
TU 493 -2	4,28	0,11	0,70	6,47	0,17	6,6	0,2	0,97	18,71		17,75	123,09	22,88	42,18
TU 493 -3	5,93	0,12	0,71	9,02	0,18			2,47	13,90		33,53	101,85	21,78	42,63
TU 493 -4	4,31	0,12	0,71	6,38	0,18			0,24	28,46		6,66	116,43	30,02	43,34
TU 493 -5	3,05	0,07	0,70	4,66	0,10			2,03	33,75		66,92	401,64	49,47	42,05
TU 496 -2	2,12	0,04	0,71	3,19	0,06	3,0	0,1	1,24	44,30		53,39	295,89	56,85	42,93
TU 496 -3	2,87	0,05	0,75	4,05	0,07			1,39	20,51		27,70	201,34	27,02	50,20
TU 496 -4	2,08	0,04	0,76	2,87	0,05			1,10	23,20		24,83	198,45	29,04	53,60
TU 496 -5	1,36	0,02	0,78	1,82	0,02			2,05	67,49		134,62	442,35	99,12	58,43
TU 499-2	5,47	0,15	0,62	8,85	0,24	9,5	0,2	5,83	3,46	0,10	20,17	1,28	8,20	37,87
TU 499-3	5,57	0,13	0,55	10,18	0,24			5,96	6,77	0,15	40,35	11,07	16,25	32,19
TU 501-1	4,17	0,04	0,71	5,89	0,06	7,4	0,1	3,82	11,67	0,09	44,51	44,45	22,13	53,27
TU 501-2	6,18	0,10	0,62	9,95	0,16			4,71	8,63	0,08	40,63	29,07	18,17	39,50
TU 501-3	5,84	0,07	0,67	8,74	0,10			5,35	12,88	0,11	68,94	27,90	29,08	44,97
TU 501-4	4,14	0,12	0,60	6,86	0,20			4,67	7,30	0,09	34,11	26,01	15,32	37,75
TU 501-5	3,33	0,05	0,61	5,46	0,07			5,14	11,41	0,11	58,72	32,88	25,21	38,48
TU 508 -1	15,95	0,20	0,70	24,45	0,31	18,4	0,3	2,62	8,81		22,48	414,86	14,09	41,06
TU 508 -2	6,94	0,14	0,70	10,40	0,22			1,14	10,99		12,25	332,19	13,87	42,41
TU 508 -3	14,16	0,18	0,70	21,58	0,28			2,14	8,00		16,69	383,86	11,93	41,26
TU 508 -4	12,66	0,15	0,77	17,18	0,21			2,57	7,25		18,15	393,15	11,52	55,60
TU 508 -5	12,14	0,16	0,71	18,30	0,24			2,10	11,42		23,40	432,01	16,92	42,49
TU 510 -1	8,71	0,23	0,74	12,43	0,34	23,2	0,4	2,16	5,81		12,23	122,75	8,68	48,92
TU 510 -2	13,42	0,16	0,68	21,62	0,26			3,46	14,51		49,02	237,45	26,03	38,24
TU 510 -3	12,47	0,17	0,71	19,11	0,26			7,63	6,71		49,90	270,53	18,44	43,15
TU 510 -4	19,79	0,33	0,70	30,30	0,51			1,57	7,70		11,81	184,84	10,48	40,98
TU 510 -5	21,87	0,27	0,72	32,62	0,41			3,11	8,37		25,40	104,22	14,34	44,70
TU 512-1	8,37	0,11	0,71	11,73	0,16	7,7	0,1	3,24	5,86	0,05	18,99	16,72	10,32	53,21
TU 512-2	2,57	0,06	0,59	4,37	0,10			5,32	8,17	0,09	43,50	19,42	18,39	36,37
TU 512-3	6,98	0,12	0,71	9,84	0,17			2,94	7,34	0,06	21,56	19,44	12,40	52,12
TU 512-4	2,38	0,03	0,75	3,17	0,04			1,09	34,19	0,26	37,23	26,06	42,94	61,11
TU 512-5	7,04	0,20	0,74	9,56	0,28			3,04	8,13	0,07	24,77	13,85	13,96	57,68
TU 515 -2	20,00	0,27	0,79	26,20	0,35	23,9	0,3	0,12	20,70		2,34	444,91	21,25	60,18
TU 515 -3	22,40	0,29	0,82	28,08	0,36			0,28	28,31		7,65	559,26	30,10	71,52
TU 515 -4	12,85	0,19	0,77	17,44	0,26			0,41	31,56		12,66	333,18	34,54	54,66

Table II-3: Analytical details of all zircon (U-Th)/He analyses.

Sample	Raw age (Ma)	Raw 1s error (Ma)	Ft	Corrected age (Ma)	Corrected 1s error (Ma)	Mean Age (Ma)	Mean error (Ma)	^{4}He (mol)	U 238 (ppm)	Th 232 (ppm)	eU (ppm)	Rs (µm)
TU491-1	110,73	1,48	0.84	135.71	1.82	136.8	1.1	$1.44*10^{-12}$	297.2	231.0	351.5	68.0
TU491-2	112,94	1,59	0.84	136.73	1.93			$1.25*10^{-12}$	264.6	142.0	298.0	71.6
TU491-3	115,96	1,64	0.86	137.99	1.97			$1.70*10^{-12}$	252.9	115.9	280.1	78.2
TU492_1	24,32	0,34	*0.77*	*33.11*	*0.47*	57.2	0.8	$3.79*10^{-12}$	*747.2*	*403.6*	*842.0*	*45.9*
TU492_2	41,08	0,54	0.75	57.21	0.76			$2.22*10^{-13}$	407.8	303.9	479.3	43.1
TU492_3	13,92	0,19	*0.81*	*17.67*	*0.24*			$1.42*10^{-13}$	*429.6*	*180.2*	*471.9*	*58.3*
TU493-1	9,54	0,14	*0.71*	*14.21*	*0.21*	57.4	0.8	$3.34*10^{-14}$	*862.9*	*200.9*	*910.2*	*36.0*
TU493-2	5,07	0,07	*0.71*	*7.55*	*0.11*			$1.28*10^{-14}$	*1299.9*	*387.5*	*1391.0*	*36.2*
TU493-3	39,08	0,53	0.72	57.42	0.79			$4.88*10^{-14}$	217.7	190.2	262.4	37.7
TU494-1	3,51	0,05	0.70	5.31	0.08	4.5	0.7	$8.00*10^{-15}$	517.0	83.39	536.6	34.9
TU494-2	2,56	0,04	0.69	3.95	0.06			$7.13*10^{-15}$	752.1	132.1	783.1	33.3
TU494-3	2,63	0,04	0.66	4.32	0.06			$2.64*10^{-15}$	433.7	287.0	501.1	29.9
TU495-1	3,81	0,05	0.78	5.05	0.07	5.3	0.5	$4.70*10^{-14}$	675.4	226.9	728.8	49.6
TU495-2	4,25	0,05	0.76	5.86	0.08			$2.08*10^{-14}$	397.7	254.3	457.5	44.6
TU495-3	3,52	0,05	0.74	4.99	0.07			$1.59*10^{-14}$	491.6	296.8	561.3	41.1
TU496-1	7,67	0,10	0.84	9.34	0.12	8.2	1.2	$5.82*10^{-13}$	1834.8	840.1	2032.2	70.3
TU496-2	5,97	0,08	0.87	7.03	0.09			$6.88*10^{-13}$	1533.1	653.9	1686.7	83.2
TU496-3	6,36	0,09	0.80	8.23	0.12			$1.18*10^{-13}$	926.7	152.6	962.6	53.7

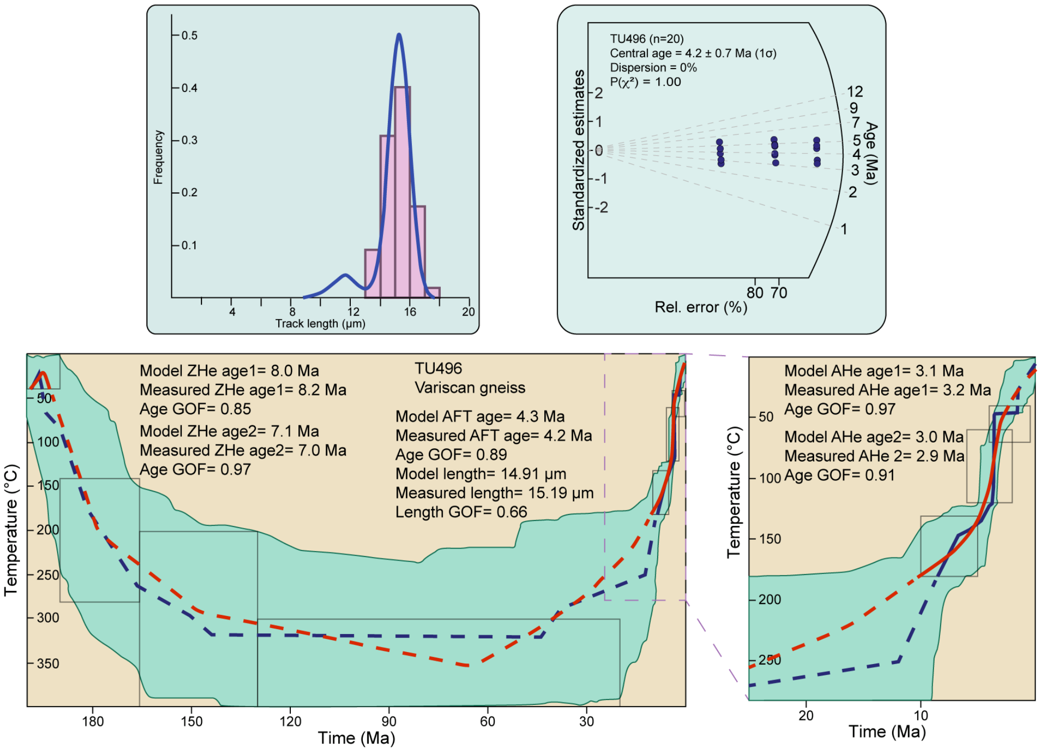

Figure II-3: Thermochronologic statistical inverse modelling results for sample TU496. Green area marks the envelope of all t-T paths having a good (GOF > 0.5) fit with the data; red line is the mean t-T path; blue line is the best-fit path. Parameters related to inverse modelling are reported: GOF (goodness-of-fit) gives an indication of the fit between observed and predicted data (values close to 1 are best). Upper left square: Histogram showing the distribution of horizontally confined fission-track lengths. Upper right square: Radial plot of single-grain AFT ages.

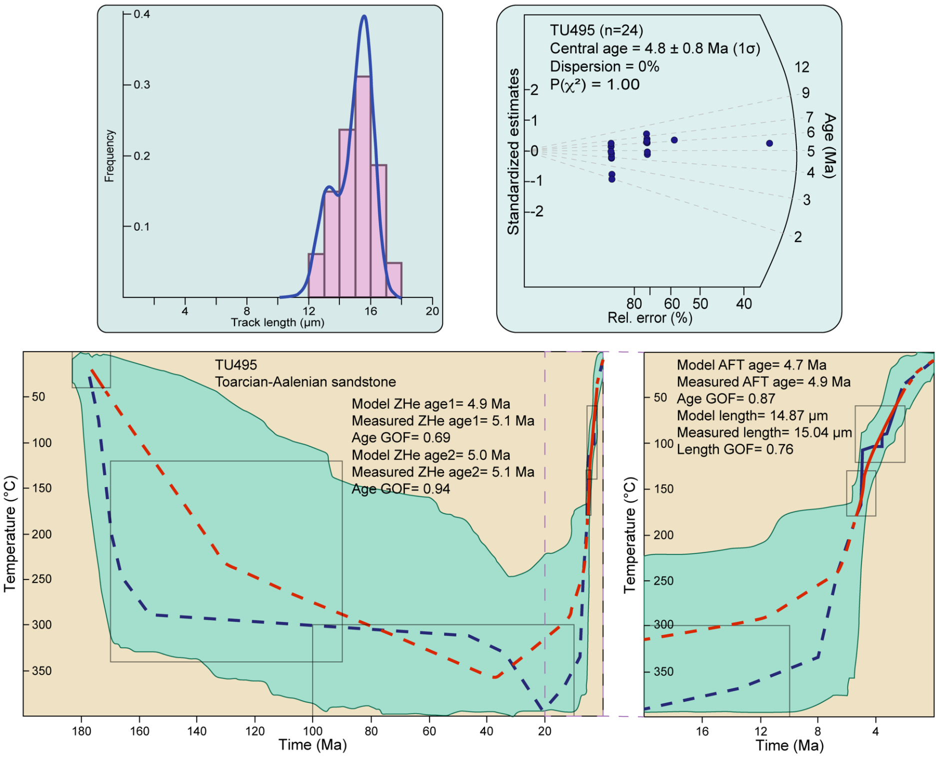

Figure II-4: Thermochronologic statistical inverse modelling results for sample TU495. Green area marks the envelope of all t-T paths having a good (GOF > 0.5) fit with the data; red line is the mean t-T path; blue line is the best-fit path. Parameters related to inverse modelling are reported: GOF (goodness-of-fit) gives an indication of the fit between observed and predicted data (values close to 1 are best). Upper left square: Histogram showing the distribution of horizontally confined fission-track lengths. Upper right square: Radial plot of single-grain AFT ages.

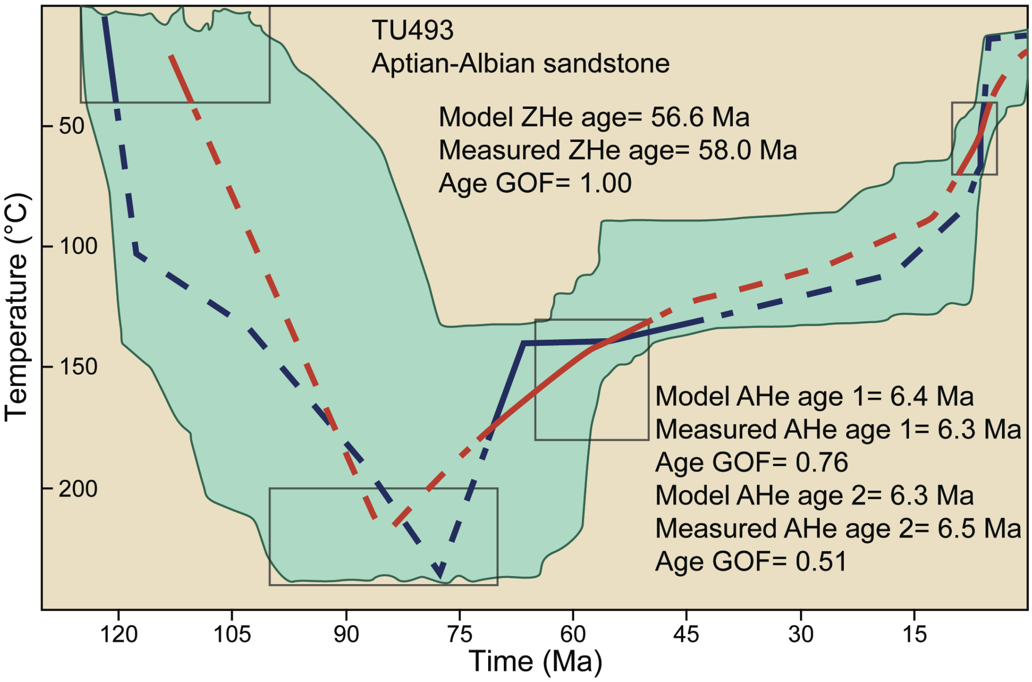

Figure II-5: Thermochronologic statistical inverse modelling results for sample TU493. Green area marks the envelope of all t-T paths having a good (GOF > 0.5) fit with the data; red line is the mean t-T path; blue line is the best-fit path. Parameters related to inverse modelling are reported: GOF (goodness-of-fit) gives an indication of the fit between observed and predicted data (values close to 1 are best). For this sample only ZHe and AHe results are available.

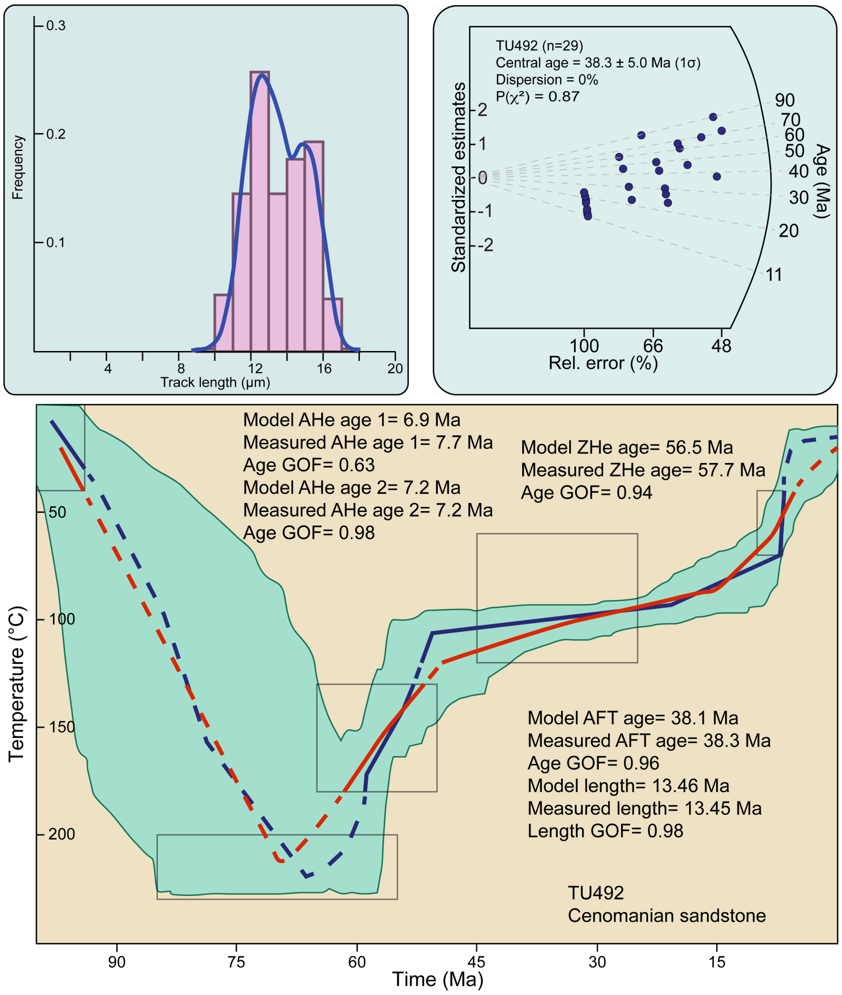

Figure II-6: Thermochronologic statistical inverse modelling results for sample TU492. Green area marks the envelope of all t-T paths having a good (GOF > 0.5) fit with the data; red line is the mean t-T path; blue line is the best-fit path. Parameters related to inverse modelling are reported: GOF (goodness-of-fit) gives an indication of the fit between observed and predicted data (values close to 1 are best). Upper left square: Histogram showing the distribution of horizontally confined fission-track lengths. Upper right square: Radial plot of single-grain AFT ages.

Figure II-7: Thermochronologic statistical inverse modelling results for sample TU483. Green area marks the envelope of all t-T paths having a good (GOF > 0.5) fit with the data; red line is the mean t-T path; blue line is the best-fit path. Parameters related to inverse modelling are reported: GOF (goodness-of-fit) gives an indication of the fit between observed and predicted data (values close to 1 are best). Upper left square: Histogram showing the distribution of horizontally confined fission-track lengths. Upper right square: Radial plot of single-grain AFT ages.

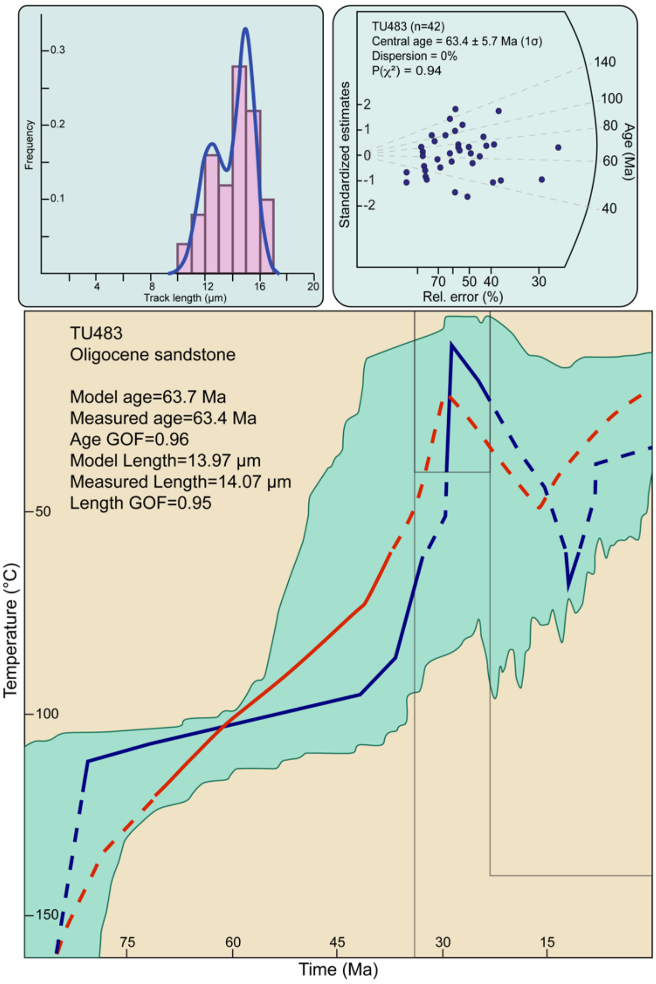

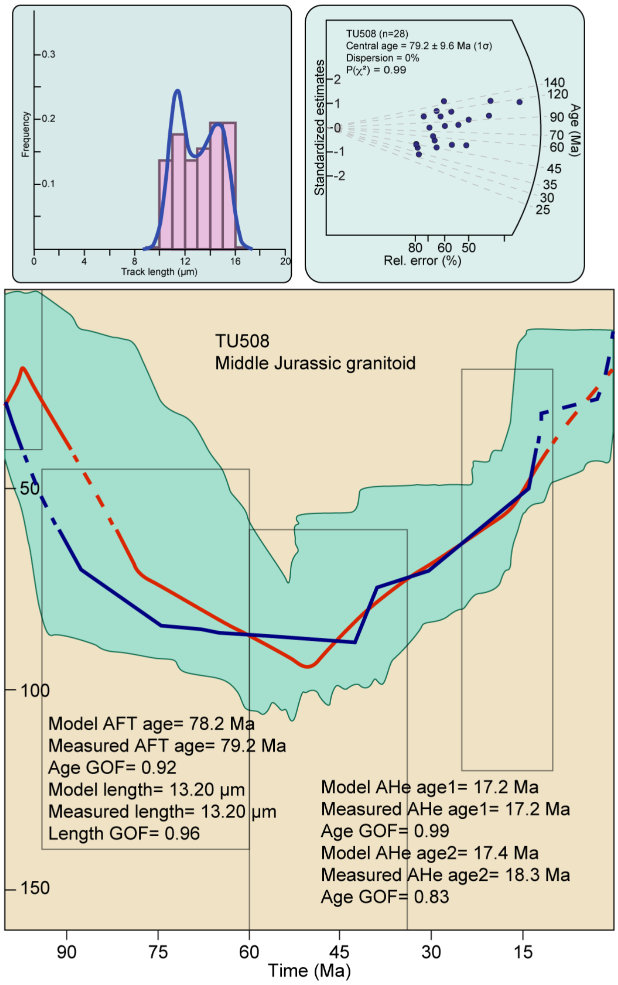

Figure II-8: Thermochronologic statistical inverse modelling results for sample TU508. Green area marks the envelope of all t-T paths having a good (GOF > 0.5) fit with the data; red line is the mean t-T path; blue line is the best-fit path. Parameters related to inverse modelling are reported: GOF (goodness-of-fit) gives an indication of the fit between observed and predicted data (values close to 1 are best). Upper left square: Histogram showing the distribution of horizontally confined fission-track lengths. Upper right square: Radial plot of single-grain AFT ages.

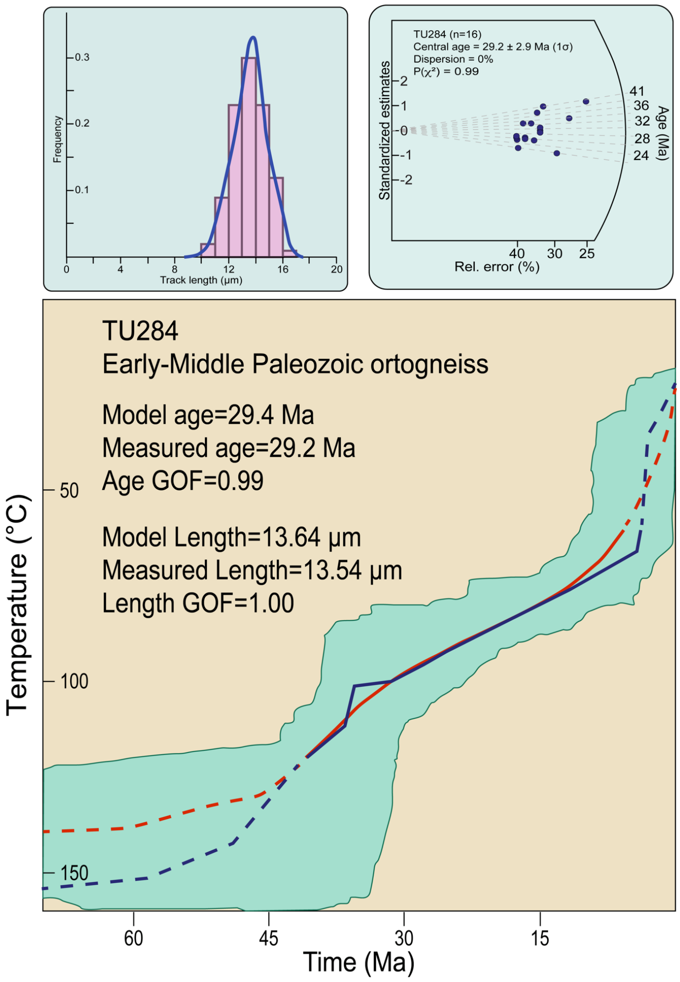

Figure II-9: Thermochronologic statistical inverse modelling results for sample TU284. Green area marks the envelope of all t-T paths having a good (GOF > 0.5) fit with the data; red line is the mean t-T path; blue line is the best-fit path. Parameters related to inverse modelling are reported: GOF (goodness-of-fit) gives an indication of the fit between observed and predicted data (values close to 1 are best). Upper left square: Histogram showing the distribution of horizontally confined fission-track lengths. Upper right square: Radial plot of single-grain AFT ages.

during the Eocene and a second pulse during Middle-Late Miocene times.

At the end of this appendix, Tables II-4 to II-10 provide details on the modelling procedures and constraints applied for the thermochronological inverse modelling results shown in Figures II-3 to II-9, compiled according to the protocol of Flowers et al. (2015).

Table II-4: Modelling details for sample TU284.

Thermochronologic data					
AFT data	*N° grains*	*Central age*	*MCTL*	*N° tracks*	*Mean Dpar*
	16	29.2 ± 2.9 Ma	13.54 ± 0.12 µm	100	2.43 µm

Additional geologic information		
Constraint	*Explanation*	*Reference*
600-800 °C at 330-300 Ma	Late Paleozoic (Variscan) metamorfism age for the ortogneiss	Rolland et al., 2011
Present-day surface temperature 20 ± 10 °C	Since specific temperature data were not available from the region, we used a standard surface temperature.	

System- and model-specific parameters						
AFT	*Annealing model*	*C-axis projection*	*Model c-axis projected lengths?*	*Default initial mean track length*	*Kinetic parameter*	*GOF metod*
	Ketcham et al., 2007	Ketcham et al., 2007, 5.0M	Yes	From Dpar	Dpar	Kuiper's Statistic
Statistical fitting criteria	acceptable paths for GOF values >0.05; good paths for GOF values >0.5					
t-T paths charachteristics	episodic history, halve two times, monotonic consistent between constraints					
Number of paths attempted:	150441					
Number of acceptable paths obtained:	1362					
Number of good paths obtained:	300					

Model output parameters	
Model age	29.4 Ma
Measured age	29.2 Ma
Age GOF	0.99
Model Length	13.64 µm
Measured length	13.54 µm
Length GOF	1.00

Table II-5: Modelling details for sample TU483.

Thermochronologic data

AFT data	*N° grains*	*Central age*	*MCTL*	*N° tracks*	*Mean Dpar*
	42	63.4 ± 5.8 Ma	14.10± 0.22 µm	50	2.91 µm

Additional geologic information

Constraint	*Explanation*	*Reference*
0-160°C at 90-34 Ma	Since no constraints are available for the pre-depositional history of the sample, we used a broad T-t box in order to avoid any forcing on the program	
0-40°C at 34-25 Ma	The depositional age of the sample is between the Early and the middle-late Oligocene	USSR geological maps
0-140°C at 23-0 Ma	Since no constraints are available for the post-depositional history of the sample, we used a broad T-t box in order to avoid any forcing on the program	
Present-day surface temperature 20 ± 10 °C	Since specific temperature data were not available from the region, we used a standard surface temperature.	

System- and model-specific parameters

AFT	*Annealing model*	*C-axis projection*	*Model c-axis projected lengths?*	*Default initial mean track length*	*Kinetic parameter*	*GOF metod*
	Ketcham et al., 2007	Ketcham et al., 2007, 5.0M	Yes	From Dpar	Dpar	Kuiper's Statistic
Statistical fitting criteria	acceptable paths for GOF values >0.05; good paths for GOF values >0.5					
t-T paths charachteristics	episodic history, halve two times, monotonic consistent between constraints					
Number of paths attempted:	66519					
Number of acceptable paths obtained:	1891					
Number of good paths obtained:	300					

Model output parameters

Model age	63.7 Ma
Measured age	63.4 Ma
Age GOF	0.96
Model Length	13.97 µm
Measured length	14.07 µm
Length GOF	0.95

Table II-6: Modelling details for sample TU492.

Thermochronologic data							
AHe data	*Replicate name*	*Uncorrected age*	*eU*	*Grain radius*	*U (ppm)*	*Th (ppm)*	*Sm (ppm)*
	TU492-1	4.74 ± 0.49 Ma	12.0	39 µm	5.2	25.1	198.7
	TU492-2	5.10 ± 0.25 Ma	15.3	52 µm	6.6	35.4	189.9
	TU492-3	4.94 ± 0.27 Ma	35.0	31 µm	13.2	86.2	353.2
AFT data	*N° grains*	*Central age*	*MCTL*	*N° tracks*	*Mean Dpar*		
	29	38.3 ± 5.0 Ma	13.45 ± 0.20 µm	62	2.86 µm		
ZHe data	*Replicate name*	*Uncorrected age*	*eU*	*Grain radius*	*U (ppm)*	*Th (ppm)*	
	TU492-2	41.08 ± 0.54 Ma	479.3	43 µm	407.8	303.9	

Additional geologic information		
Constraint	*Explanation*	*Reference*
0-40 °C at 100-94 Ma	The depositional age of the sample is Cenomaian.	USSR geological maps
200-230 °C at 85-55 Ma	Raman spectroscopy analyses demonstrated that this sample experienced maximum burial temperatures of 216 ± 13 °C. We do not have any constraints on the timing of acquisition of such thermal maturity, hence we used a large time interval for this box.	Corrado et al., 2021
130-180 °C at 65-55 Ma	The only ZHe age valid for this sample yields an age of 57.2 ± 0.8 Ma. The PRZ for ZHe is between about 130 and 180 °C.	Reiners et al., 2004
60-120°C at 45-25 Ma	The AFT central age of this sample is 38.3 ± 5.0 Ma. The PAZ for AFT is between about 60 and 120 °C.	Peyton and Carrapa, 2013
40-70 °C at 10-6 Ma	AHe single-grain ages for this sample are comprised between 9.2 ± 0.5 and 7.2 ± 0.4 Ma. The PRZ for AHe is between about 40 and 70 °C.	Peyton and Carrapa, 2013
Present-day surface temperature 20 ± 10 °C	Since specific temperature data were not available from the region, we used a standard surface temperature.	

System- and model-specific parameters						
AFT	*Annealing model*	*C-axis projection*	*Model c-axis projected lengths?*	*Default initial mean track length*	*Kinetic parameter*	*GOF metod*
	Ketcham et al., 2007	Ketcham et al., 2007, 5.0M	Yes	From Dpar	Dpar	Kuiper's Statistic
AHe	*AHe kinetic model*	*Alpha calculation*	*Age alpha correction*	*Stopping distances*	*Precision*	
	RDAAM (Flowers et al., 2009)	Ejection	Ketcham et al., 2011	Ketcham et al., 2011	Good	
ZHe	*He kinetic model*	*Alpha calculation*	*Age alpha correction*	*Stopping distances*	*Precision*	
	Guenthner et al., 2013	Ejection	Ketcham et al., 2011	Ketcham et al., 2011	Good	
Statistical fitting criteria	acceptable paths for GOF values >0.05; good paths for GOF values >0.5					
t-T paths charachteristics	episodic history, halve two times, monotonic consistent between constraints					
Number of paths attempted:	1727876					
Number of acceptable paths obtained:	4791					
Number of good paths obtained:	300					

Model output parameters					
Model age	38.1 Ma	Model AHe age1	6.9	Model ZHe age	56.5
Measured age	38.3 Ma	Measured AHe age1	7.7	Measured ZHe age	57.7
Age GOF	0.96	AHe age1 GOF	0.63	ZHe age1 GOF	0.94
Model Length	13.46 µm	Model AHe age2	7.2		
Measured length	13.45 µm	Measured AHe age2	7.2		
Length GOF	0.98	AHe age2 GOF	0.98		

Table II-7: Modelling details for sample TU493.

Thermochronologic data

	Replicate name	*Uncorrected age*	*eU*	*Grain radius*	*U (ppm)*	*Th (ppm)*	*Sm (ppm)*
AHe data	TU493-2	4.28 ± 0.11 Ma	23.4	42 µm	18.7	17.8	13.1
	TU493-3	5.93 ± 0.12 Ma	22.2	43 µm	13.9	33.5	101.9
	TU493-4	4.31 ± 0.12 Ma	30.6	43 µm	28.5	6.7	116.4
	TU493-5	3.05 ± 0.07 Ma	51.3	42 µm	33.8	66.9	401.6
ZHe data	*Replicate name*	*Uncorrected age*	*eU*	*Grain radius*	*U (ppm)*	*Th (ppm)*	
	TU493-3	39.08 ± 0.53 Ma	262.4	38 µm	217.7	190.2	
	TU486-5	2.67 ± 0.04 Ma	26.0	42 µm	10.7	65.6	43.2

Additional geologic information

Constraint	*Explanation*	*Reference*
0-40 °C at 125-100 Ma	The depositional age of the sample is Aptian-Albian.	USSR geological maps
200-240 °C at 100-70 Ma	Raman spectroscopy analyses demonstrated that this sample experienced maximum burial temperatures of 228 ± 5 °C. We do not have any constraints on the timing of acquisition of such thermal maturity, hence we used a large time interval for this box.	Corrado et al., 2021
130-180 °C at 65-55 Ma	The only ZHe age valid for this sample yields an age of 57.4 ± 0.8 Ma. The PRZ for ZHe is between about 130 and 180 °C.	Reiners et al., 2004
40-70 °C at 10-4 Ma	AHe single-grain ages for this sample are comprised between 4.7 ± 0.1 and 9.0 ± 0.2 Ma. The PRZ for AHe is between about 40 and 70 °C.	Peyton and Carrapa, 2013
Present-day surface temperature 20 ± 10 °C	Since specific temperature data were not available from the region, we used a standard surface temperature.	

System- and model-specific parameters

	He kinetic model	*Alpha calculation*	*Age alpha correction*	*Stopping distances*	*Precision*
AHe	RDAAM (Flowers et al., 2009)	Ejection	Ketcham et al., 2011	Ketcham et al., 2011	Good
ZHe	*He kinetic model*	*Alpha calculation*	*Age alpha correction*	*Stopping distances*	*Precision*
	Guenthner et al., 2013	Ejection	Ketcham et al., 2011	Ketcham et al., 2011	Good

Statistical fitting criteria	acceptable paths for GOF values >0.05; good paths for GOF values >0.5
t-T paths charachteristics	episodic history, halve two times, monotonic consistent between constraints
Number of paths attempted:	2904399
Number of acceptable paths obtained:	5759
Number of good paths obtained:	300

Model output parameters

Model AHe age1	6.4	Model ZHe age	56.6
Measured AHe age1	6.3	Measured ZHe age	58.0
AHe age1 GOF	0.76	ZHe age1 GOF	1.00
Model AHe age2	6.3		
Measured AHe age2	6.5		
AHe age2 GOF	0.51		

Table II-8: Modelling details for sample TU495.

Thermochronologic data						
AFT data	*N° grains*	*Central age*	*MCTL*	*N° tracks*	*Mean Dpar*	
	24	4.8 ± 0.8 Ma	15.04 ± 0.13 µm	85	2.61 µm	
ZHe data	*Replicate name*	*Uncorrected age*	*eU*	*Grain radius*	*U (ppm)*	*Th (ppm)*
	TU495-1	3.81 ± 0.05 Ma	728.8	50 µm	675.4	226.9
	TU495-2	4.25 ± 0.05 Ma	457.5	45 µm	397.7	254.3
	TU495-3	3.82 ± 0.05 Ma	561.3	41 µm	491.6	296.8
	TU486-5	2.67 ± 0.04 Ma	26.0	42 µm	10.7	65.6

Additional geologic information		
Constraint	*Explanation*	*Reference*
0-40 °C at 183-170 Ma	The depositional age of the sample is Toarcian-Aalenian.	USSR geological maps
120-340 °C at 170-90 Ma	This box has been put according to stratigraphic data collected in the sample area, which suggest that 7-9km of sedimentary rocks have been eroded from above this sample.	Adamia et al., 2011
300-400 °C at 100-10 Ma	Raman spectroscopy analyses demonstrated that this sample experienced maximum burial temperatures of 379 ± 9 °C. We do not have any constraints on the timing of acquisition of such thermal maturity, hence we used a large time interval for this box.	Corrado et al., 2021
130-180 °C at 4-6 Ma	ZHe single-grain ages for this sample are comprised between 4.99 ± 0.07 and 5.86 ± 0.08 Ma. The PRZ for ZHe is between about 130 and 180 °C.	Reiners et al., 2004
60-120 °C at 5-2 Ma	AFT central age of this sample is 4.8 ± 0.8 Ma. The PAZ for AFT is between about 60 and 120 °C.	Peyton and Carrapa, 2013
Present-day surface temperature 20 ± 10 °C	Since specific temperature data were not available from the region, we used a standard surface temperature.	

System- and model-specific parameters						
AFT	*Annealing model*	*C-axis projection*	*Model c-axis projected lengths?*	*Default initial mean track length*	*Kinetic parameter*	*GOF metod*
	Ketcham et al., 2007	Ketcham et al., 2007, 5.0M	Yes	From Dpar	Dpar	Kuiper's Statistic
Statistical fitting criteria	acceptable paths for GOF values >0.05; good paths for GOF values >0.5					
t-T paths charachteristics	episodic history, halve two times, monotonic consistent between constraints					
Number of paths attempted:	831906					
Number of acceptable paths obtained:	2247					
Number of good paths obtained:	300					

Model output parameters			
Model ZHe age1	4.9	Model AFT age	4.7
Measured ZHe age1	5.1	Measured AFT age	4.9
ZHe age1 GOF	0.69	AFT age GOF	0.87
Model ZHe age2	5.0	Model length	14.87 µm
Measured ZHe age2	5.1	Measured length	15.04 µm
ZHe age2 GOF	0.94	Length GOF	0.76

Table II-9: Modelling details for sample TU496.

Thermochronologic data

	Replicate name	*Uncorrected age*	*eU*	*Grain radius*	*U (ppm)*	*Th (ppm)*	*Sm (ppm)*
AHe data	TU496-2	2.12 ± 0.04 Ma	58.2	43 µm	44.3	53.4	295.9
	TU496-3	2.87 ± 0.05 Ma	27.9	50 µm	20.5	27.7	201.3
	TU496-4	2.08 ± 0.04 Ma	30.0	54 µm	23.2	24.8	198.5
	TU496-5	1.36 ± 0.02 Ma	101.1	58 µm	67.5	134.6	442.4
AFT data	*N° grains*	*Central age*	*MCTL*	*N° tracks*	*Mean Dpar*		
	20	4.2 ± 0.7 Ma	15.19 ± 0.09 µm	97	2.13 µm		
ZHe data	*Replicate name*	*Uncorrected age*	*eU*	*Grain radius*	*U (ppm)*	*Th (ppm)*	
	TU496-1	7.67 ± 0.10 Ma	2032.2	70 µm	1834.8	840.1	
	TU496-2	5.97 ± 0.08 Ma	1686.7	83 µm	1533.1	653.9	
	TU496-3	6.36 ± 0.09 Ma	962.6	54 µm	926.7	152.6	
	TU486-5	2.67 ± 0.04 Ma	26.0	42 µm	10.7	65.6	

Additional geologic information

Constraint	*Explanation*	*Reference*
0-40 °C at 200-190 Ma	Hettangian-Sinemurian unconformably overlying the sampled rocks, which means they were exposed at surface at that time.	USSR geological maps
140-280 °C at 190-70 Ma	This box has been put according to stratigraphic data collected in the sample area, which suggest that 7-9km of sedimentary rocks have been eroded from above this sample.	Adamia et al., 2011
200-400 °C at 170-130 Ma	This box has been put according to stratigraphic data collected in the sample area, which suggest that 7-9km of sedimentary rocks have been eroded from above this sample.	Adamia et al., 2011
300-400 °C at 100-10 Ma	Raman spectroscopy analyses demonstrated that sample TU495 (arguably deposited above the basement from which this sample derives) experienced maximum burial temperatures of 379 ± 9 °C, hence at least the same temperature must have been experienced by this sample. We do not have any constraints on the timing of acquisition of such thermal maturity, hence we used a large time interval for this box.	Corrado et al., 2021
130-180 °C at 10-5 Ma	ZHe single-grain ages for this sample are comprised between 7.0 ± 0.1 and 9.3 ± 0.1 Ma. The PRZ for ZHe is between about 130 and 180 °C.	Reiners et al., 2004
60-120 °C at 6-2 Ma	AFT central age of this sample is 4.2 ± 0.7 Ma. The PAZ for AFT is between about 60 and 120 °C.	Peyton and Carrapa, 2013
40-70 °C at 4-1 Ma	AHe single-grain ages fro this sample are comprised between 1.82 ± 0.02 Ma and 4.05 ± 0.07 Ma. The PRZ for ZHe is between about 40 and 70 °C.	Peyton and Carrapa, 2013
Present-day surface temperature 20 ± 10 °C	Since specific temperature data were not available from the region, we used a standard surface temperature.	

System- and model-specific parameters

AFT	*Annealing model*	*C-axis projection*	*Model c-axis projected lengths?*	*Default initial mean track length*	*Kinetic parameter*	*GOF metod*
	Ketcham et al., 2007	Ketcham et al., 2007, 5.0M	Yes	From Dpar	Dpar	Kuiper's Statistic
Statistical fitting criteria	acceptable paths for GOF values >0.05; good paths for GOF values >0.5					
t-T paths charachteristics	episodic history, halve two times, monotonic consistent between constraints					
Number of paths attempted:	2254610					
Number of acceptable paths obtained:	1838					
Number of good paths obtained:	300					

Model output parameters

Model ZHe age1	8.0	Model AFT age	4.3	Model AHe age1	3.1
Measured ZHe age1	8.2	Measured AFT age	4.2	Measured AHe age1	3.2
ZHe age1 GOF	0.85	AFT age GOF	0.89	AHe age1 GOF	0.97
Model ZHe age2	7.1	Model length	14.91 µm	Model AHe age2	3.0
Measured ZHe age2	7.0	Measured length	15.19 µm	Measured AHe age2	2.9
ZHe age2 GOF	0.97	Length GOF	0.66	AHe age2 GOF	0.91

Table II-10: Modelling details for sample TU508.

Thermochronologic data

AFT data	*N° grains*	*Central age*	*MCTL*	*N° tracks*	*Mean Dpar*		
	28	79.2 ± 9.6 Ma	13.20 ± 0.25 µm	51	2.23 µm		
AHe data	*Replicate name*	*Uncorrected age*	*eU*	*Grain radius*	*U (ppm)*	*Th (ppm)*	*Sm (ppm)*
	TU508-1	15.9 ± 0.2 Ma	16.0	41 µm	8.8	22.5	414.9
	TU508-2	6.9 ± 0.1 Ma	15.4	42 µm	11.0	12.3	332.2
	TU508-3	14.2 ± 0.2 Ma	13.7	41 µm	8.0	16.7	383.9
	TU508-4	12.7 ± 0.2 Ma	13.4	56 µm	7.3	18.2	393.2
	TU508-5	12.1 ± 0.2 Ma	18.9	42 µm	11.4	23.4	432.0

Additional geologic information

Constraint	*Explanation*	*Reference*
Near surface temperatures (0-40°C) at 100-94 Ma	Cenomanian unconformity on the top of the massif, indicating it was exposed or at very shallow levels by that time	Adamia et al, 2011; Yilmaz et al, 2014
45-140 °C between 94 and 60 Ma	1-2 km of lavas, limestones, marls and conglomerates deposited in the area from the Turonian to the Danian. Even being very conservative, thus assuming a very low geothermal gradient (25 °C/km) and an average surface temperature of 20 °C, minimum temperatures of 45-70 °C would have been obtained at the top of the massif at this stage. The upper temperature limit was set to 140 °C in order to let the model search in a wide area.	Adamia et al, 2011; Yilmaz et al, 2014
70-160 °C between 60 and 34 Ma	Additional 1-2 km of sandstones, siltstones, shales and lavas deposited between the Selandian and the Priabonian. Even being very conservative, thus assuming a very low geothermal gradient (25 °C/km) and an average surface temperature of 20 °C, minimum temperatures of 70-120 °C would have been obtained at the top of the massif at this stage. The upper temperature limit was set to 160 °C in order to let the model search in a wide area.	Adamia et al, 2011; Yilmaz et al, 2014
20-120°C between 25 and 10 Ma	AHe single-grain ages are comrpised between 24.5 ± 0.3 and 10.4 ± 0.2 Ma. The PRZ for AHe is between about 70 and 40 °C.	Peyton and Carrapa, 2013
Present-day surface temperature 20 ± 10 °C	Since specific temperature data were not available from the region, we used a standard surface temperature.	

System- and model-specific parameters

AFT	*Annealing model*	*C-axis projection*	*Model c-axis projected lengths?*	*Default initial mean track length*	*Kinetic parameter*	*GOF metod*
	Ketcham et al., 2007	Ketcham et al., 2007, 5.0M	Yes	From Dpar	Dpar	Kuiper's Statistic
AHe	*AHe kinetic model*	*Alpha calculation*	*Age alpha correction*	*Stopping distances*	*Precision*	
	RDAAM (Flowers et al., 2009)	Ejection	Ketcham et al., 2011	Ketcham et al., 2011	Good	
Statistical fitting criteria	acceptable paths for GOF values >0.05; good paths for GOF values >0.5					
t-T paths charachteristics	episodic history, halve two times, monotonic consistent between constraints					
Number of paths attempted:	1494427					
Number of acceptable paths obtained:	2308					
Number of good paths obtained:	500					

Model output parameters

Model age	78.2 Ma	Model AHe age1	17.2 Ma
Measured age	79.2 Ma	Measured AHe age1	17.2 Ma
Age GOF	0.92	AHe1 GOF	0.99
Model Length	13.20 µm	Model AHe age2	17.4 Ma
Measured length	13.20 µm	Measured AHe age2	18.3 Ma
Length GOF	0.96	AHe2 GOF	0.83